MICROBUBBLE DYNAMICS FOR DELIVERY OF NANOMEDICINE TO TUMORS

by

Seymen İlke Kaykanat

B.S., Chemical Engineering, Ege University, 2015

M.S., Chemical Engineering, Boğaziçi University, 2018

Submitted to the Institute for Graduate Studies in
Science and Engineering in partial fulfillment of
the requirements for the degree of
Master of Science

Graduate Program in Chemical Engineering

Boğaziçi University

2024

ACKNOWLEDGEMENTS

I would like to express my deepest gratitude to my advisor, Assoc. Prof. Uguz, for his invaluable guidance, support, and encouragement throughout my PhD journey. During the tough times in my life, Dr. Uguz provided not only academic mentorship but also personal support, for which I am immensely grateful. His understanding, compassion, and encouragement helped me navigate and persevere through difficult periods. I am truly thankful for his support, both professionally and personally, and for the countless hours he has invested in helping me achieve my goals. This thesis would not have been possible without his support.

I extend my deepest gratitude to the members of the jury committee, Prof. Ramazan Yıldırım, and Prof. Metin Muradoğlu for their dedication and invaluable feedback during the evaluation of this thesis. Their thoughtful insights and constructive criticism have significantly enriched the quality of the research. I would like to express my gratitude to Prof. Ahmet Kerim Avcı and Prof. Ali Koşar for his role as a defending committee member during the oral defense of this thesis. During this journey, whenever I need assistant, Prof. Avcı and Prof. Yıldırım was always there for me.

I am deeply grateful to Öner and Amable Hortaçsu for their unwavering belief in me and their continuous support throughout my academic journey. Their encouragement has been a steadfast source of motivation, and the intellectual guidance they provided has enriched my understanding in countless ways. I have learned so much from them, not only academically but also in developing a deeper appreciation for intellectual pursuits. Their faith in my potential and their nurturing support have been invaluable.

Also, I would like to extend my heartfelt thanks to my lab-mates, Yigit Ağanoğlu and Sercan Altundemir, whose support has been invaluable throughout my PhD journey, especially to Sercan Altundemir. Without Dr. Altundemir's support, intellectual exchange, and encouragement, I couldn't have finished this dissertation. The countless discussions, brainstorming sessions, and shared challenges have not only enriched my research but also

created lasting friendships. I am truly grateful for the sense of friendship we built together.

I would also like to thank my ex lab-mates, Canberk Ozan, Alperen Abacı, Hira Demirkol, Burak Hanamarian, Arda İnanç, Sima Yıldız Doğan, and Göksu Duvarcı, who have contributed significantly to my intellectual growth. Despite the distance, they have continuously encouraged me throughout this journey.

I would like to express my deepest gratitude to the members of the KB 407 Soft Matter Lab Group whom I had the chance to meet in the last quarter of my PhD education. Firstly, I extend my heartfelt thanks to Duygu Kaya and Ayşe Korkut for Their constant encouragement. Whenever I need help or talk, they are always there for me. Without they, I couldn't motivate myself for my career. Special thanks to Hafsa Doğan (and also lovely Haku and Muşu) for her constant support. Your positivity and friendship always motivate me during my journey.

I would also like to thank my dear friends, Özge Duman, Şebnem Or, Hakan Sakallıoğlu, Yiğit Kutlu, and Şafak Kılıç. Özge, your positivity, joy, and energy have been a constant source of motivation for me. Thank you so much for all your health advice when I was ill. Whenever I need you, you are always there for me. During the sleepless weeks, our fun times together were my greatest motivation. I can't imagine going through this process without you. I am truly grateful to have you in my life.

I would like to express my heartfelt gratitude to the members of the KB 402b EchemE Research Lab, especially my dear friends Ayça Fırtın, Kağan Yüksel, and Atakan Ayhan. Your constant support and encouragement have meant so much to me throughout this journey. Whether it was tackling research challenges, sharing a laugh, or simply being there when things felt overwhelming, you've made this experience so much more meaningful. A special thank you to Ayça, the kindest person in my life, whose endless compassion and warmth have been a true source of comfort and strength. I'm incredibly grateful for the friendship and memories we've created together.

I would also like to extend my deepest gratitude to Ezgi and Batuhan Altıntaş, whom I had the privilege of meeting during my master's degree. Ezgi, your unwavering support and constant presence in my life, no matter how many times our paths have diverged, has been a source of incredible comfort and inspiration. You have always been there for me, offering your encouragement and kindness when I needed it most.

I want to dedicate a paragraph to my friend, Pınar Eribol, who holds a special place in my life. I wrote this almost a year before my graduation, reflecting on our shared journey. We have been through difficult times together and also shared many wonderful experiences. Thank you for believing in me more than I believed in myself since I was a master's student.

Also, I would like to thank Merve Yüce and Özge Selçuk for always supporting and motivating me. They have never left me alone during the difficult times of this research. I want to thank my close friends Umut Çivici, Merve Tezeren, Neşe Yıldız, Cansu Köroğlu, Yonca Çayır and especially to Yiğit Akyol who are being there for me since my childhood.

Also, I would like to thank all my friends for their motivation during the time we spent in graduate education. In particular, KB404 members especially to İrem Taşpınar and KB440 members especially to Özlem Özbek, İrem Özbek Destina Genç, Müge Kasım, Ezgi Taş and Elif Esvap. Özlem and Destina, your positivity and unwavering support hold a special place in my life. You're the first people I see each morning, and your uplifting energy motivates me throughout the day. Thank you for always being there.

I would like to extend my heartfelt gratitude to Burcu Oral, Ahmet Cosgun, and Handan Akulker. We shared many classes together, and their support and insights greatly enriched my learning experience. I am truly grateful for their friendship and collaboration throughout our academic journey.

I would also like to express my sincere thanks to Ekin Yurdakul and Hamdi Erkut. Their support and encouragement have been invaluable, and I am grateful for the memorable experiences and shared learning we had together.

Last but certainly not least, I am deeply grateful to my family for their endless patience and unwavering support throughout my life, especially to my twin, Seymen Berk Kaykanat, who truly is my other half. Though we haven't been able to spend as much time together this past year, their belief in me has been a constant source of motivation and strength. I am fortunate to have such a supportive family by my side.

This thesis is dedicated to my grandmother, Nurten Seymen. As an English teacher, she was not only a role model in her dedication to education and lifelong learning but also an enduring example of resilience and compassion.

Financial support for this study was provided by TÜBİTAK through the Scientific and Technological Research Council of Turkey: 2211-C National PhD Scholarship Program in the Priority Fields in Science and Technology and by BAP Project 19465.

ABSTRACT

MICROBUBBLE DYNAMICS FOR DELIVERY OF NANOMEDICINE TO TUMORS

This dissertation explores the dynamics of spherical and nonspherical microbubble oscillations in microvessels and their implications for ultrasound-mediated therapeutic applications. The study focuses on microvessel properties, an aspect often neglected in the literature, and their impact on microbubble oscillation and stability. Simulations were conducted across various vessel and bubble properties and acoustic field parameters to analyze their effects on the resulting bubble surface area and shear stress on the microvessel wall where high shear stress values cause tissue damage ($>$ 800 Pa). In particular, the maximum shear stress reaches 30 kPa with an acoustic field pressure of 1.5 atm at 8 MHz. The maximum bubble surface area should be 900 μm^2 at resonance for Newtonian liquid, which affects the drug loading capacity and diffusion rate. Different constitutive models are applied to examine the effects of blood's non-Newtonian properties. For the bubble shell, Neo-Hookean model replaces simpler linear models, revealing significant deviations; for example, the difference between linear and nonlinear shell models reaches 60% when the pressure amplitude reaches 2.5 atm. In the literature, most studies use complex models, whether necessary or not. However, in this dissertation, a parametric range is obtained, where simple models can be used to prevent unnecessary long code runs. These insights provide a foundation for optimizing ultrasound-mediated drug delivery by carefully tuning bubble characteristics and acoustic settings to maximize therapeutic efficacy while minimizing potential vascular injury. The model also includes bubble-bubble interactions to determine the minimum distance to prevent collapse. Near resonance, this distance is found to be 12 μm. Contour maps for different shell and acoustic field properties are obtained to show where the ultrasound-mediated bubble application is safe or unsafe for the treatment application. Here, three criteria are considered: bubble surface area, wall shear stress, and distance between bubbles.

ÖZET

NANO İLACIN TÜMÖRLÜ DOKUYA MİKROKABARCIK İLE TAŞINIMI

Bu tezde, mikrodamarlardaki küresel ve küresel olmayan mikrokabarcık salınımları ile ultrason aracılığıyla gerçekleştirilen terapötik uygulamalara etkileri incelenmiştir. Çalışma, literatürde genellikle ihmal edilen mikrodamar özelliklerine ve bu özelliklerin mikrokabarcık salınımı üzerindeki etkilerine odaklanmaktadır. Çeşitli damar ve kabarcık özellikleri ile akustik alan parametreleri altında kabarcık yüzey alanı ve mikrodamar duvarındaki kayma gerilimi hesaplanmıştır. Maksimum gerilim, 8 MHz frekans ve 1.5 atm akustik alan basıncı altında 30 kPa'ya ulaşmıştır. 800 Pa'nın üzerindeki gerilim değerlerinin doku hasarına yol açtığı bilinmektedir. Kabarcık yüzey alanı, ilaç yükleme kapasitesini ve difüzyon hızını etkileyen önemli bir parametredir. Newtonyen sıvıda rezonans koşullarında maksimum yüzey alanı 900 μm^2 hesaplanmıştır. Kanın Newtonyen olmayan yapısı için çeşitli modeller kullanılmıştır. Kabarcık kabuğu için doğrusal olmayan model tercih edilerek, daha basit doğrusal modeller yerine bu model kullanılmış, önemli farklar tespit edilmiştir. Doğrusal ve doğrusal olmayan kabuk modelleri arasındaki sapma, basınç genliği 2.5 atm'ye ulaştığında %60'a ulaşmıştır. Literatürde, gerekli olmadığında bile karmaşık modellerin kullanıldığı gözlemlenmiştir. Bu tezde, uzun kod çalışma sürelerini önlemek adına, basit modellerin kullanılabileceği aralık tanımlanmıştır. Elde edilen bilgiler, potansiyel vasküler hasarı aza indirirken ilaç etkinliğini artırmak için kabarcık özelliklerin ve akustik parametrelerin optimize edilmesine yönelik bir temel sunmaktadır. Model, kabarcık etkileşimlerini içermekte, bu sayede kabarcık patlamasını önlemek için gereken mesafeyi belirlemektedir. Rezonans koşullarında bu mesafenin 12 μm'ye düştüğü görülmüştür. Ultrason aracılı kabarcık uygulamalarında tedavinin güvenli ve etkili olduğu aralıkları göster-mek amacıyla, farklı kabuk ve akustik alan özellikleri için kontur haritaları hazırlanmıştır. Bu haritalar oluşturulurken üç kriter dikkate alınmıştır: kabarcık yüzey alanı, duvar kayma gerilimi ve kabarcıklar arasındaki mesafe.

LIST OF SYMBOLS

a_n	Perturbation amplitude of shell interface
b_n	Perturbation amplitude of bubble interface
c_b	Specific heat constant
E_k	Kinetic energy
F	Surface function
G	Interfacial mass flux
G_s	Shell modulus
G_{el}	Cavity modulus
K_{el}	Cavity bulk modulus
k	Power-law index
L	Lagrangian
m	Consistency index
n	Perturbation mode
p_∞	Acoustic field pressure
p_b	Pressure inside a bubble
p_v	Vapor pressure
p_{g0}	Initial pressure inside a bubble
R	Time dependent radius of a bubble
R_b	Time-dependent bubble radius
R_g	Gas constant
R_s	Time-dependent shell radius
R_l	Time-dependent cavity radius
$\dot{R}_b$	Bubble wall velocity
$\ddot{R}_b$	Second-order time derivative of bubble radius
$\dot{R}_s$	Shell wall velocity
R_{b0}	Initial bubble radius
R_{s0}	Initial shell radius
R_{l0}	Initial cavity radius

R_{be}	Equilibrium bubble radius
R_{se}	Equilibrium shell radius
R_{le}	Equilibrium cavity radius
T_B	Temperature inside a bubble
$\mathbf{T}_e$	Elastic stress
$\mathbf{T}_s$	Total shell stress
$\mathbf{T}_v$	Liquid stress
u	Velocity of liquid in r direction
$\mathbf{v}$	Velocity vector for the surrounding liquid
W	Potential energy
w	Displacement vector for the solid
q_d	Heat flux from droplet/liquid interface
q_b	Heat flux from bubble/droplet interface
β	Ratio of initial cavity radius to initial bubble radius
χ_d	Thermal diffusivity
ε	Strain
γ	Surface tension
ζ	Bulk viscosity
κ	Polytropic exponent
κ_b	Thermal conductivity
λ	Relaxation time
μ	Viscosity of the liquid
ω	Frequency
ϕ_d	Dissipation
ρ	Density of the liquid
σ	Conductivity of the liquid
τ	Shear stress
τ_0	Yield-stress
τ_{ij}	Stress component
θ	Ratio of equilibrium bubble radius to equilibrium shell radius

ω_0	Natural frequency for spherical oscillation
ω_d	Acoustic field's driving frequency
ω_n	Natural frequency for non-spherical oscillation
ζ	Ratio of equilibrium bubble radius to equilibrium cavity radius

LIST OF ACRONYMS/ABBREVIATIONS

ADV	Acoustic Droplet Vaporization
DFB	Decafluorobutane
EPR	Enhanced Permeability and Retention
FDA	Food and Drug Administration
ODE	Ordinary Differential Equation
OFP	Octafluoropropane
PFC	Perfluorocarbon
RP	Rayleigh-Plesset
RT	Rayleigh-Taylor
UMBS	Ultrasound-Mediated Microbubbles

TABLE OF CONTENTS

ACKNOWLEDGEMENTS iii
ABSTRACT vii
ÖZET viii
LIST OF SYMBOLS ix
LIST OF ACRONYMS/ABBREVIATIONS xii
LIST OF FIGURES xviii
LIST OF TABLES xxxv
1. INTRODUCTION 1
2. LITERATURE REVIEW 7
2.1. Ultrasound and Microbubble Treatment 7
2.1.1. Therapeutic Nanocarriers for Drug Delivery 7
2.1.2. Biological Barriers for Drug Delivery 11
2.1.3. Targeting Strategies for Drug Delivery 13
2.1.4. Properties of Ultrasound and Acoustic Cavitation 19
2.1.5. Biophysical Effects of Microbubble-Mediated Ultrasound Therapy . 21
2.1.6. Therapeutic Applications of Ultrasound-Mediated Microbubbles . . 24
2.1.6.1. Therapeutic Ultrasound Applications 24
2.1.6.2. Microbubble Cavitation Applications 26
2.1.7. Acoustic Droplet Vaporization (ADV) 30
2.2. Mathematical Models for Bubbles in Acoustic Fields 33
2.2.1. Unbounded Free Bubbles 35
2.2.2. Encapsulated Microbubbles 37
2.2.3. Bubble in Confined Liquid 39
2.2.4. Numerical Studies 40
2.2.5. Shape Stability of a Bubble 43
2.3. Challenges and Outlook 45
2.3.1. Challenges and Future Directions for Clinical Applications 45
2.3.2. Challenges and Future Directions in Mathematical Modeling 48

3. PHYSICAL SYSTEM AND MODEL 50
3.1. Spherical Bubble Oscillations 50
3.1.1. Bubble in an Unbounded Liquid 50
3.1.1.1. Gas Pressure inside the Bubble 53
3.1.1.2. Bubble in an Unbounded Inviscid Liquid 54
3.1.1.3. Bubble in an Unbounded Newtonian Liquid 55
3.1.1.4. Bubble in an Unbounded Power-law Liquid 55
3.1.1.5. Bubble in an Unbounded Viscoelastic Liquid 56
3.1.2. Encapsulated Bubble in an Unbounded Liquid 58
3.1.2.1. Viscoelastic Shell 60
3.1.2.2. Linear Elastic Models 63
3.1.2.3. Encapsulated Bubble in an Unbounded Newtonian Liquid 63
3.1.2.4. Encapsulated Bubble in an Unbounded Power-law Liquid 64
3.1.2.5. Encapsulated Bubble in an Unbounded Viscoelastic Liquid 64
3.1.3. Bubble in a Liquid Cavity 65
3.1.3.1. Liquid Pressure Calculation 66
3.1.3.2. Bubble in a Newtonian Liquid Cavity 69
3.1.3.3. Bubble in a Carreau-Yasuda Liquid Cavity 69
3.1.3.4. Bubble in a Viscoelastic Liquid Cavity 70
3.1.3.5. Bubble Encapsulated with a Shell in a Liquid Cavity . . . 70
3.1.3.6. Bubble Encapsulated with a Viscoelastic Shell in a Newtonian Liquid Cavity 73
3.1.3.7. Bubble Encapsulated with Viscoelastic Shell in Viscoelastic Liquid Cavity 73
3.1.3.8. Bubble Encapsulated with Viscoelastic Shell in Carreau-Yasuda Cavity 74
3.1.4. Linearized Equations for Spherical Oscillations of a Bubble 75
3.2. Non-Spherical Oscillations of a Bubble 78
3.2.1. Field Decomposition 81
3.2.1.1. Base State: Spherical Oscillations 82
3.2.1.2. Perturbed State: Non-Spherical Oscillations 83

3.2.2. Shape Stability of a Bubble in an Unbounded Power-law Liquid . . 83
3.2.3. Shape Stability of an Encapsulated Bubble in Unbounded Liquid . . 85
3.2.3.1. Non-Spherical Oscillation for an Encapsulated Bubble in Power-Law Liquid 90
3.2.3.2. Non-Spherical Oscillation for an Encapsulated Bubble in Viscoelastic Liquid 91
3.3. Translational Motion and Bubble-Bubble Interactions 92
3.3.1. Lagrangian Method 93
3.3.2. Bubble-Bubble Interactions 97
3.4. Acoustic Droplet Vaporization (ADV) 101
3.4.1. Governing Equations 102
3.4.2. Final Equations 106
3.5. Solution Procedure 107
3.5.1. Solution Procedure for Coupled Ordinary Differential Equations . . 108
3.5.2. Solution Procedure for Shape Stability Analysis 110
3.5.3. Solution Procedure for Acoustic Droplet Vaporization 111
3.5.4. Convergence Analysis of Spectral Methods 115
3.5.5. Summary of the Solution Procedure 116
4. RESULTS AND DISCUSSION 119
4.1. Validation 119
4.2. Applicability of the Rayleigh-Plesset (RP) Equation 121
4.3. Applicability of Ideal Gas Law 123
4.4. Spherical Bubble Dynamics 127
4.4.1. Bubble in an Unbounded Liquid 128
4.4.1.1. Effect of Liquid Properties 128
4.4.1.2. Effect of Liquid Constitutive Model 131
4.4.2. Encapsulated Bubble in an Unbounded Liquid 137
4.4.2.1. Effect of Shell Properties 138
4.4.2.2. Effect of Surrounding Liquid Constitutive Model 145
4.4.3. Results for Bubble in a Liquid Cavity 149
4.4.3.1. Effect of Cavity Properties 150

4.4.3.2. Effect of Liquid Constitutive Model 152
4.4.4. Results for Encapsulated Bubble in a Liquid Cavity 155
4.4.4.1. Effect of Shell and Liquid Physical Properties 155
4.4.4.2. Effect of Cavity Properties on Spherical Oscillations . . . 160
4.4.4.3. Effect of Shell Properties 164
4.4.4.4. Effect of Liquid Constitutive Model 170
4.5. Non-Spherical Bubble Dynamics 181
4.5.1. Non-Spherical Oscillation of a Bubble in Power-law Liquid 182
4.5.2. Non-Spherical Oscillation of an Encapsulated Bubble 187
4.5.2.1. Non-Spherical Oscillation of an Encapsulated Bubble in Power-law Liquid 187
4.5.2.2. Non-Spherical Oscillation of Encapsulated Bubble in Viscoelastic Liquid 193
4.5.3. Phase Diagrams 197
4.6. Translational Motion and Bubble-Bubble Interactions 200
4.6.1. Translational Motion of an Encapsulated Bubble 201
4.6.2. Translational Motion of Two Encapsulated Bubbles 206
4.7. Acoustic Droplet Vaporization 218
4.8. Contour Maps for Biomedical Applications 225
5. CONCLUSIONS AND RECOMMENDATIONS 227
5.1. Conclusion 227
5.1.1. Spherical Oscillations 229
5.1.2. Non-Spherical Oscillations 231
5.1.3. Translational Motion and Bubble-Bubble Interactions 233
5.1.4. Acoustic Droplet Vaporization 234
5.2. Recommendations 235
REFERENCES 238
APPENDIX A: CONTINUUM MECHANICS 285
A.1. The Material Body and Motion 285
A.2. The Reference and Current Configurations 285
A.3. Deformation Gradient 287

A.4. The Left and Right Cauchy-Green Strain 288
A.5. Incompressibilty of Deformation Matrix 289
APPENDIX B: DETAILS OF THE NON-SPHERICAL OSCILLATIONS 290
B.1. Derivation of Velocity Potential for a Bubble 290
B.2. Derivation of Velocity Potential for an Encapsulated Bubble 291
B.3. Volume Change 294
APPENDIX C: MATCONT 295
APPENDIX D: AN EXAMPLE OF FLOQUET ANALYSIS 299
APPENDIX E: DIMENSIONLESS EQUATIONS 301
APPENDIX F: EFFECT OF BUBBLE AREA TO VOLUME RATIO 302
APPENDIX G: FIGURE PERMISSIONS 304

LIST OF FIGURES

Figure 1.1. Growth of the number of articles and patents [1]. 2

Figure 2.1. Nanocarrier systems for delivering drugs. Reproduced with permission from Kaykanat and Uguz, Biomicrofluidics, 17, 021502, (2023) permission from AIP Publishing [2]. 8

Figure 2.2. Biological barriers for targeted drug delivery [3] Reproduced with permission Zhao et al., Cell, 181, 151–167, (2020) permission from Elsevier. 11

Figure 2.3. Sketch of drug targeting approaches. (1) Passive targeting of nanocarriers. (2a) Active targeting of cancer cells and tumor endothelium using (2b) ligand-modified nanocarriers. (3) Stimuli-responsive nanocarriers, releasing drug by internal or external triggers. Reproduced with permission from Gagliardi et al. Front. Pharmacol., 12, 601626, 2021 [4]. Author(s), licensed under Creative Commons CC BY license. 14

Figure 2.4. Sketch of stable cavitation and inertial cavitation [5] used under Creative Commons CC BY-NC-ND. 21

Figure 2.5. The effects of ultrasound-mediated microbubbles on permeability of cell membrane for both stable and inertial cavitations [6] used under Creative Commons CC BY. 22

Figure 2.6. Scanning electron microscope images of HL-60 cells employing ultrasonic irradiation alone (a) or untreated (b), exposed to ultrasound in the presence of photosensitive drug merocyanine 540 (c–d). Reproduced with permission from Tinkov et al., J. Pharm. Sci., 98(6), 1935-1961, 2009 [7]. Copyright 2008 Wiley-Liss, Inc. 23

Figure 2.7. Fluorescent images before (t=0) and after (t=50 s) sonoporation with different acoustic pressures p_A (a) $p_A = 0.4$ MPa and (b) $p_A = 0.2$ MPa. Reproduced with permission from Wang et al. Sci. Rep. , 8(1), 1-12, 2018 [8]. Author(s), licensed under a Creative Commons Attribution (CC BY) License. 24

Figure 2.8. Sketch of a drug delivery system with ultrasound-mediated microbubble. Ultrasound-mediated microbubbles can increase blood–tumor barrier permeability and vascular perfusion, significantly improving the diffusion of agents (top right and bottom). Reproduced with permission from He et al. Pharmaceutics, 14(8), 1642, 2022 [9]. Author(s), licensed under a Creative Commons Attribution (CC BY) License. . . 25

Figure 3.1. Bubble in an unbounded liquid. 51

Figure 3.2. Encapsulated bubble in an unbounded liquid. 58

Figure 3.3. Sketch of a bubble in a liquid cavity. 66

Figure 3.4. Sketch of an encapsulated bubble in a liquid cavity. 71

Figure 3.5. Non-spherical bubble geometry in spherical coordinates. The solid and dashed lines show the spherical and non-spherical oscillations. 79

Figure 3.6. Non-spherical bubble geometry in spherical coordinates. The solid and dashed lines show the spherical and non-spherical oscillations. 86

Figure 3.7. Radial oscillation and translational motion of an encapsulated bubble in an unbounded liquid. 92

Figure 3.8. Radial oscillation and translational motion of two bubbles in unbounded liquid. 97

Figure 3.9. Configuration of acoustic droplet vaporization 102

Figure 3.10. Bubble radius versus time for different ODE solvers. 109

Figure 3.11. Bubble radius versus time for inviscid case. 111

Figure 3.12. Illustration of the microbubble shape with (left) the existence (small perturbation) and (right) growth of perturbations for order 2. Reproduced with permission from Lu et al., J. Acoust. Soc. Am. , 131, 24, (2012) permission from AIP Publishing [10]. 112

Figure 3.13. Effect of cut off frequency on convergence for N=17. Also in (a) $t =$ 0.125 μs; (b) $t = 0.25$ μs and (c) $t = 0.5$ μs. 116

Figure 3.14. Effect of cut off frequency on convergence for N=28. Also in (a) $t =$ 0.125 μs; (b) $t = 0.25$ μs and (c) $t = 0.5$ μs. 117

Figure 3.15. Effect of cut off frequency on convergence for N=56. Also in (a) $t =$ 0.125 μs; (b) $t = 0.25$ μs and (c) $t = 0.5$ μs. 117

Figure 3.16. Effect of cut off frequency on convergence for (a) N=17 and (b) N=28, $t = 50$. 118

Figure 3.17. Summary of the solution procedure for all parts. 118

Figure 4.1. Perturbation amplitude, a_n, and the bubble radius versus time: (a) our results (b) Liu's result [11]. Reproduced with permission from Liu et al., Phys. Fluids , 30, 12, (2018) permission from AIP Publishing [11]. 120

Figure 4.2. Perturbation amplitude of shell (a_n) and bubble (b_n) versus time: (a) our results (b) Lu's result [10]. Reproduced with permission from Lu et al., J. Acoust. Soc. Am. , 131, 24, (2012) permission from AIP Publishing [10]. 120

Figure 4.3. Bubble diameter, $2R_b(t)$ versus time: (a) our results (b) Doinikov's result [12]. Reproduced with permission from Doinikov et al., Phys. Fluids, 102901, 41, (2014) permission from AIP Publishing [12]. . . . 121

Figure 4.4. kR_{max} versus ω_d (condition 1). 123

Figure 4.5. $\dot{R}_{max}/c$ versus ω_d and (b) $\ddot{R}_{max}R_{max}/c$ versus ω_d (condition 2). 123

Figure 4.6. $\dot{R}_{max}/c_g$ versus ω_d and (b) $\ddot{R}_{max}R_{max}/c_g$ versus ω_d (condition 3). . . . 124

Figure 4.7. kR_{max} versus power-law index (condition 1). 124

Figure 4.8. $\dot{R}_{max}/c$ versus power-law index and (b) $\ddot{R}_{max}R_{max}/c$ versus power-law index (condition 2). 125

Figure 4.9. $\dot{R}_{max}/c_g$ versus power-law index and (b) $\ddot{R}_{max}R_{max}/c_g$ versus power-law index (condition 3). 126

Figure 4.10. $R(t)$ versus $t/(2\pi/\omega_d)$ for $p_a = 0.25$ atm and $\omega_d = 4$ MHz. 126

Figure 4.11. R(t) versus time for c = 2.5 atm, k = 1 and (a) $\omega_d = 4$ MHz (b) $\omega_d =$ 8MHz. 127

Figure 4.12. $\left|R_{\max}^{vdw} - R_{\max}^{\text{poly}}\right|$ versus p_a ($\omega_d = 2$ MHz) and (b) $\left|R_{\max}^{vdw} - R_{\max}^{\text{poly}}\right|$ versus ω_d $p_a = 0.25$ atm. 127

Figure 4.13. Spherical oscillations of a bubble in an inviscid unbounded liquid: (a) the schematic view of the bubble extraction-contraction, (b) bubble radius versus time and (c) velocity versus time. 129

Figure 4.14. Effects of (a) surface tension, σ (b) density, ρ and (c) initial bubble radius, R_{b0} on oscillation period. 130

Figure 4.15. Dimensionless bubble-wall velocity versus dimensionless bubble radius (a) Re=1 and (b) Re=10. 131

Figure 4.16. $R_b(t)$ versus $t/(2\pi/\omega_d)$ for (a) $\omega_d = 1\text{MHz} < \omega_0$, (b) $\omega_d = 2\text{MHz} \approx \omega_0/2$, (c) $\omega_d = 4\text{MHz} \approx \omega_0$ (radial resonance), and (d) $\omega_d = 8\text{MHz} > \omega_0$. Here, the blue $(k = 0.75)$, red $(k = 1)$, and black ($k = 1.25$) represent the shear-thinning, Newtonian, and shear-thickening liquids, respectively. Reproduced with permission from Kaykanat and Uguz [13]. Author(s), licensed under Creative Commons CC BY license. . . 133

Figure 4.17. $\dot{R}_b(t)$ versus R_b/R_{b0}.) for (a) $\omega_d = 1\text{MHz} < \omega_0$, (b) $\omega_d = 2\text{MHz} \approx \omega_0/2$, (c) $\omega_d = 4\text{MHz} \approx \omega_0$ (radial resonance), and (d) $\omega_d = 8\text{MHz} > \omega_0$. Here, the blue $(k = 0.75)$, red $(k = 1)$, and black ($k = 1.25$) represent the shear-thinning, Newtonian, and shear-thickening liquids, respectively. 135

Figure 4.18. a) Maximum value of bubble wall velocity $\max(\dot{R}_b)$, versus power-law index, k and (b) maximum viscosity, $\mu_{0,max}$ versus power-law index, k after 15 cycle. Reproduced with permission from Kaykanat and Uguz [13]. Author(s), licensed under Creative Commons CC BY license. . . 135

Figure 4.19. Contour plot (M versus power-law index, k) for R_{max}/R_{b0}: (a) $\omega_d =$ 1 MHz, (b) $\omega_d = 2$ MHz and (c) $\omega_d = 4$ MHz$\approx \omega_0$ after 15 cycle . Reproduced with permission from Kaykanat and Uguz [13]. Author(s), licensed under Creative Commons CC BY license. 136

Figure 4.20. Contour plot (M versus power-law index, k) for R_{max}/R_{b0}: (a) $\omega_d =$ 1 MHz, (b) $\omega_d = 2$ MHz and (c) $\omega_d = 4$ MHz$\approx \omega_0$ after 15 cycle Reproduced with permission from Kaykanat and Uguz [13]. Author(s), licensed under Creative Commons CC BY license. 137

Figure 4.21. $R_b(t)$ versus $t/(2\pi/\omega_d)$ for $\omega_d = 4$ MHz $\approx \omega_0$ and (b) Effect of liquid modulus on the natural frequency. 138

Figure 4.22. Effect of acoustic field driven frequency, ω_d, on $R_b(t)/R_{b0}$ versus $\dfrac{t}{2\pi\omega_d}$. 139

Figure 4.23. Effects of (a) shell thickness, δ and (b) shell modulus, G_s on $R_b(t)/R_{b0}$ versus $t/(2\pi/\omega_d)$. 140

Figure 4.24. Contour plot (a) δ versus G_s, and (b) p_0 versus R_{b0} for natural frequency, ω_0. 141

Figure 4.25. Contour plot G_s versus δ for natural frequency deviation, Δ. 142

Figure 4.26. Effect of shell models on $R_b(t)/R_{b0}$ versus $t/(2\pi/\omega_d)$. 142

Figure 4.27. Contour plot (δ versus G_s) (a) for maximum bubble surface area and (b) for the deviation between shell models. 143

Figure 4.28. Effect of shell thickness, δ on $R_b(t)/R_{b0}$ versus $t/(2\pi/\omega_d)$: (a) δ=15 nm, $G_s = 15$ MPa, (b) $\delta = 60$ nm, $G_s = 15$ MPa and (c) $\delta = 15$ nm, $G_s = 60$ MPa. 144

Figure 4.29. Maximum expansion and compression of microbubble versus liquid (μ_l) and shell (μ_s) viscosity. 144

Figure 4.30. Effect of power-law index on $R_b(t)/R_{b0}$ versus $t/(2\pi/\omega_d)$: (a) m =0.001 Pa$\cdot$s$^{\mathrm{k}}$ and (b) $m = 0.01$ Pa$\cdot$s$^{\mathrm{k}}$. 145

Figure 4.31. $R_b(t)/R_{b0}$ versus $t/(2\pi/\omega_d)$ for ω_d=2 MHz$< \omega_0$ 146

Figure 4.32. Contour plots (p_a versus ω_d) for maximum bubble surface area (a) $k =$ 0.5, (b) $k = 1$ and (c) $k = 1.5$. 147

Figure 4.33. Contour plots (p_a versus ω_d) for minimum bubble surface area where (a) $k = 0.5$, (b) $k = 1$ and (c) $k = 1.5$. 148

Figure 4.34. Contour plot (p_a versus k) shows the deviation between shell models (a) $m = 0.001$ Pa.s^k and (b) $m = 0.01$ Pa.s^k. 149

Figure 4.35. Effect of liquid modulus, G_{liq} on $R_b(t)/R_{b0}$ versus $t/(2\pi/\omega_d)$. 150

Figure 4.36. Effect of liquid modulus, G_{liq} on the natural frequency, ω_0 150

Figure 4.37. Effect of initial bubble radius, R_{b0} on the natural frequency, ω_0 for viscoelastic and Newtonian liquid. 151

Figure 4.38. Effect of acoustic field driven frequency, ω_d, on $R_b(t)/R_{b0}$ versus $\dfrac{t}{2\pi\omega_d}$. 152

Figure 4.39. Effects of cavity modulus, G_{el}, on natural frequency, ω_0. 152

Figure 4.40. Effect of $\beta = R_{l0}/R_{b0}$ on $R_b(t)/R_{b0}$ versus $t/(2\pi/\omega_d)$ for (a) small β and (b) large β. 153

Figure 4.41. Effect of power-law index, k on $R_b(t)/R_{b0}$ versus $t/(2\pi/\omega_d)$ for (a) $\omega_d = 7$ MHz and (b) ω_d=5 MHz. 153

Figure 4.42. Effect of initial bubble radius, R_{b0} on natural frequency, ω_0 for viscoleastic ($G_{liq} = 10^5$ Pa) and Newtonian liquid. 154

Figure 4.43. Effect of acoustic field driven frequency, ω_d, on $R_b(t)/R_{b0}$ versus $\frac{t}{2\pi\omega_d}$. 156

Figure 4.44. Effect of (a) liquid density, ρ_l and (b) shell density, ρ_s on $R_b(t)/R_{b0}$ versus $t/(2\pi/\omega_d)$. 157

Figure 4.45. Effect of (a) liquid density ρ_l and (b) shell density, ρ_s on the natural frequency, ω_0. 158

Figure 4.46. Effect of (a) bubble/shell interfacial tension σ_b and (b) interfacial tension σ_s on $R_b(t)/R_{b0}$ versus $t/(2\pi/\omega_d)$. 159

Figure 4.47. Effect of (a) liquid viscosity, μ_l and (b) shell viscosity, μ_s on $R_b(t)/R_{b0}$ versus $t/(2\pi/\omega_d)$. 160

Figure 4.48. Effect of surface tensions on the natural frequency, ω_0. The dashed and solid lines show the effects of shell/liquid (σ_s) and bubble/shell (σ_b) interfacial tensions. 160

Figure 4.49. Effect of cavity modulus, G_{el}, on $R_b(t)/R_{b0}$ versus $t/(2\pi/\omega_d)$ for (a) small, (b) moderate, and (c) large G_{el} values. 161

Figure 4.50. Effect of bulk modulus, K_{el}, on $R_b(t)/R_{b0}$ versus $t/(2\pi/\omega_d)$ for (a) small, (b) moderate, and (c) large K_{el} values. 163

Figure 4.51. Effect of radius ratio, $\beta = R_{l0}/R_{b0}$ on $R_b(t)/R_{b0}$ versus $t/(2\pi/\omega_d)$ for (a) small and (b) large β values. 163

Figure 4.52. Effect of (a) cavity modulus, G_{el} and (b) cavity bulk modulus, K_{el}, and (c) $\beta = R_{l0}/R_{b0}$ on the maximum bubble surface area. 165

Figure 4.53. Contour plot (K_{el} versus G_{el}) for natural frequency, ω_0. 166

Figure 4.54. Effect of shell modulus, G_s on $R_b(t)/R_{b0}$ versus $t/(2\pi/\omega_d)$ for (a) small, (b) moderate, and (c) large G_s values. 166

Figure 4.55. Effect of shell thickness, δ on $R_b(t)/R_{b0}$ versus $t/(2\pi/\omega_d)$ for (a) small, (b) moderate, and (c) large δ values. 167

Figure 4.56. Effect of (a) shell modulus, G_s and (b) shell thickness, δ on the maximum bubble surface area. 167

Figure 4.57. Contour plot (a) driving frequency, ω_d versus shell modulus, G_s and (b) driving frequency, ω_d versus shell thickness, δ for maximum bubble surface area. 168

Figure 4.58. Contour plot (G_s versus δ) for natural frequency, ω_0. 168

Figure 4.59. Effect of (a) acoustic field pressure amplitude, p_a and (b) driving frequency, ω_d. 169

Figure 4.60. Contour plot (δ versus G_s) shows the difference between shell models. 170

Figure 4.61. Contour plot (G_s versus δ) for the maximum bubble surface area. . . . 171

Figure 4.62. Effect of power-law index, k on $R_b(t)/R_{b0}$ versus $t/(2\pi/\omega_d)$. 172

Figure 4.63. Effect of liquid modulus on $R_b(t)/R_{b0}$ versus $t/(2\pi/\omega_d)$. 172

Figure 4.64. Effect of power-law index, k, on $R_b(t)/R_{b0}$ versus $t/(2\pi/\omega_d)$ for (a) $\beta = 100$ and (b) $\beta = 2$. 173

Figure 4.65. Effect of power-law index, k, on $R_b(t)/R_{b0}$ versus $t/(2\pi/\omega_d)$ for (a) $\omega_d = 2$ MHz, (b) for $\omega_d = 4$ MHz, and (c) $\omega_d = 16$ MHz. 174

Figure 4.66. Effect of power-law index, k, on $R_b(t)/R_{b0}$ versus $t/(2\pi/\omega_d)$ for $\omega_d =$ 2 MHz. 175

Figure 4.67. Contour plot (a) k versus β and (b) k versus p_a for maximum bubble surface area. 175

Figure 4.68. Contour plot (k versus β) (a) $\omega_d = 8$ MHz, $G_{el} = 10$ MPa, (b) $\omega_d = 4$ MHz, $G_{el} = 10$ MPa and (c) $\omega_d = 8$ MHz, $G_{el} = 100$ MPa for maximum wall pressure, p_l. 176

Figure 4.69. Contour plot k versus β (a) $p_a = 0.25$ atm and (b) $p_a = 2.25$ atm for ε. 177

Figure 4.70. Effect of power-law index, k, on $R_b(t)/R_{b0}$ versus $t/(2\pi/\omega_d)$ for (a) shear-thinning and (b) shear-thickening liquid. 177

Figure 4.71. Effect of power-law index, k, on $R_b(t)/R_{b0}$ versus $t/(2\pi/\omega_d)$ for (a) $\beta = 2$ and (b) $\omega_d = 2$ MHz. 178

Figure 4.72. Contour plot (k versus p_a) (a) $\beta = 2.5$, (b) $\beta = 10$ and (c) $\beta = 100$ for maximum stress, $max(\tau_l(R_l))$. 179

Figure 4.73. Contour plot (k versus p_a) (a) $\beta = 2.5$, (b) $\beta = 10$ and (c) $\beta = 100$ for maximum stress, $max(\tau_{rr,l}(R_l)$. 180

Figure 4.74. Contour plot (ω_d versus p_a) (a) $\beta = 2.5$, and (b) $\beta = 100$ for maximum stress, $max(\tau_{rr,l}(R_l)$. The power-law index is 0.75. 181

Figure 4.75. $a_2(t)/R_0$ versus $t/(2\pi/\omega_d)$ for (a) $\omega_d = 1$ MHz $< \omega_0$, (b) $\omega_d = 2$ MHz $\approx \omega_0/2$, (c) $\omega_d = 4$ MHz $\approx \omega_0$ (radial resonance), and (d) $\omega_d = 8$ MHz $> \omega_0$. Here, the blue, red and black lines show the shear-thinning ($k = 0.75$), Newtonian ($k = 1$) and shear-thickening ($k = 1.25$) liquid cases, respectively. Reproduced with permission from Kaykanat and Uguz [13]. Licensed under Creative Commons CC BY license. 183

Figure 4.76. $a_n(t)/R_0$ versus $t/(2\pi/\omega_d)$ for $M = 2 \times 10^{-4}$ Pa·s^k when (a) $\omega_d = 2.65$ MHz $= \omega_2$, (b) $\omega_d = 9.6$ MHz $= \omega_3$, (c) $\omega_d = 2.65$ MHz $= \omega_2$, and (d) $\omega_d = 9.6$ MHz $= \omega_3$. Here, the blue ($n = 2$), red ($n = 3$), and black ($n = 4$) represent the perturbation modes. Reproduced with permission from Kaykanat and Uguz [13]. Author(s), licensed under Creative Commons CC BY license. 185

Figure 4.77. Bubble wall acceleration, $\ddot{R}$, versus $t/(2\pi/\omega_d)$ for $\omega_d = 8$ MHz $> \omega_0$, (a) $p_a = 2.5$ atm and $k = 0.75$, (b) $p_a = 2.5$ atm and $k = 1$ and (c) $p_a = 15$ atm and $k = 1.1$. $a_n(t)/R(t)$ versus $t/(2\pi/\omega_d)$ for $\omega_d = 8$ MHz $< \omega_0$, (d) $p_a = 2.5$ atm and $k = 0.75$, (e) $p_a = 2.5$ atm and $k = 1$ and (f) $p_a = 15$ atm and $k = 1.1$. Reproduced with permission from Kaykanat and Uguz [13]. Author(s), licensed under Creative Commons CC BY license. 186

Figure 4.78. R_0 versus p_a: (a), (d) and (g), $k = 0.75$; (b), (e) and (h), $k = 1$; (c) and (f) $k = 1.25$. $n = 2$ for (a)-(c), $n = 3$ for (d)-(f) and $n = 4$ (g)-(h). . . . 186

Figure 4.79. Initial bubble radius, R_{b0} versus the most unstable mode in the parametric instability for (a) $\omega_d = 5$ MHz and (b) $\omega_d = 14$ MHz. 188

Figure 4.80. Effect of shell viscosity, μ_s on the (a) b_n/R_{b0} versus $t/(2\pi/\omega_d)$ and (b) a_n/R_{s0} versus $t/(2\pi/\omega_d)$. 189

Figure 4.81. Effect of pressure amplitude, p_a on (a)-(c) b_n/R_{b0} versus $t/(2\pi/\omega_d)$ and (b)-(d) a_n/R_{s0} versus $t/(2\pi/\omega_d)$ for $n = 2$. In (a)-(b) $\mu_s = 0.001$ kg/ms and in (c)-(d) $\mu_s = 0.05$ kg/ms. 191

Figure 4.82. Effect of pressure amplitude, p_a on (a)-(c) b_n/R_{b0} versus $t/(2\pi/\omega_d)$ and (b)-(d) a_n/R_{s0} versus $t/(2\pi/\omega_d)$ for $n = 3$. In (a)-(b) $\mu_s = 0.001$ kg/ms and in (c)-(d) $\mu_s = 0.05$ kg/ms. 192

Figure 4.83. Effect of power-law index, k on (a)-(c) b_n/R_{b0} versus $t/(2\pi/\omega_d)$ and (b)-(d) a_n/R_{s0} versus $t/(2\pi/\omega_d)$ for $n = 2$. In (a)-(b) $\delta = 15$ nm and in (c)-(d) $\delta = 30$ nm. 194

Figure 4.84. Effect of shell viscosity, μ_s on (a) bubble surface perturbation amplitude, b_n (b) shell surface perturbation amplitude, a_n (c) maximum bubble surface amplitude, $\max(b_n)$ and (d) maximum shell surface amplitude, $\max(a_n)$. 195

Figure 4.85. Effect of perturbation modes, n on (a), (c), (e) bubble surface amplitude, b_n and (b), (d), (f) shell surface amplitude, a_n. In (a)-(b) $k = 0.75$, (c)-(d) $k = 1$ and (d)-(e) $k = 1.25$. 196

Figure 4.86. Initial bubble radius, R_{b0} versus the most unstable mode, n in the parametric instability. 197

Figure 4.87. Effect of liquid modulus, G_l, on bubble ((a),(c)) and shell ((b),(d)) perturbation amplitudes for (a)-(b), $n = 2$ and (c)-(d), $n = 3$. 198

Figure 4.88. Effect of liquid modulus, G_l, on (a) maximum bubble radius, R_b, (b) maximum bubble surface perturbation amplitude, b_n, for $n = 2$, and (c) maximum bubble surface perturbation amplitude, b_n, for $n = 3$. . . . 199

Figure 4.89. Phase diagrams, R_{b0} vs. p_a for bubble in power-law liquid. Surrounding liquid is (a) shear-thinning ($k = 0.75$), (b) Newtonian and (c) shear-thickening ($k = 1.25$). 199

Figure 4.90. Phase diagrams, R_{b0} vs. p_a for an encapsulated bubble in unbounded liquid (a) shell thickness, $\delta = 150$ nm and (b) shell thickness, $\delta = 15$ nm. 200

Figure 4.91. Effect of shell modulus, G_s on (a) $z(t)/\lambda$ versus $t/(2\pi/\omega_d)$ and (b) z_{end}/λ obtained after 20 cycle of acoustic pressure. 201

Figure 4.92. Effect of shell modulus, G_s on (a) $\dot{z}(t)$ versus $t/(2\pi/\omega_d)$ and (b) $\dot{R}_b(t)$ versus $t/(2\pi/\omega_d)$. 203

Figure 4.93. Effect of shell modulus, G_s on $\dot{z}(t)$ versus $\dfrac{t}{2\pi\omega_d}$ for $\omega_d = 3.5$ MHz. . 204

Figure 4.94. Contour plot (δ versus G_s) for (a) $\omega_d = 7$ MHz and $G_l = 0$ MPa, (b) $\omega_d = 7$ MHz and $G_l = 1$ MPa, and (c) $\omega_d = 14$ MHz and $G_l = 1$ MPa show the deviation between shell models. 205

Figure 4.95. Effect of acoustic irradiation on $\dot{z}(t)$ versus $t/(2\pi/\omega_d)$ for (a) $\omega_d = 7$ MHz, $G_l = 0$ MPa and (b) $\omega_d = 14$ MHz, $G_l = 1$ MPa. 206

Figure 4.96. (a), (c), (e) $R_b(t)/R_{b0}$ and $R_{b2}(t)/R_{b20}$ versus $t/(2\pi/\omega_d)$ when $R_{b20} = 5\,\mu\text{m} = R_{b10}$ (b), (d), (f) $R_b(t)/R_{b0}$, $R_{b2}(t)/R_{b20}$ versus $t/(2\pi/\omega_d)$ when $R_{b20} = 1\,\mu\text{m} < R_{b10} = 5\,\mu\text{m}$. 208

Figure 4.97. (a), (c), (e) $\dot{z}_1(t)$ and $\dot{z}_2(t)$ versus $t/(2\pi/\omega_d)$ when $R_{b20} = 5\,\mu\text{m} = R_{b0}$ (b), (d), (f) $\dot{z}(t)$ and $\dot{z}_2(t)$ versus $t/(2\pi/\omega_d)$ when $R_{b20} = 1\,\mu\text{m} < R_{b10} = 5\,\mu\text{m}$. 209

Figure 4.98. (a), (c), (e) D versus $t/(2\pi/\omega_d)$ when $R_{b20} = 5\,\mu\text{m} = R_{b0}$ (b), (d), (f) D versus $t/(2\pi/\omega_d)$ when $R_{b20} = 1\,\mu\text{m} < R_{b10} = 5\,\mu\text{m}$. 211

Figure 4.99. F_{ex} versus $t/(2\pi/\omega_d)$ when first order (a)-(b), second order (c)-(d), and third order (e)-(f) terms of $1/D$ are considered. In (a), (c) and (e), $R_{b0} = 5\ \mu\text{m} = R_{b0}$ and In (b), (d) and (f), $R_{b0} = 5\ \mu\text{m}$, $R_{b02} = 1\ \mu\text{m}$. . 212

Figure 4.100. Effect of liquid modulus on (a) $R_{b2}(t)/R_{b20}$ versus $t/(2\pi/\omega_d)$, (b) $R_{b1}(t)/R_{b10}$, versus $t/(2\pi/\omega_d)$, (c) $\dot{z}_2$ versus $t/(2\pi/\omega_d)$, (d) $\dot{z}_1$ versus $t/(2\pi/\omega_d)$ and (e) D versus $t/(2\pi/\omega_d)$ 214

Figure 4.101. Contour plot (a) (δ versus G_s), ($G_l = 0$ and $\omega_d = 7$ MHz), (b) p_a versus G_l, ($\omega_d = 7$ MHz) and (c) p_a versus G_l ($\omega_d = 14$ MHz) for χ. 215

Figure 4.102. Contour plot (a) (δ versus G_s), ($G_l = 0$ and $\omega_d = 7$ MHz), and (c) p_a versus G_l ($\omega_d = 14$ MHz) for χ. 215

Figure 4.103. Contour plot (p_a versus ω_d) for the minimum distance between bubbles (a) $R_{b0} = R_{b02} = 5\ \mu\text{m}$ and (b) $R_{b0} = 5\ \mu\text{m}$ $R_{b02} = 1\ \mu\text{m}$ and $\omega_d = 7$ MHz. 216

Figure 4.104. Contour plot (p_a versus ω_d) for the minimum distance between bubbles without the effect of encapsulation (a) $R_{b0} = R_{b02} = 5\ \mu\text{m}$ and $R_{b0} = 5$ μm $R_{b02} = 1\ \mu\text{m}$ and $\omega_d = 4$ MHz. 217

Figure 4.105. Bubble diameter, $D_b(t)$ versus time for (a) $D_0 = 3.7$ μm and $D_0 = 2$ μm. The best-fit values of μ_l and σ_i are (a) $\mu_l = 0.0065$ Pa s, $\sigma_i =$ 0 N/m; (b) $\mu_l = 0.02$ Pa s, $\sigma_i = 0.25$ N/m. 220

Figure 4.106. Bubble surface temperature versus time for (a) $D_0 = 3.7$ μm and $D_0 =$ 2 μm. 221

Figure 4.107. Normalized mass flux versus time. for (a) $D_0 = 3.7$ μm and $D_0 = 2$ μm. 221

Figure 4.108. Bubble diameter, $2R_b(t)$ versus time for (a) $D_0 = 5.7$ μm, (b) $D_0 = 3.7$ μm, and (c) $D_0 = 2.7$ μm. The best-fit values of μ_l and σ_i are (a) $\mu_l = 0.006$ Pa s, $\sigma_i = 0$ N/m; (b) $\eta_3 = 0.0065$ Pa s, $\sigma_i = 0$ N/m; (c) $\mu_l = 0.009$ Pa s, $\sigma_i = 0$ N/m; (c) $\mu_l = 0.02$ Pa s, $\sigma_i = 0.25$ N/m. . . . 222

Figure 4.109. Effect of (a) acoustic pressure amplitude, p_a and (b) acoustic driving frequency, ω_d on bubble diameter, $2R_b(t)$. 223

Figure 4.110. Effect of power-law index, k for (a) $D_0 = 2.7$ μm and (b)$D_0 = 3.7$ μm. 223

Figure 4.111. Bubble diameter versus time for (a) shear-thinning liquids, (b) Newtonian liquids and (c) shear-thickening liquids. Here, $D_0 = 2.7$ μm. The red and black colors indicate decafluorobutane and octafluoropropane droplets. 224

Figure 4.112. Contour plot (pressure amplitude versus frequency of acoustic field) for acoustic droplet vaporization threshold, t_{ADV}. 225

Figure 4.113. Contour maps for (a) pressure amplitude versus frequency (ω_d), and (b) shell thickness versus shell modulus, highlighting the regions for efficient and safe biomedical application. 226

Figure A.1. The reference and current configurations. 286

Figure A.2. The Deformation Gradient acting on a line element 287

Figure C.1. The main menu of Matcont. 295

Figure C.2. System menu of Matcont. 295

Figure C.3. Coupled equations. 296

Figure C.4. Type menu of Matcont. 296

Figure C.5. Integrator. 297

Figure C.6. Graphic menu of Matcont. 297

Figure C.7. Compute menu of Matcont. 298

Figure F.1. Effect of area to volume ratio on drug loading capacity. 303

Figure F.2. Effect of area to volume ratio on drug diffusion rate. 303

Figure G.1. Copyright permission for Figure 2.1. 304

Figure G.2. Copyright permission for Figure 2.1 (page 2). 305

Figure G.3. Copyright permission for Figure 2.2 (page 2). 306

Figure G.4. Copyright permission for Figure 2.6. 307

Figure G.5. Copyright permission for Figure 2.6 (page 2). 308

Figure G.6. Copyright permission for Figures 2.3, 2.4, 2.5, 2.7, 2.8, 4.18, 4.19, 4.20, 4.75, 4.76, 4.77. 308

Figure G.7. Copyright permission for Figures 3.12 and 4.2. 309

Figure G.8. Copyright permission for Figure 3.12 and 4.2 (page 2). 310

Figure G.9. Copyright permission for Figure 4.1. 311

Figure G.10. Copyright permission for Tables 2.1, 2.2, 2.3, 2.4, 2.5, 2.6, 2.7, 2.8. . . 312

Figure G.11. Copyright permission for Tables (page 2). 313

Figure G.12. Copyright permission for Figure 4.3 and Table 4.4. 314

Figure G.13. Copyright permission for Figure 4.3 and Table 4.4 (page 2). 315

LIST OF TABLES

Table 2.1. Recent Food and Drug Administration-approved nanomedicines [14, 15].Reproduced with permission from Kaykanat and Uguz, Biomicrofluidics, 17, 021502, (2023) permission from AIP Publishing [2]. 10

Table 2.2. Positive aspects and drawbacks of the ligands. Reproduced with permission from Kaykanat and Uguz, Biomicrofluidics, 17, 021502, (2023) permission from AIP Publishing [2]. 16

Table 2.3. Positive aspects and drawbacks of the different stimuli types. Reproduced with permission from Kaykanat and Uguz, Biomicrofluidics, 17, 021502, (2023) permission from AIP Publishing [2]. 18

Table 2.4. Properties of an ultrasound wave. Reproduced with permission from Kaykanat and Uguz, Biomicrofluidics, 17, 021502, (2023) permission from AIP Publishing [2]. 20

Table 2.5. An overview of the historical development of therapeutic ultrasound. Reproduced with permission from Kaykanat and Uguz, Biomicrofluidics, 17, 021502, (2023) permission from AIP Publishing [2]. 26

Table 2.6. In vitro experiments of ultrasound-mediated microbubbles (UMBS). Reproduced with permission from Kaykanat and Uguz, Biomicrofluidics, 17, 021502, (2023) permission from AIP Publishing [2]. 29

Table 2.7. In vivo experiments of ultrasound-mediated microbubbles (UMBS). Reproduced with permission from Kaykanat and Uguz, Biomicrofluidics, 17, 021502, (2023) permission from AIP Publishing [2]. 30

Table 2.8. Shell models for microbubbles. Reproduced with permission from Kaykanat and Uguz, Biomicrofluidics, 17, 021502, (2023) permission from AIP Publishing [2]. 41

Table 4.1. Physical properties for a bubble in an unbounded liquid. 128

Table 4.2. Physical properties for bubble shell [16]. 138

Table 4.3. Physical parameters employed in the present study. 155

Table 4.4. Material properties of different PFCs used in simulations [12, 17]. . . . 219

1. INTRODUCTION

Cancer remains the leading cause of death globally. New cancer cases are projected to increase by 49.7% between 2020 and 2040 [18]. Traditional cancer treatments such as radiotherapy and chemotherapy come with side effects that significantly impact a patient's quality of life. These treatments often damage healthy cells contributing to further complications in addition to targeting cancerous cells. More advanced chemotherapy approaches aim to selectively target tumor tissues. These approaches include monoclonal antibodies and small-molecule inhibitors. Although these novel drugs show promise, their accumulation in both normal and tumor tissues limits their therapeutic potential. This limitation makes the application of the novel drugs in patients more challenging [19, 20]. Furthermore, in conventional drug delivery methods, only a small percentage of the dose of the administered drug (0.001–0. 01%) reaches the target area, leading to accumulation of the drug in healthy tissues [21–23]. As a result, new approaches are required to achieve higher therapeutic effectiveness. Drug-loaded nanoparticles have shown great promise for targeted delivery. However, their therapeutic potential is often hindered by biological barriers, such as the dense extracellular matrix, the effects of variable enhanced permeability and retention (EPR) and elevated pressure of the interstitial fluid in tumors [23, 24]. Recently, ultrasound-driven microbubbles have emerged as a promising tool for drug delivery. Microbubbles undergo compression and expansion during high and low-pressure cycles when exposed to an acoustic field. This oscillation creates mechanical stresses on blood vessel walls which increases vascular permeability. This process is known as sonoporation and enhances the permeability of cell membranes, facilitating improved extravasation and penetration through the extracellular matrix. As a result, the distribution and accumulation of nanoparticles and drugs in tumor tissues are significantly enhanced [23, 25]. Initial tests of this cancer treatment technique indicate that using microbubbles reduces the side effects of chemotherapy, leading to quicker patient recovery [26]. As shown in Figure 1.1, the number of articles and patents on the treatment of the delivery of ultrasonic drugs has increased in recent years.

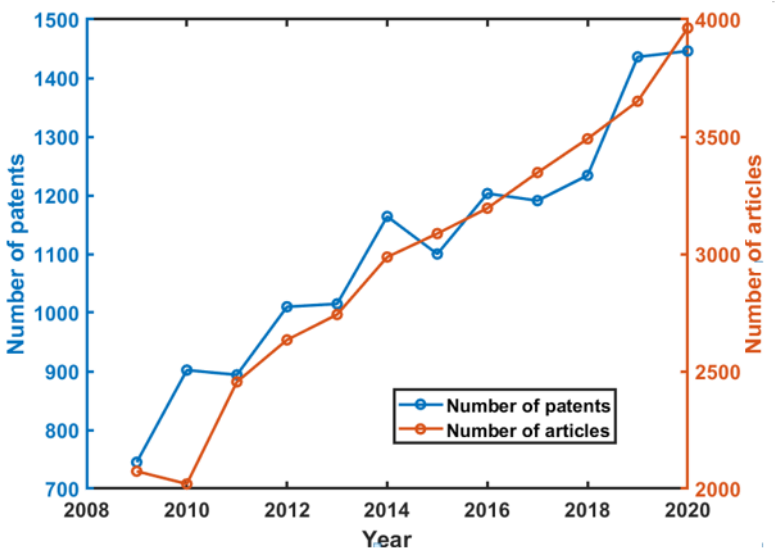

Figure 1.1. Growth of the number of articles and patents [1].

Ultrasound technology was first introduced in the 1930s and is now widely used for both diagnostic imaging [27–29] and as a therapeutic tool to induce various biological effects [30–32]. Early therapeutic uses of ultrasound focused on tissue heating [33, 34] and ablation of vestibular sense organs to treat Ménière's disease [35]. Clinical studies have also shown that focused ultrasound, which is combined with microbubbles, can facilitate the treatment of Parkinson's disease by opening the blood-brain barrier [36]. By the 1970s, therapeutic ultrasound had become a standard treatment in physiotherapy. Since then, research has expanded into more advanced applications, including neurosurgery [37] and targeted drug delivery [38–43] with promising results for cancer treatment [44].

Several complementary targeting techniques are used to increase the potential usage of ultrasound treatment with microbubbles. For instance, microbubbles are functionalized by the attachment of antibodies. However, the half-life of the microbubbles, e.g., < 5 min in circulation, is too short, which is a challenge for this method. Acoustic radiation force is a way to concentrate microbubbles and increase their binding to target sites [45]. Another approach is to incorporate magnetic material into the microbubbles and accumulate them in a target region using an external magnetic field. The combination of the magnetic and the ultrasound fields is used to delay the tumor growth and simultaneously concentrate and activate the microbubbles at the target site.

Models used to study bubble dynamics under an acoustic field are highly nonlinear due to factors such as high acoustic pressures and interactions between bubbles, as well as between bubbles and blood vessels. Recently, more complex models have been developed to better understand the behavior of microbubbles in both in vitro and in vivo experiments [32,46,47]. Most existing models for coated bubbles are based on the Rayleigh-Plesset (RP) equation which describes a bubble in an incompressible and infinite fluid. Although the RP equation can predict bubble behavior in many situations, it overlooks damping effects from sound radiation because of the assumption of fluid incompressibility. In addition, bubbles tend to be unstable and dissolve rapidly in the bloodstream, which is why microbubbles are typically coated with a shell made of a lipid, polymer, or protein. Several models have been developed to account for the dynamics of these encapsulated microbubbles.

This dissertation aims to investigate the dynamics of microbubbles within a blood vessel surrounded by elastic tissue under the influence of an acoustic field relevant to critical therapeutic applications. This thesis introduces several novel contributions to bubble dynamics and ultrasound-mediated therapeutic applications, addressing key gaps in the existing literature. By incorporating microvessel properties, the study provides a more realistic representation of in vivo conditions, an aspect often overlooked in prior work. Adopting a nonlinear Neo-Hookean shell model highlights significant deviations from traditional linear models. Additionally, blood's non-Newtonian and viscoelastic properties should be considered. Unlike many studies that rely on unnecessarily complex models, this thesis identifies parametric ranges where simplified models can be effectively used, offering a pragmatic approach to reduce computational overhead. Finally, the development of contour maps based on multiple safety and efficacy criteria, such as wall shear stress, bubble surface area, and inter-bubble distances, provides actionable guidelines for clinicians, ensuring safer and more effective therapeutic applications. These advances not only fill existing gaps in the literature but also lay the groundwork for the practical optimization of ultrasound-mediated drug delivery.

This dissertation is divided into four main parts. In the first section (Sections 3.1 and 4.4), spherical oscillations of a bubble are studied. Different non-Newtonian models

for the surrounding liquid and a nonlinear Neo-Hookean hyperelastic model for the bubble shell are employed, offering a more realistic alternative to simpler Newtonian and linear shell models. Additionally, parametric ranges for the bubble surface area and the wall shear stress exerted by the surrounding liquid are identified, supporting safer and more effective biomedical applications.

In the second part (Sections 3.2 and 4.5), the shape stability of a bubble is studied. Controlling shape stability is crucial for targeted drug delivery to regulate microbubble break-up or to determine the pressure needed for bubble collapse in tissue ablation [48,49]. The initiation of bubble break-up is directly linked to the loss of spherical form caused by the growing shape instabilities at the interface. In addition, the steady shape oscillations of bubbles are used to enhance blood tissue contrast in ultrasound imaging, thereby improving the quality of blood vessel imaging in ultrasound examinations [50]. Therefore, controlling the stability of bubbles within the bloodstream prolongs their lifespan compared to unstable bubbles, consequently extending the duration of imaging.

In the third part, the translational motion of a bubble and bubble-bubble interactions (Sections 3.3, 4.6.1 and 4.6.2) are studied. The effects of bubble-bubble interactions are investigated which is crucial for understanding the bubble dynamics for therapeutic applications. These interactions enable microbubbles to cluster at specific sites, thereby concentrating drug release. Properly managed interactions also help obtain constant bubble size which prevents premature rupture and ensures microbubbles reach their destination intact. Furthermore, minimizing acoustic shadowing through controlled spacing improves ultrasound imaging which allows more accurate guidance and real-time drug delivery monitoring.

In the fourth part (Sections 3.4 and 4.7), acoustic droplet vaporization (ADV) is studied, a promising drug delivery technique that uses ultrasound to transform liquid droplets. These droplets remain stable in the liquid state at physiological temperatures, allowing them to circulate through the bloodstream safely until they reach a targeted site. When exposed to ultrasound of sufficient intensity, the droplets rapidly vaporize and expand into gas bubbles. This phase change releases any therapeutic agents within the droplets and creates bubbles

that oscillate under ultrasound, enhancing therapeutic effects and enabling precise control of drug delivery. For instance, perfluorocarbon droplets can be loaded with chemotherapy agents and administered into the bloodstream. Once they accumulate near the tumor site, a focused ultrasound beam is applied, causing the droplets to vaporize into gas bubbles. The expansion of these bubbles disrupts tumor tissue, improving drug penetration and allowing chemotherapy drugs to enter cancer cells more effectively named as sonoporation. Sonoporation temporarily opens cell membranes, increasing drug uptake by the cancer cells and enhancing the therapeutic impact without increasing the drug dosage, thus reducing systemic side effects.

This dissertation starts with the Literature Review Section (Section 2), which reviews different nanocarrier types (Section 2.1.1), the biological barriers (Section 2.1.2), drug targeting strategies (Section 2.1.3), the properties of ultrasound and acoustic cavitation (Section 2.1.4), the biophysical effects (Section 2.1.5), and the applications (Section 2.1.6). In the second part of the Literature Review, Section 2.2, fundamental mathematical models are examined, which are essential for understanding bubble oscillations under the influence of an acoustic field. It is important to understand the effects of microbubbles and ultrasound in both in vivo and in vitro experiments, particularly for microbubble-mediated ultrasound therapy. This section reviews theoretical models that help analyze and predict the behavior of microbubbles under varying conditions. It begins by covering the basics of free-gas bubble dynamics (Section 2.2.1), followed by models for encapsulated bubbles (Section 2.2.2), bubbles in confined liquids (Section 2.2.3), and the shape stability of individual bubbles (Section 2.2.5). It concludes with a review of relevant numerical studies (Section 2.2.4).

In Section 3, the physical system and corresponding models are presented. This section is divided into four key parts: spherical oscillations (Section 3.1), non-spherical oscillations (Section 3.2), translational motion and bubble-bubble interactions (Section 3.3), and the model for acoustic droplet vaporization (Section 3.4). Section 3.1 begins with the simplest scenario—a bubble in an unbounded liquid—includes effects from encapsulation and elastic solid. Section 3.2 explores the non-spherical oscillations of a bubble, including encapsulated bubbles, within an unbounded power-law liquid. In Section 3.3, the translational

motion of a single encapsulated bubble in an unbounded viscoelastic is analyzed, followed by the introduction of the influence of a second bubble. Section 3.5 outlines the numerical solution procedures and discusses the key challenges for accurately modeling dynamic bubble oscillations.

In the Results and Discussion Section (Section 4), the model and equations are first validated (Section 4.1). Then, the suitability of the Rayleigh-Plesset equation (Section 4.2) and the ideal gas law (Section 4.3) are tested. After confirming the model's accuracy, the section discusses the findings related to spherical oscillations (Section 4.4), non-spherical oscillations (Section 4.5), bubble-bubble interactions (Section 4.6.1) and acoustic droplet vaporization (Section 4.7). The final section, Section 5, provides a conclusion for the studies.

2. LITERATURE REVIEW

The literature review delves into two parts: the description of ultrasound and microbubble treatment with biological effects (Section 2.1), and the modeling techniques employed for these applications (Section 2.2).applications (Section 2.2).

2.1. Ultrasound and Microbubble Treatment

Targeted drug delivery aims to mitigate the side effects of conventional therapeutic approaches. Drugs are encapsulated within nanoparticles which are known as nanocarriers to achieve this goal. Nanocarriers can be guided to specific sites within the body. However, biological barriers hinder the efficient delivery of these nanocarriers to their target sites. Various targeting strategies and nanoparticle formulations are employed to overcome these challenges. A novel approach to drug targeting involves the use of ultrasound-mediated microbubbles. Oscillation of microbubbles enhances endothelial barrier permeability and results in increased drug uptake at the target site. Consequently, this innovative technique allows for reduced drug doses and minimizes the side effects. In this section, the nanocarriers (Section 2.1.1), biological barriers (Section 2.1.2), targeting strategies (Section 2.1.3), ultrasound properties (Section 2.1.4), biophysical effects (Section 2.1.5) and cavitation applications (Section 2.1.6) are reviewed.

2.1.1. Therapeutic Nanocarriers for Drug Delivery

Targeted therapy involves the delivery of an appropriate dose of therapeutic agents to the target site. One strategy for achieving targeted therapy is developing safe and efficient therapeutic nanocarriers. The shape, composition and size of these nanocarriers play a crucial role in maximizing drug-carrying capacity. Delivering precise amounts of drug to target cells enhances therapeutic efficacy and minimizing toxicity. However, a significant challenge in targeted therapy lies in effectively delivering therapeutic agents to the desired site. The primary reason of this challenge is due to the poor distribution of nanocarriers in the

bloodstream and the lack of selectivity of the drug molecules.

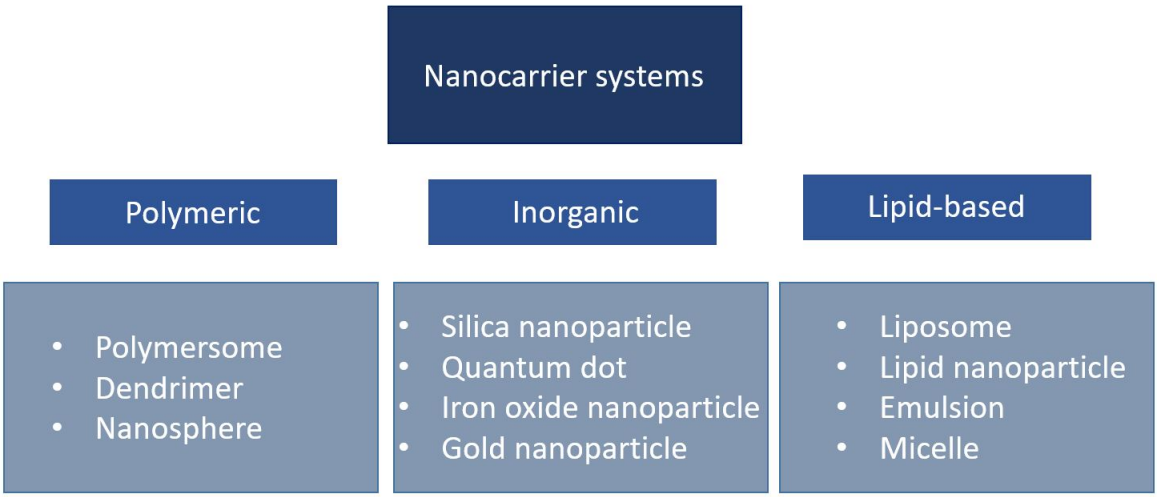

Figure 2.1. Nanocarrier systems for delivering drugs. Reproduced with permission from Kaykanat and Uguz, Biomicrofluidics, 17, 021502, (2023) permission from AIP Publishing [2].

Overcoming biological barriers represents the primary challenge in clinical applications of drug delivery systems. To address this challenge, various types of nanocarriers have been proposed. This section overviews these nanocarrier types [51–57]. As illustrated in Figure 2.1, polymeric, inorganic, and lipid-based nanocarriers are the most commonly utilized drug carriers.

The initial category is the polymeric nanocarriers. Polymeric nanocarriers can be created from either natural or synthetic materials such as monomers or preformed polymers. Within polymeric nanoparticles, the primary classifications include dendrimers, polymersomes and nanospheres. Polymersomes, consisting of amphiphilic block copolymers, form the bilayer structure of the nanocarrier. Zheng et al. [58] studied the construction of polymersomes using grafted polyphosphazenes as a novel carrier for delivering water-soluble anticancer drugs. Shae et al. [59] utilized pH-responsive polymersomes for delivering a cancer vaccine. Dendrimers represent another type of polymeric nanocarrier which are characterized by highly branched, nanoscale symmetric molecules. Nigam and Bahadur [60] explored the production and properties of cationic and biocompatible peptide dendrimers, which were used to stabilize and functionalize magnetite nanoparticles for cancer treatment. They inves-

tigated the release profiles of dimethoxyamphetamines (DOX) from dendritic nanoparticles under acidic conditions over 48 hours. It is observed that approximately 70% cumulative drug release for peptide dendrimers and 10% for poly(amidoamine) dendrimers after 15 hours [60] are obtained. Amreddy et al. [61] investigated the efficacy of anti-cancer drugs for lung cancer treatment. They engineered dendrimers with targeting ligands to interact with various surface receptors, such as the folate receptor alpha, highlighting the necessity for tailored drug delivery systems to encapsulate different agents, like a combination of small interfering RNA (siRNA) and chemotherapy.

The second category encompasses inorganic nanoparticles synthesized from metal-based materials such as quantum dots, silica, gold and iron. These nanoparticles are administered locally via injection, and external forces like magnetic fields are utilized for their manipulation. Mesoporous silica nanoparticles show considerable potential as nanocarriers for targeted drug delivery due to their enhanced intrinsic stability and biocompatibility as noted in recent research [62]. Quantum dots are another example of inorganic nanoparticles. They are artificially prepared semiconducting clusters of atoms. They were initially developed by Texas Instruments Incorporated in the 1980s [63] and have found diverse applications which include cancer diagnosis and therapy [64]. Gold nanorods showed potential in cancer treatment when irradiated with a continuous near-infrared laser at 800 nm [65]. Investigations into the in vivo tumor suppression effects of gold nanorods have been conducted, with results showing tumor disappearance after ten days of treatment [66].

The third category is the lipid-based nanocarriers which typically consist of spherical structures. These stuctures comprise a lipid bilayer encapsulating an internal aqueous core. Lipid-based nanocarriers include various types, such as liposomes, lipid nanoparticles, emulsions, and micelles, as illustrated in Figure 2.1. Liposomes, for instance, are spherical vesicles with a lipid bilayer membrane surrounding an aqueous core. These can be composed of either synthetic or natural lipids, and a notable application is the delivery of Doxorubicin using PEGylated liposomes for treating Kaposi's sarcoma in AIDS patients, aimed at minimizing opsonization and thereby increasing circulation time in the bloodstream [67].

Other clinically used examples of liposomes include Daunosome and Myocet, which exhibit shorter circulation times in the blood without PEG coating [68]. Doxil is another FDA-approved liposomal formulation. It is utilized for treating recurrent ovarian and breast cancer [69, 70]. The pH-sensitive liposomes have been developed as nanocarriers for efficient drug delivery in non-small-cell lung carcinoma recently, addressing the critical need in lung cancer treatment [71]. Lipid nanoparticles are extensively employed for nucleic acid delivery which resemble liposomes but with micellar structures in their particle cores. These structures are different from liposomes due to the presence of micellar structures. Another lipid-based nanocarrier is the nanoemulsion system, which can effectively encapsulate drugs. Studies have demonstrated the concentration of nanocarriers in breast carcinoma upon injection of lipid nanoemulsions that suggest a promising avenue for the breast cancer treatment [72]. Nanoemulsions containing anticancer drugs have been investigated with the potential for selective drug release under ultrasound-induced droplet-to-bubble transitions. These transitions provide enhanced contrast at tumor sites [73, 74]. Challenges may arise in using perfluoropentane because of its low boiling point. Lipid-based micelles represent another type of this group as demonstrated by Gao et al. [75]. Initial reports show a higher accumulation in tumors in mice. These poly(ethylene glycol)-diacyl lipid micelles exhibited high stability which show a significant portion of associated drugs such as porphyrin, tamoxifen, and taxol after incubation, suggesting their potential as stable drug carriers.

Table 2.1. Recent Food and Drug Administration-approved nanomedicines [14, 15].Reproduced with permission from Kaykanat and Uguz, Biomicrofluidics, 17, 021502, (2023) permission from AIP Publishing [2].

Type	**Drug**	**Application**	**Date of first approval**
Lipid-based	Onpattro	Transthyretin-mediated amyloidosis	2018
Polymer-based	Adynovate	Haemophilia	2015
Inorganic	Injectafer	Iron-deficiency anaemia	2013

2.1.2. Biological Barriers for Drug Delivery

It is crucial to understand the biological barriers and their impact on drug transport when a novel nanoparticle-based drug delivery system is developed.

Biological barriers pose a significant challenge for nanocarriers in transporting drugs efficiently to the target area as depicted in Figure 2.2. Therapeutic nanocarriers encounter the intravascular barrier, specifically the mononuclear phagocyte system, when they enter the bloodstream when they enter the bloodstream. This system comprises extracellular proteins known as opsonins, which form blood barrier. These opsonins bind to their surface when they are in contact with nanoparticles. Consequently, the nanocarriers become more recognizable to macrophages, which promptly identify and eliminate them before they can reach the tumor tissue. This biological mechanism is named opsonization and significantly decreases therapeutic effectiveness [76, 77].

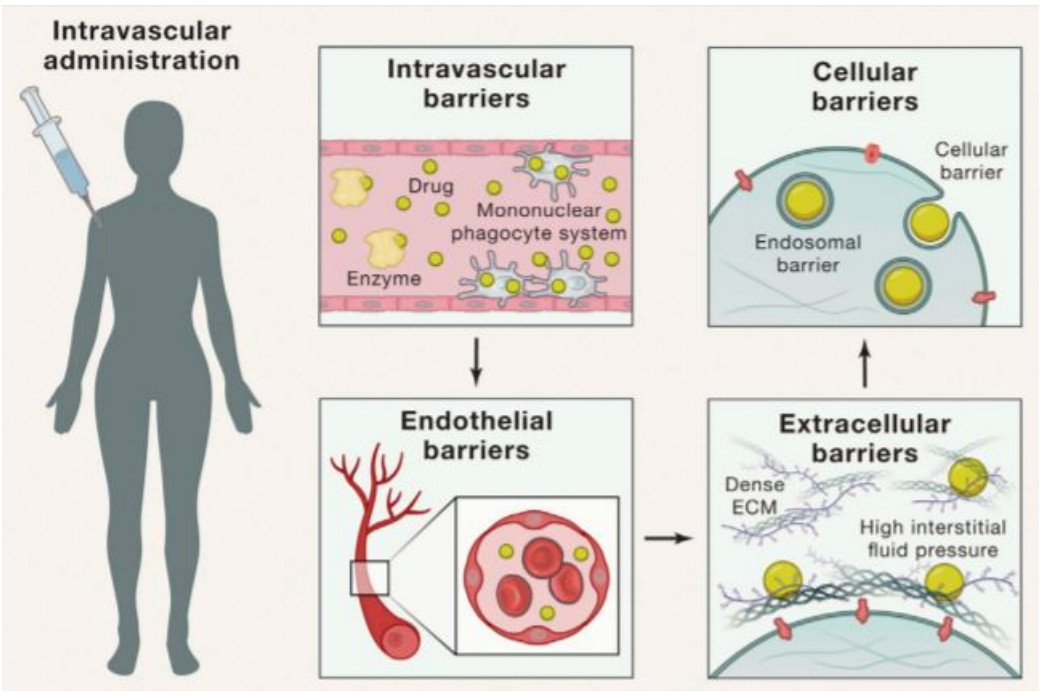

Figure 2.2. Biological barriers for targeted drug delivery [3] Reproduced with permission Zhao et al., Cell, 181, 151–167, (2020) permission from Elsevier.

Nanocarriers face the endothelial barrier after overcoming the intravascular barrier. The endothelial barrier is a semi-permeable cellular layer lining the inner walls of blood vessels. This barrier prevents the extravasation of nanocarriers to their intended target site. For instance, the endothelial layer exhibits high restrictiveness due to the dense population of endothelial cells and tight junctions between these cells, effectively preventing extravasation.

Solid tumors consist of tumor cells, stromal elements, extracellular matrix (ECM), vasculature, and immune cells. Nanocarriers navigate through the ECM, often called the extracellular barrier, when nanocarriers traverse the endothelial barrier, The ECM comprises a complex network of collagen, glycosaminoglycans, microfibrillar elastins, and proteoglycans, which form a cross-linked gel-like structure. This viscous nature of the extracellular space, or interstitium, limits fluid flow and restricts the diffusion of nanocarriers from the bloodstream toward the targeted cells. Within the tumor microenvironment, the ECM is characterized by poorly functioning vasculature, leading to elevated interstitial pressure, typically ranging between 10 to 40 mmHg across various tumor types. High interstitial pressure serves as a significant barrier to drug delivery, particularly for macromolecular drugs reliant on convective transport. Subsequently, nanocarriers penetrate the cellular barrier to release the drug within the cell membrane, marking the onset of the cellular barrier. Nanoparticles cannot passively diffuse into cells; instead, they undergo internalization through endocytic processes, including phagocytosis, pinocytosis, or endocytosis. The characteristics such as size, shape, and charge of nanocarriers can influence this internalization process.

After crossing the endothelial barrier by extravasation, the nanoparticles pass through the tumor microenvironment. The tumor vascular has an abnormal structure, which includes dead ends, unusual branches, and uneven distribution of blood vessels [76–79]. These structures create a highly heterogeneous vascular network, resulting in high vascular resistance. Due to the poorly functioning vasculature with high interstitial pressure, the dense tumor extracellular matrix limits the penetration of the nanoparticles.

By coating nanoparticles with a hydrophilic polymer, e.g., poly(ethylene glycol, the opsonization can be minimized to mitigate the effect of opsonins [80, 81]. The charge,

size, and shape of the nanoparticle affect the opsonization, which also affects the circulation time of the nanoparticle. The particle size, shape, surface charge, and hydrophobicity affect the endocytosis [82]. For instance, the cell membrane is negatively charged. So, positively charged nanoparticles quickly enter the cell membrane instead of negatively charged nanoparticles. Small (less than 10 nm) nanoparticles quickly enter the cell membrane.

2.1.3. Targeting Strategies for Drug Delivery

Nanocarriers encounter distinct biological barriers upon injection into the body, as discussed in Section 2.1.2. Various approaches are employed to overcome these barriers, which aim to enhance the accumulation and retention of nanocarriers in the desired site. Presently, three targeting strategies are utilized. The first strategy is passive targeted drug delivery, recognized as the enhanced permeability and retention effect (EPR effect). The second strategy, active targeted drug delivery, involves delivery systems conjugated with specific ligands. In the third strategy, active triggered targeting, external fields or physical stimuli are applied to the target area to augment drug accumulation (Figure 2.3).

If a nanoparticle is more significant than 10 nm, it cannot transfer healthy vessels due to the presence of continuous endothelial cells. Endothelial permeability increases under pathological conditions such as inflammation, infarcts, and tumor development. This phenomenon is known as the EPR effect which results in the preferential accumulation of molecules of specific sizes, such as nanoparticles, liposomes, and macromolecular drugs [83–85]. This targeting mechanism is termed passive targeting, and its success is closely tied to the circulation duration of the nanocarrier in the bloodstream. The charge of nanoparticles influences their stability and distribution in the blood. For instance, positively charged nanoparticles exhibit excellent stability in the bloodstream, while neutral nanoparticles demonstrate improved tissue diffusion after extravasation from tumor vessels [86–88]. Charge-conversion strategies aim to alter the nanoparticle charge at the target site in response to environmental stimuli, such as the pH of the site [89]. Yuan et al. [90] developed zwitterionic nanoparticles containing Doxorubicin which increases the nanoparticle circulation time in the bloodstream. The surface's anionic component switches to a positive charge and extravasates into tumor

microenvironments with pH levels around 6.8. Nanoparticle shape and coating material impact passive targeting efficiency. Studies indicate that rod-shaped nanoparticles exhibit superior cellular uptake compared to spheres, cylinders, and cubes [87, 91]. Parveen et al. [92] observed that PLGA coated nanoparticles with poloxamer 188 reduces macrophage uptake.

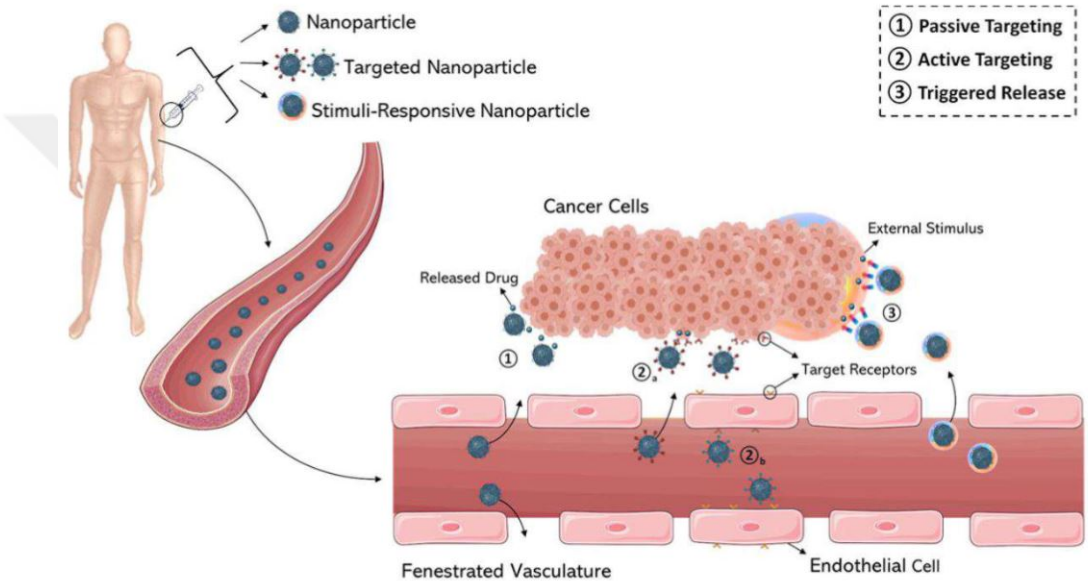

Figure 2.3. Sketch of drug targeting approaches. (1) Passive targeting of nanocarriers. (2a) Active targeting of cancer cells and tumor endothelium using (2b) ligand-modified nanocarriers. (3) Stimuli-responsive nanocarriers, releasing drug by internal or external triggers. Reproduced with permission from Gagliardi et al. Front. Pharmacol., 12, 601626, 2021 [4]. Author(s), licensed under Creative Commons CC BY license.

Active targeting is the second approach, which involves attaching a ligand to the surface of nanoparticles. This mechanism relies on the interaction between the nanoparticle's ligand and specific cell surface receptors or antigens on tumor cells. Active targeting of drug-loaded nanocarriers addresses the limitations of passive targeting by enhancing the nanoparticle's specificity to a particular site. Consequently, active targeting leads to increased drug accumulation in tumor cells, thereby reducing side effects associated with chemotherapy compared to passive targeting [93]. Watanabe et al. [94] investigated folate-polymer-coated liposomes for the targeted delivery of Doxorubicin, which resulted in a twofold increase in

cytotoxicity with Doxorubicin-loaded folic acid-conjugated liposomes. Similarly, Rana et al. [95] developed Fe_3O_4 magnetic nanoparticles conjugated with folic acid to deliver Doxorubicin which results in a threefold increase in drug accumulation in tumor cells. Transferrin, a blood plasma glycoprotein, serves as another example of a ligand. Sahoo and Labhasetwar [96] demonstrated that transferrin ligand-conjugated poly(lactic-coglycolide) nanoparticles enhance efficacy in breast cancer cells. Yang et al. [97] illustrated the synthesis of estrone-modified glycol chitosan nanoparticles for paclitaxel (PTX) delivery, showing higher PTX accumulation (81.4%) in breast cancer cells compared to pure PTX (48.8%) in mice. Additionally, Cadinoiu et al. [41] explored the formulation of liposomes with aptamer ligands to treat basal cell carcinoma, which resulted in approximately 40-fold higher overexpression of the biotin receptor in hepatocellular carcinoma cells compared to normal liver cells. The advantages and disadvantages of different ligand types are given in Table 2.2.

The final strategy for drug targeting is active triggering [98–100]. Triggers can be either internal, such as pH variations in different microenvironments, or external, including temperature, ultrasound, magnetic fields and ultraviolet/near-infrared radiation [98]. Nanocarriers can be engineered to respond to these stimuli, enabling enhanced drug release at precise locations. The tumor microenvironment differs significantly from normal tissues which exhibit distinct enzyme expression levels and an acidic pH environment [101–103]. Tumor tissues typically have lower pH values than blood and normal tissues (7.4), with even lower values observed in acidic cellular environments (4.5-5.0 for lysosomes and 5.5-6.0 for endosomes) [104]. Moreover, pH values vary widely across different segments from pH 5.5–6.8 in the small intestine to pH 6.4-7.0 in the colon and pH 1.5-3.5 in the stomach [105]. Therefore, pH-sensitive nanocarriers can be utilized for triggered targeting. For instance, Zhang et al. [106] investigated the in vitro release of Doxorubicin from micelles which release rates due to pH differences between tumor and healthy tissues. Drug release from micelles was assessed using a dialysis bag immersed in phosphate-buffered saline solutions with varying pH values (5.0, 6.5, or 7.4). Drug concentration analyzed via UV spectrophotometry. Results indicated significantly accelerated drug release when the pH environment shifted from 7.4 to 5.0. Similarly, Zhao et al. [107] demonstrated excellent anti-tumor efficacy of micelles with folate-mediated cancer targeting and pH-triggered intracellular drug delivery. Different drug

loading contents of mixed micelles were studied, with the 20:80 mixed micelles showing reduced drug release at pH 7.4 compared to pure micelles.

Another method to govern drug release is by increasing the temperature of the tumor environment. This stimulus can be either extrinsic, such as local application of heat, ultrasound, or light, or intrinsic, leading to hyperthermia. Nanocarriers release drugs at locations with elevated temperatures, such as 41°C at tumor cells, exceeding the body's physiological temperature of around 37°C. Thermosensitive liposomes represent a recent example of thermal drug delivery applications [108–110].

Table 2.2. Positive aspects and drawbacks of the ligands. Reproduced with permission from Kaykanat and Uguz, Biomicrofluidics, 17, 021502, (2023) permission from AIP Publishing [2].

Type	**Ligands**	**Binding place**	**Advantages**	**Disadvantages**
Peptides [111–113]	RGD, IL4Rep-1	Extracellular matrix	Easy fabrication Small size	Cleavable by peptidase
Aptamers [114, 115]	AS-1411, GB1-10	Nucleolin	High specificity Small size	Cleavable by nuclease, High cost
Proteins [116–118]	Antibodies, transferin	Breast cancer cell, Transferin receptor	High specifity	Large size, Low stability
Folate [119]	Folic acid	Folate receptor	Non-toxicity Small size	Insufficient folate receptor in liver, pancreas, prostate, testicles and bladder cancer cells

Liu et al. [108] developed liposomes incorporating gold nanorods and manganese-doped magnetism-engineered iron oxide nanoparticles for efficient photothermal therapy and magnetic resonance imaging. These liposomes remain stable at physiological temperatures and release drugs upon laser irradiation, with minimal morphological damage observed in normal tissues of treated mice.

Ultrasound represents another external stimulus for controlled drug release [120]. It induces transient or permanent pores on the walls of blood vessels, thereby enhancing the extravascular delivery of therapeutics. In early ultrasound applications, acoustic intensities of up to 3000 W/cm^2 were utilized [121–123]. Lower ultrasound intensities ranging from 0.2 to several W/cm^2 result in a slight temperature increase (from 41^o to 45^{o}C) and increase the cytotoxicity of chemotherapy [123–126]. The details of of therapeutic applications of ultrasound are given in Section 2.1.6.1.

An external magnetic field is also employed to direct the drug carrier. The magnetic carrier nanoparticle system typically features a core-shell structure where the core consists of magnetite (Fe_3O_4) or maghemite (Fe_2O_3). At the same, the shell is composed of a polymer, lipid, or mesoporous silica. Widder et al. investigated gene and drug delivery systems based on fine magnetic nanoparticles and microparticles [127, 128]. Doxorubicin is conjugated to magnetic particles and directed towards sarcoma tumors İn numerous animal studies. Tumor size reduction is observed across various animal models which includs small animals like rabbits and rats [129, 130], as well as larger animals such as swine [131]. Alexiou et al. [132] quantified the distribution of magnetically targeted carriers in rabbits using high-performance liquid chromatography (HPLC). The results indicate complete tumor reduction with reduced chemotherapeutic doses (20% and 50% of the regular systemic dose of 10 mg/m^2) without adverse effects. Light emerges as a promising tool for therapeutic purposes due to its easy application and noninvasive nature mong the external fields previously mentioned. Consequently, light is found to be extensively used in targeted drug delivery systems for the systemic administration of therapeutic agents. For an in-depth exploration of light-triggered drug delivery, readers are directed to [133, 134]. Table 2.3 presents the advantages and disadvantages of various triggered targeting methods.

In summary, passive targeting lacks selectivity, accumulating nanocarriers in healthy areas and resulting in side effects. In contrast, active targeting, particularly active triggered targeting, offers versatility and selectivity which effectively suppressing side effects of overdoses.

Table 2.3. Positive aspects and drawbacks of the different stimuli types. Reproduced with permission from Kaykanat and Uguz, Biomicrofluidics, 17, 021502, (2023) permission from AIP Publishing [2].

Stimuli	**Advantages**	**Disadvantages**
pH [100, 135–137]	Accumulation of nanoparticles is increased.	Drug is released before reaching the target site.
Enzyme [135, 136]	EPR-effect is increased.	Drug is released before reaching the target site.
Heat [137]	Accumulation of nanocarrier is increased.	Damage may occur from external heating. Instead of intrinsic heating, a source is necessary for deep tissue penetration.
Magnetic field [98, 135]	Nanocarrier is concentrated and manipulated in target site.	Complex equipment set-up is required.
Ultrasound [100, 135]	The stimuli is non-invasive Exposure through the tissue is easy.	High intensities and long exposures could damage tissues.
Light [100, 135]	The stimuli is non-invasive, inexpensive and easy to use.	Tissue penetration is poor

When different stimuli types are compared for active triggered targeting, the major drawback of enzyme stimuli is the heterogeneous spatial and temporal patterns of enzyme activity. This causes a decrease in the drug concentration at the target area [135,136]. Similar to other external stimuli, the disadvantages of pH stimuli are the need to avoid undesired tissue damage and the low tissue penetration depth which restrict the application in therapy [100,135–137]. As observed when pH stimuli applied, the penetration depth is low (10 mm) for light-triggered drug delivery [100, 135]. In addition, external heat stimuli may cause tissue damage. An essential advantage of ultrasound in drug delivery applications is its noninvasive nature causing less trauma. It can penetrate deep into the interior of the body and can be focused and carefully controlled. On the other hand, ultrasound has enormous advantages due to its lower cost and better sensitization [138]. Especially the combined use of ultrasound and intravascular microbubbles has shown high accumulation, distribution, and therapeutic efficacy of the drug and drug carriers in tumors and the brain, as discussed in more detail in Section 2.1.6.

2.1.4. Properties of Ultrasound and Acoustic Cavitation

Ultrasound refers to a sound wave with frequencies ranging from 20 kHz to 20 MHz which travels as a pressure wave through a medium. The amplitude of this sound wave is associated with the variations in pressure from the equilibrium state.

Therapeutic ultrasound is typically defined by parameters such as negative peak pressure, frequency, pulse repetition and duration, duty cycle, and total treatment time [139,140]. Table 2.4 provides an overview of these characteristics and their definitions. Correctly selecting ultrasound parameters for a given therapeutic application is crucial, as improper settings can result in adverse effects like hemorrhage, edema, severe inflammation, ischemia, apoptosis, or necrosis. Research also indicates that these parameters affect the effectiveness of ultrasound-mediated microbubble therapy. The duration of therapeutic ultrasound is based on the time needed to achieve the desired therapeutic effect without causing harmful impacts on the body. Negative peak pressure is used to compute the safety index, which assesses the risk of cavitation. The mechanical index (MI) reflects the potential for ultrasound beams to

cause cavitation-related biological effects and is inversely related to beam frequency. According to the FDA, the MI must remain below 1.9 to ensure safe ultrasound usage [141]. Further discussion of therapeutic ultrasound's bioeffects can be found in Section 2.1.5.

Additionally, a new safety indicator is defined based on the intra-pulse detection of ultra-harmonic events. For instance, no reliable safety indicator can predict potential damage to the blood-brain barrier. Existing methods for controlling ultrasound beam intensity, such as the mechanical index, rely on full-pulse analysis and may lack sensitivity. An intra-pulse analysis is proposed to monitor the evolution of the frequency content during ultrasound bursts to overcome this limitation [142].

Therapeutic ultrasound is classified into two types based on intensity: low-intensity (0.125–3 W cm^{-2}) and high-intensity ($\geq$ 5 W cm^{-2}) applications. High-Intensity Focused Ultrasound (HIFU) produces various biophysical effects, such as increasing blood flow and enhancing vascular permeability, which facilitates better accumulation and distribution of therapeutic agents within tumors [45, 143, 144].

Acoustic cavitation refers to the process involving the formation, growth, and collapse of bubbles created by ultrasound waves. As illustrated in Figure 2.4, when microbubbles form at low ultrasound frequencies (with acoustic pressures below 50 kPa), they oscillate in size—compressing and expanding without collapsing—a phenomenon known as stable cavitation [145]. Microbubbles are generally symmetrical and display mostly linear behavior, producing low harmonic levels or broadband acoustic emissions.

Table 2.4. Properties of an ultrasound wave. Reproduced with permission from Kaykanat and Uguz, Biomicrofluidics, 17, 021502, (2023) permission from AIP Publishing [2].

Frequency	1/Period
Pulse repetition time	1/Pulse period
Mechanical index (MI)	Peak negative pressure/$\sqrt{\text{Frequency}}$
Duty cycle	(Pulse duration/Pulse period)x100

Additionally, stable cavitation exerts push-pull effects on nearby cells, triggering intracellular signaling pathways that alter membrane permeability [146]. Moreover, the tissue adjacent to the bubble can induce non-spherical oscillations, resulting in microstreaming around the bubble.

The mechanism behind cavitation damage is quite complex. The growth and collapse of bubbles occur rapidly within blood vessels. High acoustic pressure induces inertial cavitation which leads to a greater expansion of the bubble compared to its compression, as depicted in Figure 2.4. If the inertia of the surrounding fluid overcomes the gas pressure of the bubble during its collapse, the bubble's dynamic behavior becomes nonlinear [31, 32]. Inertial cavitation results in broadband acoustic emissions that generate shock waves after the bubble collapses [30, 143, 147, 148]. Microbubbles can experience significant pressure and temperature fluctuations during collapse due to their small size. Additionally, collapsing bubbles can create asymmetric fluid flow and jets when they are near a surface.

2.1.5. Biophysical Effects of Microbubble-Mediated Ultrasound Therapy

Although the exact mechanism underlying ultrasound-mediated drug delivery is still not fully understood, researchers have recognized various biophysical effects triggered by ultrasound and microbubbles, which are sonoporation and hyperthermia [149].

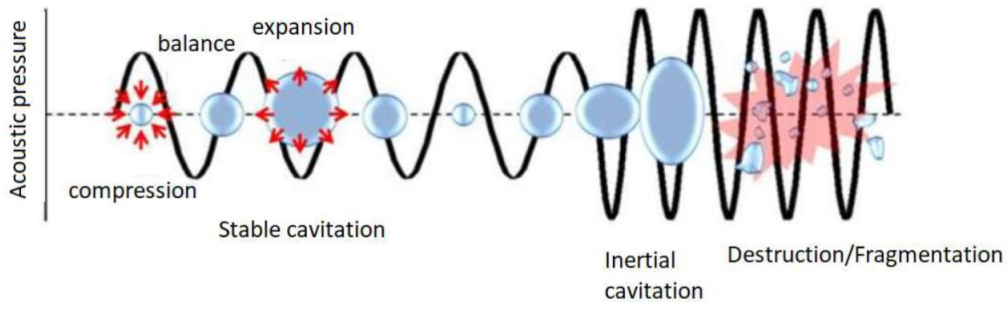

Figure 2.4. Sketch of stable cavitation and inertial cavitation [5] used under Creative Commons CC BY-NC-ND.

Sonoporation is the transient formation of pores in the cell membrane induced by an ultrasound field [25, 150–152]. Figures 2.6(a) and (b) include the electron microscope images of cells not treated and irradiated with ultrasound, respectively. When the cell is subjected to ultrasonic irradiation, transient pores are formed in the presence of the drug merocyanine 540 (Figures 2.6 (c) and (d) at different times). Transient sonoporation-induced cellular pore sizes range from approximately 30 to 100 nm to a few micrometers in diameter as shown in Figures 2.6 (c) and (d) [153]. This process increases the permeability of the cell membrane, facilitating increased intracellular transportation of drugs [153, 154]. Moreover, microbubble-mediated ultrasound therapy enhances cell membrane permeability further [30]. Oscillating microbubbles can induce pores in endothelial cell membranes through various mechanisms (as depicted in Figure 2.5). For example, stable oscillating microbubbles exert push-pull effects on the cell membrane as they cyclically expand and contract. This action triggers intracellular signaling pathways that modulate membrane permeability [146]. Additionally, as discussed in Section 2.1.4, higher acoustic pressures lead to inertial cavitation, resulting in microbubble collapse near the cell membrane. During this collapse, concentrated stress causes damage to nearby surfaces and structures.

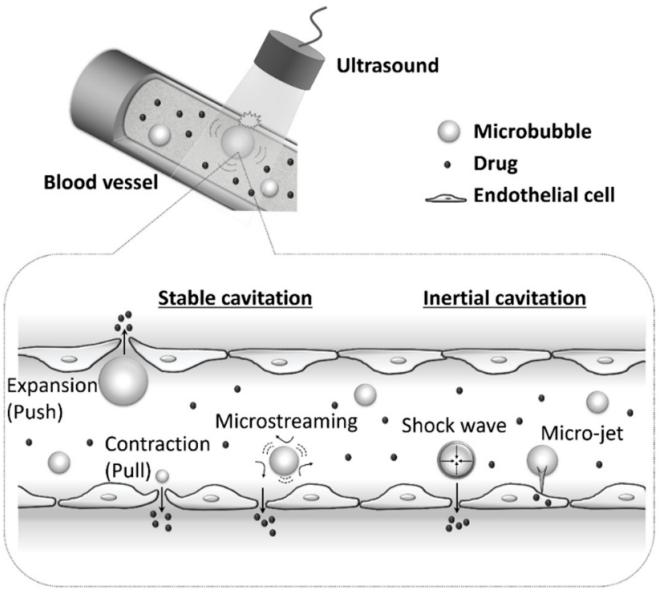

Figure 2.5. The effects of ultrasound-mediated microbubbles on permeability of cell membrane for both stable and inertial cavitations [6] used under Creative Commons CC BY.

Figures 2.7(a) and (b) show fluorescent images of cellular response induced by bubble-mediated sonoporation at different acoustic pressures where red fluorescence indicates intracellular uptake of propidium iodide (PI). The comparison of Figures 2.7 (a) ($p_A = 0.4$MPa) and (b) ($p_A = 0.2$MPa) suggests that PI uptakes are increased at higher acoustic driving pressures.

The second biophysical effect of ultrasound is hyperthermia, wherein tissue absorbs sound waves at a frequency-dependent rate. they transfer energy to the tissue in the form of both thermal and mechanical energy which causes a localized increase in temperature which is known as hyperthermia. Hyperthermia is commonly employed in conjunction with other therapies, such as chemotherapy and radiation therapy. The absorption and scattering of ultrasound result in the loss of acoustic energy [45, 143, 144]. The ultrasound wave generates radiating forces capable of causing tissue displacement and acoustic currents as the wave dissipates. Consequently, the fluidity of the phospholipid bilayer often increases, enhancing the permeability of the cell membrane and enabling nanoparticles to diffuse to the targeted area [45, 143].

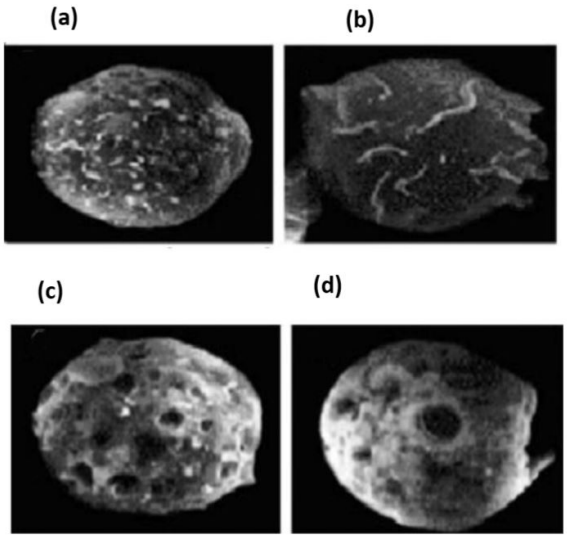

Figure 2.6. Scanning electron microscope images of HL-60 cells employing ultrasonic irradiation alone (a) or untreated (b), exposed to ultrasound in the presence of photosensitive drug merocyanine 540 (c–d). Reproduced with permission from Tinkov et al., J. Pharm. Sci., 98(6), 1935-1961, 2009 [7]. Copyright 2008 Wiley-Liss, Inc.

2.1.6. Therapeutic Applications of Ultrasound-Mediated Microbubbles

Ultrasound or ultrasound-induced-microbubble-cavitation serves dual purposes: transporting drug molecules to specific areas using microbubbles and enhancing the permeability of biological barriers such as the ECM (Extracellular Matrix), as discussed in Section 2.1.1. This section provides an overview of therapeutic ultrasound applications and ultrasound facilitated by microbubbles.

2.1.6.1. Therapeutic Ultrasound Applications. Aside from its diagnostic purposes, ultrasound finds application in therapeutic applications such as disintegrating kidney stones, treating Parkinsonian tremors, tumor ablation, and enhancing drug delivery to targeted areas while minimizing drug dosage and toxicity [33, 155–158].

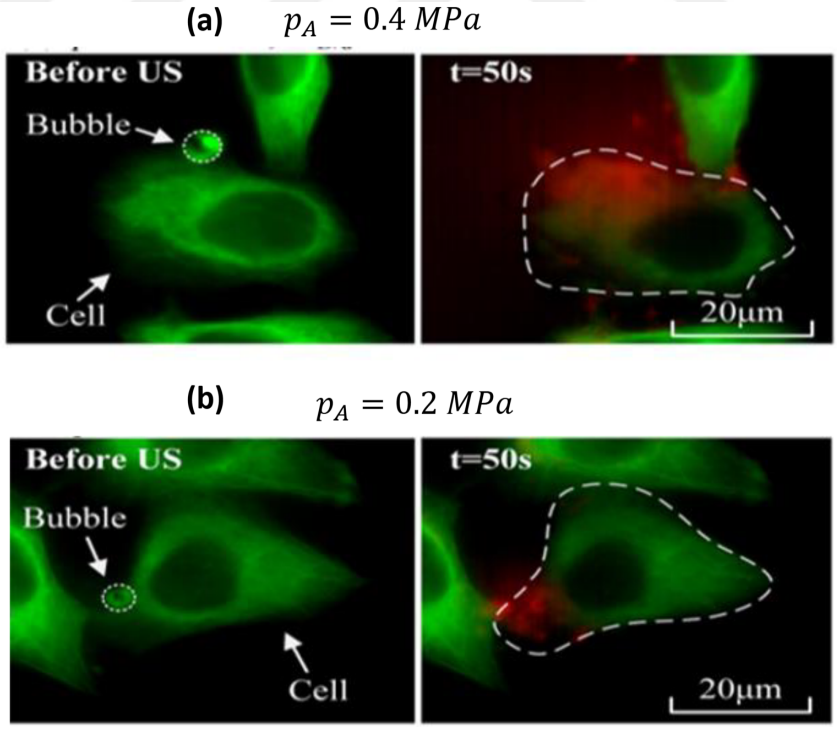

Figure 2.7. Fluorescent images before (t=0) and after (t=50 s) sonoporation with different acoustic pressures p_A (a) $p_A = 0.4$ MPa and (b) $p_A = 0.2$ MPa. Reproduced with permission from Wang et al. Sci. Rep. , 8(1), 1-12, 2018 [8]. Author(s), licensed under a Creative Commons Attribution (CC BY) License.

In recent years, different ultrasonic devices have been developed for therapeutic applications. A typical ultrasound device comprises components like a transducer, transmitter, compensating amplifiers, pulse generator, digital processors, a control unit for focusing and display systems [159]. Clinical settings commonly employ catheter-based and magnetic resonance imaging (MRI)-guided focused ultrasound techniques. Therapeutic ultrasound was primarily employed for treating soft tissue injuries, where healing is facilitated through tissue heating. High-intensity fields are utilized for thermal ablation of the targeted area, while low-intensity fields aid tissue repair without causing substantial temperature increases. Ultrasound has also been used to treate Ménière's disease, wherein a high-intensity beam is directed into the lateral semi-circular canal of the ear. This beam aims to damage the cristae's sensory neuro-epithelium [160].

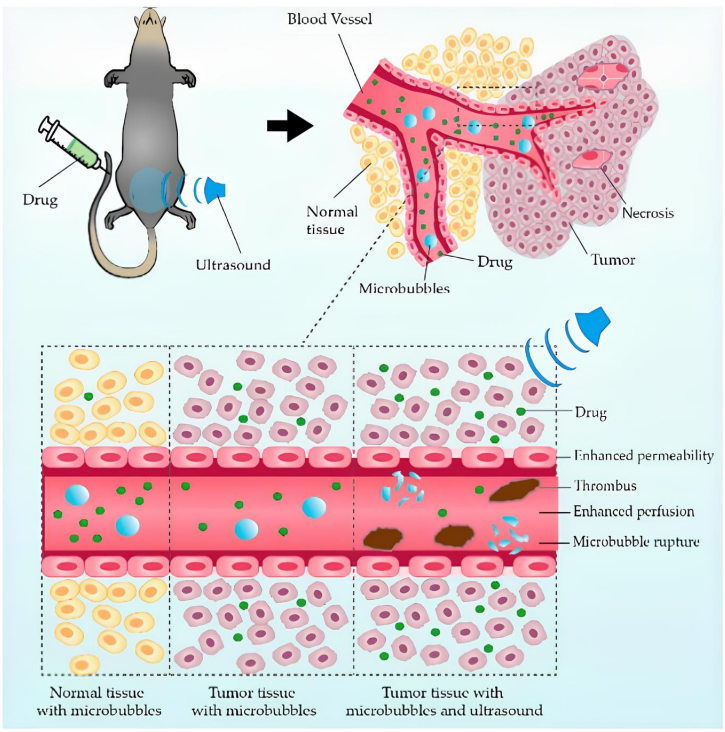

Figure 2.8. Sketch of a drug delivery system with ultrasound-mediated microbubble. Ultrasound-mediated microbubbles can increase blood–tumor barrier permeability and vascular perfusion, significantly improving the diffusion of agents (top right and bottom). Reproduced with permission from He et al. Pharmaceutics, 14(8), 1642, 2022 [9]. Author(s), licensed under a Creative Commons Attribution (CC BY) License.

Focused Ultrasound Surgery (FUS) was initially explored as a method to reduce brain tissue volumes and treat Parkinson's disease, although this approach has been supplanted by L-dopa drug therapy. Moreover, FUS has demonstrated efficacy in stopping bleeding, such as in cases of hepatic trauma. There is growing interest in employing FUS in urology, particularly for addressing benign prostatic hyperplasia (BPH). In this application, selected volumes of the prostate are targeted for ablation using FUS to decrease BPH symptoms.

The concept of utilizing ultrasound for cancer therapy was initially introduced in 1933 concerning Ehrlich's carcinoma. The earliest clinical documentation of its application in cancer treatment dates back to 1944. Furthermore, ultrasound serves as a heat source for hyperthermic cancer therapy. Various sources including phased arrays, curved transducers, lens systems and mirror systems have been developed to generate heat over a wide body area. Tumor regions located up to 12 cm beneath the skin surface can be effectively ablated using this method, with surrounding healthy tissue remaining unharmed during the process. A summary of the historical progress of therapeutic ultrasound is given in Table 2.5.

2.1.6.2. Microbubble Cavitation Applications. Recent notable progress in ultrasound and microbubble technology has been combined to enhance the permeability of blood vessel walls. This development enables oscillating microbubbles to serve as either drug carriers (Figure 2.8) or enhance the sonoporation effect for drug delivery purposes.

Table 2.5. An overview of the historical development of therapeutic ultrasound. Reproduced with permission from Kaykanat and Uguz, Biomicrofluidics, 17, 021502, (2023) permission from AIP Publishing [2].

Year	**Application**
1950s	Ménière disease: Destruction of the vestibular nerve [161]
1960s	Parkinson's diseases: Destruction of the localized tissue in the brain [162]
1970s	Physiotherapy and neurosurgery [37]
1970s	First chemotherapy and ultrasound report [44]

Employing ultrasound-mediated microbubbles represent an innovative approach for delivering drugs and genes to diverse tissues. There are three primary methods for incorporating drugs into microbubbles which are attaching drug molecules onto the shell of a microbubble, encapsulating drugs within the microbubble's core through chemical bonding like avidin-biotin interaction and utilizing adhesion forces between molecules. Additionally, electrostatic forces can facilitate the loading of drug molecules onto the surface of microbubbles.

For biomedical applications, microbubbles must be less than 10 nm in diameter so they do not block blood flow and can smoothly flow through the vasculature [147]. The gas part of the bubble is an inert high molecular weight gas, which has low blood solubility; hence, the circulation time of the microbubble in the bloodstream is increased. Furthermore, the shell of the bubbles increases the lifetime of the bubble in the bloodstream by providing stability and resistance. After the collapsing or destruction of the bubble, the shell material of the bubble is metabolized by the liver, and the gas core is exhaled through the lungs [163]. The loading capacity of drugs into the shell of lipid-stabilized microbubbles was investigated by Unger et al. [164]. They developed acoustically active lipospheres similar to lipid microbubbles containing a dense oil layer. Approximately 15 mg of paclitaxel was loaded into 1 mL of microbubble suspension (with a concentration of 10^9 bubbles/mL). Their findings revealed that 30% of healthy cells experienced apoptosis following ultrasound exposure. Bekeredjian et al. [165] explored the impact of the luciferase enzyme on drug loading into the lipid shell of microbubbles under ultrasound influence. Their rat-based experiments demonstrated that ultrasound-targeted microbubble destruction significantly enhanced the organ-specific delivery of proteins. Skachkov et al. [166] examined the impact of targeted microbubbles on the sonoporation of endothelial cells using live chicken embryos. The bubbles were subjected to sonication at frequencies of 1 MHz and peak negative sound pressures of 150 and 200 kPa. They found that endothelial cell uptake accounted for 48% of microbubble-vessel-wall complexes at 150 kPa and 33% at 200 kPa. McDannold et al. [167] demonstrated that as pulse length is increased from 0.1 to 10 ms, the degree of the brain-blood barrier permeability also increases. Microbubbles can be loaded intravenously through the blood vessel (injected into the tissue just under the skin) in a small bolus or as a dilute continuous infusion or they are

formed spontaneously by ultrasound (endogenous). They can also be loaded in an emulsion form (a fine dispersion of perfluorocarbon droplets) [31]. Microbubbles will remain in the body for a certain period. During that time, ultrasound waves are directed toward the target area. Endogenous microbubbles already exist within tissues, e.g., gaseous pockets. When the applied acoustic pressure exceeds a specific value, i.e., cavitation threshold, nuclei can be activated. The cavitation threshold depends on the frequency of the ultrasound. The advantageous part of this method is non-toxicity. Both endogenous and exogenous microbubbles can increase the permeability of the cell membranes through the formation of pores on the membrane. However, the exogenous microbubbles cannot be obtained steadily. [168]. Moreover, Xing et al. combined nanomedicine and ultrasound-mediated microbubble destruction techniques to enhance the therapeutic effect on the pancreatic cancer [169]. This study showed that three-block copolymer methoxy polyethylene glycol-polylacticco-glycolic acid-polylysine nanoparticles, combined with ultrasound-mediated microbubble treatment, substantially enhance the cellular uptake in vitro and drug retention in vivo studies in the pancreatic cancer treatment. Wang et al. [170] examined the tolerability of combining ultrasound-triggered microbubble destruction with chemotherapy. The study encompassed 12 patients, with 11 exhibiting metastatic hepatic tumors and 1 with a pancreatic tumor. The principal objective was to assess the safety threshold of the procedure concerning the MI range (0.4-1), with no instances of serious adverse effects documented. Tables 2.6 and 2.7 summarize both in vitro and in vivo investigations into ultrasound-mediated microbubble (UMBS) therapy. These tables outline the cell culture types or cancer varieties, drugs utilized, characteristic features of the ultrasound beam, and the principal conclusions obtained from the experiments.

As discussed in Section 2.1.4, under high acoustic pressures, microbubble interaction can influence cavitation and sonoporation, thereby impacting drug delivery. Decreasing the distance between microbubbles increase the microbubble lifespan [171, 172]. Arora et al. [173] demonstrated in vitro that reducing microbubble concentrations from 30 to 3 microbubbles/mL diminishes the maximum size of microbubble clusters and prolongs the cavitation duration of the cluster.

Ultrasound-targeted microbubble is also a novel therapy to deliver genes to organs. One of the main challenges in gene delivery has been developing a delivery system that is consistently safe for clinical applications. A recently developed approach to overcome this obstacle is using an ultrasound-guided microbubbles delivery system. DNA is bounded by the microbubbles, and ultrasound is applied to the target area, the ischemic myocardium [174–176]. Cavitation microbubbles can also be used for urinary stone treatment. Cavitation releases energy, producing high-speed micro jets with significant erosion capabilities that can break apart urinary stones [177–179]. To specifically target and treat urinary stones, Ramaswamy et al. [180] suggested using microbubbles within the urinary tract or kidneys, allowing the bubbles to gather on the exposed surfaces of the stones. Once accumulated, these microbubbles can be activated by an energy source (such as ultrasound) to mechanically erode, pit, and fragment the stones, effectively treating urinary stones with ultrasound-driven microbubbles [181].

Table 2.6. In vitro experiments of ultrasound-mediated microbubbles (UMBS). Reproduced with permission from Kaykanat and Uguz, Biomicrofluidics, 17, 021502, (2023) permission from AIP Publishing [2].

Cell culture type	**Drug**	**Characteristics of the ultrasound**	**Drug+UMBS vs. Drug alone**
Glioblastoma astrocytoma	Doxorubicin	1 MHz, 600-800 kPa	cell viability is 2.5 fold higher for UMBS [182]
Retinoblastoma	Doxorubicin	1 MHz, 0.3-1 W/cm^2	cell viability is 4% higher for UMBS [183]
Breast cancer cell	Taxol	0.5-2.5 MHz, MI 0.1-2.0	50% increase in cancer cell death with UMBS [184]
Head and neck squamous cell carcinoma	Cisplatin, Cetuximab	1 MHz, MI 0.5	26% decrease in tumor size [185]
Thyroid adenocarcinoma	Cisplatin	5 MHz, 6.3 and-1.2 MPa	After 24 days, tumor volume is 65% lower for UMBS [186]

Table 2.7. In vivo experiments of ultrasound-mediated microbubbles (UMBS). Reproduced with permission from Kaykanat and Uguz, Biomicrofluidics, 17, 021502, (2023) permission from AIP Publishing [2].

Animal, Cancer type	**Drug**	**Characteristics of the ultrasound**	**Drug+UMBS vs. Drug alone**
Rat, Brain cancer	1,3-bis(2-chloroethyl) -1-nitrosourea	1 MHz, 0.62 MPa 10 ms	Drug delivery increased 2 fold. Tumor growth suppressed [187].
Rat, Brain cancer	Doxorubicin	1.7 MHz, 1.2 MPa, 10 ms	Tumor growth reduced [188].
Rabbit, Liver tumor	Docetaxel	300 kHz, 2 W/cm^2 1,4,7 day treatment	Tumor growth reduced [189].
Mice, Hepatocellular carcinoma	Doxorubicin	1.3 MHz, 0.5 MPa MI: 0.48	Tumor growth suppressed. Mouse survival increased [190].
Mice, Hepatocellular carcinoma	miRNA-122 antimir-21	1.8 MHz, 5.4 MPa	Tumor growth suppressed [191].
Mice, Breast cancer	Oncolytic adenovirus in polymer	1 MHz, 1-2 W/cm^2	Tumor growth suppresssed [192].
Rat, Pancreas carcinoma	Doxorubicin	1.3 MHz, MI: 1.6, 1.2 MPa	Drug delivery increased 12 fold compared to control group. Tumor growth suppressed [193].
Mice, Pancreatic cancer	Gemcitabine	0.5 MHz, 1.2 MPa	Tumor growth suppressed [194].
Mice, malignant melanoma	Bleomycin	1 MHz, 1 W/cm^2	Tumor growth suppressed [195].

2.1.7. Acoustic Droplet Vaporization (ADV)

As mentioned in Section 2.1.6, microbubbles have been extensively employed in ultrasonic imaging to improve vascular contrast and ultrasound therapy [196, 197]. However, their circulation time is limited to minutes due to their size, and they cannot enter tumors by passing through endothelial gaps. The ADV technique can be used to increase the bubble circulation time. ADV is a physical process in which the pressure waves of ultrasound induce a phase transition that causes superheated liquid nanodroplets to form gas

bubbles [196, 198, 198, 199]. When the local pressure drops below the liquid vapor pressure, the liquid can turn to gas. In ADV, sound waves are used to manipulate the local pressure of the liquid, thus controlling the drive to turn a liquid to gas or gas to liquid. When the surrounding pressure exceeds than the vapor pressure, the condensed phase remains in its condensed form (liquid). A small droplet has a much greater probability of remaining a superheated liquid for longer than a large volume of liquid. Smaller liquid droplets can traverse the lungs more effectively than FDA-approved contrast agents like Albunex.

In principle, ADV can be used with any liquid that has a boiling point close to or below body temperature. Fluorocarbons, especially perfluorocarbons (PFCs), are promising options due to their low solubility in water-based solutions [200]. Perfluoropentane (PFC5) is commonly preferred for ADV due to its favorable transition temperature ($\approx 29^{o}$C), high vapor pressure, and low solubility in blood. Because PFC gases have low solubility and diffusion rates in water, bubbles composed of PFC can remain stable in aqueous solutions longer than air bubbles of similar size [196, 198, 198–200]. Repeated intracardiac or intravenous injections can induce ADV in specific arteries, such as renal or segmental arteries. Ninety percent of the perfluoropentane (PFP) concentration in the blood can be cleared from the body within 10 minutes after administration. During the acoustic pressure cycle, the internal pressure within the PFC droplet drops below the vapor pressure of the PFC and then increases again to values above the vapor pressure. When the internal pressure falls below the vapor pressure (a condition known as subpressurization), a driving force exists for the formation of a gas phase. Once a gas bubble is nucleated, it will continue to expand as long as subpressurization is maintained and sufficient heat transfer occurs to provide the necessary energy for gas phase formation. In an acoustic field, the pressure eventually reverses, causing the internal pressure of the droplet to surpass the vapor pressure. At this stage, the gas phase can condense into liquid, pressurizing the liquid droplet until the cycle repeats. When the insonation stops, the droplet's final state may be liquid, although, in some scenarios, a gas phase could persist. This could occur when both a condensed liquid droplet and an expanded gas phase are potential in equilibrium states, with the gas phase persisting even after ultrasound stops. ADV events will increase as the ultrasonic frequency decreases, the number of cycles in a pulse increases, the peak negative pressure of a wave increases in

magnitude, and as the Laplace pressure decreases (due to lower interfacial energy or to larger droplet radius [201–203]).

A standard experimental procedure involves a noncondensable gas (like nitrogen or oxygen) dissolved in the liquid surrounding a droplet. When the gas phase is present, dissolved noncondensable gas can diffuse to the gas-liquid interface and enter the expanding PFC gas bubble. During contraction, when the PFC condenses back into liquid due to high pressure in the acoustic cycle, the noncondensable gas does not condense with the PFC and may not fully redissolve into the surrounding liquid. This leaves behind a small bubble of noncondensable gas that can easily nucleate the next cycle of PFC boiling, resulting in a larger bubble in the subsequent cycle, with more noncondensable gas diffusing into it. After several pressure cycles in the ultrasound pulse, a stable gas bubble may that is a mixture of PFC and noncondensable gas may persist.

Numerous manufacturing methods exist for creating acoustically active capsules, such as sonication, microfluidics, or the condensation of gas cores into a liquid state. The condensation method has been employed in various studies to create perfluorocarbon-based phase-change contrast agents (PCCAs) containing highly volatile perfluorocarbons (PFCs). This method involves generating precursor gas bubbles and condensing the inner core material through a combination of low temperature and increased pressure within the sample [204]. The drawback of the condensation method is that the resulting droplets can vary in size (polydisperse) which makes it challenging to optimize the acoustic field parameters. An alternative method to produce ADV droplets is microfluidics. Martz et al. [205, 206] studied a microfluidic system to create lipid-coated perfluorocarbon (PFC) droplets that can be triggered acoustically. The size of the droplets is determined by the flow rate of the lipid solution, allowing for easy adjustment of droplet diameter. However, one disadvantage of this approach is its relatively low production rate compared to other methods.

Numerous studies indicate the potential utility of ADV droplets in diagnostic imaging, drug delivery, theranostics, thermal ablation, histotripsy and vascular therapy [196, 198, 198–200]. The induction of cell damage by ADV can have a beneficial effect in treating

tumor cells. While there are no published studies on ADV for clinical drug delivery, there are articles about delivering drugs to tumors in mice. The first study utilized a formulation comprising doxorubicin-containing block copolymer micelles mixed with perfluoropentane. The carriers were created by sonicating a mixture of drug-loaded micelles and liquid perfluoropentane at 20 kHz. By adjusting perfluoropentane to micellar suspension ratio, they obtained a mixture of droplets and micelles that was injected into mice with breast and ovarian tumors. They assumed the droplets might have been converted into drug-loaded nanobubbles through thermal activation before extravasating into mouse tumors. However, they did not measure the fraction of perfluoropentane droplets that might have been thermally activated. The tumors were exposed to ultrasound at a frequency of 3 MHz and intensity of $2W/cm^2$, with a duty cycle of 20% for 150 seconds for drug release. This led to cavitation of the thermally activated bubbles which releases the carried drug and also triggered release from nearby micelles. After receiving four treatments over two weeks, the tumors exhibited reduced growth compared to control tumors (without any carrier or ultrasound exposure) and tumors that received the carrier without ultrasound exposure. Ho et al. [204] investigated the impact of vascular disruption on drug penetration by employing a combination of advanced vaporization (ADV) and the enhanced permeability and retention (EPR) effect. Soto et al. [207] have recently designed a wearable transdermal patch comprising a drug reservoir with numerous micropores filled with lidocaine. Ultrasound exposure triggers the release of the drug, facilitating quicker and deeper skin penetration compared to ultrasound exposure, which does not generate advanced vaporization (ADV), resulting in more efficient drug delivery.

2.2. Mathematical Models for Bubbles in Acoustic Fields

Mathematical modeling of ultrasound therapy with microbubbles encompasses several stages. A comprehensive model must account for tumor formation and growth, the immune system, the biophysical effects of ultrasound on tissues, including sonoporation, the dynamics of microbubbles (including bubble formation and growth, as well as the influence of the shell), and interactions between bubbles and cells.

Several mathematical models have been proposed to describe the dynamics of tumors and the immune system, aiming to provide a quantitative understanding of cancer initiation, tumor growth, interactions between the tumor and host tissue, and the steps involved in metastasis. Numerous mathematical models also address various biological aspects of the metastasis cascade. While some of these models center on reaction-diffusion mechanisms [208–210], others focus specifically on phenomena such as haptotaxis and chemotaxis [211, 212]. Reviews on the mathematical modeling of ultrasound-mediated microbubble therapy in the literature typically concentrate on singular aspects, such as cell-related processes [213] or tumor therapy [214].

As discussed in Section 2.1.5, sonoporation primarily arises from the physical interaction between bubbles and cells, with the push-pull effects of the bubbles and microstreaming playing significant roles. The dynamic response of the bubble varies considerably due to differing physical properties among various biological tissues. In 1958, Nyborg introduced a model for acoustic microstreaming [215], which describes the vortical flow generated near a solid surface (such as a blood vessel) in the presence of high-frequency sinusoidal acoustic pressure. However, this model is specifically applicable to pulsating hemispherical-shelled microbubbles. Doinikov and Bouakaz [216] further refined Nyborg's theory to investigate spherical-shelled microbubbles detached from the plane, developing a model for the irrotational liquid velocity induced by acoustic microstreaming [217, 218].

In summary, therapeutic ultrasound and microbubble therapy encompass various biological and physical considerations. Although microbubble dynamics have been studied since the 19th century, new motivations, such as using microbubbles for treatment in the acoustic field, require investigating new aspects, as mentioned in Section 2.1.6. It is crucial to comprehend the impacts of microbubbles and ultrasound in both in vivo and in vitro experiments concerning microbubble-mediated ultrasound therapy. Consequently, this section reviews theoretical models used to analyze and forecast the behavior of microbubbles under various conditions. The section begins with the basics of free-gas bubble dynamics (Section 2.2.1). Then, the encapsulated bubble models (Section 2.2.2), the bubble in confined liquid models (Section 2.2.3), the shape stability of a single bubble (Section 2.2.5) and the numer-

ical studies (Section 2.2.4) are reviewed. The details of the theoretical models can be found in [148, 219].

2.2.1. Unbounded Free Bubbles

Besant was the first to investigate the bubble dynamics through the free gas model in 1859 [220]. Subsequently, Lamb [221] and Rayleigh [222] considered a large, hollow, spherical cavity, ignoring the interfacial tension and viscous effects. The foundation of current models for bubble dynamics lies in the Rayleigh equation for a free-gas bubble, which neglects fluid viscosity and thermal effects [222] and is given as,

$$\rho_l \left(R\ddot{R} + \frac{3}{2}\dot{R}^2 \right) = P_b - P_\infty, \tag{2.1}$$

where R is the time-dependent bubble radius, with an initial value of R_{b0}; $\dot{R}$ and $\ddot{R}$ are the velocity and the acceleration of the bubble surface, respectively. Also, ρ_{L} is the density of the surrounding fluid, and P_∞ is the pressure in the fluid far away from the bubble, which is defined as the sum of the hydrostatic pressure, P_0, and the time-varying driving pressure, $P_{\mathrm{A}}(t)$, in the fluid. P_b is the pressure in the fluid at the bubble interface. Plesset and Prosperetti [223] extended the model to incorporate viscous and surface tension terms, resulting in the Rayleigh-Plesset (RP) equation [222–224]. RP model assumes that bubbles maintain a spherical shape during oscillation, with no heat or mass transfer occurring. The surrounding fluid is assumed to be infinite, incompressible, and Newtonian. The incompressibility assumption implies that the radiation-damping of bubble oscillation is ignored. Additionally, it is assumed that the wavelength of the incident ultrasound field is sufficiently large for the pressure to become spatially uniform, allowing bubble oscillation only in the radial direction. Gravity and buoyancy are also neglected [222–224]. For an ideal gas contained within the bubble, the pressure inside (P_b) is expressed as [225, 226]:

$$P_b = P_0 \left(\frac{R_{b0}}{R} \right)^{3\kappa} - \frac{2\sigma}{R} - \frac{4\mu_{\mathrm{L}}\dot{R}}{R} + P_{\mathrm{v}}. \tag{2.2}$$

Here, σ is the surface tension at the gas-fluid interface, κ is the polytropic constant, and μ_{L} is the viscosity of the surrounding fluid. vapor pressure inside the bubble, P_v, is lower than hydrostatic and interfacial pressures at atmospheric conditions. Consequently, P_{v} is usually neglected [148]. Equation 2.2 assumes that the gas inside the bubble is non-condensable,

i.e., its mass remains constant. Also, the gas obeys a polytropic behavior characterized by the polytropic coefficient, κ. For an isothermal gas, κ is 1. It should be noted that the polytropic model is unreliable in accounting for energy dissipation by thermal processes, especially at large pulsation amplitudes. Prosperetti et al. [227] proposed a new model of bubble oscillation in which the internal pressure is obtained numerically.

The damping of bubble oscillations consists of three contributions: fluid viscosity (viscous damping), thermal conduction between the gas and surrounding fluid (thermal damping), and fluid compressibility through acoustic radiation (radiation damping). The incompressibility of the fluid is valid for small amplitude oscillations. For higher driving pressures, the effect of the compressibility (radiation damping) and the energy dissipation of acoustic emissions are added to the RP model. Hence, a first-order acoustic correction to the RP equation is derived [228–230]. In the following general equation, $\lambda_c = 0$ gives the Keller equation, and $\lambda_c = 1$ yields the Herring and Trilling equation,

$$\begin{aligned} &\left(1-(\lambda_c+1)\,\tfrac{\dot{R}}{C}\right)\rho_L R\ddot{R}+\tfrac{3}{2}\dot{R}^2\rho_L\left(1-\left(\lambda_c+\tfrac{1}{3}\right)\tfrac{\dot{R}}{C}\right)= \\ &\left(1+(1-\lambda_c)\,\tfrac{\dot{R}}{C}\right)[P_0(R)-P_\infty(t)]+\tfrac{R}{C}\dot{P}_0-4\mu_L\tfrac{\dot{R}}{R}-\tfrac{2\sigma}{R}, \end{aligned} \tag{2.3}$$

where C is the speed of the sound in the fluid. Gilmore [231] developed an expansion that includes higher-order compressibility terms. Gilmore's equation provides very close results to numerical solutions [231].

The small-amplitude (linearized) oscillations of a permanent gas bubble in a fluid were first considered by Minnaert [232], who showed that a substantial contribution to the sound emitted by running water comes from the free radial pulsations of air bubbles. More recently, the same problem was considered in greater detail by Devin [233], Plesset and Hsieh [234], Chapman and Plesset [235], and Prosperetti [236]. The evolution of the bubble radius is expressed as $R(t) = R_{b0} + \Delta R(t)$ which can be written as $R(t) = R_{b0}[1 + x(t)]$ with $x(t) = x_0 \sin(\omega t + \varphi)$, where φ is the phase shift between the acoustic forcing and the radial oscillations, and the amplitude of oscillations is small, i.e., $x_0 = \Delta R/R_{b0} \ll 1$.

Perturbation analysis to first order in the small parameter x returns in the form of a damped harmonic oscillator,

$$\ddot{x} + \delta_{\text{tot}}\dot{x} + \omega_0^2 x = -\Delta P \sin(\omega t)/\rho R_{b0}^2, \tag{2.4}$$

where δ_{tot} is the total damping [236], which is the sum of the damping contributions that arise from re-radiation of the sound, the viscous dissipation in the surrounding fluid, and the shell viscous dissipation, i.e., $\delta_{\text{tot}} = \delta_{\text{rad}} + \delta_{\text{vis}} + \delta_{\text{shell}}$. Here, $\dot{x}$ and $\ddot{x}$ are the first- and second-order derivatives of x with respect to time, ω is the angular ultrasound frequency, and ω_0 is the natural frequency given as,

$$\omega_0 = 2\pi f_0 = \frac{1}{R_{b0}}\sqrt{\frac{1}{\rho_{\text{L}}}\left(3\kappa P_0 + (3\kappa - 1)\frac{2\sigma(R_{b0})}{R_{b0}}\right)}, \tag{2.5}$$

where $\sigma(R_{b0})$ represents the interfacial tension of the bubble. As shown in Equation 2.5, the natural frequency of a bubble is inversely proportional to the microbubble size, contrary to the stiffness of the coating, χ.

In summary, while the RP model (Equation 2.1) is relatively straightforward, it suffers from a significant drawback as it does not incorporate acoustic damping, which can greatly influence bubble dynamics due to the assumption of incompressible fluid. To address this limitation, the modified Herring-Trilling [229] and Keller-Miksis [230, 237] models introduce an acoustic damping term. However, these acoustic damping models are applicable only for Mach numbers less than 1. Conversely, at high acoustic pressures of the incident-focused ultrasound, the Mach number can exceed 1. For such cases, the Gilmore [231] equation is applicable, incorporating acoustic damping and accounting for the pressure-dependent speed of sound.

2.2.2. Encapsulated Microbubbles

Microbubbles are commonly coated with a shell, composed of materials such as proteins, polymers, or (phospho)lipids [2, 238–240] as discussed in Section 2.1.6.1. These materials possess both elastic and viscous properties which render them effectively viscoelastic. The shell serves to enhance the stability of the bubble within the bloodstream. Consequently, various models have been devised, leveraging the nonlinear elasticity of the shell [241].

Models for encapsulated bubbles have progressed along two paths. Firstly, the RP equation has been adapted from empirical observations [242–244] by introducing additional terms. These models typically treat the encapsulating shell as a thin layer exhibiting both elastic and viscous characteristics. Alternatively, the second approach involves deriving models rigorously, starting from fundamental equations such as the equations of motion. In 1992, de Jong and Hoff [242] introduced a model for an elastic bubble shell adhering to Hooke's law, which characterizes the behavior of microbubbles encapsulated by an Albunex shell. Subsequently, a semi-empirical shell dissipation term was incorporated into de Jong and Hoff's model to better align with experimental findings [243]. Conversely, Church [16] integrated two pressure terms into the RP equation's right-hand side to account for the shell's elasticity and viscous dissipation. However, this model was constrained to small deformations and could not effectively address nonlinear or finite deformations of the elastic shell. In 2000, Hoff et al. [245] modeled the dynamics of microbubbles encapsulated with a thin polymeric shell by expanding upon the terms of Church's model under the limit of small ε/R_2, where ε denotes the shell thickness and R_2 represents the outer radius of a microbubble. Chatterjee and Sarkar [246] considered the encapsulation as a Newtonian viscous fluid with an infinitesimally thin interface. Allen and Rashid [247] assumed the shell to adhere to a nonlinear elasticity model, such as a nonlinear Hooke's law or neo-Hookean model. Sarkar et al. [241] assumed that the encapsulation behaves as an adsorption film on the surface of a gas bubble in a surfactant solution. As the bubble oscillates, its surface area fluctuates which causes variations in the surface concentration of the adsorbed substance. Doinikov and Dayton [248] expanded upon Church's model by assuming the encapsulating coating behaves as a viscoelastic fluid adhering to Maxwell's constitutive relations. Their findings indicated that a viscoelastic fluid might offer a more precise approximation for lipid shells than a viscoelastic solid or a simple viscous fluid. Doinikov [249] employed the Cross law to establish a relationship between shell viscosity and the initial bubble radius. However, both models overlooked non-spherical buckling during significant compression or expansion of the microbubble, an aspect addressed by Marmottant et al. [250]. They introduced terms to account for asymmetric large-amplitude oscillations of lipid-coated microbubbles. The Marmottant model primarily applies to lipid microbubbles. In this model, the surface tension $\sigma(R)$ depends on two critical values of the bubble radius: one where the shell buckles,

$R_{buckling}$, and another where the shell ruptures, $R_{ruptured}$. It also relies on the surface tension of water, σ_{water}, and the shell elastic modulus χ. Vos et al. [251] employed a finite-volume method to simulate the movement of the bubble boundary, modeling the bubble shell as a neo-Hookean membrane with an energy dissipation equation to represent shell deformation. Tsiglifis and Pelekasis [252] explored integrating the shell, comparing shear-hardening and shear-thinning models, and addressing both shell buckling and bubble stability. While Vos et al. [251] primarily concentrate on modeling oscillations, Tsiglifis and Pelekasis [252] also make strides towards modeling bubble stability. Katiyar and Sarkar [253] investigated the effects of encapsulation damping on resonance frequency. Gubadilin and Fedorov [254] examined the propagation of acoustic waves in a mixture of a liquid with gas bubbles encapsulated with a viscoelastic shell, revealing that increased damping due to small encapsulation tends to increase the resonance frequency. Vlachomitrou and Pelekasis [255] numerically studied the dynamic translation of an encapsulated microbubble inside a horizontal tube where liquid flows under constant pressure drop, disregarding the effect of gravity, treating the shell of the bubble as an infinitesimally thin viscoelastic shell with bending resistance. The Galerkin Finite Element Methodology was employed to solve the axisymmetric flow configuration. Qin et al. [256] developed a comprehensive model capable of simulating complex bubble dynamics by simultaneously considering the nonlinear viscoelastic behaviors of the shells, the bubble–bubble interactions, and the viscoelasticity of the surrounding medium. Gubaidullin [257] derived a modified RP equation, accounting for the radial oscillations of a gas bubble covered with a viscoelastic shell and located in a viscoelastic liquid. Vlachomitrou and Pelekasis [258] numerically investigated compression-only behavior in lipid-shelled contrast agents, revealing minimal impact of the wall on the initiation of compression-only behavior. Doinikov and Bouakaz [219] provided an exhaustive review of hard-shelled models, such as those involving protein shells. Furthermore, Table 2.8 shows detailed models of encapsulated microbubbles.

2.2.3. Bubble in Confined Liquid

Modeling bubbles in elastic blood vessels is particularly important due to its implications in medical science and healthcare. Medical professionals can improve patient out-

comes, develop safer medical devices and enhance therapeutic and diagnostic techniques by comprehensively understanding the dynamics of bubbles in elastic blood vessels.

Several theoretical approaches have been proposed to model bubble dynamics in a confined liquid [42, 43, 259–265]. Wang [262] and Vincent et al. [261, 266], using a quasi-static model for bubble dynamics in a fluid surrounded by an elastic solid, demonstrated that increasing both the bubble radius and the bulk modulus of the solid confinement leads to an increase in the natural frequency of bubble oscillations. Additionally, Vincent et al. [266] noted that the liquid compressibility and the elasticity modulus of the confinement contribute to ultra-fast bubble oscillations and rapid damping. More recently, Doinikov et al. [43,263–265] explored the impact of acoustic waves generated by fluid compressibility on damping bubble oscillations within a fluid enclosed by a solid confinement. They concluded that the confinement's size and elasticity strongly influence the natural frequency of bubble oscillations. Moreover, an increase in the inner radius of the confinement brings the natural frequency closer to that of a bubble within an unbounded fluid. Leonov and Akhatov [42] studied the nonlinear dynamics of a confined spherical bubble in a liquid cell. Their results showed that at relatively large liquid cells exposed to a tension exceeding the cavitation Blake threshold, the cavitation bubble abruptly expands to a finite radius, contrasting with explosive infinite bubble growth in the bulk liquid. Dollet et al. [267] provided a comprehensive review of the developments in bubble dynamics for different confinement conditions.

Most references consider three-layer models of confined bubbles, such as bubble-solid shell-liquid [16, 241, 242, 248, 267–277] or bubble-liquid- elastic solid [42, 43, 259–265]. However, understanding the interplay between encapsulated bubbles and elastic cavities is crucial for advancing biomedical technologies and improving the efficiency and precision of various diagnostic and therapeutic approaches [2, 278–285].

2.2.4. Numerical Studies

As discussed in Section 2.2.1, the majority of models for predicting the dynamics of a spherical bubble stem from the RP equation. Numerical techniques encompass conven-

Table 2.8. Shell models for microbubbles. Reproduced with permission from Kaykanat and Uguz, Biomicrofluidics, 17, 021502, (2023) permission from AIP Publishing [2].

Model	Expression	Description
de Jong Model [242–244]	$R\ddot{R}+\frac{3}{2}\dot{R}^2=\frac{1}{\rho_{\mathrm{L}}}\left[P_{\mathrm{G0}}\left(\frac{R_{b0}}{R}\right)^{3\kappa}+P_{\mathrm{v}}-\frac{2\sigma}{R}-P_0-P_{\mathrm{ac}}(t)-\delta\omega\rho_{\mathrm{L}}R\dot{R}-2S_{\mathrm{p}}\left(\frac{1}{R_{b0}}-\frac{1}{R}\right)-\frac{S_{\mathrm{f}}\dot{R}}{4\pi R^2}\right]$	ω is the angular frequency of the driving acoustic field and δ is a dimensionless damping coefficient
Church Model [16]	$R_1\ddot{R}_1\left[1+\left(\frac{\rho_{\mathrm{L}}-\rho_{\mathrm{S}}}{\rho_{\mathrm{S}}}\right)\frac{R_1}{R_2}\right]+\dot{R}_1^2\left[\frac{3}{2}+\left(\frac{\rho_{\mathrm{L}}-\rho_{\mathrm{S}}}{\rho_{\mathrm{S}}}\right)\left(\frac{4R_2^3-R_1^3}{2R_2^3}\right)\frac{R_1}{R_2}\right]=\frac{1}{\rho_{\mathrm{S}}}\left[P_0\left(\frac{R_{10}}{R_1}\right)^{3\kappa}-\frac{2\sigma_1}{R_1}-\frac{2\sigma_2}{R_2}-4\mu_{\mathrm{L}}\frac{R_1^2\dot{R}_1}{R_2^3}-P_0-P_\infty(t)+3\int_{R_1}^{R_2}\frac{\tau_{rr}^{(\mathrm{S})}(r,t)}{r}\,\mathrm{d}r\right]$.	$R_1(t)$, $R_2(t)$: inner and outer radii of shell ρ_{L}, ρ_{S}: densities of fluid and shell R_{10}: inner radius of shell at rest σ_1, σ_2: surface tension for gas-shell and shell-fluid interfaces $\tau_{rr}^{(S)}$: radial component of stress deviation of shell
Morgan Model [286]	$\rho_{\mathrm{L}}\left(R\ddot{R}+\frac{3}{2}\dot{R}^2\right)=P_0\left(\frac{R_{b0}}{R}\right)^{3\gamma}\left(1-\frac{3\gamma\dot{R}}{c}\right)-4\mu_{\mathrm{L}}\frac{\dot{R}}{R}-\frac{2\sigma}{R}\left(1-\frac{\dot{R}}{c}\right)-\frac{2\chi}{R}\left(\frac{R_{b0}}{R}\right)^2\left(1-\frac{3\dot{R}}{c}\right)-\frac{12\varepsilon\mu_{\mathrm{S}}\dot{R}}{R(R-\varepsilon)}-P_0-P_\infty(t)$.	This model is modified Herring equation [228] with two additional shell terms. ε: Shell thickness
Hoff Model [245]	$R\ddot{R}+\frac{3}{2}\dot{R}^2=\frac{1}{\rho_{\mathrm{L}}}\left[P_0\left(\frac{R_{b0}}{R}\right)^{3\kappa}-\frac{2\sigma}{R}-4\mu_{\mathrm{L}}\frac{\dot{R}}{R}-P_0-P_\infty(t)-12\mu_{\mathrm{S}}\frac{\varepsilon_0R_{b0}^2}{R^3}\left(1-\frac{R_{b0}}{R}\right)-12\mu_{\mathrm{S}}\frac{\varepsilon_0R_{b0}^2}{R^3}\frac{\dot{R}}{R}\right]$.	Infinitesimal shell thickness
Chaterjee-Sarkar Model [246]	$R\ddot{R}+\frac{3}{2}\dot{R}^2=\frac{1}{\rho_{\mathrm{L}}}\left[P_{\mathrm{G0}}\left(\frac{R_{b0}}{R}\right)^{3\kappa}-4\mu_{\mathrm{L}}\frac{\dot{R}}{R}-P_0-P_\infty(t)-4\kappa_{\mathrm{S}}\frac{\dot{R}}{R^2}-\frac{2\sigma_0}{R}-\frac{2E^{\mathrm{S}}}{R}\left(\frac{R^2}{R_{\mathrm{E}}^2}-1\right)\right]$,	E^S: dilatational elasticity R_{E}: radius at equilibrium position of shell, σ_0: Surface tension at zero area change
Marmottant Model [287]	$R\ddot{R}+\frac{3}{2}\dot{R}^2=\frac{1}{\rho_{\mathrm{L}}}\left[P_{\mathrm{G0}}\left(\frac{R_{b0}}{R}\right)^{3\kappa}\left(1-\frac{3\kappa\dot{R}}{c}\right)-4\mu_{\mathrm{L}}\frac{\dot{R}}{R}-P_0-P_\infty(t)-4\kappa_{\mathrm{S}}\frac{\dot{R}}{R^2}-\frac{2\sigma(R)}{R}\right]$.	$\sigma(R)=\begin{cases}0 & \text{if } R\le R_{\mathrm{buckling}}\\ \chi\left(\frac{R^2}{R_{\mathrm{buckling}}^2}-1\right) & \text{if } R_{\mathrm{buckling}}\le R\le R_{\text{break-up}}\\ \sigma_{\mathrm{water}} & \text{if ruptured and } R\ge R_{\mathrm{ruptured}}\end{cases}$
Maxwell Model [248, 288]	$R_1\ddot{R}_1\left[1+\left(\frac{\rho_{\mathrm{L}}-\rho_{\mathrm{S}}}{\rho_{\mathrm{S}}}\right)\frac{R_1}{R_2}\right]+\dot{R}_1^2\left[\frac{3}{2}+\left(\frac{\rho_{\mathrm{L}}-\rho_{\mathrm{S}}}{\rho_{\mathrm{S}}}\right)\left(\frac{4R_2^3-R_1^3}{2R_2^3}\right)\frac{R_1}{R_2}\right]=\frac{1}{\rho_{\mathrm{S}}}\left[P_{\mathrm{G0}}\left(\frac{R_{10}}{R_1}\right)^{3\kappa}-\frac{2\sigma_1}{R_1}-\frac{2\sigma_2}{R_2}-4\mu_{\mathrm{L}}\frac{R_1^2\dot{R}_1}{R_2^3}-P_0-P_\infty(t)-4\mu_{\mathrm{S}}\frac{D(t)\left(R_{20}^3-R_{10}^3\right)}{R_1^3R_2^3}\right]$.	An interpolation equation for intermediate cases between elastic solid and viscous fluid.
Tsiglifis-Pelekasis Model [289]	$\left(1-\frac{\dot{R}}{c}\right)R\ddot{R}+\frac{3}{2}\left(1-\frac{\dot{R}}{3c}\right)\dot{R}^2=\left(1+\frac{\dot{R}}{c}+\frac{R}{c}\frac{\mathrm{d}}{\mathrm{d}t}\right)G$ $G=\frac{1}{\rho_{\mathrm{L}}}\left[P_{\mathrm{G0}}\left(\frac{R_{b0}}{R}\right)^{\mathrm{Sn}}-\frac{2\sigma}{R}-4\mu_{\mathrm{L}}\frac{\dot{R}}{R}-P_0-P_\infty(t)-12\varepsilon\mu_{\mathrm{S}}\frac{\dot{R}}{R^2}-S_{\mathrm{el}}\right]$.	S_{el}: Shell elastic term ε: Shell thickness which is much smaller than initial radius
Doikinov Model [249]	$R\ddot{R}+\frac{3}{2}\dot{R}^2=\frac{1}{\rho_{\mathrm{L}}}\left[P_{\mathrm{G0}}\left(\frac{R_{b0}}{R}\right)^{3\kappa}-\frac{2\sigma}{R}-4\mu_{\mathrm{L}}\frac{\dot{R}}{R}-P_0-P_\infty(t)-4\chi\frac{R_{b0}}{R}\left(\frac{1}{R_{b0}}-\frac{1}{R}\right)-4\kappa_{\mathrm{S}}(\dot{R}/R)\frac{\dot{R}}{R^2}\right]$	$\kappa_{\mathrm{S}}(\dot{R}/R)=\left\lvert\frac{\kappa_0}{1+\alpha\lvert\dot{R}\rvert/R}+\kappa_1\frac{\dot{R}}{R}\right\rvert$ α; normalizing constant κ_0, κ_1: positive constants to be determined by fitting experimental data.
Paul Model [290]	$R\ddot{R}+\frac{3}{2}\dot{R}^2=\frac{1}{\rho_{\mathrm{L}}}\left[P_{\mathrm{G0}}\left(\frac{R_{b0}}{R}\right)^{3\kappa}\left(1-\frac{3\kappa\dot{R}}{c}\right)-4\mu_{\mathrm{L}}\frac{\dot{R}}{R}-P_0-P_\infty(t)-4\kappa_{\mathrm{S}}\frac{\dot{R}}{R^2}-\frac{2\sigma(R)}{R}\right]$.	$\sigma(R)=\sigma_0+E^{\mathrm{S}}\left(R^2-R_{\mathrm{E}}^2\right)/R_{\mathrm{E}}^20$,E^{S} is a function of surface area change: $E^{\mathrm{S}}=E^{\mathrm{S}}(\beta)$, where $\beta=\mathrm{d}A/A=\left(R/R_{\mathrm{E}}\right)^2-1$.

tional approaches such as the boundary element method (BEM) [291–296], finite element method (FEM) [297], finite volume method (FVM) [298–304], as well as newer methodologies like the lattice Boltzmann method (LBM) [305], smoothed particle hydrodynamics method (SPH) [306], and peridynamics method (PD) [307]. This section provides an overview of various numerical studies employing both traditional and innovative methods. For further details, readers are directed to [308–310].

Interface capturing methods like Volume of Fluid (VoF) have been demonstrated to predict bubble dynamics [311–314] accurately. Tsiglifis and Pelekasis [289] utilized the VoF method to capture bubble dynamics in hard-shell coatings. Denner et al. [314] employed the VoF method in a model accounting for liquid compressibility and viscosity, but the model neglects the surface tension. Altay et al. [304] explored single-bubble size, lifetime and multi-bubble dynamics. The COMSOL simulations highlighted the impact of surface roughness on bubble dynamics, concluding that surface roughness decreased bubble size. Miao and Gracewski [315] devised a two-dimensional hybrid model that combined the Finite Element Method (FEM) and the Boundary Element Method (BEM) algorithm to investigate the interaction between a microbubble and either a deformable structure or a microvessel.

Moreover, the front tracking method is employed to investigate bubble dynamics by solving the Navier–Stokes equation using a Finite Volume Method (FVM) on a fixed, structured grid; the interface, referred to as the front, is explicitly tracked using connected marker points [299–303].

Recently, acoustic bubble dynamics have been simulated using the Boundary Element Method (BEM) and Boundary Integral Method for a bubble in an infinite fluid [293, 294] and in proximity to a boundary under the influence of ultrasound propagating perpendicular to the boundary [316–319]. Wang and Manmi [320] investigated 3D bubble dynamics near a wall in the presence of ultrasound propagating parallel to the wall using BIM. This paper presents a computational model developed to simulate the three-dimensional dynamics of acoustic bubbles using the boundary integral method.

When exposed to high-intensity ultrasound, bubbles undergo significantly more violent collapse compared to conditions under constant ambient pressure. To address the resulting numerical challenges, several techniques were implemented. Notably, a novel hybrid approach that combined the Lagrangian method with an elastic mesh technique was used to maintain a high-quality mesh of the bubble surface. This approach prevents numerical instabilities at sharp jet surfaces while simultaneously generating the fine mesh required in these regions.A bubble collapses significantly more violently when exposed to high-intensity ultrasound compared to the normal constant ambient pressure. To address the resulting numerical challenges, several techniques are employed. Specifically, Hsiao and Chahine [295] combined a new hybrid approach combining the Lagrangian method and the elastic mesh technique to ensure a high-quality mesh around the bubble surface. A boundary integral method is used to solve the potential domain equation. Due to the proximity of the boundary and to the interaction with other bubbles, the problem is fully three-dimensional, and a spherical model is inadequate.

2.2.5. Shape Stability of a Bubble

The majority of literature in this field focuses on predicting the spherical oscillations of bubbles. However, bubble oscillations may deviate from spherical behavior, particularly in scenarios such as cavitation near an interface separating different media [321, 322] or in parametric instabilities of continuously forced bubbles [323]. These deviations can result in non-spherical oscillations, which have various consequences, including more effective gas mixing in sonochemistry [324], mitigation of temperature rise to alter the efficiency of sonochemical production [325], or the formation of high-speed liquid jets capable of causing structural damage [321, 322].

Controlling shape stability is crucial for targeted drug delivery to regulate microbubble break-up or to determine the pressure needed for bubble collapse in tissue ablation [48, 49]. The initiation of bubble break-up is directly linked to the loss of spherical form caused by the growing shape instabilities at the interface. Additionally, in ultrasound imaging, the steady shape oscillations of bubbles are used to enhance blood tissue contrast, thereby improving

the quality of blood vessel imaging in ultrasound examinations [50]. Therefore, controlling the stability of bubbles within the bloodstream prolongs their lifespan compared to unstable bubbles, consequently, extending the duration of imaging.

Previously, stability analysis of a gas bubble in water was conducted by Plesset [225] and Prosperetti [326] utilizing perturbation methods. Plesset [225] utilized spherical harmonics to represent the non-spherical bubble surface and simplified the Bernoulli equation into two ordinary differential equations (ODEs): the Rayleigh-Plesset equation for the mean bubble radius and an equation governing non-spherical mode amplitudes. Prosperetti [326] expanded this inviscid model to incorporate rotational flow by introducing two corrections: a viscous correction in the dynamic boundary condition and a rotational correction in the velocity field. This model facilitated analytical exploration of bubble shape stability, primarily driven by applications such as sonoluminescence [326–328], drug delivery [329, 330], and sonochemistry [331]. Recent advancements in experimental techniques have enabled direct observation of shape oscillations of bubbles in water [50, 323] and gelatin gels [332] under continuous forcing. Versluis et al. [323] observed the parametric instability of non-spherical modes and validated the stability analysis. Lu et al. [10] explored the stability of spherical oscillations in thick-shelled microbubbles using perturbation theory, incorporating harmonic non-spherical small perturbations and solving an eigenvalue problem under the assumption of a Newtonian surrounding liquid. Liu et al. [11] studied the shape stability of a bubble fully encompassed by an elastic solid. Klapcsik et al. [333] investigated how dissipation affects the shape stability of a harmonically excited bubble. The results indicate that the viscosity of the liquid domain prevents bubbles from deviating from their spherical shape. Gaudron et al. [334] studied the shape stability of a bubble surrounded by an elastic medium using classical perturbation theory [225]. They considered two distinct constitutive models for the surrounding medium: linear elasticity and Neo-Hookean hyperelasticity. The results show that surface tension and elasticity exert stabilizing effects, while inertia can either stabilize or destabilize depending on the interfacial velocity and acceleration. Murakami et al. [335] analytically explored the shape stability of a bubble in a Kelvin-Voigt viscoelastic medium, observing that viscosity increases the damping rate, thereby suppressing shape instability. Yang et al. [336] investigated the onset of non-spherical shapes of a bubble in a soft material

by explicitly considering nonlinear interactions between the cavitation bubble and the solid surroundings.

2.3. Challenges and Outlook

In this section, the limitations and possible future directions are reviewed both for the clinical applications and for the mathematical modeling of the acoustic-mediated microbubbles.

2.3.1. Challenges and Future Directions for Clinical Applications

Using sound fields for drug targeting can significantly reduce systemic drug doses while achieving the same localized therapeutic effects as chemotherapy. However, the dynamics of microbubbles under acoustic fields, flow conditions, and cell-bubble interactions remain insufficiently understood and controlled. Stable cavitation increases cell membrane permeability, while inertial cavitation may cause damage to nearby tissues and structures, reduce blood flow, or induce adverse effects such as ischemia, apoptosis, necrosis, edema, and hemorrhage. Ultrasound parameters must be carefully adjusted to avoid these outcomes. For instance, Kobayashi et al. [337] demonstrated in vitro that bubble bursting under ultrasonic fields damaged bovine arterial cells. To enhance safety, minimizing inertial cavitation is crucial, as Le Gac et al. [338] proposed by adjusting the distance between microbubbles to prevent cavitation. Their studies on sonoporation in microfluidic environments revealed that cells located at least four times the maximum bubble radius remain unaffected.

Microbubbles, however, face challenges in clinical applications. Being recognized as foreign by the immune system reduces their lifespan, and further studies on their degradation and clearance processes are needed to prolong their viability. Additionally, while in vitro studies provide valuable insights into drug delivery, they often fail to replicate the complexity of in vivo conditions. For effective therapeutic applications, understanding the molecular signaling mechanisms during sonoporation is critical.

The limited drug-carrying capacity of microbubble shells also restricts their potential. Advanced techniques, such as layer-by-layer polyelectrolyte assembly, have been developed to coat microbubbles, allowing them to carry multiple drugs within their layers. Overcoming these limitations, including cell targeting weaknesses, is vital for future advancements [339].

Another novel approach to improving loading capacity is using phase-change droplets with a liquid perfluorocarbon core for loading drugs. Rapoport et al. were the first group to uncage drugs using PCAs after co-loading chemotherapeutics and perfluorocarbons in micelles [154]. This group used drug-loaded (doxorubicin and paclitaxel) polymer nanodroplets to target tumors passively via the EPR effect and triggered drug release upon ultrasound exposure [340]. Droplets became a successful alternative for MBs in drug-delivery applications, and many groups showed successful drug delivery to target tissues in preclinical models [341]. One of the limitations of PCAs as drug carriers is the limited solubility of drugs in the perfluorocarbon core. To address this issue, our group conjugated droplets to liposomes for the first time to improve droplets' loading capabilities and demonstrated drug uncaging upon ultrasound application in vitro and in vivo [342].

Recent innovations aim to reduce drug toxicity. For example, inactivated prodrugs, chemically modified forms of active drugs with reduced toxicity, offer promising alternatives. Additionally, coating microbubbles with specific ligands enhances their ability to target specific cells. Ishijima et al. [343] developed a nano-complex combining a phase-change nanodroplet with an anti-cancer antibody, achieving 97.8% cancer cell targeting and killing 57% of those cells upon ultrasound exposure in in vitro experiments.

In recent years, nanobubbles (NBs) have garnered significant attention from researchers in the field of cancer treatment. However, their clinical application remains limited, with no current clinical trials utilizing NB-based therapy. An in situ study by Huynh et al. [344] was the first to demonstrate that porphyrin microbubbles can be transformed into NBs through ultrasound, suggesting the potential for enhanced drug permeability and retention in the future. Subsequently, Pellow et al. [345] conducted a comprehensive study on the extravasation of NBs to targeted tumor sites. Their work incorporated both a phantom scattering model

and an in vivo model involving mice implanted with green fluorescent protein (GFP)-tagged human FaDu squamous cell carcinoma cells. They observed that NBs remained stable for approximately 20 minutes while circulating in the vasculature. Following NB injection and ultrasound exposure, increased NB extravasation was detected over time, particularly in tumor regions compared to control groups.

Also, lab-on-a-chip experiments can be done before precilinical studies. Park et al. [346] conducted a notable study in which they used a microfluidic device to recreate the spontaneous formation of blood microvessels, enabling the visualization of microbubble- and ultrasound-assisted drug delivery across microvasculature. However, due to the significant variability in vessel sizes, achieving controlled, quantitative, and statistically robust results—such as those related to permeability—remains challenging. Recently, a relatively simple and efficient commercially available device has been introduced as a microvasculature-on-chip model [347, 348]. This optimized microfluidic network is primarily designed to study blood-brain barrier (BBB) permeability and facilitate therapeutic screening. Key advantages of this model include real-time measurement and visualization capabilities, three-dimensional channels that closely replicate microvessel sizes, appropriate perfusion rates under physiological shear stress (1–12 dyne/cm^2) [347, 348], and the ability to simulate biochemical interactions between different co-cultured tissues. For instance, in [349], the neonatal-stage BBB was recreated in vitro by co-culturing rat brain endothelial cells (RBEC) and astrocytes in separate compartments connected via a porous interface. This setup provides a platform to explore cell-cell interactions between different tissues, such as those between the immune system and tumors.

Additionally, after an initial destructive probe pulse, high cavitation activity was noted in tumors, while no cavitation occurred in healthy control groups, indicating the absence of intact NBs in these areas. A brief 2-minute sonication resulted in a significantly higher release of fluorescent materials in tumors compared to healthy controls. This finding highlights the potential of NBs, in combination with ultrasound, for targeted drug delivery to solid tumors. Further bioeffects, such as vascular disruption, vascular shutdown, and sonoprinting, were also reported following the application of ultrasound and NBs (USNBs). These studies

pave the way for incorporating NBs into clinical applications.

In contrast, microbubbles (MBs) have been extensively studied in clinical trials alongside ultrasound (USMB), often in combination with chemotherapy and/or radiation therapy. These trials have demonstrated minimal to no severe toxicity or side effects. USMB-based therapies have been successfully employed in treating a range of cancers, including breast cancer [97,98], bile duct cancer [99], gliomas [100], hepatocellular carcinoma [101], head and neck squamous cell carcinoma (NCT04431648), liver cancer [102,103], ovarian cancer [97], and pancreatic carcinoma [104]. These studies underscore the immense potential of nanobubbles and ultrasound-based therapies, warranting further exploration in clinical trials.

Emerging patents underscore growing importance of ultrasound-mediated microbubble drug delivery in clinical applications. These developments focus on improving the efficiency and safety of drug delivery systems while emphasizing the need for a deeper understanding of their underlying mechanisms and optimization for enhanced drug efficacy.

2.3.2. Challenges and Future Directions in Mathematical Modeling

Most studies modeling the dynamics of oscillating bubbles rely on the Rayleigh-Plesset (RP) equation, which originated from Lord Rayleigh's foundational work on the pressure-driven collapse of an empty cavity in an incompressible fluid [222], later expanded by Plesset (1977) to account for the gas phase inside the bubble [223]. However, the RP equation incorporates significant simplifications and does not capture the intricate behaviors of bubbles, such as laser-induced cavitation [350,351], bubble penetration into biomaterials, shock-induced collapses, or cavitation dynamics in viscoelastic media. Comprehensive modeling of these phenomena requires solving the full set of governing equations using advanced numerical methods.

As discussed in Sec. 2.1.6, microbubbles can undergo nonlinear oscillations and collapse under high acoustic pressures. Modeling such conditions demands the inclusion of interactions between bubbles and between bubbles and blood vessels. These phenomena are

computationally intensive, especially for configurations such as two bubbles near a surface within a blood vessel, a common scenario in practical applications [352–354].

Additionally, traditional linear shell models for encapsulated microbubbles fail to capture nonlinear behaviors, such as the compression-only response of lipid-coated microbubbles (where expansion is minimal) and the influence of the initial bubble radius on the material properties of the lipid shell. Segers et al.(2018) [355] demonstrated that shell viscosity depends on the bubble surface area, emphasizing the critical role of surface dilation. Future research should investigate the contributions of various shell components to acoustic bubble dynamics, with efforts like molecular interaction-based modeling [356] and molecular dynamics simulations [357] offering promising avenues.

Currently, the primary focus in bubble dynamics modeling remains on bubbles interacting with elastic solids in infinite fluid domains [262, 358–360]. However, there is a pressing need to explore factors like fluid compressibility, phase transitions, and the development of methods for simulating complex structures. In particular, modeling encapsulated microbubbles within blood—a non-Newtonian fluid—flowing through elastic blood vessels warrants further investigation.

3. PHYSICAL SYSTEM AND MODEL

This section discusses the geometry and mathematical models used in four parts of this dissertation. The first part (Section 3.1) examines the spherical oscillation of a bubble under various cases. The second part focuses on non-spherical oscillations (Section 3.2), beginning with the model for a bubble in an unbounded liquid, followed by the addition of the effects of a shell.Third part includes the translational motion and bubble-bubble interactions (Section 3.3). In the fourth part, equations for acoustic droplet vaporization are derived (Section 3.4).

3.1. Spherical Bubble Oscillations

The first part of this dissertation explores the behavior of spherical oscillations of a bubble under a variety of conditions. It considers different cases such as a bubble in an infinite liquid, an encapsulated bubble within an unbounded liquid, a bubble situated inside a liquid cavity and an encapsulated bubble within an elastic cavity.

3.1.1. Bubble in an Unbounded Liquid

The physical system comprises a bubble immersed in an unbounded liquid as depicted in Figure 3.1. The system is represented in spherical coordinates, with the bubble's position specified by a radial distance r. Here, p_∞ is the pressure in the medium far from the bubble, $p_b(t)$ is the gas pressure and p_v is the vapor pressure. $R_b(t)$ is the time-dependent bubble radius. The surrounding liquid is assumed to be either Newtonian (Section 3.1.1.3) which obeys the power-law equation (Section 3.1.1.4) or viscoelastic (Section 3.1.1.5). Additionally, it is presumed that the medium is incompressible throughout this section.

The continuity equation for the unbounded liquid is

$$\nabla \cdot \mathbf{u} = 0, \tag{3.1}$$

where **u** is the velocity field. The r component of the continuity equation is

$$\frac{1}{r^2}\frac{\partial\left(r^2u\right)}{\partial r}=0. \tag{3.2}$$

Here, u is the velocity of liquid in r direction. With the boundary condition $u(r=R_b)=\dot{R}_b$, the solution of Equation 3.2 is given as,

$$u=R_b^2\frac{\dot{R}_b}{r^2}, \tag{3.3}$$

where $\dot{R}_b$ is the rate of change of the bubble radius with respect to time, i.e., bubble wall velocity. The r component of equation of motion for the liquid is given as,

$$\rho\left(\frac{\partial u}{\partial t}+u\frac{\partial u}{\partial r}\right)=-\frac{\partial p}{\partial r}+(\nabla\cdot\boldsymbol{\tau})_r, \tag{3.4}$$

where $(\nabla\cdot\boldsymbol{\tau})_r$ is the radial component of $\nabla\cdot\boldsymbol{\tau}$. Here, ρ is the density of the liquid, and p is the pressure of the liquid. Using Equation 3.3, the left-hand side of 3.4 becomes,

$$\frac{\partial u}{\partial t}+u\frac{\partial u}{\partial r}=\frac{\ddot{R}_bR_b^2}{r^2}+2\frac{\dot{R}_b^2R_b}{r^2}-2\frac{(\dot{R}_b)^2R_b^4}{r^5}. \tag{3.5}$$

Equation 3.4 is then integrated from R_b to ∞ as,

$$\int_{R_b}^{\infty}\left(\frac{\partial u}{\partial t}+u\frac{\partial u}{\partial r}\right)dr=-\frac{\ddot{R}_bR_b^2}{r}-2\frac{\dot{R}_b^2R_b}{r}+2\frac{(\dot{R}_b)^2R_b^4}{4r^4}\Bigg|_{R_b}^{\infty}, \tag{3.6}$$

and finally, the left-hand side of Equation 3.6 becomes,

$$\int_{R_b}^{\infty}\left(\frac{\partial u}{\partial t}+u\frac{\partial u}{\partial r}\right)dr=R_b\ddot{R}_b+\frac{3}{2}(\dot{R}_b)^2. \tag{3.7}$$

The right-hand side of Equation 3.4 is integrated from the surface of the bubble to the far

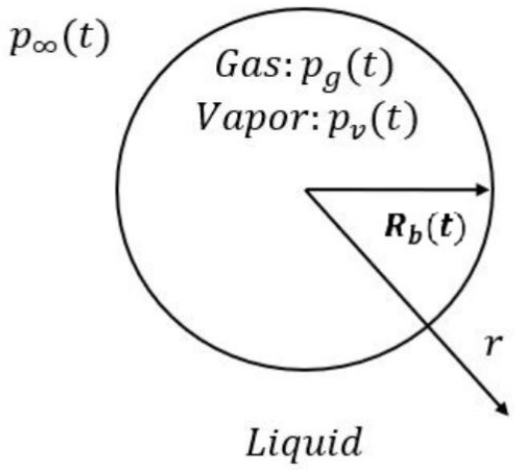

Figure 3.1. Bubble in an unbounded liquid.

field with respect to r and $u(r,t) = R_b^2\dot{R}_b/r^2$ is substituted to give,

$$\rho\left(R_b\ddot{R}_b + \frac{3}{2}\dot{R}_b^2\right) = p(R_b) - p_\infty + \int_{R_b}^{\infty}(\nabla\cdot\boldsymbol{\tau})_r \,\mathrm{d}r. \tag{3.8}$$

Equation 3.8 can be applied regardless of the rheological properties of the surrounding medium, determined by the expression of $\boldsymbol{\tau}$. Here, $p(R_b)$ represents the pressure within the medium at the interface of the bubble. If the bubble is not coated by a viscoelastic interfacial layer, the stress balance for such an uncoated microbubble is derived as follows:

$$\mathbf{n}\cdot\mathbf{T}|_l = \mathbf{n}\cdot\mathbf{T}|_g + \sigma\mathbf{n}\nabla\cdot\mathbf{n}, \tag{3.9}$$

where the subscript g represents the gas phase. σ is the surface tension and $\mathbf{T}$ is the stress tensor, and $\mathbf{n} = \frac{\nabla F}{\|\nabla F\|}$ is the outward unit normal vector, where F is the surface function. $\nabla\cdot\mathbf{n}$ represents the surface curvature. For a bubble that just undergoes spherical oscillations, $\mathbf{n} = \mathbf{e_r}$. The viscosity inside the bubble is small compared to the liquid viscosity. Therefore, the viscous effects inside the bubble can be neglected [361], and Equation 3.9 is given as,

$$\mathbf{n}\cdot\mathbf{T}|_l = \sigma\mathbf{n}\nabla\cdot\mathbf{n}, \tag{3.10}$$

where, $\mathbf{T}$ is the viscous tensor. F

Finally, the normal component of Equation 3.10, the normal stress balance becomes,

$$p(R_b) + \frac{2\sigma}{R_b} - \tau_{rr}(R_b) = p_g, \tag{3.11}$$

where $\tau_{rr}(R_b)$ is the stress component in the medium at the bubble interface. Substituting Equation 3.11 into Equation 3.8 gives,

$$\rho\left(R_b\ddot{R}_b + \frac{3}{2}\dot{R}_b^2\right) = p_\mathrm{g} - p_\infty - \frac{2\sigma}{R_b} + \tau_{rr}(R_b) + \int_{R_b}^{\infty}(\nabla\cdot\boldsymbol{\tau})_r \,\mathrm{d}r. \tag{3.12}$$

In the linear regime of deformation of a viscoelastic medium, $\boldsymbol{\tau}$ is traceless, $\tau_{\theta\theta} + \tau_{\phi\phi} = -\tau_{rr}$, hence we have the divergence of the stress tensor, and is given by

$$(\nabla\cdot\boldsymbol{\tau})_r = \frac{1}{r^2}\frac{\partial}{\partial r}\left(r^2\tau_{rr}\right) - \frac{\tau_{\theta\theta}+\tau_{\phi\phi}}{r} = \frac{1}{r^2}\left(2r\tau_{rr} + r^2\frac{\partial\tau_{rr}}{\partial r}\right) + \frac{\tau_{rr}}{r} = 3\frac{\tau_{rr}}{r} + \frac{\partial\tau_{rr}}{\partial r}. \tag{3.13}$$

Using Equation 3.13, and assuming $\tau_{rr}(r=\infty) = 0$, Equation 3.12 simplifies to [362],

$$\rho\left(R_b\ddot{R}_b + \frac{3}{2}\dot{R}_b^2\right) = p_\mathrm{g} - p_\infty - \frac{2\sigma}{R_b} + 3\int_{R_b}^{\infty}\frac{\tau_{rr}}{r}\,\mathrm{d}r. \tag{3.14}$$

This equation governs the dynamics of a spherical bubble in an incompressible medium with arbitrary rheological properties. We refer the reader to Prosperetti (1977) [362] for the complete theoretical treatment of the thermal effect.

3.1.1.1. Gas Pressure inside the Bubble. The gas pressure inside the bubble can be determined using various equations of states. At low pressures, the gas can be considered ideal. In this section, polytropic law is derived based on the ideal gas assumption, and then the Van der Waals (VdW) equation of state is presented for real gases. In Section 4.3, the results are compared.

Polytropic Law: TThe pressure within the bubble, p_b, is determined by the polytropic law, which presupposes an instantaneous thermodynamic equilibrium during the oscillations of the bubble. It is postulated that the bubble comprises a mixture of liquid-vapor and a non-condensable gas. As the bubble expands, the vapor inside it evaporates, while condensation occurs at the bubble's surface as it shrinks, thereby maintaining the vapor pressure, p_v, constant over time [363]. This assumption remains valid when the velocity of the bubble is lower than the speed of sound. Furthermore, it is assumed that the vapor and gas are sufficiently diluted to apply Dalton's Law. The internal pressure of a bubble with temperature T_B can be expressed by the polytropic law as,

$$p_g = p_v(T_B) + p_{g,eq}\left(\frac{T_B}{T_\infty}\right)\left(\frac{R_{b0}}{R_b(t)}\right)^{3\kappa}. \tag{3.15}$$

Here, $p_v(T_B)$ represents the vapor pressure and $p_{g,eq}$ denotes the equilibrium pressure. R_{b0} is the initial bubble radius. κ is the polytropic exponent which equals to the ratio of the specific heat capacity at constant pressure to the specific heat capacity at constant volume. This exponent equals to 1 for the isothermal compression of the gas. $p_{g,eq}$ signifies the pressure at equilibrium. It is assumed that the gas behaves ideally and that there is minimal heat exchange between the bubble and the liquid. Consequently, the compression and expansion of the gas are depicted as adiabatic processes. Given that the temperature of the bubble remains constant, i.e., $T_B = T_\infty$. The pressure inside the bubble can be determined as,

$$p_g = p_v + p_{g,eq}\left(\frac{R_{b0}}{R_b}\right)^{3\kappa} = \left(p_0 - p_v + \frac{2\sigma}{R_{b0}}\right)\left(\frac{R_{b0}}{R_b}\right)^{3\kappa}. \tag{3.16}$$

Van der Waals equation of state :

Van der Waals proposed the following equation of state for a real gas,

$$\left(p_b + \frac{n^2 a}{V^2}\right)(V - nb)^\kappa = nR_g T, \tag{3.17}$$

where a and b are positive constants; the ideal-gas equation is recovered when they are zero.

Also, T is temperature, R_g is gas constant, and n is the mole number of gas inside the bubble.

The bubble is assumed to include non-condensable argon gas for which no chemical instabilities (i.e., reactions) can occur. VdW constants are given as $a \approx 1.355 \frac{L^2 \text{bar}}{\text{mol}^2}$ and $b = 0.032 \frac{L}{\text{mol}}$. The density of argon is $\rho_g \approx 1.7 \frac{\text{kg}}{\text{m}^3}$ and the molecular mass of argon is $M_w = 40\ \text{g/mol}$. Thus, inside the bubble, the number of moles, n, of argon is given as,

$$n = \frac{\rho_g V_g}{M_w} = 1.7 \frac{\text{kg}}{\text{m}^3} \times \frac{4}{3} \pi R_{b0}^3\ \text{m}^3 \times \frac{1}{40 \times 10^{-3}} \frac{\text{mol}}{\text{kg}} = 42.5 R_{b0}^3\ \text{mol}, \tag{3.18}$$

Therefore, nb term in Equation 3.17 is found as,

$$nb = \frac{4}{3} \pi h^3, \tag{3.19}$$

where h is the hard core VdW radius for the argon bubble.

Substituting b and n from Equation 3.18 into Equation 3.19 yields $R_{b0}/8.9 = h$. Initial bubble gas pressure, p_{g0}, is found from Equation 3.17 as,

$$\left(p_{g0} + \frac{n^2 a}{V_0^2} \right) \left(V_0 - \frac{4}{3} \pi \left(\frac{R_{b0}}{8.9} \right)^3 \right)^{\kappa} = n R_g T, \tag{3.20}$$

where $V_0 = 4/3 \pi R_{b0}^3$.

The instantaneous gas pressure inside the bubble, p_b is found from Equation 3.17 as,

$$\left(p_b + \frac{n^2 a}{V^2} \right) \left(V - \frac{4}{3} \pi \left(\frac{R_{b0}}{8.9} \right)^3 \right)^{\kappa} = n R_g T. \tag{3.21}$$

After substituting n and a; and dividing Equation 3.20 by Equation 3.21, an expression for p_b is found as,

$$p_b = \frac{\left(p_{g0} + \dfrac{n^2 a}{\left(\frac{4}{3} \pi R_{b0}^3 \right)^2} \right) \left(R_{b0}^3 - \left(\dfrac{R_{b0}}{8.9} \right)^3 \right)^{\kappa}}{\left(R_b^3 - \left(\dfrac{R_{b0}}{8.9} \right)^3 \right)^{\kappa}} - \frac{n^2 a}{\left(\frac{4}{3} \pi R_b^3 \right)^2}. \tag{3.22}$$

3.1.1.2. Bubble in an Unbounded Inviscid Liquid. Although inviscid liquids represent an idealized and simplified approximation of fluids, they can provide insights, facilitate analysis, and aid in developing practical solutions for various applications. For this reason, viscous

forces are neglected in the first place. For the inviscid liquid, the RP equation becomes,

$$R_b\ddot{R}_b + \frac{3}{2}\left(\dot{R}_b\right)^2 = \frac{1}{\rho}\left(p_{g0}\left(\frac{R_{b0}}{R_b}\right)^{3\kappa} - p_\infty + p_v - \frac{2\sigma}{R_b}\right). \tag{3.23}$$

3.1.1.3. Bubble in an Unbounded Newtonian Liquid. Blood has been successfully modeled as a Newtonian fluid under certain conditions, such as when blood is flowing at a steady rate through large arteries or veins [364,365]. Therefore, the surrounding liquid is assumed to be Newtonian and the stress definition is given as,

$$\tau_{rr} = 2\mu\frac{\partial u}{\partial r} = -4\mu\frac{R_b^2\dot{R}_b}{r^3}. \tag{3.24}$$

After substituting Equation 3.24 into the viscous term of Equation 3.14,

$$3\int_{R_b}^{\infty}\frac{\tau_{rr}}{r}\,\mathrm{d}r = 3\left(4\mu\frac{R_b^2\dot{R}_b}{3r^3}\right)\Bigg|_R^\infty = -4\left(\mu\frac{\dot{R}_b}{R_b}\right), \tag{3.25}$$

is obtained. Here, μ is the viscosity of the liquid. Equation 3.14 becomes,

$$R_b\ddot{R}_b + \frac{3}{2}\left(\dot{R}_b\right)^2 = \frac{1}{\rho}\left(p_{g0}\left(\frac{R_{b0}}{R_b}\right)^{3\lambda} - p_\infty + p_v - \frac{2\sigma}{R_b} - \frac{4\mu}{R_b}\dot{R}_b\right). \tag{3.26}$$

3.1.1.4. Bubble in an Unbounded Power-law Liquid. In this section, instead of Newton's law of viscosity, the power-law model describes the viscosity of the surrounding liquid [366]. The relation between the stress and the deformation-rate tensor is given as,

$$\boldsymbol{\tau} = \mu\dot{\boldsymbol{\gamma}}, \tag{3.27}$$

where $\dot{\boldsymbol{\gamma}}$ is the strain-rate tensor. The apparent viscosity, μ is given by

$$\mu = m\dot{\gamma}^{k-1}. \tag{3.28}$$

Here, m is the consistency index and $\dot{\gamma}$ is the the second invariant of the strain-rate tensor, $\dot{\boldsymbol{\gamma}}$. $\dot{\gamma}$ is given as,

$$\dot{\gamma} = \sqrt{\frac{1}{2}\left(\underline{\underline{\dot{\gamma}}}:\underline{\underline{\dot{\gamma}}}\right)} = \sqrt{2\left(-2\frac{\dot{R}_bR_b^2}{r^3}\right)^2 + 2\left(\frac{\dot{R}_bR_b^2}{r^3}\right)^2 + 2\left(\frac{\dot{R}_bR_b^2}{r^3}\right)^2} = 2\sqrt{3}\left|\frac{\dot{R}_bR_b^2}{r^3}\right|. \tag{3.29}$$

Assuming blood as a non-Newtonian liquid is particularly relevant in situations such as blood flow through small capillaries or when blood is subjected to varying flow rates in the circulatory system.

After substituting Equation 3.29 into Equation 3.27, the stress component of the power-law liquid becomes,

$$\tau_{rr} = -4m(2\sqrt{3})^{n-1}\left|\frac{\dot{R}_b R_b^2}{r^3}\right|^{n-1}\left(\frac{\dot{R}_b R_b^2}{r^3}\right). \tag{3.30}$$

After substituting Equation 3.30 into the viscous term of Equation 3.14,

$$\begin{aligned} 3\int_{R_b}^{\infty}\frac{\tau_{rr}}{r}\,\mathrm{d}r &= -3\int_{R_b}^{\infty} M|\dot{R}_b|^{n-1}\dot{R}_b(R_b^{2n-2}R_b^2)r^{-3n+3-3-1}\,\mathrm{d}r \\ &= 3M|\dot{R}_b|^{n-1}\dot{R}_b(R_b^{2n})\frac{r^{-3n}}{3n}\Bigg|_{R_b}^{\infty} = -\frac{M}{n}|\dot{R}_b|^{n-1}\frac{\dot{R}_b}{R_b^n}, \end{aligned} \tag{3.31}$$

is obtained. Here, $M = 4m(2\sqrt{3})^{n-1}$. Finally, Equation 3.14 becomes,

$$\rho\left(R_b^2\ddot{R}_b + \frac{3}{2}\dot{R}_b^2\right) = p_{\mathrm{g}} - p_\infty - \frac{2\gamma}{R_b} - \frac{M}{n}|\dot{R}_b|^{n-1}\frac{\dot{R}_b}{R_b^n}. \tag{3.32}$$

After reducing the order of the second order ODE, the coupled ODEs for the spherical oscillations of the bubble becomes,

$$\dot{R}_b = V, \tag{3.33}$$

and

$$\dot{V} = \frac{\frac{1}{\rho}\left(p_{g0}\left(\frac{R_{b0}}{R_b}\right)^{3\lambda} - p_\infty - p_v - \frac{2\sigma}{R_b} - \frac{M}{n}|\dot{R}_b|^{n-1}\frac{\dot{R}_b}{R_b^n}\right) - \frac{3}{2}V^2}{R_b}. \tag{3.34}$$

These coupled ODEs are solved numerically via MATLAB. The initial conditions are $R_b(0)$ =R_{b0} and $\dot{R}_b(0) = 0$.

3.1.1.5. Bubble in an Unbounded Viscoelastic Liquid. The Kelvin-Voigt model is a foundational framework in the study of soft tissue mechanics, providing insight into biological materials' viscoelastic behavior. Muscles, tendons, and skin are examples of biological materials. Therefore, the surrounding medium is assumed to obey the Kelvin-Voigt equation. The elastic component represents the tissue's ability to store energy during deformation. The viscous component accounts for energy dissipation through internal friction or fluid flow. The Kelvin-Voigt model describes the behavior of soft tissue as a combination of a spring

and a dashpot, which represent the elastic and viscous components, respectively. This model enables understanding phenomena such as stress relaxation and creep, which are crucial in biomechanics and biomedical engineering and aid in designing prosthetics, implants, and rehabilitation strategies. The expression for τ_{rr} consists of two parts.

This section assumes that the strains are minor ($\left|\left(R_b^3 - R_o^3\right)/r^3\right| \ll 1$). Reismann and Paulik give the *rr* component of the elastic part [367] as,

$$\tau_{rre} = (\lambda + 2G)\frac{\partial \varepsilon_{rr}}{\partial r} + 2\lambda\frac{\varepsilon_{rr}}{r}, \tag{3.35}$$

where λ and G_l are the Lame constants (G_l is also known as the modulus of rigidity), and ε_{rr} is the component of the strain tensor in the radial direction. For small displacements ε_{rr}, the displacement from equilibrium, is given by,

$$\varepsilon_{rr} = \left(R_b^2/r^2\right)(R_b - R_{e1}), \tag{3.36}$$

where R_{e1} is the unstrained equilibrium position of interface. The structure of the second part, about the damping in the expression for τ_{rr}, is derived by assuming that internal friction processes occur when distinct material particles undergo relative motion. When the velocity gradient is small, damping is solely proportional to the initial derivative of velocity, $2\mu(\partial u/\partial r)$, as outlined in [368]. It is assumed that the dilatational viscosity is negligible for determining damping, as is often done in the case of rubber-like, i.e., incompressible materials [369]. The final expression for the radial component of the stress tensor is given as,

$$\tau_{rr,l} = -\frac{4R_b^2}{r^3}\left[\frac{G_l R_b}{3}\left(1 - \frac{R_{b0}^3}{R_b^3}\right) + \mu_l \dot{R}_b\right], \tag{3.37}$$

and

$$3\int_{R_b}^{\infty}\frac{\tau_{rr}}{r}\,\mathrm{d}r = \frac{4R_b^2}{r^3}\left[\frac{GR_b}{3}\left(1 - \frac{R_{b0}^3}{R_b^3}\right) + \mu\dot{R}_b\right]\Bigg|_{R_b}^{\infty} = -\frac{4}{R_b}\left[\frac{GR_b}{3}\left(1 - \frac{R_{b0}^3}{R_b^3}\right) + \mu\dot{R}_b\right]. \tag{3.38}$$

After substituting Equation 3.38 into Equation 3.14 and with the condition of incompressibility of the shell, $R_b^2\dot{R}_b = R_s^2\dot{R}_s$, Equation 3.14 becomes,

$$\rho\left(R_b^2\ddot{R}_b + \frac{3}{2}\dot{R}_b^2\right) = p_g - p_\infty - \frac{2\gamma}{R_b} - \frac{4}{R_b}\left[\frac{GR_b}{3}\left(1 - \frac{R_{b0}^3}{R_b^3}\right) + \mu\dot{R}_b\right]. \tag{3.39}$$

For the details, the reader is referred to [370].

3.1.2. Encapsulated Bubble in an Unbounded Liquid

As mentioned in Section 2, to enhance therapeutic ultrasound, microbubbles are covered with a thick shell that suspends the drug. This shell also stabilizes the encapsulated bubble, maintaining its inert state until the microbubble reaches its target. With this motivation, in this section, a model for an encapsulated bubble in an unbounded liquid is derived. The physical system is shown in Figure 3.2.

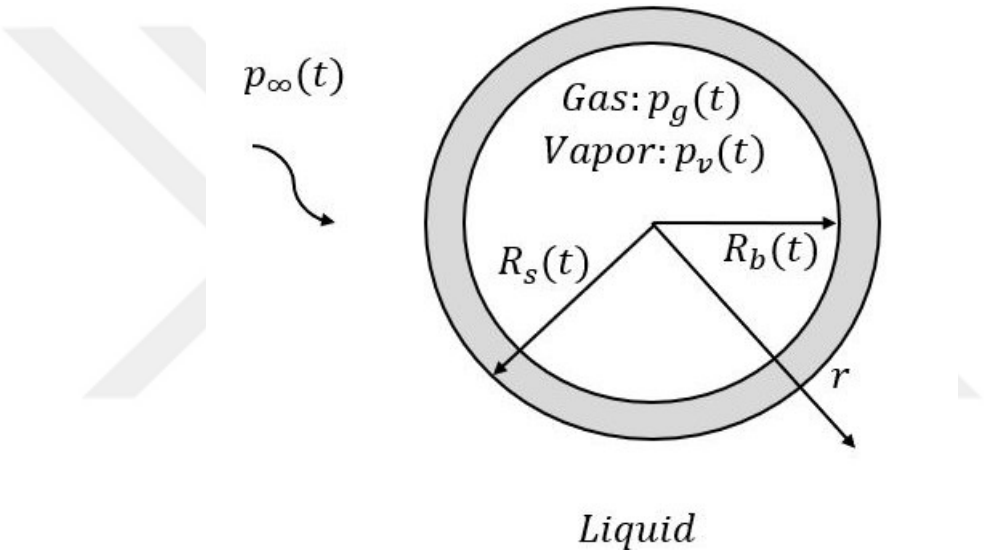

Figure 3.2. Encapsulated bubble in an unbounded liquid.

The continuity equation for the shell and liquid is given as,

$$\nabla \cdot \mathbf{u}_j = 0, \tag{3.40}$$

where the subscript $j = l, s$ represents the liquid and shell properties, respectively. With the boundary conditions $u_s(r = R_b) = \dot{R}_b$ and $u_l(r = R_s) = \dot{R}_s$, the solution of Equation 3.40 for the shell and liquid are given as,

$$u_s = R_b^2 \frac{\dot{R}_b}{r^2}, \tag{3.41}$$

and,

$$u_l = R_s^2 \frac{\dot{R}_s}{r^2}. \tag{3.42}$$

The r component of equation of the motion for the liquid and shell is given as,

$$\rho_j \left(\frac{\partial u_j}{\partial t} + u_j \frac{\partial u_j}{\partial r} \right) = -\frac{\partial p_j}{\partial r} + (\nabla \cdot \mathbf{T}_j)_r, \quad j = l, s. \tag{3.43}$$

For the liquid, the left-hand side of Equation 3.43 is integrated from R_s to R_∞, and after substituting Equation 3.42 gives,

$$\begin{aligned} \int_{R_s}^{\infty} \rho_\ell \left(\frac{\partial u}{\partial t} + u \frac{\partial u}{\partial r} \right) dr &= \rho_\ell \left(-\frac{\ddot{R}_b R_b^2}{r} - 2\frac{\dot{R}_b{}^2 R_b}{r} + 2\frac{(\dot{R}_b)^2 R_b^4}{4r^4} \right) \Bigg|_{R_s}^{\infty} \\ &= \rho_\ell \left(\frac{\ddot{R}_b R_b^2}{R_s} + 2\frac{\dot{R}_b{}^2 R_b}{R_s} - 2\frac{(\dot{R}_b)^2 R_b^4}{4R_s^4} \right), \end{aligned} \tag{3.44}$$

where R_s is the bubble radius with shell, R_b is the bubble radius and ρ_ℓ is the liquid density. For the shell, the left-hand side of Equation 3.43 is integrated from R_b to R_s, and after substituting Equation 3.41 gives,

$$\begin{aligned} \int_{R_b}^{R_s} \rho_s \left(\frac{\partial u}{\partial t} + u \frac{\partial u}{\partial r} \right) dr &= \rho_s \left(-\frac{\ddot{R}_b R_b^2}{r} - 2\frac{\dot{R}_b{}^2 R_b}{r} + 2\frac{(\dot{R}_b)^2 R_b^4}{4r^4} \right) \Bigg|_{R_b}^{R_s} \\ &= \rho_s \left(-\frac{\ddot{R}_b R_b^2}{R_s} - 2\frac{\dot{R}_b{}^2 R_b}{R_s} + 2\frac{(\dot{R}_b)^2 R_b^4}{4R_s^4} \right) + \rho_s \left(\frac{\ddot{R}_b R_b^2}{R_b} + 2\frac{\dot{R}_b{}^2 R_b}{R_b} - 2\frac{(\dot{R}_b)^2 R_b^4}{4R_b^4} \right) \\ &= \rho_s \left(-\frac{\ddot{R}_b R_b^2}{R_s} - 2\frac{\dot{R}_b{}^2 R_b}{R_s} + 2\frac{(\dot{R}_b)^2 R_b^4}{4R_s^4} \right) + \rho_s \left(\ddot{R}_b R_b + 3\frac{(\dot{R}_b)^2}{2} \right). \end{aligned} \tag{3.45}$$

Here, ρ_s is the shell density. Equations 3.44 and 3.45 are combined to give,

$$\begin{aligned} \rho_\ell \left(\frac{\ddot{R}_b R_b^2}{R_s} + 2\frac{\dot{R}_b{}^2 R_b}{R_s} - 2\frac{(\dot{R}_b)^2 R_b^4}{4R_s^4} \right) + \rho_s \left(-\frac{\ddot{R}_b R_b^2}{R_s} - 2\frac{\dot{R}_b{}^2 R_b}{R_s} + 2\frac{(\dot{R}_b)^2 R_b^4}{4R_s^4} \right) \\ + \rho_s \left(\ddot{R}_b R_b + 3\frac{(\dot{R}_b)^2}{2} \right). \end{aligned} \tag{3.46}$$

After re-arranging the terms, Equation 3.46 becomes,

$$\begin{aligned} (\rho_\ell - \rho_s) \left(\frac{\ddot{R}_b R_b^2}{R_s} + 2\frac{\dot{R}_b{}^2 R_b}{R_s} - \frac{(\dot{R}_b)^2 R_b^4}{2R_s^4} \right) + \rho_s \left(\ddot{R}_b R_b + 3\frac{(\dot{R}_b)^2}{2} \right) = \\ \rho_s R_b \ddot{R}_b \left(\frac{R_b}{R_s} \frac{\rho_\ell - \rho_s}{\rho_s} + 1 \right) + \rho_s (\dot{R}_b)^2 \left(\frac{3}{2} + \frac{\rho_\ell - \rho_s}{\rho_s} \left(\frac{R_b}{R_s} \right) \left(\frac{4R_s^3 - R_b^3}{2R_s^3} \right) \right). \end{aligned} \tag{3.47}$$

Finally, the left-hand side of Equation 3.43 becomes,

$$\rho_s R_b \ddot{R}_b F + \rho_s (\dot{R}_b)^2 H, \tag{3.48}$$

where

$$F = \frac{R_b}{R_s}\frac{\rho_\ell - \rho_s}{\rho_s} + 1 \quad \text{and} \quad H = \frac{3}{2} + \frac{\rho_\ell - \rho_s}{\rho_s}\left(\frac{R_b}{R_s}\right)\left(\frac{4R_s^3 - R_b^3}{2R_s^3}\right). \tag{3.49}$$

The right-hand side of Equation 3.43 is integrated from R_b to R_s as,

$$-p_s(R_s,t) + p_s(R_b,t) + \int_{R_b}^{R_s} (\nabla \cdot \mathbf{T}_s) r \, \mathrm{d}r. \tag{3.50}$$

Here, $p_s(R_s,t)$ and $p_s(R_b,t)$ are the shell pressure at the shell/liquid and the bubble/shell interfaces, respectively. Equation 3.43 is integrated from R_s to ∞,

$$p_l(R_s,t) - p_\infty - \tau_{rr,l}(R_s,t) + 3\int_{R_s}^{\infty} \frac{\tau_{rr,l}}{r} \, \mathrm{d}r. \tag{3.51}$$

Here, $\tau_{rr,l}(R_s,t)$ and $p_l(R_s,t)$ are the liquid stress and pressure at the shell/liquid interface. Equations 3.50 and 3.51 are combined to get the right-hand side of Equation 3.43,

$$-p_s(R_s,t) + p_s(R_b,t) + p_l(R_s,t) - p_\infty - \tau_{rr,l}(R_s,t) + \int_{R_b}^{R_s} (\nabla \cdot \mathbf{T}_s)_r \, \mathrm{d}r + 3\int_{R_s}^{\infty} \frac{\tau_{rr,l}}{r} \, \mathrm{d}r. \tag{3.52}$$

Finally, Equations 3.52 and 3.48 are combined,

$$\begin{aligned}\rho_s R_b \ddot{R}_b F + \rho_s (\dot{R}_b)^2 H = &-p_s(R_s,t) + p_s(R_b,t) + p_l(R_s,t) - p_\infty \\ &+ \int_{R_b}^{R_s} (\nabla \cdot \mathbf{T}_s)_r \, \mathrm{d}r - \tau_{rr,l}(R_s,t) + 3\int_{R_s}^{\infty} \frac{\tau_{rr,l}}{r} \, \mathrm{d}r.\end{aligned} \tag{3.53}$$

The normal stress balances at bubble/shell and shell/liquid interfaces are given as [371],

$$p_s(R_b,t) - p_b(R_b,t) + \frac{2\sigma_1}{R_b} = \tau_{rr,s}(R_b,t) - \tau_{rr,g}(R_b,t), \tag{3.54}$$

and

$$p_l(R_s,t) - p_s(R_s,t) + \frac{2\sigma_2}{R_s} = \tau_{rr,l}(R_s,t) - \tau_{rr,s}(R_s,t), \tag{3.55}$$

where σ_1 is the surface tension of the bubble/shell boundary, σ_2 is the surface tension of the shell/liquid boundary. Note that the magnitude $\tau_{rr,g}$ is smaller in order than $\tau_{rr,s}$ since the viscosity of the gas is less than the viscosity of the shell, therefore, $\tau_{rr,g}$ can be neglected.

3.1.2.1. Viscoelastic Shell. Assuming that the volume of the bubble shell remains constant during the bubble motion. The viscoelastic nature of the bubble shell is modeled by the

Kelvin-Voigt constitutive equation. Thus, the stress tensor for the shell is given as,

$$\mathbf{T}_s = \mathbf{T}_v + \mathbf{T}_e, \tag{3.56}$$

where $\mathbf{T}_e$ is the elastic stress.

The viscous stress, $\mathbf{T}_v$, is given by Newton's law of viscosity as,

$$\mathbf{T}_v = \mu_s \left(\nabla \mathbf{u}_s + \nabla \mathbf{u}_s^{\mathrm{T}} \right), \tag{3.57}$$

where μ_s is the shell viscosity. For the velocity profile given by Equation 3.41, Equation 3.57 yields the following expression for the r component of $\mathbf{T}_v$, $\tau_{rr,v}$,

$$\tau_{rr,v} = -4\mu_s \frac{R_b^2 \dot{R}_b}{r^3}. \tag{3.58}$$

$\mathbf{T}_v$ is traceless, so, $\tau_{\theta\theta,v} + \tau_{\phi\phi,v} = -\tau_{rr,v}$. For the incompressible deformations, the elastic stress tensor is

$$\mathbf{T}_e = G\mathbf{B} - \mathscr{P}\mathbf{I} = \begin{bmatrix} G_s \left(\frac{r_o}{r}\right)^4 - \mathscr{P} & 0 & 0 \\ 0 & G_s \left(\frac{r}{r_o}\right)^2 - \mathscr{P} & 0 \\ 0 & 0 & G_s \left(\frac{r}{r_o}\right)^2 - \mathscr{P} \end{bmatrix}. \tag{3.59}$$

where, $\mathscr{P}$ is the pseudo-pressure and $\mathbf{I}$ is the identity matrix. For the neo-Hookean model, $p = \mathscr{P} - G_s \left[(r_o/r)^4 + 2(r/r_o)^2 \right]/3$. G_s is the shear modulus, and $\mathbf{B} = \mathbf{F}\mathbf{F}^{\mathrm{T}}$ is the left Cauchy-Green tensor, $\mathbf{F}$ is the deformation matrix, and defined as

$$\mathbf{F} = \frac{\partial x}{\partial x_o} = \begin{bmatrix} \frac{\partial r}{\partial r_o} & 0 & 0 \\ 0 & \frac{r}{r_o} & 0 \\ 0 & 0 & \frac{r}{r_o} \end{bmatrix}, \tag{3.60}$$

Here, the original configuration is $\mathbf{x}_o = r_o \mathbf{e}_r$, and the current configuration is $\mathbf{x} = r(r_o,t)\,\mathbf{e}_r$. The near field is assumed incompressible, which gives $det(\mathbf{F}) = 1$. Thus,

$$\frac{\partial r}{\partial r_o} = \left(\frac{r_o}{r}\right)^2 \Rightarrow r(r_o,t) = \left[r_o^3 + C(t)\right]^{1/3}, \tag{3.61}$$

where $C(t)$ is an integration factor. An expression for $r_o(r,t)$ can be obtained by evaluating Equation 3.61 at the bubble wall:

$$r_o(r,t) = \left(r^3 - R_b^3 + R_{b,0}^3\right)^{1/3}. \tag{3.62}$$

After substituting the expression of the pseudo-pressure into Equation 3.229, the following expression for the elastic stress components, $\tau_{rr,e}$ and $\tau_{\theta\theta,e}$, are found as

$$\tau_{rr,e} = -2\tau_{\theta\theta,e} = \frac{2G_s}{3}\left[\left(\frac{r_0}{r}\right)^4 - \left(\frac{r}{r_0}\right)^2\right] \tag{3.63}$$

The viscous and the elastic contribution of the shell becomes

$$\int_{R_b}^{R_s} \nabla\cdot\mathbf{T}_v = \int_{R_b}^{R_s} \frac{3}{r}\tau_{rr,v}dr + \tau_{rr,v}(R_s,t) - \tau_{rr,v}(R_b,t) = \\ -4\mu_s\left(\frac{\dot{R}_s}{R_s} - \frac{\dot{R}_b}{R_s}\right) + \tau_{rr,v}(R_s,t) - \tau_{rr,v}(R_b,t), \tag{3.64}$$

and

$$\int_{R_b}^{R_s} \nabla\cdot\mathbf{T}_e = \int_{R_b}^{R_s} \frac{2}{r}\left(\tau_{rr,e} - \tau_{\theta\theta,e}\right)dr - \tau_{rr,e}(R_s,t) = \\ G_s\left(\frac{\left(4R_b^3 + R_{b0}^3\right)R_{b0}}{2R_b^4} - \frac{\left(-R_b^3 + R_{b0}^3 + R_s^3\right)^{1/3}\left(-R_b^3 + R_{b0}^3 + 5R_s^3\right)}{2R_s^4}\right) - \tau_{rr,e}(R_s,t), \tag{3.65}$$

respectively. Therefore, the total contribution of the shell is found as,

$$\int_{R_b}^{R_s} \nabla\cdot\mathbf{T}_s = \int_{R_b}^{R_s} \nabla\cdot\mathbf{T}_e + \int_{R_b}^{R_s} \nabla\cdot\mathbf{T}_v = 4\mu_s\left(\frac{\dot{R}_s}{R_s} - \frac{\dot{R}_b}{R_s}\right) - \tau_{rr,e}(R_s,t) + \tau_{rr,v}(R_s,t) - \\ \tau_{rr,v}(R_b,t) + G_s\left(\frac{\left(4R_b^3 + R_{b0}^3\right)R_{b0}}{2R_b^4} - \frac{\left(-R_b^3 + R_{b0}^3 + R_s^3\right)^{1/3}\left(-R_b^3 + R_{b0}^3 + 5R_s^3\right)}{2R_s^4}\right). \tag{3.66}$$

It is noted that in Section 3.1.1.5, the stress component is given for small strains. Here, a nonlinear neo-Hooken equation is derived for the elastic contribution of shell. Also for the details of the derivation of deformation matrix and the expressions about the continuum mechanics, the reader is referred to Appendix A. After substituting Equations 3.66, 3.54 and 3.55 into Equation 3.53, it becomes

$$\rho_s R_b\ddot{R}_b F + \rho_s(\dot{R}_b)^2 H = \quad -p_\infty + p_b + 4\mu_s\left(\tfrac{\dot{R}_s}{R_s} - \tfrac{\dot{R}_b}{R_s}\right) - \tfrac{2\sigma_1}{R_b} - \tfrac{2\sigma_2}{R_s} + \\ E_s + 3\int_{R_s}^{\infty}\tfrac{\tau_{rr,l}}{r}\,\mathrm{d}r, \tag{3.67}$$

where

$$E_s = G_s\left(\frac{\left(4R_b^3 + R_{b0}^3\right)R_{b0}}{2R_b^4} - \frac{\left(-R_b^3 + R_{b0}^3 + R_s^3\right)^{1/3}\left(-R_b^3 + R_{b0}^3 + 5R_s^3\right)}{2R_s^4}\right). \tag{3.68}$$

Although this section centers on a nonlinear neo-Hookean medium, analogous expressions can be formulated for other linear constitutive relationships (Section 3.1.2.2 are given for the elastic contribution.

3.1.2.2. Linear Elastic Models. The large strains anticipated in the relevant issues encourage employing nonlinear elastic models. Nonetheless, it's beneficial to examine the extreme scenario of infinitesimal strains, known as linear elasticity. All previous assumptions remain valid, except for the application of the generalized Hooke's law [372] for elastic stress. The elastic stress, T_e is given as,

$$T_e = 2G_s E - \mathscr{P} I, \tag{3.69}$$

where E is the linear strain tensor, G_s is the shear modulus and $\mathscr{P}(r,t)$ is a pseudo-pressure. The linear strain can be expressed in terms of the displacement gradient $H = \left(H + H^{\mathrm{T}}\right)/2 = E$, since H is diagonal. Since $F = I + H$, the Cauchy stress tensor for a linear elastic medium is given by

$$T_e = \begin{bmatrix} 2G_s\left[\left(\frac{r_o}{r}\right)^2 - 1\right] - \mathscr{P} & 0 & 0 \\ 0 & 2G_s\left[\left(\frac{r}{r_o}\right) - 1\right] - \mathscr{P} & 0 \\ 0 & 0 & 2G_s\left[\left(\frac{r}{r_o}\right) - 1\right] - \mathscr{P} \end{bmatrix}, \tag{3.70}$$

The elastic contribution of the linear elasticity is given as,

$$E_s = G_s \left(\frac{2\left(R_{b,0}^3\right)^{2/3}}{R_b^2} - \frac{2\left(-R_b^3 + R_{b,0}^3 + R_s^3\right)^{2/3}}{R_s^2} \right). \tag{3.71}$$

Additional to the linear models, Yang and Church [373] obtained a simplified model by retaining the first-order terms in the Taylor series expansions of $(r/r_o)^n$ and assuming small strains, i.e., $\left|\left(R_b^3 - R_{b,o}^3\right)/r^3\right| \ll 1$, the r-component of the Cauchy stress is given by

$$E_s = -4\left[\frac{R_s^3 - R_b^3}{R_s^3 R_b}\right] G_s \left(R_b - R_{be}\right). \tag{3.72}$$

3.1.2.3. Encapsulated Bubble in an Unbounded Newtonian Liquid. In this section, the surrounding liquid is assumed to be Newtonian, and the stress tensor is integrated from the shell radius to infinity, gives,

$$3\int_{R_s}^{\infty} \frac{\tau_{rr,l}}{r}\, \mathrm{d}r = 3\left(4\mu_l \frac{R_s^2 \dot{R}_s}{3r^3}\right)\Bigg|_{R_s}^{\infty} = -\left(4\mu_l \frac{\dot{R}_s}{R_s}\right). \tag{3.73}$$

After substituting Equation 3.73 into Equation 3.67, it becomes,

$$\rho_s R_b \ddot{R}_b F + \rho_s (\dot{R}_b)^2 H = -p_\infty + p_b + 4\mu_s\left(\frac{\dot{R}_s}{R_s} - \frac{\dot{R}_b}{R_s}\right) - \frac{2\sigma_1}{R_b} - \frac{2\sigma_2}{R_s} +$$

$$G_s\left(\frac{\left(4R_b^3+R_{b0}^3\right)R_{b0}}{2R_b^4}-\frac{\left(-R_b^3+R_{b0}^3+R_s^3\right)^{1/3}\left(-R_b^3+R_{b0}^3+5R_s^3\right)}{2R_s^4}\right)-4\mu_l\frac{\dot{R}_s}{R_s}. \quad (3.74)$$

For the details, the reader is referred to [16].

3.1.2.4. Encapsulated Bubble in an Unbounded Power-law Liquid. As mentioned in Section 3.1.1.4, the viscous contribution of the power-law liquid is derived as,

$$3\int_{R_s}^{\infty}\frac{\tau_{rr,l}}{r}\,\mathrm{d}r=3M|\dot{R}_s|^{n-1}\dot{R}_s(R_s^{2n})\frac{r^{-3n}}{3n}\bigg|_{R_s}^{\infty}=-\frac{M}{n}|\dot{R}_s|^{n-1}\frac{\dot{R}_s}{R_s^n}. \quad (3.75)$$

After substituting Equation 3.75 into Equation 3.67, it becomes,

$$\rho_s R_b\ddot{R}_b F+\rho_s(\dot{R}_b)^2H=-p_\infty+p_b+4\mu_s\left(\frac{\dot{R}_s}{R_s}-\frac{\dot{R}_b}{R_s}\right)-\frac{2\sigma_1}{R_b}-\frac{2\sigma_2}{R_s}+$$
$$G_s\left(\frac{\left(4R_b^3+R_{b0}^3\right)R_{b0}}{2R_b^4}-\frac{\left(-R_b^3+R_{b0}^3+R_s^3\right)^{1/3}\left(-R_b^3+R_{b0}^3+5R_s^3\right)}{2R_s^4}\right)-\frac{M}{n}|\dot{R}_s|^{n-1}\frac{\dot{R}_s}{R_s^n}. \quad (3.76)$$

3.1.2.5. Encapsulated Bubble in an Unbounded Viscoelastic Liquid. The viscous and elastic contribution of the viscoelastic liquid is derived as,

$$3\int_{R_s}^{\infty}\frac{\tau_{rr,l}}{r}\,\mathrm{d}r=G_l\left(-\frac{5}{2}+\frac{(4R_s^3+R_{s0}^3)R_{s0}}{2R_s^4}\right). \quad (3.77)$$

After substituting Equation 3.77 into Equation 3.67, it becomes,

$$\rho_s R_b\ddot{R}_b F+\rho_s(\dot{R}_b)^2H=-p_\infty+p_b+4\mu_s\left(\frac{\dot{R}_s}{R_s}-\frac{\dot{R}_b}{R_s}\right)-\frac{2\sigma_1}{R_b}-\frac{2\sigma_2}{R_s}+$$
$$G_s\left(\frac{\left(4R_b^3+R_{b0}^3\right)R_{b0}}{2R_b^4}-\frac{\left(-R_b^3+R_{b0}^3+R_s^3\right)^{1/3}\left(-R_b^3+R_{b0}^3+5R_s^3\right)}{2R_s^4}\right)+$$
$$G_l\left(-\frac{5}{2}+\frac{(4R_s^3+R_{s0}^3)R_{s0}}{2R_s^4}\right). \quad (3.78)$$

In the next section, Section 3.1.3, the effect of elastic blood vessel wall is added to the model. When the cavity size is very large, bubble in an unbounded liquid case can be obtained from Section 3.1.3.

3.1.3. Bubble in a Liquid Cavity

The elastic properties of cavities can impact the behavior of a bubble. Blood vessels or tissues are examples of elastic cavities. Therefore, understanding the effect of the cavity's elastic properties is crucial for advancing spherical oscillations in biomedical technologies and improving the efficiency and precision of various diagnostic and therapeutic approaches [2, 278–285]. This section investigates the effect of elastic solids on bubble dynamics. The physical system is shown in Figure 3.3. Here, $R_b(t)$ and $R_l(t)$ are the time-dependent bubble and liquid cavity radii.

The r-component of the continuity equation for compressible surrounding liquid is given as,

$$\frac{1}{r^2}\frac{\partial\left(r^2u\right)}{\partial r} = -\frac{1}{c^2\rho}\frac{dp}{dt}, \tag{3.79}$$

where,

$$\frac{d\rho}{dt} = \frac{d\rho}{dp}\frac{dp}{dt} \quad \text{and} \quad \frac{dp}{d\rho} = c^2. \tag{3.80}$$

Here, c is the speed of sound in the liquid. The initial bubble radius, R_{b0}, is used as the reference length, and $\Delta p = p_{l0} - p_{\text{sat}}$ as the constant reference pressure, where p_{l0} is the initial liquid pressure and p_{sat} is the saturated vapor pressure. The liquid density is assumed to be spatially uniform.

Equation 3.79 can be expressed in dimensionless form as follows, with dimensionless quantities denoted by an asterisk subscript:

$$\frac{1}{r_*^2}\frac{\partial\left(r_*^2u_*\right)}{\partial r_*} = -\frac{\Delta p}{\rho_0 c^2}\frac{1}{\rho_*}\frac{dp_*}{dt_*}. \tag{3.81}$$

If the reference pressure $\Delta p \leq 2.20$MPa, then $\Delta p/\left(\rho_0 c^2\right) < 0.001$, since $c \approx 1500\ \text{m s}^{-1}$ and $\rho_0 \approx 1000\ \text{kg m}^{-3}$ for water. Here, ρ_0 is the undisturbed liquid density. If the reference pressure $\Delta p < 20$ MPa, the right-hand term in Equation 3.79 becomes negligible, i.e.,

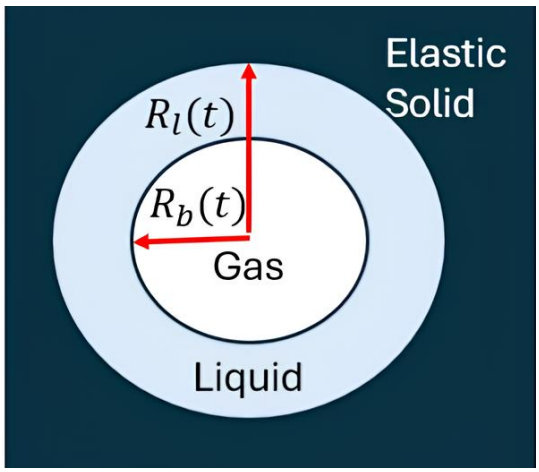

Figure 3.3. Sketch of a bubble in a liquid cavity.

$\partial\left(r^2u\right)/\partial r = 0$. Therefore, the incompressible assumption for the liquid can be used. For further details, refer to [262].

A force balance at the bubble-liquid interface is given as,

$$\tau_{rr}(R_b) + p(R_b) + \frac{2\sigma}{R_b} = p_b + p_v. \tag{3.82}$$

After substituting the force balance, Equation 3.82, into the equation of motion (Equation 3.4) and integrating from the bubble interface to the cavity surface, the right-hand side of Equation of motion becomes

$$p_b - p_{lc} - \frac{2\sigma}{R_b} + \tau_{rr}(R_b) + 3\int_{R_b}^{R_s} \frac{\tau_{rr}}{r}\,\mathrm{d}r \tag{3.83}$$

where p_{lc} is instantaneous pressure at the liquid–solid interface.

The equation of motion (Equation 3.4) is integrated from the bubble radius R_b to the cavity radius R_l, and the general form of the Rayleigh-Plesset type equation becomes,

$$\rho(2\dot{R_b}^2 + \ddot{R}_b R_b)\left(1 - \frac{R_b}{R_l}\right) + \frac{1}{2}\dot{R}_s^2\left(\frac{R_b^4}{R_l^4} - 1\right) = p_b - p_{lc} - \frac{2\sigma}{R_b} + \tau_{rr}(R_l) + 3\int_{R_b}^{R_l} \frac{\tau_{rr}}{r}\,\mathrm{d}r, \tag{3.84}$$

where the gas and liquid pressure expressions, p_b and p_{lc}, can be found in Sections 3.1.1.1 and 3.1.3.1.

3.1.3.1. Liquid Pressure Calculation. The liquid pressure at the cavity surface, p_{lc}, can be determined using different methods. The first method assumes that the liquid pressure

varies linearly with the time-dependent bubble volume (Section 3.1.3.1) [262]. In the second method, the liquid pressure is derived from the stress difference occurring at the surface of the elastic solid [40] (Section 3.1.3.1).

Liquid Pressure Depending on the Volume Change of Bubble

Here, it is assumed that the bubble's volume is much smaller than the cavity's volume, specifically, $V_b/V_c = (R_b/R_l)^3 << 1$ [261]. Therefore, the liquid pressure, depending on the bubble volume change, is given as,

$$p_{lc} - p_{10} = K\frac{V_b - V_{b0}}{V_{c0}} = K\frac{R_b^3 - R_{b0}^3}{R_{l0}^3}, K = \frac{K_c K_l}{K_c + K_l}, \tag{3.85}$$

where R_{l0} is the initial cavity radius, $R_{l0} = R_l(0)$. K is the effective bulk modulus for the system, which increases with the bulk modulus of liquid K_l and the bulk modulus of the confinement K_c. After substituting p_{lc} into Equation 3.84, it becomes

$$(2\dot{R_b}^2 + \ddot{R}_b R_b)\left(1 - \frac{R_b}{R_l}\right) + \frac{1}{2}\dot{R}_b^2\left(\frac{R_b^4}{R_l^4} - 1\right) = p_b - \left(K\frac{R_b^3 - R_{b0}^3}{R_{l0}^3} + p_{l0}\right) - \frac{2\sigma}{R_b} + \tau_{rr}(R_l) + 3\int_{R_b}^{R_l}\frac{\tau_{rr}}{r}\,\mathrm{d}r. \tag{3.86}$$

Liquid Pressure from the Stress Balance:

In the absence of body forces, the equation of motion in the solid is given as [288],

$$\rho_{el}\frac{\partial^2 u_{el}}{\partial t^2} - \nabla\cdot\mathbf{T_{el}} = 0, \tag{3.87}$$

The subscript *el* indicates the elastic solid properties. The displacement field is denoted by u_{el}, and the Cauchy stress tensor for the elastic solid is $\mathbf{T_{el}}$. Under the quasi-static assumption, where all time derivatives in the dynamic system of Equation 3.87 are set to zero gives,

$$[\nabla\cdot\mathbf{T_{el}}]_r = \frac{\partial T_{rr,el}}{\partial r} + \frac{2}{r}\left(T_{rr,el} - T_{\theta\theta,el}\right). \tag{3.88}$$

The displacement profile of the solid can be found as described in [276].

$$u_{el}(r) = ar + \frac{b}{r^2}. \tag{3.89}$$

In the case of an isotropic linear material, the components of the elastic stress are given as,

$$T_{rr,el} = (\lambda + 2\mu_{el})\,\varepsilon_{rr} + 2\lambda\,\varepsilon_{\theta\theta}, \tag{3.90}$$

and

$$T_{\theta\theta,el} = T_{\phi\phi,el} = \lambda\varepsilon_{rr} + 2(\lambda + \mu_{el})\varepsilon_{\theta\theta}, \tag{3.91}$$

with $\varepsilon_{rr,el} = \partial u_{el}/\partial r$ and $\varepsilon_{\theta\theta,el} = \varepsilon_{\phi\phi,el} = u_{el}/r$.

Finally, the r-component of the solid stress is found as

$$T_{rr,el}(r) = 3Ka - 4G\frac{b}{r^3}. \tag{3.92}$$

The shear modulus is defined as $G = \mu_{el}$, and the bulk modulus is given by $K = \lambda + \frac{2}{3}\mu_{el}$. Here, μ_{el} and λ are the Lamé constants. The boundary conditions include the continuity of the normal stress at the liquid-solid interface. Assuming the elastic solid extends infinitely, the normal stress at the outer boundary of the solid at a distance R_∞ is:

$$T_{rr,el}(R_l) = T_{rr,l}(R_l) - p_{lc}, \tag{3.93}$$

and

$$T_{rr,el}(R_\infty) = -\left(p_\infty(t)\right). \tag{3.94}$$

After substituting the general form of the displacement of the elastic solid into the boundary conditions 3.93 and 3.94, they give,

$$-p_{lc} + T_{rr,l}\big|_{r=R_l} = 3Ka - 4G\frac{b}{R_l^3}, \tag{3.95}$$

and,

$$3Ka - 4G\frac{b}{R_\infty^3} = -p_\infty(t). \tag{3.96}$$

From the boundary conditions 3.93 and 3.94, the coefficient a and b are found as,

$$a = -\frac{p_\infty(t)}{3K}, \tag{3.97}$$

and,

$$b = \frac{R_l^3}{4G}\left[p_{lc} - p_\infty(t) - T_{rr,l}\right]_{r=R_l}. \tag{3.98}$$

The incompressibility condition of the liquid gives,

$$\frac{4}{3}\pi R_l^3 - \frac{4}{3}\pi R_b^3 = \frac{4}{3}\pi R_{l0}^3 - \frac{4}{3}\pi R_{b0}^3, \tag{3.99}$$

which yields an expression for the cavity radius, $R_l(t)$. The alteration of the liquid cell volume under tension is associated with the displacement of the liquid-solid boundary as,

$$\frac{4}{3}\pi R_l^3 - \frac{4}{3}\pi R_{l0}^3 = 4\pi R_{l0}^2 u\left(R_{l0}\right). \tag{3.100}$$

Taking into account the general form of displacement in spherical coordinates $u(r)$ (Equation 3.100) and the expressions for coefficients a and b (Equations 3.96 and 3.95), one can find the equation for liquid cell alteration:

$$\frac{R_l^3 - R_{l0}^3}{R_{l0}^2 R_l} = -\frac{p_\infty(t)}{K} + \frac{3}{4G}\left[p_{lc} - T_{rr,l}\big|_{r=R_l} - p_\infty(t)\right]. \tag{3.101}$$

Finally, the unknown liquid pressure, p_{lc} can be found from 3.101 as,

$$p_{lc} = \frac{4G}{3}\left(\frac{R_l^3 - R_{l0}^3}{R_{l0}^2 R_l} + \frac{p_\infty}{K}\right) + T_{rr,l}\big|_{r=R_l} + p_\infty. \tag{3.102}$$

3.1.3.2. Bubble in a Newtonian Liquid Cavity. The viscous contribution of the Newtonian liquid is derived as,

$$3\int_{R_b}^{R_l} \frac{\tau_{rr}}{r}\,\mathrm{d}r = -3\left(4\mu\frac{R_b^2\dot{R}_b}{3r^4}\right)\Bigg|_{R_b}^{R_l} = 4\mu\left(\left(\frac{\dot{R}_b R_b^2}{R_l^3}\right) - \left(\frac{\dot{R}_b}{R_b}\right)\right), \tag{3.103}$$

and

$$\tau_{rr}(R_l) = -\left(4\mu\frac{R_b^2\dot{R}_b}{(R_l)^3}\right). \tag{3.104}$$

After substituting Equations 3.103 and 3.104 into Equation 3.86, it becomes,

$$(2\dot{R}_b^2 + \ddot{R}_b R_b)\left(1 - \frac{R_b}{R_l}\right) + \frac{1}{2}\dot{R}_b{}^2\left(\frac{R_b^4}{R_l^4} - 1\right) = p_b - p_{lc} - \frac{2\sigma}{R_b} - 4\mu\frac{\dot{R}_b}{R_b}. \tag{3.105}$$

3.1.3.3. Bubble in a Carreau-Yasuda Liquid Cavity. The viscous contribution of the Carreau Yasuda liquid is derived as,

$$\boldsymbol{\tau}_l = \mu_l \dot{\boldsymbol{\gamma}}_l, \tag{3.106}$$

where

$$\mu_l = \mu_\infty + (\mu_0 - \mu_\infty)\left(1 + (\lambda\dot{\gamma})^m\right)^{(k-1)/m}. \tag{3.107}$$

Here, μ_0 is the viscosity at zero shear rate (Pa.s), μ_∞ is the viscosity at infinite shear rate (Pa.s), λ is the characteristic time (s), m and k denote the power-law flow indices. For default, $m = 2$ The subscript l shows the liquid properties. $\dot{\gamma}$ is the the second invariant of the strain-rate tensor, $\dot{\boldsymbol{\gamma}}$. The model reduces to the Newtonian liquid when $k = 1$.

$$\tau_{rr,l} = 2\mu_l \frac{\partial u_l}{\partial r} = -4\mu_l \left(\frac{\dot{R}_b R_b^2}{r^3} \right), \tag{3.108}$$

where

$$\mu_l = \mu_\infty + (\mu_0 - \mu_\infty) \left(1 + \left(\lambda 2\sqrt{3} \left| \frac{\dot{R}_b R_b^2}{r^3} \right| \right)^2 \right)^{(k-1)/2}. \tag{3.109}$$

The viscous contribution to the right-hand side of the equation of motion becomes,

$$3 \int_{R_b}^{R_l} \frac{\tau_{rr,l}}{r} \, \mathrm{d}r + \tau_{rr,l}(R_l, t) - 4\mu_l \left(\frac{\dot{R}_b}{R_b} \right). \tag{3.110}$$

The viscous term comes from the Carreau-Yasuda liquid, $3 \int_{R_s}^{R_l} \frac{T_{rr,l}}{r} \mathrm{d}r$, cannot be found analytically. Therefore, the integral of $\frac{T_{rr,l}}{r}$ is computed numerically using the trapezoidal rule.

3.1.3.4. Bubble in a Viscoelastic Liquid Cavity. The viscous contribution of the viscoelastic liquid is derived as [16],

$$3 \int_{R}^{R_c} \frac{\tau_{rr,l}}{r} \, \mathrm{d}r = -\left(\frac{4}{R_b} - \frac{4R_b^2}{R_l^3} \right) \left[\frac{G_l R_b}{3} \left(1 - \frac{R_{b0}^3}{R_b^3} \right) + \mu_l \dot{R}_b \right], \tag{3.111}$$

and

$$\tau_{rr,l}(R_l) = -\frac{4R_b^2}{R_l^3} \left[\frac{G_l R_b}{3} \left(1 - \frac{R_{b0}^3}{R_b^3} \right) + \mu \dot{R}_b \right]. \tag{3.112}$$

After substituting Equations 3.111 and 3.112 into Equation 3.86, it becomes,

$$(2\dot{R}_b^2 + \ddot{R}_b R_b) \left(1 - \frac{R_b}{R_l} \right) + \frac{1}{2}\dot{R}^2 \left(\frac{R^4}{R_l^4} - 1 \right) = p_b - p_{lc} - \frac{2\sigma}{R_b} - \left(\frac{4}{R_b} \right) \left[\frac{G R_b}{3} \left(1 - \frac{R_{b0}^3}{R_b^3} \right) + \mu_l \dot{R}_b \right]. \tag{3.113}$$

3.1.3.5. Bubble Encapsulated with a Shell in a Liquid Cavity. In addition to the effect of the elastic solid, the effect of encapsulation of a bubble is included into the model in this

section. The physical system is shown in Figure 3.4. Here, R_b, R_s and R_l indicate the time-dependent bubble, shell, and cavity radii, respectively.

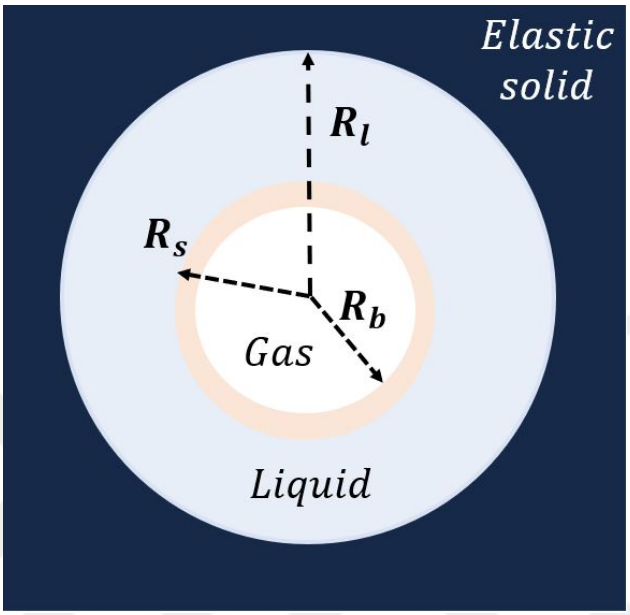

Figure 3.4. Sketch of an encapsulated bubble in a liquid cavity.

The continuity equation for the incompressible shell is given as,

$$\nabla \cdot v_s = 0. \tag{3.114}$$

Here, v is the velocity field and the subscript s shows the shell properties. The r-component of velocity, u_s, can be found from Equation 3.114 with ($u_s(r = R_b) = \dot{R}_b$) as,

$$u_s = \frac{R_b^2 \dot{R}_b}{r^2}. \tag{3.115}$$

For the bubble shell, using continuum mechanics finite-strain formalism [335, 374–376], Cauchy's equation of motion is

$$\frac{\partial v_s}{\partial t} + (v_s \cdot \nabla) v_s = \frac{1}{\rho_s} \nabla \cdot \mathbf{T_s}. \tag{3.116}$$

Here, $\mathbf{T}$ is the Cauchy stress tensor and ρ_s is the shell density. For an incompressible surrounding liquid, the continuity equation is given as,

$$\nabla \cdot v_l = 0. \tag{3.117}$$

The r-component of liquid velocity, u_l, is found from the continuity equation (Equation 3.117) with $u(r = R_s) = \dot{R}_s$ as,

$$u_l = \frac{R_s^2 \dot{R}_s}{r^2}. \tag{3.118}$$

The momentum equation for the surrounding liquid is given as

$$\rho_l \left(\frac{\partial \mathbf{v}_l}{\partial t} + \mathbf{v}_l \cdot \nabla \mathbf{v}_l \right) = -\nabla p_l + [\nabla \cdot \mathbf{T}]_l. \tag{3.119}$$

The normal stress balances at the bubble/shell and shell/liquid interfaces are given as,

$$p_s(R_b,t) - p_b(R_b,t) + \frac{2\sigma_b}{R_b} = T_{rr,s}(R_b,t) - T_{rr,b}(R_b,t), \tag{3.120}$$

and,

$$p_l(R_s,t) - p_s(R_s,t) + \frac{2\sigma_s}{R_s} = \tau_{rr,l}(R_s,t) - T_{rr,s}(R_s,t). \tag{3.121}$$

The magnitude of $T_{rr,b}$ is smaller than $T_{rr,s}$ because the viscosity of the gas is lower than that of the shell. The incompressible liquid and shell velocity profiles (Equations 3.118 and 3.115) are then substituted into Equation 3.119. Subsequently, Equation 3.119 is integrated from R_b to R_s and from R_s to R_l. The final form of the equation of motion is:

$$\rho_s R_b \ddot{R}_b F + \rho_s \left(\dot{R}_b\right)^2 H = -p_s(R_s,t) + p_s(R_b,t) + p_l(R_s,t) - p_l(R_l,t) + \tau_{rr,l}(R_l,t) - \tau_{rr,l}(R_s,t) + E_s(t) + 3\int_{R_s}^{R_l} \frac{\tau_{rr,l}}{r}\, \mathrm{d}r, \tag{3.122}$$

where

$$F = -\frac{\rho_\ell}{\rho_s}\frac{R_b}{R_l} + \frac{R_b}{R_s}\frac{\rho_\ell - \rho_s}{\rho_s} + 1, \tag{3.123}$$

and

$$H = \left(\frac{3}{2} + \frac{\rho_\ell - \rho_s}{\rho_s} \left(\frac{R_b}{R_s}\right) \left(\frac{4R_s^3 - R_b^3}{2R_s^3} \right) - 2\frac{\rho_l}{\rho_s}\frac{R_b}{R_l} + \frac{\rho_l}{\rho_s}\frac{R_b^4}{2R_l^4} \right). \tag{3.124}$$

Here, E_s is the elastic term and for neo-Hooken material, it is given as

$$E_s = G_s \left(\frac{\left(4R_b^3 + R_{b,0}^3\right) R_{b,0}}{2R_b^4} - \frac{\left(R_{b,0}^3 - R_b^3 + R_s^3\right)^{1/3} \left(R_{b,0}^3 - R_b^3 + 5R_s^3\right)}{2R_s^4} \right). \tag{3.125}$$

Although this section focuses on a nonlinear neo-Hookean medium, similar expressions concerning the elastic terms can be derived for other linear constitutive relationships (see Section 3.1.2.2). When $R_s \to \infty$, the same elastic term as Murakami et al. [335], E_s can be obtained for the bubble in an unbounded viscoelastic liquid case. The shell radius can be found from the incompressibility condition of the shell,

$$R_b^2 \dot{R}_b = R_s^2 \dot{R}_s, \tag{3.126}$$

and the expression for the liquid radius cavity, R_l and liquid pressure, p_l are found from Equations 3.99 and 3.102.

3.1.3.6. Bubble Encapsulated with a Viscoelastic Shell in a Newtonian Liquid Cavity. The viscous contribution of the Newtonian liquid is given as,

$$3\int_{R_s}^{R_c} \frac{\tau_{rr,l}}{r}\,\mathrm{d}r = 3\left(4\mu_l \frac{R_b^2 \dot{R}_b}{3r^3}\right)\Bigg|_{R_s}^{R_c} = 4\mu_l R_b^2 \dot{R}_b \left(\frac{R_b^2 \dot{R}_b}{R_s^3}\right) + \left(4\mu_l \frac{R_b^2 \dot{R}_b}{R_c^3}\right), \tag{3.127}$$

and

$$\tau_{rr,l} = -\left(4\mu_l \frac{R_b^2 \dot{R}_b}{R_l^3}\right). \tag{3.128}$$

After substituting Equations 3.127 and Equation 3.128 into Equation 3.122, it becomes,

$$\begin{aligned}\rho_s R_b F \ddot{R}_b + \rho_s H \dot{R}_b^2 = p_b - K\frac{R_b^3 - R_{b0}^3}{R_{c0}^3} - p_{10} - \frac{2\sigma_1}{R_b} - \frac{2\sigma_2}{R_s} \\ - 4\left(\frac{R_s^3 - R_b^3}{R_s^3 R_b}\right)\left[G_s\left(R_b - R_{e1}\right) + \mu_s \dot{R}_1\right] + 4\mu_l\left(\frac{R_b^2 \dot{R}_b}{R_s^3}\right).\end{aligned} \tag{3.129}$$

3.1.3.7. Bubble Encapsulated with Viscoelastic Shell in Viscoelastic Liquid Cavity. The viscous contribution of the viscoelastic linear liquid is given as

$$\begin{aligned}3\int_{R_s}^{R_c} \frac{\tau_{rr,l}}{r}\,\mathrm{d}r = \frac{4R_b^2}{r^3}\left[\frac{G_l R_b}{3}\left(1 - \frac{R_{10}^3}{R_b^3}\right) + \mu \dot{R}_b\right]\Bigg|_{R_s}^{R_c} = \\ \left(\frac{4R_b^2}{R_c^3} - \frac{4R_b^2}{R_s^3}\right)\left[\frac{G_l R_b}{3}\left(1 - \frac{R_{10}^3}{R_b^3}\right) + \mu_l \dot{R}_b\right],\end{aligned} \tag{3.130}$$

and

$$\tau_{rr,l}(R_l) = -\frac{4R_b^2}{R_l^3}\left[\frac{G_l R_b}{3}\left(1-\frac{R_{10}^3}{R_b^3}\right)+\mu\dot{R}_b\right]. \tag{3.131}$$

After substituting Equations 3.130 and Equation 3.131 into Equation 3.122, it becomes,

$$\begin{aligned}\rho_s R_b F\ddot{R}_1+\rho_s H\dot{R}_1^2 = p_b - p_{lc} - \frac{2\sigma_b}{R_b} - \frac{2\sigma_s}{R_s} \\ - \frac{4R_b^2}{R_l^3}\left[\frac{G_l R_b}{3}\left(1-\frac{R_{10}^3}{R_b^3}\right)+\mu\dot{R}_b\right] - 4\left(\frac{R_s^3-R_b^3}{R_s^3 R_b}\right)\left[G_s\left(R_b-R_{e1}\right)+\mu_s\dot{R}_1\right] + \\ \left(\frac{4R_b^2}{R_b^3}-\frac{4R_b^2}{R_s^3}\right)\left[\frac{G_l R_b}{3}\left(1-\frac{R_{10}^3}{R_b^3}\right)+\mu_l\dot{R}_b\right].\end{aligned} \tag{3.132}$$

3.1.3.8. Bubble Encapsulated with Viscoelastic Shell in Carreau-Yasuda Cavity. The surrounding liquid obeys the Carreau Yasuda model, and the stress, $\mathbf{T}_l$, is given as,

$$\boldsymbol{\tau}_l = \mu_l\dot{\boldsymbol{\gamma}}_l, \tag{3.133}$$

where

$$\mu_l = \mu_\infty + (\mu_0-\mu_\infty)\left(1+(\lambda\dot{\gamma})^m\right)^{(k-1)/m}. \tag{3.134}$$

$$\tau_{rr,l} = 2\mu_l\frac{\partial u_l}{\partial r} = -4\mu_l\left(\frac{\dot{R}_s R_s^2}{r^3}\right). \tag{3.135}$$

For $m=2$,

$$\mu_l = \mu_\infty + (\mu_0-\mu_\infty)\left(1+\left(\lambda 2\sqrt{3}\left|\frac{\dot{R}_s R_s^2}{r^3}\right|\right)^2\right)^{(k-1)/2}. \tag{3.136}$$

The momentum equation for the surrounding liquid is given as becomes,

$$\begin{aligned}\rho_s R_b\ddot{R}_b F+\rho_s\left(\dot{R}_b\right)^2 H = 3\int_{R_s}^{R_l}\frac{\tau_{rr,l}}{r}\,\mathrm{d}r+\tau_{rr,l}(R_l,t)+E_s-4\mu_s\left(\frac{R_s^3-R_b^3}{R_s^3 R_b}\right)\dot{R}_b + \\ p_v-p_l+\left(\frac{R_{b0}}{R_b}\right)^{3\kappa}\left(p_0+p_v+\frac{2\sigma_b}{R_{b0}}\right)-2\left(\frac{\sigma_s}{R_s}+\frac{\sigma_b}{R_b}\right).\end{aligned} \tag{3.137}$$

Here, E_s is the elastic term and for neo-Hooken material, it is given as

$$E_s = G_s \left(\frac{\left(4R_b^3 + R_{b,0}^3\right) R_{b,0}}{2R_b^4} - \frac{\left(R_{b,0}^3 - R_b^3 + R_s^3\right)^{1/3} \left(R_{b,0}^3 - R_b^3 + 5R_s^3\right)}{2R_s^4} \right). \tag{3.138}$$

The viscous term comes from the Carreau-Yasuda liquid, $3\int_{R_s}^{R_l} \frac{T_{rr,l}}{r}\,\mathrm{d}r$, cannot be found analytically. Therefore, the integral of $\frac{T_{rr,l}}{r}$ is computed numerically using the trapezoidal rule. When $R_s \to \infty$, the same elastic term as Murakami et al. [335] can be obtained for the bubble in an unbounded viscoelastic liquid case.

3.1.4. Linearized Equations for Spherical Oscillations of a Bubble

As the bubble radius reaches its final equilibrium radius, its oscillations are small. Consequently, Equation 3.132 can be simplified by assuming,

$$R_b(t) = R_{\mathrm{be}} + x_b(t), |x_b| \ll R_{\mathrm{be}}, \tag{3.139}$$

$$R_s(t) = R_{\mathrm{se}} + x_s(t), |x_s| \ll R_{\mathrm{se}}, \tag{3.140}$$

and

$$R_l(t) = R_{\mathrm{le}} + x_l(t), |x_l| \ll R_{\mathrm{le}}, \tag{3.141}$$

Here, R_{be}, R_{se}, and R_{le} represent the final equilibrium radii of the bubble, shell, and cavity, respectively. By substituting these expressions into Equation 3.132 and retaining only the time-independent terms, the following result is obtained.

$$p_{g,eq}\left(\frac{R_{b0}}{R_{be}}\right)^{3\kappa} - 2\left(\frac{\sigma_b}{R_{be}} + \frac{\sigma_s}{R_{se}}\right) - p_0 - \frac{p_0}{K} + 4G\frac{(R_{l0}^3 - R_{le}^3)}{3R_{l0}^3} - G_s\frac{AB^{1/3}}{2R_{se}^4} + G_s\frac{R_{b0}\left(R_{b0}^3 + 4R_{be}^3\right)}{2R_{be}^4} = 0, \tag{3.142}$$

where

$$A = R_{b0}^3 - R_{be}^3 + 5R_{se}^3, \tag{3.143}$$

and

$$B = R_{b0}^3 - R_{be}^3 + R_{se}^3. \tag{3.144}$$

This equation should be supplemented with

$$R_{le}^3 - R_{se}^3 = R_{l0}^3 - R_{s0}^3, \tag{3.145}$$

and

$$R_{se}^3 - R_{be}^3 = R_{s0}^3 - R_{b0}^3. \tag{3.146}$$

Equations 3.142 and 3.145 give the definitions of R_{be} and R_{le}. Keeping only linear time-varying terms in Equation 3.132, one obtains

$$\ddot{x}_b \rho_s R_{be}^2 \left(\frac{R_{be}}{R_{le}} \frac{\rho_l}{\rho_s} - \frac{\rho_l - \rho_s}{\rho_s} \frac{R_{be}}{R_{se}} + 1 \right) = -3 p_{b,eq} \kappa x_b + 2 \left(\frac{\sigma_b x_b}{R_{be}} + \frac{\sigma_s x_s}{R_{se}} \right) - \frac{4 G R_{le}^3 x_c}{R_{10}^3} +$$
$$x_b G_s \left(\frac{3 R_{be}^3 B^{1/3} + \frac{R_{be}^3 A}{B^{2/3}}}{2 R_{se}^4} - \frac{R_{b0} \left(4 R_{b0}^3 + 4 R_{be}^3 \right)}{2 R_{be}^4} \right) - \frac{x_s G_s \left(15 R_{se}^3 B^{1/3} - \left(4 B^{1/3} - \frac{R_{se}^3}{B^{2/3}} \right) A \right)}{2 R_{se}^4}. \tag{3.147}$$

To solve this equation, it is assumed that

$$x_b = a_b e^{-i\omega t}, \quad x_s = a_s e^{-i\omega t}, \quad x_l = a_l e^{-i\omega t}. \tag{3.148}$$

Substituting Equation 3.148 into Equation 3.147 to express a_l in terms of a_b, and then removing a_b, the following equation is obtained:

$$\omega^2 + 2 i \alpha \omega - \omega_0^2 = 0, \tag{3.149}$$

where

$$\alpha = \frac{2 \mu_s \frac{R_{se}^3 - R_{be}^3}{R_{se}^3}}{\rho_s R_{be}^2 \left(1 - \frac{R_{be}}{R_{le}} \frac{\rho_l}{\rho_s} + \frac{\rho_l - \rho_s}{\rho_s} \frac{R_{be}}{R_{se}} \right)}, \tag{3.150}$$

and

$$\omega_0^2 = -\frac{1}{\rho_s R_{be}^2 \left(1 - \frac{R_{be}}{R_{le}} \frac{\rho_l}{\rho_s} + \frac{\rho_l - \rho_s}{\rho_s} \frac{R_{be}}{R_{se}} \right)} \left[\frac{4 G R_{le}^3 \varepsilon^3}{R_{l0}^3} - 2 \left(\frac{\sigma_b}{R_{be}} + \frac{\sigma_s \varepsilon^3}{R_{se}} \right) + \right.$$

$$3\kappa(p_{atm}-p_v)+\frac{6\kappa\sigma_b}{R_{be}}-G_s\left(\frac{3R_{be}^3B^{1/3}+\frac{R_{be}^3A}{B^{2/3}}}{2R_{se}^4}-\frac{R_{b0}\left(4R_{b0}^3+4R_{be}^3\right)}{2R_{be}^4}\right)+\frac{G_s\varepsilon^3\left(15R_{se}^3B^{1/3}-\left(4B^{1/3}-\frac{R_{se}^3}{B^{2/3}}\right)A\right)}{2R_{se}^4}\Bigg]. \quad (3.151)$$

Here,

$$\beta=\frac{R_{be}}{R_{le}},\quad \varepsilon=\frac{R_{be}}{R_{se}}. \quad (3.152)$$

If $\rho_l=\rho_s$, and $\sigma_s=0=\tau_0=G_s$, the liquid pressure varies linearly with the cavity volume, and the physical properties of shell and liquid are taken same, the natural frequency for the bubble in a Newtonian liquid-cavity can be obtained as [11],

$$\omega_0=\sqrt{\frac{1}{1-\beta}\left[\frac{3\kappa R_{beq}}{\rho R_{beq}^2}+\frac{(6\kappa-2)\sigma}{\rho R_{beq}^3}+\beta^3\frac{3K}{\rho R_{beq}^2}\right]}. \quad (3.153)$$

If the pressure is found from the normal stress balance (Equation 3.85), the natural frequency for a bubble in a liquid cavity becomes

$$\omega_0=\sqrt{\frac{1}{\rho_sR_{be}^2\left(1-\frac{R_{be}}{R_{le}}\frac{\rho_l}{\rho_s}+\frac{\rho_l-\rho_s}{\rho_s}\frac{R_{be}}{R_{se}}\right)}\left[\frac{4GR_{le}^3\varepsilon^3}{R_{l0}^3}-2\left(\frac{\sigma_b}{R_{be}}+\frac{\sigma_s\varepsilon^3}{R_{se}}\right)+3\kappa(p_{atm}-p_v)+\frac{6\kappa\sigma_b}{R_{be}}\right]}. \quad (3.154)$$

For a bubble in a viscoelastic liquid cavity, the natural frequency is given as,

$$\omega_0=\sqrt{\frac{1}{\rho_sR_{be}^2\left(1-\frac{R_{be}}{R_{le}}\frac{\rho_l}{\rho_s}+\frac{\rho_l-\rho_s}{\rho_s}\frac{R_{be}}{R_{se}}\right)}\left[\frac{4GR_{le}^3\varepsilon^3}{R_{l0}^3}-2\left(\frac{\sigma_b}{R_{be}}+\frac{\sigma_s\varepsilon^3}{R_{se}}\right)+3\kappa(p_{atm}-p_v)+\frac{6\kappa\sigma_b}{R_{be}}+4G_{liq}\right]}. \quad (3.155)$$

where $4G_{liq}$ is the additional term for the viscoelastic liquid.

As $\beta^{-1} = R_{le}/R_{be} \to \infty$, we have $\omega_0 = \omega_{0\infty}$, where $\omega_{0\infty}$ is the natural frequency of radial mode for a bubble in an unbounded liquid [232] and it is given as,

$$\omega_0 = \sqrt{\left[\frac{3\kappa p_{eq}}{\rho R_{\text{beq}}^2} + \frac{(6\kappa-2)\gamma}{\rho R_{\text{beq}}^3}\right]}. \tag{3.156}$$

If the bubble is in an unbounded viscoleastic liquid, the natural frequency becomes,

$$\omega_0 = \sqrt{\left[\frac{3\kappa p_{eq}}{\rho R_{\text{beq}}^2} + \frac{(6\kappa-2)\gamma}{\rho R_{\text{beq}}^3} + 4G_{liq}\right]}. \tag{3.157}$$

For an encapsulated bubble in an unbounded Newtonian liquid ($\beta^{-1} = R_{le}/R_{be} \to \infty$), the natural frequency is found as,

$$\omega_0 = \sqrt{\left[\frac{3\kappa p_{eq}}{\rho R_{\text{beq}}^2} + \frac{(6\kappa-2)\gamma}{\rho R_{\text{beq}}^3} - G_s\left(\frac{3R_{be}^3 B^{1/3} + \frac{R_{be}^3 A}{B^{2/3}}}{2R_{se}^4} - \frac{R_{b0}\left(4R_{b0}^3 + 4R_{be}^3\right)}{2R_{be}^4}\right)\right]} + \sqrt{\left[\frac{G_s\varepsilon^3\left(15R_{se}^3 B^{1/3} - \left(4B^{1/3} - \frac{R_s^3}{B^{2/3}}\right)A\right)}{2R_{se}^4}\right]}. \tag{3.158}$$

If the encapsulated bubble is assumed to be in an unbounded ($\beta^{-1} = R_{le}/R_{be} \to \infty$) viscoelastic liquid, the natural frequency becomes,

$$\omega_0 = \sqrt{\left[\frac{3\kappa p_{eq}}{\rho R_{\text{beq}}^2} + \frac{(6\kappa-2)\gamma}{\rho R_{\text{beq}}^3} - G_s\left(\frac{3R_{be}^3 B^{1/3} + \frac{R_{be}^3 A}{B^{2/3}}}{2R_{se}^4} - \frac{R_{b0}\left(4R_{b0}^3 + 4R_{be}^3\right)}{2R_{be}^4}\right)\right]} + \sqrt{\left[\frac{G_s\varepsilon^3\left(15R_{se}^3 B^{1/3} - \left(4B^{1/3} - \frac{R_s^3}{B^{2/3}}\right)A\right)}{2R_{se}^4} + 4G_{liq}\right]}. \tag{3.159}$$

In the next section, in addition to the spherical oscillations, nonspherical oscillations of a bubble are also considered.

3.2. Non-Spherical Oscillations of a Bubble

The use of contrast agents in the delivery of targeted drugs requires controlled fragmentation of microbubbles. Bubble breakup is associated with the loss of spherical symmetry, which occurs because of the instabilities at the interface between the two fluids involved:

the gas and the host liquid. Therefore, investigating non-spherical oscillations is essential for microbubble biomedical applications. In this section, the shape stability of a bubble in an unbounded power-law liquid and then the effect of the shell on the shape stability are investigated. The physical system consists of a bubble in a homogeneous liquid described in spherical coordinates by a radial distance r and a polar angle θ, as shown in Figure 3.5.

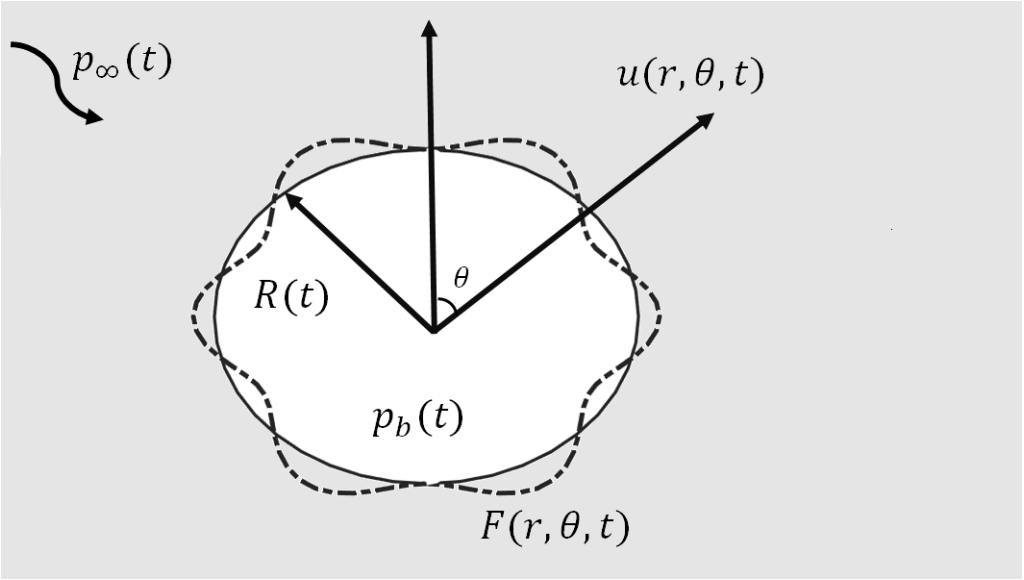

Figure 3.5. Non-spherical bubble geometry in spherical coordinates. The solid and dashed lines show the spherical and non-spherical oscillations.

The continuity and the momentum equations for the surrounding liquid are written as,

$$\nabla \cdot \mathbf{v} = \mathbf{0}, \tag{3.160}$$

and

$$\rho\left(\frac{\partial \mathbf{v}}{\partial t} + \mathbf{v}\nabla\cdot\mathbf{v}\right) = -\nabla p + [\nabla\cdot\tau], \tag{3.161}$$

In this context, $\mathbf{v}$, p, and τ represent the surrounding liquid's velocity, pressure, and stress fields, respectively. At the surface of the bubble, four boundary conditions need to be satisfied: kinematic boundary condition, no-slip conditions, and both normal and tangential stress

balances, which are described as follows:

$$\frac{\partial F}{\partial t} + (\mathbf{v} \cdot \nabla) F = 0, \tag{3.162}$$

$$\mathbf{v}_l \cdot \mathbf{t} = \mathbf{v}_\mathbf{g} \cdot \mathbf{t}, \tag{3.163}$$

$$\mathbf{n} \cdot \tau_l \mathbf{n} - \mathbf{n} \cdot \tau_g \mathbf{n} = \sigma \nabla \cdot \mathbf{n}, \tag{3.164}$$

and

$$\mathbf{n} \times \tau_l \mathbf{n} - \mathbf{n} \times \tau_g \mathbf{n} = \mathbf{0}, \tag{3.165}$$

where the subscripts l and g denote the liquid and gas phases, respectively. σ represents the surface tension. The normal vector, $\mathbf{n}$ of the interface is

$$\mathbf{n} = \frac{\nabla F}{\|\nabla F\|} = \mathbf{e}_r - \varepsilon \frac{a_n}{R} P_n' \mathbf{e}_\theta. \tag{3.166}$$

Here, $P_n' = \dfrac{dP_n(\cos\theta)}{d\theta}$. With the irrotational flow assumption, the condition $\nabla \times \mathbf{v} = \mathbf{0}$ is inherently satisfied by expressing the flow as follows:

$$\mathbf{v} = -\nabla \phi. \tag{3.167}$$

Here, ϕ is the velocity potential. The incompressiblity condition, Equation 3.160, gives,

$$\nabla^2 \phi = \frac{1}{r^2} \frac{\partial}{\partial r} \left(r^2 \frac{\partial \phi}{\partial r} \right) + \frac{1}{r^2 \sin\theta} \frac{\partial}{\partial \theta} \left(\sin\theta \frac{\partial \phi}{\partial \theta} \right) + \frac{1}{r^2 \sin^2\theta} \frac{\partial^2 \phi}{\partial \varphi^2} = 0. \tag{3.168}$$

The solutions to this equation are known as spherical harmonic functions. The system is assumed to have axial symmetry, where ϕ is independent of the angle, φ. Therefore, Equation 3.168 is considered in the form $\phi(r,\theta) = X(r)Y(\theta)$. By applying the method of separation of variables to Laplace's equation, two differential equations are obtained:

$$\frac{1}{X} \frac{d}{dr} \left(r^2 \frac{dX}{dr} \right) = \lambda, \tag{3.169}$$

and

$$\frac{1}{Y} \frac{1}{\sin\theta} \frac{\partial}{\partial \theta} \left(\sin\theta \frac{\partial Y}{\partial \theta} \right) = -\lambda, \tag{3.170}$$

respectively, and the solution is found as,

$$X = Ar^n + \frac{B}{r^{n+1}}, \quad \text{and} \quad Y = P_n(\cos\theta). \tag{3.171}$$

By combining X and Y, Equation 3.171, the potential, ϕ is found as,

$$\phi(r,\theta,t) = \frac{A_0}{r} + B_0 + \sum_{n=2}^{\infty}\left[\frac{A_n(t)}{r^{n+1}} + B_n(t)r^n\right]P_n(\cos\theta), \tag{3.172}$$

where $A_n(t)$ and $B_n(t)$ are coefficients to be determined from the kinematic boundary conditions. The details of the velocity potential derivation are given in Appendix B.1.

The bubble is assumed to be approximately spherical, while undergoing nonlinear radial oscillation and shape oscillations with small amplitude. The shape perturbation to a spherical bubble can be expanded in terms of the spherical harmonics. Therefore, the bubble surface, represented by $F(r,\theta,t)$, can be described using the Legendre polynomials:

$$F(r,\theta,t) = r - R(t) - \varepsilon a_n(t)P_n(\cos\theta) = 0. \tag{3.173}$$

In this context, εa_n represents the perturbation amplitude of the spherical harmonic mode, while P_n is a Legendre polynomial of degree $n > 2$. The parameter ε is on the order of $O\left(\frac{\|a_n\|}{R}\right)$, where $0 < \varepsilon \ll 1$. It should be noted that the summation starts from $n = 2$ because $n = 1$ pertains to the translation of the undeformed bubble, which is not considered in this section.

3.2.1. Field Decomposition

It is assumed that the velocity variations caused by non-spherical perturbations are significantly smaller compared to those from radial motion, the velocity field is thus decomposed as follows:

$$\mathbf{v} = \mathbf{v}_0 + \varepsilon\mathbf{v}_1. \tag{3.174}$$

Here, the subscripts 0 and 1 indicate the radial motion or base state and the non-spherical corrections, respectively.

The pressure field is similarly decomposed:

$$p = p_0 + \varepsilon p_1. \tag{3.175}$$

3.2.1.1. Base State: Spherical Oscillations. In the base state, a bubble undergoes spherical oscillations where the initial liquid pressure exceeds the initial gas pressure. The continuity and momentum equations for the base state are expressed in spherical coordinates as follows:

$$\frac{1}{r^2}\frac{\partial\left(r^2 u_0\right)}{\partial r} = 0, \tag{3.176}$$

and

$$\rho\left(\frac{\partial u_0}{\partial t} + u_0\frac{\partial u_0}{\partial r}\right) = -\frac{\partial p_0}{\partial r} + [\nabla\cdot\tau_{\mathbf{0}}]_{\mathbf{r}}, \tag{3.177}$$

respectively. Here, $-[\nabla\cdot\tau_{\mathbf{0}}]_r = \frac{1}{r^2}\frac{\partial\left(r^2\tau_{0,rr}\right)}{\partial r} - \frac{\tau_{0,\theta\theta}+\tau_{0,\phi\phi}}{r}$. $\tau_{0,rr}$, $\tau_{0,\theta\theta}$ and $\tau_{0,\phi\phi}$ are the stress components. τ is traceless, so, $\tau_{0,\theta\theta}+\tau_{0,\phi\phi} = -\tau_{0,rr}$. $u_{0,r}$ is the velocity component in the r-direction. The solution of Equation 3.176 with the kinematic condition, $u_0(r=R)=0$, gives

$$u_0 = R_b^2\frac{\dot{R}_b}{r^2}. \tag{3.178}$$

The normal stress balance at the bubble-liquid interface is given as,

$$\tau_{0,rr}(R_b) + p_0(R_b) + \frac{2\sigma}{R_b} = p_b. \tag{3.179}$$

The expression for p_b is provided in Equation 3.21. By substituting the velocity profile from Equation 3.178 into Equation 3.177 and integrating from R to infinity, we obtain the following differential equation describing the rate of change of the bubble radius with respect to time:

$$\rho\left(2\dot{R}^2 + \ddot{R}_b R_b\right) - \frac{1}{2}\rho{\dot{R}_b}^2 = p(R_b) - p_\infty + \tau_{0,rr}(R) + 3\int_{R_b}^{\infty}\frac{\tau_{0,rr}}{r}dr, \tag{3.180}$$

where $p_\infty = p_a\sin(\omega t)$, with p_a being the amplitude of the acoustic field pressure and ω the frequency of the acoustic field. By substituting Equation 3.179 into Equation 3.180, it becomes:

$$\rho\left(\ddot{R}_b R_b + 1.5\dot{R}_b^2\right) = p_b - p_a\sin(\omega t) - \frac{2\sigma}{R_b} + 3\int_{R_b}^{\infty}\frac{\tau_{0,rr}}{r}dr. \tag{3.181}$$

3.2.1.2. Perturbed State: Non-Spherical Oscillations. Following the field decomposition, the continuity equation and the equation of motion are expressed as:

$$\nabla \cdot v_1 = 0, \tag{3.182}$$

and

$$\rho \frac{\partial v_1}{\partial t} + \rho \left(v_0 \cdot \nabla\right) \mathbf{v}_1 + \rho \left(\mathbf{v}_1 \cdot \nabla\right) \mathbf{v}_0 + \nabla p_1 = 0, \tag{3.183}$$

respectively. The no-penetration condition at the non-spherical bubble surface is described in [225, 326, 377].

$$\mathbf{v}_1 \cdot \mathbf{n}_w = \dot{R} + \dot{a}_n P_n(\cos\theta), \tag{3.184}$$

where w represents variable evaluated at the non-spherical bubble wall, $r_w = R + a_n P_n \cos(\theta)$.

The boundary condition at infinity, where both velocity and pressure approach zero, is expressed as:

$$\mathbf{v}_1 \to 0, \quad p_1 \to 0 \quad \text{as } r \to \infty. \tag{3.185}$$

The velocity profile $\mathbf{v}_1$, upon satisfying the no-penetration condition 3.184 and 3.185, is given by [225, 326, 377],

$$\mathbf{v}_1 = \frac{\left(\dot{a}_n + \frac{2\dot{R}a_n}{R}\right) R^{n+2}}{(n+1) r^{n+2}} [(n+1) P_n(\cos\theta) e_r - P_n'(\cos\theta) e_\theta]. \tag{3.186}$$

For an incompressible and irrotational liquid, viscosity contributes only through the normal stress balance, which is given by:

$$-(p_1) + \tau_{1,rr} - 2\tau_{1,r\theta} \frac{P_n' \cos(\theta)}{R} - \sigma \left((n+2)(n-1) \frac{a_n P_n \cos(\theta)}{R^2} \right) = 0. \tag{3.187}$$

The perturbed (irrotational) pressure, p_1, is derived by substituting the perturbed velocity u_1.

3.2.2. Shape Stability of a Bubble in an Unbounded Power-law Liquid

In this section, the surrounding liquid is assumed to be an irrotational, incompressible power-law fluid. First, the equations for the base state are derived, followed by the equations for the perturbed state. The relationship between the stress and deformation-rate tensors for

the liquid is described as follows [360]:

$$\tau = \eta \dot{\gamma}, \tag{3.188}$$

where τ and $\dot{\gamma}$ represent the stress and deformation-rate tensors, respectively. The viscosity η is defined as

$$\eta = \mu \dot{\gamma}^{k-1}. \tag{3.189}$$

To obtain the spherical and non-spherical oscillation equations, field decomposition is applied as shown in Section 3.2.1. The base state equations are the same as obtained in Section 3.1.1.4. Therefore, here, just the non-spherical equations are given. For a detailed discussion on the spherical oscillations of a bubble in a power-law liquid, the reader is referred to [360]. When $k = 1$, the spherical oscillation of a bubble in an unbounded Newtonian liquid can be obtained (Section 3.1.1).

The perturbed stress equations are

$$\tau_{1,rr} = 2\left(\mu_{0,rr}\frac{\partial u_1}{\partial r} + \mu_{1,rr}\frac{\partial u_0}{\partial r}\right), \tag{3.190}$$

$$\tau_{1,\theta\theta} = 2\left(\mu_{0,\theta\theta}\left(\frac{1}{r}\frac{\partial w_1}{\partial \theta} + \frac{u_1}{r} + \mu_{1,\theta\theta}\frac{u_0}{r}\right)\right), \tag{3.191}$$

and

$$\tau_{1,r\theta} = \mu_{0,r\theta}\left(r\frac{\partial w_1}{\partial r} + \frac{1}{r}\frac{\partial u_1}{\partial \theta}\right). \tag{3.192}$$

Here, w and u are the θ and r components of the surrounding liquid's velocity. The specifics of the perturbed state shear stress equations, namely Equations (3.190-3.192), can be found in [378–380]. The perturbed (irrotational) pressure, p_1, is determined by substituting the perturbed velocity, u_1, and the stress components, $\tau_{1,rr}$ and $\tau_{1,r\theta}$, into Equation 3.187. The governing equation for the perturbation amplitude, $a_n(t)$, is derived by integrating the equation of motion, Equation 3.161, from the non-spherical bubble surface to infinity and substituting in p_1 from Equation 3.187. To the order of $O(a_n)$, a linear ODE for the perturbation

amplitude of the non-spherical mode $a_n(t)$ is obtained as follows:

$$\ddot{a}_n(t) + A_n(t)\dot{a}_n(t) + B_n(t)a_n(t) = 0, \tag{3.193}$$

where

$$A_n = 3\frac{\dot{R}}{R} + \frac{2M(n+2)(n+1)}{\rho R^2}\left(\left\|\frac{\partial u_0}{\partial r}\right\|^{k-1} - 2(k-1)\left\|\frac{\partial u_0}{\partial r}\right\|^{k-2}\frac{\dot{R}}{R}\right), \tag{3.194}$$

and

$$B_n = -(n-1)\frac{\ddot{R}}{R} + (n-1)(n+1)(n+2)\frac{\sigma}{\rho R^3} + 4(n+1)\frac{M\dot{R}}{\rho R^3}\left((n-1)\left\|\frac{\partial u_0}{\partial r}\right\|^{k-1} - 2(k-1)(n+2)\frac{\dot{R}}{R}\left\|\frac{\partial u_0}{\partial r}\right\|^{k-2}\frac{\partial u_0}{\partial r}\right). \tag{3.195}$$

When $k = 1$, the non-spherical model simplifies to the Newtonian model proposed by Prosperetti [326].

3.2.3. Shape Stability of an Encapsulated Bubble in Unbounded Liquid

In this section, the non-spherical oscillations of an encapsulated bubble are investigated. Two different cases are studied where the surrounding liquid is assumed to be power-law (Section 3.2.3.1) or viscoelastic liquid (Section 3.2.3.2). This setup is described using spherical coordinates (r, θ, ϕ), centered at the bubble's core, as shown in Figure 3.6. The radii of the bubble (inner) and the shell (outer) vary with time and are represented by $R_b(t)$ and $R_s(t)$, respectively. In the figure, the pressure $p_\infty(t) = p_{atm} + p_a \sin(\omega_d t)$. The velocity field is denoted by the vector $\mathbf{v}$, $p_b(t)$ is the pressure inside the bubble, and t represents time. The detailed expression of the p_b and the assumptions can be found in Section 3.1.1.

With the axisymmetric deformation assumption, the bubble, $F^{(1)}(r,\theta,t)$, and shell $F^{(2)}(r,\theta,t)$, surface functions can be expressed by the Legendre polynomials,

$$F^{(1)}(r,\theta,t) = r - R_b(t) - \sum_{n=2}^{\infty} b_n(t)P_n(\cos\theta) = 0, \tag{3.196}$$

and

$$F^{(2)}(r,\theta,t) = r - R_s(t) - \sum_{n=2}^{\infty} a_n(t)P_n(\cos\theta) = 0, \tag{3.197}$$

where b_n and a_n are the perturbation amplitudes of the bubble and shell surfaces, respectively. It is assumed that $|b_n(t)| \ll R_b(t)$ and $|a_n(t)| \ll R_s(t)$. P_n is a Legendre polynomial of degree $n \geqslant 2$.

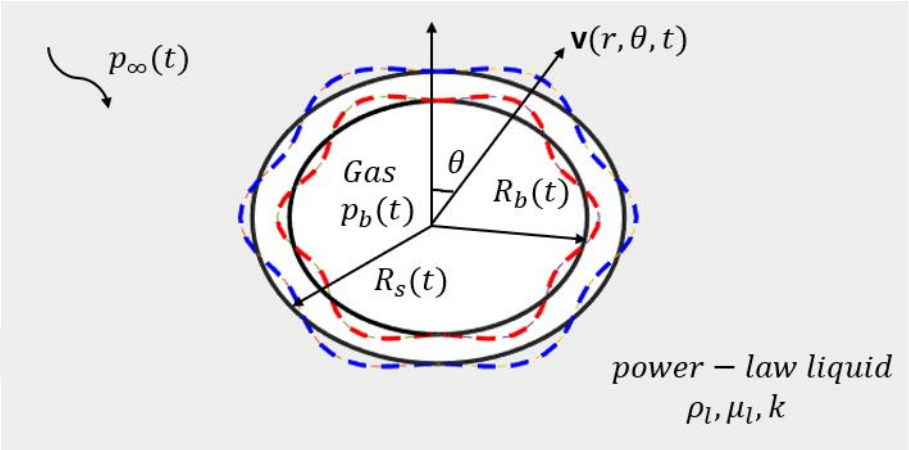

Figure 3.6. Non-spherical bubble geometry in spherical coordinates. The solid and dashed lines show the spherical and non-spherical oscillations.

The continuity and the momentum equations for the surrounding liquid and shell are written as,

$$\nabla \cdot \mathbf{v}_j = 0, \quad j = l, s, \tag{3.198}$$

and

$$\rho_j \left(\frac{\partial \mathbf{v_j}}{\partial t} + \mathbf{v_j} \cdot \nabla \mathbf{v_j} \right) = -\nabla p_j + \nabla \cdot \tau_j, \quad j = l, s, \tag{3.199}$$

respectively. The subscripts l and s denote the properties of the liquid and the shell, respectively.

At the interface between the bubble and the shell, the kinematic condition, no-slip condition, and stress balance are described as follows:

$$\frac{\partial F^{(1)}}{\partial t} + (\mathbf{v}_s \cdot \nabla^{(1)}) F^{(1)} = 0, \tag{3.200}$$

$$\mathbf{v}_s \cdot \mathbf{t}^{(\mathbf{1})} = \mathbf{v}_\mathbf{g} \cdot \mathbf{t}^{(\mathbf{1})}, \tag{3.201}$$

and

$$\mathbf{n}^{(\mathbf{1})} \cdot \tau_s - \mathbf{n}^{(\mathbf{1})} \cdot \tau_g = \sigma^{(1)} \mathbf{n}^{(\mathbf{1})} \nabla \cdot \mathbf{n}^{(\mathbf{1})}, \tag{3.202}$$

where the subscript g represents the gas phase, σ is the surface tension, $\mathbf{T}$ is the stress tensor, and $\mathbf{n} = \frac{\nabla F}{\|\nabla F\|}$ is the outward unit normal vector [326]. The superscript (1) shows bubble/shell interface properties.

At the shell/liquid interface, kinematic condition, no-slip, and stress balance are given as

$$\frac{\partial F^{(2)}}{\partial t} + (\mathbf{v}_l \cdot \nabla^{(2)}) F^{(2)} = 0, \tag{3.203}$$

$$\mathbf{v_l} \cdot \mathbf{t}^{(\mathbf{2})} = \mathbf{v_s} \cdot \mathbf{t}^{(\mathbf{2})}, \tag{3.204}$$

and

$$\mathbf{n}^{(\mathbf{2})} \cdot \tau_l - \mathbf{n}^{(\mathbf{2})} \cdot \tau_s = \sigma^{(2)} \mathbf{n}^{(\mathbf{2})} \nabla \cdot \mathbf{n}^{(\mathbf{2})}. \tag{3.205}$$

The superscript (2) shows shell/liquid interface properties. To obtain the spherical and non-spherical oscillation equations, field decomposition is applied as shown in Section 3.2.1. The base state equations are the same, as obtained in Section 3.1.2.4. Therefore, here, just the non-spherical equations are given.

The continuity equation and the irrotational equation of motion for non-spherical oscillations are expressed as follows:

$$\nabla \cdot \mathbf{v}_{1,j} = 0, \tag{3.206}$$

and

$$\rho_j \left(\frac{\partial \mathbf{v}_{1,j}}{\partial t} + \left(\mathbf{v}_{0,j} \cdot \nabla \right) \mathbf{v}_{1,j} + \left(\mathbf{v}_{1,j} \cdot \nabla \right) \mathbf{v}_{0,j} \right) + \nabla p_{1,j} - \nabla \cdot \tau_{1,ej} = 0, \quad j = l, s, \tag{3.207}$$

respectively. For an incompressible and irrotational liquid and shell, the viscous effects arise from the normal stress conditions. Additionally, the elastic contribution ($\tau_{1,ej}$) in the last term of Equation 3.207 is zero in the shell phase. Also, when the surrounding liquid is assumed to be power-law, this term is zero. The boundary conditions at infinity are given as follows:

$$\mathbf{v}_{1,l} \to 0, \quad p_{1,l} \to 0 \quad \text{as } r \to \infty. \tag{3.208}$$

The velocity at the interface in the radial direction is given by [225, 326, 377],

$$\mathbf{v}_{1,l} \cdot n|_{w_2} = \dot{a}_n P_n(\cos\theta), \tag{3.209}$$

and

$$\mathbf{v}_{1,s} \cdot n|_{w_1} = \dot{b}_n P_n(\cos\theta), \tag{3.210}$$

where w_2 and w_1 denote the variable evaluated at the non-spherical shell and bubble wall, respectively. The velocity profiles u_1, upon satisfying the conditions 3.208, and 3.209, are given by [377],

$$\mathbf{v}_{1,l} = \frac{\left(\dot{a}_n + \dfrac{2\dot{R}_s a_n}{R_s} \right) R_s^{n+2}}{(n+1) r^{n+2}} [(n+1) P_n(\cos\theta) - P_n'(\cos\theta) e_\theta], \tag{3.211}$$

and

$$\mathbf{v}_{1,s} = \frac{\left(\dot{b}_n + \dfrac{2\dot{R}_b b_n}{R_b} \right) R_b^{n+2}}{(n+1) r^{n+2}} [(n+1) P_n(\cos\theta) - P_n'(\cos\theta) e_\theta], \tag{3.212}$$

respectively. Here, $P_n' = \frac{dP_n(\cos\theta)}{d\theta}$. The details of the velocity derivation are given in Appendix B.2.

For an incompressible and irrotational liquid and shell, the contribution of viscosity arises from the normal stress balances at the non-spherical interfaces between the bubble and shell (1) and the shell and liquid (2). These are expressed to order ε as follows:

$$p_{1,s}^{(1)} - T_{1,rrs}^{(1)} + \sigma_b(n+2)(n-1)\frac{a_n P_n \cos(\theta)}{R_b^2} = 0, \tag{3.213}$$

and

$$p_{1,s}^{(2)} - T_{1,rrs}^{(2)} + \sigma_s(n+2)(n-1)\frac{b_n P_n \cos(\theta)}{R_s^2} = p_{1,l}^{(2)} - T_{1,rrl}^{(2)}, \tag{3.214}$$

respectively. The perturbed pressures, p_1, are derived by substituting the perturbed stress components from Equations 3.190 into Equations 3.213 and 3.214. The governing equation for the perturbation amplitude, $a_n(t)$, is obtained by integrating the equation of motion, Equation 3.207, from the non-spherical bubble surface to infinity and substituting p_1 from Equation 3.213. To order ε, a linear ODE for the perturbation amplitude of the non-spherical mode, $a_n(t)$, is derived as follows:

$$A_n(t)\ddot{b}_n(t) + B_n(t)\dot{b}_n(t) + C_n(t)\dot{a}_n(t) + D_n(t)b_n(t) + E_n(t)a_n(t) = F_{surf} + F_{viscous} + F_{elastic}. \tag{3.215}$$

Here, the time-dependent expressions are given as,

$$A_n(t) = \frac{R_b}{n+1}\left(\left(\frac{R_b}{R_s}\right)^{n+1}(\rho_s - \rho_\ell) - \rho_s\right), \tag{3.216}$$

$$B_n(t) = \left(\frac{\dot{R}_b}{n+1}\left(\frac{R_b}{R_s}\right)^{n+1}(\rho_s - \rho_\ell) - \frac{\rho_s \dot{R}_b}{n+1}\right), \tag{3.217}$$

$$C_n(t) = \dot{R}_s(\rho_\ell - \rho_s), \tag{3.218}$$

$$D_n(t) = \left(2(\rho_s - \rho_\ell)\left(\frac{R_b^2}{R_s}\left(\frac{R_b}{R_s}\right)^n + \frac{\ddot{R}_b}{n+1}\left(\frac{R_b}{R_s}\right)^{n+1}\right) - \rho_s(n+1)\ddot{R}_b\right), \tag{3.219}$$

and

$$E_n(t) = \frac{R_b}{R_s^2}(\rho_s - \rho_\ell)\left(\ddot{R}_b R_b + 2\dot{R}_b{}^2\right). \tag{3.220}$$

At the right-hand side of the equation, F_{surf} , F_{viscous} , F_{elastic} show the surface tension, viscous and elastic contributions to the system, and given as,

$$F_{\text{surf}} = 2(n-1)(n+2)\left(\frac{b_n}{R_b^2}\sigma_i + \frac{a_n}{R_s^2}\sigma_o\right). \tag{3.221}$$

The definitions for F_{viscous} and F_{elastic} are given in Sections 3.2.3.1 and 3.2.3.2.

3.2.3.1. Non-Spherical Oscillation for an Encapsulated Bubble in Power-Law Liquid. The non-Newtonian liquid surrounding the bubble follows a power-law constitutive model. The relationship between the stress and the deformation-rate tensor is described as follows [360],

$$\tau_l = \mu_l \dot{\boldsymbol{\gamma}}_l. \tag{3.222}$$

The apparent viscosity, μ is given by

$$\mu_l = m\dot{\gamma}_l^{k-1}, \tag{3.223}$$

where, m is the consistency index, and $\dot{\gamma}_l$ represents the second invariant of the strain-rate tensor, $\dot{\boldsymbol{\gamma}}$. The perturbed stress equation for the liquid is

$$T_{1,rrl} = \mu_{0,l}\left(u_{0,l}\right)\dot{\gamma}_{1,rrl}\left(u_{1,l}\right) + \mu_{1,l}\left(u_{1l}\right)\dot{\gamma}_{0,rrl}\left(u_{0,l}\right), \tag{3.224}$$

where

$$\mu_{1,l} = \frac{\partial\mu\left(u_{0,l}\right)}{\partial\dot{\gamma}_{rr}}\dot{\gamma}_{1,rrl} = M(k-1)\left|\frac{\partial u_{0,l}}{\partial r}\right|^{(k-3)}\left(\frac{\partial u_{0,l}}{\partial r}\right)\left(\frac{\partial u_{1,l}}{\partial r}\right). \tag{3.225}$$

The viscous term, which is used in the perturbed state equation for the power-law liquid is find as,

$$F_{\text{viscous}} = -b_n\left\{4\dot{R}_b(n+2)\left(\frac{\mu_s}{R_b^2} + \frac{R_b^{n+1}}{R_s^{(n+3)}}\left(\mu_s - M\left(\left|\frac{\partial u_{l,0}}{\partial r_0}\right|^{k-1} + \left|\frac{\partial u_{l,0}}{\partial r_0}\right|^{k-2}\frac{\partial u_{l,0}}{\partial r_0}(1-k)\right)\right)\right) - \left.\frac{\partial\tau_{s,0}}{\partial r_0}\right|_{r_0=R_b}\right\} - \dot{b}_n 2(n+2)\left\{\frac{\mu_s}{R_b} + \frac{R_b^{n+2}}{R_s^{(n+3)}}\left(\mu_s - M\left(\left|\frac{\partial u_{l,0}}{\partial r_0}\right|^{k-1} + \left|\frac{\partial u_{l,0}}{\partial r_0}\right|^{k-2}\frac{\partial u_{l,0}}{\partial r_0}(1-k)\right)\right)\right\} + a_n\left\{\left.\frac{\partial\tau_{l,0}}{\partial r_0}\right|_{r_0=R_s} - \left.\frac{\partial\tau_{s,0}}{\partial r_0}\right|_{r_0=R_s}\right\}, \tag{3.226}$$

When $k = 1$, the model is reduced to Newtonian surrounding liquid. Furthermore, for this case, $F_{\text{elastic}} = 0$.

3.2.3.2. Non-Spherical Oscillation for an Encapsulated Bubble in Viscoelastic Liquid. The viscoelastic properties of the surrounding liquid are represented using the Kelvin-Voigt model, where the Cauchy stress tensor is expressed as follows:

$$\tau_l = \tau_v + \tau_e, \tag{3.227}$$

where τ_e represents the elastic stress. The viscous stress, τ_v, is described by Newton's law of viscosity as follows:

$$\tau_v = \mu_s \left(\nabla \mathbf{v}_s + \nabla \mathbf{v}_s^{\mathrm{T}} \right), \tag{3.228}$$

The viscous stress tensor τ_v is traceless, which implies that $\tau_{\theta\theta,v} + \tau_{\phi\phi,v} = -\tau_{rr,v}$. For incompressible deformations, the elastic stress tensor is given by,

$$\tau_e = \begin{bmatrix} G_l \left(\frac{r_0}{r}\right)^4 - \mathscr{P} & G_l \frac{r}{r_0^2} \frac{\partial r}{\partial \theta} & G_l \frac{r}{r_0^2 \sin\theta} \frac{\partial r}{\partial \varphi} \\ G_l \frac{r}{r_0^2} \frac{\partial r}{\partial \theta} & G_l \left(\frac{r}{r_0}\right)^2 - \mathscr{P} & 0 \\ G_l \frac{r}{r_0^2 \sin\theta} \frac{\partial r}{\partial \varphi} & 0 & G_l \left(\frac{r}{r_0}\right)^2 - \mathscr{P} \end{bmatrix} \tag{3.229}$$

where $\mathscr{P}$ denotes the pseudo-pressure and $\mathbf{I}$ is the identity matrix. In the neo-Hookean model, the pressure p is expressed as $\mathscr{P} - \dfrac{G_l \left[(r_o/r)^4 + 2 (r/r_o)^2 \right]}{3}$, where G_l is the shear modulus. The details of the viscoelastic model is given as Section 3.1.2.1.

For this section, the viscous term is same which is given in Equation 3.226 when, the power-law index, $k = 1$. In addition tho this term, the elastic contribution of the viscoelastic liquid is found as,

$$F_{\text{elastic}} = \frac{G_l}{R_s} \left[2 \frac{R_{seq}}{R_s} + 2 \left(\frac{R_{seq}}{R_s} \right)^4 + \frac{n(n+1)}{1 + \frac{R_{seq}}{R_s} + \left(\frac{R_{seq}}{R_s} \right)^2} \right]. \tag{3.230}$$

3.3. Translational Motion and Bubble-Bubble Interactions

The translational motion of a bubble plays a significant role in bubble interactions within a fluid. The motion of bubbles generates flow fields that influence the behavior of nearby bubbles as they move through the fluid. This interaction is governed by the principles of fluid dynamics, where the velocity and pressure fields created by one bubble can attract or repel.

The Lagrangian method is crucial for analyzing the translational motion of a bubble within a fluid. This method provides a comprehensive framework to account for energy transformations within the system. Energy transformations refer to converting one form of energy to another, such as kinetic energy (the energy of motion) transforming into potential energy (the energy of position) and vice versa. This method relies on energy conservation principles, which combine kinetic and potential energies to form the Lagrangian function. Therefore, in this section, the Lagrangian method is first described, then the translational motion and the effect of bubble-bubble interactions are shown.

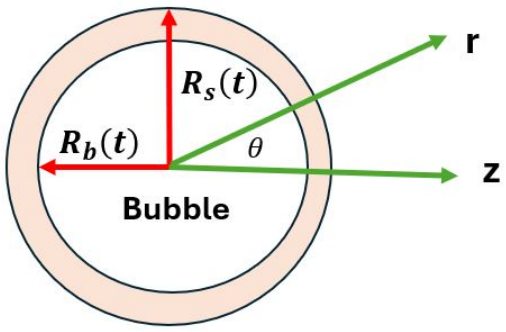

Figure 3.7. Radial oscillation and translational motion of an encapsulated bubble in an unbounded liquid.

The physical system is shown in Figure 3.7. Here, the bubble with radius R_b is encapsulated with a shell with radius R_s. A spherical coordinate system is introduced with its origin at the center of the cavity and the z-axis passing through the bubble center. In this coordinate system, the position vector r is expressed as (r, θ, ε). The bubble has its own

local spherical coordinate system, with its origin at the bubble's moving center. The position vector r_j in the bubble's coordinate system is given by $\left(r_j, \theta_j, \varepsilon_j\right)$. The position of the bubble's center relative to the cavity's center is denoted as z. Due to symmetry, the translational motion of the bubble can only occur along the z-axis.

3.3.1. Lagrangian Method

The Lagrangian method relies on energy balances, providing equations that can often be solved in closed form, enabling thorough system analysis for various applications. The Lagrangian represents the balance of non-dissipative energies. By combining kinetic energy with potential energy, the Lagrangian for the bubble in the confined liquid cell can be expressed as follows [40, 42]:

$$L = E_k - \Delta W, \tag{3.231}$$

This section includes the translational motion of the bubble is modeled using the Lagrangian method. In Equation 3.231, E_k indicates the kinetic energy and it is given for the liquid and shell parts as,

$$E_{k,l} = \int_0^{\pi} \int_{R_s(t))}^{\infty} \pi \rho_l \mathbf{v_l}^2 sin(\theta) r^2 dr d\theta, \tag{3.232}$$

and

$$E_{k,s} = \int_0^{\pi} \int_{R_b(t)}^{R_s(t)} \pi \rho_l \mathbf{v_s}^2 sin(\theta) r^2 dr d\theta. \tag{3.233}$$

where the velocity vector of the incompressible liquid velocity, $\mathbf{v_l}$ is found from the continuity equation as,

$$\mathbf{v_l} = \left[\frac{R_s^2 \dot{R}_s}{r^2} + \frac{\dot{z}}{2} \left(\frac{3R_s}{r} - \frac{R_s^3}{r^3} \right) \cos\theta \right] - \frac{\dot{z}}{4} \left(\frac{3R_s}{r} + \frac{R_s^3}{r^3} \right) \sin\theta e_\theta, \tag{3.234}$$

which satisfies the kinematic condition at the shell-liquid interface,

$$\frac{\partial \varphi_l}{\partial r} = \dot{R}_s + \dot{z}\cos\theta \quad \text{at } r = R_s(t), \tag{3.235}$$

where φ_l is the velocity potential of the liquid, $z(t)$ is the time-dependent position of the center of the bubble. The incompressible r-component shell velocity, u_s is given as,

$$u_s = \frac{R_b^2 \dot{R}_b}{r^2}. \tag{3.236}$$

First, the velocity profiles (Equations 3.115 and 3.118) are substituted into Equations 3.232 and 3.233. Then, Equations 3.232 and 3.233 are integrated from R_b to R_s and R_s to R_l, respectively. The final form of the kinetic energy equations become:

$$E_{k,l} = 2\pi\rho_L \left(R_s^3 \dot{R}_2^2 + \frac{1}{6} R_s^3 \dot{x}^2 \right), \tag{3.237}$$

and

$$E_{k,s} = 2\pi\rho_s R_b(t)^3 \dot{R}_b^2 - \frac{2\pi\rho_s R_b(t)^4 \dot{R}_b^2}{R_s^3}. \tag{3.238}$$

The total kinetic energy of the system, E_k is given as,

$$E_k = E_{k,l} + E_{k,s}. \tag{3.239}$$

To determine the potential energy, the increase in energy stored in the lshell and gas is equal to

$$\delta W = \int_{V_S} \mathscr{E}_s dV + \int_{V_l} \mathscr{E}_l dV \left[p_b + p_V(T) \right] 4\pi R_b^2 (-\delta R_b) + \frac{2\sigma_b}{R_b} 4\pi R_b^2 \delta R_b + \frac{2\sigma_s}{R_s} 4\pi R_s^2 \delta R_s. \tag{3.240}$$

where $\mathscr{E}$ is the elastic energy density. In this context, the first and second terms indicate the potential energy contributions due to the shell and liquid elasticity. Depending on the linear or nonlinear viscoelastic model of shell, the definition of $\mathscr{E}$ differs (Section 3.1.2.2). The third term reflects the work done on the gas and vapor inside the bubble, while the fourth and fifth terms represent the additional energy required to form the bubble-shell and liquid-shell interfaces.

By integrating Equation 3.240 from R_{s0} to R_s for the first term and from R_{b0} to R_b for the other terms, the change in the total potential energy of the bubble within the unbounded viscoelastic liquid due to cavitation inception can be determined. The gas pressure, p_b, can be found in Section 3.1.1.1. Note that if the system volume expands against a force, work is done by the system. If the system volume contracts under a force, work is done on the

system. The Rayleigh dissipation functions for the liquid, F_l, and shell,$F_{s,d}$, parts are given as,

$$F_l = \frac{\mu_l}{2} \int_{R_s(t)}^{R_l(t)} \Phi_l 4\pi r^2 dr, \tag{3.241}$$

and

$$F_{s,d} = \frac{\mu_s}{2} \int_{R_b(t)}^{R_s(t)} \Phi_s 4\pi r^2 dr, \tag{3.242}$$

where

$$\begin{aligned} \Phi_j =& 2\left[\left(\frac{\partial v_r}{\partial r}\right)^2 + \left(\frac{1}{r}\frac{\partial v_\theta}{\partial \theta} + \frac{v_r}{r}\right)^2 + \left(\frac{1}{r\sin\theta}\frac{\partial v_\phi}{\partial \phi} + \frac{v_r + v_\theta \cot\theta}{r}\right)^2\right] \\ &+ \left[r\frac{\partial}{\partial r}\left(\frac{v_\theta}{r}\right) + \frac{1}{r}\frac{\partial v_r}{\partial \theta}\right]^2 + \left[\frac{\sin\theta}{r}\frac{\partial}{\partial \theta}\left(\frac{v_\phi}{\sin\theta}\right) + \frac{1}{r\sin\theta}\frac{\partial v_\theta}{\partial \phi}\right]^2, \quad j = s,l. \end{aligned} \tag{3.243}$$

The primary Bjerknes force arises from the acoustic pressure gradient and is computed as

$$F_{B1} = -V(t)\nabla p_A(z,t). \tag{3.244}$$

The term $\nabla p_A(z,t)$ represents the pressure gradient at the center of the bubble. Hereby, $v_{ex}(z,t)$ is the liquid velocity induced by the acoustic irradiation calculated at the center of bubble. $p_A(z,t)$ is the harmonic forcing. This term is written as

$$p_A(z,t) = P_A \cdot \cos(kz) \cdot \sin(2\pi f t), \tag{3.245}$$

and

$$\dot{p}_A(z,t) = P_A \cdot 2\pi f \cdot \cos(kz) \cdot \cos(2\pi f t). \tag{3.246}$$

Since the motion is constrained to one dimension, the pressure gradient has a single component, which is

$$\nabla p_A(z,t) = -P_A \cdot k \cdot \sin(kz) \cdot \sin(2\pi f t), \tag{3.247}$$

The velocity of the liquid generated by acoustic irradiation at the center of the bubble is given by

$$v_{ex}(z,t) = -\frac{p_A}{\rho_l c_L} \cdot \sin(kz) \cdot \cos(2\pi f t). \tag{3.248}$$

The shell total external force becomes

$$F_s = F_{sd} + F_{ext}. \tag{3.249}$$

The total dissipation function is,

$$F = F_l + F_s. \tag{3.250}$$

The corresponding equation for bubble dynamics can be derived as the Euler equation for this Lagrangian, including the dissipative term is given as,

$$\frac{d}{dt}\left(\frac{\partial L}{\partial \dot{R}_b}\right) - \frac{\partial L}{\partial R_b} = -\frac{\partial F}{\partial \dot{R}_b}, \tag{3.251}$$

and

$$\frac{d}{dt}\left(\frac{\partial L}{\partial \dot{z}}\right) - \frac{\partial L}{\partial z} = -\frac{\partial F}{\partial \dot{z}}. \tag{3.252}$$

Here, the generalized coordinates are chosen as R_b and z. After the differentiation of Equation 3.251, Equation 3.253 is obtained which is the same as Equation 3.129.

$$\rho_s R_b F \ddot{R}_b + \rho_s H \dot{R}_b^2 = p_b - p_{ac}(z,t) - \frac{2\sigma_b}{R_b} - \frac{2\sigma_s}{R_s} - 4\mu_s \dot{R}_b \left(\frac{R_s^3 - R_b^3}{R_s^3 R_b}\right) + 4\mu_l \left(\frac{R_b^2 \dot{R}_b}{R_s^3}\right) + G_s E_s + G_l E_l. \tag{3.253}$$

Here, $F(t)$ and $H(t)$ are given in Equation 3.49. The viscoelastic contribution of shell and liquid, E_s and E_l are given in Section 3.1.2.2. The translational motion equation is obtained from Equation 3.252 as,

$$m_b \ddot{z} + \frac{2\pi}{3}\rho_l \frac{d}{dt}\left(R_s^3 \dot{z}\right) = -\frac{4\pi}{3} R_s^3 \frac{\partial}{\partial z} p_{ac}(z,t) - 6\pi\mu_l R_s \dot{z}. \tag{3.254}$$

Here, it is assumed that the mass inside the bubble (m_b) can be neglected. If $\sigma_s = 0$, and the physical properties of the liquid are assumed to be equal to the shell properties, the same coupled equations for the spherical and translational motion of a bubble in an unbounded

liquid can be obtained.

3.3.2. Bubble-Bubble Interactions

Bubbles in liquids are subject to various hydrodynamic forces. The most familiar is the buoyancy force, which corresponds to the pressure force that a sphere of liquid, replacing the bubble, would experience. This principle holds even in an accelerating liquid, with the generalized buoyancy force experienced by the bubble given by $-V\nabla\mathscr{P}$, where $\mathscr{P}(r,t)$ is the pressure that would be present at the bubble's center if the bubble were absent, and $V(t)$ is the bubble volume. For a bubble oscillating radially in a sound field, both $\mathscr{P}(r,t)$ and $V(t)$ are oscillatory quantities, resulting in a non-zero time average of their product over one cycle. Consequently, the bubble experiences a net force known as the primary Bjerknes force.

$$F_B = -\langle V\nabla\mathscr{P}\rangle. \tag{3.255}$$

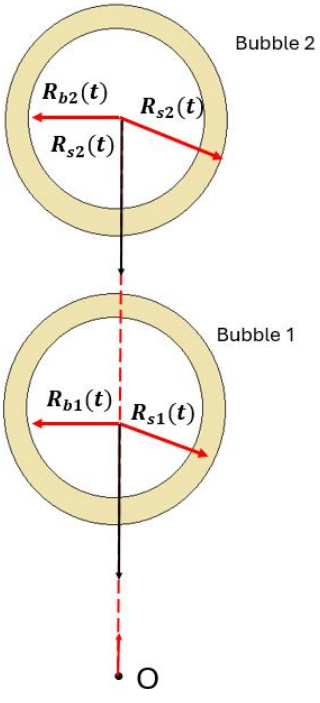

Figure 3.8. Radial oscillation and translational motion of two bubbles in unbounded liquid.

In this section, two gas bubbles in an unbounded liquid cavity driven by a stationary sound field are considered, where the wavelength is large compared to both the radii of the bubbles and the distance between their centers. The system is indicated in Figure 3.8, where R_b R_s are the bubble and shell radii of bubble 1 and R_{b2}, and R_{s2} are the bubble and shell radii of bubble 2. As a result, both bubbles experience pressure oscillations with the same amplitude and phase. When the distance between the bubbles is much greater than their sizes, it can be assumed that the bubbles remain spherical at all times. Additionally, the motion of the liquid around the first oscillating bubble can be considered spherically symmetric. In the region near an oscillating bubble, the incompressible liquid approximation holds (Section 3.1.3), and the velocity field $u_l(r,t)$ can be expressed as

$$u_l = \frac{R_{b1}^2 \dot{R}_{b1}}{r^2}. \tag{3.256}$$

Here, the origin of the coordinate system coincides with the center of the first bubble. To calculate the respective pressure field, the equation of motion is used,

$$\rho_l \frac{\partial u_l}{\partial t} + \frac{\partial p_1}{\partial r} = 0, \tag{3.257}$$

where p_1 represents the pressure in the liquid generated by the first bubble. The nonlinear convective term $u_l\,(\partial u_l/\partial r)$ is omitted because it is on the order of r^{-5}, making it much smaller than the first term. By substituting Equation 3.256 into Equation 3.257 and performing integration, the following expressions are obtained for the pressure gradient and the pressure:

$$\frac{\partial p}{\partial r} = -\frac{\rho}{r^2}\frac{d}{dt}\left(R_s^2 \dot{R}_s\right), \quad p = \frac{\rho}{r}\frac{d}{dt}\left(R_s^2 \dot{R}_s\right). \tag{3.258}$$

The pressure gradient field is the source of the Bjerknes force acting from the first bubble on the second, and the pressure field represents an additional driving pressure for the second bubble.

The additional terms for the potential energy, W (Equation 3.240), are given as

$$W_b = -p_1 V_1 - p_2 V_2, \tag{3.259}$$

where p_j is the scattered pressure at the surface of the j th bubble, $V_j = 4\pi R_j^3/3$ is the time-varying volume of the jth bubble. The new potential energy is found by adding Equation

3.259 to Equation 3.240. After adding the effect of bubble-bubble interactions, the Rayleigh-Plesset type equation for bubbles 1 and 2 are found as,

$$\rho_{s1}R_{b1}F_1\ddot{R}_{b1}+\rho_{s1}H?1\dot{R}_{b1}^2=p_{b1}-p_\infty-\frac{2\sigma_{b1}}{R_{b1}}-\frac{2\sigma_{s1}}{R_{s1}}-4\mu_{s1}\dot{R}_{b1}\left(\frac{R_{s1}^3-R_{b1}^3}{R_{s1}^3R_{b1}}\right)+$$
$$4\mu_l\left(\frac{R_{b1}^2\dot{R_{b1}}}{R_{s1}^3}\right)+E_{s1}+O\left(\frac{1}{D}\right)+O\left(\frac{1}{D}\right)^2+O\left(\frac{1}{D}\right)^3, \quad (3.260)$$

and

$$\rho_{s2}R_{b2}F_2\ddot{R}_{b2}+\rho_{s2}H_2\dot{R}_{b2}^2=p_{b2}-p_\infty-\frac{2\sigma_{b2}}{R_{b2}}-\frac{2\sigma_{s2}}{R_{s2}}-4\mu_{s2}\dot{R}_{b2}\left(\frac{R_{s2}^3-R_{b2}^3}{R_{s2}^3R_{b2}}\right)+$$
$$4\mu_l\left(\frac{R_{b2}^2\dot{R_{b2}}}{R_{s2}^3}\right)+E_{s2}+O\left(\frac{1}{D}\right)+O\left(\frac{1}{D}\right)^2+O\left(\frac{1}{D}\right)^3. \quad (3.261)$$

$F_j(t)$ and $H_j(t)$ are derived from Equations 3.123 and 3.124, respectively, for each individual bubble. D is the distance between the bubble centers, $D=z-z_2$. The first order terms acting on the equation of motion of first and second bubbles are given as,

$$O\left(\frac{1}{D}\right)=-\frac{R_{s2}^2\ddot{R}_{s2}+2R_{s2}\ddot{R}_{s2}^2}{D}, \quad (3.262)$$

and

$$O\left(\frac{1}{D}\right)=-\frac{R_{s1}^2\ddot{R}_{s1}+2R_{s1}\ddot{R}_{s1}^2}{D}, \quad (3.263)$$

respectively. The second order terms acting on the equation of motion of first and second bubbles are given as,

$$O\left(\frac{1}{D}\right)^2=\frac{R_{s2}^2\left(\dot{z}\dot{R}_{s2}+R_{s2}\ddot{z}_2+5\dot{R}_{s2}\dot{z}_2\right)}{2D^2}, \quad (3.264)$$

and

$$O\left(\frac{1}{D}\right)^2=-\frac{R_{s1}^2\left(\dot{z1}_2\dot{R}_{s1}+R_{s1}\ddot{z}_1+5\dot{R}_{s1}\dot{z}_1\right)}{2D^2}, \quad (3.265)$$

respectively. The third order terms acting on the equation of motion of first and second bubbles are given as,

$$O\left(\frac{1}{D}\right)^3=-\frac{R_{s2}^3\dot{z}_2\left(\dot{z}_1+2\dot{z}_2\right)}{2D^3}, \quad (3.266)$$

and

$$O\left(\frac{1}{D}\right)^3 = -\frac{R_{s1}^3 \dot{z}_1 \left(\dot{z}_2 + 2\dot{z}_1\right)}{2D^3}, \tag{3.267}$$

respectively. Here, $E_{s,j}$ is also given by

$$E_{sj} = G_s \left(\frac{\left(4R_{b,j}^3 + R_{b,j0}^3\right) R_{b,j0}}{2R_{b,j}^4} - \frac{\left(R_{b,j0}^3 - R_{b,j}^3 + R_{s,j}^3\right)^{1/3} \left(R_{b,j0}^3 - R_{b,j}^3 + 5R_{s,j}^3\right)}{2R_{s,j}^4} \right) + G_l \left(\frac{\left(4R_{b,j}^3 + R_{b,j0}^3\right) R_{b,j0}}{2R_{b,j}^4} - \frac{5}{2} \right), \tag{3.268}$$

for the first bubble and,

$$E_{s2} = G_{s2} \left(\frac{\left(4R_{b2}^3 + R_{b2,0}^3\right) R_{b2,0}}{2R_{b2}^4} - \frac{\left(R_{b2,0}^3 - R_{b2}^3 + R_{s2}^3\right)^{1/3} \left(R_{b2,0}^3 - R_{b2}^3 + 5R_{s2}^3\right)}{2R_{s2}^4} \right) + G_l \left(\frac{\left(4R_{b2}^3 + R_{b2,0}^3\right) R_{b2,0}}{2R_{b2}^4} - \frac{5}{2} \right). \tag{3.269}$$

The translational motion ODE for the first and second bubbles are given as,

$$\frac{R_{s1}\ddot{z}_1}{3} + \dot{R}_{s1}\dot{z}_1 + \frac{1}{D^2}\frac{d}{dt}\left(R_{s1}R_{s2}^2\dot{R}_{s2}\right) - \frac{R_{s2}^2\left(R_{s1}R_{s2}\ddot{z}_2 + R_{s2}\dot{R}_{s1}\dot{z}_2 + 5R_{s1}\dot{R}_{s2}\dot{z}_2\right)}{D^3} = \frac{F_{ex1}}{2\pi\rho_l R_{s1}^2}, \tag{3.270}$$

and

$$\frac{R_{s2}\ddot{z}_2}{3} + \dot{R}_{s2}\dot{z}_2 + \frac{1}{D^2}\frac{d}{dt}\left(R_{s2}R_{s1}^2\dot{R}_{s1}\right) - \frac{R_{s1}^2\left(R_{s2}R_{s1}\ddot{z}_1 + R_{s1}\dot{R}_{s2}\dot{z}_1 + 5R_{s2}\dot{R}_{s1}\dot{z}_1\right)}{D^3} = \frac{F_{ex2}}{2\pi\rho_l R_{s2}^2}, \tag{3.271}$$

respectively. The secondary Bjerknes forces acting on first (F_{ex1}) and second bubbles (F_{ex2}) are given as,

$$F_{ex1} = -12\pi\eta R_{s1}\left(\dot{z}_1 - v_2\right), \tag{3.272}$$

and

$$F_{ex2} = -12\pi\eta R_{s2}\left(\dot{z}_2 - v_1\right). \tag{3.273}$$

Here v_2 and v_1 denote the liquid velocity that is generated by the second and first bubble at the center of the other bubble. Up to order D^{-3}, v_2 and v_1 are given by

$$v_2 = -\frac{R_{s2}^2\dot{R}_{s2}}{D^2} + \frac{R_{s2}^3\dot{z}_2}{D^3}, \tag{3.274}$$

and

$$v_1 = \frac{R_{1s}^2\dot{R}_{s1}}{D^2} + \frac{R_{s1}^3\dot{z}_1}{D^3}. \tag{3.275}$$

3.4. Acoustic Droplet Vaporization (ADV)

The circulation time of microbubbles is limited to minutes due to their size and they cannot penetrate tumors through endothelial gaps. In contrast, liquefied gas nanoparticles can rapidly transform into a gaseous state under an acoustic field after just a few exposure cycles without causing significant heating. This rapid and efficient process is known as acoustic droplet vaporization (ADV) and is a key factor in its potential for biomedical applications. Therefore, understanding the dynamics of ADV is crucial for our research.

Figure 3.9 depicts the model's geometry. It assumes a spherical vapor bubble with a radius of $R_b(t)$ that is situated at the center of a droplet of spherical perfluorocarbon (PFC) with a radius of $R_d(t)$ and surrounded by an unbounded liquid. The interior of the vapor bubble is referred to as medium 1, the droplet as medium 2, and the surrounding liquid (host liquid) as medium 3. Media 2 and 3 are incompressible viscous liquids that follow the equation of continuity and the Navier-Stokes equation.

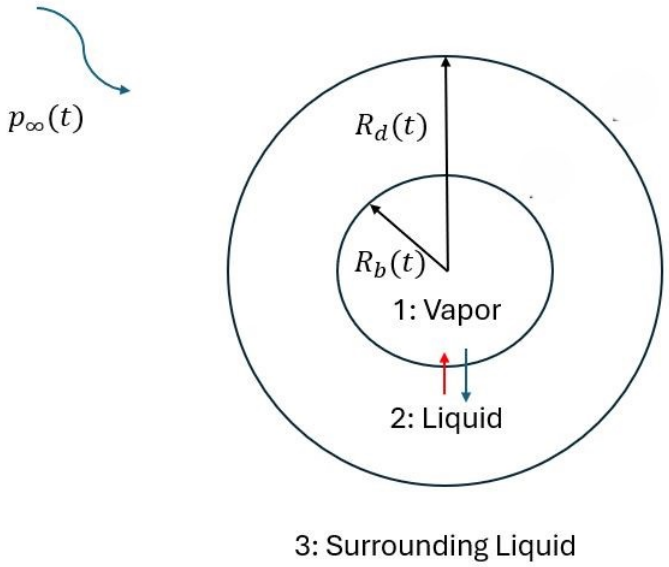

Figure 3.9. Configuration of acoustic droplet vaporization

3.4.1. Governing Equations

First, the governing equations are outlined for each domain, and then the interface conditions are provided.

Medium 1 (Vapor) ($r < R_b$):

The vapor nucleus of radius R_b is supposed to be centered in the droplet and already present at the initial time t = 0. The enthalpy equation for a perfect gas may be written [381, 382]

$$\rho_b c_b \frac{\mathrm{d}T_b}{\mathrm{d}t} - \frac{\mathrm{d}p_b}{\mathrm{d}t} = \nabla \cdot (\kappa_b \nabla T_b), \tag{3.276}$$

where, c_b, T_b and p_b are the specific heat at constant pressure, the temperature and the pressure inside the bubble. κ_b is the thermal conductivity. A common simplification is to assume that the internal temperature of the bubble is spatially uniform. This assumption, which is based on the low Mach number of the vapor flow, is also valid for vapor bubbles [381], [383]. Therefore, Equation 3.276 becomes,

$$\rho_b c_b \frac{\partial T_b}{\partial t} = \frac{\partial p_b}{\partial t}. \tag{3.277}$$

The continuity equation for the vapor is given as,

$$\frac{1}{r^2}\frac{\partial}{\partial r}\left(r^2 u_b \rho_b\right) = -\frac{\partial \rho_b}{\partial t}. \tag{3.278}$$

The vapor in the bubble obeys the ideal gas law, and the vapor density is not constant in time. Therefore, the density of the bubble can be given as,

$$\rho_b = \frac{p_b}{R_{g1} T_b}, \tag{3.279}$$

where $R_{g1} = R_g/m_b$ is the gas constant of the vapor, R_g is the universal gas constant, and m_b is the molar mass of the vapor. Equation 3.278 is multiplied by $c_b T_b$ and added to Equation 3.277 to yield,

$$\frac{\partial\left(\rho_b c_b T_b\right)}{\partial t} + \frac{c_b \rho_b T_b}{r^2}\frac{\partial}{\partial r}\left(r^2 u_b\right) - \frac{\partial p_b}{\partial t} = 0. \tag{3.280}$$

Finally, Equation 3.279 is substituted into Equation 3.280 and then, Equation 3.280 is integrated with respect to r. The velocity inside the bubble is found as,

$$u_b = -\frac{r}{3\gamma_b}\frac{\dot{p}_b}{p_b}. \tag{3.281}$$

It is conventional to assume that T_b equals to the saturation temperature corresponding to the pressure, p_b, inside the bubble. This assumption allows one to use the Clapeyron-Clausius equation [12, 381],

$$T_b = \left[\frac{1}{T_{s0}} - \frac{R_g}{\mathscr{L}}\ln\left(\frac{p_b}{p_{s0}}\right)\right]^{-1}, \tag{3.282}$$

where T_{s0} is the saturation temperature at the reference pressure p_{s0} and $\mathscr{L}$ is the latent heat of vaporization

Medium 2 (Droplet):

The incompressible continuity and Navier–Stokes equations for medium 2 are given as:

$$\frac{1}{r^2}\frac{\partial}{\partial r}\left(r^2 u_d\right) = 0, \tag{3.283}$$

and

$$\rho_d\left(\frac{\partial u_d}{\partial t} + u_d\frac{\partial u_d}{\partial r}\right) = -\frac{\partial p_d}{\partial r} + (\nabla\cdot\tau_d)_r, \tag{3.284}$$

respectively. Subscript d shows the droplet phase.

$$\frac{\partial T_d}{\partial t} + v_d \frac{\partial T_d}{\partial r} - \frac{1}{r^2}\frac{\partial}{\partial r}\left(\chi_d r^2 \frac{\partial T_d}{\partial r}\right) = \mu_d \Phi_d. \tag{3.285}$$

Here, $\chi_d = \kappa_d/(\rho_d c_d)$ is the thermal diffusivity of the droplet. κ_d and c_d are the thermal conductivity, and the specific heat of droplet, respectively. Φ_d is the dissipation.

Medium 3 (Host Liquid):

The continuity equation and equation of motion for medium 3 are given as:

$$\frac{1}{r^2}\frac{\partial}{\partial r}\left(r^2 u_l\right) = 0, \tag{3.286}$$

and

$$\rho_l\left(\frac{\partial u_l}{\partial t} + u_l \frac{\partial u_l}{\partial r}\right) = -\frac{\partial p_l}{\partial r} + (\nabla \cdot \tau_l)_r, \tag{3.287}$$

respectively.

Interface Conditions (Bubble/Droplet Interface) @$r = R_b$:

The conservation of mass condition across the liquid–vapor interface is given as,

$$\rho_d\left(\mathbf{v}_d - \mathbf{U}\right)\cdot\mathbf{n} = \rho_b\left(\mathbf{v}_b - \mathbf{U}\right)\cdot\mathbf{n} = G, \tag{3.288}$$

where G is the interfacial mass flux (positive for evaporation). $\mathbf{v}_b$ and $\mathbf{v}_d$ are the vapor and liquid velocities at $r = R_b$, $\mathbf{U}$ is the bubble-wall velocity. The energy balance at interface A is given as,

$$\begin{aligned}&\rho_L\left(\mathbf{v}_d - \mathbf{u}\right)\left\{\mathscr{L} + \frac{1}{2}\left(\left(\mathbf{v}_d - \mathbf{u}\right)^2 - \left(\mathbf{v}_b - \mathbf{u}\right)^2\right)\right\}\cdot\mathbf{n} \\ &+ \left(\mathbf{q}_d - \mathbf{q}_b\right)\cdot\mathbf{n} - \left\{S_d\cdot\left(\mathbf{v}_d - \mathbf{u}\right) - S_b\cdot\left(\mathbf{v}_b - \mathbf{u}\right)\right\}\cdot\mathbf{n} = \mathbf{0}.\end{aligned} \tag{3.289}$$

In Equation 3.289, it is assumed that the kinetic energy and the deviatoric stress can be neglected and $\kappa_b << \kappa_d$. Therefore, the final version of Equation 3.289 becomes

$$G = \frac{\kappa_d}{\mathscr{L}}\left(\frac{\partial T_d}{\partial r}\right). \tag{3.290}$$

The stress balance is given as:

$$\left\{\rho_d\left(\mathbf{v}_d - \mathbf{u}\right)\mathbf{v}_d - T_d\right\}\cdot\mathbf{n} + \sigma_i 2H\mathbf{n} - \left\{\rho_G\left(\mathbf{v}_G - \mathbf{u}\right)\mathbf{v}_G - T_G\right\}\cdot\mathbf{n}. \tag{3.291}$$

Here, σ_i is the interfacial tension at bubble/droplet interface. The temperature continuity at bubble/liquid interface is given as,

$$T_d = T_b. \tag{3.292}$$

Interface Conditions (Droplet/Liquid Interface) $r = R_d$:

The stress balance at droplet/liquid interface is given as,

$$\{\rho_L (\mathbf{v}_L - \mathbf{u}) \mathbf{v}_L - T_L\} \cdot \mathbf{n} + \sigma_o 2H\mathbf{n} - \{\rho_d (\mathbf{v}_d - \mathbf{u}) \mathbf{v}_d - T_d\} \cdot \mathbf{n}. \tag{3.293}$$

Here, σ_o is the interfacial tension of interface B. he temperature and the velocity of liquid and droplet are equal at interface B are given as,

$$T_d = T_l, \tag{3.294}$$

and

$$u_d = u_l, \tag{3.295}$$

respectively.

Boundary conditions ($r \to \infty$)

The boundary conditions at $r \to \infty$ are specified as,

$$u_l = 0, \tag{3.296}$$

$$p_l = p_\infty, \tag{3.297}$$

and

$$T_l = T_\infty, \tag{3.298}$$

where p_∞ is the acoustic pressure imposed at far field.

3.4.2. Final Equations

From Equation 3.288, the vapor and liquid velocities at bubble/droplet interface are found as,

$$u_b = \dot{R}_b - G/\rho_b, \quad u_d = \dot{R}_b - G/\rho_d \quad \text{at } r = R_b(t), \tag{3.299}$$

Following the substitution of Equations 3.295 and 3.299, the velocity profiles for media 2 and 3 are determined from the incompressible continuity equations as,

$$u_d = \frac{R_b^2\left(\dot{R}_b - G/\rho_d\right)}{r^2} \quad \text{and } u_l = \frac{R_b^2\left(\dot{R}_b - G/\rho_d\right)}{r^2}. \tag{3.300}$$

The vapor radial velocity is substituted into Equation 3.281 to find an expression for the bubble pressure:

$$R_b\dot{p}_b + 3\gamma p_b\left(\dot{R}_b - \frac{G}{\rho_b}\right) = 0. \tag{3.301}$$

The incompressible host liquid and droplet velocity profiles (Equation 3.300), are substituted into Equations 3.284 and 3.287. Then, Equations 3.284 and 3.287 are integrated from R_b to R_d and R_d to ∞. The final form of the equation of motion becomes:

$$\begin{aligned} R_b\left(\ddot{R}_b - \frac{\dot{G}}{\rho_d}\right)\left[\rho_d + (\rho_l - \rho_d)\frac{R_b}{R_d}\right] + \frac{3}{2}\left(\dot{R}_b - \frac{G}{\rho_d}\right)\left\{\dot{R}_b\left[\rho_d + (\rho_l - \rho_d)\frac{R_b}{3R_d}\left(4 - \frac{R_b^3}{R_b^3}\right)\right]\right. \\ \left. + \frac{G}{3\rho_b}\left[\rho_d + (\rho_l - \rho_d)\frac{R_b^4}{R_d^4}\right]\right\} = p_d(R_b,t) + p_l(R_d,t) - p_\infty(t) - p_d(R_d,t) \\ + \tau_{rr,d}(R_d,t) - \tau_{rr,d}(R_b,t) - \tau_{rr,l}(R_d,t) + 3\int_{R_b}^{R_d}\frac{\tau_{rr,d}}{r}\,\mathrm{d}r + 3\int_{R_d}^{\infty}\frac{\tau_{rr,l}}{r}\,\mathrm{d}r. \end{aligned} \tag{3.302}$$

After substituting Equations 3.291 and 3.293 into Equation 3.302, Equation 3.302 becomes,

$$\begin{aligned} R_b\left(\ddot{R}_b - \frac{\dot{G}}{\rho_d}\right)\left[\rho_d + (\rho_l - \rho_d)\frac{R_b}{R_d}\right] + \frac{3}{2}\left(\dot{R}_b - \frac{G}{\rho_d}\right)\left\{\dot{R}_b\left[\rho_d + (\rho_l - \rho_d)\frac{R_b}{3R_d}\left(4 - \frac{R_b^3}{R_b^3}\right)\right]\right. \\ \left. + \frac{G}{3\rho_b}\left[\rho_d + (\rho_l - \rho_d)\frac{R_b^4}{R_d^4}\right]\right\} = p_b - p_\infty(t) - \frac{2\sigma_A}{R_b} - \frac{2\sigma_B}{R_d} - G^2\left(\frac{1}{\rho_d} - \frac{1}{\rho_l}\right) \\ + 3\int_{R_b}^{R_d}\frac{\tau_{rr,d}}{r}\,\mathrm{d}r + 3\int_{R_d}^{\infty}\frac{\tau_{rr,l}}{r}\,\mathrm{d}r. \end{aligned} \tag{3.303}$$

Equation 3.303 is derived for a host liquid (Medium 2) with any type of rheology. If the host liquid obeys the power-law constitutive equation, Equation 3.303 becomes,

$$R_b\left(\ddot{R}_b-\frac{\dot{G}}{\rho_d}\right)\left[\rho_d+(\rho_l-\rho_d)\frac{R_b}{R_d}\right]+\frac{3}{2}\left(\dot{R}_b-\frac{G}{\rho_d}\right)\left\{\dot{R}_b\left[\rho_d+(\rho_l-\rho_d)\frac{R_b}{3R_d}\left(4-\frac{R_b^3}{R_b^3}\right)\right]+\frac{G}{3\rho_b}\left[\rho_d+(\rho_l-\rho_d)\frac{R_b^4}{R_d^4}\right]\right\}=p_b-p_\infty(t)-\frac{2\sigma_A}{R_b}-\frac{2\sigma_B}{R_d}-G^2\left(\frac{1}{\rho_d}-\frac{1}{\rho_l}\right)-\frac{2M}{n}\dot{R}_d\left|\dot{R}_d\right|^{n-1}R_d^{-1}. \quad (3.304)$$

When $n=1$, the liquid model is reduced to Newtonian liquid [12].

The droplet radius R_d can be determined by using the mass conservation condition for the droplet. This condition is expressed as

$$\frac{d}{dt}\left[\frac{4\pi}{3}\left(R_d^3-R_b^3\right)\rho_d\right]=-4\pi R_b^2 G. \quad (3.305)$$

From Equation 3.305, an expression for the droplet radius, R_d, is found as,

$$\dot{R}_d=\frac{R_b^2}{R_d^2}\left(\dot{R}_b-\frac{G}{\rho_d}\right). \quad (3.306)$$

Equation 3.285 describes the temperature distribution inside the droplet which affects the evaporation rate, and is solved under the conditions given in Equations 3.292 and 3.294.

When the PFC droplet fully transitions into a vapor bubble, the bubble's oscillation is characterized by the Keller-Miksis equation.

$$(1-\frac{\dot{R}_b}{c})R_b\ddot{R}_b+\frac{3}{2}\left(1-\frac{\dot{R}_b}{3c}\right)\dot{R}_b^2=\frac{1}{\rho}\left(1+\frac{\dot{R}_b}{c}+\frac{R_b}{c}\frac{d}{dt}\right)\left[p_{b0}\left(\frac{R_{b0}}{R_b}\right)^{3\gamma}-\frac{2\sigma}{R_b}-\frac{2M}{n}\dot{R}_b\left|\dot{R}_b\right|^{n-1}R_b^{-1}-p_\infty\right]. \quad (3.307)$$

3.5. Solution Procedure

In this section, the solution procedures for spherical (Section 3.1) and non-spherical (Section 3.2) bubble oscillations,translational motion of a bubble, bubble-bubble interactions (Section 3.3) and acoustic droplet vaporization (ADV) (Section 3.4) are presented. For the spherical oscillation and translational motion sections (Sections 3.1 and 3.3), coupled

ordinary differential equations (ODEs) are solved using MATLAB. For the non-spherical oscillations (Section 3.2), in addition to solving the ODEs, Floquet analysis is applied for stability analysis.

In the ADV section (Section 3.4), coupled partial differential equations are solved using MATLAB. For time and spatial discretization, finite difference and spectral methods are employed, respectively. Details of the solution procedures for spherical and non-spherical oscillations and ADV are provided in Sections 3.5.1, 3.5.2 and 3.5.3, respectively.

3.5.1. Solution Procedure for Coupled Ordinary Differential Equations

In Sections 3.1-3.2, second-order ordinary differential equations for the bubble radius are derived with respect to time. A standard method for solving higher-order ordinary differential equations is to transform them into systems of first-order differential equations, which can then be solved. Here, only the reduced equations from Section 3.1.1 are provided as an example.

Reducing the order, Equation 3.23 becomes,

$$\dot{R} = V, \tag{3.308}$$

and

$$\dot{V} = \frac{\frac{1}{\rho}\left(+p_{g0}\left(\frac{R_{b0}}{R}\right)^{3\lambda} - p_\infty + p_v - \frac{2\sigma}{R}\right) - \frac{3}{2}V^2}{R}. \tag{3.309}$$

These coupled ODEs are solved numerically via MATLAB. The initial conditions are $R_b(0) = R_{b0}$ and $\dot{R}(0) = 0$.

When solving ODEs via MATLAB, the solver selection and the absolute and relative tolerance values are important, which affect the bubble radius behavior. The ode45 solver performs well with most ODE problems and is typically the preferred first choice. However, solvers like ode23, ode78, ode89, and ode113 may be more efficient depending on whether

the problem requires looser or tighter accuracy. Figure 3.10 shows the effect of solver type on the solution of a bubble in an unbounded inviscid liquid. It is known that when the initial bubble pressure is larger than the liquid pressure, the bubble radius oscillates at the same amplitude when the liquid is assumed to be inviscid. However, as shown in Figure 3.10, only ode89 gives the expected result. At the beginning of Figure 3.10, the differences between the solvers are small. To observe the difference between the solvers, the behavior of bubble radius is obtained after 80 μs. The detailed solutions of a bubble in an unbounded inviscid liquid are given in Section 4.4.1.

Also, relative and absolute tolerances are essential. Relative tolerance (RelTol) assesses the error about the magnitude of each solution component. In simple terms, it governs the number of accurate digits in all solution components, except for those more minor than the absolute tolerance, AbsTol. AbsTol sets a threshold, indicating that solution values below it are negligible.

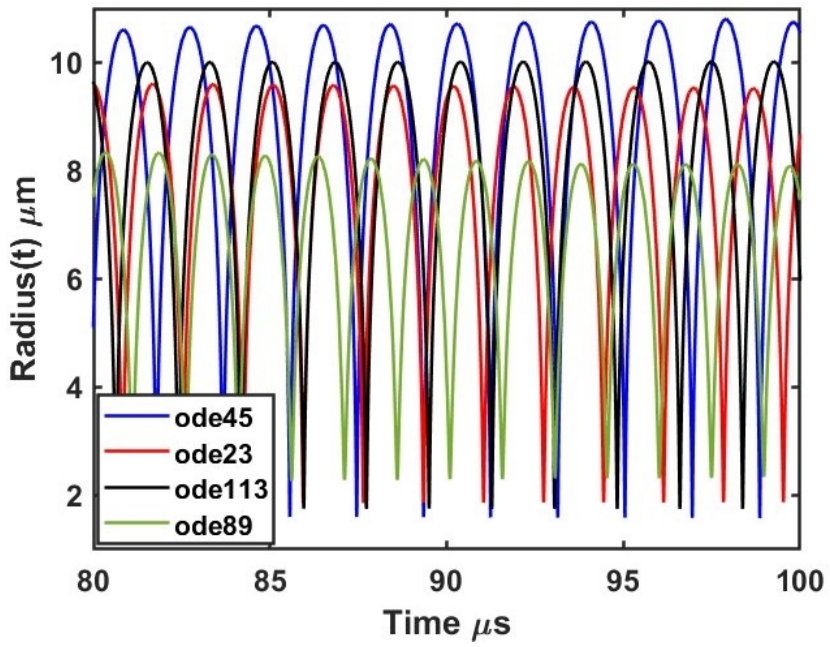

Figure 3.10. Bubble radius versus time for different ODE solvers.

Figure 3.11 shows the effect of AbsTol and RelTol on the solution of a bubble in an unbounded inviscid liquid. As shown in Figure 3.11, for the default options of ode45 (RelTol=10^{-3} and AbsTol=10^{-3}), the bubble radius increases over time, which is unexpected. However, the expected bubble radius can be obtained when RelTol=10^{-8} and AbsTol= 10^{-10}. It is observed that AbsTol and Reltol should always be used together. For accuracy, it is observed that AbTol be set at least two orders of magnitude smaller than RelTol.

Also, the coupled equations can be solved via MatCont, which is a GUI-Matlab package. MatCont is a numerical tool for analyzing parameterized dynamical systems, specifically for studying bifurcations. The solution manual of Matcont to solve coupled ODE systems is described in Appendix C.

3.5.2. Solution Procedure for Shape Stability Analysis

After solving the coupled ODEs to find the stability regions of the perturbation amplitude, a_n in Section 3.2, the Floquet theory is applied. Based on Floquet theory, the stability analysis method is about the solution to linear dynamic systems with periodic coefficients. Hence, stability analysis under actual operating conditions requires that the general dynamic equations be linearized around a periodic solution [384].

In Section 3.2.2, coupled ODEs are solved to find the solution of a_n and R_b, where the bubble is assumed to be in an unbounded power-law liquid. After the spherical oscillations according to Equation 3.193 reach a steady periodic state in time with frequency $1/T$, the coefficients in Equations 3.194 and 3.195 are periodic functions of time. Therefore, Floquet theory is applied, according to which the solution at the end of a cycle $(a_n, \dot{a}_n)_{t=t_0+1}$ is linearly related to the value at the beginning of a cycle $(a_n, \dot{a}_n)_{t=t_0}$. Thus, the parametric instability of the system is analyzed. The parametric instability occurs whenever the magnitude of the maximal eigenvalue of the Floquet transition matrix $F_n(T)$ is more significant than one. When $max(\lambda) > 1$, the oscillations increase over time and they are considered unstable; otherwise, they remain stable. With mode $n = 2$, the bubble surface takes on an el-

lipsoidal shape and as the perturbation increases, the bubble tends to divide into two smaller bubbles, as shown in Figure 3.12.

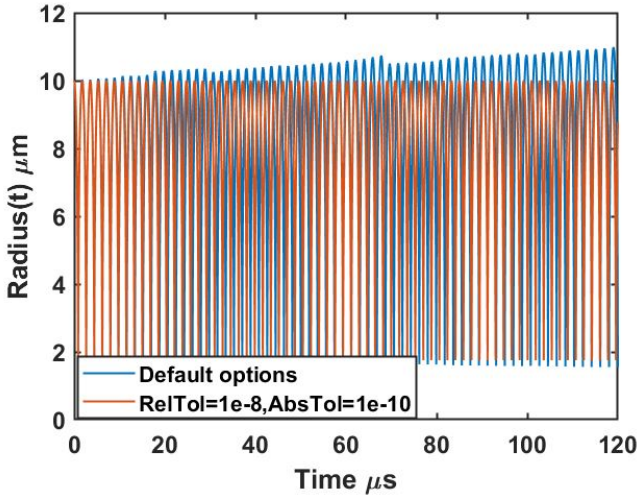

Figure 3.11. Bubble radius versus time for inviscid case.

The Floquet transition matrix $F_n(T)$ is defined by

$$\begin{pmatrix} a_n(T) \\ \dot{a}_n(T) \end{pmatrix} = F_n(T) \begin{pmatrix} a_n(0) \\ \dot{a}_n(0) \end{pmatrix}. \tag{3.310}$$

By numerically computing the eigenvalues of the Floquet transition matrix, the phase diagrams of stability are obtained.

The same procedure is applied to Section 3.1.2.4, where the Floquet transition matrix is obtained for an encapsulated bubble in an unbounded power-law liquid.

3.5.3. Solution Procedure for Acoustic Droplet Vaporization

In this section, the numerical procedure of Section 3.4 is given. The bubble, droplet, and host media radii equations form coupled nonlinear partial differential equations (PDEs) that vary with time and space. The time derivatives are discretized using the finite difference method.

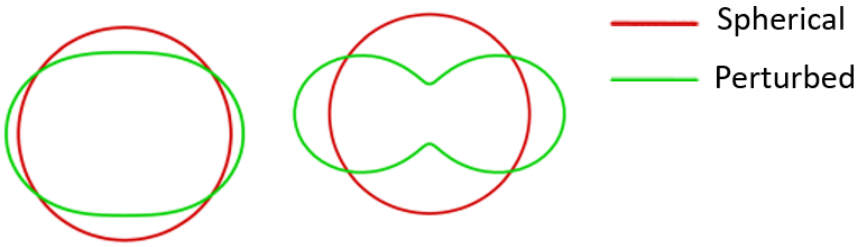

Figure 3.12. Illustration of the microbubble shape with (left) the existence (small perturbation) and (right) growth of perturbations for order 2. Reproduced with permission from Lu et al., J. Acoust. Soc. Am. , 131, 24, (2012) permission from AIP Publishing [10].

For instance, for the bubble radius, R_b, the first and second-order derivatives are given as,

$$\frac{dR_b}{dt} = \frac{R_b^{n+1} - R_b^n}{\Delta t}, \tag{3.311}$$

and

$$\frac{d^2R_b}{dt} = \frac{R_b^{n+1} - R_b^{n-1}}{2\Delta t}, \tag{3.312}$$

respectively.

For the spatial derivative, spectral methods are used. Spectral methods discretize derivative matrices by transforming the problem into the spectral domain using basis functions such as Fourier series or Chebyshev polynomials. The function to be differentiated is expanded in terms of these basis functions. Here, Chebyshev polynomials are used [385]. To construct the derivative matrix, a grid of points r_j is defined where the function values are sampled. For Chebyshev methods, Gauss-Lobatto nodes are used given as,

$$r_p = -\cos\left(p\frac{\pi}{N}\right) \quad p = 0, 1, \ldots N, \tag{3.313}$$

where N is the cut-off frequency. A transformation matrix $\mathbf{F}$ is then created to convert the function values at these grid points to the spectral coefficients. In the spectral domain, the differentiation matrix $\mathbf{D}$ is constructed. In this section, $\mathbf{D}$ and $\mathbf{D2}$ indicate the first and second

derivatives, i.e., $\frac{d}{dr}$ and $\frac{d^2}{dr^2}$, respectively.

Finally, the arranged equations for the MATLAB code are given as,

$$T_d^{(n+1)} = \Delta t\,(-conv + cond+)\,T_d^{(n)} + visc_{disp}, \tag{3.314}$$

where,

$$conv = u_d \mathbf{D} T_d^{(n)}, \tag{3.315}$$

$$u_d = \left(\dot{R}_b^{(n)} - \frac{G^{(n)}}{\rho_d}\right)\frac{(R_b^{(n)})^2}{r^2}, \tag{3.316}$$

$$cond = \chi_d \left(D2T_d^{(n)} + \frac{2\mathbf{D}T_d^{(n)}}{r}\right), \tag{3.317}$$

and

$$visc_{disp} = \frac{12\mu_d u_d^2}{\rho_d c_d r^2}. \tag{3.318}$$

Here, *conv*, *cond* and $visc_{disp}$ are the convection, conduction and viscous dissipation terms, respectively. The evaporation rate and its derivative are given as,

$$G^{(n+1)} = \frac{\kappa_d}{\mathscr{L}} \mathbf{D} T_d^{(n)}, \tag{3.319}$$

and

$$\dot{G}^{(n+1)} = \frac{G^{(n+1)} - G^{(n)}}{\Delta t}. \tag{3.320}$$

The bubble-wall velocity is given as,

$$\dot{R}_b^{(n+1)} = \dot{R}_b^{(n)} + \Delta t \frac{(RHS - H2 - H)}{F}, \tag{3.321}$$

where

$$F = \frac{R_b^{(n)}(\rho_d + (\rho_l - \rho_d)R_b^{(n)})}{R_d^{(n)}}, \tag{3.322}$$

$$H = 1.5\left(\dot{R}_b^{(n)} - \frac{G^{(n)}}{\rho_d}\right)(\dot{R}_b^{(n)}(\rho_d + (\rho_l - \rho_d)\frac{R_b^{(n)}}{3R_d^{(n)}}\left(4 - \frac{(R_b^{(n)})^3}{R_d(n)^3}\right) + \frac{G^{(n)}}{3\rho_d}\left(\rho_d + (\rho_l - \rho_d)\frac{(R_b^{(n)})^4}{(R_d^{(n)})^4}\right), \tag{3.323}$$

$$H2 = -\frac{\dot{G}^{(n)}}{\rho_d F}, \tag{3.324}$$

$$RHS = p_b^{(n)} - (G^{(n)})^2\left(\frac{1}{\rho_b} - \frac{1}{\rho_d}\right) - 2\left(\frac{\sigma_A}{R_b^{(n)}} + \frac{\sigma_B}{R_s^{(n)}}\right) - \frac{4}{R_b^{(n)}}\left(\dot{R}_b^{(n)} - \frac{G^{(n)}}{\rho_d}\right)\left(\mu_d + (\mu_l - \mu_d)\frac{(R_b^{(n)})^3}{(R_d^{(n)})^3}\right) - p_\infty^{(n)}. \tag{3.325}$$

The pressure and the density inside the bubble are given as,

$$p_b^{(n+1)} = p_b^{(n)} + \frac{\Delta t}{R_b^{(n)}}\left(-3\gamma p_b^{(n)}\left(\dot{R}_b^{(n)} - \frac{G(n)}{\rho_b}\right)\right), \tag{3.326}$$

and

$$\rho_b = \frac{p_b^{(n)}}{R_{g1}T_b}, \tag{3.327}$$

respectively. Here, T_b is given as,

$$T_b = \left[\frac{1}{T_{s0}} - \frac{R_{g1}}{\mathscr{L}}\ln\left(\frac{p_b}{p_{s0}}\right)\right]^{-1}. \tag{3.328}$$

The droplet wall velocity, droplet and bubble radii equations are given as,

$$\dot{R}_d^{(n+1)} = \frac{(Rb^{(n)})^2}{(R_s^{(n)})^2}\left(\dot{R}_b^{(n)} - \frac{G^{(n)}}{\rho_d}\right), \tag{3.329}$$

$$R_d^{(n+1)} = R_d^{(n)} + \Delta t \dot{R}_d^{(n)}, \tag{3.330}$$

and

$$R_b^{(n+1)} = R_b^{(n)} + \Delta t \dot{R}_b^{(n)}, \tag{3.331}$$

respectively.

3.5.4. Convergence Analysis of Spectral Methods

n this section, the convergence analysis of the spectral method is done. An inverse Chebyshev transform matrix is obtained to convert the values of spatial functions into spectral coefficients which represent functions in terms of Chebyshev polynomials. The stability and accuracy of the spectral method are affected by the pseudospectrum of the differentiation matrices. When the solution is highly sensitive to perturbations, the pseudospectrum reveals regions where even minor numerical errors or perturbations can lead to significant changes in the solution. Large pseudospectral regions indicate that the computed spectral coefficients may be highly sensitive and potentially impacting solution accuracy. By examining the pseudospectrum of the Chebyshev differentiation matrix, the cut-off frequency can be found which helps to improve stability and ensure reliable results. In Figures 3.13-3.15, the effect of the cut-off number on the convergence is studied. The challenge for the acoustic droplet vaporization part is the moving boundaries. The bubble radius (inner boundary) and the droplet radius (outer boundary) depend on time. When the bubble radius is close to the droplet radius, complete evaporation is obtained. At this point, the distance between the boundaries is small, which causes divergence. Compared to the final time, the cut-off frequency should be high at the beginning to prevent the initial divergence. To overcome this problem, an optimum cut-off frequency is chosen, which is not too high or small. The temperature profiles are obtained when $t = 0.125$ μs (Figures 3.13(a), 3.14(a) and 3.15(a)), when $t = 0.25$ μs (Figures 3.13(b), 3.14(b) and 3.15(b)) and when $t = 0.5$ μs (Figures 3.13(c), 3.14(c) and 3.15(c)). In Figures 3.13 the cut-off frequency, N=17, in Figures 3.14 N=28 and in Figures 3.15 N=56. In Figure 3.16, the final convergence figures are obtained at the

final stage, when $t = 75$ μs. The N = 56 results cannot be obtained because the temperature profiles diverge. As mentioned, in the early stages (Figures 3.13), the lower value of N gives low convergence in contrast to the final stages (Figures 3.16(a) and (b)).

3.5.5. Summary of the Solution Procedure

In Figure 3.17, the solution procedures and their interrelationships are outlined for all parts of this dissertation. In the first part (Section 3.1), coupled ordinary differential equations (ODEs) are derived to describe the spherical oscillations, which serve as the base state equations. In Part 2 (Section 3.2), two additional coupled ODEs are introduced to account for non-spherical oscillations. These four coupled ODEs (two from the base state and two from the perturbed state) are solved simultaneously. In Part 3 (Section 3.3), the effect of Bjerknes forces is incorporated into the equations, resulting in two coupled ODEs for each bubble. Finally, in Part 4 (Section 3.4), phase change equations at the interface between the bubble and the liquid droplet, along with the temperature field within the droplet (described by partial differential equations, PDEs), are solved using MATLAB.

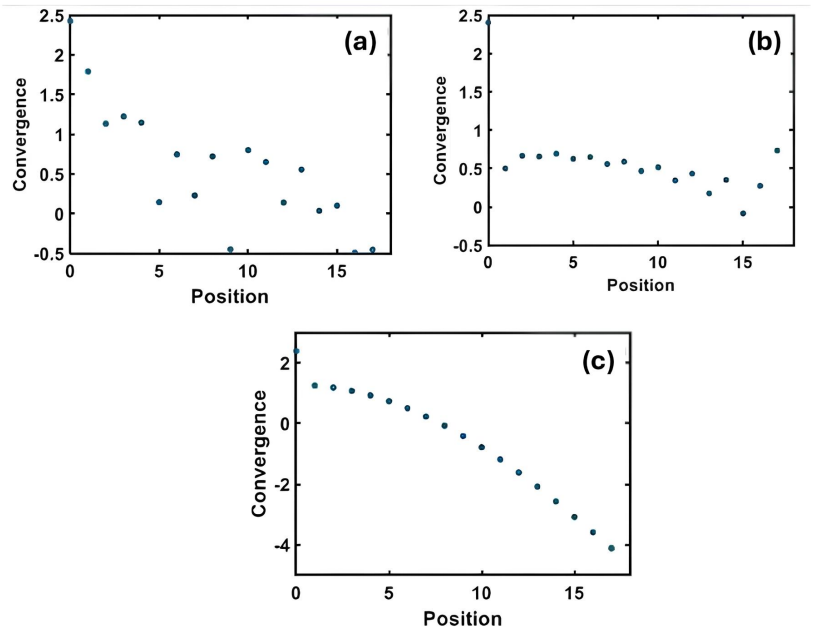

Figure 3.13. Effect of cut off frequency on convergence for N=17. Also in (a) $t = 0.125$ μs; (b) $t = 0.25$ μs and (c) $t = 0.5$ μs.

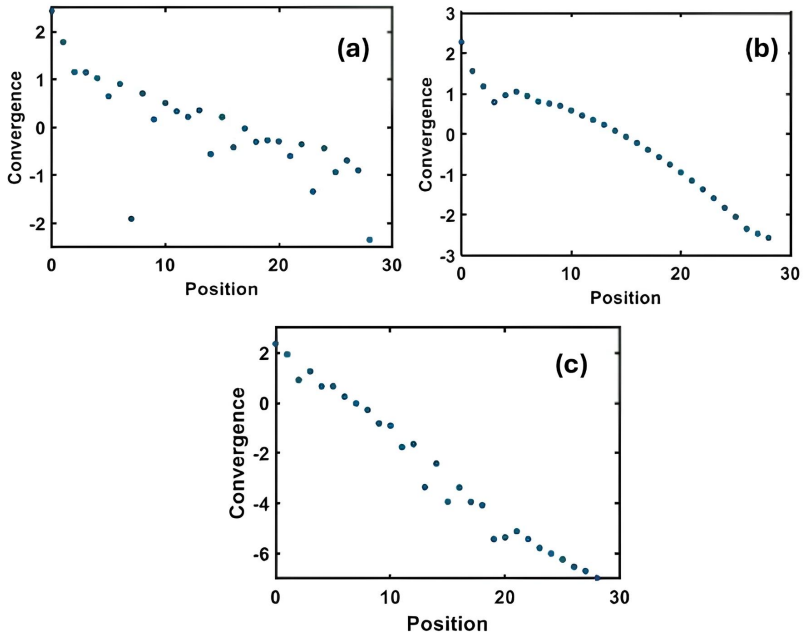

Figure 3.14. Effect of cut off frequency on convergence for N=28. Also in (a) $t = 0.125\ \mu$s; (b) $t = 0.25\ \mu$s and (c) $t = 0.5\ \mu$s.

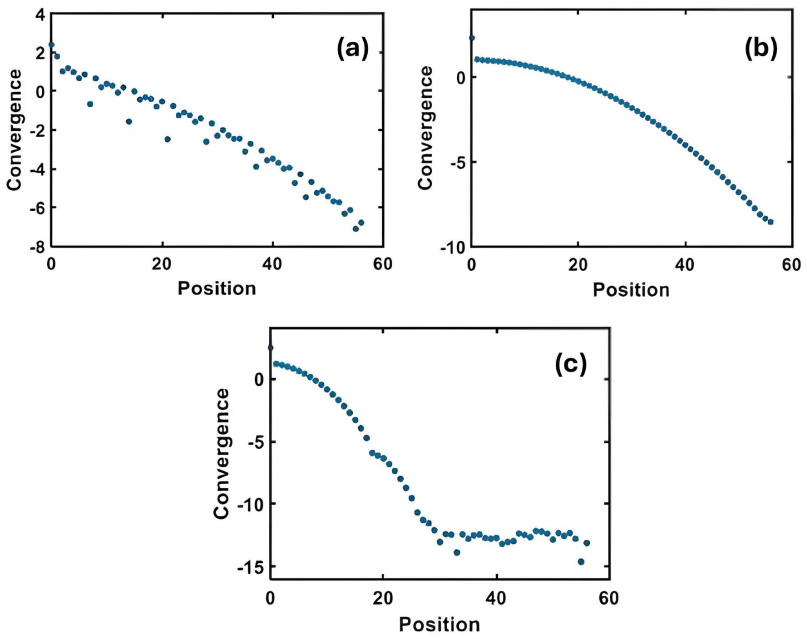

Figure 3.15. Effect of cut off frequency on convergence for N=56. Also in (a) $t = 0.125\ \mu$s; (b) $t = 0.25\ \mu$s and (c) $t = 0.5\ \mu$s.

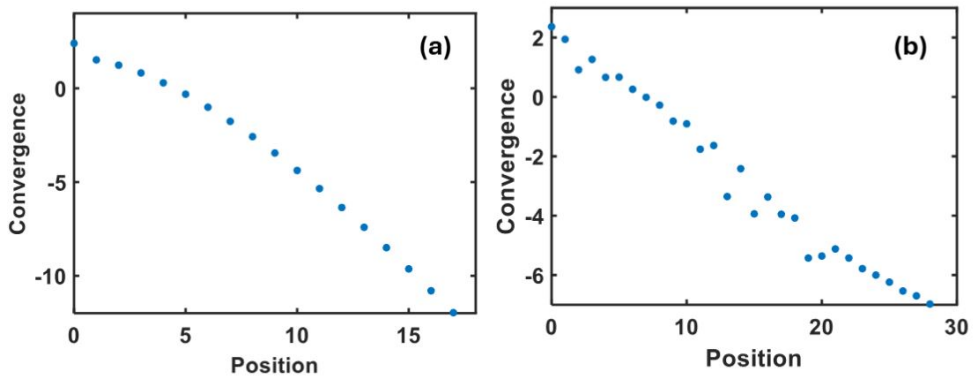

Figure 3.16. Effect of cut off frequency on convergence for (a) N=17 and (b) N=28, $t = 50$.

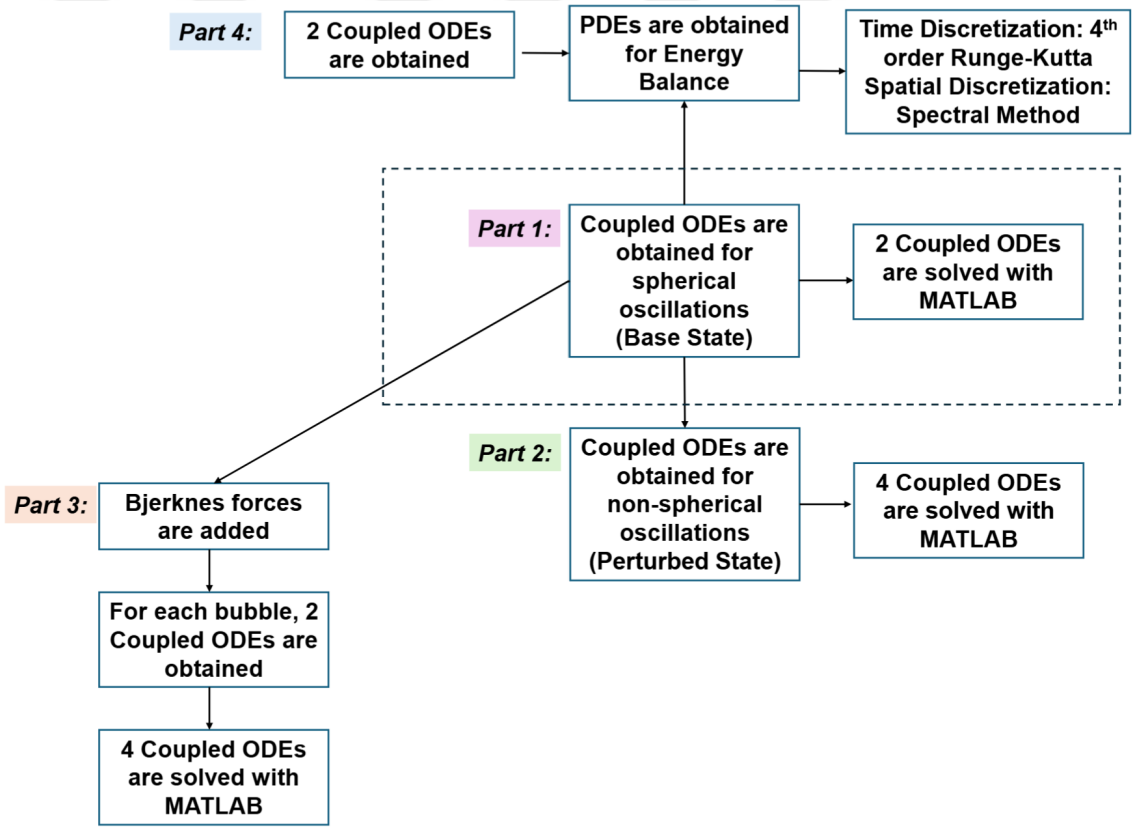

Figure 3.17. Summary of the solution procedure for all parts.

4. RESULTS AND DISCUSSION

In the results section, the model and equations are first validated (Section 4.1). Following this validation, the applicability of the Rayleigh-Plesset (Section 4.2) equation and the ideal gas law (Section 4.3) is tested.

After validating the model, the section presents the results for spherical (Section 4.4) and non-spherical oscillations (Section 4.5), translational motion and bubble-bubble interactions (Section 4.6) as well as acoustic droplet vaporization (Section 4.7).

4.1. Validation

In this section, the results of references [11], [10] and [12] are reproduced. Liu et al. [11] examines the a non-spherical and spherical bubble oscillations under the effect of acoustic field. Their physical systems are same as our system which is depicted in Figure 3.3. Here, it is assumed that bubble is in a liquid cavity. They also cover the results of a bubble in an unbounded liquid.

In Figure 4.1, the spherical bubble radius, R_b and the perturbation amplitude, a_n, profiles are obtained for bubble in an unbounded liquid. Figures 4.1(a) and (b) show our and Liu's [11] results, respectively. Here, n shows the perturbation amplitude. The parameters are chosen according to the standard water-gas system with liquid density $\rho = 1000$ kg m^{-3}, viscosity $\mu = 1 \times 10^{-3}$ kg $/$ m s^{-1}, surface tension $\gamma = 0.0729$ N m^{-1}, and polytropic index $\gamma = 1.4$. The external acoustic field, $p_\infty = p_0 + p_a \sin(\omega_d t)$ where p_a =1 atm and $\omega_d = 2.65$ MHz.

In Figure 4.2, the results of Lu et al. [10] are reproduced. The physical system is same as our system given in Figure 3.6. Contrary to our case where the shell is assumed to be viscoelastic, Lu et al. [10] assumed that bubble is encapsulated by thick, Newtonian shell. Figures 4.2(a) and (b) show our and Lu's [10] results, respectively. Three-dimensional small

perturbations are applied to the spherical oscillations of a bubble. Again, the liquid and shell is assumed to be water. The acoustic pressure frequency is $f = 2.5$ MHz. The initial inner and outer radius of the bubble are $R_{b0} = 1.2\mu$m, $R_{a0} = 1.7\mu$m.

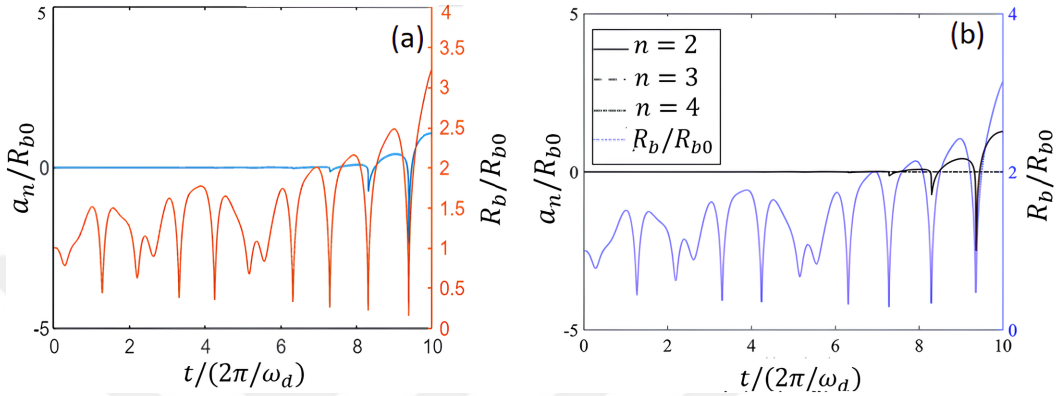

Figure 4.1. Perturbation amplitude, a_n, and the bubble radius versus time: (a) our results (b) Liu's result [11]. Reproduced with permission from Liu et al., Phys. Fluids , 30, 12, (2018) permission from AIP Publishing [11].

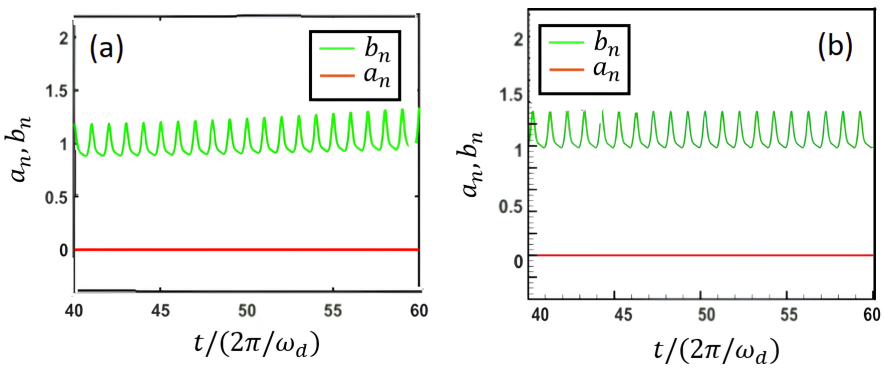

Figure 4.2. Perturbation amplitude of shell (a_n) and bubble (b_n) versus time: (a) our results (b) Lu's result [10]. Reproduced with permission from Lu et al., J. Acoust. Soc. Am. , 131, 24, (2012) permission from AIP Publishing [10].

Finally, the results of Doinikov et al. [12] are reproduced for the acoustic bubble vaporization section, Section 3.4. The model's geometry is illustrated in Figure 3.9. Figures 4.3(a) and (b) show our and Doinikov's [12] results, respectively. It is assumed that a spherical vapor bubble with a radius of $R_b(t)$ is situated at the center of a spherical Perfluorocarbon

(PFC) droplet with a radius of $R_d(t)$, which is surrounded by an infinite liquid medium. The droplet phase is assumed to be octafluoropropane (OFP). Thus, the specific heat c_d = 1028.5 J/(kg K), saturation temperature T_{s0} =-36.79 ^{o}C and pressure p_{s0}=101.3 kPa, density, ρ_d = 1603 kg/m^3, viscosity, μ_d=108.25 μPa.s, specific heat c_d =0.0385 W/(m K), thermal condıctivity κ_d=1268.5 J/(kg K) and latent heat of evaporation is 242.85 kJ/kg.

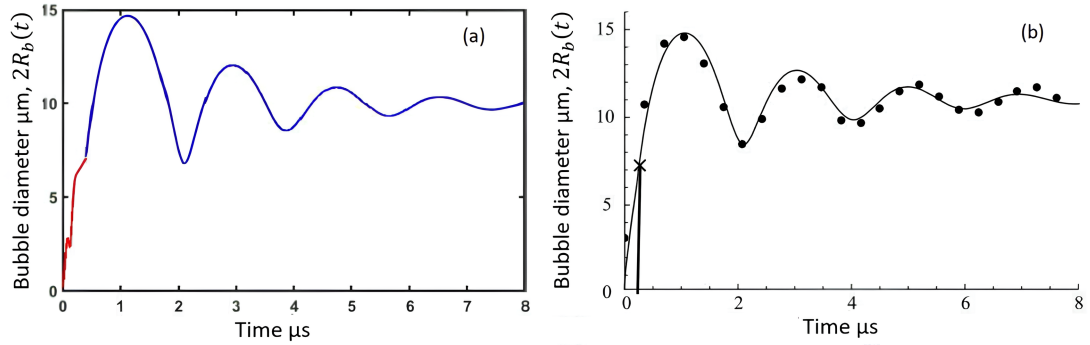

Figure 4.3. Bubble diameter, $2R_b(t)$ versus time: (a) our results (b) Doinikov's result [12]. Reproduced with permission from Doinikov et al., Phys. Fluids, 102901, 41, (2014) permission from AIP Publishing [12].

4.2. Applicability of the Rayleigh-Plesset (RP) Equation

The applicability of the RP equation to bubble dynamics is limited by several approximations underlying its derivation [386]. The first condition that the wavelength of the driving field (such as an acoustic or pressure wave) should be large compared to the radius of the bubble is important to ensure that the bubble experiences the driving field as a uniform pressure throughout its volume. Thus, the first condition is given as,

$$kR_{max} \ll 1 \text{ (condition 1)} , \tag{4.1}$$

where k is the wave number of the sound field. The compressibility of the liquid can be checked using the Mach number M, which is the ratio of the bubble wall velocity $\dot{R}_b$ to the speed of sound in the liquid c. Further, the analysis requires that the motion of the bubble wall be slow compared to the speed of sound in the liquid,

$$\frac{\dot{R}_{\max}}{c} \ll 1; \quad \frac{\ddot{R}_b R_b}{c^2} \ll 1 \text{ (condition 2)} , \tag{4.2}$$

where c is the speed of sound in the liquid ($c \approx 1500$m/s).

The final condition ensures that pressure disturbances can propagate fast enough through the gas inside the bubble to maintain the assumption of uniform pressure. When this condition is violated, the gas dynamics inside the bubble become complex, with non-uniform pressure fields and possible shock waves, requiring more sophisticated models to describe the bubble's behavior accurately. Therefore, the comparison of (instantaneous) speed of sound in the gas is given as,

$$\frac{\dot{R}_{\max}}{c_g} \ll 1; \quad \frac{\ddot{R}R}{c_g^2} \ll 1 \text{ (condition 3)} . \tag{4.3}$$

Here, c_g is found from

$$c_g^2(R) = \frac{\left(c_0^2 R_0^{3(\kappa-1)} R^6\right)}{\left(R^3 - a^3\right)^{\kappa+1}}, \tag{4.4}$$

where R_0 is the initial bubble radiıs and $R_0/a = 8.9$ for argon. c_0 is the speed of sound in the gas at these conditions, with $c_0 = 323\,$m/s and $\kappa = 1.4$. After 15 cycles of the acoustic field, $R_{\max}, \dot{R}_{\max}$, and $\ddot{R}_{\max}$ are obtained, which correspond to the maximum bubble radius, bubble wall velocity, and acceleration, respectively. It is assumed here that the bubble is in an unbounded viscous liquid. It is assumed that the surrounding liquid obeys the power-law constitutive law (Section 3.1.1.4. The amplitude of the acoustic pressure is 0.25 atm ($p_\infty = p_0 + p_a \sin(\omega_d t)$). In Figures 4.4-4.6, the physical properties for the liquid are taken from Table 4.1. Additionally, the liquid viscosity is 0.001 kg/(ms).

Figures 4.4-4.6 show the effect of the power-law index, k on kR_{max} (condition 1), on $\dot{R}_{\max}/c$ and $\ddot{R}_{\max}R_{\max}/c$ (condition 2) and; $\dot{R}_{\max}/c_g$ and $\ddot{R}_{\max}R_{\max}/c_g$ (condition 3) for different frequencies. Figures 4.7- 4.9 show the effect of the power-law index on kR_{max}, on $\dot{R}_{\max}/c$ and $\ddot{R}_{\max}R_{\max}/c$ and; $\dot{R}_{\max}/c_g$ and $\ddot{R}_{\max}R_{\max}/c_g$. After 5 cycles of the acoustic field, $R_{\max}, \dot{R}_{\max}$ and $\ddot{R}_{\max}$ are obtained.

As shown in Figures 4.4-4.8, the RP conditions are satisfied. In Figures 4.4-4.6, the amplitude of acoustic field is low, e.g., $p_a = 0.25$ atm. In Figures 4.7-4.9, higher pressure

amplitudes are used to test the applicability of RP equation, e.g., $p_a = 2.5$ atm. Higher pressure amplitudes mean the bubble wall velocities are higher. Although the acceleration of liquid is high, compressible effects on the spherical oscillations are expected to be small because R/c are small, where c is the speed of sound in liquid ($c \approx 1500 \frac{\text{m}}{\text{s}}$ in water).

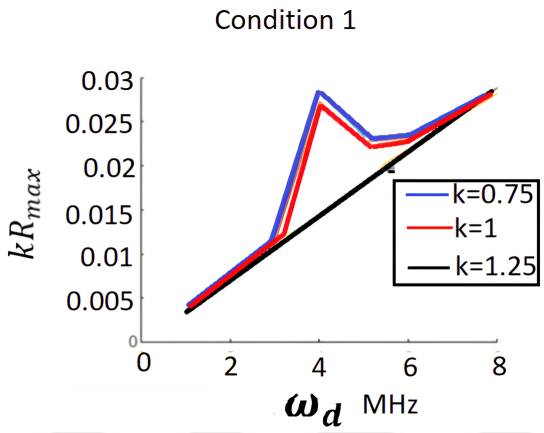

Figure 4.4. kR_{max} versus ω_d (condition 1).

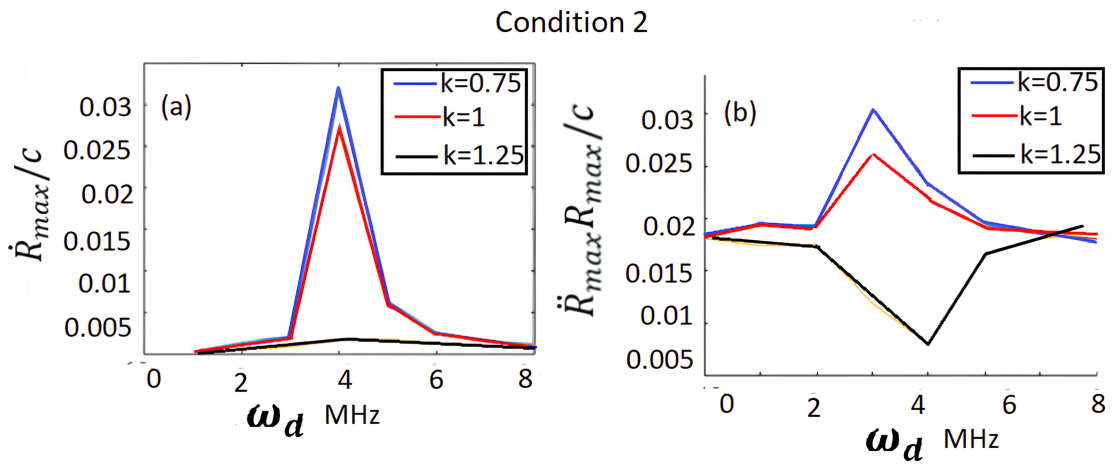

Figure 4.5. $\dot{R}_{max}/c$ versus ω_d and (b) $\ddot{R}_{max}R_{max}/c$ versus ω_d (condition 2).

4.3. Applicability of Ideal Gas Law

In Section 3.1.1.1, different equations of state are provided for ideal and real gases (Equations 3.16 and 3.17). In this dissertation, the results are obtained by assuming the gas

inside the bubble is ideal. Therefore, in this section, the applicability of ideal gas law is evaluated by comparing the results obtained using polytropic law and Van der Waals' law.

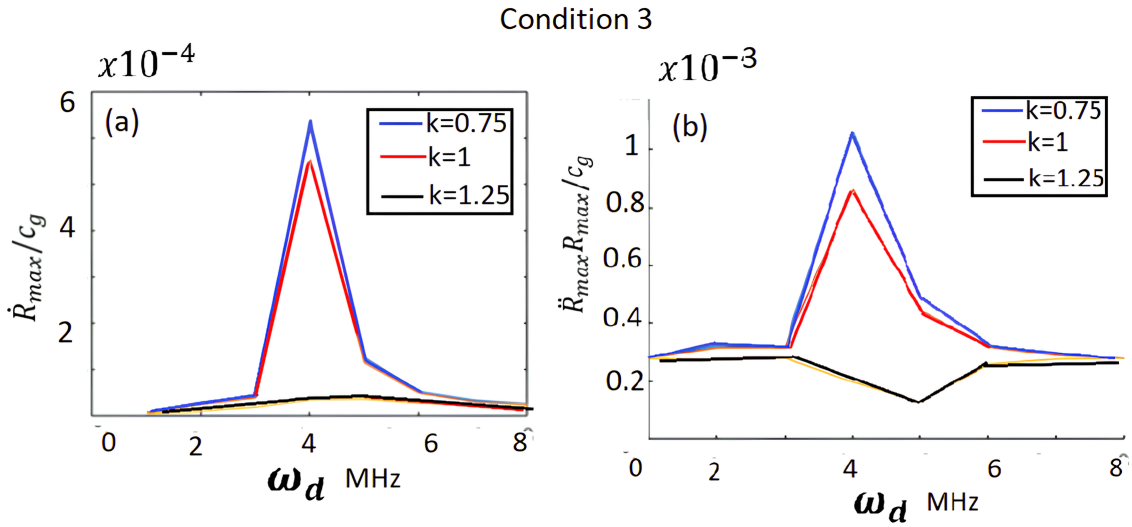

Figure 4.6. $\dot{R}_{max}/c_g$ versus ω_d and (b) $\ddot{R}_{max}R_{max}/c_g$ versus ω_d (condition 3).

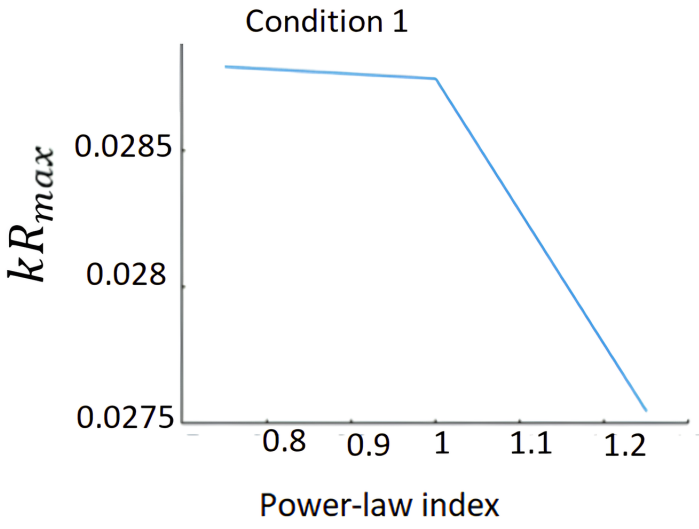

Figure 4.7. kR_{max} versus power-law index (condition 1).

In Figures 4.10 and 4.11, Van der Waals law for the gas pressure (VdW) is compared with the polytropic law. Two different pressure amplitudes are used. As seen in Figure 4.10,

when the applied acoustic pressure amplitude is low, i.e., 0.25 atm , the polytropic law (red line) and the VdW (blue line) yield the same results. This result is also valid at different acoustic field frequencies. However, for higher acoustic field pressure amplitudes in Figure 4.11(a), i.e., $p_a = 2.5$ atm, the difference between the polytropic law and VdW increases with time. For instance, after 5 cycles, the difference between the polytropic law and VdW becomes apparent. In Figure 4.11(b), again, $p_a = 2.5$ atm and f = 8MHz. In Figure 4.11(b), the polytropic law and the VdW yield the same results.

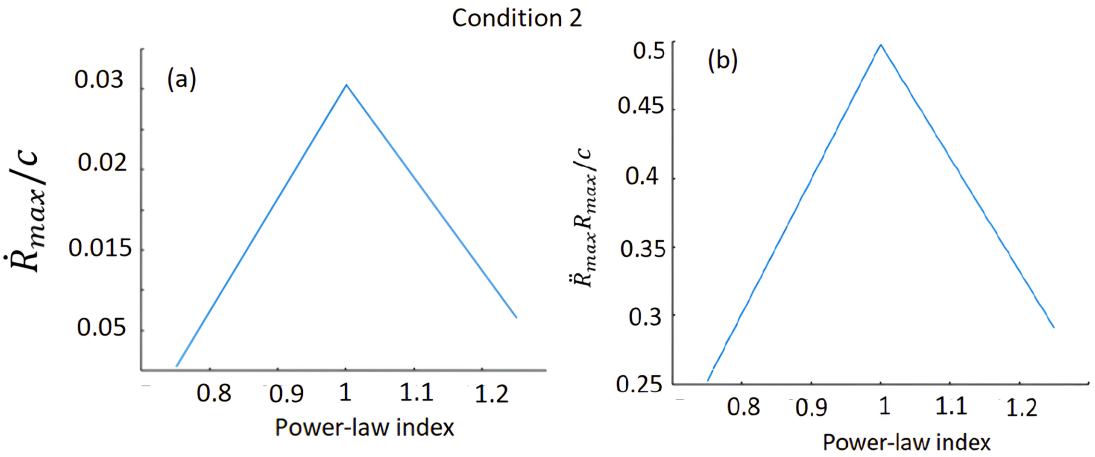

Figure 4.8. $\dot{R}_{max}/c$ versus power-law index and (b) $\ddot{R}_{max}R_{max}/c$ versus power-law index (condition 2).

Finally, the pressure amplitude is found where the difference between the polytropic law and VdW is noticeable. The maximum bubble radius values over 5 cycles of acoustic field are compared. In Figure 4.12, $R_{\max}^{vdw}$ is the maximum bubble radius obtained from VdW, and $R_{\max}^{\text{poly}}$ is obtained from the polytropic law. Figures 4.12(a) and (b) show the effects of pressure amplitude and the frequency on the maximum bubble radius. As shown in Figure 4.12(a), when $p_a = 6$ atm, the difference between the maximum radius becomes larger. However, the frequency slightly affects the difference between $R_{\max}^{vdw}$ and $R_{\max}^{\text{poly}}$.

In conclusion, the polytropic law yields consistent results for low pressures and high frequencies, making it a valid assumption for these parameters. The polytropic law is valid when the system can be approximated as behaving like an ideal gas. For the polytropic law

to be valid, the gas must remain ideal, meaning intermolecular forces are negligible, and the process occurs quasi-statically to maintain thermodynamic equilibrium.

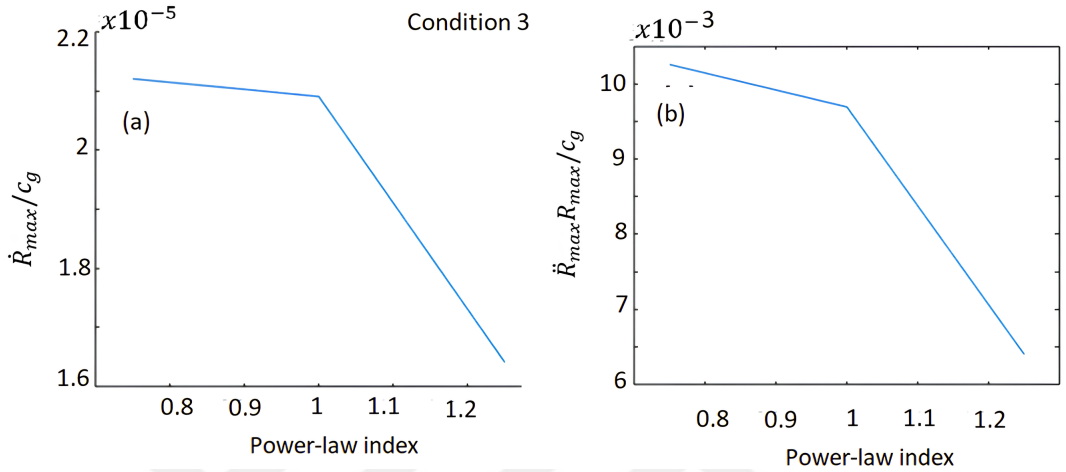

Figure 4.9. $\dot{R}_{max}/c_g$ versus power-law index and (b) $\ddot{R}_{max}R_{max}/c_g$ versus power-law index (condition 3).

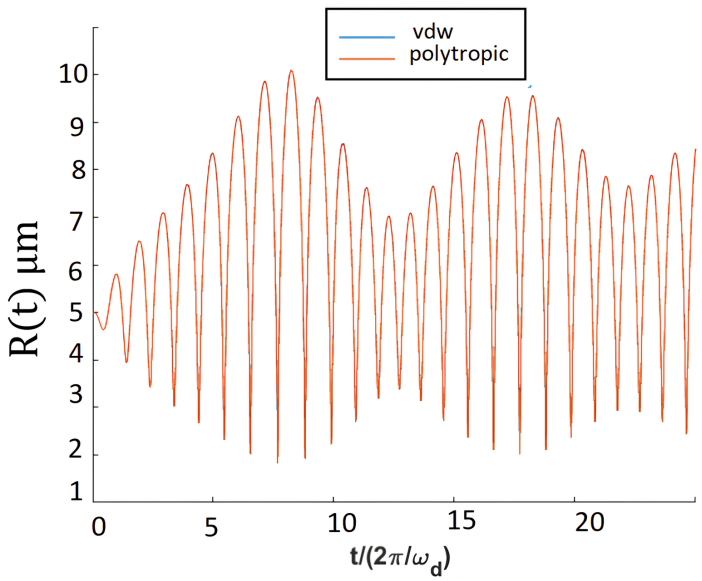

Figure 4.10. $R(t)$ versus $t/(2\pi/\omega_d)$ for $p_a = 0.25$ atm and $\omega_d = 4$ MHz.

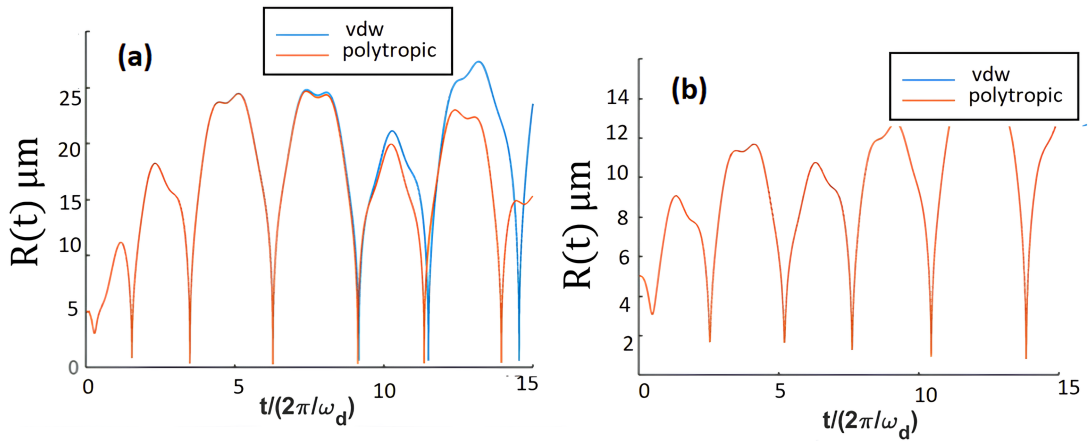

Figure 4.11. R(t) versus time for c = 2.5 atm, k = 1 and (a) $\omega_d = 4$ MHz (b) $\omega_d = 8$MHz.

4.4. Spherical Bubble Dynamics

In this section, the oscillations of a spherical bubble in an unbounded liquid are studied using the model presented in Section 3.1. First, the results for a bubble in an unbounded liquid are provided (Section 4.4.1). Next, the effect of encapsulation is incorporated into this configuration (Section 4.4.2). Finally, the results for a bubble in a liquid cavity are discussed (Section 4.4.3), including the effect of encapsulation (Section 4.4.4).

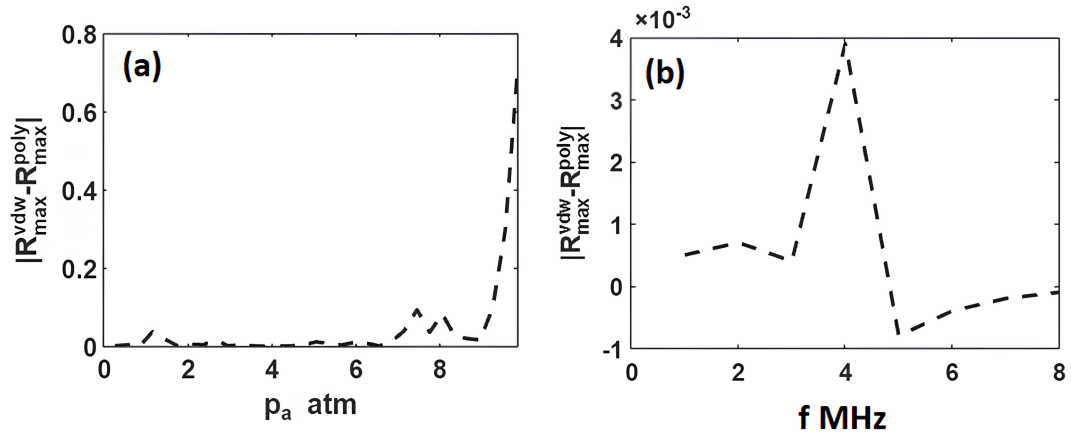

Figure 4.12. $\left|R_{\max}^{vdw} - R_{\max}^{\text{poly}}\right|$ versus p_a ($\omega_d = 2$ MHz) and (b) $\left|R_{\max}^{vdw} - R_{\max}^{\text{poly}}\right|$ versus ω_d $p_a = 0.25$ atm.

4.4.1. Bubble in an Unbounded Liquid

The spherical oscillations of a bubble in an unbounded inviscid liquid are first examined to establish the fundamental dynamics of bubble behavior. This analysis provides insight into the oscillatory motion driven by external forces such as acoustic fields or pressure variations. Subsequently, the influence of viscosity is introduced to investigate how energy dissipation alters the oscillation characteristics. The physical system for this section is illustrated in Figure 3.1. The liquid is assumed to be water. The physical properties of the system are provided in Table 4.1.

Table 4.1. Physical properties for a bubble in an unbounded liquid.

Surface tension, σ	0.072 N/m
Initial radius, R_{b0}	10^{-5} m
Vapor pressure, p_v	2300 Pa
Liquid density, ρ	1000 kg/m^3
Ratio of specific heat, κ	5/3
Initial bubble pressure, p_{g0}	2500 Pa
External pressure, p_∞	10^5 Pa

4.4.1.1. Effect of Liquid Properties. Here, the liquid's viscosity, density and the surface tension effects are investigated.

Figure 4.13(a) presents a schematic view of a bubble's expansion and contraction in an unbounded inviscid liquid when the acoustic field is turned off. Initially, the pressure inside the bubble is lower than the liquid pressure, which causes the bubble to contract. Figures 4.13(b) and (c) show the bubble radius and the dimensionless bubble wall velocity as functions of time, respectively. The scale definitions, such as $\dot{R}_b^\star$ and $t^\star$, are provided in Equation E.1. In the figure, the bubble experiences negative velocity at small radii, indicating contraction (C-D). This occurs because surface tension dominates at small scales, pulling the bubble inward. When the velocity is positive, the bubble radius increases (A-B). The

figure also shows that the bubble radius oscillates with the same amplitude when the liquid is assumed to be inviscid and the external acoustic field is turned off.

Figure 4.14 illustrates the effects of surface tension (Figure 4.14(a)), liquid density (Figure 4.14(b)) and initial bubble radius (Figure 4.14(c)) on the oscillation period. The period is defined as the interval between two successive maxima of the bubble radius. The figure shows that higher liquid density and initial bubble radius increase the oscillation period while surface tension decreases. The period of oscillations is related to the natural frequency of the system by the equation, $T = \frac{2\pi}{\omega_0}$ where $\omega_0 \propto \sqrt{\frac{\sigma}{\rho_l R_{b0}^3}}$ is the natural frequency without the effect of damping and external forces. Here, T is the oscillation period. The period of bubble oscillations decreases with increasing liquid density because the system's natural frequency increases. This is due to the greater inertia provided by the liquid which causes the bubble to oscillate more rapidly and reduces the period of each oscillation cycle. Also, a larger bubble has a greater volume and more inertia which slows down its response to the restoring forces, e.g., surface tension forces. As a result, the bubble takes longer to complete each oscillation, leading to a more extended period.

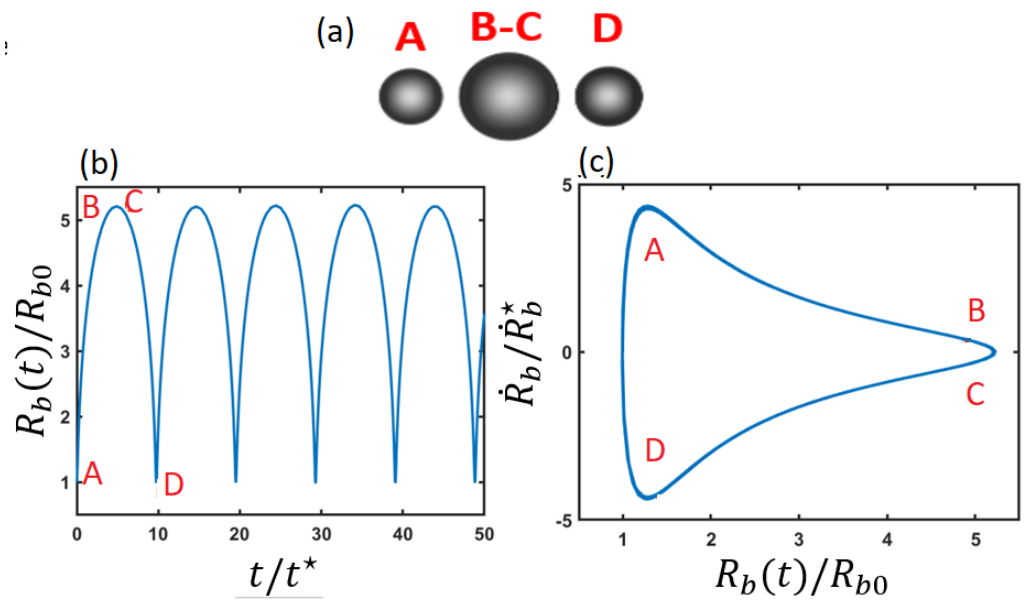

Figure 4.13. Spherical oscillations of a bubble in an inviscid unbounded liquid: (a) the schematic view of the bubble extraction-contraction, (b) bubble radius versus time and (c) velocity versus time.

Second, the effect of viscosity is added to the system in Figure 4.15. Here, the liquid is assumed to be Newtonian. In Figure 4.15(a), the Reynolds number, $Re = 1$, and in Figure 4.15(b) $Re = 10$. The definition of the Reynolds number is given in Equation E.3. The figure shows that the amplitude of oscillations decreases due to viscous damping effects. In Figure 4.13(c), the curve forms a loop which indicates that the motion is undamped. Therefore, the bubble achieves higher velocities during its expansion and contraction phases.

For viscous liquid (Figure 4.15), the bubble's velocity decreases over time and gradually approaches zero. This indicates that the bubble is losing energy over time due to viscous effects, which causes a more controlled and slower expansion and contraction. At high Reynolds numbers (Figure 4.15(b)), the inertial forces are stronger than the viscous forces, which allow the bubble to maintain its motion with less damping. The phase diagram reflects this with closed loops representing continued oscillations with less energy loss.

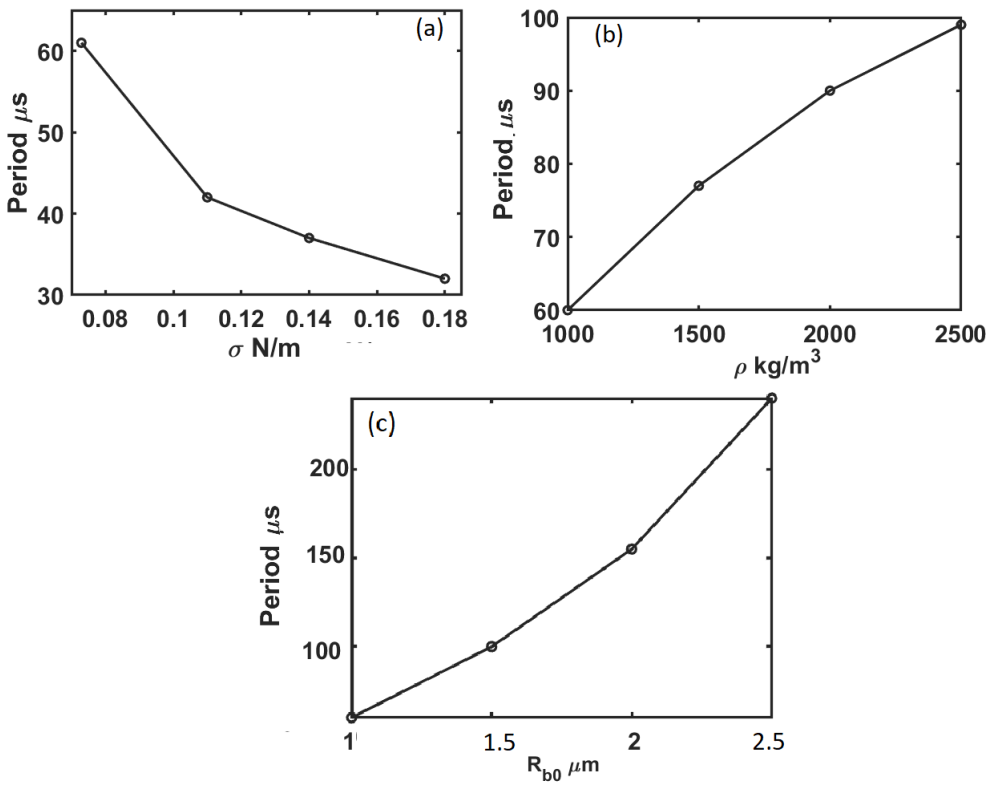

Figure 4.14. Effects of (a) surface tension, σ (b) density, ρ and (c) initial bubble radius, R_{b0} on oscillation period.

4.4.1.2. Effect of Liquid Constitutive Model. Here, the liquid is assumed to be power-law or viscoelastic. For the power-law constitutive model, a parametric analysis is performed to explore the effects of the consistency index m, power-law index k, driving frequency ω_d, and initial bubble radius R_0. Then, the surrounding liquid is assumed to be viscoelastic, and the parametric study is conducted to understand the effect of liquid modulus, G_{liq}.

In Figure 4.16, the radial oscillations of a bubble are studied both for the Newtonian and power-law liquid (Section 3.1.1.4). Here, the blue $(k = 0.75)$, red $(k = 1)$, and black $(k = 1.25)$ represent the shear-thinning, Newtonian and shear-thickening liquids, respectively. Also, the external acoustic field is turned on in Figure 4.16, $p_\infty = p_0 + p_a \sin(\omega_d t)$, where p_a is the amplitude of the acoustic field and $p_a = 0.25$ atm. The physical properties of the unbounded liquid are taken from Table 4.1. In addition to the these properties, the apparent viscosity of the power-law liquid, m, is 0.001 Pa·s^k.

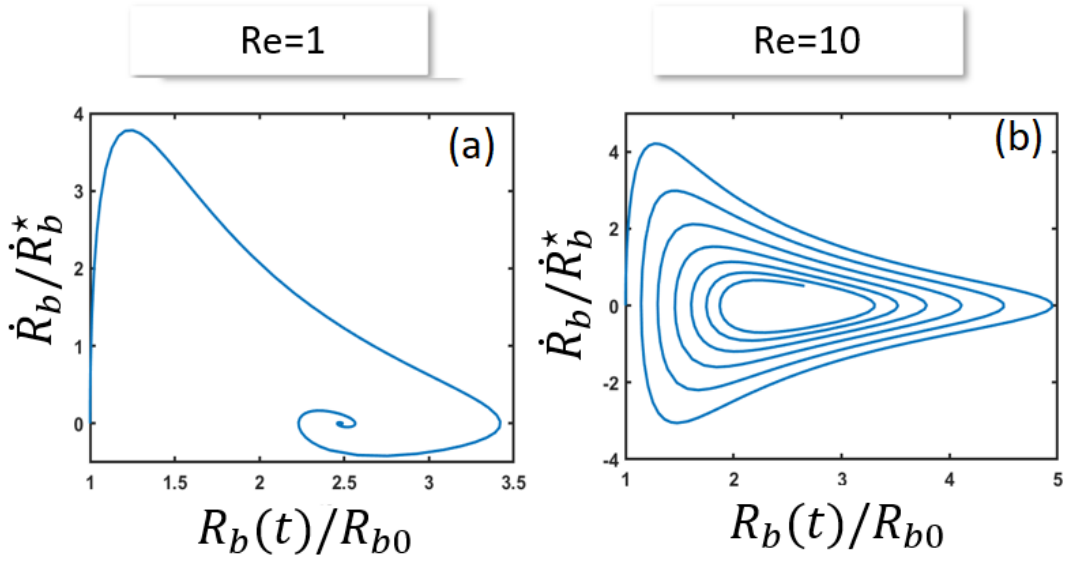

Figure 4.15. Dimensionless bubble-wall velocity versus dimensionless bubble radius (a) Re=1 and (b) Re=10.

For Newtonian liquid, $m = \mu$. The dynamic behavior of the radial modes is illustrated for different acoustic field frequencies: $\omega_d = 1$ MHz $< \omega_0$ (Figure 4.16(a)), $\omega_d = 2$ MHz $= \omega_0/2$ (Figure 4.16(b)), $\omega_d = 4$ MHz $= \omega_0$ (radial resonance, where the driving frequency approximately matches the natural frequency of radial oscillation [387]) (Figure 4.16(c)),

and $\omega_d = 10\,\text{MHz} > \omega_0$ (Figure 4.16(d)) for various values of k. Here, ω_0, the natural frequency of the radial mode, is approximately 4 MHz which causes radial resonance. The definition of the natural frequency of a bubble in an unbounded liquid is calculated from Equation 3.156. Also, a small figure is placed into Figure 4.16(a) to show the minimum radius values at the end of each period of oscillations.

In the case of radial resonance, depicted in Figure 4.16(c), the amplitude of radial oscillation is significantly greater than in the non-resonant cases (Figures 4.16(a)-(b) and (d)). Additionally, the amplitude of radial oscillation decreases as the power-law index k increases, as shown in Figures 4.16(b)-(d). Higher k values result in a reduced strain rate and increased dissipation rate, leading to dampened oscillations.

In Figures 4.17(a)-(d), the dimensionless bubble wall velocity, $\dot{R}_b$, is plotted against $R_b(t)/R_{b0}$ for different values of k and ω_d. In Figure 4.17(a), the driving frequency is $\omega_d = 1\,\text{MHz}$. Here, the phase diagram forms a nearly perfect circular loop for the Newtonian liquid which indicates stable and periodic oscillations with minimal distortion. The shear-thickening liquid shows a phase diagram that deviates slightly from the circular shape and takes on a more elliptical form. This suggests that the oscillations in a shear-thickening fluid are influenced by its resistance to deformation, which causes slight variations in both the amplitude and velocity of the bubble's oscillations compared to the Newtonian case. In contrast, the shear-thinning liquid exhibits a more complex phase diagram with multiple smaller loops, which indicates a non-linear response. As the driving frequency increases to $\omega_d = 2\,\text{MHz}$ in Figure 4.17(b), the oscillatory behavior becomes more complex across all liquids. The phase diagram shows multiple inner loops for the Newtonian liquid. This indicates that the bubble's response incorporates more complex dynamics as the driving frequency increases. The shear-thickening liquid's phase diagram remains elliptical but with more pronounced deviations, reflecting an increase in the bubble's oscillation amplitude and velocity variability. The shear-thinning liquid, however, shows numerous overlapping loops. At $\omega_d = 4\,\text{MHz}$, Figure 4.17(c), the phase diagram for the Newtonian liquid becomes tighter with more overlapping paths, indicating rapid oscillations with smaller changes in radius. This suggests that the system is nearing or at its natural frequency, where the bubble's re-

sponse is more confined but faster.

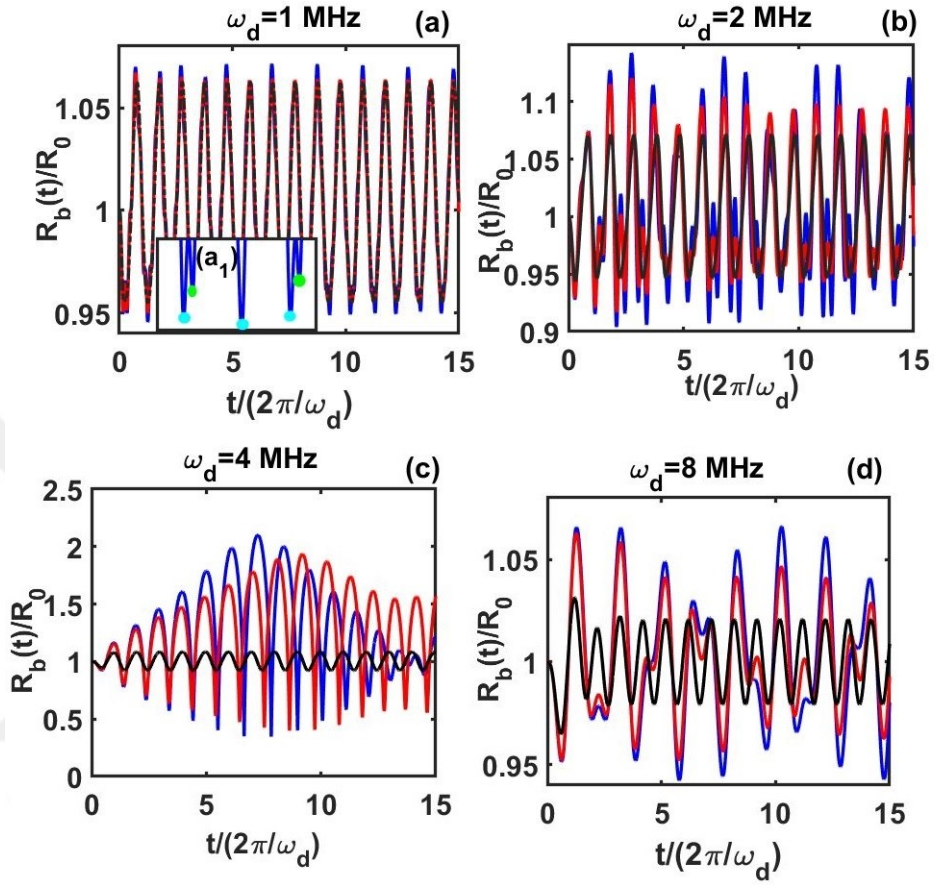

Figure 4.16. $R_b(t)$ versus $t/\left(2\pi/\omega_d\right)$ for (a) $\omega_d = 1\text{MHz} < \omega_0$, (b) $\omega_d = 2\text{MHz} \approx \omega_0/2$, (c) $\omega_d = 4\text{MHz} \approx \omega_0$ (radial resonance), and (d) $\omega_d = 8\text{MHz} > \omega_0$. Here, the blue $(k = 0.75)$, red $(k = 1)$, and black ($k = 1.25$) represent the shear-thinning, Newtonian, and shear-thickening liquids, respectively. Reproduced with permission from Kaykanat and Uguz [13]. Author(s), licensed under Creative Commons CC BY license.

Finally, the Newtonian liquid loops become very tight and densely packed, indicating rapid oscillations with minimal changes in the bubble radius when $\omega_d = 8\,\text{MHz}$ in Figure 4.17(d). This suggests that the system operates in a high-frequency regime, where the bubble's response is rapid but stable. The shear-thickening liquid shows a much tighter loop pattern than lower frequencies, reflecting a higher-frequency response. However, the overall complexity is less than that of the shear-thinning case. Therefore, Newtonian liquid (red) exhibits more regular and predictable oscillations across all frequencies. The shear-thickening

liquid shows increasing complexity with frequency but remains more regular than the shear-thinning case. Shear-thinning liquid displays the most complex and chaotic behavior with significant changes in both amplitude and velocity, especially at higher frequencies. As the driving frequency increases from 1 MHz to 8 MHz, the phase diagrams for all liquids become more complex, indicating a transition from regular periodic oscillations to more chaotic and non-linear behavior.

As illustrated in Figure 4.16, the influence of k on the dynamic bubble radius depends on ω_d. To assess the effect of ω_d on viscosity, the maximum bubble wall velocity (Figure 4.18(a)), followed by the maximum viscosity $\mu_{0,max}$ (Figure 4.18(b)), and $max\left(\left|\dot{R}_b/R_b\right|\right)^{(k-1)}$ are calculated for different k after 15 cycles of the acoustic field. In the radial resonance case, the bubble wall velocity is substantially higher than in non-resonant cases, as depicted in Figure 4.18(a). The bubble wall velocity significantly impacts the behavior of the power-law liquid viscosity contrary to the Newtonian liquid.

For a Newtonian liquid, while the bubble wall velocity varies with ω_d, the viscosity remains constant, which highlights the effect of the power-law liquid. The influence of M, which is linked to the consistency index, m, ($M = 2m(2\sqrt{3})^{k-1}$), and the power-law index k on the maximum bubble radius R_{max}/R_{b0} is illustrated in Figure 4.19 for $\omega_d = 1$ MHz (Figure 4.19(a)), $\omega_d = 2$ MHz (Figure 4.19(b)), and $\omega_d = 4$ MHz (Figure 4.19(c)). In Figure 4.19(a), the variation of R_{max}/R_{b0} with respect to M and k is minimal compared to Figures 4.19(b) and (c). As a result, changes in R_{max}/R_{b0} are not easily observed in Figure 4.19(a). An inset figure with different color codes is provided for Figure 4.19(a) to highlight the effects of M and k on R_{max}/R_{b0}. Across all cases, when M is low, R_{max}/R_{b0} is high and becomes independent of k.

The damping rate is relatively low for small M, corresponding to smaller consistency indexes. Consequently, lower M values, as described in Equation 3.30, lead to an increase in the oscillations of the bubble radius over time. Conversely, higher M values enhance the damping due to the increased dissipation rate, thereby reducing the amplitude of the oscillations.

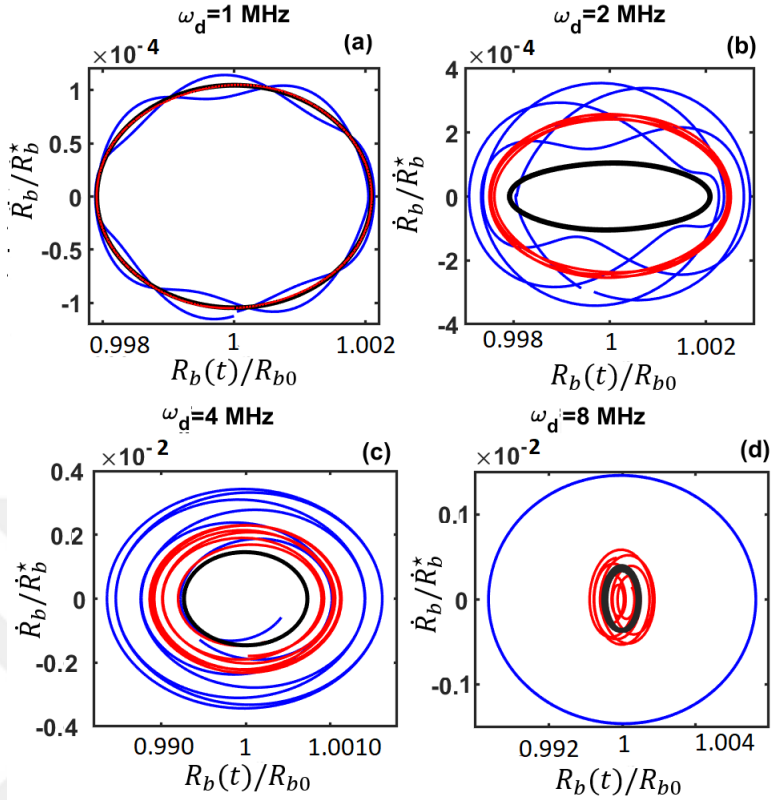

Figure 4.17. $\dot{R}_b(t)$ versus R_b/R_{b0}.) for (a) $\omega_d = 1\text{MHz} < \omega_0$, (b) $\omega_d = 2\text{MHz} \approx \omega_0/2$, (c) $\omega_d = 4\text{MHz} \approx \omega_0$ (radial resonance), and (d) $\omega_d = 8\text{MHz} > \omega_0$. Here, the blue $(k = 0.75)$, red $(k = 1)$, and black ($k = 1.25$) represent the shear-thinning, Newtonian, and shear-thickening liquids, respectively.

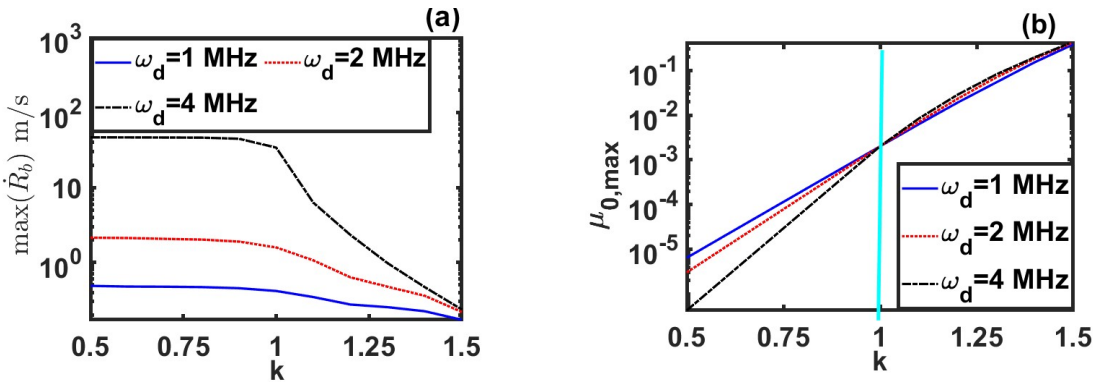

Figure 4.18. a) Maximum value of bubble wall velocity max($\dot{R}_b$), versus power-law index, k and (b) maximum viscosity, $\mu_{0,max}$ versus power-law index, k after 15 cycle. Reproduced with permission from Kaykanat and Uguz [13]. Author(s), licensed under Creative Commons CC BY license.

Although this dissertation primarily focuses on microbubbles due to their biomedical applications, Figure 4.20 examines the effects of R_{b0} and k on $|R_{max}/R_{b0}|$ for $\omega_d = 2$ MHz. The maximum bubble values are measured after 15 cycles of the acoustic field. In Figure 4.20, the amplitude of the acoustic field is set to 0.25 atm. The power-law index k has little impact on the maximum bubble radius for large bubbles. However, small bubbles are more influenced by surface forces which have a larger surface area relative to their volume than larger bubbles. The dependence of bubble radius on bubble dynamics is also evident in Equation 3.32. The effect of the power-law index on bubble dynamics diminishes because the dissipation term in Equation 3.32 ($\frac{2M}{k}|\dot{R}|^{k-1}\frac{\dot{R}}{R^k}$) becomes smaller which plays a more significant role in the dynamics of smaller bubbles.

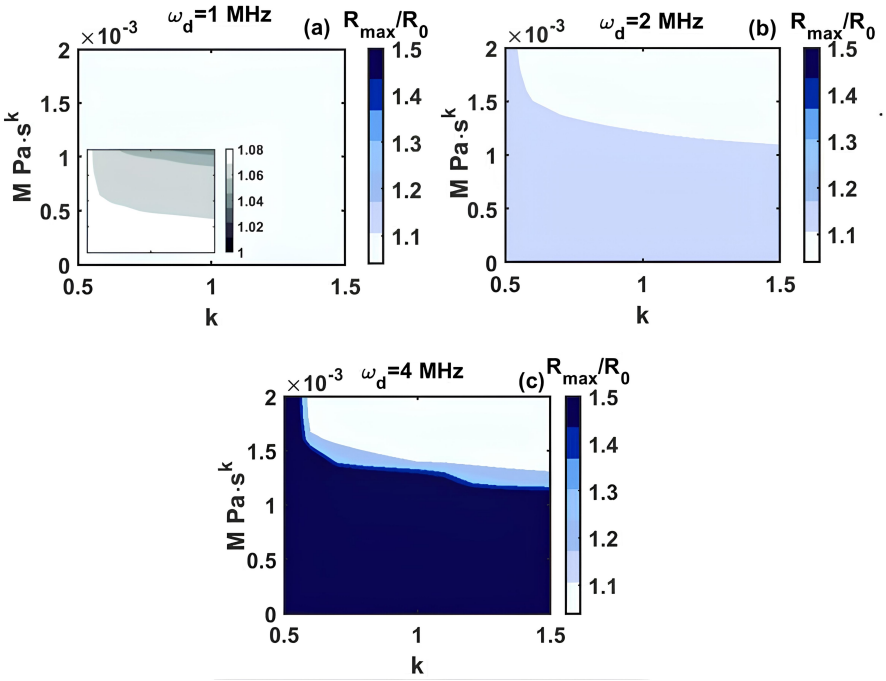

Figure 4.19. Contour plot (M versus power-law index, k) for R_{max}/R_{b0}: (a) $\omega_d = 1$ MHz, (b) $\omega_d = 2$ MHz and (c) $\omega_d = 4$ MHz$\approx \omega_0$ after 15 cycle . Reproduced with permission from Kaykanat and Uguz [13]. Author(s), licensed under Creative Commons CC BY license.

Finally, a bubble in an unbounded viscoelastic liquid is studied as discussed in Section 3.1.1.5. The impact of the liquid's viscoelastic modulus G_{liq} on the bubble radius is examined in Figure 4.21(a). The figure shows that the bubble oscillations progressively dampen as G_{liq}

increases. Moreover, the viscoelastic properties of the liquid influence not only the damping of oscillations but also the system's natural frequency. Unlike purely viscous forces, the viscoelastic modulus G_{liq} significantly affects the natural frequency. The natural frequency of the bubble's oscillation increases with G_{liq} as derived in Equation 3.157. This relationship is shown in Figure 4.21(b), where the natural frequency increases with G_{liq}, The natural frequency increases with G_{liq} due to the additional restorative force provided by the liquid's elasticity. In a viscoelastic medium, the liquid not only resists the deformation caused by the bubble's expansion and contraction but also exerts a force that tends to restore the bubble to its equilibrium state more quickly. This leads to faster oscillations, reflected in the higher natural frequency.

4.4.2. Encapsulated Bubble in an Unbounded Liquid

In this section, the spherical oscillations of an encapsulated bubble in an unbounded liquid are examined. First, the surrounding liquid is assumed to be Newtonian, and then, the effect of non-Newtonian surrounding liquid is investigated. The physical system for this section is shown in Figure 3.2, and the physical properties of the liquid and shell are provided in Tables 4.1 and 4.2, respectively. An external acoustic field, $p_\infty = p_0 + p_a \sin(\omega_d t)$, is applied with an amplitude, $p_a = 0.25$ atm.

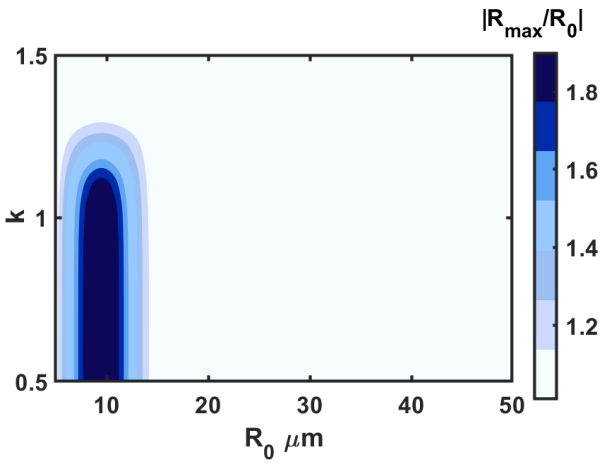

Figure 4.20. Contour plot (M versus power-law index, k) for R_{max}/R_{b0}: (a) $\omega_d = 1$ MHz, (b) $\omega_d = 2$ MHz and (c) $\omega_d = 4$ MHz$\approx \omega_0$ after 15 cycle Reproduced with permission from Kaykanat and Uguz [13]. Author(s), licensed under Creative Commons CC BY license.

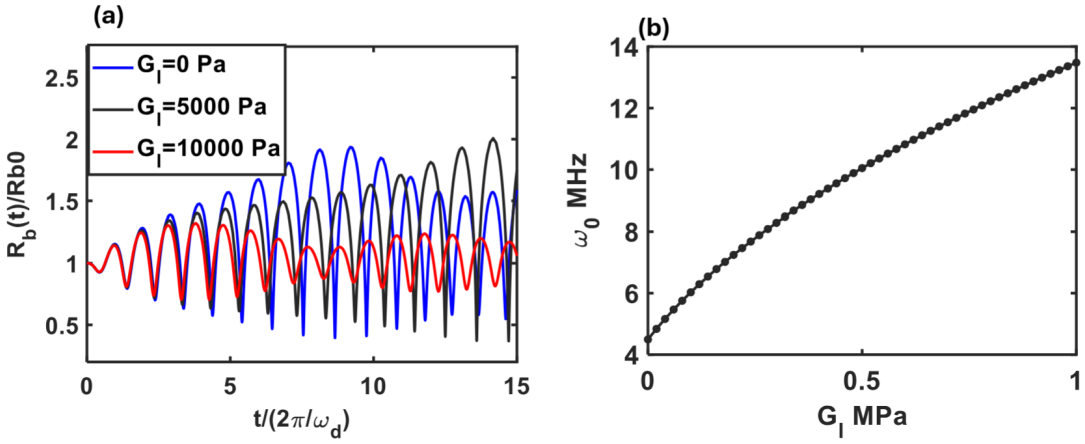

Figure 4.21. $R_b(t)$ versus $t/(2\pi/\omega_d)$ for $\omega_d = 4$ MHz $\approx \omega_0$ and (b) Effect of liquid modulus on the natural frequency.

4.4.2.1. Effect of Shell Properties. Here, the effects of shell modulus, G_s and the shell thickness, δ, on the dynamic bubble oscillations and the natural frequency are investigated.

The natural frequency of an encapsulated bubble in an unbounded liquid is given by Equation 3.158. The viscoelastic shell increases the system's natural frequency. In the previous section, for a bubble in an unbounded liquid, the natural frequency was 4 MHz. With the same properties, the encapsulated bubble in an unbounded liquid has a natural frequency of 7 MHz. As shown in Figure 4.22, when the acoustic field's driven frequency is adjusted at the natural frequency of the system, i.e., $\omega_d = 7$ MHz, radial resonance occurs, which causes the growth of the oscillation of bubble radius, R_b.

Table 4.2. Physical properties for bubble shell [16].

Shell thickness, δ	15 nm
Shell viscosity, μ_s	0.05 kg/(ms)
Modulus of rigidity, G_s	15 MPa
Shell density, ρ_s	1100 kg/m^3
Interfacial tension (bubble/shell), σ_b	0.04 N/m
Interfacial tension (shell/liquid), σ_s	0.005 N/m

Figure 4.23 illustrates the effects of shell thickness (δ) and shell modulus (G_s) on the dynamic behavior of bubble radius. Increasing either δ or G_s dampens the oscillations of a bubble as shown in the figure. Notably, this damping effect can be achieved through either a thicker or higher shell modulus. Therefore, a bubble can be encapsulated with a thick and high modulus shell to prevent bubble bursting and dampen oscillations. However, it is important to note that if the shell modulus is too high, it may thoroughly dampen the oscillations which potentially causes an overly rigid system with diminished responsiveness to external stimuli. Figure 4.24 presents contour plots of shell thickness (δ) vs. shell modulus (G_s) (Figure 4.24(a)) and reference pressure amplitude (p_0) vs. initial bubble radius (R_{b0}) (Figure 4.24(b)) for the natural frequency (ω_0) of an encapsulated bubble in unbounded liquid. The shell modulus, G_s, defines the stiffness of the encapsulating layer and it significantly influences the bubble's resistance to deformation. A higher G_s increases the system's natural frequency by making oscillations more resistant to external forces, as seen in Figure 4.24(a). Similarly, an increase in shell thickness (δ) adds structural rigidity which furtherincreases ω_0. When $G_s < 5\,\text{MPa}$ and $\delta < 5\,\text{nm}$, the shell's influence becomes negligible which causes the bubble to behave like a free bubble. The region is marked by the "UB" in Figure 4.24(a). In Figure 4.24(b), higher values of p_0 increase the inertial forces, and their effect on ω_0 becomes more pronounced with larger bubble radii (R_{b0}).

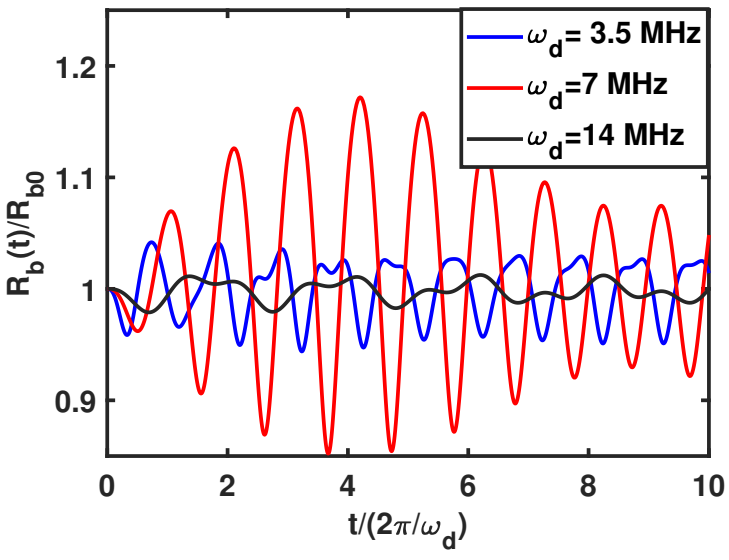

Figure 4.22. Effect of acoustic field driven frequency, ω_d, on $R_b(t)/R_{b0}$ versus $\dfrac{t}{2\pi\omega_d}$.

Figure 4.25 illustrates natural frequency difference between an encapsulate and unencapsulated bubble defined as $\Delta = \frac{(\omega_{0,UB} - \omega_{0,EC})}{\omega_{0,UB}}$. The subscript UB refers to the natural frequency of the unencapsulated bubble, while EC refers to the natural frequency of the encapsulated bubble. When the initial bubble radius (R_{b0}) and the reference pressure amplitude (p_0) are small, the difference in natural frequency, Δ, is significant. This is because smaller bubbles are more strongly influenced by the encapsulating shell which alters the dynamics of the bubble oscillation compared to an unencapsulated bubble. However, as R_{b0} and p_0 increase Δ decreases. This can be attributed to the fact that larger bubbles are less affected by the material properties of shell as the effects of inertial forces begin to dominate over the constraints imposed by the shell. Similarly, the increased external forcing overcomes the damping effect of the shell, reducing the natural frequency difference at higher pressure amplitudes, p_0.

As detailed in Section 3.1.2.2, the behavior of the shell can be described using either linear or nonlinear viscoelastic models. Linear viscoelasticity typically applies only to small deformations, while nonlinear deformations occur when deformations are large or when the material's properties change under deformation. Figure 4.26 illustrates the impact of the shell model on the system. Initially, the difference between the models is minimal, but becomes more pronounced over time.

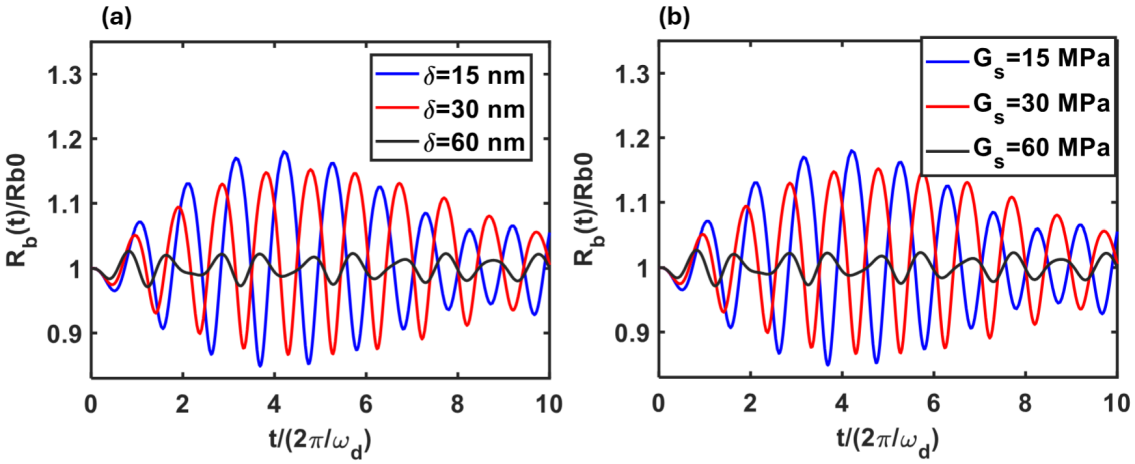

Figure 4.23. Effects of (a) shell thickness, δ and (b) shell modulus, G_s on $R_b(t)/R_{b0}$ versus $t/(2\pi/\omega_d)$.

A contour plot of δ vs. G_s is presented in Figure 4.27 to illustrate the effects of varying shell thickness (δ) and modulus (G_s) on two key metrics: the maximum bubble surface area (Figure 4.27(a)) and the deviation between the linear and nonlinear shell models, denoted as χ (Figure 4.27(b)). The behavior of the shell can be described using either linear [16] or nonlinear viscoelastic models [335, 376]. The maximum bubble surface area, $4\pi \max(R_b)^2$, is determined from the maximum bubble radius observed after 25 oscillation cycles. The deviation, $\chi = \max(\text{Area})|_{\text{linear}} - \max(\text{Area})|_{\text{nonlinear}}$, quantifies the difference in predicted surface areas between the linear and nonlinear shell models, also calculated after 25 cycles. There is a distinct region in the δ-G_s contour plot where the maximum bubble surface area reaches approximately 600 μm^2 as shown in Figure 4.27(a). This region is defined by specific combinations of shell modulus (G_s) and shell thickness (δ) with the corners of this region located at $G_s \approx 15$ MPa with $\delta \approx 15$ nm, $G_s \approx 15$ MPa with $\delta \approx 30$ nm, $G_s \approx 20$ MPa with $\delta \approx 30$ nm, and $G_s \approx 30$ MPa with $\delta \approx 15$ nm. This region is referred to as the resonance region where the bubble's oscillations are significantly amplified as depicted in Figure 4.22. Figure 4.27(b) highlights the regions where the deviation between the linear and nonlinear shell models exceeds 10%, indicating the boundaries where the linear approximation begins to break down. In Figure 4.27(b), the contour plot reveals that in the vicinity of these resonance region, the deviation between the linear and nonlinear shell models, χ, becomes more pronounced. This increase in deviation is attributed to the resonant amplification of the bubble's oscillations, where nonlinear deformations of the shell become significant. As the bubble oscillates near resonance, the linear model fails to capture these nonlinear effects accurately, leading to larger errors predicting of the maximum bubble surface area.

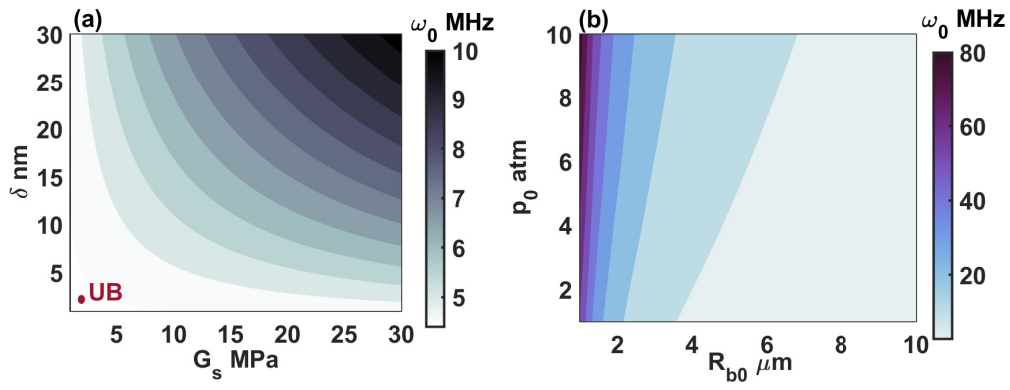

Figure 4.24. Contour plot (a) δ versus G_s, and (b) p_0 versus R_{b0} for natural frequency, ω_0.

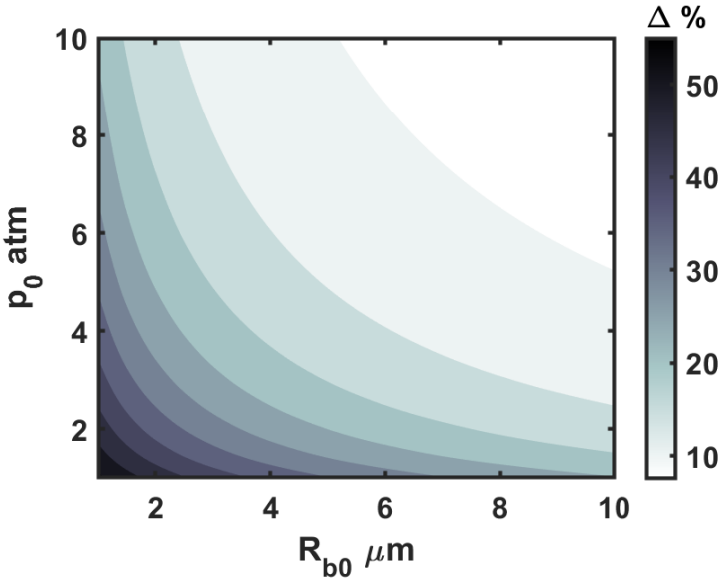

Figure 4.25. Contour plot G_s versus δ for natural frequency deviation, Δ.

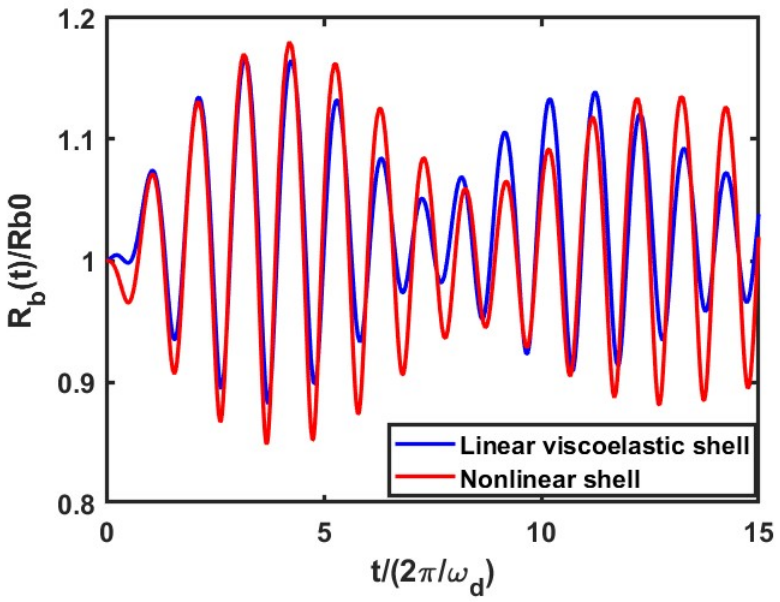

Figure 4.26. Effect of shell models on $R_b(t)/R_{b0}$ versus $t/(2\pi/\omega_d)$.

Figure 4.28 illustrates the behavior of the shell and bubble radii for different shell thicknesses and modulus: $\delta = 30\,\text{nm}$ and $G_s = 15$ MPa in Figure 4.28(a), $\delta = 60\,\text{nm}$ and $G_s = 15$ MPa in Figure 4.28(b), and $\delta = 15\,\text{nm}$ and $G_s = 60$ MPa in Figure 4.28(c). In the case of a thin shell ($\delta = 30\,\text{nm}$) (Figure 4.28(a)), the shell radius closely follows the bubble

radius throughout oscillation, indicating that for small shell thicknesses, the shell's response is tightly coupled to the bubble's motion. This behavior reflects the thin shell's lower inertia and minimal resistance to deformation, allowing it to move in near synchronization with the bubble. However, with a thicker shell ($\delta = 60\,\text{nm}$) (Figure 4.28(b)), a noticeable lag develops between the shell and bubble radii. Also, a higher shell modulus bit increases the difference between the behavior of the bubble and shell radii (Figure 4.28(c)). The increased stiffness of the thicker shell slows its response to oscillations, reducing its expansion and contraction amplitude compared to the bubble.

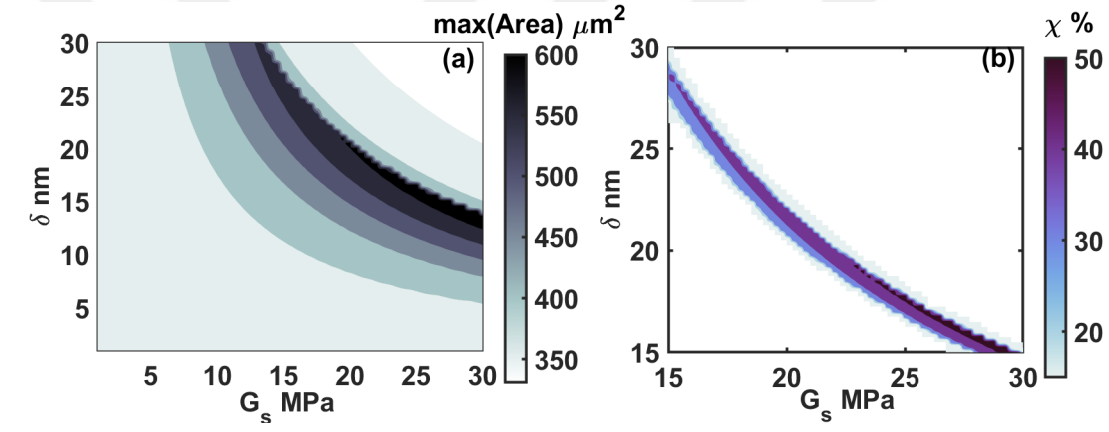

Figure 4.27. Contour plot (δ versus G_s) (a) for maximum bubble surface area and (b) for the deviation between shell models.

Figure 4.29 analyzes the impact of shell and liquid viscosities on the maximum expansion and compression of an encapsulated bubble after 25 oscillation cycles. Increasing the liquid viscosity (μ_l) reduces expansion and increases contraction due to greater energy dissipation which dampens oscillations by converting kinetic energy. Similarly, Figure 4.29 illustrates that higher shell viscosity (μ_s) slowly decreases expansion and increases contraction by adding dissipation to the system. The thicker shell increases the energy required for oscillations further reducing the oscillatory amplitude. However, bubble oscillations are particularly sensitive to changes in μ_l, where even small variations can significantly affect amplitude and stability. This sensitivity is critical in applications like acoustic imaging and drug delivery where precise control of bubble dynamics is essential. The maximum expansion decreases while the contraction increases without the effect of encapsulating shell.

However, when the driving frequency of acoustic field matches the natural frequency for the unencapsulated bubble, ω_d =4, MHz the expansion is greater and the compression is more significant of an unencapsulated bubble compared to the encapsulated bubble.

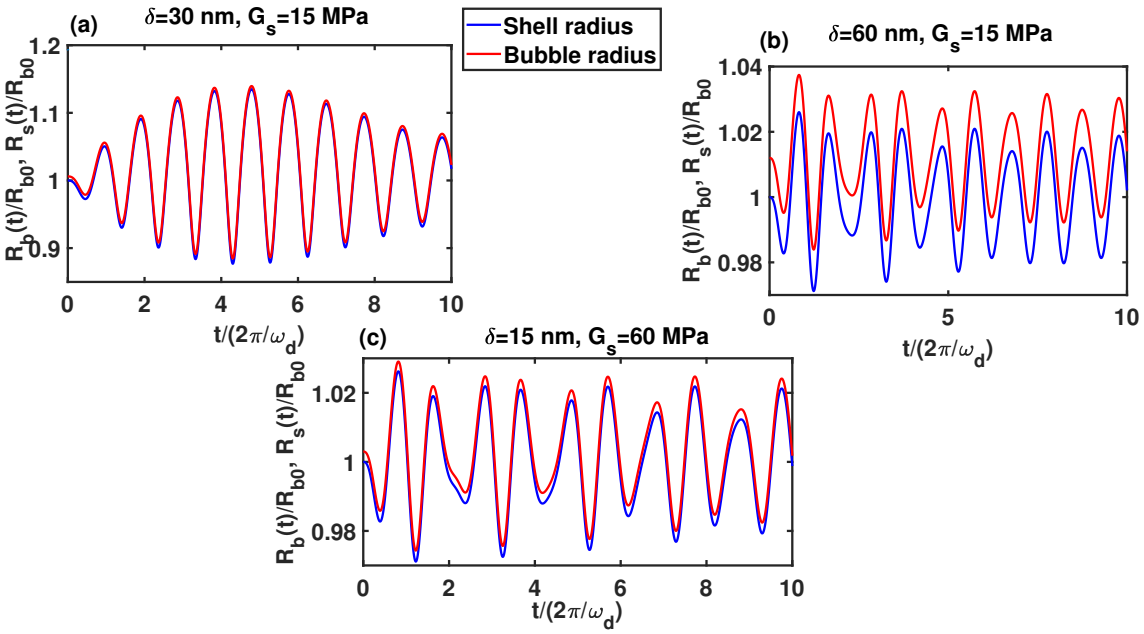

Figure 4.28. Effect of shell thickness, δ on $R_b(t)/R_{b0}$ versus $t/(2\pi/\omega_d)$: (a) δ=15 nm, $G_s = 15$ MPa, (b) $\delta = 60$ nm, $G_s = 15$ MPa and (c) $\delta = 15$ nm, $G_s = 60$ MPa.

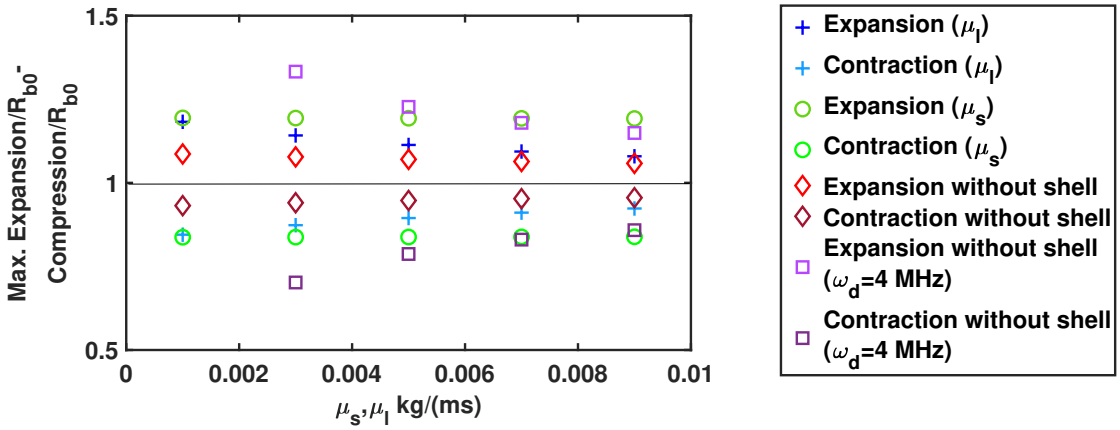

Figure 4.29. Maximum expansion and compression of microbubble versus liquid (μ_l) and shell (μ_s) viscosity.

4.4.2.2. Effect of Surrounding Liquid Constitutive Model. Here, the effect of the surrounding liquid model is studied. Different constitutive models for liquid, e.g., power-law and viscoelastic, are used.

In Figure 4.30, the surrounding liquid is modeled using a power-law constitutive law (Section 3.1.2.4). The blue, red, and black lines show the shear-thinning ($k = 0.75$), Newtonian ($k = 1$), and shear-thickening ($k = 1.25$) liquid cases, respectively. When the apparent viscosity, m, is 0.001 Pa $\cdot$ s$^{\mathrm{k}}$, the influence of the power-law index, k, on the system's behavior is minimal as depicted in Figure 4.30(a). However, the impact of k becomes more pronounced which causes noticeable differences in the system's response as the value of m increases . This suggests that the effect of the power-law index is more significant in fluids with higher apparent viscosities, where non-Newtonian characteristics play a larger role in determining the overall dynamics.

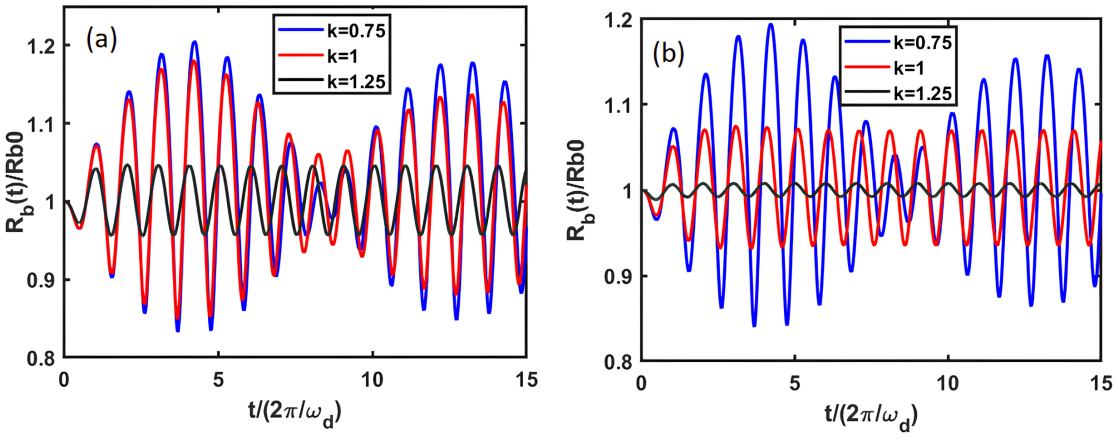

Figure 4.30. Effect of power-law index on $R_b(t)/R_{b0}$ versus $t/(2\pi/\omega_d)$: (a) m =0.001 Pa $\cdot$ s$^{\mathrm{k}}$ and (b) $m = 0.01$ Pa $\cdot$ s$^{\mathrm{k}}$.

As discussed in Section 4.4.1 in Figure 4.16(a), the power-law index has a subtle impact on the amplitude of oscillation in the non-resonance scenario. This phenomenon is similarly observed in Figure 4.31. The reason for this result is the relatively low inertia of the system in the non-resonance case, which makes the oscillations less sensitive to changes in the power-law index. The reduced inertia not only diminishes the system's overall re-

sponse but also affects the effective viscosity of the power-law liquid. In power-law fluids, the effective viscosity depends on the shear rate and at lower inertia, the shear rates generated during oscillations are lower . This results in a smaller change in the effective viscosity with varying power-law indices, further contributing to the slight modification in the oscillation amplitude. This contrasts with resonance conditions, where higher inertia leads to larger shear rates and a more significant impact of the power-law index on both the effective viscosity and the amplitude of oscillations, as observed in Figures 4.16(c) and 4.30(a).

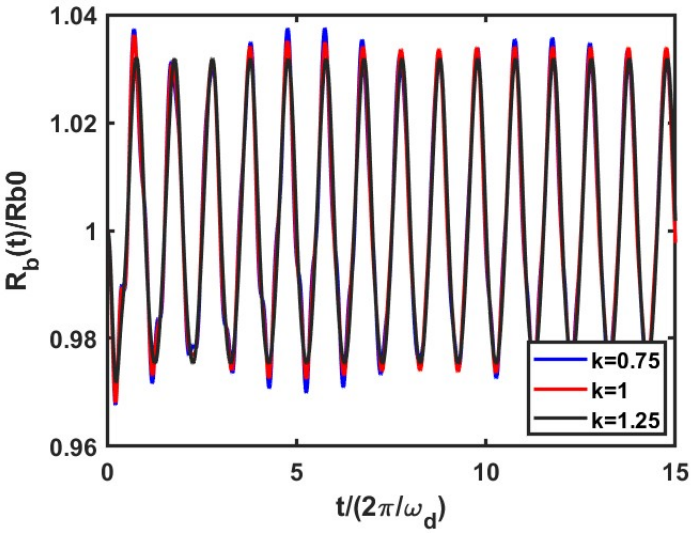

Figure 4.31. $R_b(t)/R_{b0}$ versus $t/(2\pi/\omega_d)$ for ω_d=2 MHz$< \omega_0$

Figure 4.32 presents contour plots of p_a versus ω_d for both (a)-(c) the maximum bubble surface area and Figure 4.33 (a)-(c) shows the minimum bubble surface area, reflecting the bubble's maximum expansion and contraction, respectively. Figure 4.32 (a) and Figure 4.33 (a) correspond to a shear-thinning liquid ($k = 0.5$), Figure 4.32 (b) and Figure 4.33(b) to a Newtonian liquid ($k = 1$), and Figure 4.32 (c) and Figure 4.33 (c) to a shear-thickening liquid ($k = 1.5$).

Although the maximum and minimum areas for shear-thinning and Newtonian liquids show similar behavior (Figures 4.32(a)-(b) and -Figure 4.33 (a)-(b)), the shear-thickening liquid significantly reduces the maximum bubble surface area (Figure 4.32(c)). However, the minimum area for the shear-thickening liquid (Figure 4.33(c)) is comparable to that of

the shear-thinning and Newtonian liquids. Within the range $4.5\,\text{MPa} < \omega_d < 7.5\,\text{MPa}$, the effect of pressure amplitude becomes more pronounced in Figures 4.32(a)-(b) and Figures 4.33(a)-(b). Outside of this range, the pressure amplitude has only a minor influence on the bubble surface area. This pattern is also observed for the minimum surface area. However, this region is not observed for the shear-thickening liquid, where the thickening behavior suppresses the effects of pressure amplitude and frequency.

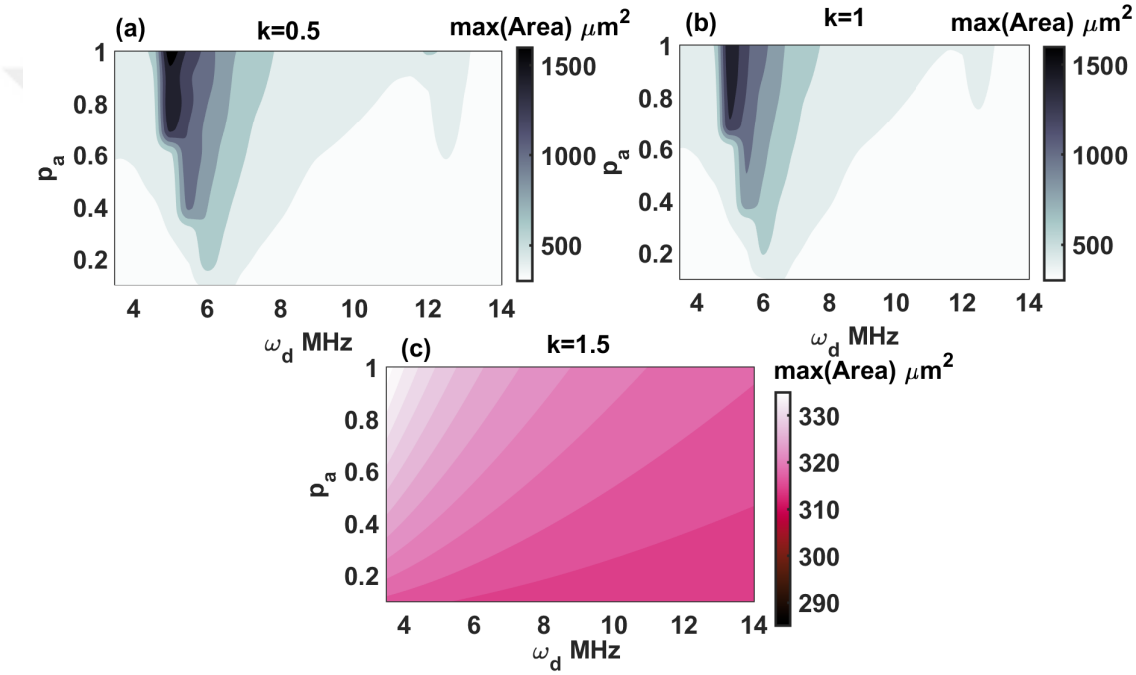

Figure 4.32. Contour plots (p_a versus ω_d) for maximum bubble surface area (a) $k = 0.5$, (b) $k = 1$ and (c) $k = 1.5$.

Figure 4.34 presents two contour plots (p_a vs. k) that depict the deviation between shell models for different apparent liquid viscosities, m. The apparent viscosity is $m = 0.001\,\text{Pa}\cdot\text{s}^k$ in Figure 4.34(a), while $m = 0.01\,\text{Pa}\cdot\text{s}^k$ in Figure 4.34(b). As expected, the deviation between the shell models increases with higher acoustic field amplitude, p_a. For lower values of m, particularly $m = 0.001\,\text{Pa}\cdot\text{s}^k$, the deviation is more pronounced for shear-thinning liquids (i.e., when $k < 1$). On the other hand, The deviation is more significant for shear-thickening liquids (i.e., when $k > 1$) for higher m values, such as $m = 0.01\,\text{Pa}\cdot\text{s}^k$. Finally, for higher values of m, the deviation between the shell models increases compared to lower

viscosity values. This occurs because higher m values correspond to lower viscosities for shear-thickening liquids which causes higher strain rates and a greater discrepancy between the predictions of the shell models (Figure 4.34(b)). Additionally, increased acoustic pressure amplitude further raises the strain rate which causes nonlinear deformations (Figures 4.34(a) and (b)). This analysis emphasizes the importance of accounting for both the rheological properties of liquid and the strength of the acoustic field when comparing shell models. The interaction between viscosity, shear rate dependence, and acoustic forces can significantly influence model outcomes.

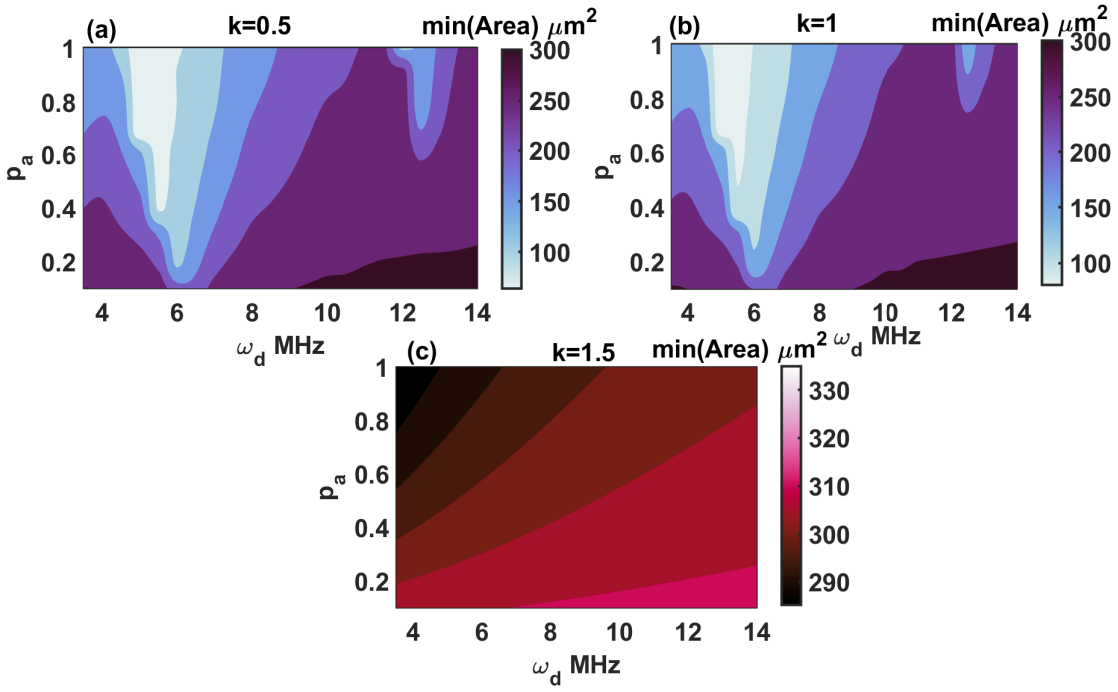

Figure 4.33. Contour plots (p_a versus ω_d) for minimum bubble surface area where (a) $k = 0.5$, (b) $k = 1$ and (c) $k = 1.5$.

In Figure 4.35, the surrounding liquid is assumed to be linear viscoelastic as described in Section 3.1.2.1. Higher G_{liq} values dampen the oscillations of the bubble radius. This damping effect is due to the inherent energy dissipation properties of viscoelastic materials where the resistance to deformation of the liquid grows stronger with higher G_{liq}. Higher G_{liq} causes the reduced oscillatory motion. Additionally, the viscoelastic modulus influences the natural frequency of the system. The natural frequency of a bubble in an unbounded

viscoelastic liquid is given in Equation 3.157. Figure 4.36 demonstrates that the natural frequency increases with increasing G_{liq} as also observed in Figure 4.21(b). This rise in ω_0 can be attributed to the increased stiffness of the viscoelastic liquid. A higher viscoelastic modulus makes the liquid more deformation-resistant which causes the bubble to oscillate at a higher frequency. In Figure 4.37, the natural frequencies for viscoelastic and Newtonian liquids are compared for different initial bubble radius values. For better visualiation, y-axis is in logarithmic scale. The figure shows that the natural frequency of the Newtonian liquid is consistently lower than that of the viscoelastic liquid. However, this difference becomes more pronounced at lower R_b values. The viscoelasticity dampens the oscillations and enhances the natural frequency, particularly in scenarios involving smaller bubbles. This behavior contrasts with Newtonian liquids, where the absence of viscoelastic effects results in lower natural frequencies across the range of bubble sizes examined.

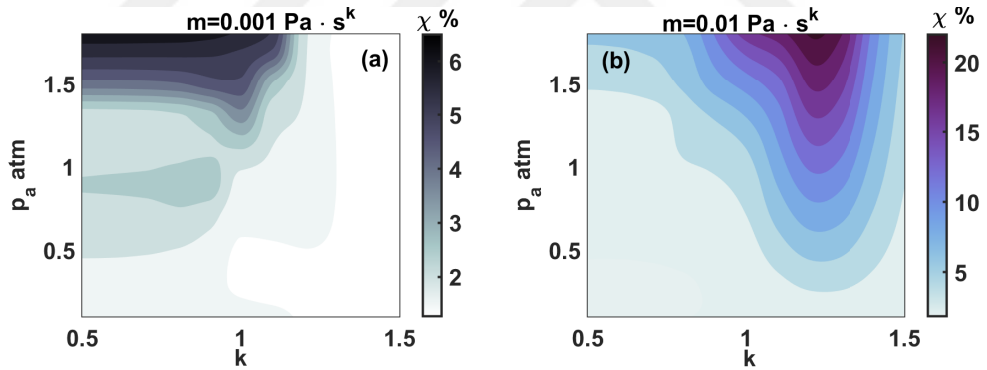

Figure 4.34. Contour plot (p_a versus k) shows the deviation between shell models (a) $m = 0.001$ Pa.s^k and (b) $m = 0.01$ Pa.s^k.

4.4.3. Results for Bubble in a Liquid Cavity

In this section, the spherical oscillations of a bubble in a liquid cavity are examined. First, liquid is assumed to be Newtonian, and then, the effect of non-Newtonian liquid is investigated. The physical system for this section is shown in Figure 3.3, and the physical properties of the liquid are provided in Table 4.1. An external acoustic field, $p_\infty = p_0 + p_a \sin(\omega_d t)$, is applied with an amplitude, $p_a = 0.25$ atm. The shear and bulk modulus of the solid are given as $G_{el} = 10$ MPa and K_{el}=10 MPa.

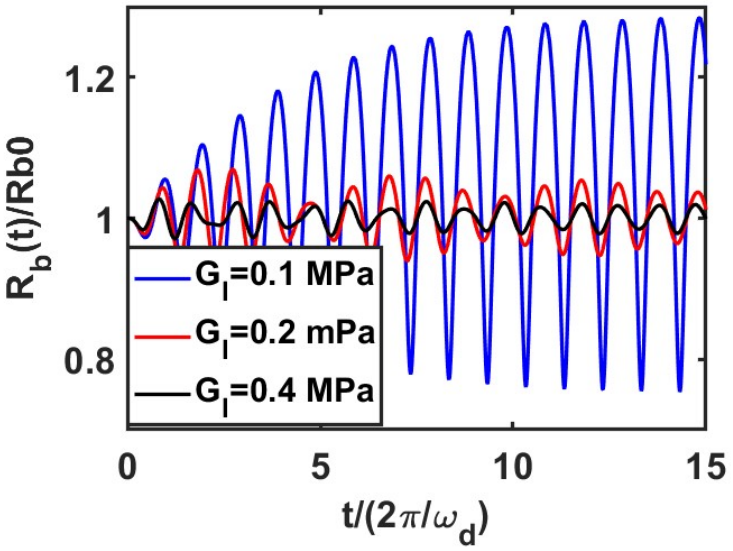

Figure 4.35. Effect of liquid modulus, G_{liq} on $R_b(t)/R_{b0}$ versus $t/(2\pi/\omega_d)$.

4.4.3.1. Effect of Cavity Properties. Here, the effect of cavity properties, i.e., the ratio of initial cavity radius to bubble radius, $\beta = R_{l0}/R_{b0}$, and the cavity modulus, G_{el}, are investigated on the dynamic bubble oscillations and the natural frequency.

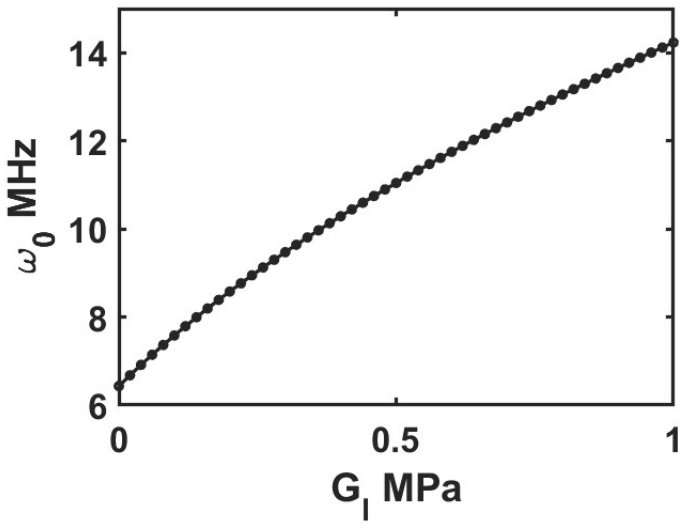

Figure 4.36. Effect of liquid modulus, G_{liq} on the natural frequency, ω_0

The natural frequency of a bubble in a Newtonian liquid cavity is determined by Equation 3.158. In the previous section, the natural frequency for a bubble in an unbounded liquid was calculated to be 4 MHz. As illustrated in Figure 4.38, when the acoustic field's driving frequency is set to match the system's natural frequency, $\omega_d = 7$ MHz, radial resonance occurs, leading to an amplification in the oscillation of the bubble radius, R_b. Figure 4.39 examines the effect of cavity modulus on natural frequency, as described by Equation 3.154. The figure demonstrates that an increase in the solid's elastic modulus (G_{el}) leads to a corresponding increase in the natural frequency (ω_0). This relationship indicates that a stiffer cavity, characterized by a higher elastic modulus, results in higher oscillation frequencies for the system. Figure 4.40 shows the effect of the initial radius ratio $\beta = R_{l0}/R_{b0}$ on the system's behavior. Smaller β values are examined in Figure 4.40(a), while Figure 4.40(b) focuses on larger β values. The results indicate that when β is large, it has little to no impact on the behavior of the bubble radius, R_b. Additionally, there is no apparent direct dependency of the oscillation amplitudes on β for larger β values. This suggests that while the ratio β influences the system's dynamics, its effect is not straightforward and may depend on other factors or parameters within the system. The lack of a direct correlation between β and oscillation amplitudes for small values highlights the complex interplay between the bubble and its surrounding environment.

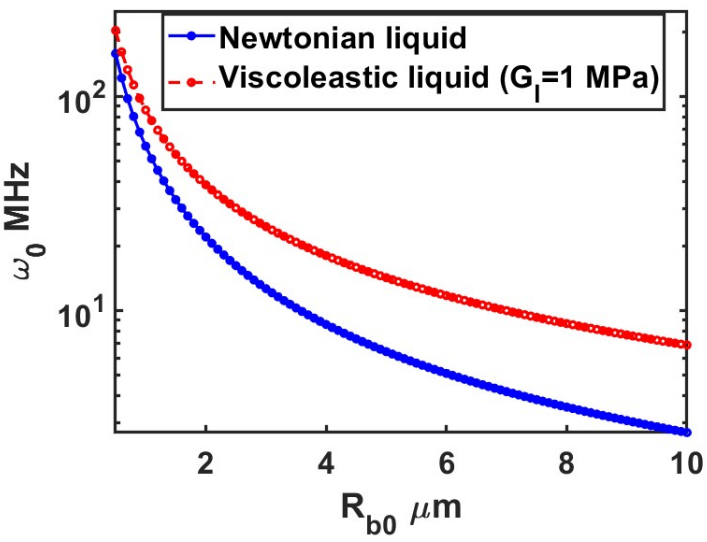

Figure 4.37. Effect of initial bubble radius, R_{b0} on the natural frequency, ω_0 for viscoelastic and Newtonian liquid.

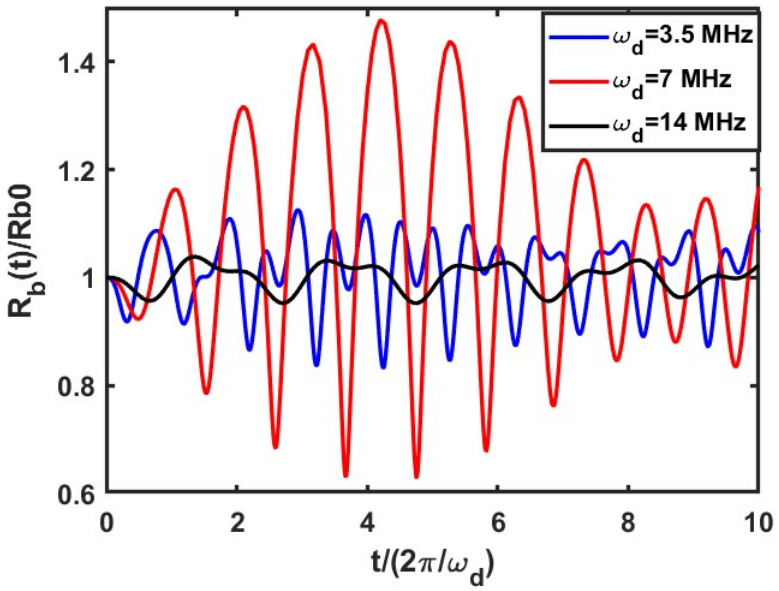

Figure 4.38. Effect of acoustic field driven frequency, ω_d, on $R_b(t)/R_{b0}$ versus $\dfrac{t}{2\pi\omega_d}$.

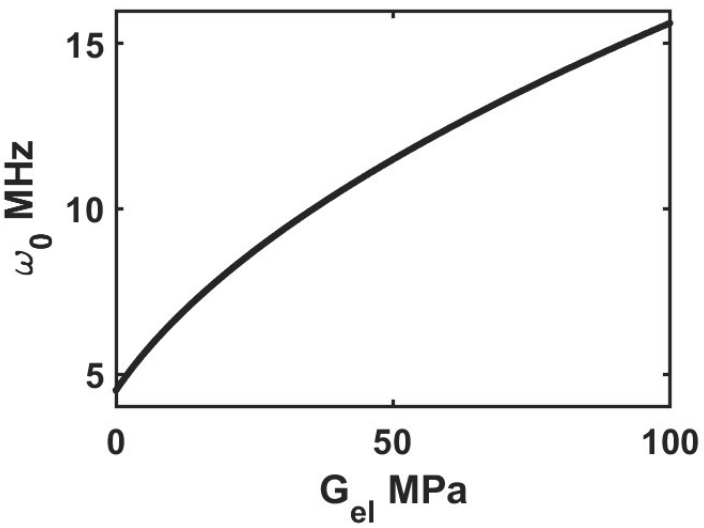

Figure 4.39. Effects of cavity modulus, G_{el}, on natural frequency, ω_0.

4.4.3.2. Effect of Liquid Constitutive Model. Here, the effect of the liquid constitutive model is investigated. The liquid is assumed to obey the power-law or viscoelastic model.

In Figure 4.41, it is assumed that the surrounding liquid follows a constitutive power law equation (Section 3.1.3.3). The apparent viscosity of the liquid, m, is 0.001 Pa·s^k. Figures 4.41(a) and (b) illustrate the effect of the power law index, k, for different driving fre-

quencies of the acoustic field: in Figure 4.41 (a), $\omega_d = 7$ MHz (the natural frequency), and in Figure 4.41(b), $\omega_d = 5$ MHz. At natural frequency, radial resonance is observed, leading to an increase in the bubble wall velocity and the liquid strain rate, which, in turn, increases the viscosity of the power-law liquid. Consequently, the effect of the power-law index k is more pronounced in Figure 4.41(a) than in Figure 4.41(b).

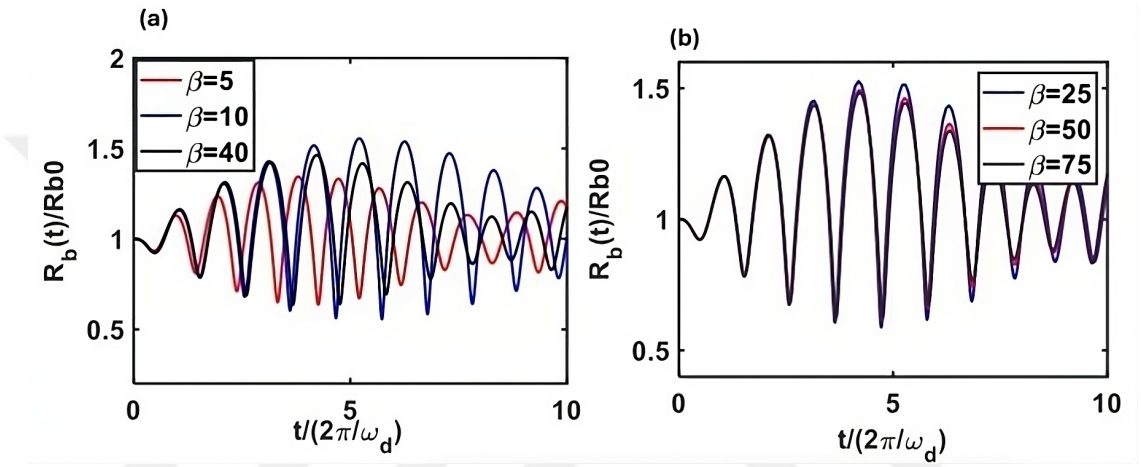

Figure 4.40. Effect of $\beta = R_{l0}/R_{b0}$ on $R_b(t)/R_{b0}$ versus $t/(2\pi/\omega_d)$ for (a) small β and (b) large β.

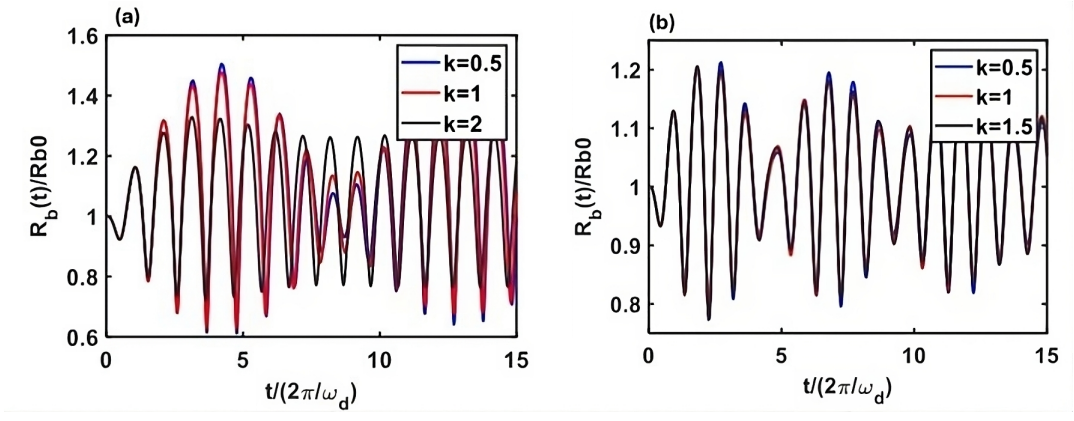

Figure 4.41. Effect of power-law index, k on $R_b(t)/R_{b0}$ versus $t/(2\pi/\omega_d)$ for (a) $\omega_d = 7$ MHz and (b) ω_d=5 MHz.

Finally, in Figure 4.42, the surrounding liquid is modeled as viscoelastic. A linear viscoelastic model is employed for the liquid, as detailed by Church [16]. The figure examines

the effect of the initial bubble radius, R_{b0}, on the natural frequency, ω_0, for both viscoelastic and Newtonian liquids. The expression for the natural frequency, ω_0, is provided in Equation 3.155. Compared to the Newtonian liquid case (Equation 3.154), the viscoelastic model introduces an additional term, $4G_{liq}$, which arises from the elasticity of liquid. This additional term not only modifies the natural frequency but also influences the equilibrium bubble radius which causes an increase in the natural frequency for viscoelastic liquids. Specifically, the elasticity enhances the stiffness of the system which increase the natural frequency. This effect becomes more pronounced as the initial bubble radius decreases and shows the interplay between bubble size and the viscoelastic properties of the surrounding medium. The increased natural frequency in viscoelastic liquids can lead to different resonance conditions than Newtonian liquids which affects processes such as ultrasound imaging, drug delivery and cavitation.

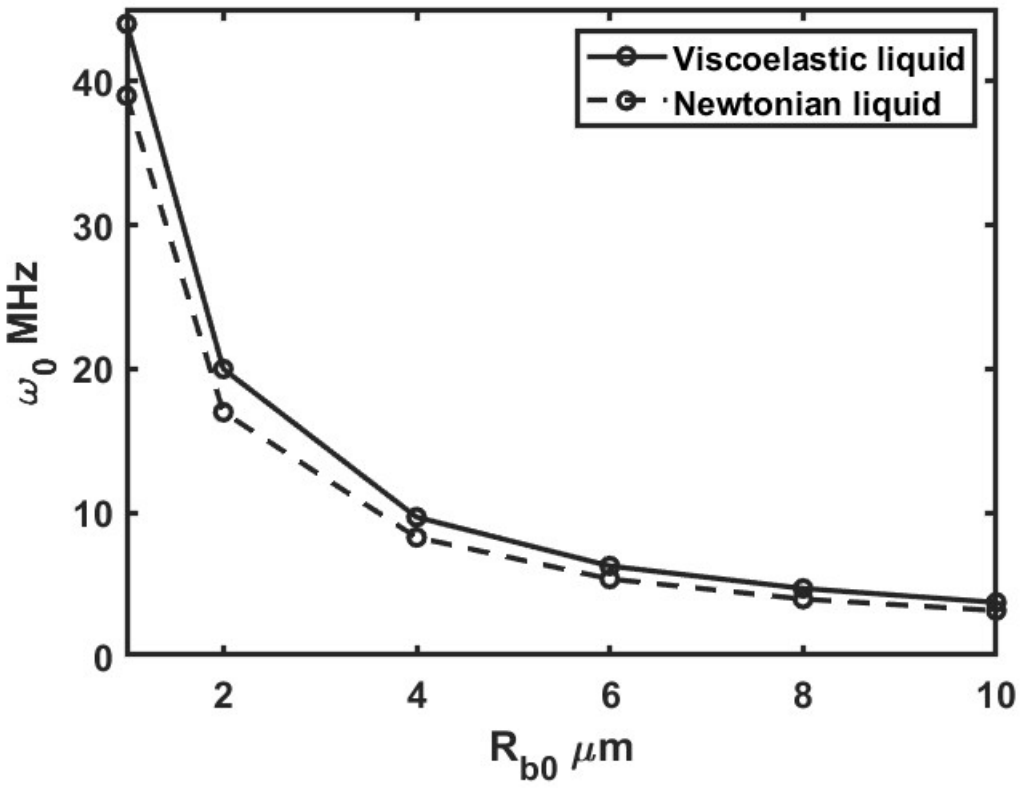

Figure 4.42. Effect of initial bubble radius, R_{b0} on natural frequency, ω_0 for viscoleastic ($G_{liq} = 10^5$ Pa) and Newtonian liquid.

4.4.4. Results for Encapsulated Bubble in a Liquid Cavity

In this section, the spherical oscillations of an encapsulated bubble in a liquid cavity are examined. First, liquid is assumed to be Newtonian and then, the effect of non-Newtonian liquid is investigated. The physical system for this section is shown in Figure 3.132, and the physical properties of the liquid and shell are provided in Table 4.1 and 4.2. An external acoustic field, $p_\infty = p_0 + p_a \sin(\omega_d t)$ is applied with the amplitude, $p_a = 0.25$ atm. The shear and bulk modulus of the solid are given as $G_{el} = 10$ MPa and K_{el}=10 MPa. The liquid pressure at the cavity surface, p_l is found from the stress balance at the cavity surface (Equation 3.102). The physical properties are given in Table 4.3.

The natural frequency of a bubble within a Newtonian liquid cavity is defined by Equation 3.151. As shown in Figure 4.43, when the driving frequency of the acoustic field is adjusted to match the system's natural frequency, $\omega_d = 8$MHz, radial resonance occurs, resulting in an amplification of the oscillations.

Table 4.3. Physical parameters employed in the present study.

Parameter	Value	Parameter	Value
Shell thickness, δ	15 nm	Viscosity at zero shear rate, μ_0	0.001 kg/(ms)
Shell viscosity, μ_s	0.05 kg/(ms)	Viscosity at infinite shear rate, μ_∞	0.0001 kg/(ms)
Shell modulus, G_s	15 MPa	Characteristic time, λ	1 s
Shell density, ρ_s	1100 kg/m^3	Liquid density, ρ_l	1000 kg/m^3
Initial radius ratio, $\beta = R_{l0}/R_{b0}$	100	Initial bubble radius, R_{b0}	5 μm
Cavity modulus, G_{el}	10 MPa	Vapor pressure, p_v	2300 Pa
Interfacial tension (bubble/shell), σ_b	0.05 N/m	Cavity bulk modulus, K_{el}	10 MPa
Interfacial tension (shell/liquid), σ_s	0.004 N/m	Polytropic index, κ	1.4
Acoustic field pressure amplitude, p_a	0.25-3 atm	Acoustic field frequency, ω_d	2-16 MHz

4.4.4.1. Effect of Shell and Liquid Physical Properties. Here, the effect of liquid and shell properties, specifically density, viscosity and surface tension on bubble dynamics is investigated.

In Figure 4.44, the impact of the liquid density, ρ_l, and the shell density, ρ_s, on the dynamic oscillations of a bubble encapsulated within a cavity is analyzed. Figure 4.44 is divided into two parts. Figure 4.44(a) examines the influence of the ρ_l and Figure 4.44(b) focuses on tρ_s. An increase in ρ_l leads to a damping effect on the radial oscillations of a bubble as depicted in Figure 4.44(a). The density of the liquid directly influences the inertia of the system. Higher densities increase the mass that must be displaced during oscillation. This increased inertia reduces the amplitude of the oscillations as more energy is required to sustain the motion. The bubble oscillations are particularly sensitive to changes in ρ_l. Even slight variations in ρ_l can significantly change the amplitude and stability of the oscillations. This sensitivity emphasizes the importance of accurately accounting for liquid density in applications where precise modulation of bubble dynamics is crucial such as in acoustic imaging or drug delivery systems. Figure 4.44(b) illustrates the effect of ρ_s on bubble oscillations. An increase in ρ_s also dampens the oscillations similar to the liquid density. The shell adds layer of mass around the bubble, which increases the system's overall inertia. As a result, the energy required to maintain oscillations increases which causes a reduction in oscillatory amplitude.

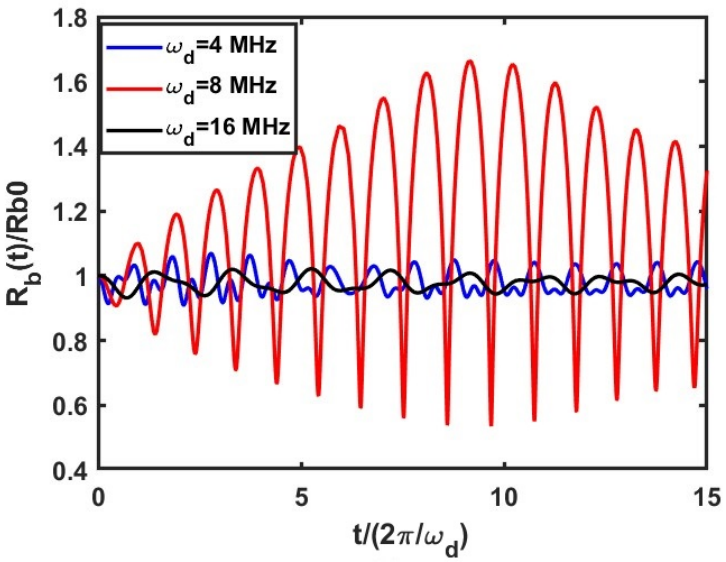

Figure 4.43. Effect of acoustic field driven frequency, ω_d, on $R_b(t)/R_{b0}$ versus $\dfrac{t}{2\pi\omega_d}$.

Although both ρ_l and ρ_s contribute to the damping of oscillations, the effect of ρ_l is more pronounced. This is because the surrounding liquid plays a more dominant role in governing bubble oscillations dynamics than the shell. The density of the liquid directly influences the resistance of a bubble during expansion and contraction which makes it a more critical factor in determining the overall oscillatory behavior.

In Figure 4.45, the effects of (a) liquid density, ρ_l, and (b) shell density, ρ_s, on the natural frequency, ω_0, are investigated. liquid density (ρ_l) has a more pronounced effect on the natural frequency compared to the shell density (ρ_s) as observed from the results. The surrounding liquid contributes more substantially to the system's overall inertia with its larger volume and mass. An increase in ρ_l leads to a decrease in ω_0 since natural frequency is inversely related to the square root of the system's inertia. For both ρ_l and ρ_s, the natural frequency ω_0 decreases as density increases. This inverse relationship is a fundamental characteristic of oscillatory systems, where increased mass or inertia leads to slower oscillations. However, the magnitude of this effect differs between the liquid and the shell. The liquid density playing a more dominant role.

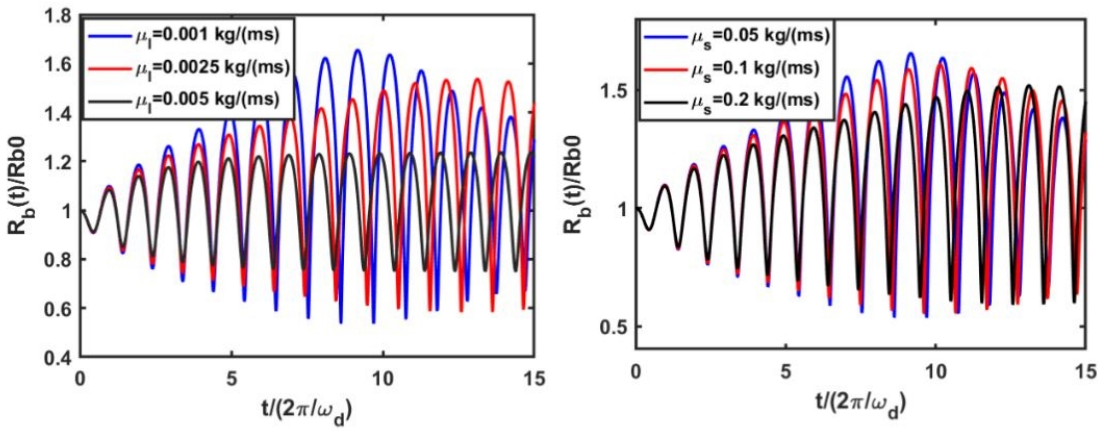

Figure 4.44. Effect of (a) liquid density, ρ_l and (b) shell density, ρ_s on $R_b(t)/R_{b0}$ versus $t/(2\pi/\omega_d)$.

The impact of both liquid viscosity, μ_l and shell viscosity, μ_s, on the dynamic behavior of an encapsulated bubble is analyzed in Figure 4.47, Figure 4.47(a) shows that as the liquid viscosity, μ_l, increases, the amplitude of the bubble's oscillations decreases significantly.

This effect is an indication of enhanced energy dissipation within the surrounding liquid. The stronger the viscosity of the liquid, the more pronounced this damping effect becomes. The shell viscosity, μ_s, also contributes to the damping of bubble oscillations, as shown in Figure 4.47(b). The viscosity of shell influences the interaction between the bubble and its encapsulating shell which adds another layer of energy dissipation. As μ_s increases, the internal friction within the shell material causes additional resistance to the expansion and contraction of a bubble, further reducing the oscillation amplitude. The results demonstrate that the damping effect due to liquid viscosity is more substantial than that of shell viscosity, μ_s. This dominance is likely due to the larger volume of the liquid surrounding the bubble which provides a more significant medium for energy dissipation. The viscosity of liquid impacts not only the surface interactions but also the fluid bulk motion which makes it a critical factor in determining the overall oscillatory behavior of the bubble.

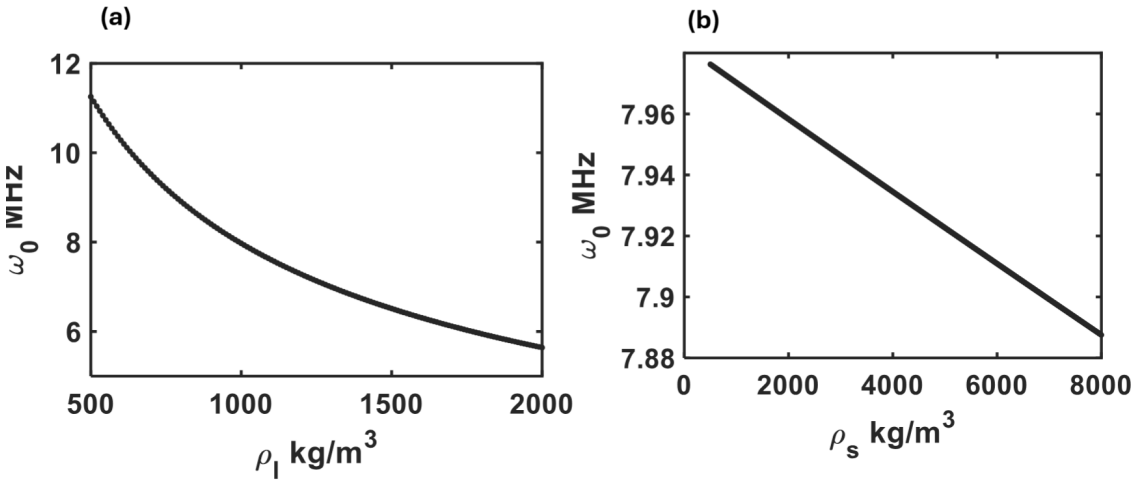

Figure 4.45. Effect of (a) liquid density ρ_l and (b) shell density, ρ_s on the natural frequency, ω_0.

In Figure 4.46, the influence of interfacial tension on the dynamics of an encapsulated bubble is analyzed which focuses on two interfaces: (a) the bubble/shell surface (σ_b) and (b) the shell/liquid surface (σ_s). As depicted in Figure 4.46f(a), despite the increase in amplitude, the bubble/shell interfacial tension does not significantly alter the stability of the oscillations. Greater interfacial tension enhances the restoring force at the bubble/shell interface which causes the bubble to oscillate more vigorously. Figure 4.46(b) illustrates the effect

of shell/liquid interfacial tension on bubble dynamics. Similar to the bubble/shell interface, The effect of shell/liquid surface tension on oscillation amplitude is comparable to that of the bubble/shell surface tension, but the impact is slightly less pronounced. The shell/liquid interfacial tension contributes to the overall energy balance of the system with higher tension providing a more vital restoring force as the bubble expands and contracts within the shell. This results in more pronounced oscillatory behavior. The bubble/shell interface is slightly more influential in determining the oscillation amplitude while both interfaces contribute to the overall dynamics. This difference could be attributed to the fact that the bubble/shell interface is closer to the core of the oscillatory motion, where the effects of interfacial forces are more directly felt.

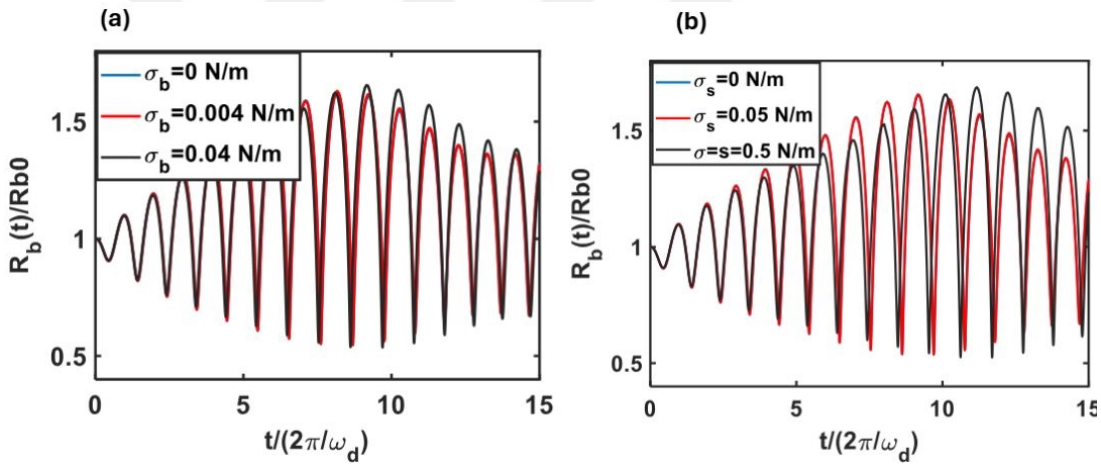

Figure 4.46. Effect of (a) bubble/shell interfacial tension σ_b and (b) interfacial tension σ_s on $R_b(t)/R_{b0}$ versus $t/(2\pi/\omega_d)$.

In Figure 4.48, the impact of interfacial tensions on the natural frequency, ω_0, of an encapsulated bubble in a liquid cavity is explored. The analysis distinguishes between the effects of shell/liquid interfacial tension (σ_s) and bubble/shell interfacial tension (σ_b), which are represented by dashed and solid lines, respectively. As shown by the dashed lines in Figure 4.48, an increase in shell/liquid interfacial tension, σ_s, results in a corresponding rise in ω_0. This behavior can be attributed to the additional restoring force provided by the higher interfacial tension at the shell/liquid boundary. Contrary to the effect of σ_s, an increase in bubble/shell interfacial tension, σ_b, leads to a decrease in the natural frequency, as depicted

by the solid lines in Figure 4.48.

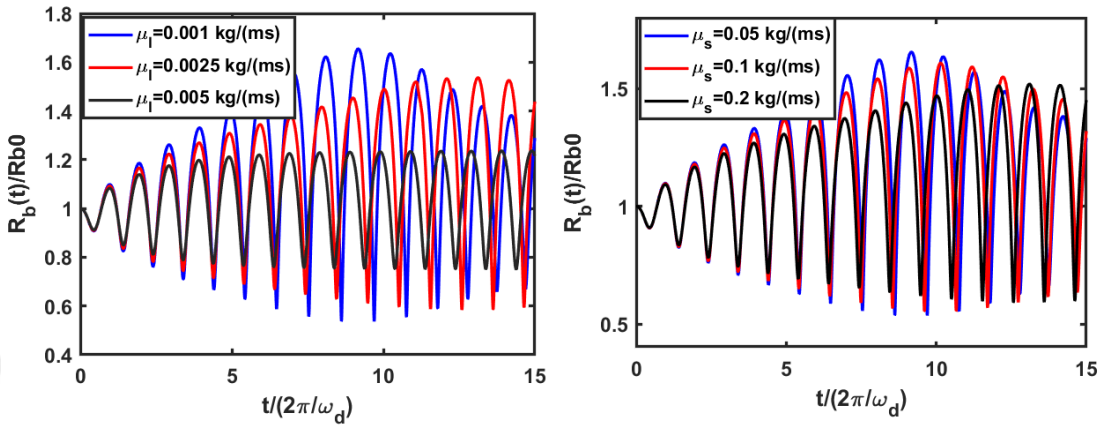

Figure 4.47. Effect of (a) liquid viscosity, μ_l and (b) shell viscosity, μ_s on $R_b(t)/R_{b0}$ versus $t/(2\pi/\omega_d)$.

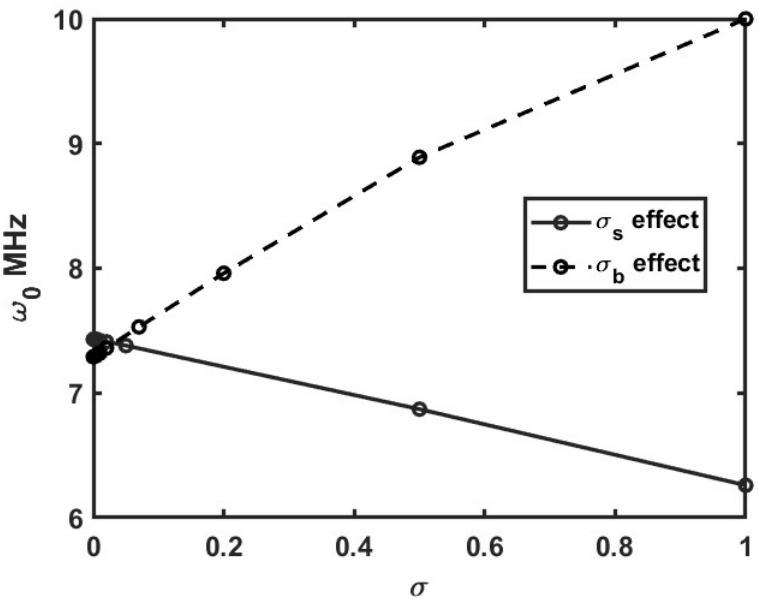

Figure 4.48. Effect of surface tensions on the natural frequency, ω_0. The dashed and solid lines show the effects of shell/liquid (σ_s) and bubble/shell (σ_b) interfacial tensions.

4.4.4.2. Effect of Cavity Properties on Spherical Oscillations. Here, effect of cavity properties, K_{el} and G_{el} on the dynamic bubble oscillation and the natural frequency, ω_0 is investigated. Figure 4.49 examines the influence of the cavity modulus, G_{el}, on the radial

oscillations of the bubble. As depicted in Figure 4.49(a), at low G_{el} values, the amplitude of the bubble's radial oscillations is not affected by G_{el}. However, for moderate G_{el} values, the amplitude of oscillations increases with G_{el} (Figure 4.49(b)). For high G_{el} values, the oscillations are dampened with G_{el} (Figure 4.49(c)).

Figure 4.50 analyzes the impact of the cavity's bulk modulus, K_{el}, on the radial oscillations of the bubble. As illustrated in Figure 4.50(a), at lower values of K_{el}, the amplitude of the bubble's radial oscillations increases. For moderate values, K_{el} dampens the oscillations (Figure 4.50(b)). At higher K_{el} values, there is a slight increase in the oscillations (Figure 4.50(c) $G_{el} = 40$ and 50 MPa).

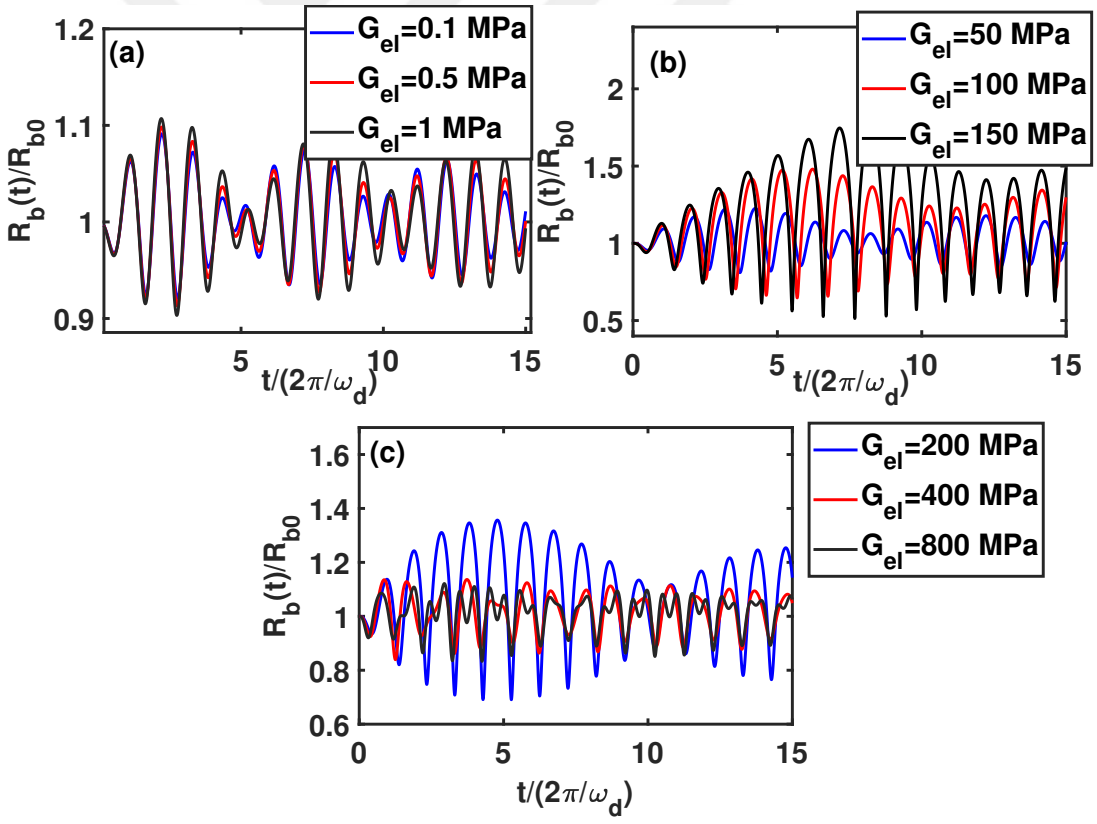

Figure 4.49. Effect of cavity modulus, G_{el}, on $R_b(t)/R_{b0}$ versus $t/(2\pi/\omega_d)$ for (a) small, (b) moderate, and (c) large G_{el} values.

Figure 4.51 presents the influence of the ratio of the initial cavity radius to the bubble radius, denoted as $\beta = R_{l0}/R_{b0}$. In Figure 4.51(a)), when β is small, meaning the cavity radius is close to the bubble radius, the oscillations are significantly damped. This suggests that in smaller cavities, the surrounding liquid has a less capacity to absorb and dissipate the energy, leading to damped amplitudes of oscillations. When β is large (Figure 4.51(b)), where the cavity radius is large compared to the bubble radius, the damping effect of β is minimal, and the oscillations remain relatively unaffected.

Figure 4.52 investigates the effects of cavity modulus, G_{el} (Figure 4.52(a)), cavity bulk modulus, K_{el} (Figure4.52(b)), and $\beta = R_{l0}/R_{b0}$ (Figure4.52(c)) on the maximum bubble surface area. Similar to what was observed in Figure 4.56, three distinct effects are noted. The maximum bubble surface area increases for small values of the parameters ($G_{el} < 22$ MPa, $K_{el} < 4$ MPa, $\beta < 15$) in Region 1; it decreases in Region 2, and remains unaffected in Region 3. However, the surface area stabilizes at a higher value than Figures 4.52(a) and 4.52(b) when β no longer significantly affects the maximum surface area in Region 3.

In conclusion, when G_{el} reaches higher values (Figure 4.52(a)), the amplitude of the oscillations becomes less sensitive to changes in G_{el}. As K_{el} continues to increase, the amplitude of the oscillations shows diminishing sensitivity to further changes in the bulk modulus, as highlighted in Figure 4.52(b). When the cavity becomes less compressible (high K_{el}), the energy stored in the system increases which causes more damped oscillations. The compressibility of the cavity has reached a level where it exerts a limiting effect on further oscillatory growth (cavity becomes incompressible). In large cavities (large β) (Figure 4.52(c)), the system is more capable of dissipating energy, leading to greater damping of oscillations. In contrast, in small cavities (small β), the confined space restricts energy dissipation, resulting in more sustained oscillations.

Figure 4.53 analyzes the effects of the cavity modulus G_{el} and the bulk modulus K_{el} on the natural frequency ω_0 of the system (Equation 3.158). The figure indicates that increased G_{el} and K_{el} make the cavity more resistant to deformation, resulting in a higher ω_0. This explanation is valid until K_{el} reaches a critical point at $K_{el} \approx 20$ MPa. Beyond this point,

the cavity behaves like an incompressible medium, limiting further increase in the natural frequency and the natural frequency of the system becomes < 10 MHz, which is close to ω_∞, the natural frequency of a bubble in an unbounded liquid.

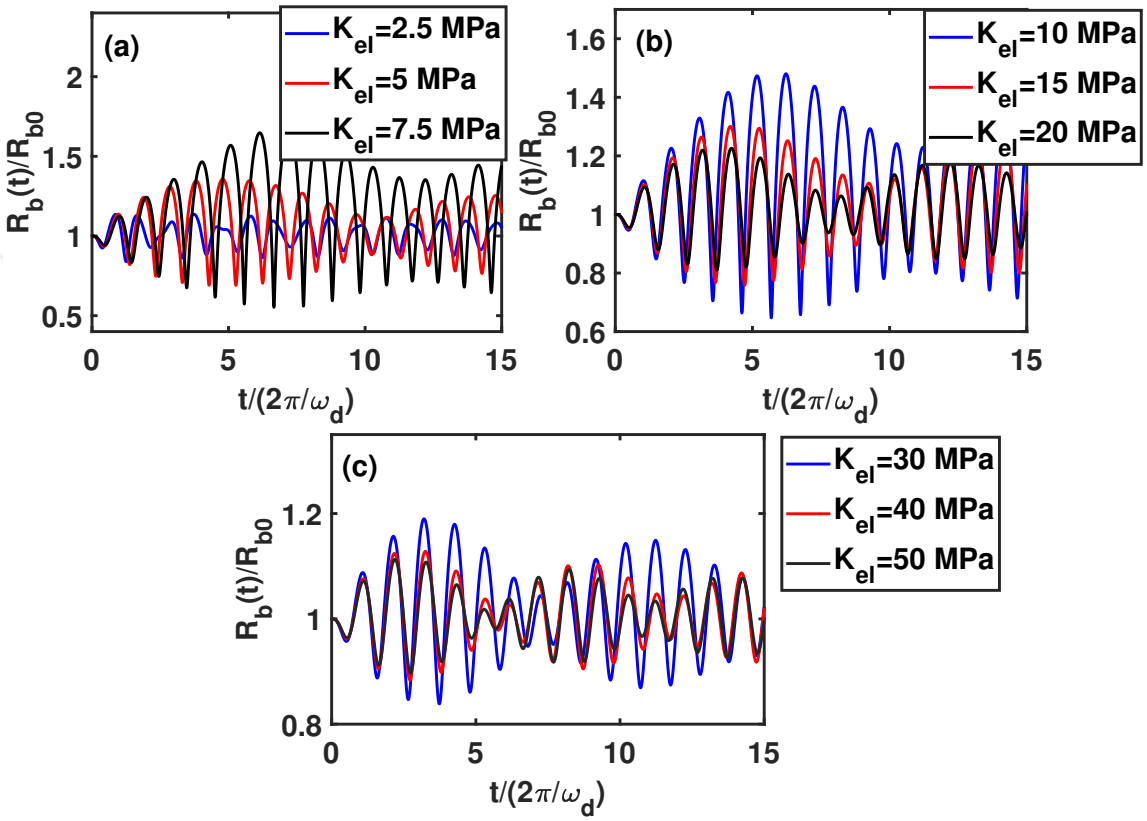

Figure 4.50. Effect of bulk modulus, K_{el}, on $R_b(t)/R_{b0}$ versus $t/(2\pi/\omega_d)$ for (a) small, (b) moderate, and (c) large K_{el} values.

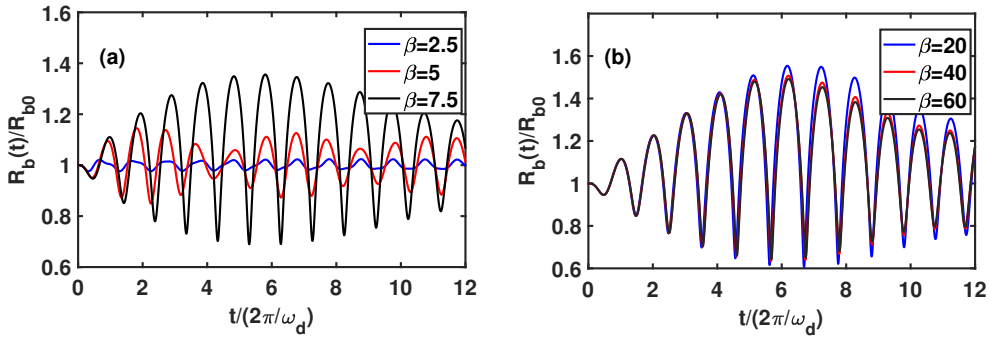

Figure 4.51. Effect of radius ratio, $\beta = R_{l0}/R_{b0}$ on $R_b(t)/R_{b0}$ versus $t/(2\pi/\omega_d)$ for (a) small and (b) large β values.

4.4.4.3. Effect of Shell Properties. In this section the effects of shell properties, shell thickness and shell modulus on the natural frequency and the dynamic bubble oscillation are investigated.

The effect of the shell modulus, G_s, on the dynamic oscillations of a bubble is explored across three different ranges of G_s in Figure 4.54. At low values of G_s (Figure 4.54(a)), the shell's influence on the bubble's oscillations is negligible. The bubble behaves similarly to one without an encapsulating shell, with the oscillations primarily governed by the surrounding liquid and cavity characteristics. which indicates that the shell is too soft to significantly alter the system's dynamics, which allows the bubble to oscillate freely. The effect of G_s on the bubble dynamics becomes evident As the shell modulus increases (Figure 4.54(b)). The shell increases the amplitude of the oscillations. The shell begins to dampen the oscillations For higher values of G_s (Figure 4.54(c)). This damping effect is beneficial in specific applications, as it helps control the amplitude of the oscillations. When G_s reaches very high values (Figure 4.54(c) $G_s = 40$ and 50 MPa), the shell becomes very stiff which significantly damps the bubble's oscillations.

Figure 4.55 shows the impact of the shell thickness, δ, on the oscillations of an encapsulated bubble. The effect of shell thickness is negligible For small δ values (Figure 4.55(a)), as similarly observed for the effect of G_s. In this region, the shell is too thin to significantly alter the bubble's dynamics, which allows the bubble to oscillate freely with little resistance. The influence of δ becomes more pronounced and increases the amplitude of oscillations when the shell thickness increases (Figure 4.55(b)). The shell stiffness is enhanced for larger δ values (Figure 4.55(c)) and the bubble's oscillations are dampened.

Figures 4.56(a) and 4.56(b) illustrate the effects of shell modulus, G_s, and shell thickness, δ, on the maximum bubble surface area, respectively. The maximum bubble surface area, $4\pi max(R_b)^2$, is determined based on the maximum bubble radius obtained after 25 cycles. Three distinct regions of G_s and δ are observed from Figures 4.56(a) and 4.56(b). In Region 1 ($1 < G_s < 27$ MPa and $0.1 < \delta < 27$ nm), the maximum surface area of the bubble increases with G_s and δ. When $G_s \approx 15$ MPa and $\delta \approx 15$ nm, the system's natural

frequency matches the driven frequency, $\omega_0 = 8$ MHz. In Region 2, G_s and δ dampen the oscillations, and finally, in Region 3, for very high G_s and δ, the shell becomes excessively stiff, and the oscillations are almost entirely suppressed. This can be undesirable, especially in biomedical applications where bubble oscillations are often used for therapeutic effects, such as in targeted drug delivery or ultrasound imaging.

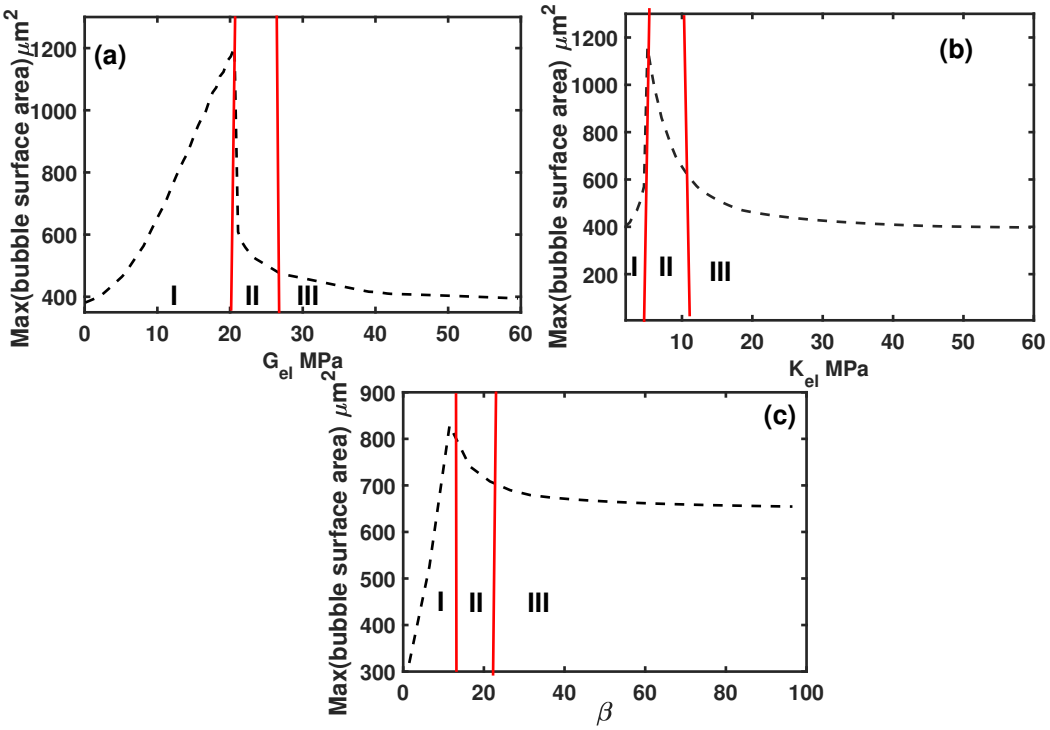

Figure 4.52. Effect of (a) cavity modulus, G_{el} and (b) cavity bulk modulus, K_{el}, and (c) $\beta = R_{l0}/R_{b0}$ on the maximum bubble surface area.

Figure 4.57 presents a contour plot for driving frequencies, $\omega_d < \omega_0$. The three regions in Figures 4.56(a) and 4.56(b) are not observed anymore. When the driving frequency does not match the natural frequency, the maximum bubble surface area decreases with both G_s and δ. Near resonance, a higher G_s and δ enhance the oscillations due to efficient energy storage and release.

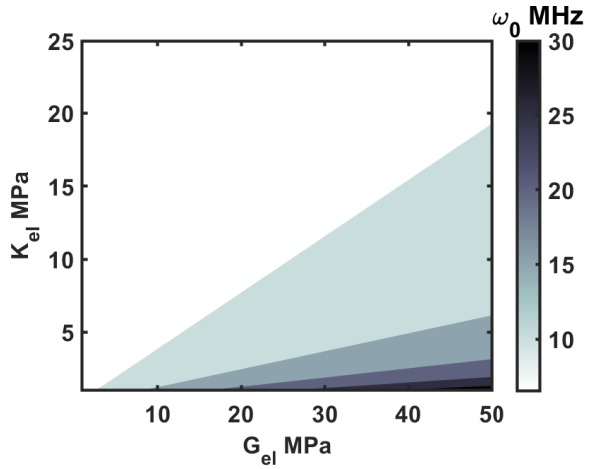

Figure 4.53. Contour plot (K_{el} versus G_{el}) for natural frequency, ω_0.

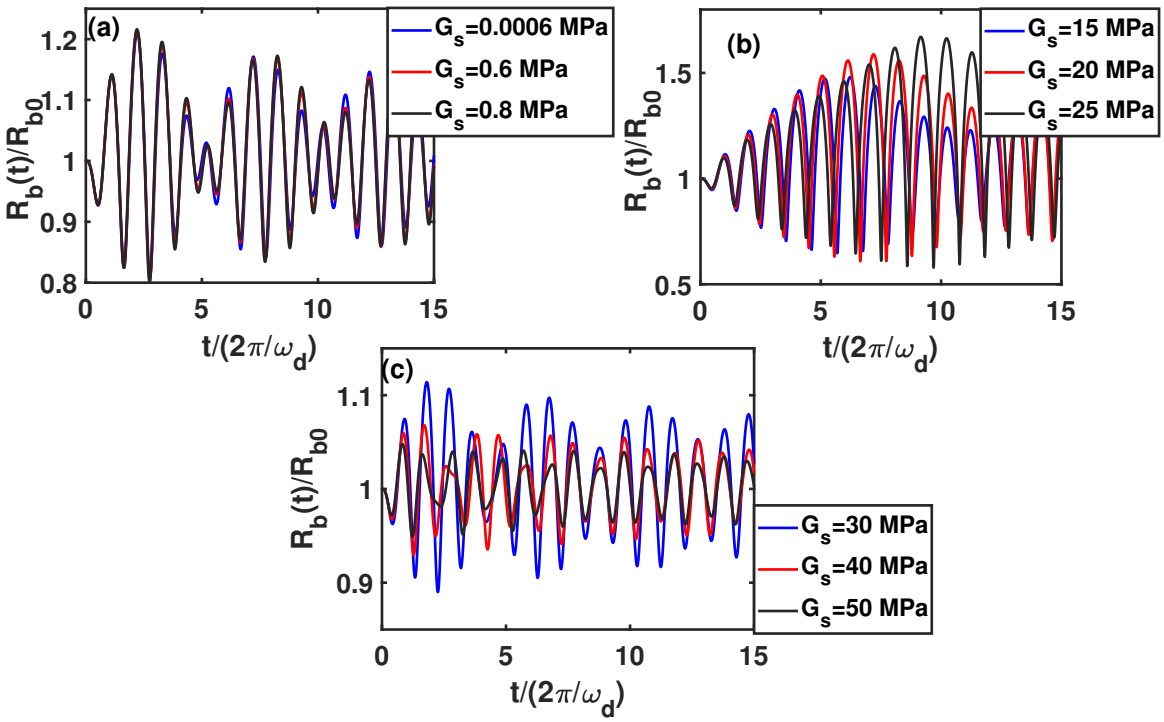

Figure 4.54. Effect of shell modulus, G_s on $R_b(t)/R_{b0}$ versus $t/(2\pi/\omega_d)$ for (a) small, (b) moderate, and (c) large G_s values.

Figure 4.58 examines the impacts of shell thickness, δ, and shell modulus, G_s, on the natural frequency, ω_0 (Equation 3.158). The natural frequency of the bubble increases with δ and G_s due to an increase in the overall stiffness of the system. The stiffer the shell, the higher the natural frequency, as the bubble becomes less able to deform and oscillate freely.

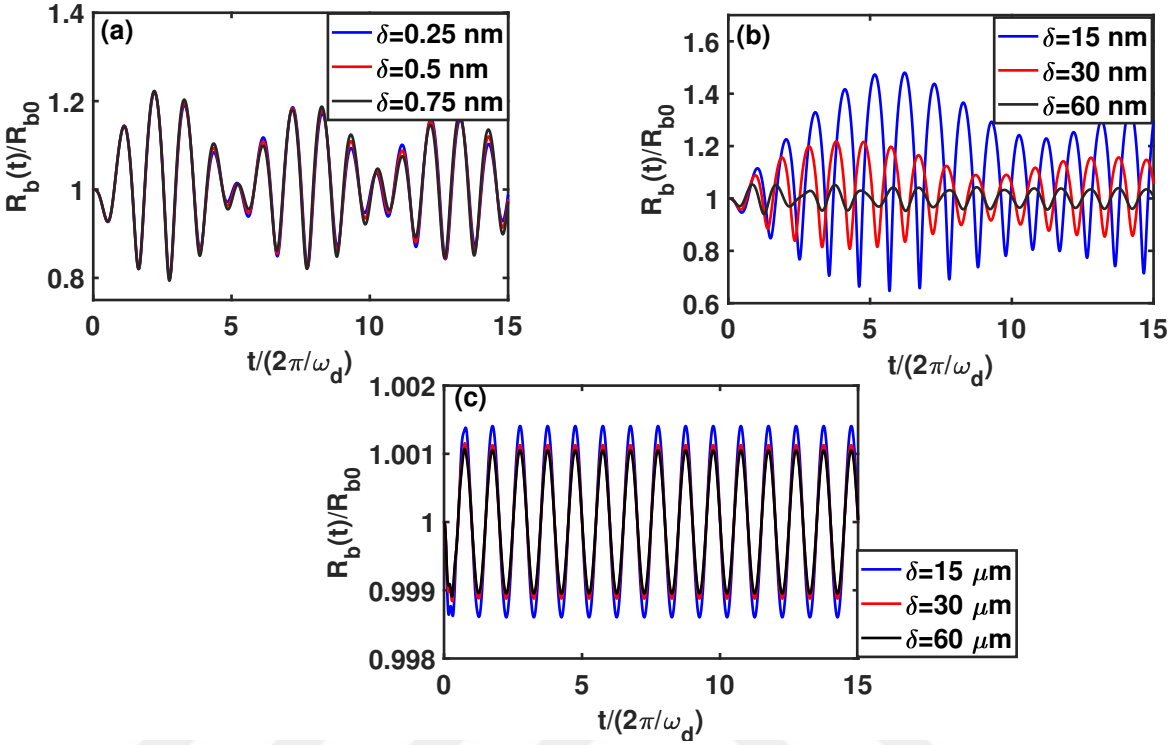

Figure 4.55. Effect of shell thickness, δ on $R_b(t)/R_{b0}$ versus $t/(2\pi/\omega_d)$ for (a) small, (b) moderate, and (c) large δ values.

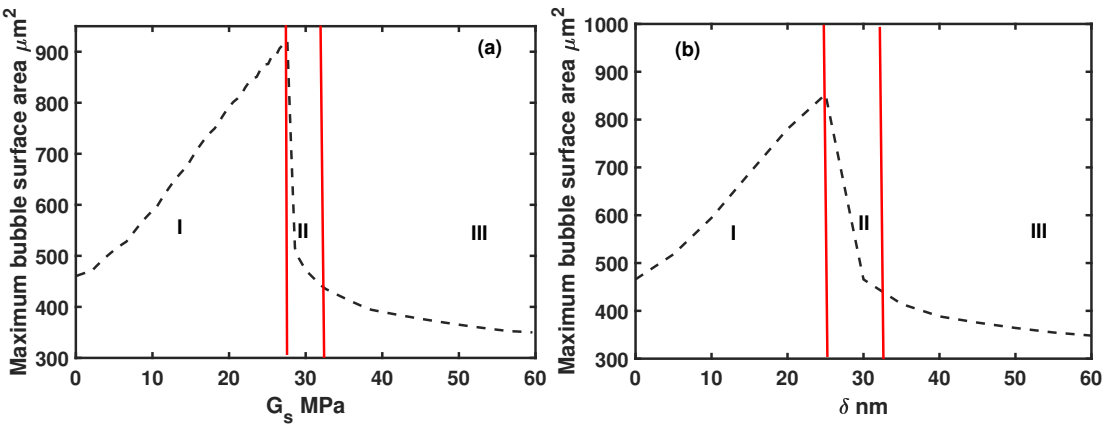

Figure 4.56. Effect of (a) shell modulus, G_s and (b) shell thickness, δ on the maximum bubble surface area.

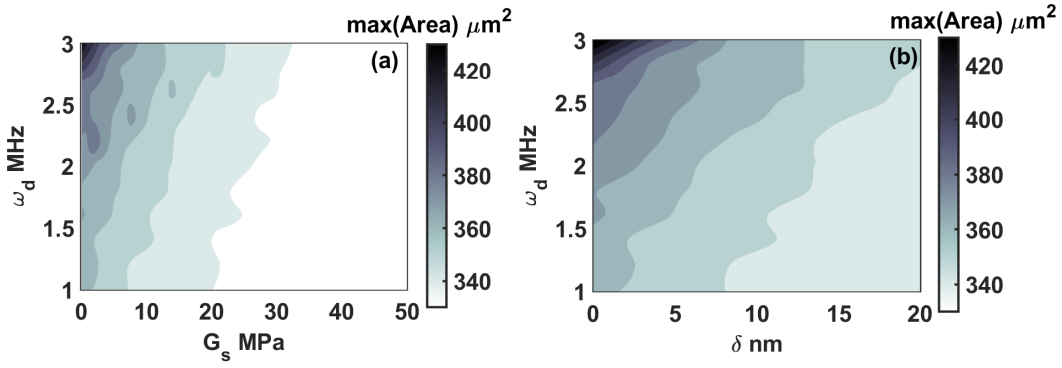

Figure 4.57. Contour plot (a) driving frequency, ω_d versus shell modulus, G_s and (b) driving frequency, ω_d versus shell thickness, δ for maximum bubble surface area.

As detailed in Section 3.1.2.2, the behavior of the shell can be described using either linear [16] or nonlinear viscoelastic models [335, 376]. Figure 4.59 illustrates the impact of the shell model on the system for different pressure amplitudes (Figure 4.59(a)) and driving frequencies (Figure 4.59(b)). Figure 4.59(a) shows that the effect of the shell model on the maximum area becomes evident for larger pressure amplitudes (p_a >1.5 atm), which also increases the nonlinear deformations. However, the driving frequency slightly affects the maximum area for different shell models.

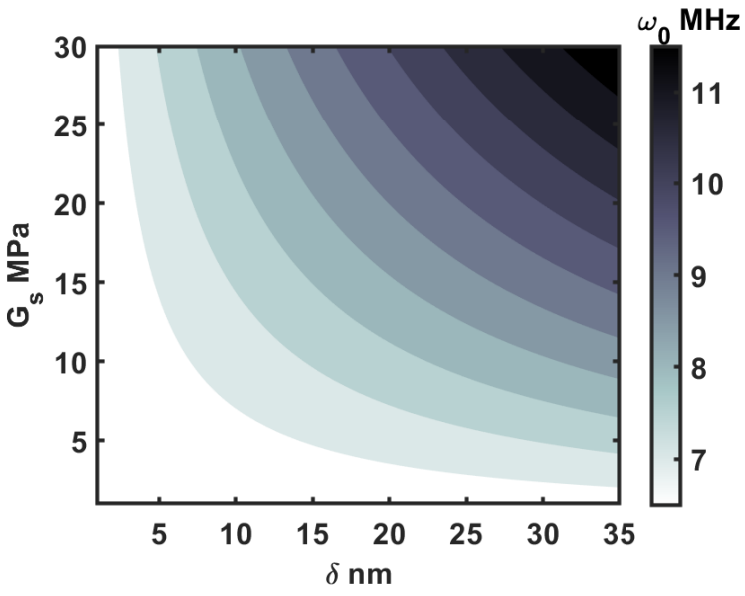

Figure 4.58. Contour plot (G_s versus δ) for natural frequency, ω_0.

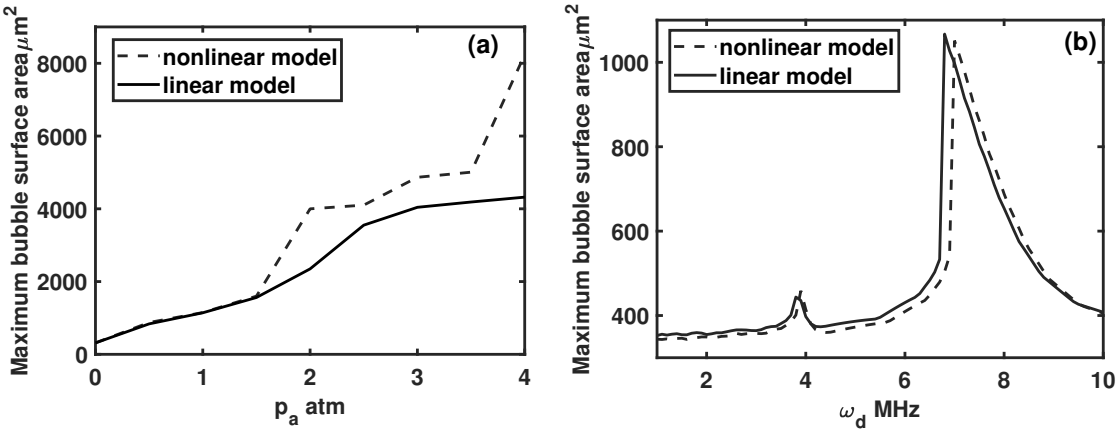

Figure 4.59. Effect of (a) acoustic field pressure amplitude, p_a and (b) driving frequency, ω_d.

A contour plot of δ vs. G_s is generated to examine their effects on t To highlight the effects of large and small δ and G_s on , $\chi = \left|\frac{\max(R_b)^2_{\text{nlin}} - \max(R_b)^2_{\text{lin}}}{\max(R_b)^2_{\text{nlin}}}\right|$, two inset figures with different color codes are provided for Figure 4.60. Here, χ is the deviation obtained from the maximum area difference between the linear and nonlinear shell models. The maximum bubble surface area is obtained after 25 cycles. It is observed from the figure that when G_s and δ are either small ($G_s < 15$ MPa and $\delta < 15$ nm, $\chi < 5$) or large ($G_s > 25$ MPa and $\delta > 25$ nm, $\chi < 2.5$), the deviation, χ is minimized. As shown in Figure 4.56(a) and (b), the maximum area peaks approximately when $G_s = 27$ MPa and $\delta = 25$ nm. In this region, the difference between the linear and nonlinear shell models increases due to the effect of resonance. Therefore, close to resonance, the selection of the appropriate shell model becomes important. At resonance, the effects of nonlinear deformations become significant, which the linear shell model cannot accurately capture.

The behavior observed with varying shell thickness, δ, closely mirrors that seen with changes in the shell modulus, G_s. Both parameters—δ and G_s—influence the bubble's oscillatory behavior by modifying the overall stiffness of the shell. When either G_s or δ is too small or too large, the bubble's oscillations are significantly damped, which decreases the bubble's surface area. This reduction in surface area is undesirable in biomedical applications, particularly in targeted drug delivery, where controlled and sustained bubble oscillations are crucial for enhancing drug uptake at the target site. Therefore, optimizing the shell

thickness and modulus is essential to balance control and responsiveness in bubble dynamics. Proper optimization ensures that the bubble maintains sufficient oscillatory amplitude to effectively interact with the surrounding medium, thereby maximizing the therapeutic efficacy of the encapsulated drug while avoiding excessive damping that could hinder the delivery process.

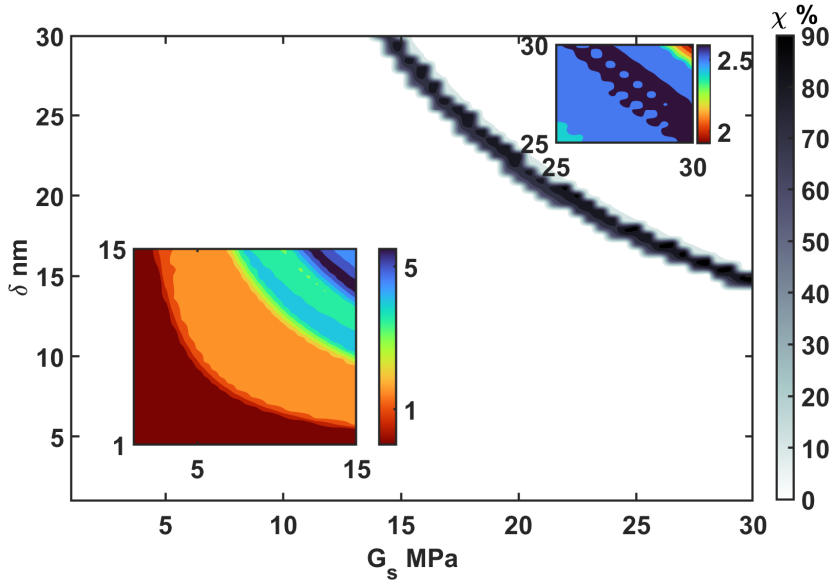

Figure 4.60. Contour plot (δ versus G_s) shows the difference between shell models.

4.4.4.4. Effect of Liquid Constitutive Model. In this section the effect of liquid model on the natural frequency and the dynamic bubble oscillations is investigated. The liquid model is assumed to be power-law, viscoelastic or Carreau-Yasuda (Sections 3.1.3.8 and 3.1.3.7).

In Figure 4.62, the surrounding liquid is modeled according to the power-law constitutive model, as described in Section 3.1.3.8. The apparent viscosity of the power-law liquid is set at 0.001 Pa $\cdot$ s$^{\mathrm{k}}$ which is denoted by m. For shear-thinning fluids (where $k < 1$), viscosity decreases with increasing shear rate, which can lead to more vigorous bubble oscillations. In contrast, viscosity increases with shear rate for shear-thickening fluids (where $k > 1$), potentially damping the oscillations more effectively. The presence of a shell further amplifies these effects (compared to Figure 4.41, as the rigidity of shell can either enhance or counteract the influence of the surrounding liquid's viscosity, depending on the value of

k.

Second, the surrounding liquid is assumed to be viscoelastic (Section 3.1.3.7)) As shown in Figure 4.63, the modulus of visoelastic liquid, G_{liq} dampens the dynamic oscillations of bubble.

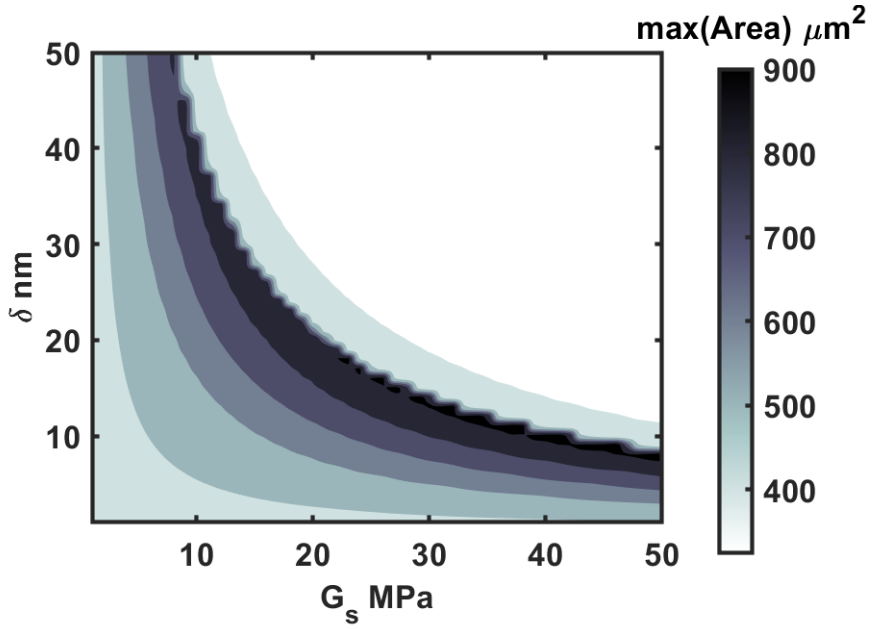

Figure 4.61. Contour plot (G_s versus δ) for the maximum bubble surface area.

Finally, the liquid is assumed to be Carreau-Yasuda. Figure 4.64 illustrates that a lower initial radius ratio, $\beta = R_{l0}/R_{b0}$ suppresses the influence of the power-law index, k on bubble oscillations. When β is small, the confinement imposed by the surrounding medium limits the bubble's ability to respond to variations in k, leading to reduced oscillations. For larger β values, the bubble is less restricted and the nonlinear effects of the power-law fluid become more significant which amplifies the oscillations. Furthermore, as observed from the figures, shear-thinning behavior amplifies the oscillations due to the reduced viscosity at higher shear rates. In contrast, shear-thickening behavior dampens the oscillations, as the increased viscosity at higher shear rates imposes greater resistance to bubble deformation.

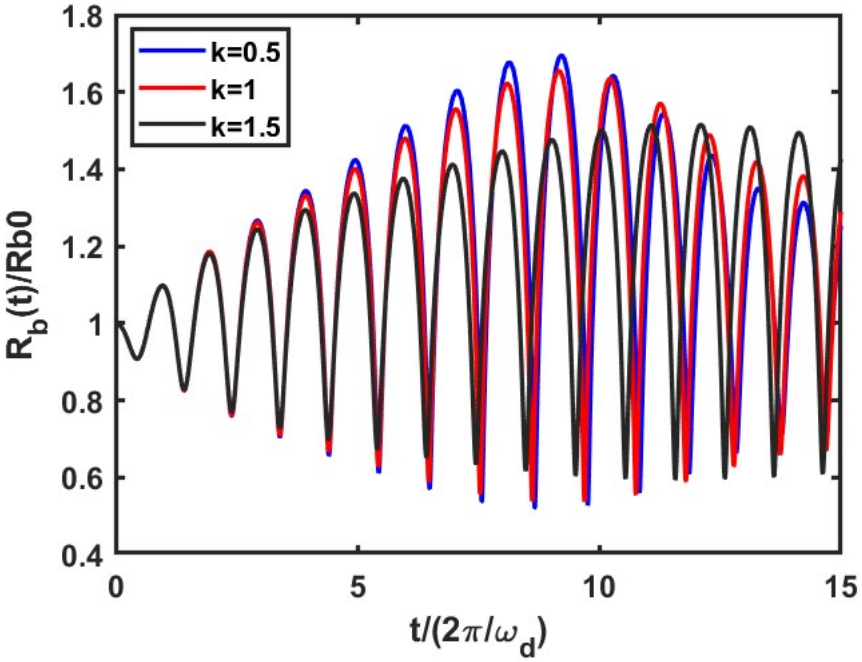

Figure 4.62. Effect of power-law index, k on $R_b(t)/R_{b0}$ versus $t/(2\pi/\omega_d)$.

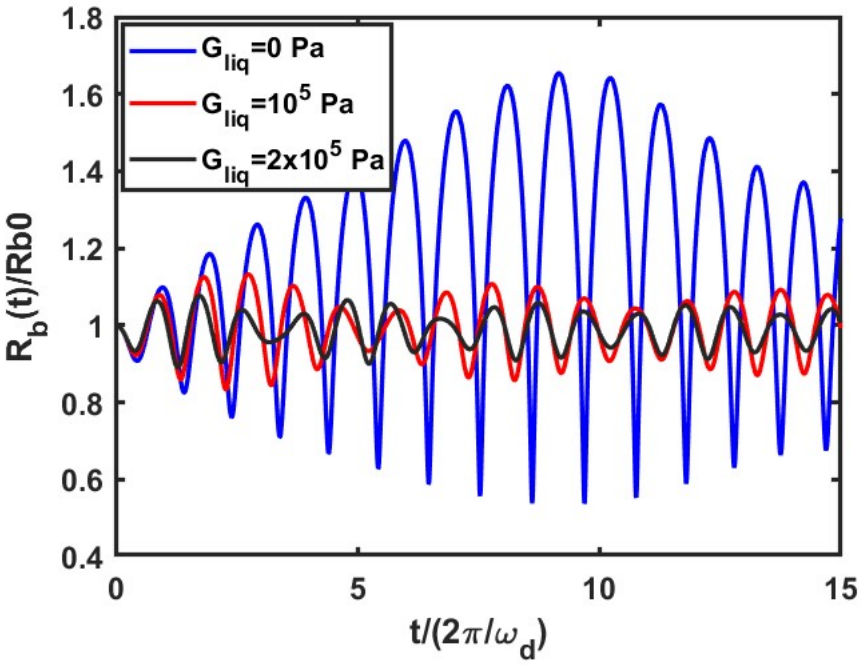

Figure 4.63. Effect of liquid modulus on $R_b(t)/R_{b0}$ versus $t/(2\pi/\omega_d)$.

Figure 4.65 illustrates the effect of the power-law index, k, for different acoustic field driving frequencies. At the natural frequency (Figure 4.64(a)), radial resonance is observed,

increasing both the bubble wall velocity and the liquid strain rate. This, in turn, raises the viscosity of the power-law fluid (Figure 4.64(a)). As a result, the impact of the power-law index, k, is more significant in Figure 4.64(a) than in Figure 4.65(a), where $\omega_d = 2$ MHz$<$ ω_0. Subharmonic oscillations (Figure 4.65(b)) at $\omega_d = 4$ MHz $=\omega_0/2$, and superharmonic oscillations (Figure 4.65(c)) at $\omega_d = 16$ MHz $= 2\omega_0$, arise due to nonlinear effects in bubble dynamics. In both cases, bubble oscillations are amplified because of the interaction between the subharmonic and superharmonic driving frequencies and the bubble's natural dynamics.

Figure4.66 shows the influence of the power-law index, k, on the dynamic oscillations of a bubble under the conditions of $p_a = 1$ atm and $\omega_d = 2$ MHz. The results show that, under these parameters, the variations in k affect the bubble's oscillatory behavior although $\omega_d = 2$ MHz as opposed to what was observed in Figure 4.65(a) as the driving pressure increases to $p_a = 1$ atm, the influence of the power-law index becomes pronounced. Higher acoustic pressures induce greater strain in the fluid, enhancing the effective viscosity.

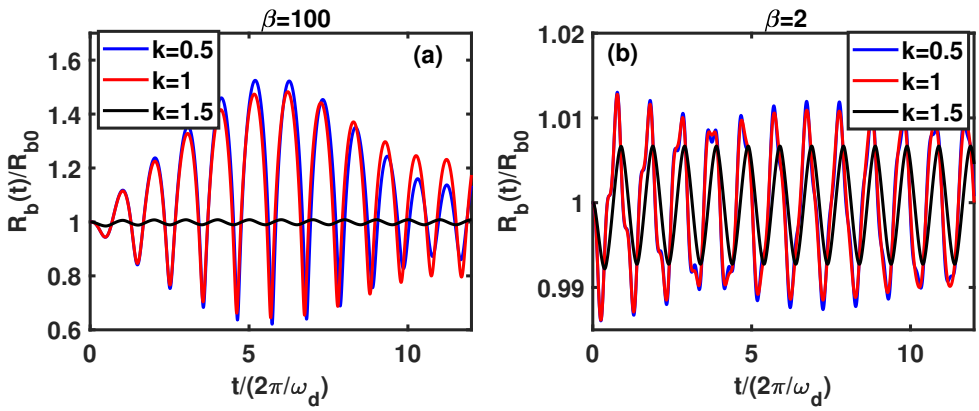

Figure 4.64. Effect of power-law index, k, on $R_b(t)/R_{b0}$ versus $t/(2\pi/\omega_d)$ for (a) $\beta = 100$ and (b) $\beta = 2$.

Two contour plots are generated to illustrate the maximum bubble surface area as a function of the power-law index, k, versus the initial radius ratio, $\beta = R_{l0}/R_{b0}$ (Figure 4.67(a)) and k versus the pressure amplitude, p_a (Figure 4.67(b)). For shear-thinning fluids ($k < 1$), higher p_a and lower β values significantly increase the maximum bubble surface area. This effect is due to the reduced viscosity in shear-thinning fluids at higher p_a and

lower β, which allows the bubble to expand more readily under the influence of the acoustic field, resulting in larger surface oscillations. In contrast, for shear-thickening fluids ($k > 1$), the effect of p_a and β on the maximum bubble surface area is less pronounced. The increased viscosity in shear-thickening fluids resists the deformation caused by the acoustic field and β, effectively dampening the bubble's expansion.

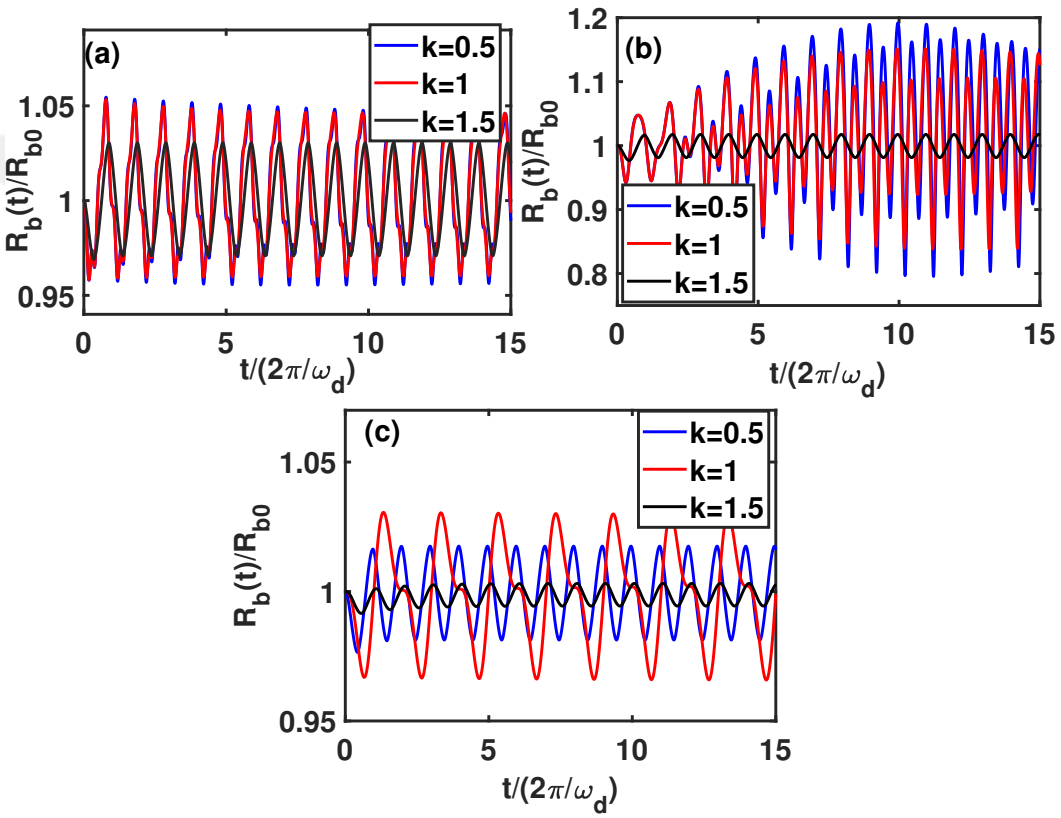

Figure 4.65. Effect of power-law index, k, on $R_b(t)/R_{b0}$ versus $t/(2\pi/\omega_d)$ for (a) $\omega_d = 2$ MHz, (b) for $\omega_d = 4$ MHz, and (c) $\omega_d = 16$ MHz.

Figure 4.69 illustrates the effect of the power-law index k and the initial radius ratio $\beta = R_{l0}/R_{b0}$ on the deviation of the bubble surface area, comparing the results of the linear shell model [16]) with the nonlinear model [335, 376]. In Figures 4.69(a) and (b), the acoustic pressure amplitudes, p_a, are 0.25 atm and 2.25 atm, respectively. In Figure 4.69(a), ε is large at lower β values. For higher β, the shear-thickening behavior of the liquid leads to an increase in ε. For high-pressure amplitudes (Figure 4.69(b)), the choice of shell model becomes critical when dealing with shear-thinning liquids, whereas for lower

pressure amplitudes (Figure 4.69(a)), the model's importance increases for smaller cavities and shear-thickening liquids.

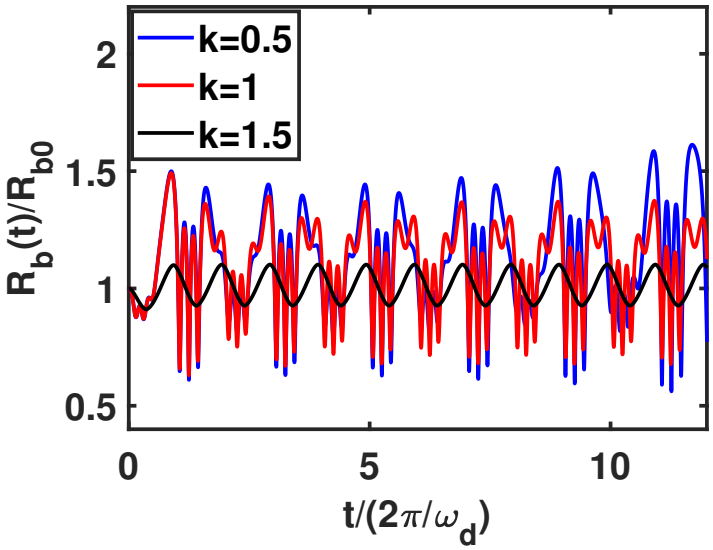

Figure 4.66. Effect of power-law index, k, on $R_b(t)/R_{b0}$ versus $t/(2\pi/\omega_d)$ for $\omega_d = 2$ MHz.

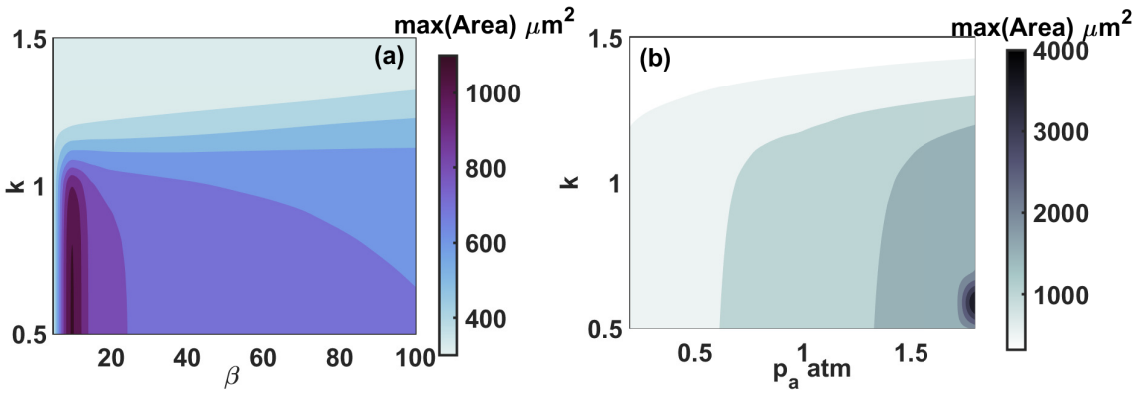

Figure 4.67. Contour plot (a) k versus β and (b) k versus p_a for maximum bubble surface area.

In the final case, the physical properties of real blood are used for the surrounding liquid. Specifically, $m = 0.64$, $\mu_0 = 0.056$ Pa.s, and $\mu_\infty = 0.0035$ Pa.s, based on values from the literature [388], to simulate non-Newtonian effects (Figures 4.70-4.71).

Figure 4.70 illustrates the effects of shear-thinning (Figure 4.70 (a)) and shear-thinning tendency (Figure 4.70 (b)) on bubble oscillations. The influence of the shear-thinning tendency (Figure 4.70(a)), and particularly shear-thickening tendency, becomes more pronounced compared to the previous case (Figure 4.64(a)) where the viscosities at zero and infinite shear rates are low ($\mu_0 = 0.001$ kg/(ms) and $\mu_\infty = 10^{-4}$ kg/(ms)). Figure 4.71 investigates the effect of the power-law index, k, for (a) $\beta = 2$ and (b) $\omega_d = 2$ MHz. In contrast to the behavior observed in Figures 4.64 and 4.41, the shear-thickening effect on bubble oscillations is evident here and where it dampens the oscillations.

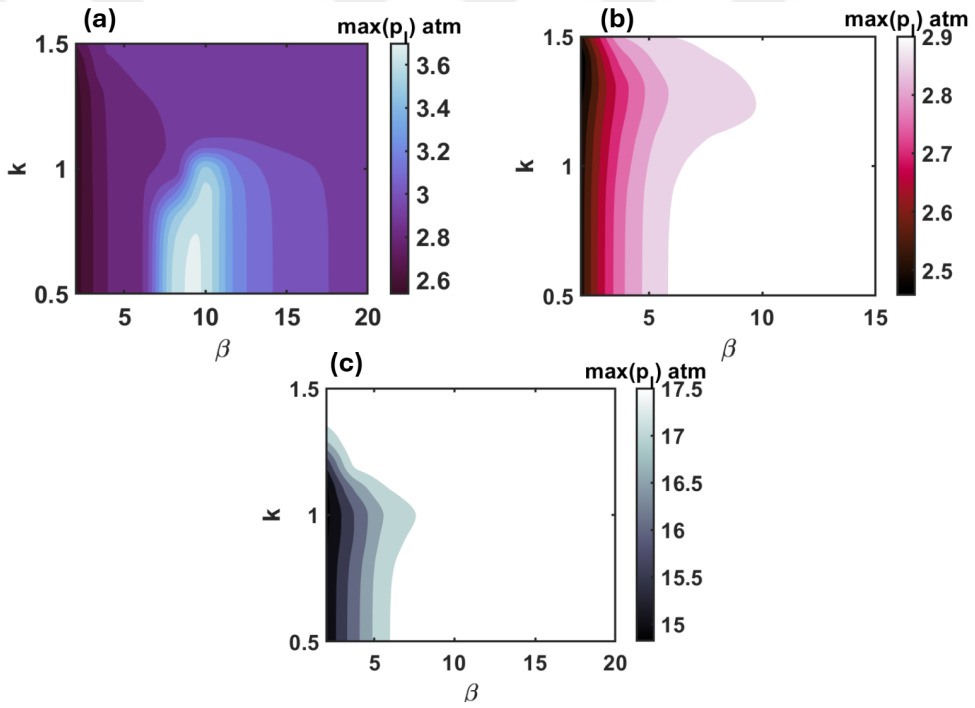

Figure 4.68. Contour plot (k versus β) (a) $\omega_d = 8$ MHz, $G_{el} = 10$ MPa, (b) $\omega_d = 4$ MHz, $G_{el} = 10$ MPa and (c) $\omega_d = 8$ MHz, $G_{el} = 100$ MPa for maximum wall pressure, p_l.

The maximum liquid shear stress exerted on the wall of the blood vessel $\max(\tau_{rr,l}(R_l))$ is essential to assess vascular permeability and the risk of vessel damage when pressure levels exceed safe thresholds. This information is precious for optimizing therapeutic parameters while ensuring patient safety. Previous studies have suggested that wall shear stresses in the 100–800 range Pa may enhance permeability. In contrast, higher stress levels could lead to cell detachment or membrane damage [389, 390].

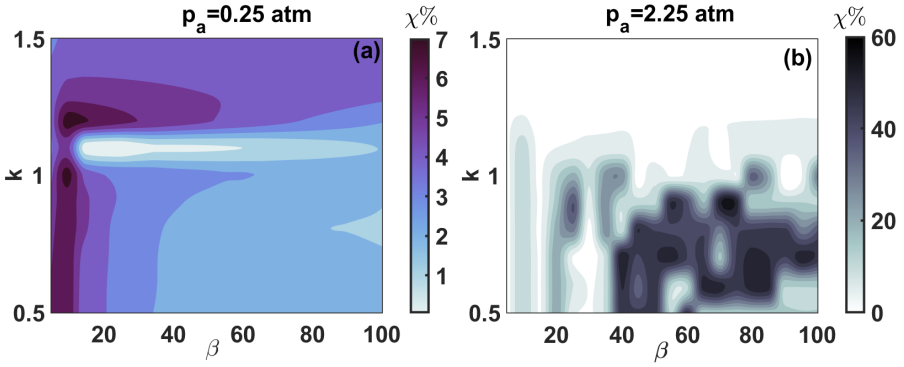

Figure 4.69. Contour plot k versus β (a) $p_a = 0.25$ atm and (b) $p_a = 2.25$ atm for ε.

Figure 4.68 illustrates the effects of the power-law index, k, and the amplitude of the acoustic field pressure, p_a on the maximum wall shear stress, $\max(\tau_{rr,l}(R_l))$, at different radius ratios, $\beta = R_{l0}/R_{b0}$. Specifically, Figure 4.72(a) corresponds to $\beta = 2.5$, Figure 4.72(b) corresponds to $\beta = 10$, and Figure 4.72(c) corresponds to $\beta = 100$. The maximum $\tau_{rr,l}(R_l)$ is computed after 25 cycles. In Figure 4.72(a), there is a region where the wall liquid shear stress is maximized, particularly for $k \approx 1.5$ and $p_a > 1.5$ atm. The peak $\tau_{rr,l}(R_l)$ reaches approximately 3000 Pa. In Figure 4.72(b), the maximum wall shear stress is 500 Pa, occurring when $k \approx 1.2$.

Additionally, Figure 4.72(c) demonstrates that a higher cavity size, e.g., large β, decreases the resulting wall shear stress. Therefore, wall shear stress becomes high in smaller blood vessels, which may cause important bioeffects.

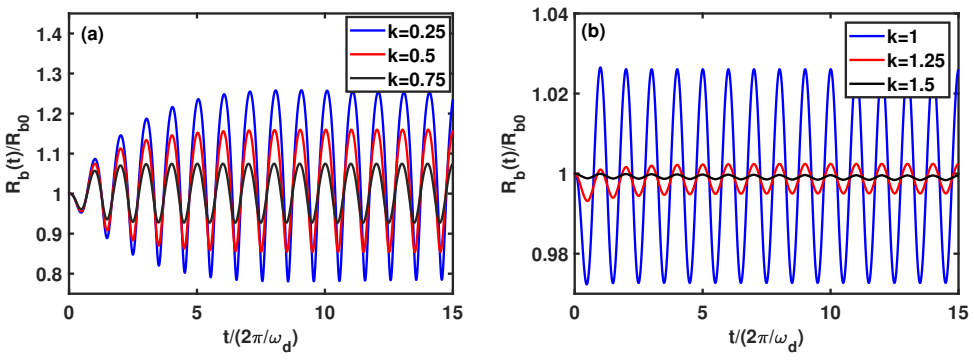

Figure 4.70. Effect of power-law index, k, on $R_b(t)/R_{b0}$ versus $t/(2\pi/\omega_d)$ for (a) shear-thinning and (b) shear-thickening liquid.

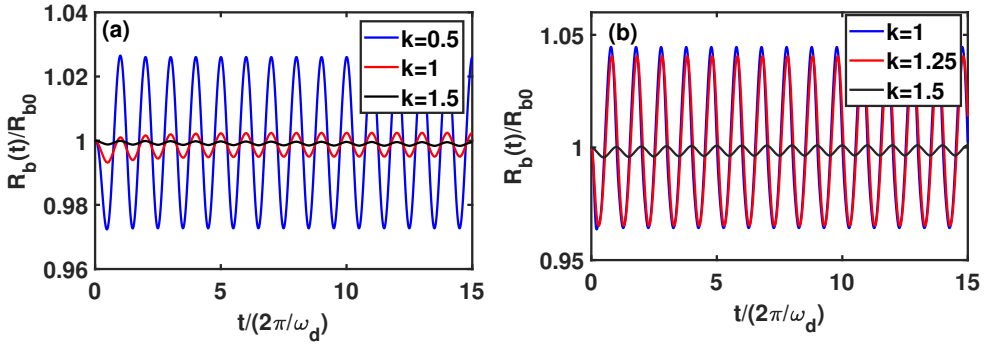

Figure 4.71. Effect of power-law index, k, on $R_b(t)/R_{b0}$ versus $t/(2\pi/\omega_d)$ for (a) $\beta = 2$ and (b) $\omega_d = 2$ MHz.

Figure 4.73 illustrates the effects of the power-law index k and the amplitude of the acoustic field pressure p_a on the maximum wall shear stress, $\max(\tau_{rr,l}(R_l))$, under various acoustic driving frequencies, ω_d, and cavity moduli, G_{el}. In particular, Figure 4.73(a) represents the case where $\omega_d = 8$ MHz and $G_{el} = 10$ MPa, while Figure 4.73(b) corresponds to $\omega_d = 2$ MHz and $G_{el} = 10$ MPa. Meanwhile, Figure 4.73(c) shows the results for $\omega_d = 8$ MHz and $G_{el} = 1$ MPa. The physical properties used in the simulations are provided in Table 4.3. Moreover, to account for non-Newtonian effects, the surrounding liquid properties are modeled using the physical parameters of real blood, specifically $m = 0.64$, $\mu_0 = 0.056$ Pa·s, and $\mu_\infty = 0.0035$ Pa·s, based on values reported in the literature [388]. These properties are also used in the context of Figures 4.70-4.71. Across Figures 4.73(a)-(c), a region is observed where the wall liquid shear stress is maximized. Notably, in Figure 4.73(a), the maximum occurs around $k \approx 1$, whereas in Figure 4.73(b), it is around $k \approx 1.2$. In Figure 4.73(c), the maximum is observed near $k \approx 0.75$. Among these cases, the peak $\tau_{rr,l}(R_l)$ reaches approximately 800 Pa in Figure 4.73(a).

Figure 4.74 illustrates the effect of the pressure amplitude of the acoustic field, p_a, and the acoustic field driving frequency, ω_d, on the maximum wall shear stress. In Figure 4.74(a), the parameter $\beta = 2.5$, while in Figure 4.74(b), $\beta = 100$. From these figures, it is evident that when β is low (Figure 4.74(a)), the wall shear stress reaches up to 2000 Pa at $p_a = 15$ atm. In contrast, when β is high (Figure 4.74(b)), the wall shear stress is significantly reduced, reaching only 2 Pa at $p_a = 1$ atm and $\omega_d = 1.5$ MHz. These results suggest that microvessel

pores cannot be created in larger vessels ($\tau_l < 100$ Pa) in contrary to this, high wall shear stress values cause cell damage inside the small vessels ($\tau_l > 800$ Pa).

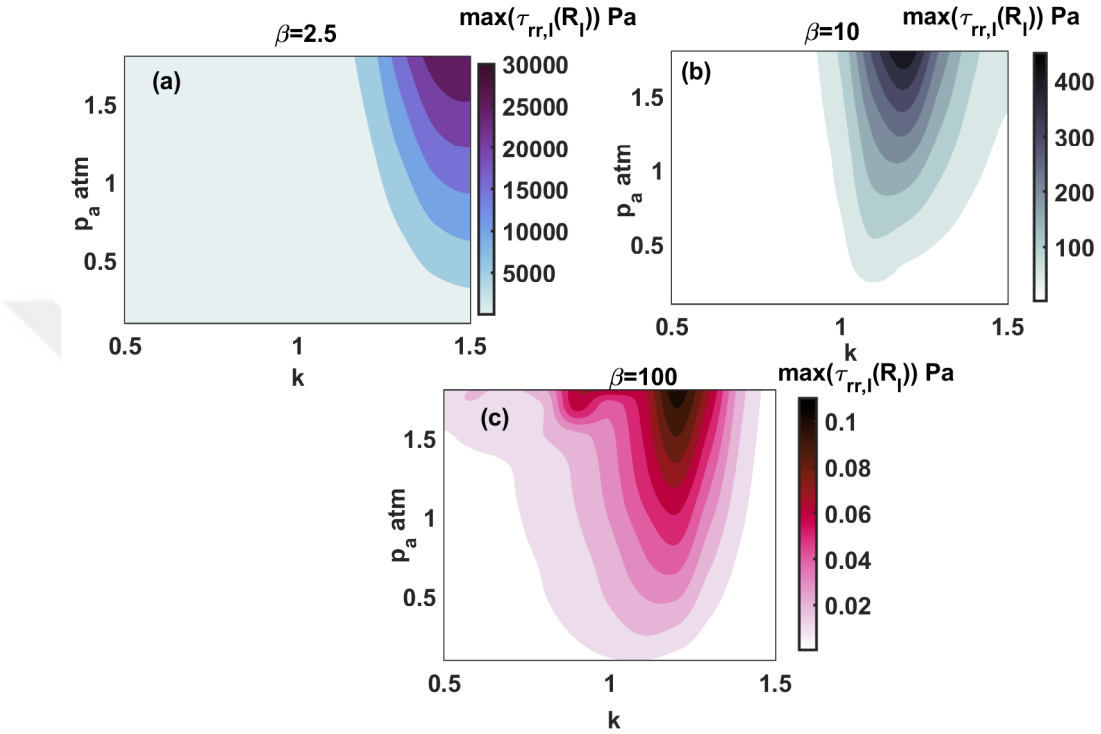

Figure 4.72. Contour plot (k versus p_a) (a) $\beta = 2.5$, (b) $\beta = 10$ and (c) $\beta = 100$ for maximum stress, $max(\tau_l(R_l))$.

In summary, both the bubble surface area and wall shear stress values affect the drug efficiency and the safety of the biomedical applications. To prevent the cell damage, the wall shear stress should be less than 800 Pa, however, to create pores, it should be larger than 100 Pa. The desired bubble surface area for the biomedical applications are between 12 to 1200 μm^2 which affects the drug diffusion rate and drug loading capacity. These two criteria are important for drug efficiency and the safety of the biomedical applications.

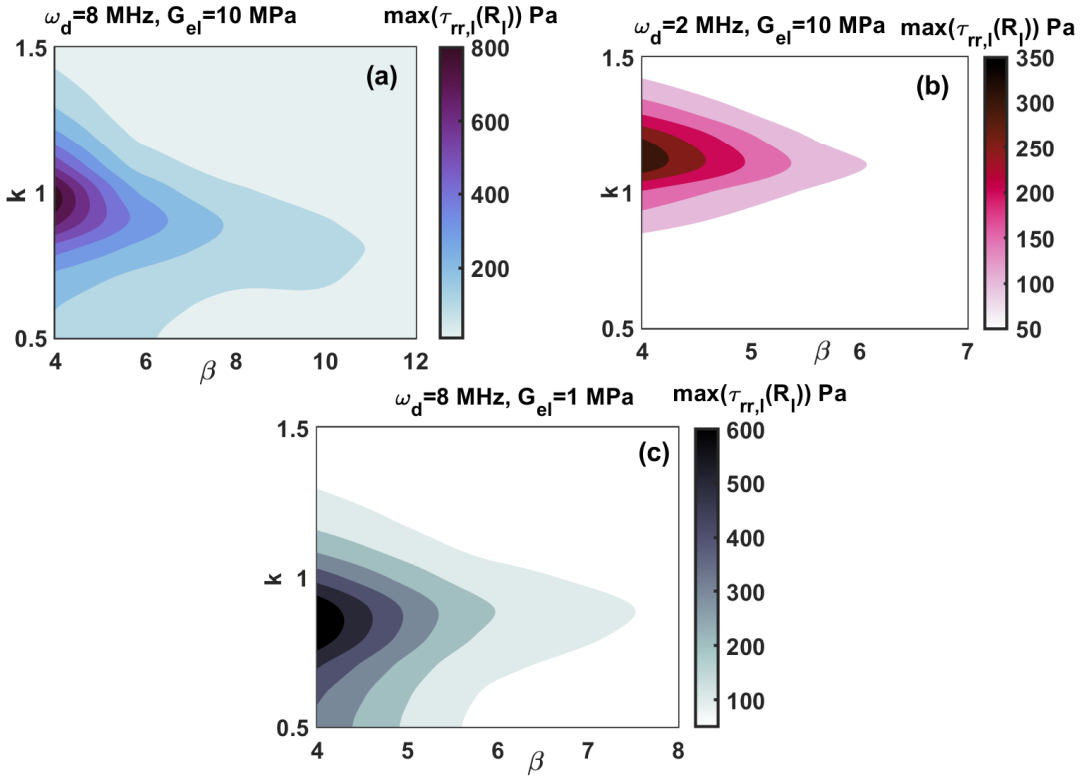

Figure 4.73. Contour plot (k versus p_a) (a) $\beta = 2.5$, (b) $\beta = 10$ and (c) $\beta = 100$ for maximum stress, $max(\tau_{rr,l}(R_l)$.

The drug loading capacity of bubbles increases with the augmentation of the Area-Volume Ratio (AVR), as a higher surface area provides more sites for drug binding. However, this increase reaches a saturation point where further growth in AVR no longer significantly enhances loading efficiency. Conversely, the drug diffusion rate decreases with increasing AVR. This is because smaller bubbles, which inherently have higher AVR, are less stable, leading to reduced diffusion efficiency and potentially compromising the therapeutic effectiveness. Therefore, drug loading capacity is high in large bubbles, however, drug diffusion rate is small. A small example is added to Appendix F is added to show how AVR affects the drug diffusion rate.

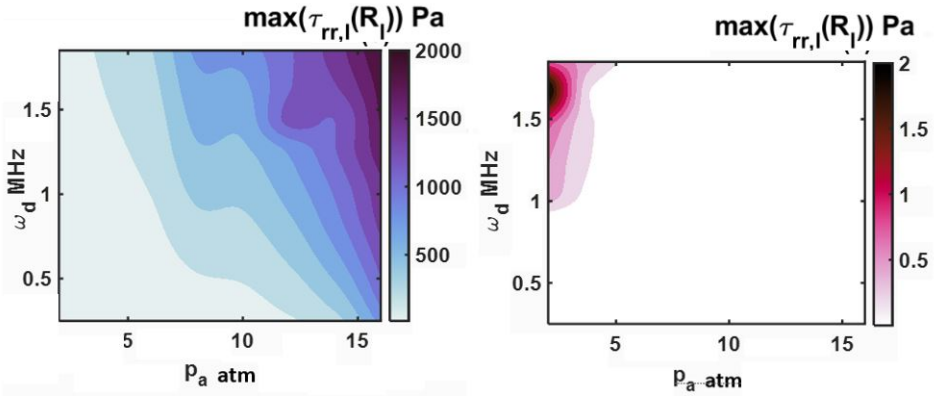

Figure 4.74. Contour plot (ω_d versus p_a) (a) $\beta = 2.5$, and (b) $\beta = 100$ for maximum stress, $max(\tau_{rr,l}(R_l)$. The power-law index is 0.75.

4.5. Non-Spherical Bubble Dynamics

In this section, the non-spherical oscillations of a bubble in an unbounded liquid are investigated. First, it is assumed that the bubble is in an unbounded power liquid (Section 4.5.1), then, the effect of encapsulating shell is added to this configuration (Section 4.5.2).

Two distinct types of instabilities are identified: Rayleigh–Taylor (RT) instabilities and parametric instabilities [11, 327, 328, 381, 391]. Parametric instability arises from the resonance between spherical oscillations and non-spherical perturbations, which happens when the condition $2\omega_n/\omega_d = j$ is met [392, 393]. Here, j is typically either 1 or 2 [11, 394, 394], and ω_n represents the natural frequency of mode n [11, 394]. The parametric instability associated with mode $n = 0$ is examined in Section 4.4 by analyzing the natural frequency of the spherical mode. If a disturbance amplifies over several cycles, it is likely that the bubble will eventually rupture under these conditions [395–397]. While parametric instability develops over multiple oscillations of the bubble, RT instability manifests during a single, intense bubble collapse.

4.5.1. Non-Spherical Oscillation of a Bubble in Power-law Liquid

In this section, the non-spherical oscillations of a bubble in power-law liquid is investigated. The physical system consists of a bubble in a homogeneous and non-Newtonian fluid described in spherical coordinates by a radial distance r, and a polar angle θ, as shown in Figure 3.5. The effects of power-law index, k, acoustic field driven frequency, ω_d , pressure amplitude, p_a, perturbation mode, n, and initial bubble radius, R_0 are investigated.

Figure 4.75 illustrates the dynamic behavior of the second mode amplitudes for various power-law indices and frequencies. It can be observed that as the power-law index k increases, particularly at $k = 1$ and $k = 1.25$, the oscillations of the perturbed mode amplitudes are more heavily damped. For cases where the system is not in radial resonance ($\omega_d \approx \omega_0$) and for higher power-law indices like $k = 1$ and $k = 1.25$, the initial disturbances in the shape modes are quickly damped, preventing shape instabilities from occurring at this pressure amplitude. The dissipation rate increases with the power-law index, leading to a faster decrease in oscillation amplitude, allowing the bubble to reach its equilibrium radius more rapidly.

At radial resonance, the strong radial oscillations cause shape instability when $k = 0.75$. For lower power-law indices, like $k = 0.75$, the dissipation rate decreases which results in small amplitude non-spherical modes, making the oscillations nearly spherical. The time scale for shape oscillation aligns closely with that of radial oscillation. In Figure 4.75(c), mode $n = 2$ grows significantly after several oscillations due to radial resonance, leading to a deviation from the spherical shape of the bubble. At radial resonance ($\omega_d = 4$ MHz), the amplitude of the non-spherical oscillations is linked to the amplitude of the radial oscillations (Figure 4.16(c)). Consequently, non-spherical oscillations are more likely to occur when the bubble is at its radial resonance. This behavior reflects typical characteristics of parametric instabilities, where the applied ultrasound does not directly trigger surface modes but is instead driven by radial oscillations.

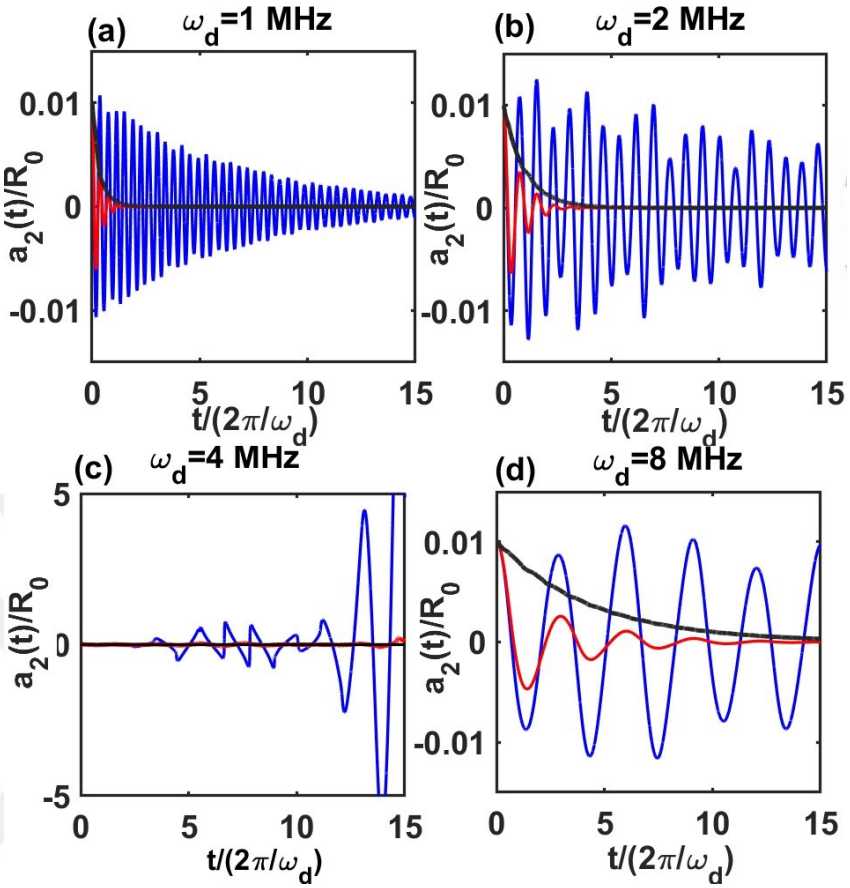

Figure 4.75. $a_2(t)/R_0$ versus $t/(2\pi/\omega_d)$ for (a) $\omega_d = 1$ MHz $< \omega_0$, (b) $\omega_d = 2$ MHz $\approx \omega_0/2$, (c) $\omega_d = 4$ MHz $\approx \omega_0$ (radial resonance), and (d) $\omega_d = 8$ MHz $> \omega_0$. Here, the blue, red and black lines show the shear-thinning ($k = 0.75$), Newtonian ($k = 1$) and shear-thickening ($k = 1.25$) liquid cases, respectively. Reproduced with permission from Kaykanat and Uguz [13]. Licensed under Creative Commons CC BY license.

In Figure 4.76, the impact of perturbation mode n on shape stability is analyzed by setting the driving frequencies to match the natural frequencies of the shape modes rather than the radial mode: $\omega_d = 2.65$ MHz = ω_2 for $n = 2$ and $\omega_d = 9.6$ MHz = $2\omega_3$ for $n = 3$ [11], with a lower consistency index, such as $M = 2 \times 10^{-4}$ Pa.s^k. When the consistency index decreases, the damping effect of the power-law index is reduced, leading to the emergence of parametric instabilities in both shear-thinning ($k = 0.75$) and Newtonian liquid ($k = 1$) cases, as the driving frequencies are equal to or near multiples of the natural frequency (2.65 MHz and 9.6 MHz). Unlike in Newtonian liquids, the damping factor for the power-law liquid is

diminished. The damping factor is given as,

$$\frac{M(n+2)(n+1)}{\rho R^2}\left|\frac{\dot{R}}{R}\right|^{k-3}\left(\left(\frac{\dot{R}}{R}\right)^2+4(k-1)\frac{\dot{R}^2}{R}\right), \tag{4.5}$$

which depends on the bubble wall velocity and the power-law index (Equation 3.194).

Rayleigh-Taylor (RT) instability occurs near the point of minimum bubble radius, where the acceleration $\ddot{R}$ of the bubble wall is positive (i.e., the gas accelerates into the fluid, and vice versa). The normalized solutions of perturbation amplitudes ($n = 2$ to $n = 4$) by the mean bubble radius are illustrated in Figure 4.77. The acceleration of bubble wall reaches a peak value of $10.5 \times 10^9\,\mathrm{m/s^2}$ (Figure 4.77(a)), $6.3 \times 10^9\,\mathrm{m/s^2}$ (Figure 4.77(b)), and $1.9 \times 10^{10}\,\mathrm{m/s^2}$ (Figure 4.77(c)), then rapidly decreases to $-8 \times 10^8\,\mathrm{m/s^2}$ in 0.020 μs (Figure 4.77(a)), $-0.49 \times 10^8\,\mathrm{m/s^2}$ in 0.025 μs (Figure 4.77(b)), and $-1.75 \times 10^9\,\mathrm{m/s^2}$ in 0.015 μs (Figure 4.77(c)) during inertial collapse. This instability arises due to the significant acceleration of the power-law liquid into the gas and adjacent gases. Despite the high acceleration of the liquid, compressible effects on both non-spherical and spherical oscillations are expected to be minimal because $\dot{a}_n/c_\infty$ and $\dot{R}/c_\infty$ remain small. The maximum unperturbed an perturbed bubble wall velocities are normalized by the speed of sound in the liquid,$\dot{a}_{\max}/c_\infty = 0.1$ and $\dot{R}_{\max}/c_\infty = 0.04$, where $c_\infty \approx 1500\,\mathrm{m/s}$. For this set of parameters, the most unstable mode is $n = 3$. Additionally, Figure 4.77 explores the effect of the power-law index on the RT-type instability of a bubble. The RT instability is only weakly influenced by viscous effects because the maximum acceleration of the bubble is independent of viscosity in a Newtonian liquid. Unlike the Newtonian case, the power-law index alters the evolution of the mean bubble radius. Consequently, the bubble wall acceleration increases (Figures 4.77(a)-(c)), which is the key factor inducing the RT-type instability. At higher power-law indexes, the acceleration is reduced, leading to a corresponding reduction in perturbation growth (red line in Figures 4.77(a)-(b)). For larger values of k (e.g., $k = 1.1$), the non-spherical perturbation diminishes. Thus, the amplitude of the acoustic pressure must be increased to achieve RT-type instability, as seen with $p_a = 15$ atm in Figure 4.77(c).

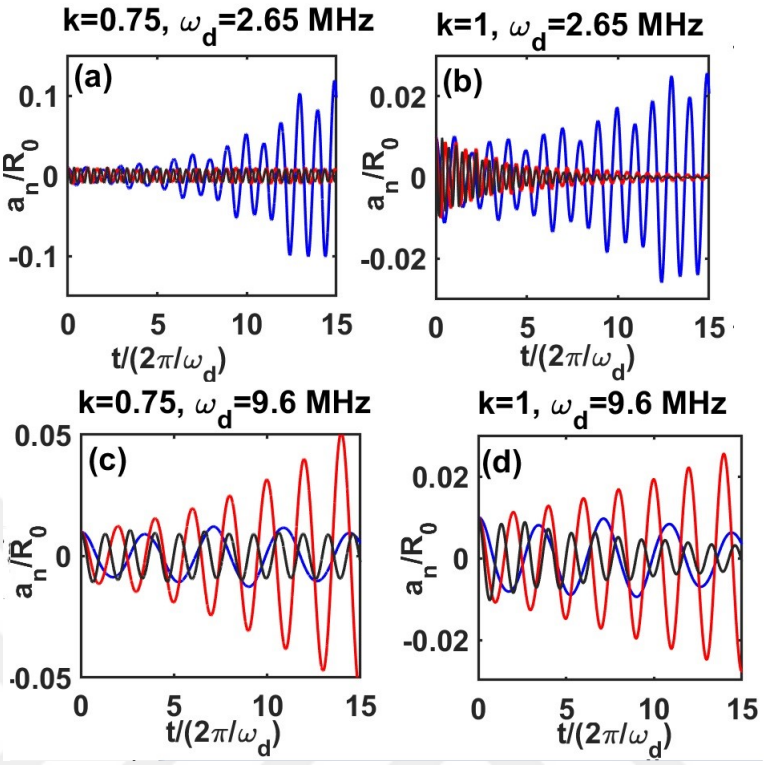

Figure 4.76. $a_n(t)/R_0$ versus $t/(2\pi/\omega_d)$ for $M = 2 \times 10^{-4}$ Pa·s^k when (a) $\omega_d = 2.65$ MHz $= \omega_2$, (b) $\omega_d = 9.6$ MHz $= \omega_3$, (c) $\omega_d = 2.65$ MHz $= \omega_2$, and (d) $\omega_d = 9.6$ MHz $= \omega_3$. Here, the blue ($n = 2$), red ($n = 3$), and black ($n = 4$) represent the perturbation modes. Reproduced with permission from Kaykanat and Uguz [13]. Author(s), licensed under Creative Commons CC BY license.

Finally, Figure 4.78 is obtained for different p_a and R_0 values to find regions with large non-spherical oscillations. Figures 4.78(a)-(c) are obtained for perturbation mode, $n = 2$, Figures 4.78(d)-(f) for mode 3 and Figures 4.78(g)-(h) are for mode 4. Also in Figures 4.78(a), (d) and (g), $k = 0.75$, in Figures 4.78(b), (e) and (h), $k = 1$ and in Figures 4.78(c) and (f), $k = 1.25$. At dark blue region, $\max_{t\subset[0,N(2\pi/\omega)]} \left|\frac{a_n}{R}\right| \geqslant 1$. Here, N is the large number. The light blue regions show the region where $\max \left|\frac{a_n}{R}\right| < 1$. Mostly, for the larger p_a, the system becomes unstable for all modes and the shear-thinning behavior of the viscosity; again, the system becomes unstable. In summary, parametric instability occurs before the Rayleigh-Taylor (RT) instability. The parametric instability operates over a long timescale (approximately ten cycles). Furthermore, the RT instability is only weakly influenced by viscosity since the maximum acceleration of the bubble is essentially independent of it.

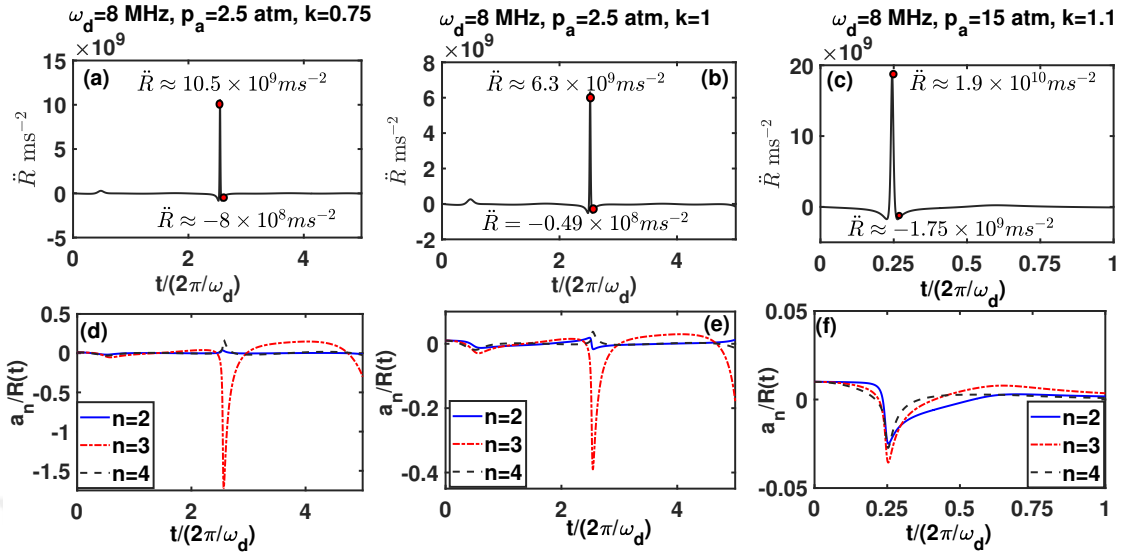

Figure 4.77. Bubble wall acceleration, $\ddot{R}$, versus $t/(2\pi/\omega_d)$ for $\omega_d = 8$ MHz $> \omega_0$, (a) $p_a = 2.5$ atm and $k = 0.75$, (b) $p_a = 2.5$ atm and $k = 1$ and (c) $p_a = 15$ atm and $k = 1.1$. $a_n(t)/R(t)$ versus $t/(2\pi/\omega_d)$ for $\omega_d = 8$ MHz $< \omega_0$, (d) $p_a = 2.5$ atm and $k = 0.75$, (e) $p_a = 2.5$ atm and $k = 1$ and (f) $p_a = 15$ atm and $k = 1.1$. Reproduced with permission from Kaykanat and Uguz [13]. Author(s), licensed under Creative Commons CC BY license.

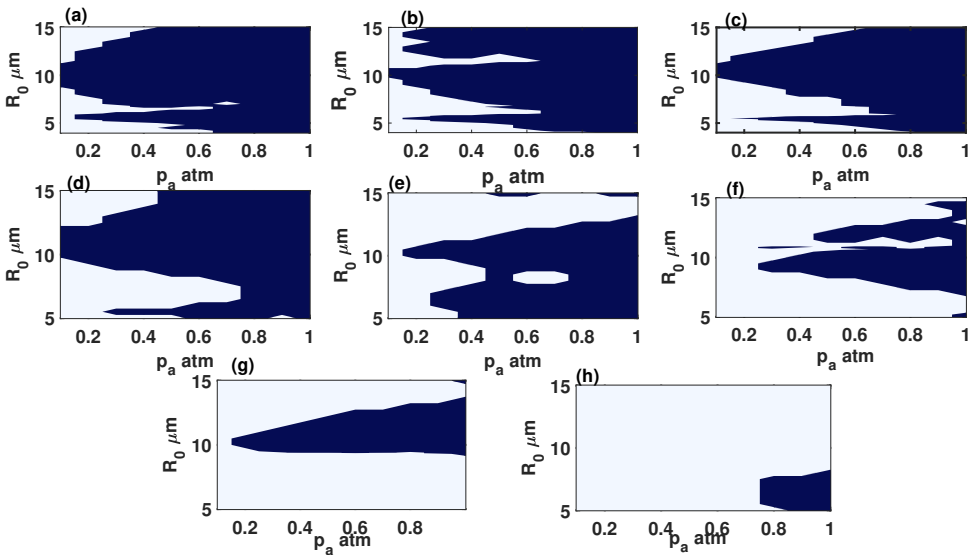

Figure 4.78. R_0 versus p_a: (a), (d) and (g), $k = 0.75$; (b), (e) and (h), $k = 1$; (c) and (f) $k = 1.25$. $n = 2$ for (a)-(c), $n = 3$ for (d)-(f) and $n = 4$ (g)-(h).

4.5.2. Non-Spherical Oscillation of an Encapsulated Bubble

In this section, the non-spherical oscillations of an encapsulated bubble in an unbounded liquid are investigated. The physical system consists of a bubble in a homogeneous fluid described in spherical coordinates by a radial distance r and a polar angle θ, as shown in Figure 3.6. The physical properties for this section are given in Tables 4.1 and 4.2.

Two different cases are investigated. First, the surrounding liquid is assumed to obey power-law constitutive model. Second, the surrounding liquid is assumed to be viscoelastic. For both cases, the bubble is encapsulated with a thick Newtonian shell.

4.5.2.1. Non-Spherical Oscillation of an Encapsulated Bubble in Power-law Liquid. In this Section, the non-spherical oscillation of an encapsulated bubble in a power-law liquid is studied. The thick encapsulated layer is assumed to be Newtonian, and the unbounded liquid obeys the power-law constitutive model. The natural frequency of the spherical oscillation is 5 MHz, found in Equation 3.157. Neglecting the transient change in R_b and R_s in Equation 3.215, the square of the natural frequency of the non-spherical oscillations, ω_n, can be determined as

$$\omega_n^2 = \left\{ \sigma_b \frac{(n-1)(n+1)(n+2)}{R_{b,eq}^3} \left(1 + \frac{\sigma_s}{\sigma_b} \left(\frac{R_{b,eq}}{R_{s,eq}} \right)^{n+4} \right) \right\} \text{x} \left((\rho_\ell - \rho_s) \left(\frac{R_{b,eq}}{R_{s,eq}} \right)^{n+1} + \rho_s \right)^{-1} \quad (4.6)$$

Equation 4.6 links the most unstable mode number, n, to the equilibrium bubble radius R_{beq} for a constant driving frequency. The most unstable mode indicates parametric instability, which occurs when $\omega_d = 2\omega_n$. In Figure 4.79, the initial values of the bubble radius are determined for a given acoustic field driving frequency, with $\omega_d = 5$ MHz in Figure 4.79(a) and $\omega_d = 7$ MHz in Figure 4.79(b). For example, when $\omega_d = 5$ MHz, the mode $n = 2$ is identified as the most unstable parameter instability mode for an uncoated bubble with $R_{beq} = 12\,\mu$m and a coated bubble with $R_{beq} = 13\,\mu$m. As mentioned, the typical bubble radius range for drug delivery applications is 1–10 μm [2]. Within this radius range (1-10μm), parametric resonance does not occur for $\omega_d = 5$ MHz because the conditions required for instability are

not satisfied (R_{b0} should be in the order of 0.001 m). However, when the driving frequency ω_d is increased to 7 MHz and the bubble has a smaller initial radius, a parametric instability is expected ($\omega_n = 14MHz$). For example, with an initial radius of $R_{b0} = 6\,\mu$m, the most unstable mode, $n = 2$, will grow over time which shows the onset of parametric instability in the system. This growth highlights the potential for resonance-driven amplification of the oscillation mode, which could have practical implications in scenarios where bubble oscillations increase the permeability of the target site for drug diffusion.

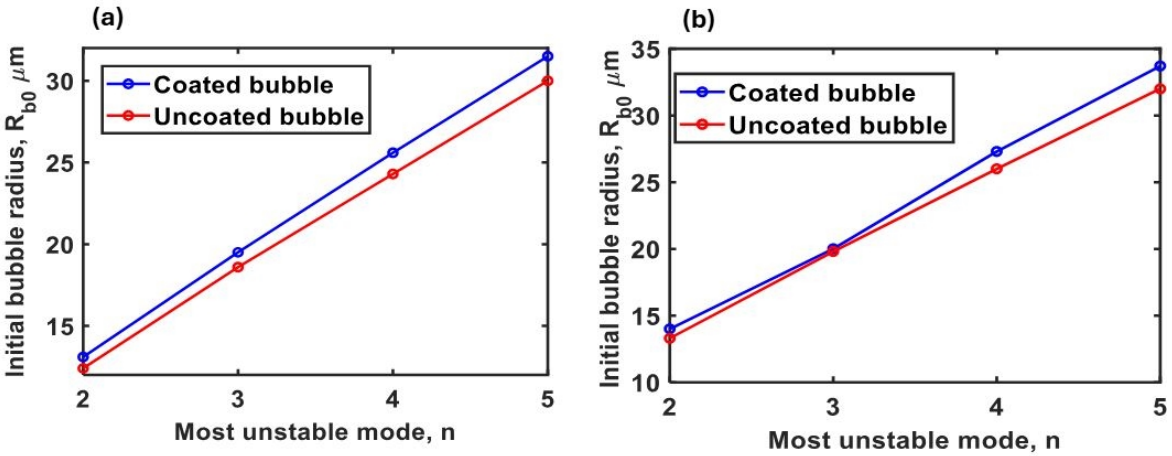

Figure 4.79. Initial bubble radius, R_{b0} versus the most unstable mode in the parametric instability for (a) $\omega_d = 5$ MHz and (b) $\omega_d = 14$ MHz.

First, the results are obtained for an acoustic driving frequency of $\omega_d = 5$ MHz, which matches the natural frequency of spherical oscillations for an encapsulated bubble with an initial radius $R_{b0} = 5\,\mu$m. The initial shell thickness is set to 15 nm, and the surrounding unbounded liquid is assumed to be Newtonian. The pressure amplitude, $p_a = 0.25$ atm. As shown in Figure 4.80, the viscosity of the shell has a significant damping effect on non-spherical oscillations, both at the shell surface (Figure 4.80(b)) and at the bubble surface (Figure 4.80(a)). Despite the acoustic field's frequency being tuned to the natural frequency of spherical oscillations, a shell viscosity of $\mu_s = 0.05$ kg/ms is sufficient to completely dampen the non-spherical mode-2 perturbations on both the bubble and shell surfaces. This behavior suggests that the shell's viscous resistance effectively suppresses non-spherical oscillations, even under resonant conditions. The presence of a highly viscous shell increases energy

dissipation, which prevents the growth of non-spherical perturbations, maintaining a more stable spherical oscillation mode.

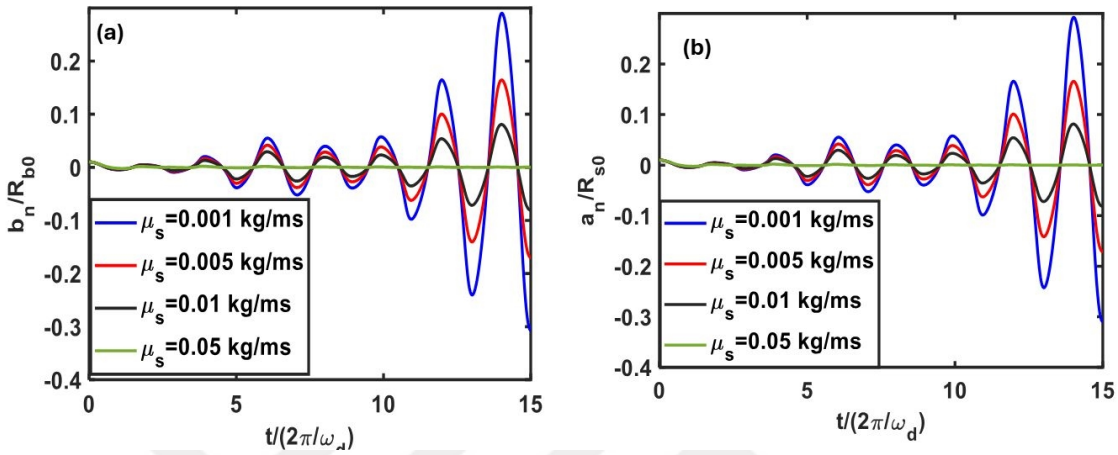

Figure 4.80. Effect of shell viscosity, μ_s on the (a) b_n/R_{b0} versus $t/(2\pi/\omega_d)$ and (b) a_n/R_{s0} versus $t/(2\pi/\omega_d)$.

Figure 4.81 illustrates the effects of pressure amplitude on the perturbation amplitudes of the bubble surface, b_n (Figures 4.81(a) and (c)), and the shell surface, a_n (Figures 4.81(b) and (d)), to better understand the dynamics under varying shell viscosities and driving pressures. Here, the perturbation amplitude for both surfaces is $n = 2$. In Figures 4.81(a) and (b), the shell viscosity, μ_s, is set to 0.001 kg/ms, while in Figures 4.81(c) and (d), the shell viscosity is 0.05 kg/ms. When $\mu_s = 0.001$ kg/ms (Figures 4.81(a) and (b)), the perturbation amplitudes are damped, and higher acoustic pressure amplitudes lead to pronounced oscillations on both the bubble and shell surfaces. When $\mu_s = 0.05$ kg/ms (Figures 4.81(c) and (d)), the more considerable viscosity value dampens the perturbation amplitudes effectively, reducing the oscillatory responses of both the bubble and the shell surfaces. However, even with this higher damping effect, an increase in pressure amplitude (e.g., $p_a = 0.45$ atm) leads to growth in the oscillations of both surfaces. This indicates that higher driving pressures can overcome the damping effects of shell viscosity, which promotes larger surface perturbations when the driving frequency equals the natural frequency. These observations suggest that while shell viscosity plays a crucial role in damping perturbations, high driving pressures can induce significant oscillations regardless of viscosity.

Similar to Figure 4.81, Figure 4.82 demonstrates how pressure amplitude affects the perturbation amplitudes on both the bubble surface, b_n (Figures 4.82(a) and (c)), and the shell surface, a_n (Figures 4.82(b) and (d)). However, in this case, the perturbation amplitude for each surface is analyzed at $n = 3$. In Figures 4.82(a) and (b), the shell viscosity μ_s is set to 0.001 kg/ms, while in Figures 4.82(c) and (d), it is increased to 0.05 kg/ms. Perturbation amplitudes undergo less damping in the lower viscosity case ($\mu_s = 0.001$ kg/ms), which results in pronounced oscillations at higher pressure amplitudes (Figures 4.82(a) and (b))In the lower viscosity case ($\mu_s = 0.001$ kg/ms). With increased viscosity ($\mu_s = 0.05$ kg/ms) (Figures 4.82(c) and (d)), damping becomes more effective, significantly reducing oscillations for both the bubble and shell surfaces as observed for perturbation mode 2 in Figures 4.81. Higher pressure amplitudes are applied to increase the perturbation amplitudes in both cases. Here, the greater oscillation amplitudes result from Rayleigh-Plesset instability rather than the effect of the natural frequency of spherical oscillations, as described in Section 4.5.1.

Using the power-law constitutive equation, the surrounding liquid is modeled to capture non-Newtonian behavior in Figure 4.83. Here, the driving frequency is set to $\omega_d = 5$ MHz, the initial bubble radius is $R_{b0} = 5\,\mu$m and the perturbation amplitude is $n = 2$. Figures 4.83(a) and (b) show results with a shell thickness of 15 nm, while Figures 4.83(c) and (d) illustrate behavior with an increased shell thickness of 30 nm. Newtonian behavior effectively damps the perturbed oscillations on both the bubble (Figure 4.83 (a)) and the shell surfaces (Figure 4.83(b)). However, the perturbation amplitudes increase for both surfaces when the surrounding liquid exhibits shear-thinning behavior, which leads to pronounced oscillations. This effect indicates that shear-thinning liquids amplify surface perturbations as observed in Section 4.5.1. In addition, increasing the thickness of the shell (Figures 4.83(c) and (d)) further dampens the oscillations, as the thicker shell adds stiffness and resistance to deformation. This added resistance reduces the amplitude of the oscillations and influences the natural frequency of the spherical oscillations, which shifts due to the altered mechanical properties of the bubble-shell system.

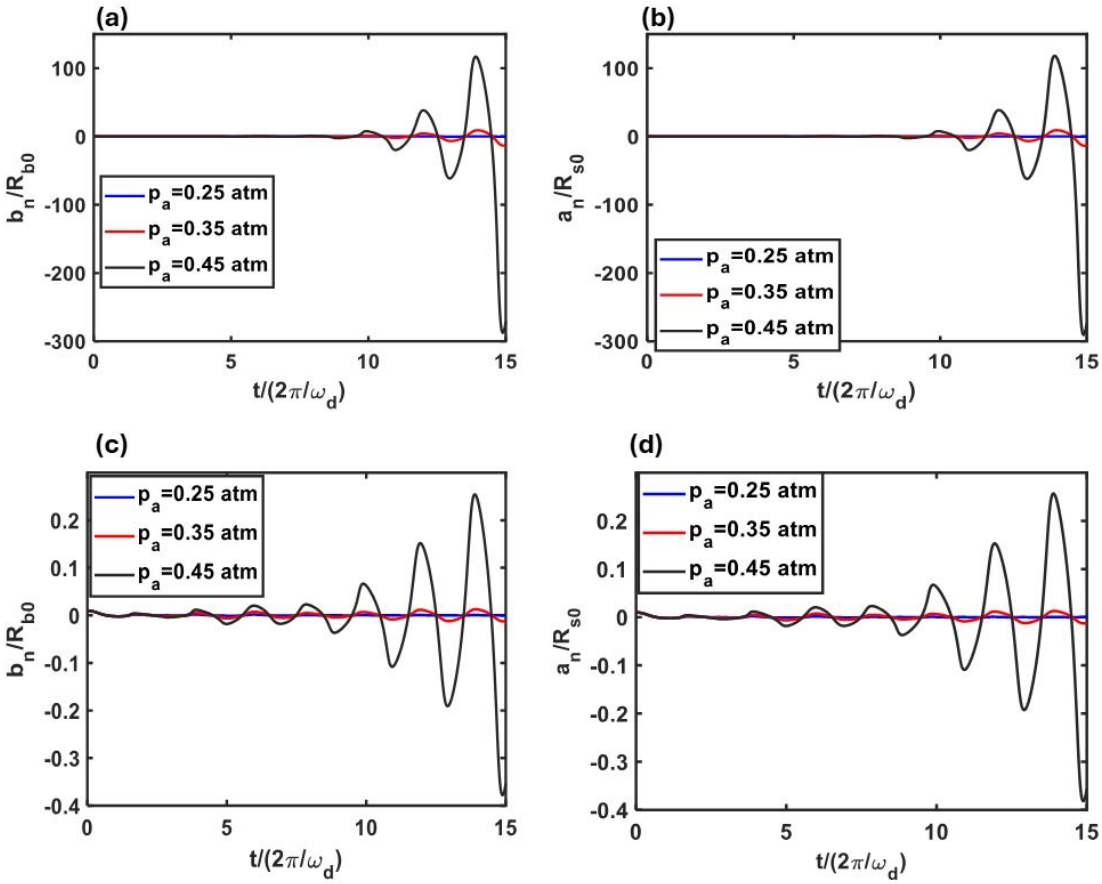

Figure 4.81. Effect of pressure amplitude, p_a on (a)-(c) b_n/R_{b0} versus $t/(2\pi/\omega_d)$ and (b)-(d) a_n/R_{s0} versus $t/(2\pi/\omega_d)$ for $n = 2$. In (a)-(b) $\mu_s = 0.001$ kg/ms and in (c)-(d) $\mu_s = 0.05$ kg/ms.

Figure 4.84 explores the impact of shell viscosity μ_s on the oscillation behavior of a bubble with a surrounding shell in a non-Newtonian fluid, described by a power-law index k. In Figures 4.83(a) and (b), the power-law index is set to $k = 0.5$ which represents a shear-thinning fluid. The results show that lower viscosities allow for greater oscillatory amplitudes, with higher viscosities progressively dampening the oscillations. To further understand this relationship, Figures 4.83(c) and (d) plot the maximum perturbation amplitudes for the bubble and shell surfaces, recorded after 10 cycles. As shell viscosity μ_s increases, the maximum perturbation amplitude decreases, illustrating the effectiveness of viscosity in damping surface oscillations. Depending on the power-law index, maximum bubble radius behavior differs. For instance, when $k = 0.75$, the maximum bubble radius first increases until a threshold, and then decreases contrary to the $k = 0.95$ which is also observed for the

maximum shell amplitude. This complex interplay between shell viscosity and the power-law index k provides key insights into the role of non-Newtonian behavior in bubble stability. In applications such as ultrasound imaging, therapeutic ultrasound, and drug delivery, controlling the oscillatory behavior of encapsulated bubbles is essential. Shear-thinning fluids with lower values of k may support larger oscillation amplitudes, and, thus greater mechanical impact, which can be beneficial for targeted drug delivery or enhanced permeability and retention (EPR) effects in tissues. Conversely, using fluids with higher viscosities or a power-law index closer to 1 can dampen oscillations, which might be preferred in applications requiring precision and minimal bubble deformation.

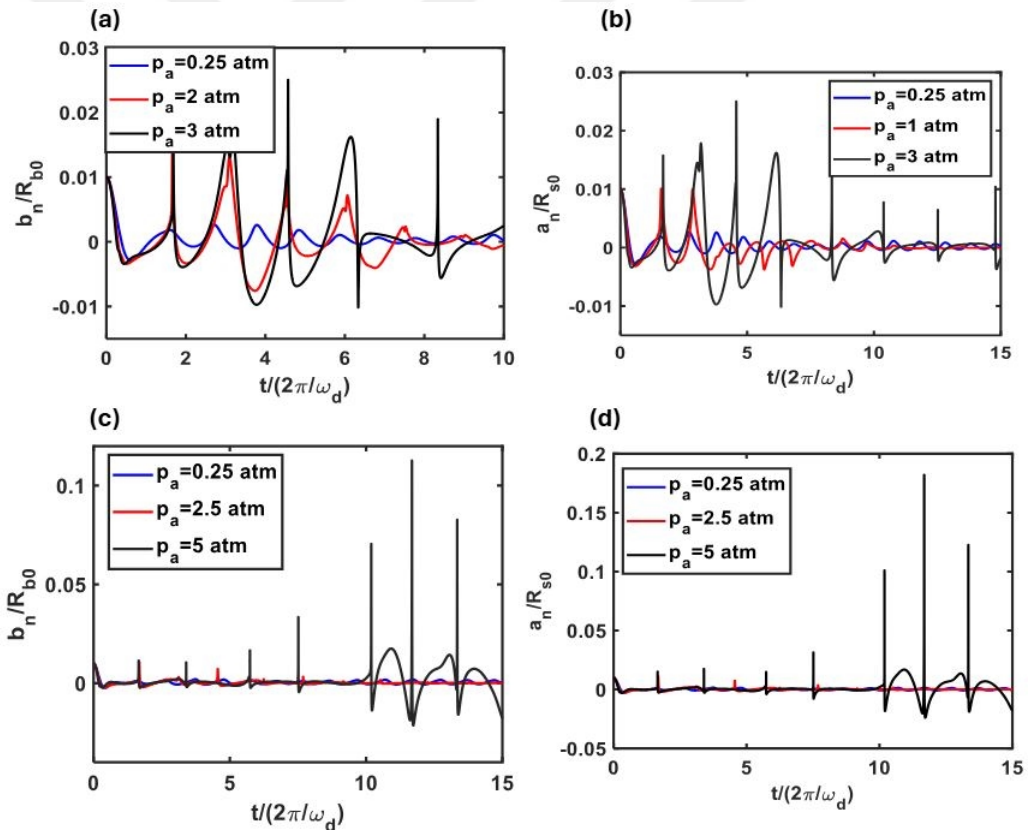

Figure 4.82. Effect of pressure amplitude, p_a on (a)-(c) b_n/R_{b0} versus $t/(2\pi/\omega_d)$ and (b)-(d) a_n/R_{s0} versus $t/(2\pi/\omega_d)$ for $n = 3$. In (a)-(b) $\mu_s = 0.001$ kg/ms and in (c)-(d) $\mu_s = 0.05$ kg/ms.

Figure 4.85 illustrates the impact of perturbation amplitudes, n, in shear-thinning (Figures 4.85(a) and (b)), Newtonian (Figures 4.85(c) and (d)), and shear-thickening liquids (Fig-

ures 4.85(e) and (f)). As discussed in Section 4.5.1, parametric instability arises from resonance between spherical oscillations and non-spherical perturbations, occurring when the condition $2\omega_n/\omega_d = j$ is met [392, 393]. Here, j is typically either 1 or 2 [11, 394, 394] and ω_n represents the natural frequency of mode n. In Figure 4.85, the driving frequency ω_d is set to match the natural frequency of the shape mode $n = 2$ (i.e., $\omega_d = 7$ MHz = ω_2), rather than the natural frequency of the radial mode. This frequency alignment is intended to amplify shape perturbations. The initial bubble radius is 4.5 μm. The results show that mode $n = 2$ perturbations are significantly amplified on both the bubble and shell surfaces, particularly in Newtonian (Figures 4.85(c) and (d)) and shear-thinning liquids (Figures 4.85(a) and (b)). In these cases, resonance conditions increase oscillation amplitudes, which makes the bubble and shell surfaces unstable. In contrast, shear-thickening behavior has a dampening effect on these oscillations, which reduces the amplitude of the perturbations and thus improves stability against parametric instability (Figures 4.85(e) and (f)). This damping effect in shear-thickening fluids likely arises from the increased viscosity at higher shear rates, which resists deformation and prevents resonance from fully developing.

4.5.2.2. Non-Spherical Oscillation of Encapsulated Bubble in Viscoelastic Liquid. In this section, the non-spherical oscillation of an encapsulated bubble in a viscoelastic fluid is examined. By neglecting transient variations in R_b and R_s, the square of the natural frequency for non-spherical oscillations, ω_n, can be calculated in Equation 4.7 as

$$\omega_n^2 = \left\{ \sigma_b \frac{(n-)(n+1)(n+2)}{R_{b,eq}^3} \left(1 + \frac{\sigma_s}{\sigma_b} \left(\frac{R_{b,eq}}{R_{s,eq}} \right)^{n+4} \right) \right. \\ \left. (n+1) \frac{G_l}{\rho_\infty R_{s,eq}^2} \left[4 + \frac{n(n+1)}{3} \right] \right\} \left((\rho_\ell - \rho_s) \left(\frac{R_{b,eq}}{R_{s,eq}} \right)^{n+1} + \rho_s \right)^{-1} \quad (4.7)$$

Equation 4.7 links the most unstable mode number, n, to the equilibrium bubble radius R_{beq} For a fixed driving frequency. As mentioned, the most unstable mode is related to the parametric instability. In Figure 4.86, the initial values of the bubble radius are determined for a driving frequency of $\omega_d = 7$ MHz. Various cases are examined, including an uncoated bubble in a Newtonian liquid and a coated bubble in a viscoelastic liquid with $G_l = 10$ kPa.

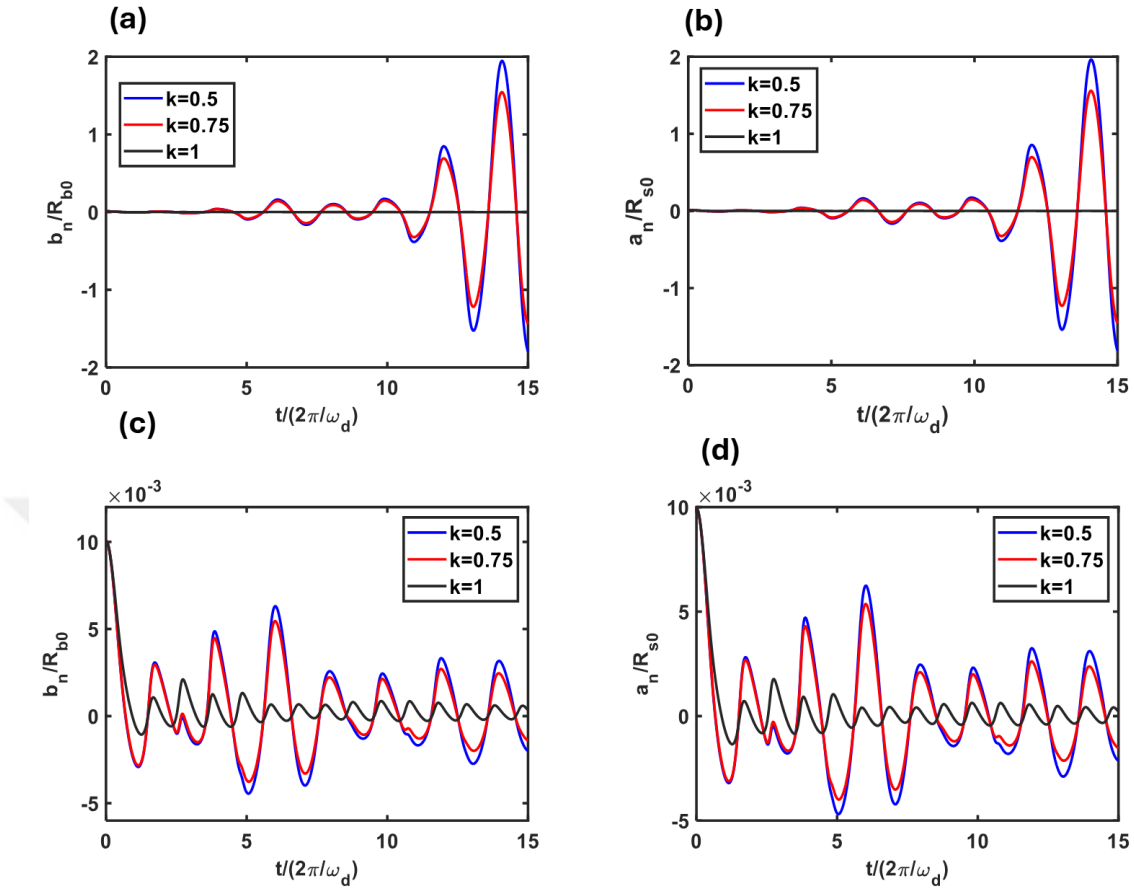

Figure 4.83. Effect of power-law index, k on (a)-(c) b_n/R_{b0} versus $t/(2\pi/\omega_d)$ and (b)-(d) a_n/R_{s0} versus $t/(2\pi/\omega_d)$ for $n=2$. In (a)-(b) $\delta = 15$ nm and in (c)-(d) $\delta = 30$ nm.

For example, mode $n=2$ is identified as the most unstable mode for an encapsulated bubble in a Newtonian liquid with $R_{beq} = 6.26\,\mu$m and for an encapsulated bubble in a viscoelastic liquid with $R_{beq} = 4.21\,\mu$m when $G_l = 10$ kPa. As observed, increasing G_l results in higher equilibrium radius values.

In Figure 4.87, the effect of the liquid modulus, G_l, on the perturbation amplitudes of both the bubble ((a), (c)) and shell ((b), (d)) surfaces is shown, focusing specifically on modes $n=2$ (Figures (a)-(b)) and $n=3$ (Figures (c)-(d)). The results indicate that, at $G_l = 100$ kPa, the perturbation amplitudes are higher compared to cases when $G_l = 10$ and 1000 kPa. This behavior is similar to the response observed in cases where the encapsulating layer has an elastic modulus and the bubble is surrounded by an unbounded liquid (see Section 4.4.2). Figure 4.88 is obtained to gain a more detailed understanding of this behavior which indicates

the effect of liquid modulus on the maximum spherical bubble radius (Figure 4.88(a)), as well as the perturbation amplitudes for modes $n = 2$ (Figure 4.88(b)) and $n = 3$ (Figure 4.88(c)). The maximum values are obtained after 15 cycles. This additional analysis provides insights into how different modulus values influence both radial and non-spherical oscillations across varying modes.

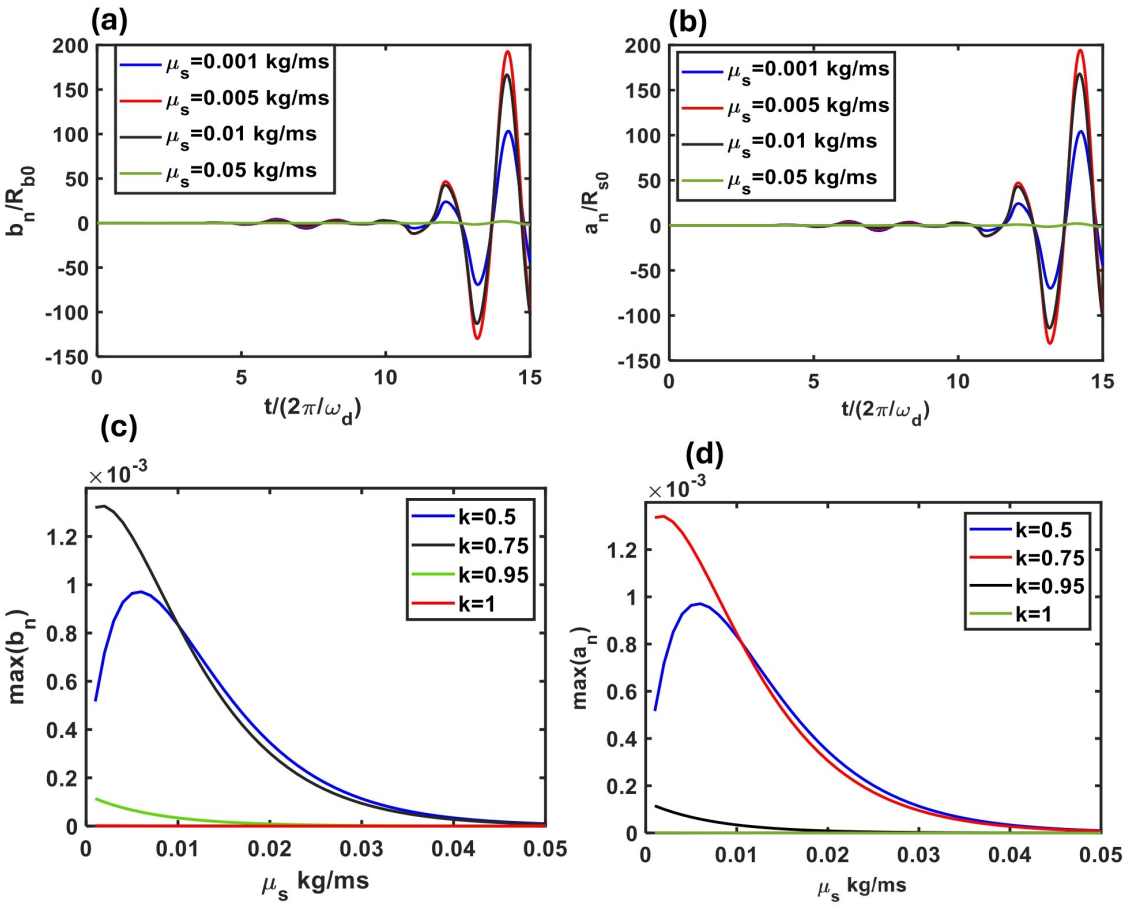

Figure 4.84. Effect of shell viscosity, μ_s on (a) bubble surface perturbation amplitude, b_n (b) shell surface perturbation amplitude, a_n (c) maximum bubble surface amplitude, $\max(b_n)$ and (d) maximum shell surface amplitude, $\max(a_n)$.

In Figure 4.88(a), a peak in the maximum bubble radius occurs around $G_l \approx 0.1$ MPa. Before reaching this modulus value, the maximum bubble radius increases steadily with G_l (region 1), indicating that higher liquid modulus values initially support larger bubble expansion. Beyond this (Region 2 and 3) peak, however, the maximum radius begins to decrease

as G_l continues to increase, eventually reaching a point where it remains constant. This peak in bubble radius also corresponds to an amplification of non-spherical perturbations for both mode $n = 2$ and mode $n = 3$, as seen in Figures 4.88(b) and 4.88(c). The observed behavior suggests a resonance-like effect around $G_l \approx 0.1$ MPa, where the bubble's oscillatory dynamics promote maximum expansion and enhance non-spherical perturbations. This amplification of both radial and non-spherical oscillations may result from the elastic response of the surrounding liquid, which allows for energy transfer into higher-order oscillatory modes at this specific modulus value.

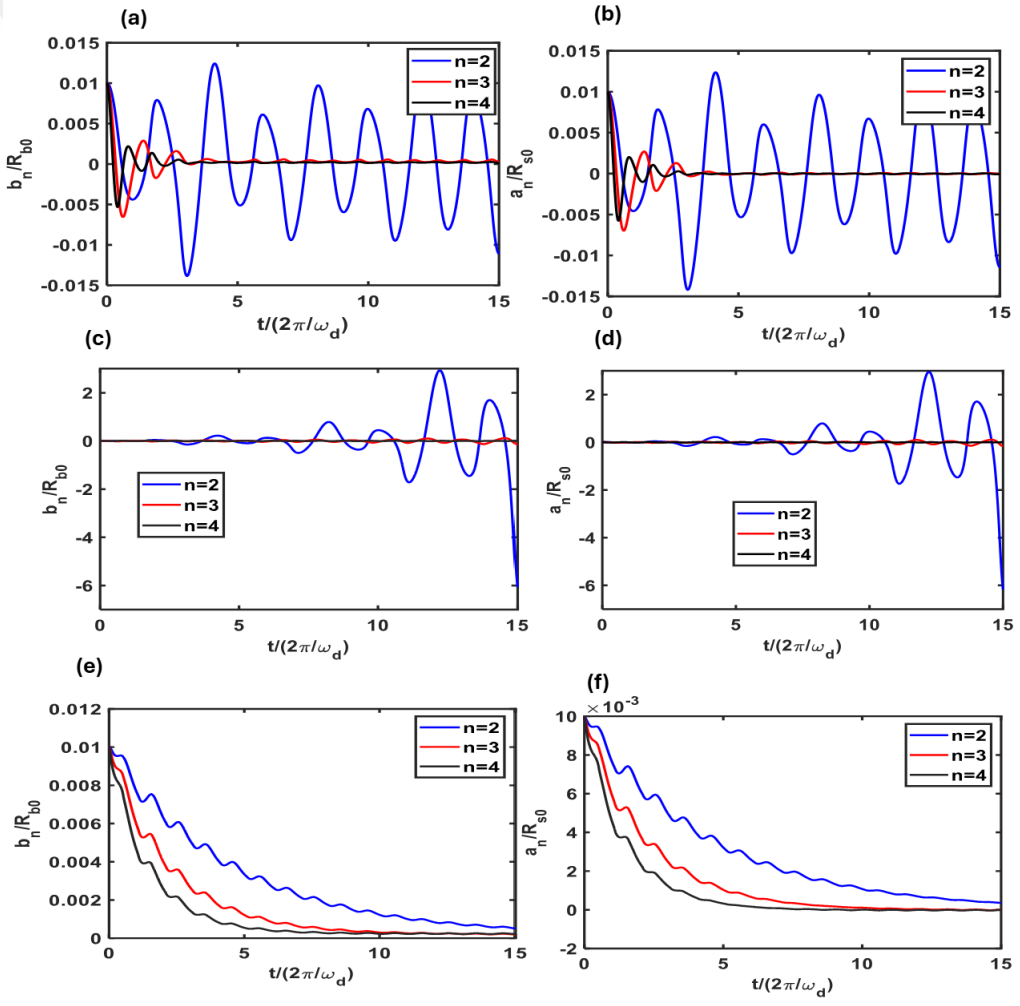

Figure 4.85. Effect of perturbation modes, n on (a), (c), (e) bubble surface amplitude, b_n and (b), (d), (f) shell surface amplitude, a_n. In (a)-(b) $k = 0.75$, (c)-(d) $k = 1$ and (d)-(e) $k = 1.25$.

4.5.3. Phase Diagrams

Once the spherical oscillations reach a steady periodic state, Floquet theory is applied, where the solution at the end of each cycle is linearly related to its value at the beginning, as detailed in Section 3.5.2. Shape stability phase diagrams are generated as a function of the initial bubble radius and the forcing pressure amplitude for $n = 2$. In these diagrams, black regions indicate instability (where the maximum modulus of the eigenvalues exceeds 1), while white regions represent stable areas.

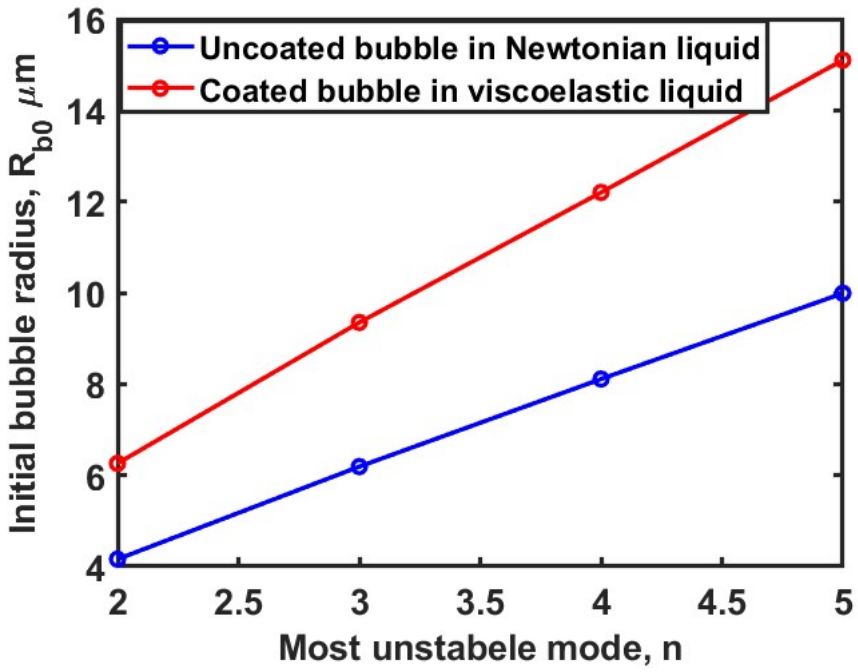

Figure 4.86. Initial bubble radius, R_{b0} versus the most unstable mode, n in the parametric instability.

First, phase diagrams for a bubble in an unbounded power-law liquid are presented, with the surrounding liquid's properties provided in Table 4.1. The acoustic field frequency is 2.65 MHz, the resonance frequency for mode 2. Figures 4.89(a), (b), and (c) illustrate cases where the surrounding liquid is shear-thinning, Newtonian, and shear-thickening, respectively. The diagrams show that for larger values of p_a and R_{b0}, the bubble becomes unstable, though the detailed structure of the phase diagrams is complex. Additionally, as

the power-law index increases, the bubble becomes stable. When the surrounding liquid is shear-thinning (Figure 4.89(a)), the black regions expand relative to the Newtonian (Figure 4.89(b)) and shear-thickening (Figure 4.89(c)) cases, suggesting that a lower power-law index enhances stability.

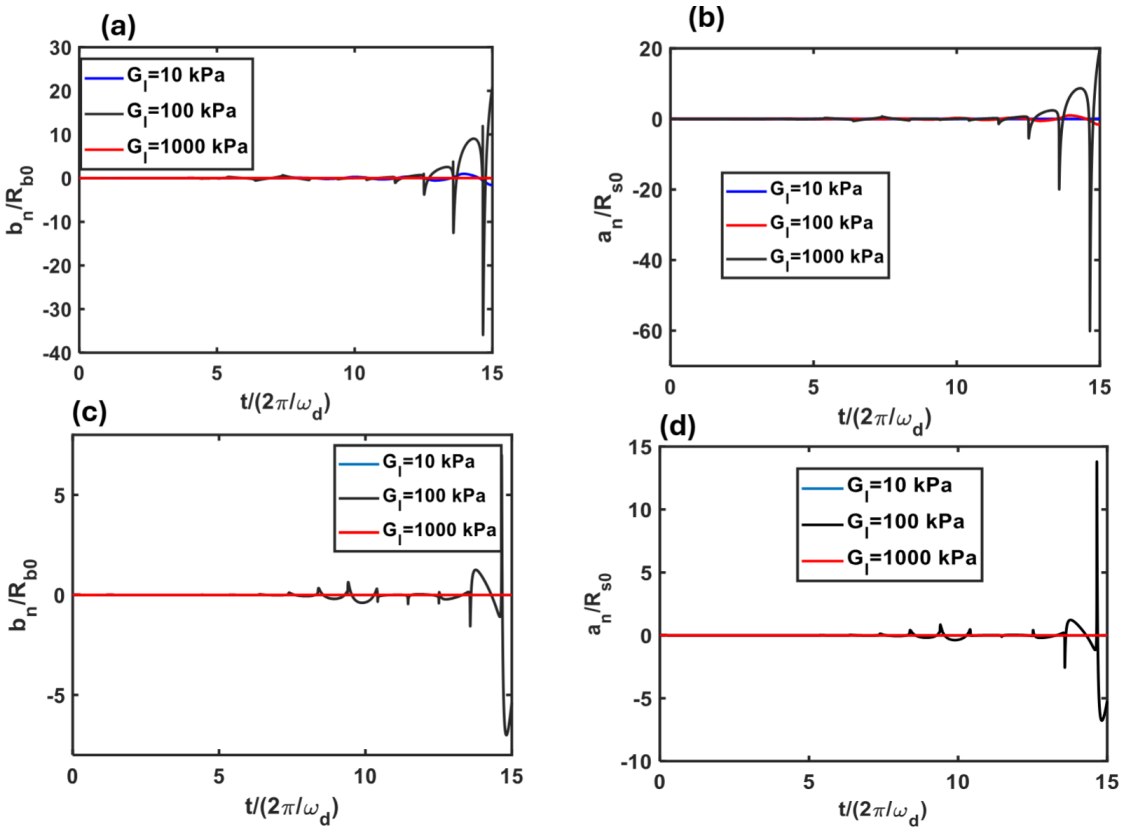

Figure 4.87. Effect of liquid modulus, G_l, on bubble ((a),(c)) and shell ((b),(d)) perturbation amplitudes for (a)-(b), $n = 2$ and (c)-(d), $n = 3$.

In Figure 4.90, phase diagrams are presented for an encapsulated bubble in an unbounded, thick Newtonian liquid. As shown, the unstable regions remain large when the shell thickness is low (Figure 4.90(a), $\delta = 15$ nm) due to the resonance frequency (2.2 MHz) being close to the driving frequency of the acoustic field. However, with thicker shells, the stabilizing effect of the shell becomes evident in the phase diagrams (Figure 4.90(b), $\delta = 150$ nm), where the resonance frequency increases to 7 MHz, as calculated in 4.6.

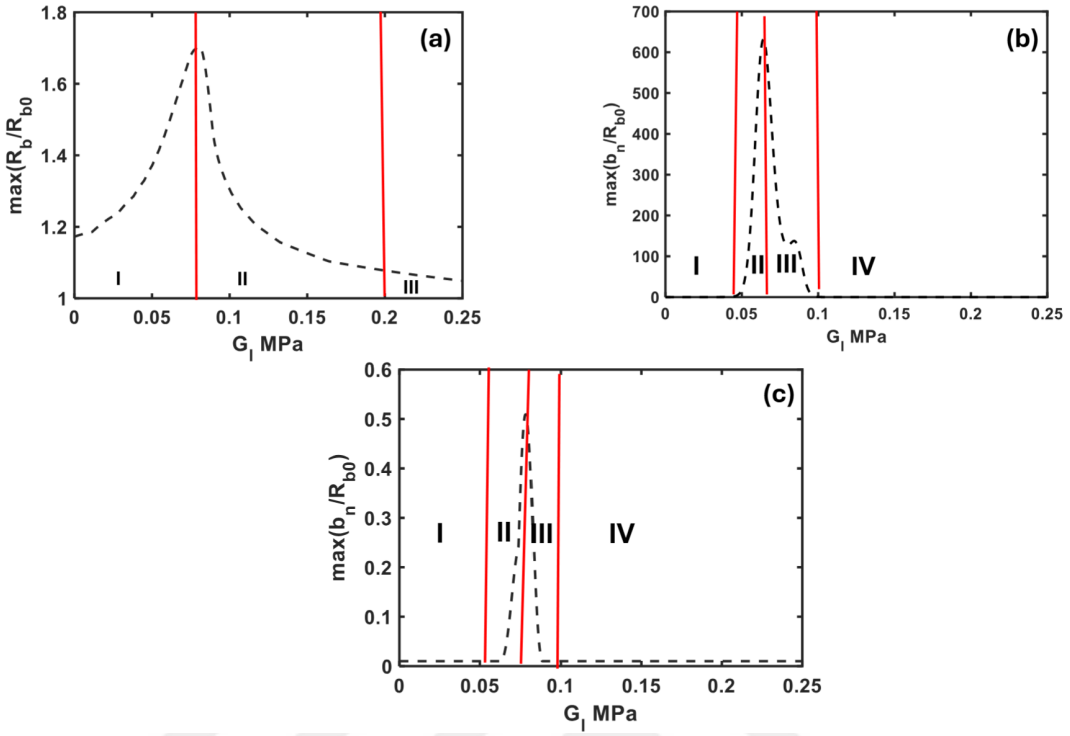

Figure 4.88. Effect of liquid modulus, G_l, on (a) maximum bubble radius, R_b, (b) maximum bubble surface perturbation amplitude, b_n, for $n = 2$, and (c) maximum bubble surface perturbation amplitude, b_n, for $n = 3$.

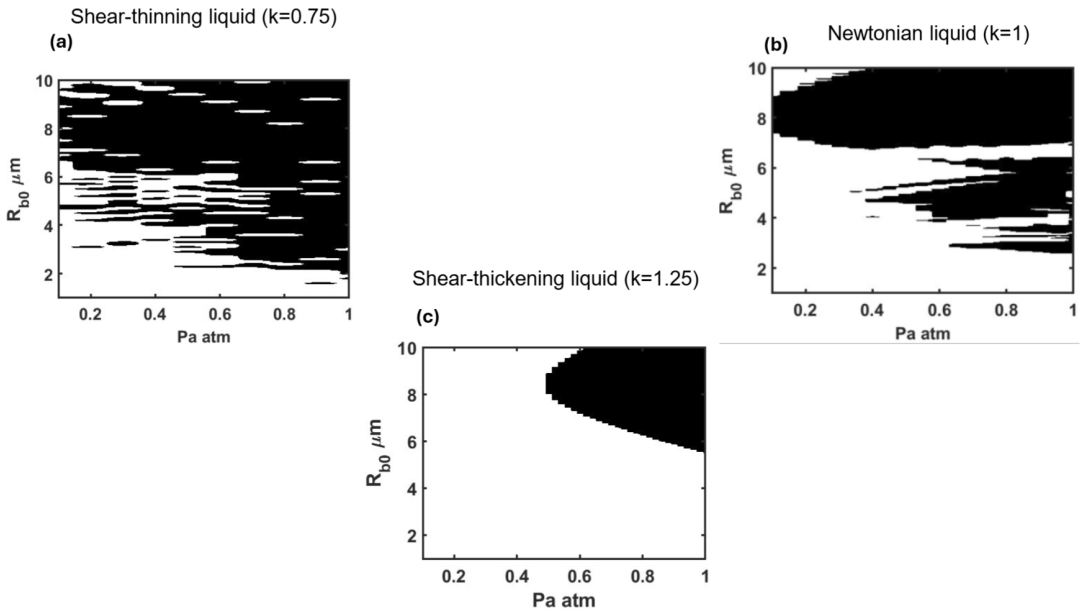

Figure 4.89. Phase diagrams, R_{b0} vs. p_a for bubble in power-law liquid. Surrounding liquid is (a) shear-thinning ($k = 0.75$), (b) Newtonian and (c) shear-thickening ($k = 1.25$).

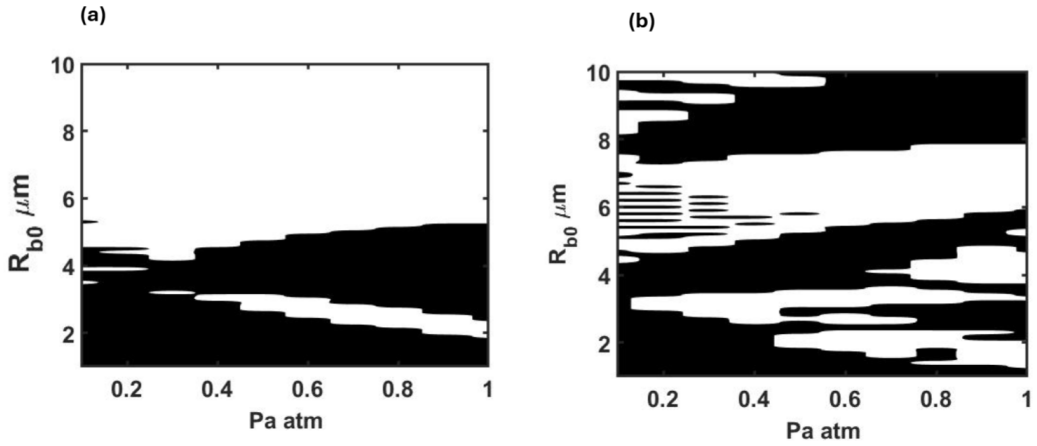

Figure 4.90. Phase diagrams, R_{b0} vs. p_a for an encapsulated bubble in unbounded liquid (a) shell thickness, $\delta = 150$ nm and (b) shell thickness, $\delta = 15$ nm.

4.6. Translational Motion and Bubble-Bubble Interactions

Translational motion and bubble-bubble interactions are critical in various fluid dynamics applications, from industrial processes to biological systems. Understanding the behavior of bubbles as they move through a liquid medium and how they interact with one another is essential for improving technologies like ultrasound imaging, chemical reactors and underwater acoustics. These interactions are influenced by bubble size, proximity, liquid properties and external forces like pressure or temperature. Researchers can optimize processes involving multiphase flows and contribute to advancements in fields ranging from medicine to environmental engineering by analyzing the dynamics of translational motion and bubble-bubble interactions.

In this section, first, the effect of shell thickness, modulus, acoustic field's amplitude, driving frequency, and power-law index is studied for an encapsulated bubble (Section 4.6.1) and two encapsulated bubbles in an unbounded viscoelastic liquid (Section 4.6.2), respectively. The physical properties of the liquid and shell are given in Tables 4.1 and 4.2.liquid and shell are given in Tables 4.1 and 4.2.

4.6.1. Translational Motion of an Encapsulated Bubble

This section investigates the translational motion of an encapsulated bubble in an unbounded viscoelastic liquid by adding the effect of primary Bjerknes force. The primary Bjerknes force is the force exerted directly on a single bubble due to the pressure gradient of the acoustic field. It causes the bubble to move toward either high or low pressure regions, depending on the bubble's natural frequency relative to the driving frequency: in-phase oscillations pull the bubble toward high-pressure zones, while out-of-phase oscillations drive it to low-pressure regions. The study begins by considering the surrounding liquid to be Newtonian. Then, the effect of a viscoelastic liquid is introduced into the model. Both linear and nonlinear viscoelastic models are employed to capture the complex rheological behavior of the liquid and their results are compared to find a parametric range where complex nonlinear models are necessary. The effects of shell modulus, G_s, shell thickness, δ, acoustic field's pressure amplitude, p_a, acoustic field's driving frequency, ω_d, and liquid modulus, G_l, on the translational motion of the bubble are investigated. The acoustic field pressure amplitude is 0.25 atm, and the driving frequency is 7 MHZ, which matches the natural frequency.

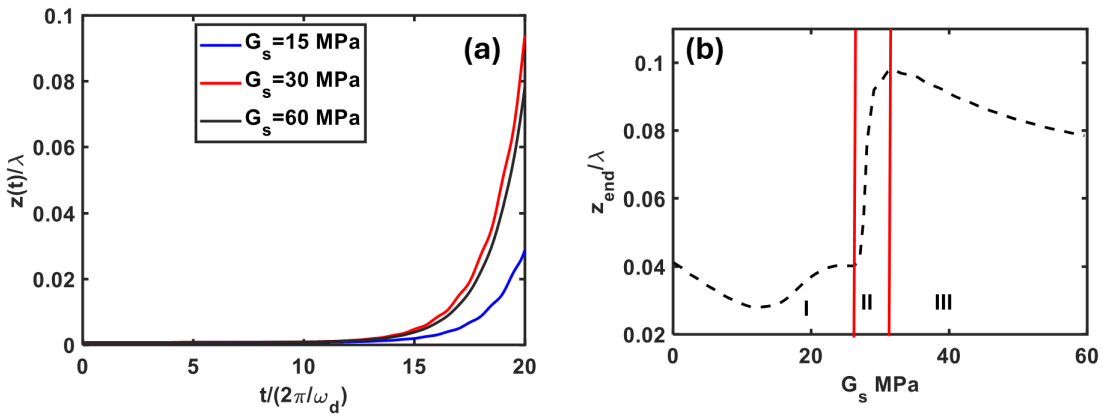

Figure 4.91. Effect of shell modulus, G_s on (a) $z(t)/\lambda$ versus $t/(2\pi/\omega_d)$ and (b) z_{end}/λ obtained after 20 cycle of acoustic pressure.

The effect of the shell modulus (G_s) on the translational displacement of the bubble is examined in Figure 4.91. The shell modulus G_s represents the elastic stiffness of the shell and it plays a significant role in determining how the bubble responds to external forces such as

acoustic waves. Translational displacement, $z(t)$, is normalized by the acoustic wavelength λ. Here, $\lambda = c_L/f_d$ is the wavelength, f_d and c_L are the frequency of the acoustic field and the speed of sound in liquid. As shown in Figure 4.91(a), the relationship between G_s and the dimensionless displacement $z(t)/\lambda$ over time shows a more complex behavior.

Figure 4.91(b) focuses on the final displacement after 20 cycles of the acoustic field to gain further insight into how G_s affects the overall translational displacement. The parameter z_{end}/λ represents the position of a bubble after experiencing prolonged acoustic excitation which allows for the identification of any cumulative effects of the shell modulus over time. Three distinct regions are observed which is similar to the behavior in Figure 4.56(a). The shell is relatively soft In Region 1 which indicats it can deform more quickly in response to the acoustic field. As a result, the translational motion remains limited and the final displacement z_{end}/λ is relatively small. In Region 2, the bubble reaches a threshold where its translational displacement sharply increases as G_s increases. At this point, the bubble can harness the energy from the acoustic field more effectively, resulting in a pronounced displacement. The abrupt increase in z_{end}/λ may be linked to a resonance-like phenomenon where the mechanical properties of the shell match the frequency of the external acoustic excitation which maximizes the translational response. In Region 3, as G_s continues to increase beyond the threshold observed in Region 2, the bubble's translational displacement diminishes slightly. The shell becomes increasingly stiff in this region, restricting the bubble's ability to deform and respond dynamically to the acoustic field. This indicates that overly stiff shells may hinder the bubble's mobility, as the energy from the acoustic field is no longer efficiently transferred into translational motion.

Figure 4.92 presents the influence of the shell modulus (G_s) on both the translational velocity (Figure 4.92(a)) and the radial velocity (Figure 4.92(b)) of the bubble. At lower driving frequency cycles of the acoustic field, the bubble exhibits relatively small translational motion, with its dynamics primarily governed by radial expansion and contraction rather than translational displacement. This behavior can be attributed to the fact that, at lower cycles, the oscillating pressure field does not impart sufficient energy to overcome the resistances from the surrounding liquid and the shell, limiting the bubble's translational motion, as also

observed in the translational displacement shown in Figure 4.91. However, as the number of acoustic cycles increases, a noticeable shift occurs, and the translational motion of the bubble becomes more dominant than its radial velocity particularly after reaching approximately 17 cycles. This indicates a transition in the bubble's dynamic response where the cumulative energy imparted by the acoustic field allows the bubble to overcome the resistance and move more significantly in the translational direction. Furthermore, as observed for translational displacement, the effect of the shell modulus on translational motion exhibits a complex and non-linear relationship. At higher acoustic field cycles, such as after 15 cycles, the effect of G_s becomes more pronounced which influences the bubble's translational motion more noticeably. This observation emphasizes the significant role that the shell modulus plays in bubble dynamics at larger cycle counts, where the interaction between the bubble and the surrounding medium intensifies. It highlights the importance of our research in understanding and predicting the behavior of bubbles under varying acoustic frequencies.

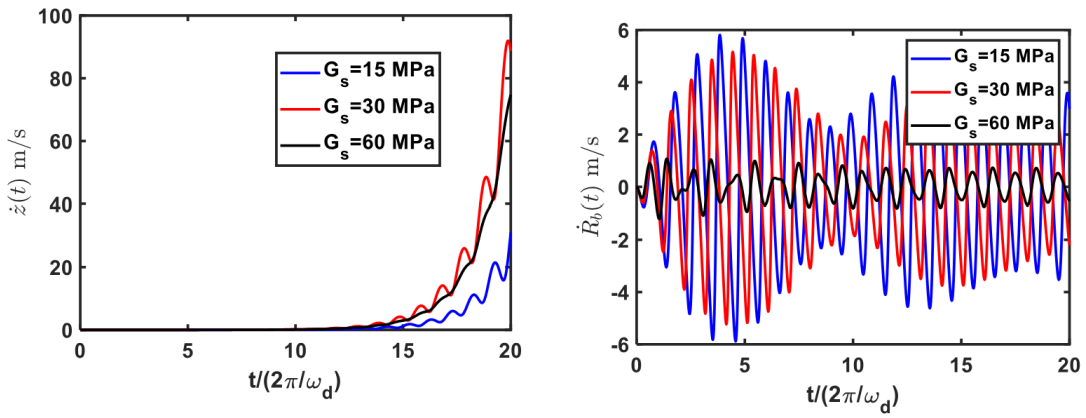

Figure 4.92. Effect of shell modulus, G_s on (a) $\dot{z}(t)$ versus $t/(2\pi/\omega_d)$ and (b) $\dot{R}_b(t)$ versus $t/(2\pi/\omega_d)$.

Figure 4.93 illustrates the effect of G_s on the translational velocity $\dot{z}$ when the driving frequency $\omega_d = 3.5\,\text{MHz} \approx \omega_0/2$ (i.e., the driving frequency is lower than the bubble's natural resonance frequency). In such conditions, it is observed that as G_s decreases, $\dot{z}$ increases slightly which indicates an inverse relationship between the translational velocity and the damping coefficient. When G_s is high, it dampens the radial oscillations, as seen in Figure 4.57, where the amplitude of radial displacement decreases with increasing G_s. In

the sub-resonant regime $\omega_d < \omega_0$, the damping effect is especially pronounced on the radial oscillations. Despite the overall damping of radial oscillations for high G_s, the translational velocity slightly increases with G_s. This suggests that while G_s restricts radial motion, it may enhance energy transfer into translational motion under specific acoustic conditions. Figure 4.94 presents contour plots that illustrate the deviation of the linear model from the nonlinear viscoelastic shell model.

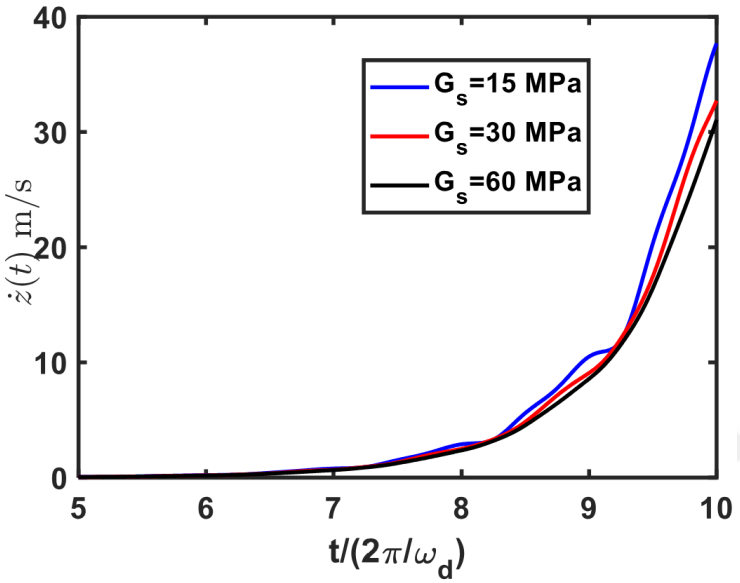

Figure 4.93. Effect of shell modulus, G_s on $\dot{z}(t)$ versus $\dfrac{t}{2\pi\omega_d}$ for $\omega_d = 3.5$ MHz.

The deviation, denoted by χ, is calculated based on the translational motion after 20 cycles. Specifically, χ is defined in Equation 4.8 as:

$$\chi = \left| \frac{\dot{z}_{\text{end, nlin}} - \dot{z}_{\text{end, lin}}}{\dot{z}_{\text{end, nlin}}} \right|, \tag{4.8}$$

where the subscripts lin and nlin refer to the end values of the translational motion derived from the linear and nonlinear viscoelastic shell models, respectively. In Figure 4.94(a), the deviation behavior is similar to that observed in the radial motion depicted in Figure 4.27(b). As shown in Figure 4.94(b), when $G_l = 1$ MPa, the deviation χ is minimal, suggesting that the linear shell model can be effectively used in place of the nonlinear model. This reduced deviation is attributed to the increased natural frequency of the system. The viscoelasticity of the liquid raises the natural frequency of the system to approximately 14 MHz as illustrated in Figure 4.35. For this reason, Figure 4.94(c) examines the case where $\omega_d = 14$ MHz.

Slightly larger deviations are observed compared to Figure 4.94(b) as shown the figure which indicates a higher sensitivity to the driving frequency when it approaches the system's natural frequency.

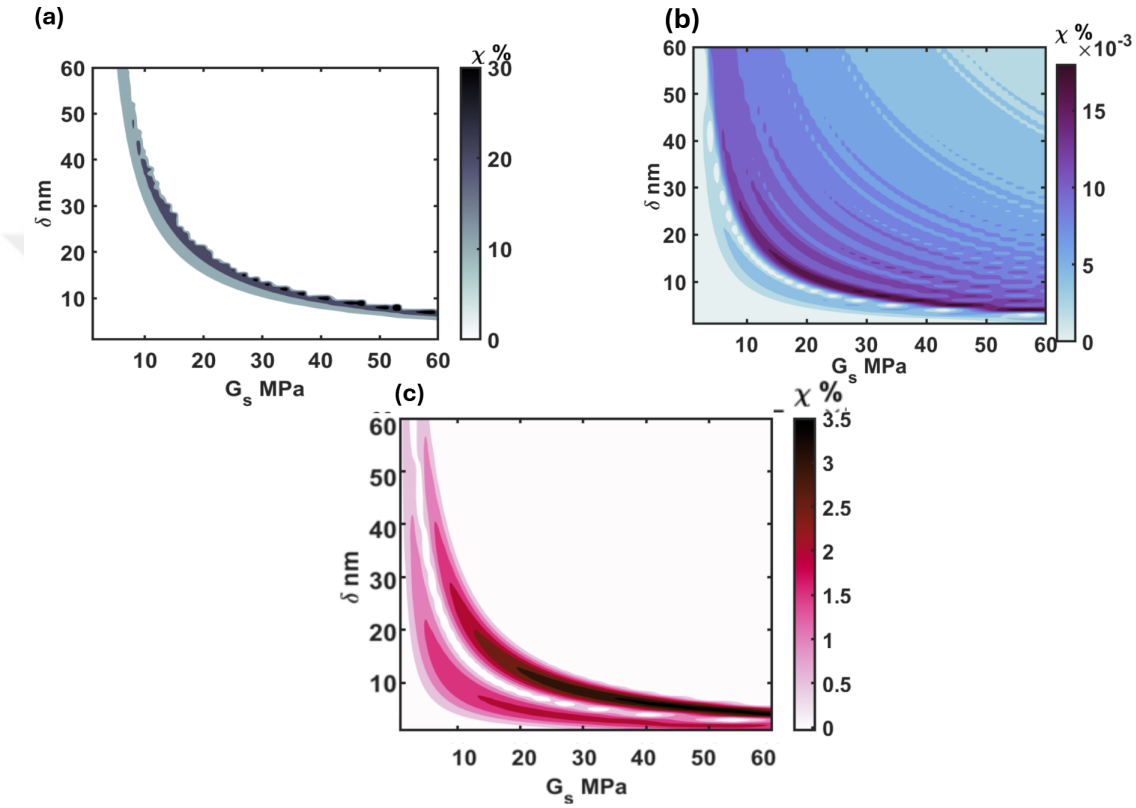

Figure 4.94. Contour plot (δ versus G_s) for (a) $\omega_d = 7$ MHz and $G_l = 0$ MPa, (b) $\omega_d = 7$ MHz and $G_l = 1$ MPa, and (c) $\omega_d = 14$ MHz and $G_l = 1$ MPa show the deviation between shell models.

The impact of acoustic irradiation on the translational motion of the bubble is analyzed in Figure 4.95. Two cases are presented: Figure 4.95(a) shows results for $\omega_d = 7$ MHz and $G_l = 0$ MPa, while Figure 4.95(b) corresponds to $\omega_d = 14$ MHz and $G_l = 1$ MPa. The contribution of the external velocity field v_{ex} (as expressed in Equation 3.248) is either included or excluded from the model in order to isolate and investigate the effect of acoustic irradiation. Additionally, to amplify the effect of acoustic irradiation, the amplitude of the acoustic field is increased to 1 atm. When the elastic properties of the liquid are not considered ($G_l = 0$ MPa), the effect of acoustic irradiation becomes more pronounced As seen in Figure 4.95(a).

The translational motion of a bubble is more strongly influenced by the acoustic pressure gradient without resistance from the viscoelastic behavior of the liquid. This suggests that in an elastic-free medium, the acoustic field can efficiently induce bubble movement with the translational velocity, $\dot{z}$, which reflects the direct impact of the external acoustic force. In contrast, even though the driving frequency $\omega_d = 14$ MHz matches the natural frequency, the effect of acoustic irradiation on the bubble's translational motion is less noticeable in Figure 4.95(b). This can be attributed to the liquid elasticity ($G_=$1 MPa), which dampens the response of the bubble to the acoustic field. The elastic properties of the liquid restrict the radial oscillations of the bubble, which in turn limits the energy transfer from the radial to the translational motion. Consequently, the bubble exhibits less pronounced movement under acoustic irradiation despite the resonance condition.

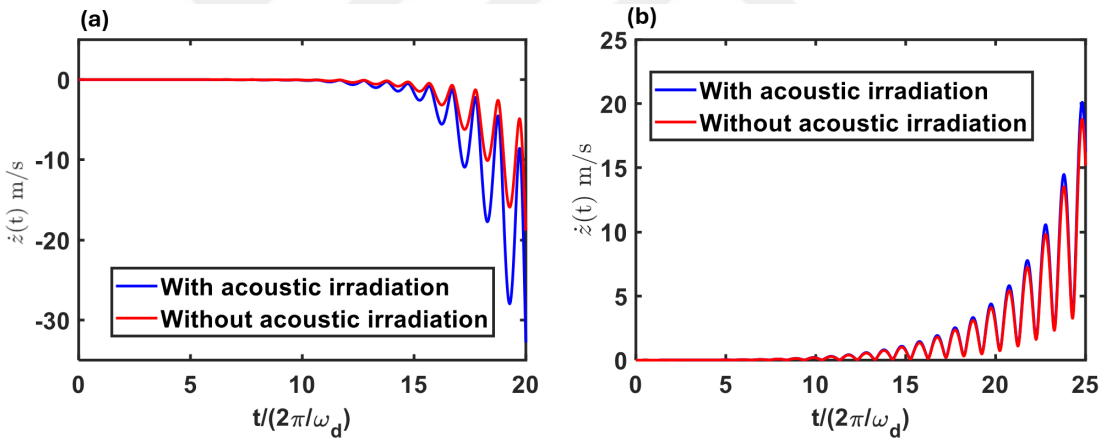

Figure 4.95. Effect of acoustic irradiation on $\dot{z}(t)$ versus $t/(2\pi/\omega_d)$ for (a) $\omega_d = 7$ MHz, $G_l = 0$ MPa and (b) $\omega_d = 14$ MHz, $G_l = 1$ MPa.

4.6.2. Translational Motion of Two Encapsulated Bubbles

In this section, the translational motion of an encapsulated bubble is analyzed, with adding the influence of a second bubble. The study begins by assuming that the surrounding liquid is Newtonian and then the liquid is assumed to be viscoelasitc. The impact of primary Bjerknes forces was investigated in Section 4.6.1. Here, the focus is on the effects of secondary Bjerknes forces which arise from the interaction between two or more oscillating

bubbles. The secondary Bjerknes forces depend on the relative phase of their oscillations leading to either attraction or repulsion. Bubbles experience an attractive force when they oscillate in phase, while out-of-phase oscillations cause repulsion which results in complex motion patterns. These interactions can significantly impact applications such as medical ultrasound and targeted drug delivery, where bubble dynamics are key to effective performance.

To investigate the effects of $1/D$ terms on bubble dynamics, Figure 4.96 displays results for cases where only first-order terms are considered. Section 3.3 discusses the terms of first, second, and third order $1/D$ in detail. In Figures 4.96(a), (c), and (e), both bubbles have an initial radius of $R_{b10} = R_{b20} = 5\,\mu$m, while in Figures 4.96(b), (d), and (f), the radii are $R_{b10} = 5\,\mu$m and $R_{b20} = 1\,\mu$m. The acoustic driving frequency is set to the natural frequency, $\omega_d = 7$ MHz, for a system with two encapsulated bubbles (bubbles 1 and 2). This natural frequency, which is obtained for an encapsulated bubble in a Newtonian unbounded liquid, is illustrated in Figure 4.58 and is defined by Equation 3.158. When the bubbles approach a 1 μm separation, the simulation is stopped to prevent collapse. Both bubbles exhibit similar dynamic behavior when only first-order terms are applied, as shown in Figure 4.96(a), reflecting the typical encapsulated bubble motion predominantly influenced by radial oscillations (see Figure 4.22). The initial center-to-center distance between the bubbles is 19 μm. However, the dynamic differences between bubbles 1 and 2 remain negligible after introducing second- and third-order $1/D$ terms, as illustrated in Figures 4.96 (b), (d) and (f).

In Figure 4.97, the impact of higher-order $1/D$ terms on the translational motion of bubbles is analyzed. When only first-order $1/D$ terms are included, the translational motion amplitude remains relatively low, as shown in Figures 4.97(a) and (b). However, introducing second-order terms significantly increases translational motion amplitude which shows a distinct change in behavior (Figures 4.97(c) and (d)). Without these second-order terms, both configurations—where $R_{b10} = R_{b20} = 5\,\mu$m and $R_{b20} = 1\,\mu\text{m} < R_{b10} = 5\,\mu$m—display low translational motion amplitudes (Figures 4.97(a) and (b)). For the configuration with $R_{b20} = 1\,\mu\text{m} < R_{b10} = 5\,\mu$m, the translational motion of the first bubble gradually approaches zero after approximately six cycles (Figures 4.97 (b), (d) and (f)), while the second bubble

exhibits an oscillatory translational motion.

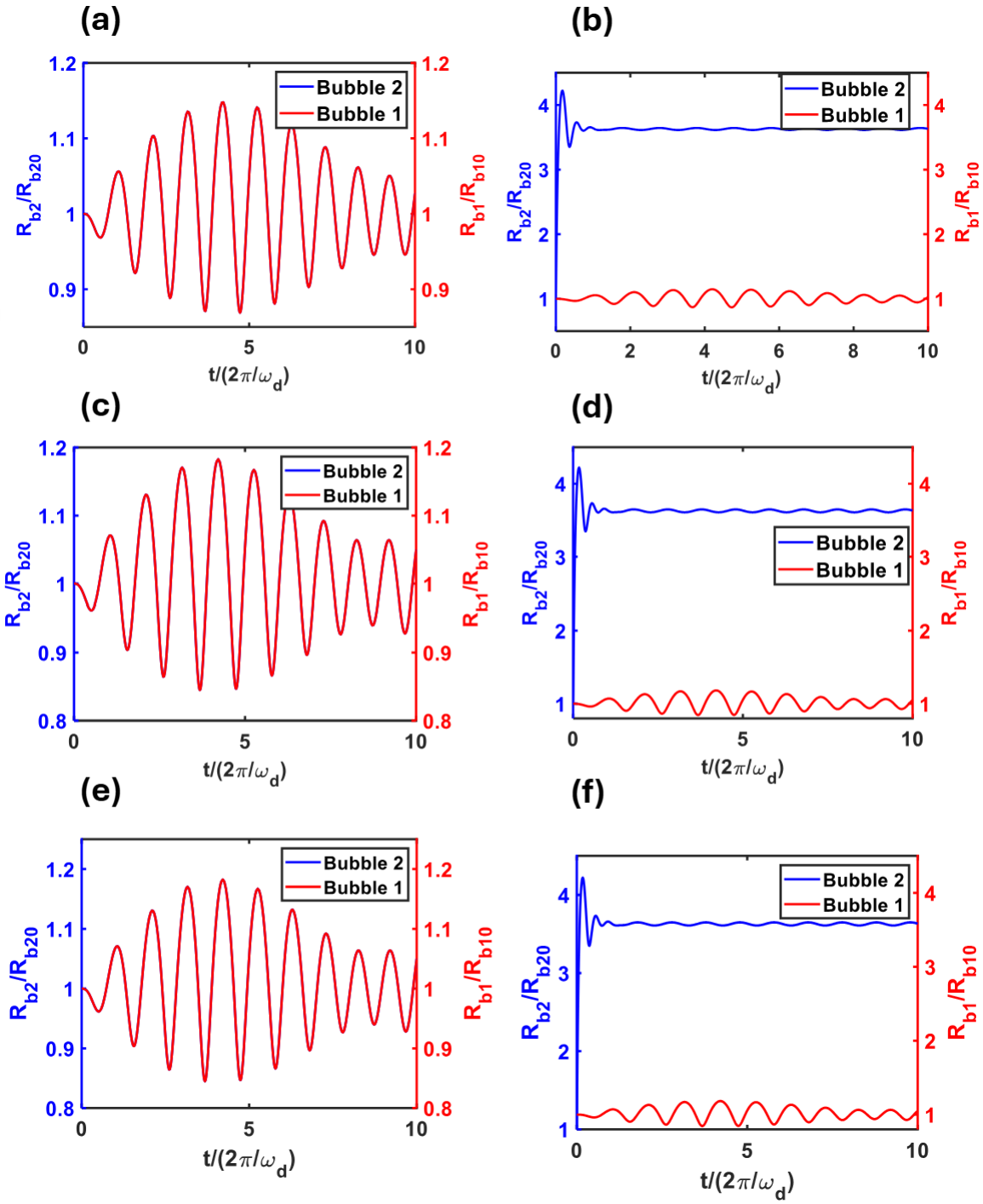

Figure 4.96. (a), (c), (e) $R_b(t)/R_{b0}$ and $R_{b2}(t)/R_{b20}$ versus $t/(2\pi/\omega_d)$ when $R_{b20} = 5\,\mu\text{m} = R_{b10}$ (b), (d), (f) $R_b(t)/R_{b0}$, $R_{b2}(t)/R_{b20}$ versus $t/(2\pi/\omega_d)$ when $R_{b20} = 1\,\mu\text{m} < R_{b10} = 5\,\mu\text{m}$.

This translational behavior inversely mirrors the radial oscillations, where the first bubble ceases motion while the second continues oscillating. Furthermore, differences in bubble size have no significant effect on the inclusion of third-order terms.

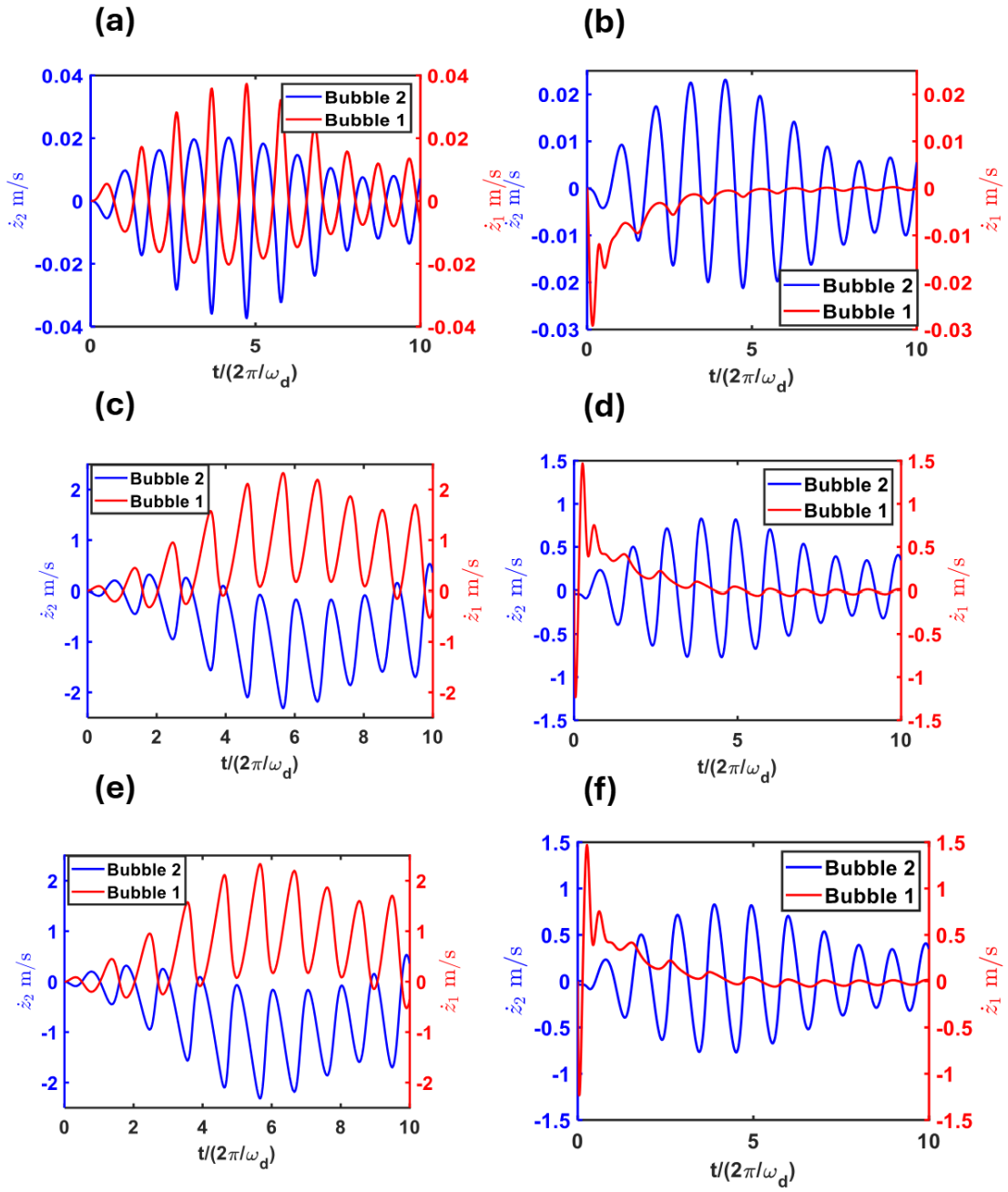

Figure 4.97. (a), (c), (e) $\dot{z}_1(t)$ and $\dot{z}_2(t)$ versus $t/(2\pi/\omega_d)$ when $R_{b20} = 5\,\mu\text{m} = R_{b0}$ (b), (d), (f) $\dot{z}(t)$ and $\dot{z}_2(t)$ versus $t/(2\pi/\omega_d)$ when $R_{b20} = 1\,\mu\text{m} < R_{b10} = 5\,\mu\text{m}$.

In Figure 4.98, the effect of higher-order $1/D$ terms on the center-to-center distance between bubbles, D, is analyzed. Figures 4.98(a) and (b) show results with only first-order terms; Figures 4.98(c) and (d) include second-order terms; and Figures 4.98(e) and (f) incorporate third-order $1/D$ terms. Each figure also examines how varying acoustic field pressure amplitudes affect D. In Figures 4.98(a), (c), and (e), both bubbles have equal initial radii, $R_{b20} = R_{b10} = 5\,\mu$m, while in Figures 4.98(b), (d), and (f), $R_{b20} = 1\,\mu$m, making it smaller than $R_{b10} = 5\,\mu$m.

The distance D changes minimally with only first-order terms, following the trends observed in the translational motion of bubbles (Figure 4.97). At a low amplitude of acoustic pressure ($p_a = 0.05$ atm), D remains consistent regardless of the inclusion of second- or third-order terms, indicating that higher-order terms have a limited effect on D in weak acoustic fields. However, as the acoustic pressure amplitude increases, the impact of second-order terms becomes more pronounced. Under stronger acoustic excitation, D increases significantly when second-order terms are included (Figures 4.98(c) and (d)), suggesting that these higher-order terms enhance bubble separation by amplifying the response to the acoustic field. However, the addition of third-order $1/D$ terms does not produce a noticeable difference between Figures 4.98(c) and (e) and Figures (d) and (f).

When $R_{b20} = 1\,\mu\text{m} < R_{b10} = 5\,\mu$m, the distance D between the bubbles is not affected by higher pressure amplitudes. (Figures 4.98(b), (d) and (f)). This size discrepancy dampens the sensitivity of the smaller bubble to nonlinear inter-bubble forces, thereby reducing the influence of the amplitude of the acoustic field.

Figure 4.99 depicts the secondary Bjerknes forces exerted on bubbles 1 (F_{ex1}) and 2 (F_{ex2}) with varying orders of $1/D$ terms. In Figure 4.99 (a), only first-order $1/D$ terms are included, both F_{ex1} and F_{ex2} oscillate with similar amplitudes around 10^{-8} N, displaying periodic attractive and repulsive interactions. With the addition of second-order $1/D$ terms in Figure 4.99(c), the oscillations in F_{ex1} and F_{ex2} become slightly stronger which indicates an enhancement in the interaction strength between the bubbles. This results in more pronounced oscillatory forces, although the amplitude increase remains modest.

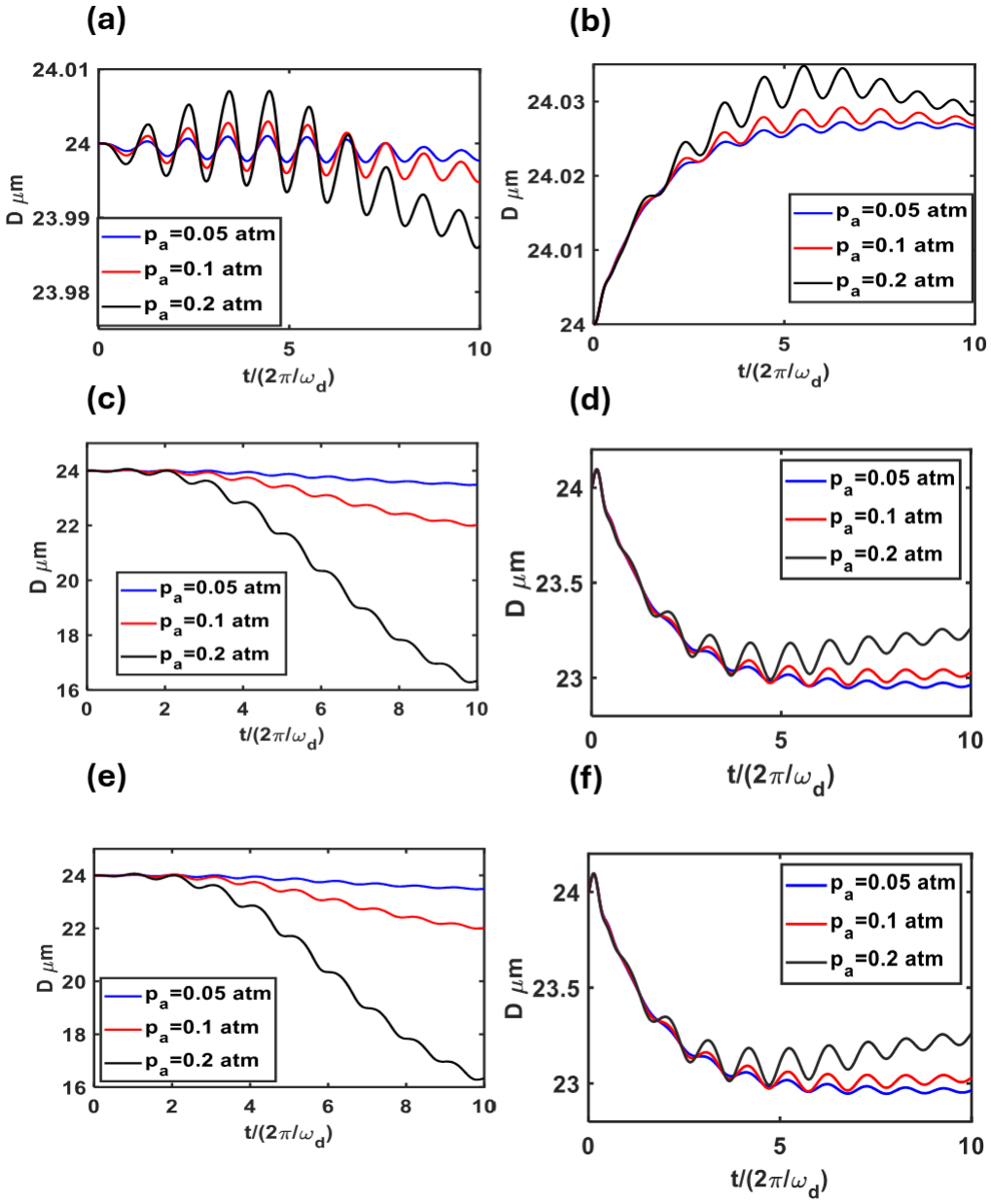

Figure 4.98. (a), (c), (e) D versus $t/(2\pi/\omega_d)$ when $R_{b20} = 5\,\mu\text{m} = R_{b0}$ (b), (d), (f) D versus $t/(2\pi/\omega_d)$ when $R_{b20} = 1\,\mu\text{m} < R_{b10} = 5\,\mu\text{m}$.

In Figure 4.99(e), where third-order $1/D$ terms are introduced, the forces experience an unimportant amplification, reaching the order of 10^{-7} N. When $R_{b20} = 1\,\mu\text{m} < R_{b10} = 5\,\mu\text{m}$, the force F_{ex1}, exerted on the first bubble by the second bubble, becomes zero after six cycles. This occurs because, the translational motion of the first bubble gradually diminishes to zero in this configuration. As a result, the Bjerknes force acting on the second bubble, F_{ex2} is solely influenced by radial motion. However, F_{ex1} is affected by both translational ($\dot{z}_2$) and

radial motion, causing it to completely diminish after approximately six cycles.

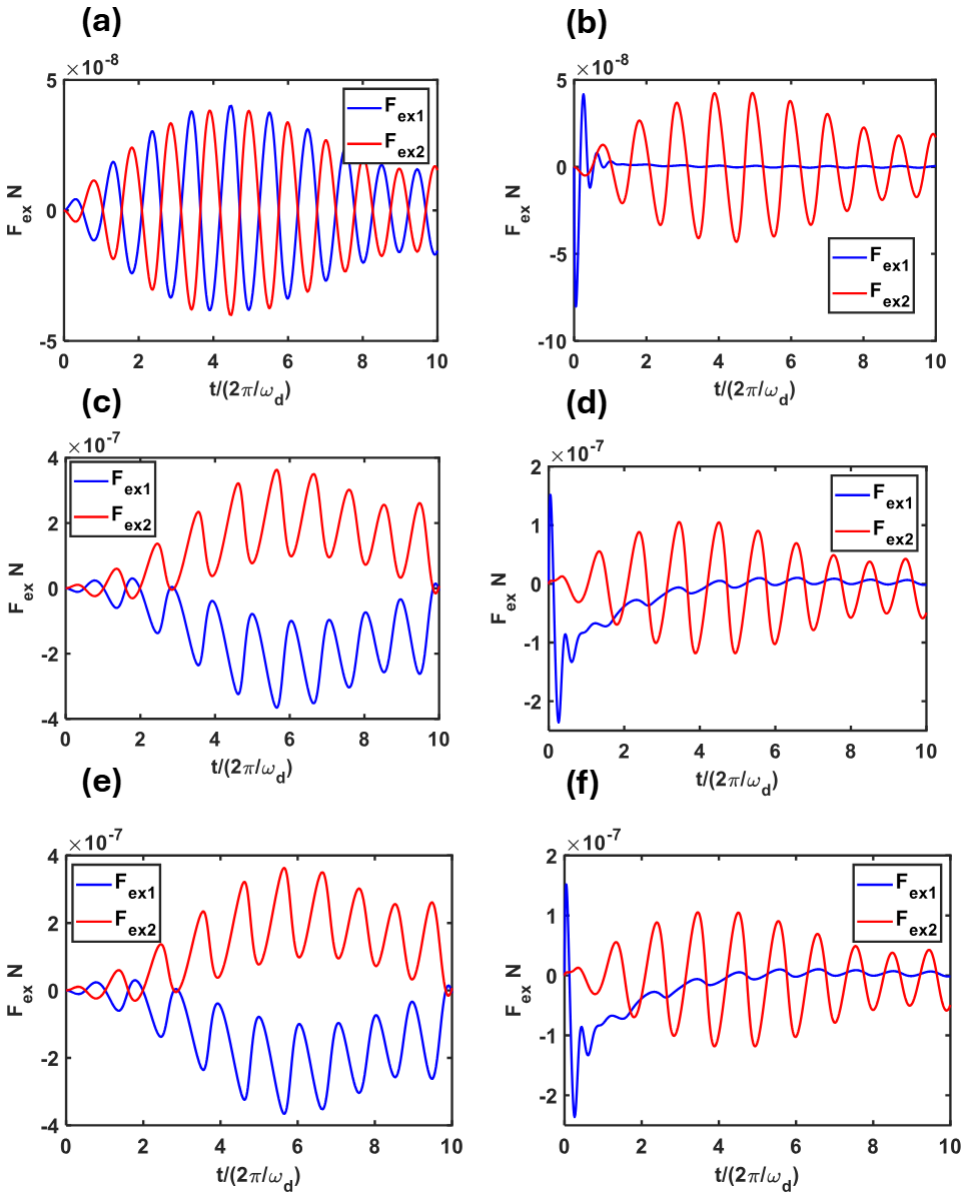

Figure 4.99. F_{ex} versus $t/(2\pi/\omega_d)$ when first order (a)-(b), second order (c)-(d), and third order (e)-(f) terms of $1/D$ are considered. In (a), (c) and (e), $R_{b0} = 5\ \mu$m$= R_{b0}$ and In (b), (d) and (f), $R_{b0} = 5\ \mu$m $, R_{b02} = 1\ \mu$m.

Including of second-order terms introduces significant nonlinear effects, leading to stronger and more dynamic inter-bubble interactions. This progression demonstrates that as the order of the $1/D$ terms increases, the secondary Bjerknes forces become more intense

and intricate, amplifying the interaction between the bubbles. Therefore, this intense effect of secondary Bjerknes forces increases the amplitude of the translational motion of bubbles (Figures 4.96(e) and 4.97(e)). In Figures 4.99 (d) and (f), the bubble radii are set to $R_{b10} = 1\,\mu$m and $R_{b20} = 5\,\mu$m. The magnitudes of the Bjerknes forces are relatively small compared to Figure 4.99(b) in this case and the significance of third-order $1/D$ terms becomes less pronounced. In Figure 4.100, the behavior of bubbles in a viscoelastic medium, characterized by its modulus G_l, which reflects the liquid's elastic properties, is modeled. The liquid behaves like a Newtonian fluid when $G_l = 0$. A critical effect of introducing viscoelasticity is an increase in the system's natural frequency. The system exhibits a natural frequency of 7 MHz without elasticity as shown in Figure 4.22 and defined in Equation 3.158. As the elasticity of the liquid increases, the effective stiffness surrounding the bubbles also increases, raising the system's natural frequency to 14 MHz (for $G_l = 1$ MPa), as illustrated in Figure 4.36 and defined in Equation 3.157. In Figure 4.100, the driving frequency is set to 14 MHz. Higher values of G_l not only increase the natural frequency but also dampen both the radial (Figures 4.100(a)–(b)) and translational (Figures 4.100(c)–(d)) motions of the bubbles. Additionally, when the elastic modulus is high, the distance between the bubbles remains nearly constant (Figure 4.100(e)). In Figure 4.101, the deviation between results obtained from models incorporating third-order and first-order $1/D$ terms is shown. The deviation χ is defined in Equation 4.9 as,

$$\chi = \frac{\min(D)_3 - \min(D)_1}{\min(D)_3}, \tag{4.9}$$

where subscripts 3 and 1 represent the minimum bubble distances derived from the third- and first-order models after 10 cycles. The initial center-to-center bubble distance is set to 24 μm. Figure 4.101(a) examines how shell thickness (δ) and shell modulus (G_s) influence χ. The plot shows contour bands of χ, with values ranging from light to dark shades which represents higher deviation. The black region indicates a significant discrepancy between the results of the third- and first-order models where χ reaches its highest values. The initial radii of bubbles 1 and 2 are set to 5 μm. In Figure 4.101(a), the surrounding fluid is assumed to be Newtonian, with an acoustic driving frequency of 7 MHz and an amplitude of 0.1 atm. At $\delta = 15$ nm and $G_s = 15$ MPa, the system's natural frequency matches the driving frequency of 7 MHz which results in a resonance condition. Close to the resonance region

(darker region), the oscillations of the bubbles become more pronounced which leads to larger amplitude changes in the bubble dynamics. This intensified response means that the influence of higher-order terms (such as the third-order $1/D$ term) becomes more significant, causing greater deviation from the first-order model predictions.

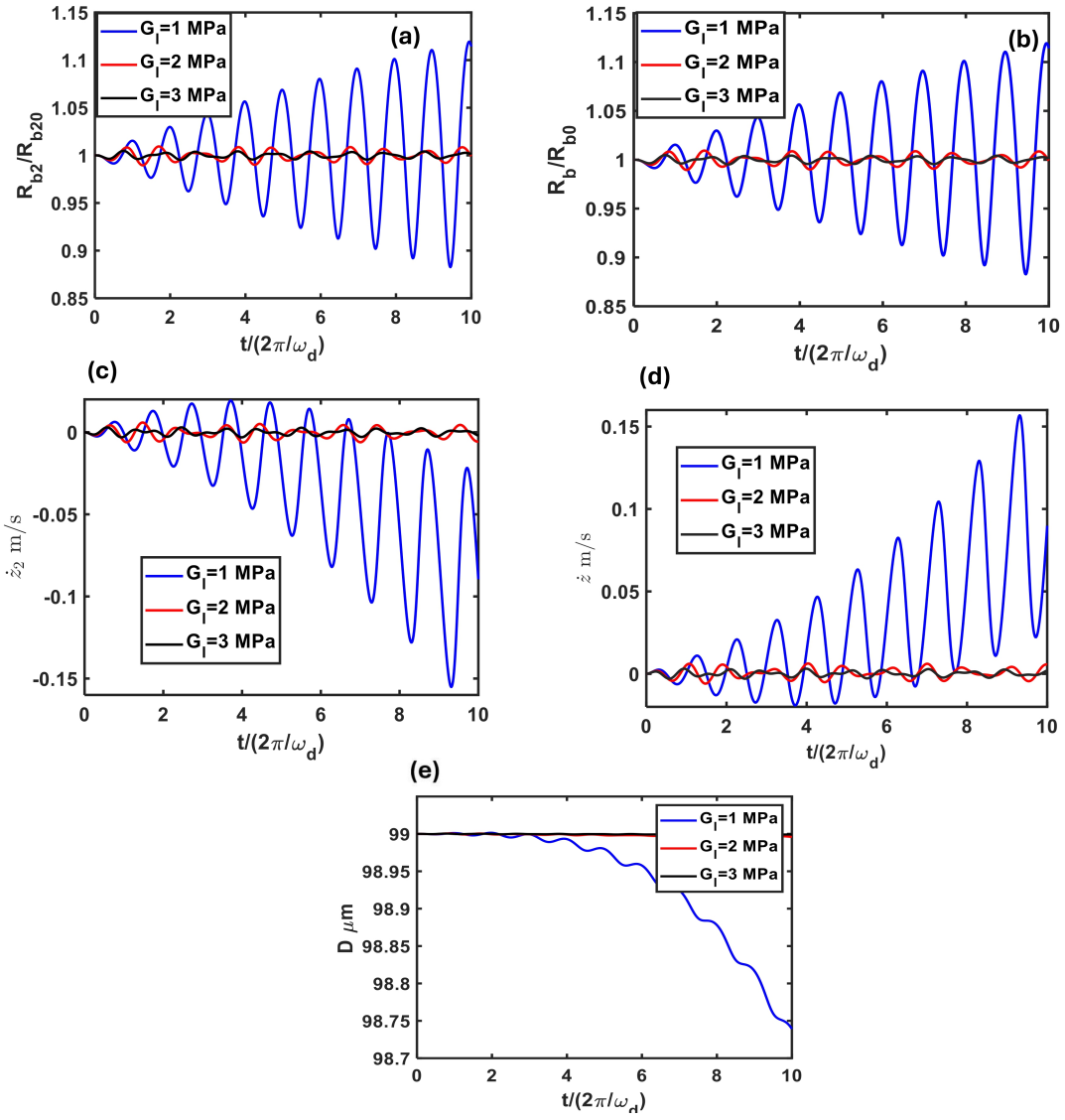

Figure 4.100. Effect of liquid modulus on (a) $R_{b2}(t)/R_{b20}$ versus $t/(2\pi/\omega_d)$, (b) $R_{b1}(t)/R_{b10}$, versus $t/(2\pi/\omega_d)$, (c) $\dot{z}_2$ versus $t/(2\pi/\omega_d)$, (d) $\dot{z}_1$ versus $t/(2\pi/\omega_d)$ and (e) D versus $t/(2\pi/\omega_d)$.

The surrounding fluid is assumed to be viscoelastic and the effects of pressure amplitude (p_a) and the modulus of the viscoelastic liquid are examined in Figure 4.101(b). A

higher deviation (χ) is observed at high pressure amplitudes and low viscoelastic moduli when the driving frequency ω_d is 7 MHz. Increased viscoelasticity dampens both radial and translational oscillations which reduces nonlinear behavior and thereby decreasing χ. In Figure 4.101(c), the driving frequency $\omega_d = 14$ MHz matches the natural frequency of the bubble in an unbounded viscoelastic liquid with $G_l = 1$ MPa. Similar to Figure 4.101(a), resonance conditions at this frequency lead to an increase in the deviation χ, highlighting the amplified effect of higher-order terms at resonance.

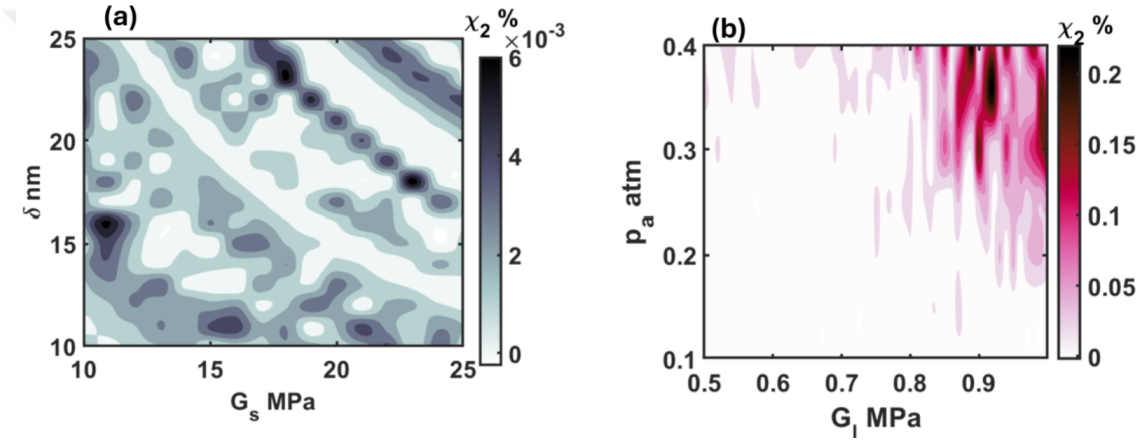

Figure 4.101. Contour plot (a) (δ versus G_s), ($G_l = 0$ and $\omega_d = 7$ MHz), (b) p_a versus G_l, ($\omega_d = 7$ MHz) and (c) p_a versus G_l ($\omega_d = 14$ MHz) for χ.

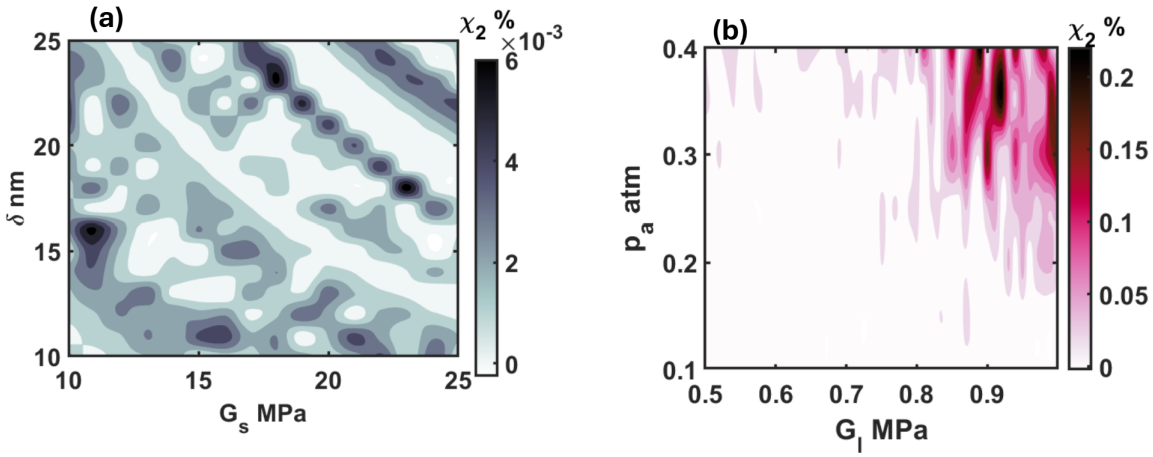

Figure 4.102. Contour plot (a) (δ versus G_s), ($G_l = 0$ and $\omega_d = 7$ MHz), and (c) p_a versus G_l ($\omega_d = 14$ MHz) for χ.

The radial deviation, (χ_2), between results obtained from models incorporating third-order and first-order $1/D$ terms is presented in Figure 4.102 . The deviation χ_2 is defined as $\chi_2 = \frac{\max(|R_{b1,3}|)-\max(|R_{b1,1}|)}{\max(|R_{b1,3}|)}$, where subscripts 3 and 1 represent the maximum bubble radius derived from the third- and first-order models after 10 cycles. As also observed in Figure 4.96, the effect of $1/D$ terms is minimal on the radial motion of the bubbles. The initial radii of bubbles 1 and 2 set to 5 μm. Figure 4.102(a) illustrates the effect of shell modulus and thickness on the deviation, χ_2, with $\omega_d = 7$ MHz and a pressure amplitude of 0.1 atm. The surrounding liquid is assumed to be Newtonian and the initial center-to-center distance between the bubbles is 24 μm. Unlike Figure 4.101(a), the influence of $1/D$ terms on χ_2 is minimal. In Figure 4.102(b), the effect of the liquid modulus (G_l) and pressure amplitude (p_a) on χ_2 is examined. Again, in contrast to Figure 4.101(c), the impact of G_l and p_a on χ_2 remains minimal, even when the acoustic driving frequency matches the natural frequency. This suggests that the higher-order $1/D$ terms have a negligible influence on the radial deviation under these conditions.

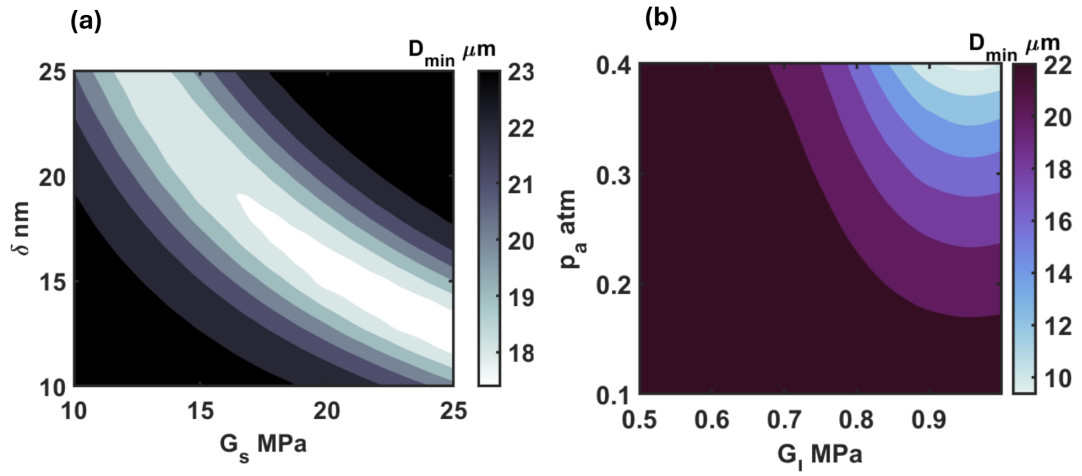

Figure 4.103. Contour plot (p_a versus ω_d) for the minimum distance between bubbles (a) $R_{b0} = R_{b02} = 5$ μm and (b) $R_{b0} = 5$ μm $R_{b02} = 1$ μm and $\omega_d = 7$ MHz.

The contour plots in Figure 4.103 depict the minimum distance ($D_{\min}$) between two bubbles as a function of shell thickness (δ) and shell modulus (G_s). The color scale represents $D_{\min}$ where darker shades indicating smaller distances between the bubbles. The initial radii of both bubbles are identical at 5 μm, with a driving frequency of $\omega_d = 7$ MHz in Figure

4.103(a). The surrounding liquid is assumed to be Newtonian. The plot shows a region in the middle where $D_{\min}$ is smallest which suggest a resonance region. This region corresponds to the area in Figure 4.101(a) where the maximum deviation between models is observed. The effects of pressure amplitude (p_a) and liquid viscoelasticity (G_l) on $D_{\min}$ are investigated in Figure 4.103(b), with $\omega_d = 14$ MHz. Again, near the resonance region ($G_l \approx 1$ MPa), $D_{\min}$ reaches its smallest values which indicates that resonance enhances bubble interactions and reduces the separation distance between them.

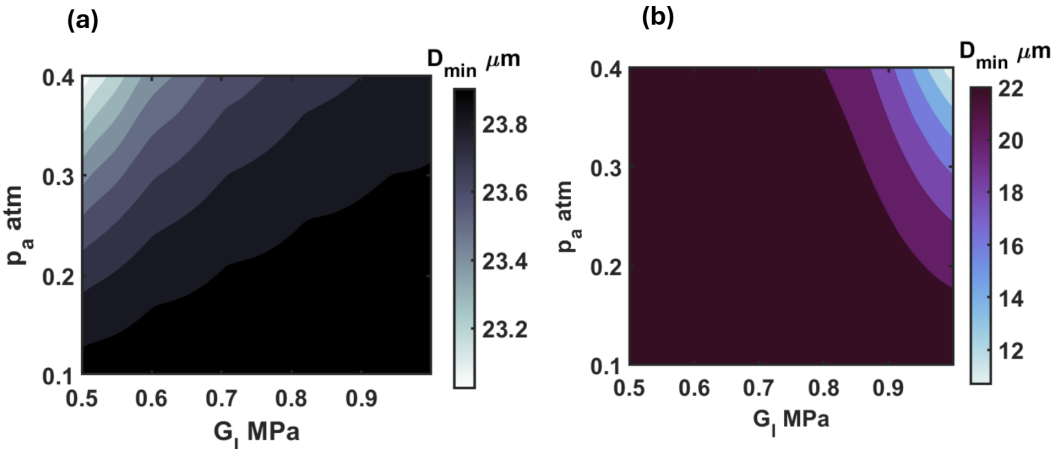

Figure 4.104. Contour plot (p_a versus ω_d) for the minimum distance between bubbles without the effect of encapsulation (a) $R_{b0} = R_{b02} = 5$ μm and $R_{b0} = 5$ μm $R_{b02} = 1$ μm and $\omega_d = 4$ MHz.

In Figure 4.104, the contour plots illustrate the minimum distance ($D_{\min}$) between two non-encapsulated bubbles as a function of pressure amplitude (p_a) and liquid modulus (G_l). Unlike Figure 4.103, these plots show the behavior of free bubbles under the same acoustic parameters which focuses on encapsulated bubbles. Here, the initial radii of bubbles 1 and 2 are both 5 μm. The driving frequencies are $\omega_d = 7$ MHz and $\omega_d = 14$ MHz, respectively in Figures 4.104(a) and (b).

The minimum distance values for non-encapsulated bubbles are lower than those for encapsulated bubbles when comparing Figure 4.104(a) with Figure 4.103(a). This difference is again related to the natural frequency of the system. When the driving acoustic frequency matches the system's natural frequency, the minimum distance between the bubble

centers decreases, as observed in Figure 4.103(b) for encapsulated bubbles.

The observed behavior in the contour plots can be attributed to the interplay between acoustic pressure amplitude, acoustic frequency and the secondary Bjerknes forces acting on the bubbles. The oscillations of each bubble become more intense at higher pressure amplitudes, which leads to stronger secondary Bjerknes forces. When these forces are sufficiently strong, they drive the bubbles closer together, which reduces $D_{\min}$. Higher pressure amplitudes and lower frequencies typically result in stronger Bjerknes forces and reduced $D_{\min}$ in a Newtonian liquid, as seen in Figures 4.103. However, the elastic component resists bubble deformation and restricts their movement, thereby limiting the attraction between bubbles in a viscoelastic medium. Overall, viscoelasticity reduces the bubbles' responsiveness to the acoustic field which dampens oscillations and mitigating the secondary Bjerknes forces. This results in a relatively constant minimum distance $D_{\min}$ which could be beneficial in applications requiring controlled bubble separation in complex media such as in biomedical or material processing environments where bubble coalescence must be minimized.

4.7. Acoustic Droplet Vaporization

Perfluorocarbon (PFC) microdroplets can be transferred from liquid to gas when stimulated by an external acoustic pulse. These microdroplets are known as phase-change contrast agents (PCCAs). PCCAs made from volatile PFCs, such as decafluorobutane (DFB, C_4F_{10}) and octafluoropropane (OFP, C_3F_8) which can be easily vaporized under the effect of an acoustic pulse. As a result, a PFC droplet transforms into a vapor bubble. This method is an innovative application in ultrasound medicine. This section aims to develop a theoretical model to obtain the vaporization dynamics of volatile PFC droplets and to validate this model against in vitro experimental data. The surrounding liquid is assumed to follow a power-law constitutive model to represent the blood viscosity.

The parameters for media 1 and 2 used in the simulations are detailed in Table 4.4, reflecting gaseous and liquid OFP and DFB at 37°C. Here, m_v is the molar mass of the vapor, c_p is the specific heat of the vapor at constant pressure, T_{s0} is the saturation temperature at

the reference pressure p_{s0}. σ is the interfacial tension at bubble/droplet and droplet/liquid interfaces, μ_d is the droplet viscosity, c_d is the specific heat of the droplet, κ_d is the thermal conductivity of the droplet, and $\mathscr{L}$ is the latent heat of evaporation. Medium 3 is defined with $p_0 = 101.3$kPa, $\rho_l = 993.25$ kg/m^3, $\sigma_o = 0.0035$ N/m, and $c = 1520$ m/s, which correspond to water at $T_0 = 37^\circ$C. A two-cycle, 8MHz, 500kPa Gaussian pulse is used and the initial bubble radius R_{b0} is set to 0.1 μm [12, 17].

Table 4.4. Material properties of different PFCs used in simulations [12, 17].

	m_v kg/mol	c_p J/(kg K)	T_{s0} ^{o}C	p_{s0} kPa	σ_i mN/m	ρ_d kg/m^3	μ_d μPa · s	c_d	κ_d W/(mK)	$\mathscr{L}$ (kJ/kg)
OFP	$188.02 \cdot 10^{-3}$	1028.5	-36.79	101.3	2.629	1601	108.25	1268.5	0.0385	242.85
DFB	$238.03 \cdot 10^{-3}$	892	-2.081	101.3	6.025	1594	188.9	1113.5	0.0405	239.7

In Figures 4.105(a) and (b), the effect of droplet diameter on the bubble diameter oscillations are observed. Here, $D_b(t)$ is the time-dependent bubble behavior. Notably, after the complete vaporization of the droplet, the color of the line changes from red to blue. At this point, the surface tension of the bubble-host liquid interface is recalculated. The experimental data validating the model were obtained from the study detailed in [17]. In Doinikov et al. [12], the simulated results were adjusted to fit the experimental data [17] using the least squares method. This involved varying the viscosity μ_l of the host liquid and the surface tension σ_i between the PFC vapor and the host liquid while keeping all other parameters constant. The initial values for μ_l and σ_i were set to the viscosity of water (0.001 Pas) and the surface tension of the air-water interface (0.07 N/m), respectively. The optimal values of μ_l and σ_i are listed in the captions of Figures 4.105 (a) and (b). After using the calculated values from Doinikov [12], the simulations fit the experimental data well.

In Figure 4.105(a) and b, the initial droplet radii are 3.7 μm and 2 μm, respectively. As observed from the Figures that the whole droplet vaporizes approximately at the same point however, the maximum bubble diameter is higher when the initial droplet diameter is higher.

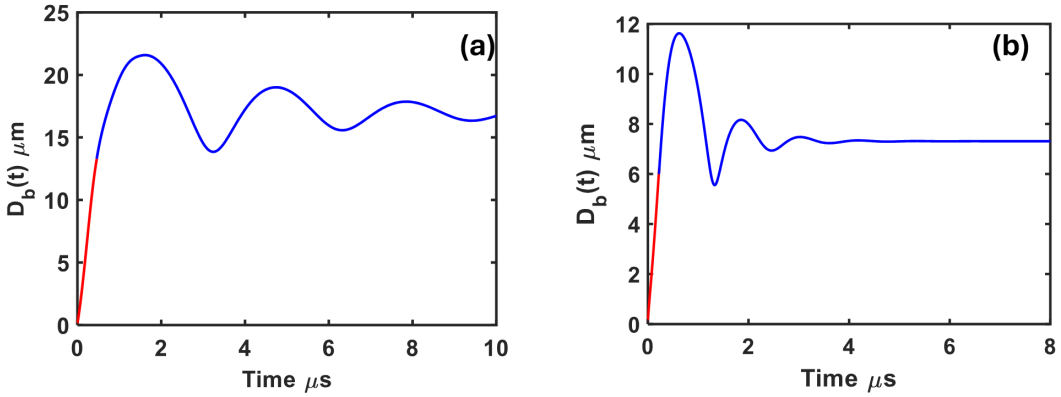

Figure 4.105. Bubble diameter, $D_b(t)$ versus time for (a) $D_0 = 3.7$ μm and $D_0 = 2$ μm. The best-fit values of μ_l and σ_i are (a) $\mu_l = 0.0065$ Pa s, $\sigma_i = 0$ N/m; (b) $\mu_l = 0.02$ Pa s, $\sigma_i = 0.25$ N/m.

Figure 4.106 is obtained to simulate the bubble surface temperature versus time for different initial bubble diameters, in Figure 4.106(a), the initial droplet radius is 3.7 μm and in Figure 4.106(b), the initial droplet radius is 2 μm. Figure 4.107 indicates the behavior of normalized mass flux ($G/(\omega R_{b0}\rho_d)$) versus time for two different cases: in Figure 4.107(a), the initial droplet radius is 3.7 μm and in Figure 4.107(b), the initial droplet radius is 2 μm. When the bubble surface temperature increases (Figure 4.106(a)) initially, mass flux also increases Figure 4.107(b) (gas evaporates to the liquid phase). In evaporation, convection accelerates the process by transferring heat to the liquid surface and removing vapor from the interface, facilitating a higher evaporation rate. In condensation, convection aids by removing latent heat from the liquid surface and bringing vapor closer to the condensing region, thereby speeding up the phase change. Therefore, convection works in opposing ways in these processes: in evaporation, it supplies heat and removes vapor, while in condensation, it dissipates heat and facilitates vapor transport to the surface. In Figure 4.108, the effect of the initial droplet radius on the diameter of the bubble is examined. Unlike in Figure 4.105, the bubble is subjected to Gaussian pressure for a longer duration. The pressure is turned off and then reapplied when the droplet has fully evaporated. The figures show that the maximum bubble radii in all cases are larger than those in Figure 4.105. Beyond this point, ultrasound exposure increases, meaning that it is cycled off and on again precisely at the point of complete droplet evaporation.

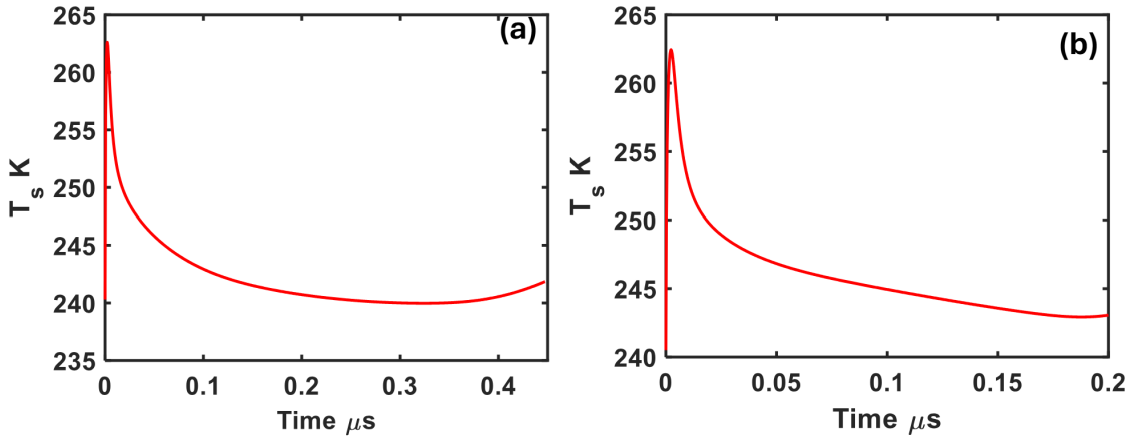

Figure 4.106. Bubble surface temperature versus time for (a) $D_0 = 3.7$ μm and $D_0 = 2$ μm.

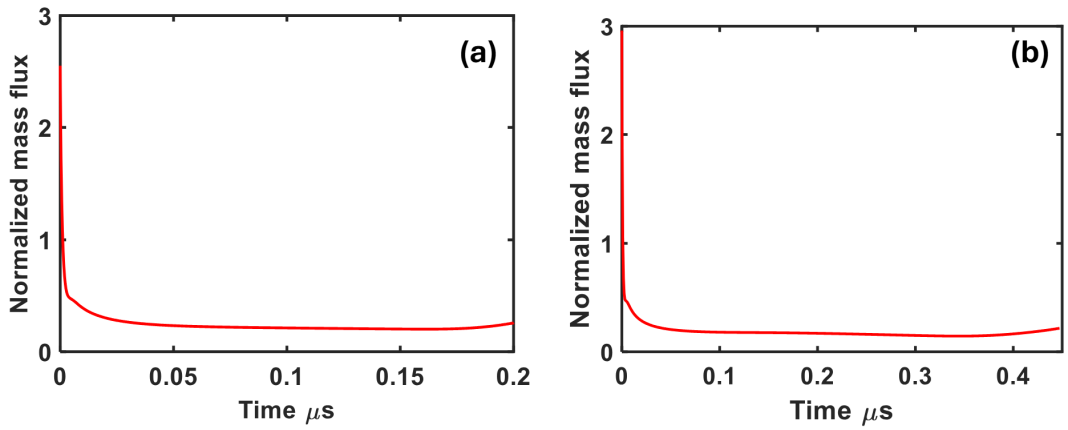

Figure 4.107. Normalized mass flux versus time. for (a) $D_0 = 3.7$ μm and $D_0 = 2$ μm.

In Figures 4.109(a) and (b), the effects of the pressure amplitude and driving frequency of the acoustic field on the diameter of the bubble are analyzed. The initial droplet diameter is assumed to be 2.7 μm. As expected, the maximum diameter of the bubble also increases with an increase in the pressure amplitude. When the pressure amplitude increases by a factor of 10 (from 5 to 50 atm), the maximum diameter of the bubble increases by 100%. In comparison to the effect of the pressure amplitude, the system is much more sensitive to changes in the acoustic field's driving frequency. At a driving frequency of $\omega_d = 4$ MHz, the bubble collapses at approximately $t \approx 1.7$ μs, illustrating a rapid response to acoustic forcing. However, at a higher driving frequency of $\omega_d = 16$ MHz, the bubble quickly reaches its equilibrium diameter without undergoing collapse. In this case, the equilibrium diameter is smaller than the equilibrium diameter observed at $\omega_d = 8$ MHz. It is suggested that higher

frequencies suppress bubble expansion because of shorter oscillation periods.

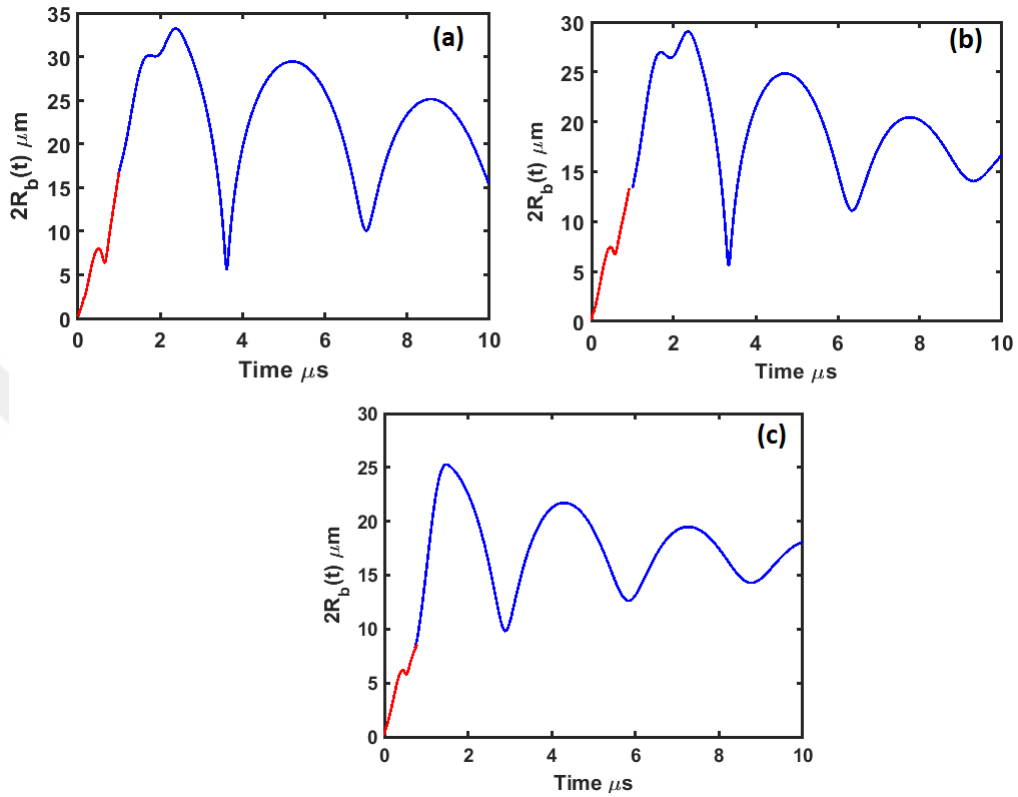

Figure 4.108. Bubble diameter, $2R_b(t)$ versus time for (a) $D_0 = 5.7$ μm, (b) $D_0 = 3.7$ μm, and (c) $D_0 = 2.7$ μm. The best-fit values of μ_l and σ_i are (a) $\mu_l = 0.006$ Pa s, $\sigma_i = 0$ N/m; (b) $\eta_3 = 0.0065$ Pa s, $\sigma_i = 0$ N/m; (c) $\mu_l = 0.009$ Pa s, $\sigma_i = 0$ N/m; (c) $\mu_l = 0.02$ Pa s, $\sigma_i = 0.25$ N/m.

Figure 4.110 illustrates the effect of the power-law index, k, on the bubble dynamics for two different initial droplet diameters. Specifically, Figure 4.110(a) corresponds to an initial droplet diameter of $D_0 = 2.7$ μm, while Figure 4.110(b) presents the results for a larger initial droplet diameter of $D_0 = 3.7$ μm. For smaller droplets, the difference in behavior between shear-thinning ($k < 1$) and Newtonian liquids is not relatively evident. However, a more significant divergence occurs when $k > 1$ indicates a shear-thickening liquid. In this case, the bubble rapidly reaches an equilibrium diameter smaller than the equilibrium diameter in a Newtonian liquid. This suggests that shear-thickening fluids provide greater resistance to bubble expansion. Unlike the Newtonian and shear-thinning cases, the bubble

in a shear-thickening fluid undergoes two rebounds before its diameter reduces to zero, indicating the possibility of bubble collapse. When the initial droplet diameter is larger, as shown in Figure 4.110(b) for $D_0 = 3.7$ μm, the behavior differs. The bubble does not collapse and the bubble diameter reaches its equilibrium diameter in shear-thinning liquids. However, in shear-thickening liquids, the bubble still reaches an equilibrium diameter smaller than that in the Newtonian case. This indicates that shear-thickening fluids tend to suppress bubble expansion more effectively than Newtonian fluids, regardless of the initial droplet size. Furthermore, the bubble in the shear-thinning fluid avoids collapse, whereas the shear-thickening case results in an equilibrium diameter smaller than in the Newtonian case.

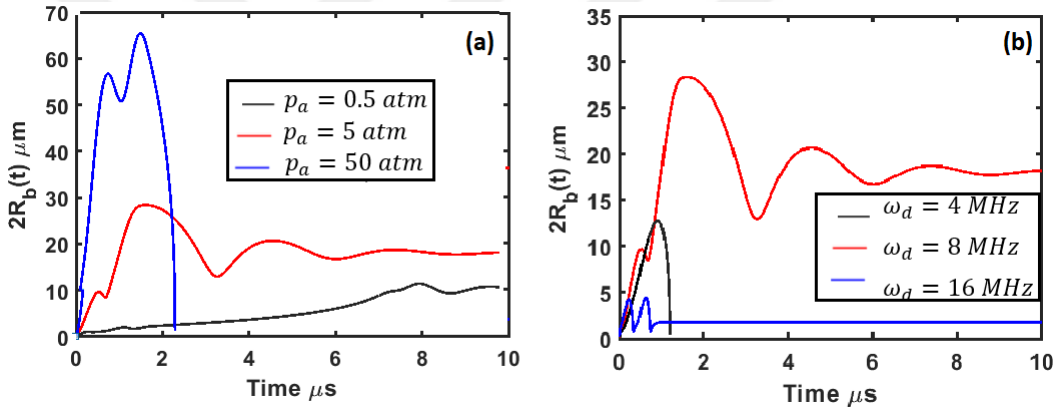

Figure 4.109. Effect of (a) acoustic pressure amplitude, p_a and (b) acoustic driving frequency, ω_d on bubble diameter, $2R_b(t)$.

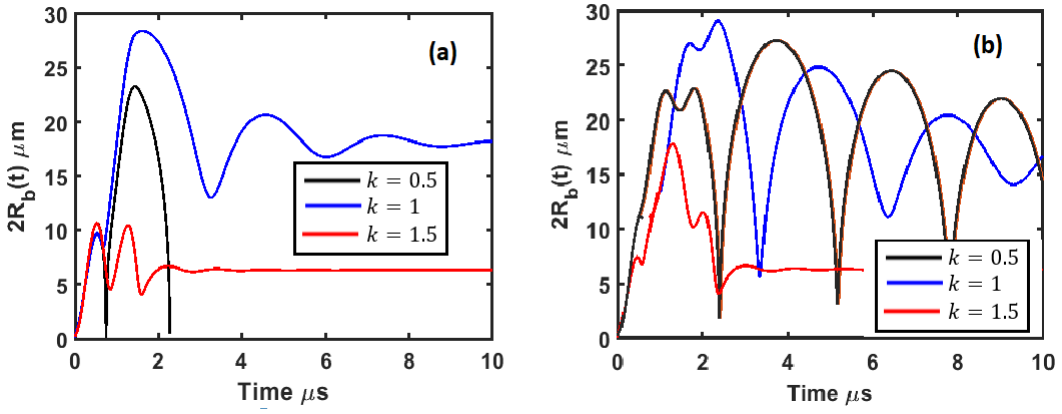

Figure 4.110. Effect of power-law index, k for (a) $D_0 = 2.7$ μm and (b)$D_0 = 3.7$ μm.

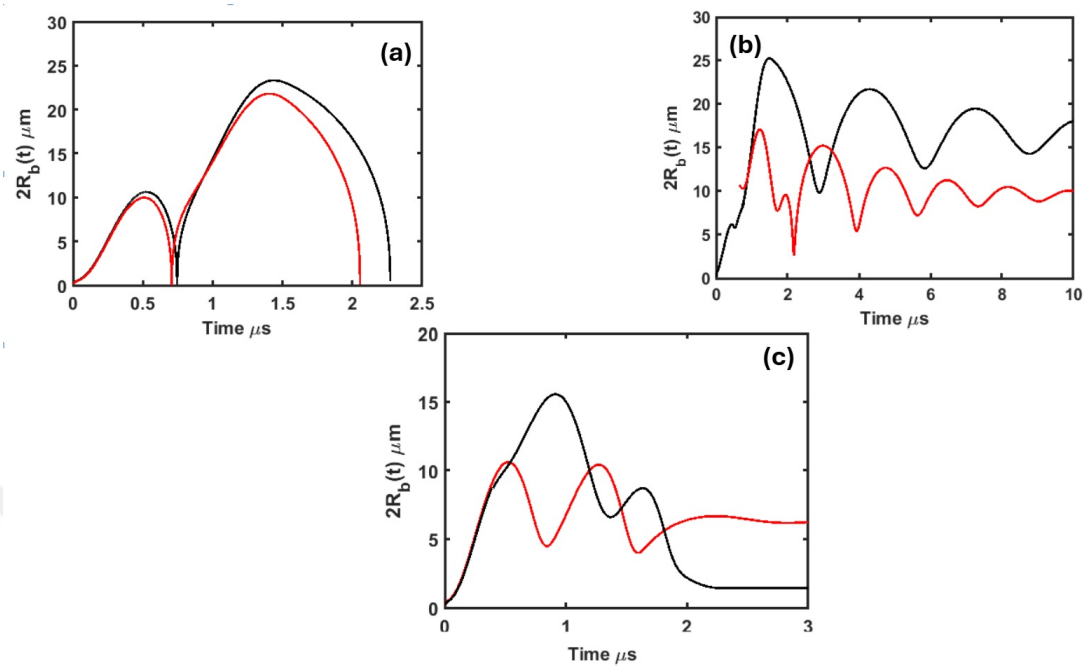

Figure 4.111. Bubble diameter versus time for (a) shear-thinning liquids, (b) Newtonian liquids and (c) shear-thickening liquids. Here, $D_0 = 2.7$ μm. The red and black colors indicate decafluorobutane and octafluoropropane droplets.

Figure 4.111 shows how the power-law index of the host-liquid affects bubble dynamics in a DFB or OFB droplet. In Figure 4.111(a), the power-law index is $k = 0.5$, representing a shear-thinning liquid; in Figure 4.111(b), $k = 1$, a Newtonian liquid; and in Figure 4.111(c), $k = 1.5$, a shear-thickening liquid. In a Newtonian liquid (Figure 4.111(b)), the bubble in a DFB droplet reaches an equilibrium diameter smaller than in an OFB droplet under similar conditions. When the host liquid is shear shear (Figure 4.111 (c)), the bubble in the DFB droplet reaches equilibrium at a diameter larger than that of an OFB droplet. Finally, the acoustic droplet vaporization (ADV) threshold time, t_{ADV}, is presented in Figure 4.112 for various acoustic pressure amplitudes and frequencies. The drug is encapsulated within the droplet, and upon complete evaporation of the droplet, the drug is released at the target site. Consequently, the ADV time, which corresponds to the complete evaporation process, is directly associated with the drug release time. As illustrated in the figure, t_{ADV} decreases with increasing pressure amplitudes or frequencies of the acoustic field.

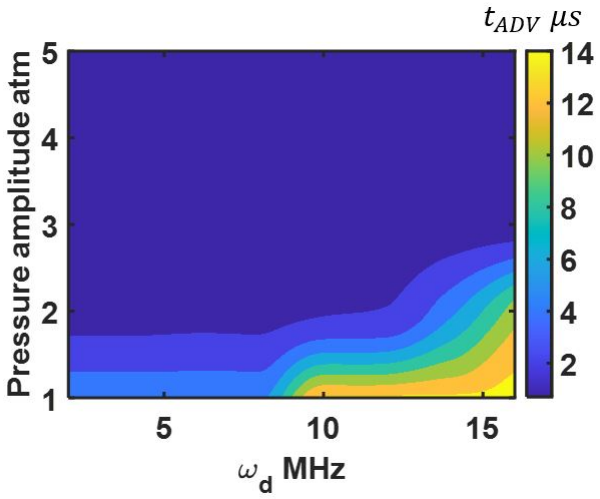

Figure 4.112. Contour plot (pressure amplitude versus frequency of acoustic field) for acoustic droplet vaporization threshold, t_{ADV}.

4.8. Contour Maps for Biomedical Applications

In this section, a parametric range is established to ensure the safe and effective application of ultrasound-mediated microbubbles. Sections 4.4, 4.5, and 4.6 address three key criteria essential for achieving efficient drug delivery while maintaining safety during the application. These criteria are:

- $12\,\mu\text{m}^2 <$ Bubble surface area $< 1200\,\mu\text{m}^2$
- $100\,\text{Pa} <$ Wall shear stress $< 800\,\text{Pa}$
- Distance between bubbles $> 1\,\mu\text{m}$

In Figure 4.113, the contour maps are obtained where these three criteria are satisfied. The first map is obtained for the acoustic field properties which are the pressure amplitude and the frequency and the second map is obtained for the shell properties. Here, the properties of acoustic field and shell are chosen which can be adjusted before the biomedical application.

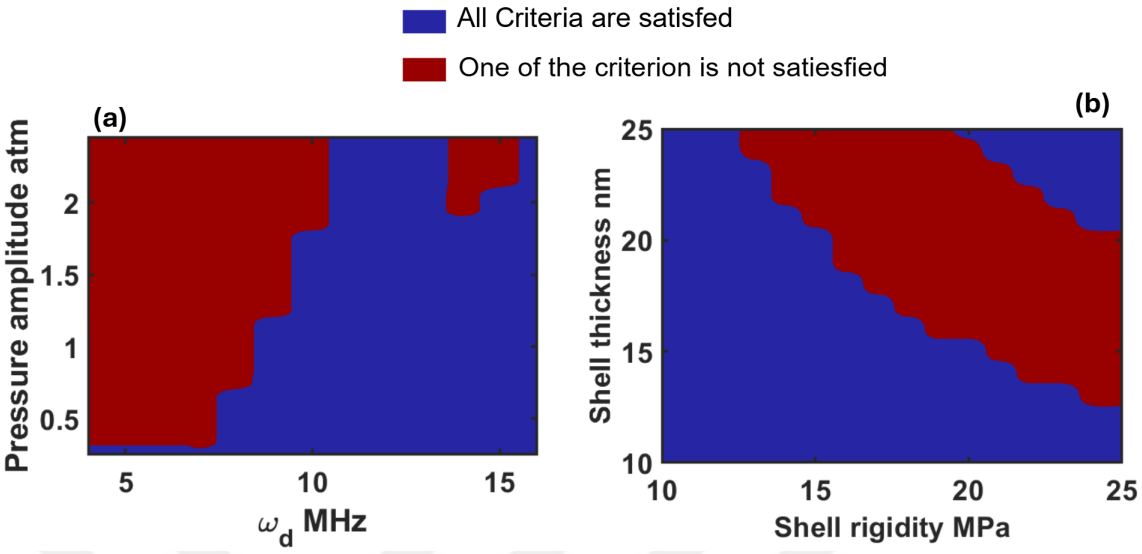

Figure 4.113. Contour maps for (a) pressure amplitude versus frequency (ω_d), and (b) shell thickness versus shell modulus, highlighting the regions for efficient and safe biomedical application.

5. CONCLUSIONS AND RECOMMENDATIONS

5.1. Conclusion

Microbubbles are notable for their ability to improve visualization of blood vessels and tissue perfusion. Microbubbles enhance imaging and drug delivery across the blood-brain barrier which are encapsulated by lipid, protein or polymer shells. They can also potentially improve stroke treatment by improving thrombolysis and improving molecular imaging sensitivity. Challenges remain while acoustic fields offer a promising approach to reduce chemotherapeutic drug doses. The complex interactions between microbubbles and the surrounding liquid have become a critical focus in biomedical research. Microbubble technology could transform these areas of medicine, leading to more effective targeted treatments and more precise imaging techniques.

This dissertation focuses on theoretical modeling of microbubble oscillations within an elastic microvessel. This research aims to optimize drug delivery systems by improving the understanding of microbubble interactions with blood vessels, which contributes to more accurate diagnoses and better patient outcomes. The stabilizing microbubble shell, which plays a critical role in its behavior, remains a factor to be fully explored.

This dissertation explores microbubbles' dynamics within a blood vessel surrounded by elastic tissue, subjected to an acoustic field relevant to critical therapeutic applications. The research presents several innovative contributions to bubble dynamics and ultrasound-mediated therapies, addressing significant gaps in the existing body of work. By integrating microvessel properties, the study offers a more accurate representation of in vivo conditions, which is previously neglected. A nonlinear Neo-Hookean shell model reveals critical deviations from conventional linear models while accounting for blood's non-Newtonian and viscoelastic nature. Unlike studies that employ overly complex models, this work identifies parameter ranges where simplified models are effective, providing a practical strategy to reduce computational demands. Furthermore, developing contour maps based on safety and efficacy

metrics—such as wall shear stress, bubble surface area, and inter-bubble distances—offers clinicians guidelines for safer and more effective therapies. These advancements address critical gaps in the literature and pave the way for optimizing ultrasound-mediated drug delivery in practice. The dissertation is organized into four main sections.

The first part examines the spherical oscillations of a bubble (Sections 3.1 and 4.4). Various non-Newtonian models for the surrounding liquid and a nonlinear Neo-Hookean model for the bubble shell are used which provides a realistic alternative to simpler Newtonian and linear shell models. Parameters for the bubble's surface area and the wall shear stress exerted by the surrounding liquid are identified to support safer and more effective biomedical applications.

The second part (Sections 3.2 and 4.5) explores bubble shape stability. Controlling shape stability is essential for targeted drug delivery, as it regulates bubble break-up. Shape instability at the interface triggers bubble break-up, while stable shape oscillations enhance contrast in ultrasound imaging which improves blood vessel imaging quality. Thus, stabilizing bubbles in the bloodstream extends their lifespan and enhances the imaging duration.

The bubble translational motion and the bubble-bubble interactions (Sections 3.3, 4.6.1 and 4.6.2) are analyzed in the third part. Understanding these interactions is vital for therapeutic applications, as they allow microbubbles to cluster at target sites, concentrating drug release and minimizing healthy tissue exposure. Properly managed interactions also help to maintain bubble size which prevents premature rupture and ensuring intact delivery. Reducing acoustic shadowing through controlled spacing enhances ultrasound imaging which facilitates accurate guidance and real-time monitoring of drug delivery.

The fourth part addresses acoustic droplet vaporization (ADV) (Sections 3.4 and 4.7). ADV is an innovative drug delivery method that uses ultrasound to transform liquid droplets. These droplets circulate safely until they reach the target site where focused ultrasound induces rapid vaporization into gas bubbles. This phase transition releases therapeutic agents and oscillating bubbles that enhance therapeutic effects. For example, drug-loaded perfluo-

rocarbon droplets accumulate near tumors and ultrasound vaporizes them into bubbles. The expanding bubbles improve drug penetration which increases cancer cell drug uptake without raising the dosage, thereby reducing side effects.

5.1.1. Spherical Oscillations

This part of the dissertation explores the behavior of an encapsulated bubble within a spherical liquid cell which is enclosed by an infinite elastic solid. The surrounding liquid is modeled as either a Newtonian or a non-Newtonian liquid such as a Carreau-Yasuda fluid or a viscoelastic fluid to simulate the complex rheological properties of blood. The bubble shell is characterized by either linear elasticity or Neo-Hookean hyperelasticity.

To validate the results of the complex code and equations, initial analytical solutions are derived. For this purpose, it is first assumed that the bubble exists in an unbounded liquid. Subsequently, the effects of a non-Newtonian fluid and bubble encapsulation are incorporated into the analysis.

For applications that require precise and responsive bubble oscillations, such as biomedical therapies, it is crucial to optimize the properties of the shell and elastic solid. The resonance frequency is determined parametrically. The shell and elastic solid properties enhance bubble oscillations depending on their values near resonance. These properties dampen the oscillations when the natural frequency of the system exceeds the driving frequency of the acoustic field. If the modulus of the shell is too low or the thickness is too thin, the shell has minimal impact. In contrast, an excessively high modulus or thick shell restricts the bubble motion. Thus, the properties of the shell must be adjusted to the application's specific needs, allowing effective oscillation without being too restricted by a rigid shell.

This dissertation also explores a parameter range where both the liquid's non-Newtonian properties and the shell's nonlinear behavior play a vital role, requiring an advanced model to capture bubble oscillation dynamics accurately. Resonance occurs when the shell modulus and thickness produce a natural frequency near the driving frequency of the acoustic

field which causes the results from the nonlinear shell model to diverge from those of the linear shell model. The acoustic field pressure amplitude, cavity radius and the behavior of the power-law index further influence this divergence. For this particular parameter set, significant deviations between the linear and nonlinear shell models emerge at low-pressure amplitudes when the cavity is small and the liquid shows shear-thinning behavior. The shear-thickening behavior increases these deviations as the cavity size increases. The shear-thinning behavior leads to noticeable inconsistencies at higher pressure amplitudes. Therefore, factors such as cavity size, the power-law index and the acoustic field amplitude are vital in selecting the appropriate shell model.

In biomedical applications, the bubble radius typically ranges from 1 to 10 μm which corresponds to surface areas between 13 and 1200 μm^2. While oscillating, several factors affect the bubble's surface area which includes the shell properties, cavity size, power-law index, acoustic field pressure amplitude and frequency. An increase in cavity size, shear-thinning behavior and acoustic pressure amplitude generally leads to a larger maximum bubble surface area within this parameter range. Moreover, when the natural frequency of the bubble matches the driving frequency of the acoustic field, the surface area reaches its peak at resonance. If the shell properties lead to resonance, the maximum surface area increases, whereas the maximum area decreases in the absence of resonance. For this parameter set, when the acoustic field pressure exceeds 1 atm at resonance, the maximum bubble surface area can exceed the desirable range for biomedical applications, i.e., 1200 μm^2. Additionally, the maximum liquid shear stress at the bubble wall is crucial for evaluating vascular permeability and the risk of vessel damage, as excessive stress levels can be harmful. In this dissertation, the maximum wall shear stress can exceed 3000 Pa in small cavities at resonance, surpassing safe limits. This emphasizes optimizing therapeutic parameters to ensure effectiveness and patient safety.

To the best of our knowledge, no prior study has combined all the critical criteria—bubble surface area, wall shear stress, and inter-bubble distances—into a unified framework to comprehensively evaluate the safety and efficacy of ultrasound-mediated therapeutic applications. This thesis bridges that gap by integrating these parameters and developing detailed

contour maps that delineate safe and unsafe zones for treatment. This holistic approach ensures a balanced consideration of therapeutic outcomes and vascular safety, providing a much-needed practical tool for optimizing bubble-based drug delivery systems.

This dissertation also emphasizes the importance of the power-law index, along with factors such as the ultrasound driving frequency, pressure amplitude, Carreau-Yasuda parameters, and cavity size, in influencing the damping effect. The impact of the power-law index becomes particularly noticeable at resonance or when the cavity size is large. Furthermore, even when the acoustic field's driving frequency does not match the natural frequency, the power-law index continues to play a significant role, provided the acoustic pressure amplitude is sufficiently high.

In contrast to the Newtonian liquid case, the viscoelastic liquid model introduces an additional stiffness to the system, which accounts for the elasticity of the liquid. The viscoelasticity alters the natural frequency and impacts the equilibrium bubble radius which results in a higher natural frequency. Specifically, the elasticity increases the system's stiffness which increases the natural frequency. This effect becomes more prominent as the initial bubble radius decreases.

5.1.2. Non-Spherical Oscillations

Shape stability is crucial for targeted drug delivery, as it helps regulate microbubble breakup and is also essential to estimate the collapse pressure of bubbles during tissue ablation. The initiation of bubble break-up is closely tied to the loss of a spherical shape because of the development of shape instabilities at the interface. Stable shape oscillations of bubbles are employed to enhance blood-tissue contrast which improves the image quality of blood vessels during examination in ultrasound imaging. In this context, stable bubbles persist longer in the bloodstream than unstable bubbles which extend the imaging duration.

This section of the dissertation investigates different cases of the dynamics of non-spherical oscillations of a bubble. First, a bubble in an unbounded power-law liquid is

investigated. Then, the effect of the Newtonian thick shell and viscoelastic surrounding liquid is added to the model. A model for non-spherical bubbles is developed by extending perturbation analysis for a spherical interfaces between bubble/shell and shell/liquid. This approach provides deeper insight into surface mode oscillations which allows for the classification of stable and unstable conditions. This system identifies two types of instabilities: Rayleigh–Taylor instability and parametric instability. The amplitude of non-spherical oscillations is particularly high when shape mode resonance occurs under two conditions: when the driving frequency meets the radial resonance condition or satisfies the Mathieu condition $\omega_d = 2\omega_n/j$, where j equals 1 or 2. Higher power-law indices lead to reduced oscillations for non-spherical bubble oscillations due to increased damping. This damping effect can be mitigated by lowering the consistency index. Unlike Newtonian liquids, the driving frequency affects the bubble wall velocity and, consequently, the apparent viscosity. The power-law index also influences the evolution of the mean bubble radius, which affects the bubble wall acceleration and induces Rayleigh-Taylor instability—a phenomenon not observed in Newtonian liquids.

Furthermore, thicker shells and higher shell moduli suppress non-spherical oscillations, increasing bubble stability. Conversely, non-spherical oscillations in shear-thinning or viscoelastic fluids are more pronounced, suggesting that such fluid properties could amplify bubble oscillations in applications requiring enhanced mechanical effects.

This part provides an in-depth analysis of the non-spherical oscillations of an encapsulated bubble in an unbounded liquid which shows important insights into how these oscillations respond to different liquid and shell properties. By exploring two distinct cases, one where the surrounding liquid follows a power-law model and another where it is viscoelastic, the study offers a detailed understanding of how the bubble behavior changes under non-Newtonian and elastic influences. The results demonstrate that both the shell characteristics, such as thickness and modulus and the properties of the surrounding liquid, play significant roles in stabilizing or amplifying nonspherical perturbations. By fine-tuning parameters such as shell thickness, fluid viscosity and elasticity, it may be possible to enhance the stability of bubbles or induce instability for therapeutic purposes. For example, the observed resonance

effects at specific liquid modulus values suggest higher non-spherical oscillations, enhancing the mechanical impact of bubble oscillations for drug penetration across biological barriers.

5.1.3. Translational Motion and Bubble-Bubble Interactions

Translational motion and bubble-bubble interactions are crucial in various fluid dynamics applications, from industrial processes to biological systems. Gaining insight into how bubbles move through a liquid and interact with one another is crucial in advancing technologies such as ultrasound imaging, chemical reactors and underwater acoustics. These interactions depend on factors like bubble size, distance between bubbles and properties of the liquid. Researchers can improve multiphase flow processes in fields from medicine to environmental engineering by studying the dynamics of translational motion and bubble interactions.

First, the translational motion of an encapsulated bubble in an unbounded viscoelastic liquid is investigated via incorporating the effect of the primary Bjerknes force. This force is generated by the acoustic field's pressure gradient and influences bubble motion based on the alignment between the bubble's natural frequency and the driving frequency. Through a series of model refinements, beginning with Newtonian assumptions and advancing to complex viscoelastic conditions, both linear and nonlinear viscoelastic shell models are examined to capture the translational motion of a bubble.

Key parameters, including shell modulus (G_s), shell thickness (δ), acoustic field pressure amplitude (p_a), driving frequency (ω_d) and liquid modulus (G_l), are analyzed to investigate their effects on bubble displacement and velocity. Results indicate that variations in the shell modulus significantly impact the bubble's translational response which shows three distinct behavioral regions and highlighting a resonance-like response at intermediate shell stiffness. These three regions are also observed in the radial oscillation section. Further, the influence of acoustic cycles on translational versus radial motion became evident, with the translational component dominating as the number of cycles increased.

Comparative analyses of linear and nonlinear viscoelastic shell models emphasize the relevance of nonlinearity near resonance frequencies. The deviation between the linear and nonlinear shell models is most pronounced under specific driving frequencies and liquid moduli. The response of bubbles to acoustic irradiation is also explored, which indicates the importance of liquid elasticity in moderating bubble displacement, especially in resonance conditions. These findings emphasize the need to consider both shell elasticity and the rheological properties of the surrounding medium when modeling bubble dynamics, particularly in applications where precise control over translational motion is critical.

The translational motion and interactions between two encapsulated bubbles are investigated in a liquid medium, which examines Newtonian and viscoelastic fluid conditions in the second part of this section. The focus of this section is understanding the secondary Bjerknes force. The interaction between oscillating bubbles generates the secondary Bjerknes force, which causes either attraction or repulsion based on the phase difference of their oscillations. Resonance amplifies translational motion, and the Bjerknes force reduces the minimum distance between bubbles. Additionally, introducing viscoelasticity dampens oscillations and stabilizes bubble spacing, showing how fluid elasticity can control bubble interactions.

In conclusion, this section highlights the role of the bubble shell modulus, acoustic field properties and liquid properties on the translational motion and bubble-bubble interactions in optimizing ultrasound-assisted drug delivery. Controlling bubble-bubble interactions allows precise management of the distance between bubbles. This capability enables the formation of bubble clusters at targeted sites or helps prevent bubble collapse by maintaining optimal spacing.

5.1.4. Acoustic Droplet Vaporization

This section investigates the vaporization dynamics of perfluorocarbon (PFC) microdroplets which are known as phase-change contrast agents (PCCAs) PCCAs are converted from liquid to gas upon exposure to an acoustic pulse. PCCAs composed of volatile PFCs

such as decafluorobutane (DFB) and octafluoropropane (OFP) can rapidly vaporize when acoustically stimulated, producing vapor bubbles that enhance contrast in ultrasound imaging and offer the potential for targeted drug delivery.

A theoretical model is developed to examine these vaporization dynamics in this section. The validation of the theoretical model is done against in vitro experimental data. The study aimed to accurately capture the complex rheological behavior of blood surrounding the droplet By assuming a power-law model to represent blood viscosity. Effects of droplet size, acoustic pressure amplitude, driving frequency and the power-law index of the host liquid are analyzed to understand their effects on bubble expansion and stability. Results show that both conduction and convection affect heat transfer around the bubble, with convection significantly enhancing bubble expansion, particularly at smaller droplet sizes. Moreover, higher acoustic pressure and frequency influence bubble growth and collapse rates, with the system proving more responsive to frequency changes.

This section's findings show promise for using PCCAs (phase-change contrast agents) in medical imaging. Better bubble control could lead to clearer images and more accurate visualizations. This research opens doors for more experiments and clinical applications, especially in customizing PCCA properties for specific medical needs, ultimately leading to safer and more effective treatments and imaging methods. Also, by including both basic and advanced viscoelastic models, a better understanding of how PFC droplets interact with blood-like environments is gained. This makes it possible to fine-tune ultrasound settings to boost droplet response while reducing the risk of tissue damage.

5.2. Recommendations

While this dissertation addresses the challenges of targeted drug delivery and enhances bubble dynamics models by incorporating non-Newtonian behavior, the elastic properties of the blood vessel wall and finite-thickness shell behavior for both spherical and non-spherical oscillations, there are still limitations in the current model that future research should address. Three main recommendations are proposed to improve the existing model.

The first recommendation to enhance the model is to incorporate the effects of blood pulsatile flow. This addition would provide a more accurate representation of in vivo conditions and significantly improve the model's ability to capture the interaction between microbubbles and the dynamic nature of the surrounding blood. The model's accuracy could be significantly enhanced by accounting for time-dependent variations in shear stress and pressure gradients, which significantly influence bubble behavior, shape stability and oscillation dynamics. This addition could introduce additional instabilities or modulate existing ones, affecting both bubble break-up and collapse pressures in therapeutic applications, such as drug delivery or tissue ablation. Moreover, considering the impact of pulsatile flow on bubble stability could improve the accuracy of ultrasound imaging models, particularly in extending the imaging time by predicting the lifespan of stable bubbles under physiological flow conditions.

Second, the blood vessel wall is modeled as a single elastic layer in this dissertation. However, both arteries and veins have three distinct layers: the tunica intima, tunica media, and tunica externa (or adventitia) [398]. The innermost layer, the tunica intima, features a surface layer of endothelium along with a basement membrane. Modeling the blood vessel wall as a membrane would enable incorporating its mechanical properties, such as elasticity, viscoelasticity and thickness. These properties are critical in influencing how microbubbles interact with the vessel walls. The model can account for stress distributions during bubble oscillations and pulsatile blood flow by treating the vessel wall as a flexible membrane. This would lead to a more accurate model of the forces exerted on the bubbles and the vessel wall which impacts the stability and dynamics of the bubbles in real time physiological conditions. Furthermore, this membrane model could facilitate the exploration of phenomena such as the transmission of pressure waves through the vessel wall and the potential for bubble-induced shear stress on the endothelial layer.

Third, our model is constrained by assumptions of vessel geometry and homogeneity in vessel properties. While these simplifications facilitate numerical simulations, they only partially capture the complex interactions between biological tissues and their responses to fluid. In this dissertation, the surrounding liquid cavity is assumed to be a perfect sphere

with constant solid properties. However, the biological structure of blood vessels is more complex, including inhomogeneities, branching, and the presence of plaques. In future iterations, such inhomogeneities could be incorporated into the model. Additionally, rather than modeling the vessel as a single, unbounded elastic solid, the distinct arterial layers—intima, media, and adventitia—could be represented individually to more accurately reflect the vessel's layered structure [398].

REFERENCES

1. Scopus, www.elsevier.com/products/scopus, accessed on Nov 1, 2024.

2. Kaykanat, S. and A. Uguz, "The Role of Acoustofluidics and Microbubble Dynamics for Therapeutic Applications and Drug Delivery", *Biomicrofluidics*, Vol. 17, No. 2, p. 021502, 2023.

3. Zhao, Z., A. Ukidve, J. Kim and S. Mitragotri, "Targeting Strategies for Tissue Specific Drug Delivery", *Cell*, Vol. 181, No. 1, pp. 151–167, 2020.

4. Gagliardi, A., E. Giuliano, E. Venkateswararao, M. Fresta, S. Bulotta, V. Awasthi and D. Cosco, "Biodegradable Polymeric Nanoparticles for Drug Delivery to Solid Tumors", *Frontiers in Pharmacology*, Vol. 12, No. 1, p. 601626, 2021.

5. Liu, H.-L., C.-H. Fan, C.-Y. Ting and C.-K. Yeh, "Combining Microbubbles and Ultrasound for Drug Delivery to Brain Tumors: Current Progress and Overview", *Theranostics*, Vol. 4, No. 4, p. 432, 2014.

6. Endo-Takahashi, Y. and Y. Negishi, "Microbubbles and Nanobubbles with Microbubbles for Systemic Gene Delivery", *Pharmaceutics*, Vol. 12, No. 10, p. 964, 2020.

7. Tinkov, S., R. Bekeredjian, G. Winter and C. Coester, "Microbubbles as Ultrasound Triggered Drug Carriers", *Journal of Pharmaceutical Sciences*, Vol. 98, No. 6, pp. 1935–1961, 2009.

8. Wang, M., Y. Zhang, C. Cai, J. Tu, X. Guo and D. Zhang, "Sonoporation Induced Cell Membrane Permeabilization and Cytoskeleton Disassembly at Varied Acoustic and Microbubble Cell Parameters", *Scientific Reports*, Vol. 8, No. 1, pp. 1–12, 2018.

9. He, J., Z. Liu, X. Zhu, H. Xia, H. Gao and J. Lu, "Ultrasonic Microbubble Cavitation Enhanced Tissue Permeability and Drug Diffusion in Solid Tumor Therapy", *Pharma-*

ceutics, Vol. 14, No. 8, p. 1642, 2022.

10. Lu, X., G. L. Chahine and C.-T. Hsiao, "Stability Analysis of Ultrasound Thick Shell Contrast Agents", *The Journal of the Acoustical Society of America*, Vol. 131, No. 1, pp. 24–34, 2012.

11. Liu, Y., Q. Wang and A. Zhang, "Surface Stability of a Bubble in a Liquid Fully Confined by an Elastic Solid", *Physics of Fluids*, Vol. 30, No. 12, p. 127106, 2018.

12. Doinikov, A. A., P. S. Sheeran, A. Bouakaz and P. A. Dayton, "Vaporization Dynamics of Volatile Perfluorocarbon Droplets: A Theoretical Model and in Vitro Validation", *Medical Physics*, Vol. 41, No. 10, p. 102901, 2014.

13. Kaykanat, S. I. and K. Uguz, "Shape Stability of a Microbubble in a power–law Liquid", *The European Physical Journal Special Topics*, pp. 1–11, 2024.

14. Anselmo, A. C. and S. Mitragotri, "Nanoparticles in the Clinic: An Update", *Bioengineering Translational Medicine*, Vol. 4, No. 3, p. e10143, 2019.

15. Fenton, O. S., K. N. Olafson, P. S. Pillai, M. J. Mitchell and R. Langer, "Advances in Biomaterials for Drug Delivery", *Advanced Materials*, Vol. 30, No. 29, p. 1705328, 2018.

16. Church, C. C., "The Effects of an Elastic Solid Surface Layer on the Radial Pulsations of Gas Bubbles", *The Journal of the Acoustical Society of America*, Vol. 97, No. 3, pp. 1510–1521, 1995.

17. Sheeran, P. S., T. O. Matsunaga and P. A. Dayton, "Phase Change Events of Volatile Liquid Perfluorocarbon Contrast Agents Produce Unique Acoustic Signatures", *Physics in Medicine & Biology*, Vol. 59, No. 2, p. 379, 2013.

18. Sung, H., J. Ferlay, R. L. Siegel, M. Laversanne, I. Soerjomataram, A. Jemal and F. Bray, "Global Cancer Statistics 2020: Globocan Estimates of Incidence and Mor-

tality Worldwide for 36 Cancers in 185 Countries", *Cancer Journal for Clinicians*, Vol. 71, No. 3, pp. 209–249, 2021.

19. Park, J. W., K. Hong, D. B. Kirpotin, G. Colbern, R. Shalaby, J. Baselga, Y. Shao, U. B. Nielsen, J. D. Marks, D. Moore, D. Papahadjopoulos and C. Benz, "Anti-HER2 Immunoliposomes: Enhanced Efficacy Attributable to Targeted Delivery", *Clinical Cancer Research*, Vol. 8, No. 4, pp. 1172–1181, 2002.

20. Gottesman, M. M., "Mechanisms of Cancer Drug Resistance", *Annual Review of Medicine*, Vol. 53, No. 1, pp. 615–627, 2002.

21. Epenetos, A. A., D. Snook, H. Durbin, P. M. Johnson and J. Taylor-Papadimitriou, "Limitations of Radiolabeled Monoclonal Antibodies for Localization of Human Neoplasms", *American Association for Cancer Research*, Vol. 46, No. 6, pp. 3183–3191, 1986.

22. Kolkman, J. A. and D. A. Law, "Nanobodies from llamas to Therapeutic Proteins", *Drug Discovery Today: Technologies*, Vol. 7, No. 2, pp. e139–e146, 2010.

23. Deprez, J., G. Lajoinie, Y. Engelen, S. De Smedt and I. Lentacker, "Opening Doors with Ultrasound and Microbubbles: Beating Biological Barriers to Promote Drug Delivery", *Advanced Drug Delivery Reviews*, Vol. 172, No. 1, pp. 9–36, 2021.

24. Zhou, Y., X. Chen, J. Cao and H. Gao, "Overcoming the Biological Barriers in the Tumor Microenvironment for Improving Drug Delivery and Efficacy", *Journal of Materials Chemistry B*, Vol. 8, No. 31, pp. 6765–6781, 2020.

25. Carugo, D., D. N. Ankrett, P. Glynne-Jones, L. Capretto, R. J. Boltryk, X. Zhang, P. A. Townsend and M. Hill, "Contrast Agent Free Sonoporation: The Use of an Ultrasonic Standing Wave Microfluidic System for the Delivery of Pharmaceutical Agents", *Biomicrofluidics*, Vol. 5, No. 4, p. 044108, 2011.

26. Tu, J., H. Zhang, J. Yu, C. Liufu and Z. Chen, "Ultrasound Mediated Microbubble De-

struction: A New Method in Cancer Immunotherapy", *Oncology Targets and Therapy*, Vol. 11, No. 1, p. 5763, 2018.

27. Feng, S., L. Jin, Y. Wang, W. Zhao, H. Peng and H. Qiao, "An Efficient Algorithm Based on Spectrum Migration for High Frame Rate Microbubbles Imaging", *Computer Modeling in Engineering and Sciences*, Vol. 126, No. 2, pp. 739–754, 2021.

28. An, Y., S. Hu, S. Liu, J. Zhao and Y.-D. Zhang, "The Research of Automatic Classification of Microbubbles Thyroid Nodules", *Computer Modeling in Engineering and Sciences*, Vol. 128, No. 1, pp. 203–222, 2021.

29. Errico, C., J. Pierre, S. Pezet, Y. Desailly, Z. Lenkei, O. Couture and M. Tanter, "Ultrafast Ultrasound Localization Microscopy for Deep Super Resolution Vascular Imaging", *Nature*, Vol. 527, No. 7579, pp. 499–502, 2015.

30. Kooiman, K., S. Roovers, S. A. Langeveld, R. T. Kleven, H. Dewitte, M. A. O'Reilly, J.-M. Escoffre, A. Bouakaz, M. D. Verweij and K. Hynynen, "Microbubbles Responsive Cavitation Nuclei for Therapy and Drug Delivery", *Microbubbles in Medicine and Biology*, Vol. 46, No. 6, pp. 1296–1325, 2020.

31. Chowdhury, S. M., L. Abou-Elkacem, T. Lee, J. Dahl and A. M. Lutz, "Microbubbles and Microbubble Mediated Therapeutic Delivery: Underlying Mechanisms and Future Outlook", *Journal of Controlled Release*, Vol. 326, No. 1, pp. 75–90, 2020.

32. Roovers, S., T. Segers, G. Lajoinie, J. Deprez, M. Versluis, S. C. De Smedt and I. Lentacker, "The Role of Ultrasound Driven Microbubble Dynamics in Drug Delivery: From Microbubble Fundamentals to Clinical Translation", *Langmuir*, Vol. 35, No. 31, pp. 10173–10191, 2019.

33. Ter Haar, G., "Therapeutic Microbubbles", *European Journal of Ultrasound*, Vol. 9, No. 1, pp. 3–9, 1999.

34. Field, S. and N. Bleehen, "Hyperthermia in the Treatment of Cancer", *Cancer Treat-*

ment Reviews, Vol. 6, No. 2, pp. 63–94, 1979.

35. Merchant, S., S. Rauch and J. Nadol, "Meniere's Disease", *Eur Arch Otorhinolaryngol*, Vol. 252, No. 2, pp. 63–75, 1995.

36. Pandit, R., L. Chen and J. Götz, "The Blood-Brain Barrier: Physiology and Strategies for Drug Delivery", *Advanced Drug Delivery Reviews*, Vol. 165, No. 1, pp. 1–14, 2020.

37. Wells, P., "Ultrasonics in Medicine and Biology", *Physics in Medicine & Biology*, Vol. 22, No. 4, p. 629, 1977.

38. Akkoyun, F., S. Gucluer and A. Ozcelik, "Potential of the Acoustic Micromanipulation Technologies for Biomedical Research", *Biomicrofluidics*, Vol. 15, No. 6, p. 061301, 2021.

39. McMahon, D., M. A. O'Reilly and K. Hynynen, "Therapeutic Agent Delivery Across the Blood–Brain Barrier Using Focused Microbubbles", *Annual Review of Biomedical Engineering*, Vol. 23, No. 1, pp. 89–113, 2021.

40. Leonov, K. and I. Akhatov, "Dynamics of an Externally Driven Cavitation Bubble in an Elastic Microconfinement", *Physical Review E*, Vol. 104, No. 1, p. 015105, 2021.

41. Cadinoiu, A. N., D. M. Rata, L. I. Atanase, C. T. Mihai, S. E. Bacaita and M. Popa, "Formulations Based on Drug Loaded Aptamer-Conjugated Liposomes as a Viable Strategy for the Topical Treatment of Basal Cell Carcinoma—In Vitro Tests", *Pharmaceutics*, Vol. 13, No. 6, p. 866, 2021.

42. Leonov, K. and I. Akhatov, "Towards a Theory of Dynamics of a Single Cavitation Bubble in a Rigid Microconfinement", *International Journal of Multiphase Flow*, Vol. 130, No. 1, p. 103369, 2020.

43. Doinikov, A. A., D. Bienaimé, S. R. Gonzalez-Avila, C.-D. Ohl and P. Marmottant, "Nonlinear Dynamics of Two Coupled Bubbles Oscillating Inside a Liquid-Filled Cav-

ity Surrounded by an Elastic Medium", *Physical Review E*, Vol. 99, No. 5, p. 053106, 2019.

44. Kremkau, F. W., "Cancer Therapy with Ultrasound: A Historical Review", *Journal of Clinical Microbubbles*, Vol. 7, No. 4, pp. 287–300, 1979.

45. Dayton, P., A. Klibanov, G. Brandenburger and K. Ferrara, "Acoustic RadiationForce in Vivo: a Mechanism to Assist Targeting of Microbubbles", *Microbubbles in Medicine and Biology*, Vol. 25, No. 8, pp. 1195–1201, 1999.

46. Liu, Y., X. Lai, Y. Zhu, F. Guo, L. Su, G. Arkin, T. He, J. Xu and H. Ran, "Contrast-Enhanced Ultrasound Imaging Using Long-Circulating Cationic Magnetic Microbubbles in Vitro and in Vivo Validations", *International Journal of Pharmaceutics*, Vol. 616, No. 1, p. 121299, 2022.

47. Sharma, D., H. Cartar, N. Law, A. Giles, G. Farhat, M. Oelze and G. J. Czarnota, "Optimization of Microbubble Enhancement of Hyperthermia for Cancer Therapy in an in Vivo Breast Tumour Model", *Public Library of Science One*, Vol. 15, No. 8, p. e0237372, 2020.

48. Ibsen, S., C. E. Schutt and S. Esener, "Microbubble Mediated Ultrasound Therapy: A Review of Its Potential in Cancer Treatment", *Drug Design, Development and Therapy*, Vol. 111, No. 222, pp. 375–388, 2013.

49. Brennen, C. E., "Cavitation in Medicine", *Interface Focus*, Vol. 5, No. 5, p. 20150022, 2015.

50. Dollet, B., S. M. van Der Meer, V. Garbin, N. de Jong, D. Lohse and M. Versluis, "Non-spherical Oscillations of Ultrasound Contrast Agent Microbubbles", *Microbubbles in Medicine and Biology*, Vol. 34, No. 9, pp. 1465–1473, 2008.

51. Lin, X., R. Gao, Y. Zhang, N. Qi, Y. Zhang, K. Zhang, H. He and X. Tang, "Lipid Nanoparticles for Chemotherapeutic Applications: Strategies to Improve Anticancer

Efficacy", *Expert Opinion on Drug Delivery*, Vol. 9, No. 7, pp. 767–781, 2012.

52. Lasa-Saracibar, B., A. Estella-Hermoso de Mendoza, M. Guada, C. Dios-Vieitez and M. J. Blanco-Prieto, "Lipid Nanoparticles for Cancer Therapy: State of the Art and Future Prospects", *Expert Opinion on Drug Delivery*, Vol. 9, No. 10, pp. 1245–1261, 2012.

53. Ansari, M. T., T. A. Ramlan, N. N. Jamaluddin, N. Zamri, R. Salfi, A. Khan, F. Sami, S. Majeed and M. S. Hasnain, "Lipid Based Nanocarriers for Cancer and Tumor Treatment", *Current Pharmaceutical Design*, Vol. 26, No. 34, pp. 4272–4276, 2020.

54. Avramović, N., B. Mandić, A. Savić-Radojević and T. Simić, "Polymeric Nanocarriers of Drug Delivery Systems in Cancer Therapy", *Pharmaceutics*, Vol. 12, No. 4, p. 298, 2020.

55. Tong, R. and J. Cheng, "Anticancer Polymeric Nanomedicines", *Journal of Polymer Science: Macromolecular Reviews*, Vol. 47, No. 3, pp. 345–381, 2007.

56. Chen, J., F. Saeki, B. J. Wiley, H. Cang, M. J. Cobb, Z.-Y. Li, L. Au, H. Zhang, M. B. Kimmey and X. Li, "Gold Nanocages: Bioconjugation and Their Potential Use as Optical Imaging Contrast Agents", *Nano Letters*, Vol. 5, No. 3, pp. 473–477, 2005.

57. Hirsch, L. R., A. M. Gobin, A. R. Lowery, F. Tam, R. A. Drezek, N. J. Halas and J. L. West, "Metal Nanoshells", *Annals of Biomedical Engineering*, Vol. 34, No. 1, pp. 15–22, 2006.

58. Zheng, C., L. Qiu and K. Zhu, "Novel Polymersomes Based on Amphiphilic Graft Polyphosphazenes and Their Encapsulation of Water Soluble Anticancer Drug", *Polymer*, Vol. 50, No. 5, pp. 1173–1177, 2009.

59. Shae, D., K. W. Becker, P. Christov, D. S. Yun, A. K. Lytton-Jean, S. Sevimli, M. Ascano, M. Kelley, D. B. Johnson and J. M. Balko, "Endosomolytic Polymersomes Increase the Activity of Cyclic Dinucleotide Sting Agonists to Enhance Cancer Im-

munotherapy", *Nature Nanotechnology*, Vol. 14, No. 3, pp. 269–278, 2019.

60. Nigam, S. and D. Bahadur, "Dendrimer-Conjugated Iron Oxide Nanoparticles as Stimuli Responsive Drug Carriers for Thermally Activated Chemotherapy of Cancer", *Colloids and Surfaces B*, Vol. 155, No. 1, pp. 182–192, 2017.

61. Amreddy, N., A. Babu, J. Panneerselvam, A. Srivastava, R. Muralidharan, A. Chen, Y. D. Zhao, A. Munshi and R. Ramesh, "Chemobiologic Combinatorial Drug Delivery Using Folate Receptor Targeted Dendrimer Nanoparticles for Lung Cancer Treatment", *Nanomedicine: Nanotechnology, Biology and Medicine*, Vol. 14, No. 2, pp. 373–384, 2018.

62. Baeza, A., D. Ruiz-Molina and M. Vallet-Regí, "Recent advances in Porous Nanoparticles for Drug Delivery in antitumoral Applications: Inorganic Nanoparticles and Nanoscale Metal Organic Frameworks", *Expert Opinion on Drug Delivery*, Vol. 14, No. 6, pp. 783–796, 2017.

63. Drbohlavova, J., V. Adam, R. Kizek and J. Hubalek, "Quantum Dots—Characterization, Preparation and Usage in Biological Systems", *International Journal of Molecular Sciences*, Vol. 10, No. 2, pp. 656–673, 2009.

64. Bagher, A. M., "Quantum Dots Applications", *Sensors & Transducers*, Vol. 198, No. 3, p. 37, 2016.

65. Huang, X., I. H. El-Sayed, W. Qian and M. A. El-Sayed, "Cancer Cell Imaging and Photothermal Therapy in the Near Infrared Region by Using Gold Nanorods", *Journal of the American Chemical Society*, Vol. 128, No. 6, pp. 2115–2120, 2006.

66. Von Maltzahn, G., J.-H. Park, A. Agrawal, N. K. Bandaru, S. K. Das, M. J. Sailor and S. N. Bhatia, "Computationally Guided Photothermal Tumor Therapy Using Long Circulating Gold Nanorod Antennas", *American Association for Cancer Research*, Vol. 69, No. 9, pp. 3892–3900, 2009.

67. James, N., R. Coker, D. Tomlinson, J. Harris, M. Gompels, A. Pinching and J. Stewart, "Liposomal Doxorubicin (Doxil): an Effective New Treatment for Kaposi's Sarcoma in AIDS", *Journal of Clinical Oncology*, Vol. 6, No. 5, pp. 294–296, 1994.

68. Peer, D., J. M. Karp, S. Hong, O. C. Farokhzad, R. Margalit and R. Langer, "Nanocarriers as an Emerging Platform for Cancer Therapy", *Nature Nanotechnology*, Vol. 2, No. 12, pp. 751–760, 2007.

69. Muggia, F. M., "Clinical Efficacy and Prospects for Use of Pegylated Liposomal Doxorubicin in the Treatment of Ovarian and Breast Cancers", *Drugs*, Vol. 54, No. 4, pp. 22–29, 1997.

70. Barenholz, Y. C., "Doxil®—the First FDA Approved Nano Drug: Lessons Learned", *Journal of Control Release*, Vol. 160, No. 2, pp. 117–134, 2012.

71. Park, Y. I., S.-H. Kwon, G. Lee, K. Motoyama, M. W. Kim, M. Lin, T. Niidome, J. H. Choi and R. Lee, "PH Sensitive Multidrug Liposomes Targeting Folate Receptor β for Efficient Treatment of Nonsmall Cell Lung Cancer", *Journal of Controlled Release*, Vol. 330, No. 1, pp. 1–14, 2021.

72. Mendes, S., S. Graziani, T. Vitório, A. Padoveze, R. Hegg, S. Bydlowski and R. Maranhão, "Uptake by Breast Carcinoma of a Lipidic Nanoemulsion After Intralesional Injection into the Patients: A New Strategy for Neoadjuvant Chemotherapy", *Gynecologic Oncology*, Vol. 112, No. 2, pp. 400–404, 2009.

73. Rapoport, N., Z. Gao and A. Kennedy, "Multifunctional Nanoparticles for Combining Ultrasonic Tumor Imaging and Targeted Chemotherapy", *Journal of the National Cancer Institute*, Vol. 99, No. 14, pp. 1095–1106, 2007.

74. Rapoport, N., K.-H. Nam, R. Gupta, Z. Gao, P. Mohan, A. Payne, N. Todd, X. Liu, T. Kim and J. Shea, "Ultrasound Mediated Tumor Imaging and Nanotherapy Using Drug Loaded, Block Copolymer Stabilized Perfluorocarbon Nanoemulsions", *Journal*

of Controlled Release, Vol. 153, No. 1, pp. 4–15, 2011.

75. Gao, Z., A. N. Lukyanov, A. Singhal and V. P. Torchilin, "Diacyllipid Polymer Micelles as Nanocarriers for Poorly Soluble Anticancer Drugs", *Nano Letters*, Vol. 2, No. 9, pp. 979–982, 2002.

76. Jain, R. K. and T. Stylianopoulos, "Delivering Nanomedicine to Solid Tumors", *Nature Reviews Clinical Oncology*, Vol. 7, No. 11, p. 653, 2010.

77. Huang, Q. and J. Du, *New Nanomaterials and Techniques for Tumor- Targeted System*, Springer, Shanghai, China, 2020.

78. Sriraman, S. K., B. Aryasomayajula and V. P. Torchilin, "Barriers to Drug Delivery in Solid Tumors", *Tissue Barriers*, Vol. 2, No. 3, p. e29528, 2014.

79. Nakamura, Y., A. Mochida, P. L. Choyke and H. Kobayashi, "Nanodrug Delivery: Is the Enhanced Permeability and Retention Effect Sufficient for Curing Cancer?", *Bioconjugate Chemistry*, Vol. 27, No. 10, pp. 2225–2238, 2016.

80. Gabizon, A. and F. Martin, "Polyethylene Glycol Coated (Pegylated) Liposomal Doxorubicin", *Drugs*, Vol. 54, No. 4, pp. 15–21, 1997.

81. Nunes, S. S., R. S. Fernandes, C. H. Cavalcante, I. da Costa César, E. A. Leite, S. C. A. Lopes, A. Ferretti, D. Rubello, D. M. Townsend and M. C. de Oliveira, "Influence of PEG Coating on the Biodistribution and Tumor Accumulation of PH Sensitive Liposomes", *Drug Delivery and Translational Research*, Vol. 9, No. 1, pp. 123–130, 2019.

82. Oh, N. and J.-H. Park, "Endocytosis and Exocytosis of Nanoparticles in Mammalian Cells", *International Journal of Nanomedicine*, Vol. 9, No. Suppl 1, p. 51, 2014.

83. Matsumura, Y. and H. Maeda, "A New Concept for Macromolecular Therapeutics in Cancer Chemotherapy: Mechanism of Tumoritropic Accumulation of Proteins and the Antitumor Agent Smancs", *American Association for Cancer Research*, Vol. 46, No.

12 Part 1, pp. 6387–6392, 1986.

84. Fang, J., H. Nakamura and H. Maeda, "The EPR Effect: Unique Features of Tumor Blood Vessels for Drug Delivery, Factors Involved, and Limitations and Augmentation of the Effect", *Advanced Drug Delivery Reviews*, Vol. 63, No. 3, pp. 136–151, 2011.

85. Iyer, A. K., G. Khaled, J. Fang and H. Maeda, "Exploiting the Enhanced Permeability and Retention Effect for Tumor Targeting", *Drug Discovery Today*, Vol. 11, No. 17-18, pp. 812–818, 2006.

86. Miller, C. R., B. Bondurant, S. D. McLean, K. A. McGovern and D. F. O'Brien, "Liposome Cell Interactions in Vitro: Effect of Liposome Surface Charge on the Binding and Endocytosis of Conventional and Sterically Stabilized Liposomes", *Biochemistry*, Vol. 37, No. 37, pp. 12875–12883, 1998.

87. Gratton, S. E., P. A. Ropp, P. D. Pohlhaus, J. C. Luft, V. J. Madden, M. E. Napier and J. M. DeSimone, "The Effect of Particle Design on Cellular Internalization Pathways", *Proceedings of the National Academy of Sciences of the United States of America*, Vol. 105, No. 33, pp. 11613–11618, 2008.

88. Osaka, T., T. Nakanishi, S. Shanmugam, S. Takahama and H. Zhang, "Effect of Surface Charge of Magnetite Nanoparticles on Their Internalization into Breast Cancer and Umbilical Vein Endothelial Cells", *Colloids and Surfaces B*, Vol. 71, No. 2, pp. 325–330, 2009.

89. Lee, Y., S. Fukushima, Y. Bae, S. Hiki, T. Ishii and K. Kataoka, "A Protein Nanocarrier from Charge Conversion Polymer in Response to Endosomal PH", *Journal of the American Chemical Society*, Vol. 129, No. 17, pp. 5362–5363, 2007.

90. Yuan, Y.-Y., C.-Q. Mao, X.-J. Du, J.-Z. Du, F. Wang and J. Wang, "Surface Charge Switchable Nanoparticles Based on Zwitterionic Polymer for Enhanced Drug Delivery to Tumor", *Advanced Materials*, Vol. 24, No. 40, pp. 5476–5480, 2012.

91. Albanese, A., P. S. Tang and W. C. Chan, "The Effect of Nanoparticle Size, Shape, and Surface Chemistry on Biological Systems", *Annual Review of Biomedical Engineering*, Vol. 14, No. 11, pp. 1–16, 2012.

92. Parveen, S. and S. K. Sahoo, "Long Circulating Chitosan/PEG Blended PLGA Nanoparticle for Tumor Drug Delivery", *European Journal of Pharmacology*, Vol. 670, No. 2-3, pp. 372–383, 2011.

93. Bazak, R., M. Houri, S. El Achy, S. Kamel and T. Refaat, "Cancer Active Targeting by Nanoparticles: A Comprehensive Review of Literature", *Journal of American Association for Cancer Research and Journal of Clinical Oncology*, Vol. 141, No. 5, pp. 769–784, 2015.

94. Watanabe, K., M. Kaneko and Y. Maitani, "Functional Coating of Liposomes Using a Folate Polymer Conjugate to Target Folate Receptors", *International Journal of Nanomedicine*, Vol. 7, No. 1, p. 3679, 2012.

95. Rana, S., N. G. Shetake, K. Barick, B. Pandey, H. Salunke and P. Hassan, "Folic Acid Conjugated Fe_3O_4 Magnetic Nanoparticles for Targeted Delivery of Doxorubicin", *Dalton Transactions*, Vol. 45, No. 43, pp. 17401–17408, 2016.

96. Sahoo, S. K. and V. Labhasetwar, "Enhanced Antiproliferative Activity of Transferrin Conjugated Paclitaxel Loaded Nanoparticles is Mediated via Sustained Intracellular Drug Retention", *Molecular Pharmaceutics*, Vol. 2, No. 5, pp. 373–383, 2005.

97. Yang, H., C. Tang and C. Yin, "Estrone-Modified PH Sensitive Glycol Chitosan Nanoparticles for Drug Delivery in Breast Cancer", *Acta Biomaterialia*, Vol. 73, No. 1, pp. 400–411, 2018.

98. Mura, S., J. Nicolas and P. Couvreur, "Stimuli-Responsive Nanocarriers for Drug Delivery", *Nature Materials*, Vol. 12, No. 11, pp. 991–1003, 2013.

99. Torchilin, V. P., "Multifunctional, Stimuli-Sensitive Nanoparticulate Systems for Drug

Delivery", *Nature Reviews Drug Discovery*, Vol. 13, No. 11, pp. 813–827, 2014.

100. Bawa, P., V. Pillay, Y. E. Choonara and L. C. Du Toit, "Stimuli-Responsive Polymers and Their Applications in Drug Delivery", *Biomedical Materials*, Vol. 4, No. 2, p. 022001, 2009.

101. Shahriari, M., M. Zahiri, K. Abnous, S. M. Taghdisi, M. Ramezani and M. Alibolandi, "Enzyme Responsive Drug Delivery Systems in Cancer Treatment", *Journal of Controlled Release*, Vol. 308, No. 11, pp. 172–189, 2019.

102. Cao, Z., W. Li, R. Liu, X. Li, H. Li, L. Liu, Y. Chen, C. Lv and Y. Liu, "PH-and Enzyme-Triggered Drug Release as an Important Process in the Design of Antitumor Drug Delivery Systems", *Biomedicine & PharmacoTherapy*, Vol. 118, No. 1, p. 109340, 2019.

103. Hu, Q., P. S. Katti and Z. Gu, "Enzyme-Responsive Nanomaterials for Controlled Drug Delivery", *Nanoscale*, Vol. 6, No. 21, pp. 12273–12286, 2014.

104. Yang, Q., S. Wang, P. Fan, L. Wang, Y. Di, K. Lin and F.-S. Xiao, "PH-Responsive Carrier System Based on Carboxylic Acid Modified Mesoporous Silica and Polyelectrolyte for Drug Delivery", *Chemistry of Materials*, Vol. 17, No. 24, pp. 5999–6003, 2005.

105. Balamuralidhara, V., T. Pramodkumar, N. Srujana, M. Venkatesh, N. V. Gupta, K. Krishna and H. Gangadharappa, "PH Sensitive Drug Delivery Systems: A Review", *American Journal of Drug Discovery and Development*, Vol. 1, No. 1, p. 25, 2011.

106. Zhang, C. Y., Y. Q. Yang, T. X. Huang, B. Zhao, X. D. Guo, J. F. Wang and L. J. Zhang, "Self-Assembled PH-Responsive MPEG-b-(PLA-co-PAE) Block Copolymer Micelles for Anticancer Drug Delivery", *Biomaterials*, Vol. 33, No. 26, pp. 6273–6283, 2012.

107. Zhao, H., H. H. P. Duong and L. Y. L. Yung, "Folate-Conjugated Polymer Micelles with PH-Triggered Drug Release Properties", *Macromolecular Rapid Communica-*

tions, Vol. 31, No. 13, pp. 1163–1169, 2010.

108. Liu, K.-C., A. Arivajiagane, S.-J. Wu, S.-C. Tzou, C.-Y. Chen and Y.-M. Wang, "Development of a Novel Thermal-Sensitive Multifunctional Liposome with Antibody Conjugation to Target EGFR-Expressing Tumors", *Nanomedicine: Nanotechnology, Biology and Medicine*, Vol. 15, No. 1, pp. 285–294, 2019.

109. Dorjsuren, B., B. Chaurasiya, Z. Ye, Y. Liu, W. Li, C. Wang, D. Shi, C. E. Evans, T. J. Webster and Y. Shen, "Cetuximab-Coated Thermo-Sensitive Liposomes Loaded with Magnetic Nanoparticles and Doxorubicin for Targeted EGFR-Expressing Breast Cancer Combined Therapy", *International Journal of Nanomedicine*, Vol. 15, No. 1, p. 8201, 2020.

110. Koga, K., T. Tagami and T. Ozeki, "Gold Nanoparticle-Coated thermosensitive Liposomes for the Triggered Release of Doxorubicin , and Photothermal Therapy Using a Near-Infrared Laser", *Colloids and Surfaces A: Physicochemical and Engineering*, Vol. 626, No. 1, p. 127038, 2021.

111. Chi, L., M.-H. Na, H.-K. Jung, S. M. P. Vadevoo, C.-W. Kim, G. Padmanaban, T.-I. Park, J.-Y. Park, I. Hwang and K. U. Park, "Enhanced Delivery of Liposomes to Lung Tumor through Targeting Interleukin-4 Receptor on both Tumor Cells and Tumor Endothelial Cells", *Journal of Controlled Release*, Vol. 209, No. 11, pp. 327–336, 2015.

112. Lu, Z., Y. Long, X. Cun, X. Wang, J. Li, L. Mei, Y. Yang, M. Li, Z. Zhang and Q. He, "A Size Shrinkable Nanoparticle Based Combined Antitumor and Antiinflammatory Strategy for Enhanced Cancer Therapy", *Nanoscale*, Vol. 10, No. 21, pp. 9957–9970, 2018.

113. Sugahara, K. N., T. Teesalu, P. P. Karmali, V. R. Kotamraju, L. Agemy, D. R. Greenwald and E. Ruoslahti, "Coadministration of a Tumor Penetrating Peptide Enhances the Efficacy of Cancer Drugs", *Science*, Vol. 328, No. 5981, pp. 1031–1035, 2010.

114. Duo, Y., M. Yang, Z. Du, C. Feng, C. Xing, Y. Wu, Z. Xie, F. Zhang, L. Huang and X. Zeng, "CX-5461 Loaded Nucleolus Targeting Nanoplatform for Cancer Therapy Through Induction of Pro-Death Autophagy", *Acta Biomaterialia*, Vol. 79, No. 1, pp. 317–330, 2018.

115. He, X., X. Chen, L. Liu, Y. Zhang, Y. Lu, Y. Zhang, Q. Chen, C. Ruan, Q. Guo and C. Li, "Sequentially Triggered Nanoparticles with Tumor Penetration and Intelligent Drug Release for Pancreatic Cancer Therapy", *Advanced Science*, Vol. 5, No. 5, p. 1701070, 2018.

116. Roncato, F., F. Rruga, E. Porcù, E. Casarin, R. Ronca, F. Maccarinelli, N. Realdon, G. Basso, R. Alon and G. Viola, "Improvement and Extension of Anti-EGFR Targeting in Breast Cancer Therapy by Integration with the Avidin-Nucleic-Acid-Nano-Assemblies", *Nature Communications*, Vol. 9, No. 1, pp. 1–11, 2018.

117. Smith, B., I. Lyakhov, K. Loomis, D. Needle, U. Baxa, A. Yavlovich, J. Capala, R. Blumenthal and A. Puri, "Hyperthermia Triggered Intracellular Delivery of Anticancer Agent to HER2+ Cells by HER2-Specific Affibody (ZHER2-GS-Cys)-Conjugated Thermosensitive Liposomes (HER2+ Affisomes)", *Journal of Controlled Release*, Vol. 153, No. 2, pp. 187–194, 2011.

118. Clark, A. J. and M. E. Davis, "Increased Brain Uptake of Targeted Nanoparticles by Adding an Acid Cleavable Linkage between Transferrin and the Nanoparticle Core", *Proceedings of the National Academy of Sciences of the United States of America*, Vol. 112, No. 40, pp. 12486–12491, 2015.

119. Zwicke, G. L., G. Ali Mansoori and C. J. Jeffery, "Utilizing the Folate Receptor for Active Targeting of Cancer Nanotherapeutics", *Nano Reviews*, Vol. 3, No. 1, p. 18496, 2012.

120. Schroeder, A., J. Kost and Y. Barenholz, "Microbubbles, Liposomes, and Drug Delivery: Principles for Using Ultrasound to Control the Release of Drugs from Liposomes",

Chemistry and Physics of Lipids, Vol. 162, No. 1-2, pp. 1–16, 2009.

121. Chapelon, J., J. Margonari, F. Vernier, F. Gorry, R. Ecochard and A. Gelet, "In Vivo Effects of High-Intensity Ultrasound on Prostatic Adenocarcinoma Dunning R3327", *American Association for Cancer Research*, Vol. 52, No. 22, pp. 6353–6357, 1992.

122. Madersbacher, S., M. Pedevilla, L. Vingers, M. Susani and M. Marberger, "Effect of High-Intensity Focused Ultrasound on Human Prostate Cancer in Vivo", *American Association for Cancer Research*, Vol. 55, No. 15, pp. 3346–3351, 1995.

123. Cheng, S.-Q., X.-D. Zhou, Z.-Y. Tang, Y. Yu, H.-Z. Wang, S.-S. Bao and D.-C. Qian, "High-Intensity Focused Ultrasound in the Treatment of Experimental Liver Tumour", *Journal of American Association for Cancer Research and Journal of Clinical Oncology*, Vol. 123, No. 4, pp. 219–223, 1997.

124. Kremkau, F. W., J. S. Kaufmann, M. M. Walker, P. G. Burch and C. L. Spurr, "Ultrasonic Enhancement of Nitrogen Mustard Cytotoxicity in Mouse Leukemia", *Cancer*, Vol. 37, No. 4, pp. 1643–1647, 1976.

125. Harrison, G. H., E. Balcer-Kubiczek and H. Eddy, "Potentiation of Chemotherapy by Low-Level Ultrasound", *International Journal of Radiation Biology*, Vol. 59, No. 6, pp. 1453–1466, 1991.

126. Saad, A. H. and G. M. Hahn, "Ultrasound-Enhanced Effects of Adriamycin against Murine Tumors", *Microbubbles in Medicine and Biology*, Vol. 18, No. 8, pp. 715–723, 1992.

127. Widder, K. J., R. M. Morris, G. A. Poore, D. P. Howard and A. E. Senyei, "Selective Targeting of Magnetic Albumin Microspheres Containing Low-Dose Doxorubicin : Total Remission in Yoshida Sarcoma Bearing Rats", *European Journal of Cancer and Clinical Oncology*, Vol. 19, No. 1, pp. 135–139, 1983.

128. Widder, K. J., A. E. Senyei and D. G. Scarpelli, "Magnetic Microspheres: a Model

System for Site Specific Drug Delivery in Vivo", *Proceedings of the Society for Experimental Biology and Medicine.*, Vol. 158, No. 2, pp. 141–146, 1978.

129. Alexiou, C., W. Arnold, R. J. Klein, F. G. Parak, P. Hulin, C. Bergemann, W. Erhardt, S. Wagenpfeil and A. S. Luebbe, "Locoregional Cancer Treatment with Magnetic Drug Targeting", *American Association for Cancer Research*, Vol. 60, No. 23, pp. 6641–6648, 2000.

130. Pulfer, S. K., S. L. Ciccotto and J. M. Gallo, "Distribution of Small Magnetic Particles in Brain Tumor-Bearing Rats", *Journal of Neuro Oncology*, Vol. 41, No. 2, pp. 99–105, 1999.

131. Goodwin, S., C. Peterson, C. Hoh and C. Bittner, "Targeting and Retention of Magnetic Targeted Carriers Enhancing Intra Arterial Chemotherapy", *Journal of Magnetism and Magnetic Materials*, Vol. 194, No. 1-3, pp. 132–139, 1999.

132. Alexiou, C., R. Jurgons, R. Schmid, A. Hilpert, C. Bergemann, F. Parak and H. Iro, "In Vitro and in Vivo investigations of Targeted Chemotherapy with Magnetic Nanoparticles", *Journal of Magnetism and Magnetic Materials*, Vol. 293, No. 1, pp. 389–393, 2005.

133. Tao, Y., H. F. Chan, B. Shi, M. Li and K. W. Leong, "Light: A Magical Tool for Controlled Drug Delivery", *Advanced functional Materials*, Vol. 30, No. 49, p. 2005029, 2020.

134. Rapp, T. L. and C. A. DeForest, "Targeting Drug Delivery with Light: A Highly Focused Approach", *Advanced Drug Delivery Reviews*, Vol. 171, No. 1, pp. 94–107, 2021.

135. Qiao, Y., J. Wan, L. Zhou, W. Ma, Y. Yang, W. Luo, Z. Yu and H. Wang, "Stimuli-Responsive Nanotherapeutics for Precision Drug Delivery and Cancer Therapy", *Wiley Interdisciplinary Reviews: Nanomedicine and Nanobiotechnology*, Vol. 11, No. 1, p.

e1527, 2019.

136. Chen, H., D. Liu and Z. Guo, "Endogenous Stimuli-Responsive Nanocarriers for Drug Delivery", *Chemistry Letters*, Vol. 45, No. 3, pp. 242–249, 2016.

137. Ganta, S., H. Devalapally, A. Shahiwala and M. Amiji, "A Review of Stimuli-Responsive Nanocarriers for Drug and Gene Delivery", *Journal of Controlled Release*, Vol. 126, No. 3, pp. 187–204, 2008.

138. Xia, H., D. Yang, W. He, X. Zhu, Y. Yan, Z. Liu, T. Liu, J. Yang, S. Tan, J. Jiang, X. Hou, H. Gao, L. Ni and J. Lu, "Ultrasound Mediated Microbubbles Cavitation Enhanced Chemotherapy of Advanced Prostate Cancer by Increasing the Permeability of Blood-Prostate Barrier", *Translational Oncology*, Vol. 14, No. 10, p. 101177, 2021.

139. O'Brien Jr, W. D., "Microbubbles Biophysics Mechanisms", *Progress in Biophysics and Molecular Biology*, Vol. 93, No. 1-3, pp. 212–255, 2007.

140. Fulgham, P. F., *Physical Principles of Ultrasound*, pp. 13–30, Springer International Publishing, Cham, 2021.

141. Şen, T., O. Tüfekçioğlu and Y. Koza, "Mechanical Index", *Anatolian Journal of Cardiology*, Vol. 15, No. 4, p. 334, 2015.

142. Novell, A., H. Kamimura, A. Cafarelli, M. Gerstenmayer, J. Flament, J. Valette, P. Agou, A. Conti, E. Selingue and R. A. Badin, "A New Safety Index Based on Intrapulse Monitoring of Ultraharmonic Cavitation During Ultrasound-Induced Blood-Brain Barrier Opening Procedures", *Scientific Reports*, Vol. 10, No. 1, pp. 1–12, 2020.

143. Frenkel, V., "Microbubbles Mediated Delivery of Drugs and Genes to Solid Tumors", *Advanced Drug Delivery Reviews*, Vol. 60, No. 10, pp. 1193–1208, 2008.

144. Hernot, S. and A. L. Klibanov, "Microbubbles in Ultrasound-Triggered Drug and Gene Delivery", *Advanced Drug Delivery Reviews*, Vol. 60, No. 10, pp. 1153–1166, 2008.

145. Coussios, C. C. and R. A. Roy, "Applications of Acoustics and Cavitation to Noninvasive Therapy and Drug Delivery", *Annual Review of Fluid Mechanics*, Vol. 40, No. 1, pp. 395–420, 2008.

146. Qin, P., T. Han, C. Alfred and L. Xu, "Mechanistic Understanding the Bioeffects of Ultrasound Driven Microbubbles to Enhance Macromolecule Delivery", *Journal of Controlled Release*, Vol. 272, No. 1, pp. 169–181, 2018.

147. Udroiu, I., "Ultrasonic Drug Delivery in Oncology", *Journal of Medical and Biological Engineering*, Vol. 20, No. 2, pp. 381–90, 2015.

148. Versluis, M., E. Stride, G. Lajoinie, B. Dollet and T. Segers, "Microbubbles Contrast Agent Modeling: A Review", *Microbubbles in Medicine and Biology*, Vol. 46, No. 9, pp. 2117–2144, 2020.

149. Dalecki, D., "Mechanical Bioeffects of Ultrasound", *Annual Review of Biomedical Engineering*, Vol. 6, No. 1, pp. 229–248, 2004.

150. Ward, M., J. Wu and J.-F. Chiu, "Microbubbles-Induced Cell Lysis and Sonoporation Enhanced by Contrast Agents", *The Journal of the Acoustical Society of America*, Vol. 105, No. 5, pp. 2951–2957, 1999.

151. Hu, Y., J. M. Wan and C. Alfred, "Membrane Perforation and Recovery Dynamics in Microbubble Mediated Sonoporation", *Microbubbles in Medicine and Biology*, Vol. 39, No. 12, pp. 2393–2405, 2013.

152. Eck, M., R. Aronovich and T. Ilovitsh, "Efficacy Optimization of Low Frequency Microbubble Mediated Sonoporation as a Drug Delivery Platform to Cancer Cells", *International Journal of Pharmaceutics: X*, Vol. 4, No. 1, p. 100132, 2022.

153. Tachibana, K., T. Uchida, K. Ogawa, N. Yamashita and K. Tamura, "Induction of Cell-Membrane Porosity by Ultrasound", *Lancet*, Vol. 353, No. 9162, p. 1409, 1999.

154. Fan, Z., D. Chen and C. Deng, "Improving Ultrasound Gene Transfection Efficiency by Controlling Ultrasound Excitation of Microbubbles", *Journal of Controlled Release*, Vol. 170, No. 3, pp. 401–413, 2013.

155. Mohr, J., P. A. Wolf, M. A. Moskowitz, M. R. Mayberg and R. Von Kummer, *Stroke E-Book: Pathophysiology, Diagnosis, and management*, Elsevier Health Sciences, Philadelphia, 2011.

156. Miller, D. L., N. B. Smith, M. R. Bailey, G. J. Czarnota, K. Hynynen, I. R. S. Makin and B. C. of the American Institute of Microbubbles in Medicine, "Overview of Therapeutic Ultrasound Applications and Safety Considerations", *Journal of Medical Microbubbles*, Vol. 31, No. 4, pp. 623–634, 2012.

157. Abbasiasl, T., H. E. Sutova, S. Niazi, G. Celebi, Z. Karavelioglu, U. G. Kirabali, A. Yilmaz, H. Uvet, O. Kutlu, S. Ekici, M. Ghorbani and A. Kosar, "A Flexible Cystoscope Based on Hydrodynamic Cavitation for Tumor Tissue Ablation", *Institute of Electrical and Electronics Engineers Transactions on Biomedical Engineering*, Vol. 69, No. 1, pp. 513–524, 2021.

158. Dongsar, T. S., T. T. Dongsar, N. Molugulu, S. Annadurai, S. Wahab, N. Gupta and P. Kesharwani, "Targeted Therapy of Breast Tumor by PLGA-Based Nanostructures: The Versatile Function in Doxorubicin Delivery", *Environmental Research*, Vol. 1, No. 1, p. 116455, 2023.

159. Carovac, A., F. Smajlovic and D. Junuzovic, "Application of Ultrasound in Medicine", *Acta Informatica Medica*, Vol. 19, No. 3, p. 168, 2011.

160. James, J. A., "Clinical Aspects of the Surgical Treatment of Meniere's Disease with Ultrasound", *Ultrasonics*, Vol. 5, No. 2, pp. 102–104, 1967.

161. Lehmann, J., "The Biophysical Basis of Biologic Ultrasonic Reactions with Special Reference to Ultrasonic Therapy.", *Archives of Physical Medicine and Rehabilitationl*,

Vol. 34, No. 3, pp. 139–152, 1953.

162. Newell, J., "Ultrasonics in Medicine", *Physics in Medicine & Biology*, Vol. 8, No. 3, p. 241, 1963.

163. Goldberg, B. B., J.-B. Liu and F. Forsberg, "Microbubbles Contrast Agents: A Review", *Microbubbles in Medicine and Biology*, Vol. 20, No. 4, pp. 319–333, 1994.

164. Unger, E. C., T. P. McCreery, R. H. Sweitzer, V. E. Caldwell and Y. Wu, "Acoustically Active Lipospheres Containing Paclitaxel: A New Therapeutic Ultrasound Contrast Agent", *Investigative Radiology*, Vol. 33, No. 12, pp. 886–892, 1998.

165. Bekeredjian, R., S. Chen, P. A. Grayburn and R. V. Shohet, "Augmentation of Cardiac Protein Delivery Using Ultrasound Targeted Microbubble Destruction", *Microbubbles in Medicine and Biology*, Vol. 31, No. 5, pp. 687–691, 2005.

166. Skachkov, I., Y. Luan, A. F. van der Steen, N. de Jong and K. Kooiman, "Targeted Microbubble Mediated Sonoporation of Endothelial Cells in Vivo", *Institute of Electrical and Electronics Engineers Transactions on Ultrasonics, Ferroelectrics, and Frequency Control*, Vol. 61, No. 10, pp. 1661–1667, 2014.

167. McDannold, N., N. Vykhodtseva and K. Hynynen, "Effects of Acoustic Parameters and Ultrasound Contrast Agent Dose on Focused-Ultrasound Induced Blood-Brain Barrier Disruption", *Microbubbles in Medicine and Biology*, Vol. 34, No. 6, pp. 930–937, 2008.

168. Maxwell, A. D., C. A. Cain, T. L. Hall, J. B. Fowlkes and Z. Xu, "Probability of Cavitation for Single Ultrasound Pulses Applied to Tissues and Tissue-Mimicking Materials", *Microbubbles in Medicine and Biology*, Vol. 39, No. 3, pp. 449–465, 2013.

169. Xing, L., Q. Shi, K. Zheng, M. Shen, J. Ma, F. Li, Y. Liu, L. Lin, W. Tu and Y. Duan, "Ultrasound Mediated Microbubble Destruction (UMMD) Facilitates the Delivery of CA19-9 Targeted and Paclitaxel Loaded mPEG-PLGA-PLL Nanoparticles in Pancreatic Cancer", *Theranostics*, Vol. 6, No. 10, p. 1573, 2016.

170. Wang, Y., Y. Li, K. Yan, L. Shen, W. Yang, J. Gong and K. Ding, "Clinical Study of Ultrasound and Microbubbles for Enhancing Chemotherapeutic Sensitivity of Malignant Tumors in Digestive System", *Chinese Journal of Cancer Research*, Vol. 30, No. 5, p. 553, 2018.

171. Quinto-Su, P. A. and C.-D. Ohl, "Interaction between Two Laser-Induced Cavitation Bubbles in a Quasi-Two-Dimensional Geometry", *Journal of Fluid Mechanics*, Vol. 633, No. 1, pp. 425–435, 2009.

172. Lauterborn, W. and C.-D. Ohl, "Cavitation Bubble Dynamics", *Ultrasonics Sonochemistry*, Vol. 4, No. 2, pp. 65–75, 1997.

173. Arora, M., C.-D. Ohl and D. Lohse, "Effect of Nuclei Concentration on Cavitation Cluster Dynamics", *The Journal of the Acoustical Society of America*, Vol. 121, No. 6, pp. 3432–3436, 2007.

174. Unger, E. C., T. O. Matsunaga, T. McCreery, P. Schumann, R. Sweitzer and R. Quigley, "Therapeutic Applications of Microbubbles", *European journal of Radiology*, Vol. 42, No. 2, pp. 160–168, 2002.

175. Unger, E. C., E. Hersh, M. Vannan and T. McCreery, "Gene Delivery Using Ultrasound Contrast Agents", *Echocardiography*, Vol. 18, No. 4, pp. 355–361, 2001.

176. Liu, S., Y. Zhang, Y. Liu, W. Wang, S. Gao, W. Yuan, Z. Sun, L. Liu and C. Wang, "Microbubbles- Targeted Microbubble Destruction Remodels Tumour Microenvironment to Improve immunotherapeutic Effect", *British Journal of Cancer*, Vol. 128, No. 5, pp. 715–725, 2023.

177. Yoshizawa, S., T. Ikeda, A. Ito, R. Ota, S. Takagi and Y. Matsumoto, "High Intensity Focused Ultrasound Lithotripsy with Cavitating Microbubbles", *Medical & Biological Engineering & Computing*, Vol. 47, No. 8, pp. 851–860, 2009.

178. Bailey, M. R., Y. A. Pishchalnikov, O. A. Sapozhnikov, R. O. Cleveland, J. A. McA-

teer, N. A. Miller, I. V. Pishchalnikova, B. A. Connors, L. A. Crum and A. P. Evan, "Cavitation Detection During Shock Wave Lithotripsy", *Microbubbles in Medicine & Biology*, Vol. 31, No. 9, pp. 1245–1256, 2005.

179. Johnsen, E. and T. Colonius, "Shock-Induced Collapse of a Gas Bubble in Shock Wave Lithotripsy", *The Journal of the Acoustical Society of America*, Vol. 124, No. 4, pp. 2011–2020, 2008.

180. Ramaswamy, K., V. Marx, D. Laser, T. Kenny, T. Chi, M. Bailey, M. D. Sorensen, R. H. Grubbs and M. L. Stoller, "Targeted Microbubbles: A Novel Application for the Treatment of Kidney Stones", *British Journal of Urology*, Vol. 116, No. 1, pp. 9–16, 2015.

181. Pishchalnikov, Y. A., W. M. Behnke-Parks, K. Schmidmayer, K. Maeda, T. Colonius, T. W. Kenny and D. J. Laser, "High-Speed Video Microscopy and Numerical Modeling of Bubble Dynamics Near a Surface of Urinary Stone", *The Journal of the Acoustical Society of America*, Vol. 146, No. 1, pp. 516–531, 2019.

182. Escoffre, J.-M., J. Piron, A. Novell and A. Bouakaz, "Doxorubicin Delivery into Tumor Cells with Ultrasound and Microbubbles", *Molecular Pharmaceutics*, Vol. 8, No. 3, pp. 799–806, 2011.

183. Lee, N. G., J. L. Berry, T. C. Lee, A. T. Wang, S. Honowitz, A. L. Murphree, N. Varshney, D. R. Hinton and A. A. Fawzi, "Sonoporation Enhances Chemotherapeutic Efficacy in Retinoblastoma Cells in Vitro", *Investigative Ophthalmology and Visual Science*, Vol. 52, No. 6, pp. 3868–3873, 2011.

184. Sorace, A. G., J. M. Warram, H. Umphrey and K. Hoyt, "Microbubble Mediated Ultrasonic Techniques for Improved Chemotherapeutic Delivery in Cancer", *Journal of Drug Targeting*, Vol. 20, No. 1, pp. 43–54, 2012.

185. Heath, C. H., A. Sorace, J. Knowles, E. Rosenthal and K. Hoyt, "Microbubble Ther-

apy Enhances Antitumor Properties of Cisplatin and Cetuximab in Vitro and in Vivo", *Otolaryngology–Head and Neck Surgery*, Vol. 146, No. 6, pp. 938–945, 2012.

186. Sasaki, N., N. Kudo, K. Nakamura, S. Y. Lim, M. Murakami, W. B. Kumara, Y. Tamura, H. Ohta, M. Yamasaki and M. Takiguchi, "Microbubbles Image-Guided Therapy Enhances Antitumor Effect of Cisplatin", *Journal of Medical Microbubbles*, Vol. 41, No. 1, pp. 11–21, 2014.

187. Liu, H.-L., M.-Y. Hua, P.-Y. Chen, P.-C. Chu, C.-H. Pan, H.-W. Yang, C.-Y. Huang, J.-J. Wang, T.-C. Yen and K.-C. Wei, "Blood-Brain Barrier Disruption with Focused Ultrasound Enhances Delivery of Chemotherapeutic Drugs for Glioblastoma Treatment", *Radiology*, Vol. 255, No. 2, pp. 415–425, 2010.

188. Treat, L. H., N. McDannold, Y. Zhang, N. Vykhodtseva and K. Hynynen, "Improved Antitumor Effect of Liposomal Doxorubicin After Targeted Blood-Brain Barrier Disruption by MRI-Guided Focused Ultrasound in Rat Glioma", *Microbubbles in Medicine and Biology*, Vol. 38, No. 10, pp. 1716–1725, 2012.

189. Kang, J., X. Wu, Z. Wang, H. Ran, C. Xu, J. Wu, Z. Wang and Y. Zhang, "Antitumor Effect of Docetaxel-Loaded Lipid Microbubbles Combined with Ultrasound- Targeted Microbubble Activation on VX2 Rabbit Liver Tumors", *Journal of Medical Microbubbles*, Vol. 29, No. 1, pp. 61–70, 2010.

190. Zhu, F., Y. Jiang, F. Luo and P. Li, "Effectiveness of Localized Ultrasound- Targeted Microbubble Destruction with Doxorubicin Liposomes in H22 Mouse Hepatocellular Carcinoma Model", *Journal of Drug Targeting*, Vol. 23, No. 4, pp. 323–334, 2015.

191. Chowdhury, S. M., T.-Y. Wang, S. Bachawal, R. Devulapally, J. W. Choe, L. Abou Elkacem, B. K. Yakub, D. S. Wang, L. Tian and R. Paulmurugan, "Microbubbles-Guided Therapeutic Modulation of Hepatocellular Carcinoma Using Complementary MicroRNAs", *Journal of Controlled Release*, Vol. 238, No. 1, pp. 272–280, 2016.

192. Carlisle, R., J. Choi, M. Bazan-Peregrino, R. Laga, V. Subr, L. Kostka, K. Ulbrich, C.-C. Coussios and L. W. Seymour, "Enhanced Tumor Uptake and Penetration of Virotherapy Using Polymer Stealthing and Focused Ultrasound", *Journal of the National Cancer Institute*, Vol. 105, No. 22, pp. 1701–1710, 2013.

193. Tinkov, S., C. Coester, S. Serba, N. A. Geis, H. A. Katus, G. Winter and R. Bekeredjian, "New Doxorubicin -Loaded Phospholipid Microbubbles for Targeted Tumor Therapy: In-Vivo Characterization", *Journal of Controlled Release*, Vol. 148, No. 3, pp. 368–372, 2010.

194. Kotopoulis, S., A. Delalande, M. Popa, V. Mamaeva, G. Dimcevski, O. H. Gilja, M. Postema, B. T. Gjertsen and E. McCormack, "Sonoporation-Enhanced Chemotherapy Significantly Reduces Primary Tumour Burden in an Orthotopic Pancreatic Cancer Xenograft", *Molecular Imaging and Biology*, Vol. 16, No. 1, pp. 53–62, 2014.

195. Sonoda, S., K. Tachibana, E. Uchino, T. Yamashita, K. Sakoda, K.-H. Sonoda, T. Hisatomi, Y. Izumi and T. Sakamoto, "Inhibition of Melanoma by Ultrasound-Microbubble-Aided Drug Delivery Suggests Membrane Permeabilization", *Cancer Biology & Therapy*, Vol. 6, No. 8, pp. 1282–1289, 2007.

196. Lin, C.-Y. and W. G. Pitt, "Acoustic Droplet Vaporization in Biology and Medicine", *Bimedical Research International*, Vol. 2013, No. 1, pp. 1–18, 2013.

197. Zhou, Y., "Application of Acoustic Droplet Vaporization in Ultrasound Therapy", *Journal of Therapeutic Ultrasound*, Vol. 3, No. 1, pp. 1–18, 2015.

198. Loskutova, K., D. Grishenkov and M. Ghorbani, "Review on Acoustic Droplet Vaporization in Ultrasound diagnostics and Therapeutics", *Bimedical Research International*, Vol. 2019, No. 1, pp. 1–18, 2019.

199. Aliabouzar, M., O. D. Kripfgans, J. B. Fowlkes and M. L. Fabiilli, "Bubble Nucleation and Dynamics in Acoustic Droplet Vaporization: A Review of Concepts, Applications,

and New Directions", *Zeitschrift für Medizinische Physik*, Vol. 33, No. 3, pp. 387–406, 2023.

200. Aliabouzar, M., K. N. Kumar and K. Sarkar, "Acoustic Vaporization Threshold of Lipid-Coated Perfluoropentane Droplets", *The Journal of the Acoustical Society of America*, Vol. 143, No. 4, pp. 2001–2012, 2018.

201. Kripfgans, O. D., J. B. Fowlkes, D. L. Miller, O. P. Eldevik and P. L. Carson, "Acoustic Droplet Vaporization for Therapeutic and Diagnostic Applications", *Microbubbles in Medicine & Biology*, Vol. 26, No. 7, pp. 1177–1189, 2000.

202. Strohm, E., M. Rui, I. Gorelikov, N. Matsuura and M. Kolios, "Vaporization of Perfluorocarbon Droplets Using Optical Irradiation", *Biomedical Optics Express*, Vol. 2, No. 6, pp. 1432–1442, 2011.

203. Rapoport, N., "Phase Shift, Stimuli-Responsive Perfluorocarbon Nanodroplets for Drug Delivery to Cancer", *Wiley Interdisciplinary Reviews: Nanomedicine and Nanobiotechnology*, Vol. 4, No. 5, pp. 492–510, 2012.

204. Ho, Y.-J., Y.-C. Chang and C.-K. Yeh, "Improving Nanoparticle Penetration in Tumors by Vascular Disruption with Acoustic Droplet Vaporization", *Theranostics*, Vol. 6, No. 3, p. 392, 2016.

205. Martz, T. D., D. Bardin, P. S. Sheeran, A. P. Lee and P. A. Dayton, "Microfluidic Generation of Acoustically Active Nanodroplets", *Small*, Vol. 8, No. 12, pp. 1876–1879, 2012.

206. Teston, E., V. Hingot, V. Faugeras, C. Errico, M. Bezagu, M. Tanter and O. Couture, "A Versatile and Robust Microfluidic Device for Capillary-Sized Simple or Multiple Emulsions Production", *Biomedical Microdevices*, Vol. 20, No. 1, pp. 1–12, 2018.

207. Soto, F., I. Jeerapan, C. Silva-López, M. A. Lopez-Ramirez, I. Chai, L. Xiaolong, J. Lv, J. F. Kurniawan, I. Martin, K. Chakravarthy and J. Wang, "Noninvasive Transdermal

Delivery System of Lidocaine Using an Acoustic Droplet-Vaporization Based Wearable Patch", *Small*, Vol. 14, No. 49, p. 1803266, 2018.

208. Gatenby, R. A. and E. T. Gawlinski, "A Reaction-Diffusion Model of Cancer Invasion", *Cancer Research*, Vol. 56, No. 24, pp. 5745–5753, 1996.

209. Jeon, J., V. Quaranta and P. T. Cummings, "An Off-Lattice Hybrid Discrete-Continuum Model of Tumor Growth and Invasion", *Biophysical Journal*, Vol. 98, No. 1, pp. 37–47, 2010.

210. Chaplain, M. A. and G. Lolas, "Mathematical Modelling of Cancer Invasion of Tissue: Dynamic Heterogeneity", *Networks and Heterogeneous Media*, Vol. 1, No. 3, p. 399, 2006.

211. Meral, G., "DRBEM-FDM Solution of a Chemotaxis–Haptotaxis Model for Cancer Invasion", *Journal of Computational and Applied Mathematics*, Vol. 354, No. 1, pp. 299–309, 2019.

212. Waldeland, J. O. and S. Evje, "A Multiphase Model for Exploring Tumor Cell Migration Driven by Autologous Chemotaxis", *Chemical Engineering Science*, Vol. 191, No. 1, pp. 268–287, 2018.

213. Altrock, P. M., L. L. Liu and F. Michor, "The Mathematics of Cancer: Integrating Quantitative Models", *Nature Reviews Cancer*, Vol. 15, No. 12, pp. 730–745, 2015.

214. Gerisch, A. and M. A. Chaplain, "Mathematical Modelling of Cancer Cell Invasion of Tissue: Local and Non-Local Models and the Effect of Adhesion", *Journal of Theoretical Biology*, Vol. 250, No. 4, pp. 684–704, 2008.

215. Nyborg, W. L., "Acoustic Streaming Near a Boundary", *The Journal of the Acoustical Society of America*, Vol. 30, No. 4, pp. 329–339, 1958.

216. Doinikov, A. A. and A. Bouakaz, "Theoretical Investigation of Shear Stress Generated

by a Contrast Microbubble on the Cell Membrane as a Mechanism for Sonoporation", *The Journal of the Acoustical Society of America*, Vol. 128, No. 1, pp. 11–19, 2010.

217. Doinikov, A. A., "Translational Motion of Two Interacting Bubbles in a Strong Acoustic Field", *Physical Review E*, Vol. 64, No. 2, p. 026301, 2001.

218. Allen, J. S., D. E. Kruse, P. A. Dayton and K. W. Ferrara, "Effect of Coupled Oscillations on Microbubble Behavior", *The Journal of the Acoustical Society of America*, Vol. 114, No. 3, pp. 1678–1690, 2003.

219. Doinikov, A. A. and A. Bouakaz, "Review of Shell Models for Contrast Agent Microbubbles", *Institute of Electrical and Electronics Engineers Transactions on Ultrasonics, Ferroelectrics, and Frequency Control*, Vol. 58, No. 5, pp. 981–993, 2011.

220. Besant, W. H., *A Treatise on Hydrostatics and Hydrodynamics*, Deighton, Bell, Cambridge, 1859.

221. Lamb, H., *A Treatise on the Mathematical Theory of the Motion of Fluids*, The University Press, Cambridge, 1879.

222. Rayleigh, L., "VIII. On the Pressure Developed in a Liquid During the Collapse of a Spherical Cavity", *The London, Edinburgh, and Dublin Philosophical Magazine and Journal of Science*, Vol. 34, No. 200, pp. 94–98, 1917.

223. Plesset, M. S. and A. Prosperetti, "Bubble Dynamics and Cavitation", *Annual Review of Fluid Mechanics*, Vol. 9, No. 1, pp. 145–185, 1977.

224. Noltingk, B. E. and E. A. Neppiras, "Cavitation Produced by Ultrasonics", *Proceedings of the Physical Society. Section B*, Vol. 63, No. 9, p. 674, 1950.

225. Plesset, M., "On the Stability of Fluid Flows with Spherical symmetry", *Journal of Applied Physics*, Vol. 25, No. 1, pp. 96–98, 1954.

226. Leighton, T., "The Inertial Terms in Equations of Motion for Bubbles in Tubular Vessels or Between Plates", *The Journal of the Acoustical Society of America*, Vol. 130, No. 5, pp. 3333–3338, 2011.

227. Prosperetti, A., L. A. Crum and K. W. Commander, "Nonlinear Bubble Dynamics", *The Journal of the Acoustical Society of America*, Vol. 83, No. 2, pp. 502–514, 1988.

228. Herring, C., *Theory of the Pulsations of the Gas Bubble Produced by an Underwater Explosion*, Ph.D. Thesis, Columbia University, 1941.

229. Trilling, L., "The Collapse and Rebound of a Gas Bubble", *Journal of Applied Physics*, Vol. 23, No. 1, pp. 14–17, 1952.

230. Keller, J. B. and I. I. Kolodner, "Damping of Underwater Explosion Bubble Oscillations", *Journal of Applied Physics*, Vol. 27, No. 10, pp. 1152–1161, 1956.

231. Gilmore, F. R., *The Growth or Collapse of a Spherical Bubble in a Viscous Compressible Liquid*, California Institute of Technology, Ph.D. Thesis, 1952.

232. Minnaert, M., "XVI. On Musical Air-Bubbles and the Sounds of Running Water", *The London, Edinburgh, and Dublin Philosophical Magazine and Journal of Science*, Vol. 16, No. 104, pp. 235–248, 1933.

233. Devin Jr, C., "Survey of Thermal, Radiation, and Viscous Damping of Pulsating Air Bubbles in Water", *The Journal of the Acoustical Society of America*, Vol. 31, No. 12, pp. 1654–1667, 1959.

234. Plesset, M. S. and D.-Y. Hsieh, "Theory of Gas Bubble Dynamics in Oscillating Pressure Fields", *Physics of Fluids*, Vol. 3, No. 6, pp. 882–892, 1960.

235. Chapman, R. B. and M. S. Plesset, "Thermal Effects in the Free Oscillation of Gas Bubbles", *Journal of Basic Engineering*, Vol. 93, No. 3, pp. 373–376, 1971.

236. Prosperetti, A., "Thermal Effects and Damping Mechanisms in the Forced Radial Oscillations of Gas Bubbles in Liquids", *The Journal of the Acoustical Society of America*, Vol. 61, No. 1, pp. 17–27, 1977.

237. Keller, J. B. and M. Miksis, "Bubble Oscillations of Large Amplitude", *The Journal of the Acoustical Society of America*, Vol. 68, No. 2, pp. 628–633, 1980.

238. Allan, P. L., G. M. Baxter and M. J. Weston, *Clinical Microbubbles*, Elsevier Health Sciences, Glasgow, 2011.

239. Stride, E. and N. Saffari, "Microbubble Ultrasound Contrast Agents: A Review", *Proceedings of the Institution of Mechanical Engineers. H*, Vol. 217, No. 6, pp. 429–447, 2003.

240. Faez, T., M. Emmer, K. Kooiman, M. Versluis, A. F. van der Steen and N. de Jong, "20 Years of Ultrasound Contrast Agent Modeling", *Institute of Electrical and Electronics Engineers Transactions on Ultrasonics, Ferroelectrics, and Frequency Control*, Vol. 60, No. 1, pp. 7–20, 2012.

241. Sarkar, K., W. T. Shi, D. Chatterjee and F. Forsberg, "Characterization of Ultrasound Contrast Microbubbles Using in Vitro Experiments and Viscous and Viscoelastic Interface Models for Encapsulation", *The Journal of the Acoustical Society of America*, Vol. 118, No. 1, pp. 539–550, 2005.

242. de Jong, N., L. Hoff, T. Skotland and N. Bom, "Absorption and Scatter of Encapsulated Gas Filled Microspheres: Theoretical Considerations and Some Measurements", *Ultrasonics*, Vol. 30, No. 2, pp. 95–103, 1992.

243. De Jong, N. and L. Hoff, "Microbubbles Scattering Properties of Albunex Microspheres", *Ultrasonics*, Vol. 31, No. 3, pp. 175–181, 1993.

244. De Jong, N., R. Cornet and C. d. Lancée, "Higher Harmonics of Vibrating Gas-Filled Microspheres. Part One: Simulations", *Ultrasonics*, Vol. 32, No. 6, pp. 447–453, 1994.

245. Hoff, L., P. C. Sontum and J. M. Hovem, "Oscillations of Polymeric Microbubbles: Effect of the Encapsulating Shell", *The Journal of the Acoustical Society of America*, Vol. 107, No. 4, pp. 2272–2280, 2000.

246. Chatterjee, D. and K. Sarkar, "A Newtonian Rheological Model for the Interface of Microbubble Contrast Agents", *Microbubbles in Medicine and Biology*, Vol. 29, No. 12, pp. 1749–1757, 2003.

247. Allen, J. and M. Rashid, "Dynamics of a Hyperelastic Gas-Filled Spherical Shell in a Viscous Fluid", *Journal of Applied Mechanics*, Vol. 71, No. 2, pp. 195–200, 2004.

248. Doinikov, A. A. and P. A. Dayton, "Maxwell Rheological Model for Lipid-Shelled Ultrasound Microbubble Contrast Agents", *The Journal of the Acoustical Society of America*, Vol. 121, No. 6, pp. 3331–3340, 2007.

249. Doinikov, A. A., J. F. Haac and P. A. Dayton, "Modeling of Nonlinear Viscous Stress in Encapsulating Shells of Lipid-Coated Contrast Agent Microbubbles", *Ultrasonics*, Vol. 49, No. 2, pp. 269–275, 2009.

250. Marmottant, P., A. Bouakaz, N. d. Jong and C. Quilliet, "Buckling Resistance of Solid Shell Bubbles under Ultrasound", *The Journal of the Acoustical Society of America*, Vol. 129, No. 3, pp. 1231–1239, 2011.

251. Vos, H. J., B. Dollet, M. Versluis and N. de Jong, "Nonspherical Shape Oscillations of Coated Microbubbles in Contact with a Wall", *Microbubbles in Medicine & Biology*, Vol. 37, No. 6, pp. 935–948, 2011.

252. Tsiglifis, K. and N. A. Pelekasis, "Parametric Stability and Dynamic Buckling of an Encapsulated Microbubble Subject to Acoustic Disturbances", *Physics of Fluids*, Vol. 23, No. 1, pp. 1–10, 2011.

253. Katiyar, A. and K. Sarkar, "Effects of Encapsulation Damping on the Excitation Threshold for Subharmonic Generation from Contrast Microbubbles", *The Journal of*

the Acoustical Society of America, Vol. 132, No. 5, pp. 3576–3585, 2012.

254. Gubaidullin, D. and Y. V. Fedorov, "Acoustic Waves in a Liquid with Gas Bubbles Covered by a Viscoelastic Shell", *Fluid Dynamics*, Vol. 54, No. 2, pp. 270–278, 2019.

255. Vlachomitrou, M., A. Lytra and N. Pelekasis, "Dynamic Simulations of an Encapsulated Microbubble Translating in a Tube at Low Capillary and Reynolds Numbers", *Journal of Engineering Mathematics*, Vol. 129, No. 1, p. 8, 2021.

256. Qin, D., Q. Zou, S. Lei, W. Wang and Z. Li, "Cavitation Dynamics and Inertial Cavitation Threshold of Lipid Coated Microbubbles in Viscoelastic Media with Bubble–Bubble Interactions", *Micromachines*, Vol. 12, No. 9, p. 1125, 2021.

257. Gubaidullin, D., D. Gubaidullina and Y. V. Fedorov, "Radial Oscillations of a Shell-Covered Gas Bubble in a Viscoelastic Liquid", *Lobachevskii Journal of Mathematics*, Vol. 42, No. 1, pp. 2124–2128, 2021.

258. Vlachomitrou, M. and N. Pelekasis, "The Compression-Only Behavior of Coated Microbubbles in a Wall Restricted Flow", *The Journal of the Acoustical Society of America*, Vol. 155, No. 1, pp. 452–464, 2024.

259. Zhang, X., F. Li, C. Wang, J. Guo, R. Mo, J. Hu, S. Chen, J. He and H. Liu, "Radial Oscillation and Translational Motion of a Gas Bubble in a Micro-Cavity", *Ultrasonics Sonochemistry*, Vol. 84, No. 1, p. 105957, 2022.

260. Vincent, O., P. Marmottant, P. A. Quinto-Su and C.-D. Ohl, "Birth and Growth of Cavitation Bubbles within Water under Tension Confined in a Simple Synthetic Tree", *Physical Review Letters*, Vol. 108, No. 18, p. 184502, 2012.

261. Vincent, O., P. Marmottant, S. R. Gonzalez-Avila, K. Ando and C.-D. Ohl, "The fast Dynamics of Cavitation Bubbles within Water Confined in Elastic Solids", *Soft Matter*, Vol. 10, No. 10, pp. 1455–1461, 2014.

262. Wang, Q., "Oscillation of a Bubble in a Liquid Confined in an Elastic Solid", *Physics of Fluids*, Vol. 29, No. 7, p. 072101, 2017.

263. Doinikov, A. A., B. Dollet and P. Marmottant, "Model for the growth and the Oscillation of a Cavitation Bubble in a Spherical Liquid-Filled Cavity Enclosed in an Elastic Medium", *Physical Review E*, Vol. 97, No. 1, p. 013108, 2018.

264. Doinikov, A. A. and P. Marmottant, "Natural Oscillations of a Gas Bubble in a Liquid-Filled Cavity Located in a Viscoelastic Medium", *Journal of Sound and Vibration*, Vol. 420, No. 1, pp. 61–72, 2018.

265. Doinikov, A. A., B. Dollet and P. Marmottant, "Cavitation in a Liquid-Filled Cavity Surrounded by an Elastic Medium: Intercoupling of Cavitation Events in Neighboring Cavities", *Physical Review E*, Vol. 98, No. 1, p. 013108, 2018.

266. Vincent, O. and P. Marmottant, "On the statics and Dynamics of Fully Confined Bubbles", *Journal of Fluid Mechanics*, Vol. 827, No. 1, pp. 194–224, 2017.

267. Dollet, B., P. Marmottant and V. Garbin, "Bubble Dynamics in Soft and Biological Matter", *Annual Review of Fluid Mechanics*, Vol. 51, No. 1, pp. 331–355, 2019.

268. Qin, D., S. Lei, X. Wang, X. Zhong, X. Ji and Z. Li, "Resonance Behaviors of Encapsulated Microbubbles Oscillating Nonlinearly with Ultrasonic Excitation", *Ultrasonics Sonochemistry*, Vol. 94, No. 1, p. 106334, 2023.

269. Kawahata, R., T. Kanagawa and G. Chabouh, "Nonlinear Ultrasound Propagation in Liquid Containing Multiple Microbubbles Coated by Shell Incorporating Anisotropy", *Physics of Fluids*, Vol. 35, No. 7, p. 073312, 2023.

270. Abu-Nab, A. K. and A. F. Abu-Bakr, "On the Theory of Multiple Encapsulated Microbubbles Interaction: Effect of Lipid Shell Thickness", *Case Studies in Thermal Engineering*, Vol. 45, No. 1, p. 102901, 2023.

271. Kanagawa, T., M. Honda and Y. Kikuchi, "Nonlinear Acoustic Theory on Flowing Liquid Containing Multiple Microbubbles Coated by a Compressible Visco-Elastic Shell: Low and High Frequency Cases", *Physics of Fluids*, Vol. 35, No. 2, p. 023303, 2023.

272. Yusefi, H. and B. Helfield, "Subharmonic Resonance of Phospholipid Coated Ultrasound Contrast Agent Microbubbles", *Ultrasonics Sonochemistry*, Vol. 102, No. 1, p. 106753, 2024.

273. Jiménez-Fernández, J., "Nonlinear Response to Ultrasound of Encapsulated Microbubbles", *Ultrasonics*, Vol. 52, No. 6, pp. 784–793, 2012.

274. Shao, W. and W. Chen, "The Rupture of Viscoelastic Shell Bubble under High Intensity Ultrasound Drive", *Journal of Applied Physics*, Vol. 117, No. 2, p. 024702, 2015.

275. De Jong, N., A. Bouakaz and P. Frinking, "Basic Acoustic Properties of Microbubbles", *Echocardiography*, Vol. 19, No. 3, pp. 229–240, 2002.

276. Chabouh, G., B. Dollet, C. Quilliet and G. Coupier, "Spherical Oscillations of Encapsulated Microbubbles: Effect of Shell Compressibility and Anisotropy", *The Journal of the Acoustical Society of America*, Vol. 149, No. 2, pp. 1240–1257, 2021.

277. Abu-Bakr, A. F. and A. K. Abu-Nab, "Growth of Lipid-Coated Multi-Microbubbles in Viscoelastic Tissues", *The European Physical Journal Plus*, Vol. 137, No. 4, pp. 1–27, 2022.

278. Fournier, L., T. de La Taille and C. Chauvierre, "Microbubbles for Human Diagnosis and Therapy", *Biomaterials*, Vol. 294, No. 1, p. 122025, 2023.

279. Akkoyun, F., S. Gucluer and A. Ozcelik, "Potential of the Acoustic Micro Manipulation Technologies for Biomedical Research", *Biomicrofluidics*, Vol. 15, No. 6, p. 061301, 2021.

280. McMahon, D., M. A. O'Reilly and K. Hynynen, "Therapeutic Agent Delivery Across-

the Blood–Brain Barrier Using Focused Ultrasound", *Annual Review of Biomedical Engineering*, Vol. 23, No. 1, pp. 89–113, 2021.

281. Frenkel, V., "Microbubbles Mediated Delivery of Drugs and Genes to Solid Tumors", *Advanced Drug Delivery Reviews*, Vol. 60, No. 10, pp. 1193–1208, 2008.

282. Hernot, S. and A. L. Klibanov, "Microbubbles in Ultrasound-Triggered Drug and Gene Delivery", *Advanced Drug Delivery Reviews*, Vol. 60, No. 10, pp. 1153–1166, 2008.

283. Mitragotri, S., "Healing Sound: The Use of Ultrasound in Drug Delivery and Other Therapeutic Applications", *Nature Reviews Drug Discovery*, Vol. 4, No. 3, pp. 255–260, 2005.

284. Roovers, S., T. Segers, G. Lajoinie, J. Deprez, M. Versluis, S. C. De Smedt and I. Lentacker, "The Role of Ultrasound Driven Microbubble Dynamics in Drug Delivery: From Microbubble Fundamentals to Clinical Translation", *Langmuir*, Vol. 35, No. 31, pp. 10173–10191, 2019.

285. Bose, N., X. Zhang, T. K. Maiti and S. Chakraborty, "The Role of Acoustofluidics in Targeted Drug Delivery", *Biomicrofluidics*, Vol. 9, No. 5, pp. 1–20, 2015.

286. Morgan, K. E., J. S. Allen, P. A. Dayton, J. E. Chomas, A. Klibaov and K. W. Ferrara, "Experimental and Theoretical Eevaluation of Microbubble Behavior: Effect of Transmitted Phase and Bubble Size", *Institute of Electrical and Electronics Engineers Transactions on Ultrasonics, Ferroelectrics, and Frequency Control*, Vol. 47, No. 6, pp. 1494–1509, 2000.

287. Marmottant, P., S. Van Der Meer, M. Emmer, M. Versluis, N. De Jong, S. Hilgenfeldt and D. Lohse, "A Model for Large Amplitude Oscillations of Coated Bubbles Accounting for Buckling and Rupture", *The Journal of the Acoustical Society of America*, Vol. 118, No. 6, pp. 3499–3505, 2005.

288. Landau, L. D., E. M. Lifvsic, E. M. Lifshitz, A. M. Kosevich and L. P. Pitaevskii,

Theory of Elasticity: Volume 7, Elsevier, Moscow, 1986.

289. Tsiglifis, K. and N. A. Pelekasis, "Nonlinear Radial Oscillations of Encapsulated Microbubbles Subject to Ultrasound: The Effect of Membrane Constitutive Law", *The Journal of the Acoustical Society of America*, Vol. 123, No. 6, pp. 4059–4070, 2008.

290. Paul, S., A. Katiyar, K. Sarkar, D. Chatterjee, W. T. Shi and F. Forsberg, "Material Characterization of the Encapsulation of an Ultrasound Contrast Microbubble and Its Subharmonic Response: Strain-Softening Interfacial Elasticity Model", *The Journal of the Acoustical Society of America*, Vol. 127, No. 6, pp. 3846–3857, 2010.

291. Zhang, Y., K. Yeo, B. Khoo and C. Wang, "3D Jet Impact and Toroidal Bubbles", *Journal of Computational Physics*, Vol. 166, No. 2, pp. 336–360, 2001.

292. Zhang, A. and Y.-L. Liu, "Improved Three-Dimensional Bubble Dynamics Model Based on Boundary Element Method", *Journal of Computational Physics*, Vol. 294, No. 1, pp. 208–223, 2015.

293. Calvisi, M. L., O. Lindau, J. R. Blake and A. J. Szeri, "Shape Stability and Violent Collapse of Microbubbles in Acoustic Traveling Waves", *Physics of Fluids*, Vol. 19, No. 4, p. 047101, 2007.

294. Wang, Q. and J. Blake, "Non-Spherical Bubble Dynamics in a Compressible Liquid. Part 1. Travelling Acoustic Wave", *Journal of Fluid Mechanics*, Vol. 659, No. 1, pp. 191–224, 2010.

295. Hsiao, C.-T. and G. L. Chahine, "Breakup of Finite Thickness Viscous Shell Microbubbles by Ultrasound: A Simplified Zero-Thickness Shell Model", *The Journal of the Acoustical Society of America*, Vol. 133, No. 4, pp. 1897–1910, 2013.

296. Li, S., Y. Saade, D. van der Meer and D. Lohse, "Comparison of Boundary Integral and Volume-of-Fluid Methods for Compressible Bubble Dynamics", *International Journal of Multiphase Flow*, Vol. 145, No. 1, p. 103834, 2021.

297. Tian, Z., Y. Liu, A. Zhang and S. Wang, "Analysis of Breaking and Reclosure of a Bubble Near a Free Surface Based on the Eulerian Finite Element Method", *Computers & Fluids*, Vol. 170, No. 1, pp. 41–52, 2018.

298. Koukouvinis, P., M. Gavaises, O. Supponen and M. Farhat, "Simulation of Bubble Expansion and Collapse in the Vicinity of a Free Surface", *Physics of Fluids*, Vol. 28, No. 5, p. 052103, 2016.

299. Yu, P.-W., S. L. Ceccio and G. Tryggvason, "The Collapse of a Cavitation Bubble in Shear Flows—A Numerical Study", *Physics of Fluids*, Vol. 7, No. 11, pp. 2608–2616, 1995.

300. Bunner, B. and G. Tryggvason, "Direct Numerical Simulations of Three-Dimensional Bubbly Flows", *Physics of Fluids*, Vol. 11, No. 8, pp. 1967–1969, 1999.

301. Bunner, B. and G. Tryggvason, "Effect of Bubble Deformation on the Properties of Bubbly Flows", *Journal of Fluid Mechanics*, Vol. 495, No. 1, pp. 77–118, 2003.

302. Muradoglu, M. and H. A. Stone, "Motion of Large Bubbles in Curved Channels", *Journal of Fluid Mechanics*, Vol. 570, No. 1, pp. 455–466, 2007.

303. Feng, J., M. Muradoglu, H. Kim, J. T. Ault and H. A. Stone, "Dynamics of a Bubble Bouncing at a Liquid/Liquid/Gas Interface", *Journal of Fluid Mechanics*, Vol. 807, No. 1, pp. 324–352, 2016.

304. Altay, R., A. K. Sadaghiani, M. I. Sevgen, A. Şişman and A. Koşar, "Numerical and Experimental Studies on the Effect of Surface Roughness and Ultrasonic Frequency on Bubble Dynamics in Acoustic Cavitation", *Energies*, Vol. 13, No. 5, p. 1126, 2020.

305. Peng, C., S. Tian, G. Li and M. C. Sukop, "Single-Component Multiphase Lattice Boltzmann Simulation of Free Bubble and Crevice Heterogeneous Cavitation Nucleation", *Physical Review E*, Vol. 98, No. 2, p. 023305, 2018.

306. Peng-Nan, S., L. Yun-Bo and M. Fu-Ren, "Numerical Simulation on the Motion Characteristics of Freely Rising Bubbles Using Smoothed Particle Hydrodynamics Method", *Acta Physica Sinica*, Vol. 64, No. 17, p. 194701, 2015.

307. Fan, H. and S. Li, "A Peridynamics-SPH Modeling and Simulation of Blast Fragmentation of Soil under Buried Explosive Loads", *Computer Methods in Applied Mechanics and Engineering*, Vol. 318, No. 1, pp. 349–381, 2017.

308. Ohl, S.-W., E. Klaseboer and B. C. Khoo, "Bubbles with Shock Waves and Ultrasound: A Review", *Interface Focus*, Vol. 5, No. 5, p. 20150019, 2015.

309. Wang, S.-P., A. Zhang, Y.-L. Liu, S. Zhang and P. Cui, "Bubble Dynamics and Its Applications", *Journal of Hydrodynamics*, Vol. 30, No. 6, pp. 975–991, 2018.

310. Tamidi, A., K. Lau and S. Khalit, "A Review of Recent Development in Numerical Simulation of Ultrasonic-Assisted Gas-Liquid Mass Transfer Process", *Computers & Chemical Engineering*, Vol. 155, No. 1, p. 107498, 2021.

311. Ye, Y., Y. Liang, C. Dong, Y. Xu and Z. Zhang, "Treating the Phase Change of Cavitation as the Source of Vapor Inside Bubbles", *Modern Physics Letters B*, Vol. 35, No. 05, p. 2150093, 2021.

312. Ding, S.-T., B. Luo and G. Li, "A Volume of Fluid Based Method for Vapor-Liquid Phase Change Simulation with Numerical Oscillation Suppression", *International Journal of Heat and Mass Transfer*, Vol. 110, No. 1, pp. 348–359, 2017.

313. Gonzalez-Avila, S. R., F. Denner and C.-D. Ohl, "The Acoustic Pressure Generated by the Cavitation Bubble Expansion and Collapse Near a Rigid Wall", *Physics of Fluids*, Vol. 33, No. 3, p. 032118, 2021.

314. Denner, F., F. Evrard and B. van Wachem, "Modeling Acoustic Cavitation Using a Pressure-Based Algorithm for Polytropic Fluids", *Fluids*, Vol. 5, No. 2, p. 69, 2020.

315. Miao, H. and S. M. Gracewski, "Coupled FEM and BEM Code for Simulating Acoustically Excited Bubbles Near Deformable Structures", *Computational Mechanics*, Vol. 42, No. 1, pp. 95–106, 2008.

316. Curtiss, G., D. Leppinen, Q. Wang and J. Blake, "Ultrasonic Cavitation Near a Tissue Layer", *Journal of Fluid Mechanics*, Vol. 730, No. 1, pp. 245–272, 2013.

317. Calvisi, M., J. Iloreta and A. Szeri, "Dynamics of Bubbles Near a Rigid Surface Subjected to a Lithotripter Shock Wave. Part 2. Reflected Shock Intensifies Nonspherical Cavitation Collapse", *Journal of Fluid Mechanics*, Vol. 616, No. 1, pp. 63–97, 2008.

318. Klaseboer, E. and B. Khoo, "An Oscillating Bubble Near an Elastic Material", *Journal of Applied Physics*, Vol. 96, No. 10, pp. 5808–5818, 2004.

319. Klaseboer, E. and B. Khoo, "Boundary Integral Equations as Applied to an Oscillating Bubble Near a Fluid-Fluid Interface", *Computational Mechanics*, Vol. 33, No. 2, pp. 129–138, 2004.

320. Wang, Q. and K. Manmi, "Three Dimensional Microbubble Dynamics Near a Wall Subject to High Intensity Ultrasound", *Physics of Fluids*, Vol. 26, No. 3, p. 032104, 2014.

321. Brujan, E.-A., K. Nahen, P. Schmidt and A. Vogel, "Dynamics of Laser-Induced Cavitation Bubbles Near an Elastic Boundary", *Journal of Fluid Mechanics*, Vol. 433, No. 1, pp. 251–281, 2001.

322. Brujan, E., T. Ikeda, K. Yoshinaka and Y. Matsumoto, "The Final Stage of the Collapse of a Cloud of Bubbles Close to a Rigid Boundary", *Ultrasonics Sonochemistry*, Vol. 18, No. 1, pp. 59–64, 2011.

323. Versluis, M., D. E. Goertz, P. Palanchon, I. L. Heitman, S. M. van Der Meer, B. Dollet, N. de Jong and D. Lohse, "Microbubble Shape Oscillations Excited through Ultrasonic Parametric Driving", *Physical Review E*, Vol. 82, No. 2, p. 026321, 2010.

324. Mettin, R., C. Cairós and A. Troia, "Sonochemistry and Bubble Dynamics", *Ultrasonics Sonochemistry*, Vol. 25, No. 1, pp. 24–30, 2015.

325. Yasui, K., T. Tuziuti and Y. Iida, "Optimum Bubble Temperature for the Sonochemical Production of Oxidants", *Ultrasonics*, Vol. 42, No. 1-9, pp. 579–584, 2004.

326. Prosperetti, A., "Viscous Effects on Perturbed Spherical Flows", *Quarterly of Applied Mathematics*, Vol. 34, No. 4, pp. 339–352, 1977.

327. Brenner, M. P., D. Lohse and T. F. Dupont, "Bubble Shape Oscillations and the Onset of Sonoluminescence", *Physical Review Letters*, Vol. 75, No. 5, p. 954, 1995.

328. Hilgenfeldt, S., D. Lohse and M. P. Brenner, "Phase Diagrams for Sonoluminescing Bubbles", *Physics of Fluids*, Vol. 8, No. 11, pp. 2808–2826, 1996.

329. Liu, Y., K. Sugiyama, S. Takagi and Y. Matsumoto, "Surface Instability of an Encapsulated Bubble Induced by an Ultrasonic Pressure Wave", *Journal of Fluid Mechanics*, Vol. 691, No. 1, p. 315, 2012.

330. Liu, Y., K. Sugiyama and S. Takagi, "On the Interaction of Two Encapsulated Bubbles in an Ultrasound Field", *Journal of Fluid Mechanics*, Vol. 804, No. 1, pp. 58–89, 2016.

331. Zhang, Y., X. Du, H. Xian and Y. Wu, "Instability of Interfaces of Gas Bubbles in Liquids under Acoustic Excitation with Dual Frequency", *Ultrasonics Sonochemistry*, Vol. 23, No. 1, pp. 16–20, 2015.

332. Hamaguchi, F. and K. Ando, "Linear Oscillation of Gas Bubbles in a Viscoelastic Material under Ultrasound Irradiation", *Physics of Fluids*, Vol. 27, No. 11, 2015.

333. Klapcsik, K. and F. Hegedűs, "Study of Nonspherical Bubble Oscillations under Acoustic Irradiation in Viscous Liquid", *Ultrasonics Sonochemistry*, Vol. 54, No. 1, pp. 256–273, 2019.

334. Gaudron, R., K. Murakami and E. Johnsen, "Shape Stability of a Gas Cavity Surrounded by Linear and Nonlinear Elastic Media", *Journal of the Mechanics and Physics of Solids*, Vol. 143, No. 1, p. 104047, 2020.

335. Murakami, K., R. Gaudron and E. Johnsen, "Shape Stability of a Gas Bubble in a Soft Solid", *Ultrasonics Sonochemistry*, Vol. 67, No. 1, p. 105170, 2020.

336. Yang, J., A. Tzoumaka, K. Murakami, E. Johnsen, D. L. Henann and C. Franck, "Predicting Complex Nonspherical Instability Shapes of Inertial Cavitation Bubbles in Viscoelastic Soft Matter", *Physical Review E*, Vol. 104, No. 4, p. 045108, 2021.

337. Kobayashi, N., T. Yasu, S. Yamada, N. Kudo, M. Kuroki, M. Kawakami, K. Miyatake and M. Saito, "Endothelial Cell Injury in Venule and Capillary Induced by Contrast Ultrasonography", *Microbubbles in Medicine and Biology*, Vol. 28, No. 7, pp. 949–956, 2002.

338. Le Gac, S., E. Zwaan, A. van den Berg and C.-D. Ohl, "Sonoporation of Suspension Cells with a Single Cavitation Bubble in a Microfluidic Confinement", *Lab on a Chip*, Vol. 7, No. 12, pp. 1666–1672, 2007.

339. Aghdam, A. S., M. Ghorbani, G. Deprem, F. Ç. Cebeci and A. Koşar, "A New Method for intense Cavitation Bubble Generation on Layer-by-Layer Assembled Slips", *Scientific Reports*, Vol. 9, No. 1, pp. 1–13, 2019.

340. Escoffre, J.-M. and A. Bouakaz, *Therapeutic Ultrasound*, Springer, London, 2016.

341. Zhang, W., Y. Shi, S. Abd Shukor, A. Vijayakumaran, S. Vlatakis, M. Wright and M. Thanou, "Phase Shift Nanodroplets as an Emerging Sonoresponsive Nanomaterial for Imaging and Drug Delivery Applications", *Nanoscale*, Vol. 14, No. 8, pp. 2943–2965, 2022.

342. Lee, H., H. Kim, H. Han, M. Lee, S. Lee, H. Yoo, J. H. Chang and H. Kim, "Microbubbles used for Contrast Enhanced Ultrasound and Theragnosis: A Review of Principles

to Applications", *Biomedical Engineering Letters*, Vol. 7, No. 2, pp. 59–69, 2017.

343. Ishijima, A., K. Minamihata, S. Yamaguchi, S. Yamahira, R. Ichikawa, E. Kobayashi, M. Iijima, Y. Shibasaki, T. Azuma and T. Nagamune, "Selective Intracellular Vaporisation of Antibody-Conjugated Phase-Change Nanodroplets in Vitro", *Scientific Reports*, Vol. 7, No. 1, pp. 1–10, 2017.

344. Huynh, E., C. S. Jin, B. C. Wilson and G. Zheng, "Aggregate Enhanced Trimodal Porphyrin Shell Microbubbles for Ultrasound, Photoacoustic, and Fluorescence Imaging", *Bioconjugate Chemistry*, Vol. 25, No. 4, pp. 796–801, 2014.

345. Pellow, C., E. C. Abenojar, A. A. Exner, G. Zheng and D. E. Goertz, "Concurrent Visual and Acoustic Tracking of Passive and Active Delivery of Nanobubbles to Tumors", *Theranostics*, Vol. 10, No. 25, p. 11690, 2020.

346. Park, Y. C., C. Zhang, S. Kim, G. Mohamedi, C. Beigie, J. O. Nagy, R. G. Holt, R. O. Cleveland, N. L. Jeon and J. Y. Wong, "Microvessels-on-a-Chip to Assess Targeted Ultrasound-Assisted Drug Delivery", *The American Community Survey Applied Materials & Interfaces*, Vol. 8, No. 46, pp. 31541–31549, 2016.

347. Terrell-Hall, T. B., A. G. Ammer, J. I. Griffith and P. R. Lockman, "Permeability Acrossa Novel Microfluidic Blood-Tumor Barrier Model", *Fluids and Barriers of the Central Nervous System*, Vol. 14, No. 1, pp. 1–10, 2017.

348. Tarbell, J. M., "Shear Stress and the Endothelial Transport Barrier", *Cardiovascular Research*, Vol. 87, No. 2, pp. 320–330, 2010.

349. Deosarkar, S. P., B. Prabhakarpandian, B. Wang, J. B. Sheffield, B. Krynska and M. F. Kiani, "A Novel Dynamic Neonatal Blood-Brain Barrier on a Chip", *Public Library of Science One*, Vol. 10, No. 11, p. e0142725, 2015.

350. Lechner, C., M. Koch, W. Lauterborn and R. Mettin, "Pressure and Tension Waves from Bubble Collapse Near a Solid Boundary: A Numerical Approach", *The Journal*

of the Acoustical Society of America, Vol. 142, No. 6, pp. 3649–3659, 2017.

351. Zeng, Q., S. R. Gonzalez-Avila, R. Dijkink, P. Koukouvinis, M. Gavaises and C.-D. Ohl, "Wall Shear Stress from Jetting Cavitation Bubbles", *Journal of Fluid Mechanics*, Vol. 846, No. 1, pp. 341–355, 2018.

352. Hayes, B., G. Whiting and R. MacCurdy, "Modeling of Contactless Bubble–Bubble Interactions in Microchannels with Integrated Inertial Pumps", *Physics of Fluids*, Vol. 33, No. 4, p. 042002, 2021.

353. Huang, G., M. Zhang, L. Han, X. Ma and B. Huang, "Physical Investigation of Acoustic Waves Induced by the Oscillation and Collapse of the Single Bubble", *Ultrasonics Sonochemistry*, Vol. 72, No. 1, p. 105440, 2021.

354. Goncalves da Silva, E. and P. Parnaudeau, "Numerical Study of Pressure Loads Generated by a Shock-Induced Bubble Collapse", *Physics of Fluids*, Vol. 33, No. 11, p. 113318, 2021.

355. Segers, T., E. Gaud, M. Versluis and P. Frinking, "High Precision Acoustic Measurements of the Nonlinear Dilatational Elasticity of Phospholipid Coated Monodisperse Microbubbles", *Soft Matter*, Vol. 14, No. 47, pp. 9550–9561, 2018.

356. Borden, M. A., "Intermolecular Forces Model for Lipid Microbubble Shells", *Langmuir*, Vol. 35, No. 31, pp. 10042–10051, 2018.

357. van Opheusden, J. H. and J. Molenaar, "Lipid Aggregate Formation at an Oscillating Bubble Surface: A Simulation Study", *Physical Review E*, Vol. 83, No. 5, p. 051606, 2011.

358. Wang, Q., "Local Energy of a Bubble System and Its Loss due to Acoustic Radiation", *Journal of Fluid Mechanics*, Vol. 797, No. 1, pp. 201–230, 2016.

359. Wang, Q., K. Manmi and K.-K. Liu, "Cell Mechanics in Biomedical Cavitation", *In-*

terface Focus, Vol. 5, No. 5, p. 20150018, 2015.

360. Arefmanesh, A., M. M. Arani and A. A. A. Arani, "Dynamics of a Bubble in a Power-Law Fluid Confined within an Elastic Solid", *European Journal of Mechanics*, Vol. 94, No. 1, pp. 29–36, 2022.

361. Brenner, H., *Interfacial Transport Processes and Rheology*, Elsevier, Stoneham, 2013.

362. Prosperetti, A., "A Generalization of the Rayleigh–Plesset Equation of Bubble Dynamics", *Physics of Fluids*, Vol. 25, No. 3, pp. 409–410, 1982.

363. Farnes, J. S., "A Unifying Theory of Dark Energy and Dark Matter: Negative Masses and Matter Creation within a Modified ΛCDM Framework", *Astronomy & Astrophysics*, Vol. 620, No. 1, p. A92, 2018.

364. Mann, D. E. and J. M. Tarbell, "Flow of Nonnewtonian Blood Analog Fluids in Rigid Curved andStraight Artery Models", *Biorheology*, Vol. 27, No. 5, pp. 711–733, 1990.

365. Crawshaw, H. M., W. C. Quist, E. Serrallach, C. R. Valeri and F. W. LoGerfo, "Flow Disturbance at the Distal End-to-Side Anastomosis: Effect of Patency of the Proximal Outflow Segment and Angle of Anastomosis", *Archives of Surgery*, Vol. 115, No. 11, pp. 1280–1284, 1980.

366. Anand, M., K. Rajagopal and K. Rajagopal, "A Model Incorporating Some of the Mechanical and Biochemical Factors Underlying Clot Formation and Dissolution in Flowing Blood", *Journal of Theoretical Medicine*, Vol. 5, No. 3-4, pp. 183–218, 2003.

367. Huston, R. and H. Josephs, *Practical Stress Analysis in Engineering Design*, CRC Press, Livermore, 2008.

368. Landau, L., *Em Lifshitz, Fluid Mechanics*, Vol. 6, Elsevier, Moscow, 1959.

369. Kolsky, H., *Stress Waves in Solids*, Vol. 1098, Courier Corporation, New York, 1963.

370. Gubaidullin, D. A. and Y. V. Fedorov, "Acoustics of a Viscoelastic Medium with Encapsulated Bubbles", *Journal of Hydrodynamics*, Vol. 33, No. 1, pp. 55–62, 2021.

371. Landau, L. D. and E. M. Lifshitz, *Course of Theoretical Physics*, Elsevier, Moscow, 2013.

372. Hoger, A. and B. E. Johnson, "Linear Elasticity for Constrained Materials: Incompressibility", *Journal of Elasticity*, Vol. 38, No. 1, pp. 69–93, 1995.

373. Yang, X. and C. C. Church, "A Model for the Dynamics of Gas Bubbles in Soft Tissue", *The Journal of the Acoustical Society of America*, Vol. 118, No. 6, pp. 3595–3606, 2005.

374. Mooney, M., "A Theory of Large Elastic Deformation", *Journal of Applied Physics*, Vol. 11, No. 9, pp. 582–592, 1940.

375. Holzapfel, A. G., *Nonlinear Solid Mechanics II*, John Wiley & Sons, Incorporated, New York, 2000.

376. Gaudron, R., M. Warnez and E. Johnsen, "Bubble Dynamics in a Viscoelastic Medium with Nonlinear Elasticity", *Journal of Fluid Mechanics*, Vol. 766, No. 1, pp. 54–75, 2015.

377. Liu, Y., K. Sugiyama, S. Takagi and Y. Matsumoto, "Surface Instability of an Encapsulated Bubble Induced by an Ultrasonic Pressure Wave", *Journal of Fluid Mechanics*, Vol. 691, No. 1, pp. 315–340, 2012.

378. Picchi, D., I. Barmak, A. Ullmann and N. Brauner, "Stability of Stratified Two-Phase Channel Flows of Newtonian/Nonnewtonian Shear-thinning Fluids", *International Journal of Multiphase Flow*, Vol. 99, No. 1, pp. 111–131, 2018.

379. Nouar, C. and I. Frigaard, "Stability of Plane Couette–Poiseuille Flow of Shear-thinning Fluid", *Physics of Fluids*, Vol. 21, No. 6, p. 064104, 2009.

380. Sahu, K., P. Valluri, P. Spelt and O. Matar, "Linear Instability of Pressure Driven Channel Flow of a Newtonian and a Herschel-Bulkley Fluid", *Physics of Fluids*, Vol. 19, No. 12, p. 122101, 2007.

381. Hao, Y. and A. tti, "The Effect of Viscosity on the Spherical Stability of Oscillating Gas Bubbles", *Physics of Fluids*, Vol. 11, No. 6, pp. 1309–1317, 1999.

382. Nigmatulin, R. I., *Dynamics of Multiphase Media*, Vol. 2, CRC Press, Moscow, 1990.

383. Shpak, O., L. Stricker, M. Versluis and D. Lohse, "The Role of Gas in Ultrasonically Driven Vapor Bubble Growth", *Physics in Medicine & Biology*, Vol. 58, No. 8, p. 2523, 2013.

384. Nayfeh, A. H. and B. Balachandran, *Applied Nonlinear Dynamics: Analytical, Computational, and Experimental Methods*, John Wiley & Sons, New York, 2008.

385. Guo, W., G. Labrosse and R. Narayanan, *The Application of the Chebyshev-Spectral Method in Transport Phenomena*, Springer Science & Business Media, Florida, 2013.

386. Löfstedt, R., B. P. Barber and S. J. Putterman, "Toward a Hydrodynamic Theory of Sonoluminescence", *Physics of Fluids A: Fluid Dynamics*, Vol. 5, No. 11, pp. 2911–2928, 1993.

387. Ashokkumar, M., *Theoretical and Experimental Sonochemistry Involving Inorganic Systems*, Springer Science & Business Media, Tokyo, 2010.

388. Lynch, S., N. Nama and C. A. Figueroa, "Effects of Nonnewtonian Viscosity on Arterial and Venous Flow and Transport", *Scientific Reports*, Vol. 12, No. 1, p. 20568, 2022.

389. Ohl, C.-D. and B. Wolfrum, "Detachment and Sonoporation of Adherent HeLa-Cells by Shock Wave-Induced Cavitation", *Biochimica et Biophysica Acta-General Subjects*, Vol. 1624, No. 1-3, pp. 131–138, 2003.

390. Xie, Y., J. Hu, W. Lei and S. Qian, "Prediction of Vascular Injury by Cavitation Microbubbles in a Focused Ultrasound Field", *Ultrasonics Sonochemistry*, Vol. 88, No. 1, p. 106103, 2022.

391. Brenner, M. P., S. Hilgenfeldt and D. Lohse, "Single-Bubble Sonoluminescence", *Reviews of Modern Physics*, Vol. 74, No. 2, p. 425, 2002.

392. Versluis, M., D. E. Goertz, P. Palanchon, I. L. Heitman, S. M. van Der Meer, B. Dollet, N. de Jong and D. Lohse, "Microbubble Shape Oscillations Excited Through Ultrasonic Parametric Driving", *Physical Review E*, Vol. 82, No. 2, p. 026321, 2010.

393. Morse, P. M. and H. Feshbach, "Methods of Theoretical Physics", *American Journal of Physics*, Vol. 22, No. 6, pp. 410–413, 1954.

394. Bender, C. M. and S. A. Orszag, *Advanced Mathematical Methods for Scientists and Engineers I: Asymptotic Methods and Perturbation Theory*, Springer Science & Business Media, New York, 1999.

395. Dollet, B., S. M. van Der Meer, V. Garbin, N. de Jong, D. Lohse and M. Versluis, "Nonspherical Oscillations of Ultrasound Contrast Agent Microbubbles", *Microbubbles in Medicine and Biology*, Vol. 34, No. 9, pp. 1465–1473, 2008.

396. Versluis, M., D. E. Goertz, P. Palanchon, I. L. Heitman, S. M. van Der Meer, B. Dollet, N. de Jong and D. Lohse, "Microbubble Shape Oscillations Excited Through Ultrasonic Parametric Driving", *Physical Review E*, Vol. 82, No. 2, p. 026321, 2010.

397. Poulichet, V., A. Huerre and V. Garbin, "Shape Oscillations of Particle-Coated Bubbles and directional Particle expulsion", *Soft Matter*, Vol. 13, No. 1, pp. 125–133, 2017.

398. Altundemir, S., S. S. Lashkarinia, K. Pekkan and A. K. Uğuz, "Interstitial Flow, Pressure and Residual Stress in the Aging Carotid Artery Model in FEBio", *Biomechanics and Modeling in Mechanobiology*, Vol. 23, No. 1, pp. 179–192, 2024.

APPENDIX A: CONTINUUM MECHANICS

Continuum mechanics plays a pivotal role in understanding and characterizing the behavior of viscoelastic materials, which exhibit both elastic and viscous properties. By treating viscoelastic materials as continuous media, continuum mechanics provides a comprehensive framework for analyzing their complex mechanical response to external forces and deformations over time. Understanding the interplay between elastic and viscous components in viscoelastic materials is crucial for various applications, including biomechanics.

In this Section, the basic concept of the expressions for the continuum mechanics and the derivation of the deformation matrix is given.

A.1. The Material Body and Motion

In real-world scenarios, physical materials are represented using a theoretical construct known as a body within mathematical frameworks. This body comprises an infinite collection of material particles where a body B containing a material particle P. It's important to differentiate between this body and the surrounding space in which it exists and moves. By fixing the material particles of the body to points in space, one has a configuration of the body $\bar{\chi}$. A configuration can be expressed as a mapping of the particles P to the point $\mathbf{x}$,

$$\mathbf{x} = \bar{\chi}(P). \tag{A.1}$$

A motion of the body is a family of configurations parameterised by time t,

$$\mathbf{x} = \bar{\chi}(P,t). \tag{A.2}$$

At any time t, Equation A.2 gives the location in space $\mathbf{x}$ of the material particle P.

A.2. The Reference and Current Configurations

A reference configuration is chosen where the movement can then be assessed in relation to this chosen configuration as illustrated in Figure A.1. The reference configuration

could be the state occupied by the material at time $t = 0$, commonly referred to as the initial configuration. In the case of a solid, it might be intuitive for a configuration where the material experiences no stress, often termed the undeformed configuration.

A Cartesian coordinate system is introduced using base vectors $\mathbf{E}_i$ for the reference configuration. In this system, a material particle P located in the reference configuration can be given a specific position vector $\mathbf{X} = X_i\mathbf{E}_i$ with respect to the origin of the axes. The set of coordinates (X_1, X_2, X_3) associated with the particle is termed material coordinates, also known as Lagrangian coordinates or referential coordinates. At a later time, at time t, the material occupies a different configuration, referred to as the current configuration (or deformed configuration). A second Cartesian coordinate system using base vectors $\mathbf{e}_i$ for this current configuration is introduced, as depicted in Figure A.1. In this current configuration, the same particle P now occupies the position $\mathbf{x}$, which can be represented by a position vector $\mathbf{x} = x_i\mathbf{e}_i$. The coordinates (x_1, x_2, x_3) associated with this new position are termed spatial coordinates, also known as Eulerian coordinates.

Each particle is characterized by two sets of coordinates. The material coordinates associated with the particle remain fixed throughout its motion, while the spatial coordinates of the particle alter as it moves. In practical applications, it's common to align the material and spatial axes, making the base vectors $\mathbf{E}_i$ and $\mathbf{e}_i$ identical.

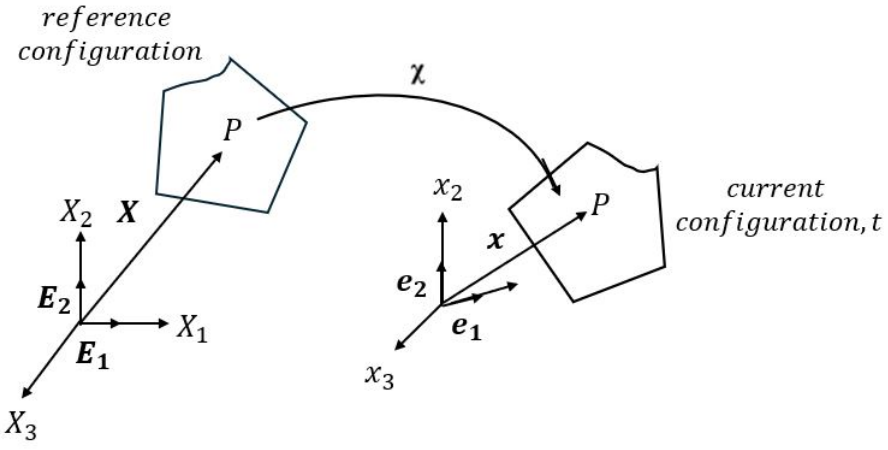

Figure A.1. The reference and current configurations.

A.3. Deformation Gradient

The deformation gradient **F** is the measure of the deformation and it is a second-order tensor that maps line elements in the reference configuration into line element.

A line element $d\mathbf{X}$ starting from position **X** in the reference configuration is considered, which transforms into $d\mathbf{x}$ in the current configuration, as depicted in Figure A.2. The definition of $d\mathbf{X}$ is given as,

$$d\mathbf{x} = \chi(\mathbf{X} + d\mathbf{X}) - \chi(\mathbf{X}) = (\text{Grad}\,\chi)d\mathbf{X}. \tag{A.3}$$

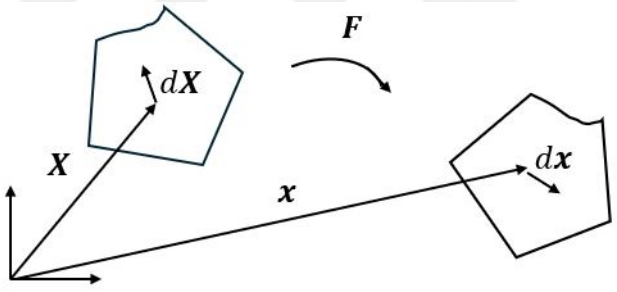

Figure A.2. The Deformation Gradient acting on a line element

A line element, $d\mathbf{X}$, emanating from position X in the reference configuration is considered which becomes $d\mathbf{x}$ in the current configuration. Then, using Equation A.2,

$$\mathbf{F} = \frac{\partial \mathbf{x}}{\partial \mathbf{X}}, \quad F_{iJ} = \frac{\partial x_i}{\partial X_J}. \tag{A.4}$$

The deformation gradient characterizes the transformation of a line element from the reference configuration to the current configuration. While it provides insights into deformation (change of shape) and rigid body rotation, it doesn't account for potential rigid body translations.

A.4. The Left and Right Cauchy-Green Strain

The Left Cauchy-Green Strain and Right Cauchy-Green Strain tensors quantify the lengths of line elements and angles between line elements, as determined by the vector dot product, change between configuration.

To obtain the Right Cauchy-Green Strain, two line elements in the reference configuration $d\mathbf{X}^{(1)}, d\mathbf{X}^{(2)}$ are considered which are mapped into the line elements $d\mathbf{x}^{(1)}, d\mathbf{x}^{(2)}$ in the current configuration. The mapping terms is given as,

$$d\mathbf{x}^{(1)} \cdot d\mathbf{x}^{(2)} = \left(\mathbf{F}d\mathbf{X}^{(1)}\right) \cdot \left(\mathbf{F}d\mathbf{X}^{(2)}\right) = d\mathbf{X}^{(1)} \left(\mathbf{F}^{\mathrm{T}}\mathbf{F}\right) d\mathbf{X}^{(2)} = d\mathbf{X}^{(1)}\mathbf{C}d\mathbf{X}^{(2)}, \tag{A.5}$$

where,

$$\mathbf{C} = \mathbf{F}^{\mathrm{T}}\mathbf{F}, \quad C_{IJ} = F_{kI}F_{kJ} = \frac{\partial x_k}{\partial X_I}\frac{\partial x_k}{\partial X_J} \quad \text{Right Cauchy-Green Strain .} \tag{A.6}$$

The Right Cauchy-Green Strain is a symmetric, positive definite tensor, which implies that it has real positive eigenvalues.

To obtain the Left Cauchy-Green Strain,

$$d\mathbf{X}^{(1)} \cdot d\mathbf{X}^{(2)} = \left(\mathbf{F}^{-1}d\mathbf{x}^{(1)}\right) \cdot \left(\mathbf{F}^{-1}d\mathbf{x}^{(2)}\right) = d\mathbf{x}^{(1)} \left(\mathbf{F}^{-\mathrm{T}}\mathbf{F}^{-1}\right) d\mathbf{x}^{(2)} = d\mathbf{x}^{(1)}\mathbf{B}^{-1}d\mathbf{x}^{(2)}, \tag{A.7}$$

where, $\mathbf{B}$ is the left Cauchy-Green Strain. Again, the left Cauchy-Green Strain is a symmetric, positive definite tensor. $\mathbf{B}$ is defined in the current configuration and so is called a spatial tensor. $\mathbf{B}$ is given as,

$$\mathbf{B} = \mathbf{F}\mathbf{F}^{\mathrm{T}}, \quad B_{ij} = F_{iK}F_{jK} = \frac{\partial x_i}{\partial X_K}\frac{\partial x_j}{\partial X_K}. \tag{A.8}$$

The inverse of $\mathbf{B}, \mathbf{B}^{-1}$, is called the Cauchy deformation tensor.

A.5. Incompressibilty of Deformation Matrix

The irrotational deformations are consider: the original configuration is $\mathbf{x}_0 = r_0\mathbf{e}_r$ and the current configuration is $\mathbf{x} = r(r_0,\theta,\varphi,t)\,\mathbf{e}_r$. Then, the deformation gradient tensor is

$$\mathbf{F} = \frac{\partial \mathbf{x}}{\partial \mathbf{x}_0} = \begin{bmatrix} \frac{\partial r}{\partial r_0} & \frac{1}{r_0}\frac{\partial r}{\partial \theta} & \frac{1}{r_0\sin\theta}\frac{\partial r}{\partial \varphi} \\ 0 & \frac{r}{r_0} & 0 \\ 0 & 0 & \frac{r}{r_0} \end{bmatrix}. \tag{A.9}$$

The Jacobian is defined as

$$J = \det(\mathbf{F}). \tag{A.10}$$

It is a measure of the volume change produced by a deformation. The volume change is given as,

$$\frac{dV}{dV_0} = \det(\mathbf{F}) = J. \tag{A.11}$$

The deformation is also incompressible ($\det\mathbf{F} = 1$), which leads to

$$V = V_0 \rightarrow \frac{r^3}{r_0^3} = 1 \rightarrow \frac{\partial r}{\partial r_0} = \left(\frac{r_0}{r}\right)^2. \tag{A.12}$$

If a material is incompressible, its volume remains constant. This requires $\mathbf{J} = \mathbf{1}$.

APPENDIX B: DETAILS OF THE NON-SPHERICAL OSCILLATIONS

In this appendix, the detailed derivations of the perturbed potential profiles are found for the bubble in an unbounded liquid (Section B.1) and for the encapsulated bubble in an unbounded liquid (Section B.2).

B.1. Derivation of Velocity Potential for a Bubble

The kinematic condition is given as

$$\frac{dF^{(1)}}{dt} = \frac{\partial F^{(1)}}{\partial t} + \mathbf{v}\cdot\nabla F^{(1)}\Big|_{F^{(1)}=0} = 0, \text{ with } \quad \mathbf{v} = \nabla\phi. \tag{B.1}$$

$\frac{\partial F^{(1)}}{\partial t}$, $\nabla F^{(1)}\Big|_{F^{(1)}=0}$ and $\mathbf{v}|_{F^{(1)}=0}$ are given as,

$$\frac{\partial F^{(1)}}{\partial t} = -R - \varepsilon \dot{a}_n P_n(\cos\theta), \tag{B.2}$$

$$\nabla F^{(1)}\Big|_{F^{(1)}=0} = \begin{pmatrix} 1 \\ -\varepsilon\dfrac{a_n}{R}\partial_\theta P_n(\cos\theta) \end{pmatrix} + O\left(\varepsilon^2\right), \tag{B.3}$$

and

$$\mathbf{v}|_{F^{(1)}=0} = \begin{pmatrix} \dfrac{\partial\phi_0}{\partial r} + \varepsilon\left(\dfrac{\partial\phi'}{\partial r} + \dfrac{\partial^2\phi_0}{\partial r^2}a_n P_n(\cos\theta)\right) \\ \dfrac{\varepsilon}{R}\dfrac{\partial\phi'}{\partial\theta} \end{pmatrix}_{r=R} + O\left(\varepsilon^2\right). \tag{B.4}$$

Here, the velocity vector is decomposed as (Section 3.2.1),

$$\mathbf{v} = \mathbf{v}_0 + \varepsilon\mathbf{v}_1 = v_0 + \varepsilon\left(\mathbf{v}' + \underbrace{\frac{d\mathbf{v}_0}{dr}anP_n(cos\theta)}_{Mapping \quad term}\right). \tag{B.5}$$

Equations B.2-B.4 are substituted into Equation B.1 and it becomes,

$$\left(-\dot{R}+\frac{\partial\phi_0}{\partial r}\right)\Big|_{r=R}+\quad \varepsilon\left(-\dot{a}_nP_n(\cos\theta)+\frac{\partial\phi'}{\partial r}+\frac{\partial^2\phi_0}{\partial r^2}a_nP_n(\cos\theta)\right)\Big|_{r=R}+ O\left(\varepsilon^2\right)=0. \tag{B.6}$$

To order $\varepsilon^{(0)}$ Equation B.6 is

$$\left(-\dot{R}+\frac{\partial\phi_0}{\partial r}\right)\Big|_{R}=0. \tag{B.7}$$

To order $\varepsilon^{(1)}$ Equation B.6 is

$$\left(-\dot{a}_nP_n(\cos\theta)+\frac{\partial\phi'}{\partial r}+\frac{\partial^2\phi_0}{\partial r^2}a_nP_n(\cos\theta)\right)\Big|_{r=R}=0. \tag{B.8}$$

The boundary conditions are given as,

$$r\to\infty,\quad \phi=0,\quad \phi'=0. \tag{B.9}$$

The potential profile, found in Equation 3.172, is given as,

$$\phi'(r,\theta,t)=\sum_{n=2}^{n}\left(A_nr^nl+B_nr^{-n-1}\right)P_n(\cos\theta). \tag{B.10}$$

The coefficient A_n is found from the Equation B.9 as,

$$r\to\infty\quad \phi'=0,\quad A_n=0. \tag{B.11}$$

From kinematic boundary condition at $r=R$

$$B_n=-\left(2a_n\dot{R}+\dot{a}_nR\right)(R)^{n+2}\frac{1}{n+1}. \tag{B.12}$$

After substituting the coefficients A_n and B_n (Equations B.11 and B.12) into the potential, Equation B.10, it becomes

$$\phi'(r,\theta,t)=-\varepsilon\left(2a_n\dot{R}+\dot{a}_nR\right)\left(\frac{R}{r}\right)^{n+1}\frac{P_n(\cos\theta)}{n+1}. \tag{B.13}$$

B.2. Derivation of Velocity Potential for an Encapsulated Bubble

For shell and liquid parts, the velocity potentials are given as,

$$\phi_l'(r,\theta,t)=\sum_{n=2}^{\infty}\left[\frac{A_n}{r^{n+1}}+B_n(t)r^n\right]P_n(\cos\theta), \tag{B.14}$$

and

$$\phi_s'(r,\theta,t) = \sum_{l=2}^{\infty} \left[\frac{A_l}{r^{l+1}} + B_l r^l \right] P_l(\cos\theta), \tag{B.15}$$

respectively. For the thick shell model, the kinematic condition at the shell-liquid interface, $F^{(2)}$, is given as,

$$\frac{dF^{(2)}}{dt} = \frac{\partial F^{(2)}}{\partial t} + \mathbf{v}_l \cdot \nabla F^{(2)}\Big|_{F^{(2)}=0} = 0, \text{ with} \quad \mathbf{v}_l = \nabla\phi_l. \tag{B.16}$$

$\frac{\partial F^{(2)}}{\partial t}$, $\nabla F^{(2)}\Big|_{F^{(2)}=0}$ and $\mathbf{v}|_{F^{(2)}=0}$ are given as,

$$\frac{\partial F^{(2)}}{\partial t} = -R_s - \varepsilon \dot{a}_n Y_n^m, \tag{B.17}$$

$$\nabla F^{(2)}\Big|_{F^{(2)}=0} = \begin{pmatrix} 1 \\ -\varepsilon \frac{a_n}{R_s} \partial_\theta P_n(\cos(\theta)) \end{pmatrix} + O\left(\varepsilon^2\right), \tag{B.18}$$

and

$$\mathbf{v}_l|_{F^{(2)}=0} = \left(\begin{array}{c} \frac{\partial \phi_{l0}}{\partial r} + \varepsilon \left(\frac{\partial \phi_l'}{\partial r} + \frac{\partial^2 \phi_{l0}}{\partial r^2} a_n P_n(\cos\theta) \right) \\ \frac{\varepsilon}{R_s} \frac{\partial \phi_l'}{\partial \theta} \end{array} \right) \Bigg|_{r=R_s} + O\left(\varepsilon^2\right). \tag{B.19}$$

Equations B.17-B.19 are substituted into Equation B.1 and it becomes,

$$\begin{aligned} \left(-\dot{R}_s + \tfrac{\partial \phi_{l0}}{\partial r}\right)\Big|_{r=R_s} + \quad \varepsilon \left(-\dot{a}_n P_n(\cos\theta) + \tfrac{\partial \phi_l'}{\partial r} + \tfrac{\partial^2 \phi_{l0}}{\partial r^2} a_n P_n(\cos\theta)\right)\Big|_{r=R_s} + \\ O\left(\varepsilon^2\right) = 0. \end{aligned} \tag{B.20}$$

Equation B.20 is separated into the $\varepsilon^{(0)}$ order:

$$\left(-\dot{R}_s + \frac{\partial \phi_{l0}}{\partial r}\right)\Big|_{R_s} = 0. \tag{B.21}$$

Equation B.20 is separated into the $\varepsilon^{(1)}$ order:

$$\left(-\dot{a}_n P_n(\cos\theta) + \frac{\partial \phi_l'}{\partial r} + \frac{\partial^2 \phi_{l0}}{\partial r^2} a_n P_n(\cos\theta)\right)\Big|_{r=R_s} = 0. \tag{B.22}$$

The boundary condition at far field is given as,

$$r \to \infty, \quad \phi_{i0} = 0, \quad \phi_l' = 0. \tag{B.23}$$

The velocity potential of the outer domain (Equation 3.172) is found after applying Equation B.23

$$\phi_{1,l} = -\frac{R_s^2 \dot{R}_s}{r} - \varepsilon \left(2a_n \dot{R}_s + \dot{a}_n R_s\right) \left(\frac{R_s}{r}\right)^{n+1} \frac{P_n(\cos\theta)}{n+1}. \tag{B.24}$$

For the microbubble shell part, the velocity potential is ϕ_s, and the kinematical condition on the interface shell-host liquid can be written as:

$$\frac{\partial F^{(1)}}{\partial t} + \mathbf{v}_s \cdot \nabla F^{(1)}\Big|_{F^{(1)}=0} = 0 \text{ with} \quad \mathbf{v}_s = \nabla \phi_s, \tag{B.25}$$

and

$$\phi_l|_{F^{(2)}=0} = \phi_s|_{F^{(2)}=0}. \tag{B.26}$$

After applying the interface conditions for ϕ_s, it is found as

$$\phi_s - \frac{R_b^2 \dot{R}_b}{r} - \varepsilon \left(2b_l \dot{R}_b + \dot{b}_l R_s\right) \left(\frac{R_b}{r}\right)^{l+1} \frac{P_l(\cos\theta)}{l+1}. \tag{B.27}$$

By substituting Equations B.24 and B.27 to Equation B.26, and separating the order of each term:

$$\left(2b_n \dot{R}_s + \dot{b}_n R_s\right) (R_s)^{n+1} P_n(\cos\theta) = \left(2a_l \dot{R}_1 + \dot{a}_l R_b\right) (R_b)^{n+1} P_l(\cos\theta). \tag{B.28}$$

Due to the orthogonality of the harmonic functions, $n = l$ and $m = k$,

$$\left(2b_n \dot{R}_2 + \dot{b}_n R_s\right) (R_s)^{n+1} = \left(2a_n \dot{R}_1 + \dot{a}_n R_b\right) (R_b)^{n+1}, \tag{B.29}$$

Therefore, the perturbation amplitude of interface $F^{(2)}$, a_n, can be written in terms of the perturbation amplitude of interface $F^{(1)}$, b_n.

B.3. Volume Change

The microbubble volume remains constant after the perturbation because

$$\begin{aligned} V &= \int_0^{2\pi}\int_0^{\pi}\int_0^{R+\varepsilon a_n Y_n^m} r^2 dr \sin\theta d\theta d\varphi \\ &= \frac{1}{3}\int_0^{2\pi}\int_0^{\pi}\left(R+\varepsilon a_n P_n^m e^{im\varphi}\right)^3 \sin\theta d\theta d\varphi \\ &= \frac{1}{3}\int_0^{2\pi}\int_0^{\pi}\left(R^3+3R^2\varepsilon a_n P_n^m e^{im\varphi}\right)\sin\theta d\theta d\varphi + O\left(\varepsilon^2\right) \\ &= \frac{4\pi R^3}{3} - 3R^2\varepsilon a_n \int_0^{2\pi} e^{im\varphi} d\varphi \int_0^{\pi} P_n^m(\cos\theta) d(\cos\theta) + O\left(\varepsilon^2\right), \end{aligned} \tag{B.30}$$

$$\int_0^{\pi} P_n^m(\cos\theta) d(\cos\theta) = 0. \tag{B.31}$$

Therefore, up to order ε, the perturbation's contribution to the microbubble's volume is zero.

APPENDIX C: MATCONT

After downloading the Matcont package, it is opened via MATLAB. The main menu of the package is:

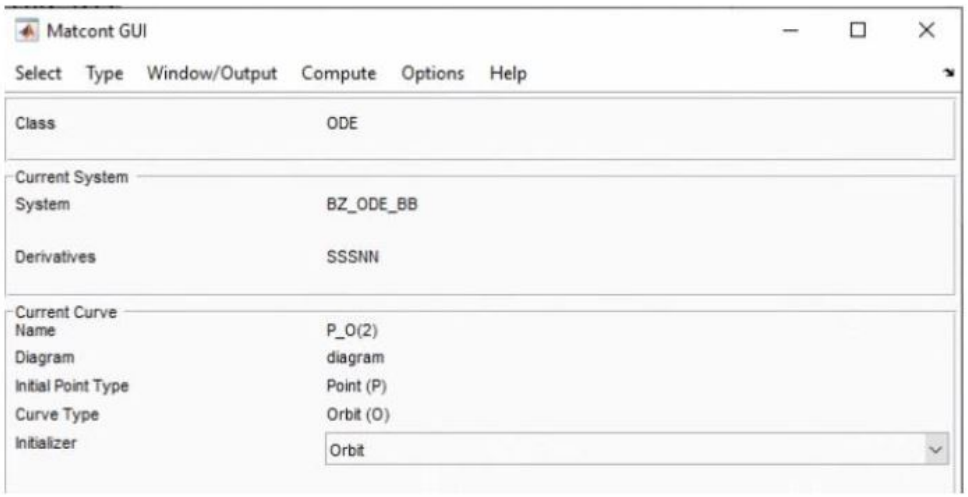

Figure C.1. The main menu of Matcont.

New system is created for coupled ODE equations.

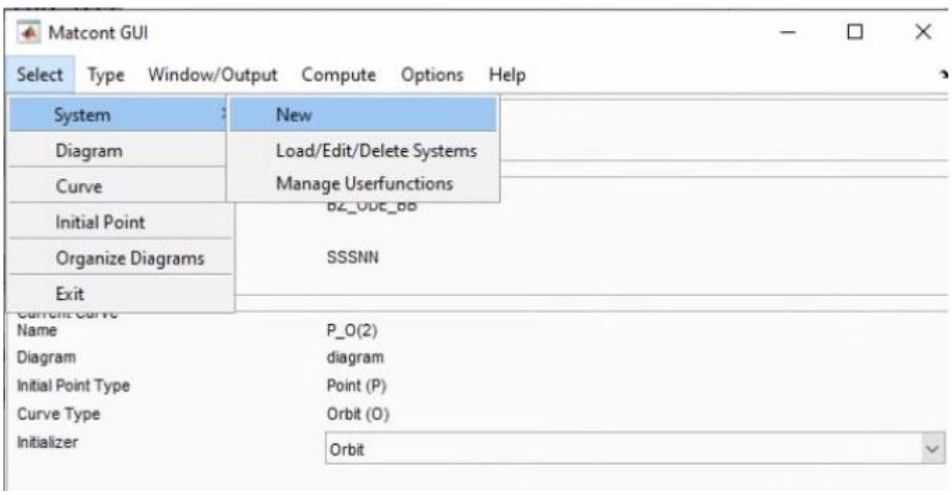

Figure C.2. System menu of Matcont.

Nonlinear differential equations are entered. Here, coordinates are dependent parameters.

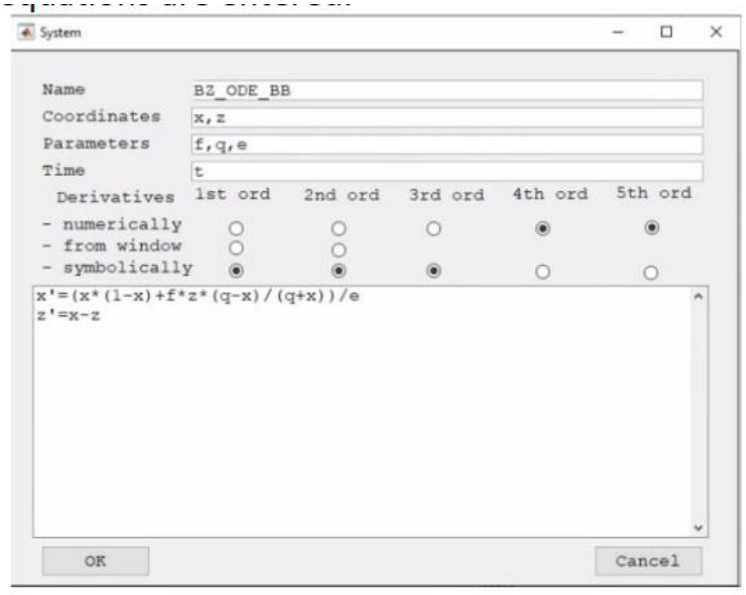

Figure C.3. Coupled equations.

The problem type is chosen as Initial point.

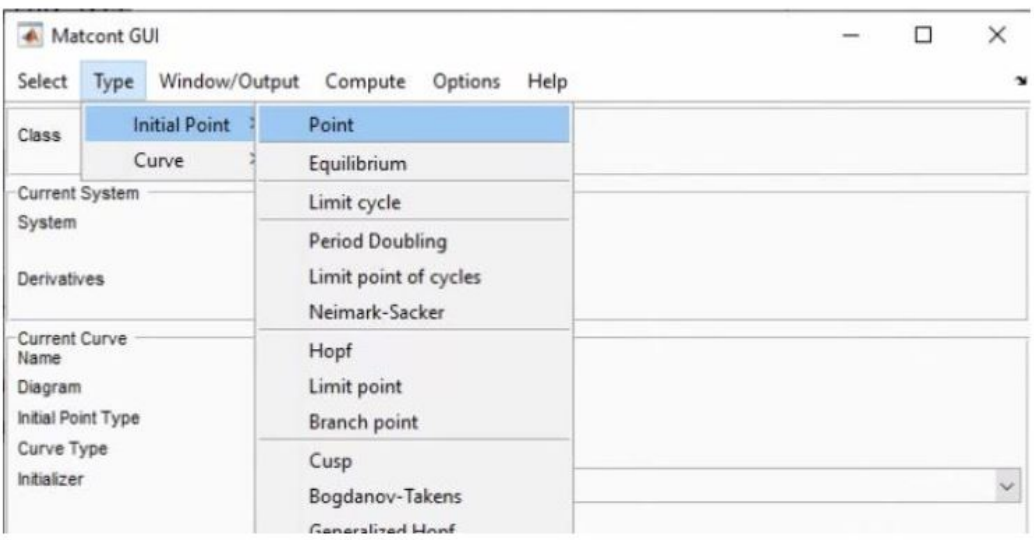

Figure C.4. Type menu of Matcont.

The initial point are set.

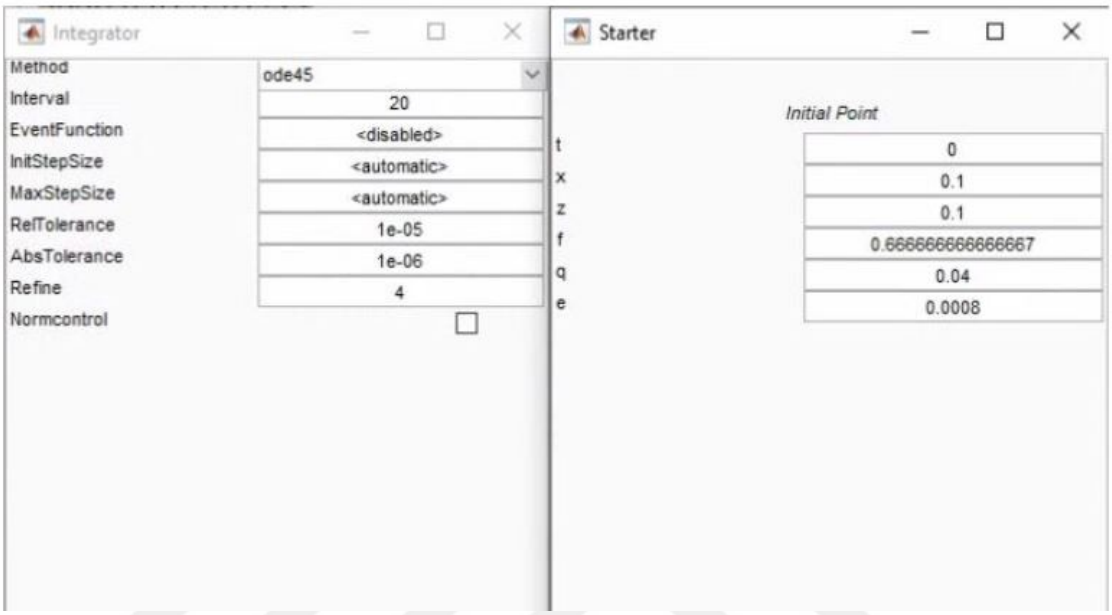

Figure C.5. Integrator.

The graphs are opened.

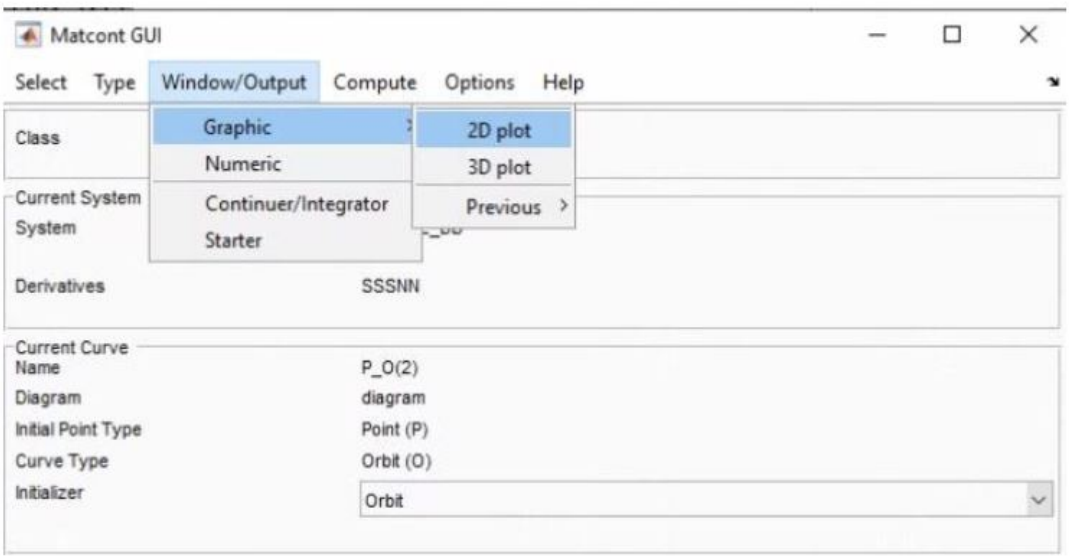

Figure C.6. Graphic menu of Matcont.

The system is computed forward.

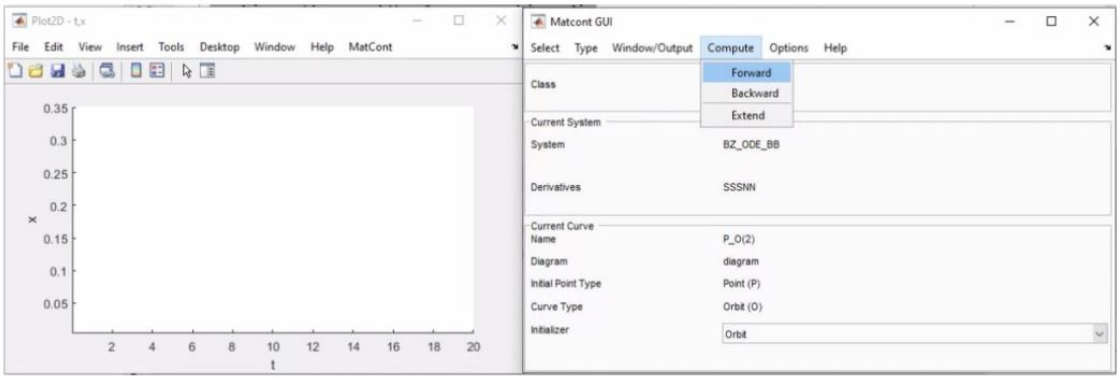

Figure C.7. Compute menu of Matcont.

APPENDIX D: AN EXAMPLE OF FLOQUET ANALYSIS

1.Rewrite the ODE as a first-order system.

2. Find the solution of the ODE over one period, and use it to construct the monodromy matrix. The monodromy matrix describes how the solution evolves over one period.

3. Find the eigenvalues of the monodromy matrix. These are known as the Floquet multipliers.

4. Use the Floquet multipliers to compute the Floquet exponents. The Floquet exponents are the logarithms of the Floquet multipliers, divided by the period of the ODE.

5. The eigenvalues of the Floquet matrix are given by the Floquet multipliers raised to the power of the period of the ODE.

Here's an example to illustrate the steps:

t Consider the following ODE with periodic coefficients:

$$y''(t) + (2 + cos(t))y(t) = 0. \tag{D.1}$$

We can rewrite this ODE as a first-order system by introducing a new variable $z(t) = y'(t)$. The resulting system is:

$$y'(t) = z(t), \tag{D.2}$$

and

$$z'(t) = -(2 + cos(t))y(t). \tag{D.3}$$

To find the eigenvalues using Floquet theory, we can follow the steps: Rewrite the system as a matrix equation:

$$y'(t) = A(t)y(t), \tag{D.4}$$

where $y(t) = [y(t), z(t)]'$, and $A(t)$ is the coefficient matrix:

$$A(t) = [0, 1; -(2 + cos(t)), 0]. \tag{D.5}$$

Find the solution of the system over one period, from t=0 to t=T, where $T = 2 * \pi$. We can use any numerical method to solve the system, such as ode45 in MATLAB. Let y_0 be the initial condition at t=0. We can use the solution at t=T to construct the monodromy matrix:

$$M = [y(T), z(T); z(T), -y(T)]. \tag{D.6}$$

Find the eigenvalues of the monodromy matrix M. These are the Floquet multipliers.

Compute the Floquet exponents by taking the logarithms of the Floquet multipliers, and dividing by the period T:

$$\lambda = log(eig(M))/T. \tag{D.7}$$

Finally, the eigenvalues of the Floquet matrix are given by:

$$exp(\lambda * T). \tag{D.8}$$

These are the eigenvalues we seek. Note that in practice, we would use a numerical method to solve the ODE and construct the monodromy matrix, and then use MATLAB's built-in functions eig and log to find the eigenvalues and Floquet exponents.

APPENDIX E: DIMENSIONLESS EQUATIONS

In this section, dimensionless equation are given for a bubble in an unbounded liquid. The time pressure and length scales are given as

$$t^\star = \sqrt{\frac{\rho R_{b0}^2}{p_0}}, \quad p^\star = p_0, \text{ and } R_b^\star = R_{b0}. \tag{E.1}$$

Dimensionless Rayleigh-Plesset equation is given as,

$$R\frac{d^2R}{dt^2} + \frac{3}{2}\left(\frac{dR}{dt}\right) = p_{g0}^\star \left(\frac{R_{b0}}{R}\right)^{3\kappa} - 1 - \frac{2We}{R} - \frac{4}{Re}\frac{dR}{dt}\frac{1}{R} - F_{acc}(t). \tag{E.2}$$

where the dimensionless numbers are given as,

$$Re = \frac{R_{b0}\sqrt{\Delta p \rho}}{\mu}, \quad We = \frac{R_{b0}\Delta p}{\sigma}, \quad p_{g0}^\star = \frac{p_{g0}}{\Delta p} \text{ and } \Delta p = p_\infty - p_v. \tag{E.3}$$

and the dimensionless external force is,

$$F_{acc}(t) = p_{g0}^\star(1 + A\cos(\omega t)). \tag{E.4}$$

APPENDIX F: EFFECT OF BUBBLE AREA TO VOLUME RATIO

Surface Area-Driven Loading; Drug loading capacity is proportional to the surface area of the bubble. Since the Area-to-Volume Ratio (AVR) is defined as:

$$\text{AVR} = \frac{\text{Surface Area}}{\text{Volume}}. \tag{F.1}$$

The drug loading capacity (C) can be related to AVR as:

$$C \propto \text{AVR} \times \text{Volume}. \tag{F.2}$$

Bubble Volume Dependence; Assuming the bubble volume is fixed, the drug loading capacity simplifies to:

$$C = k_1 \cdot \text{AVR}, \tag{F.3}$$

where k_1 is a proportionality constant.

Saturation Effects; In practice, drug loading capacity does not increase indefinitely with AVR because surface area binding sites become saturated at high AVR. This effect can be modeled using a saturation curve:

$$C = C_{\max} \cdot \left(1 - e^{-k_2 \cdot \text{AVR}}\right), \tag{F.4}$$

where, $C_{\max}$ is the maximum drug-loading capacity, and k_2 is the saturation rate constant.

Since drug diffusion rate depends on the amount of drug available on the bubble surface, it can be related to the loading capacity (C):

$$R_{\text{diff}} = k_d \cdot C, \tag{F.5}$$

where, k_d is drug release rate constant (s^{-1}) and C is the Drug loading capacity mg/bubble. If C follows a saturation model:

$$R_{\text{diff}} = k_d \cdot C_{\max} \cdot \left(1 - e^{-k_2 \cdot \text{AVR}}\right). \tag{F.6}$$

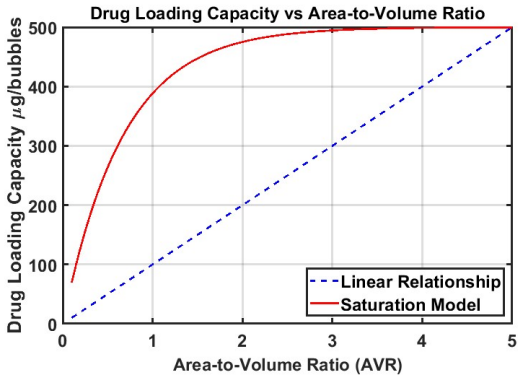

Figure F.1. Effect of area to volume ratio on drug loading capacity.

Drug Diffusion Rate:

$$R_{\text{diff}} = k_d \cdot C. \tag{F.7}$$

Fickian Diffusion-Based Rate:

$$R_{\text{diff}} = -D_0 \cdot \frac{\Delta C}{\Delta x} \cdot (\text{AVR} \cdot V). \tag{F.8}$$

These equations can be used in theoretical modeling or experimental data fitting for bubble-based drug delivery systems.

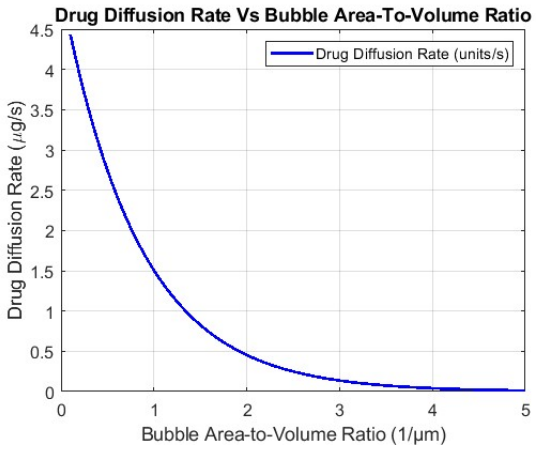

Figure F.2. Effect of area to volume ratio on drug diffusion rate.

APPENDIX G: FIGURE PERMISSIONS

Nov 11, 2024

This Agreement between Bogazici University ("You") and AIP Publishing ("AIP Publishing") consists of your license details and the terms and conditions provided by AIP Publishing and Copyright Clearance Center.

License Number	5905950579189
License date	Nov 11, 2024
Licensed Content Publisher	AIP Publishing
Licensed Content Publication	Biomicrofluidics
Licensed Content Title	The role of acoustofluidics and microbubble dynamics for therapeutic applications and drug delivery
Licensed Content Author	Kaykanat, S. I.; Uguz, A. K.
Licensed Content Date	Apr 10, 2023
Licensed Content Volume	17
Licensed Content Issue	2
Type of Use	Thesis/Dissertation
Requestor type	Author (original article)
Format	Print and electronic
Portion	Figure/Table

Figure G.1. Copyright permission for Figure 2.1.

Dec 12, 2024

This Agreement between Bogazici University ("You") and Elsevier ("Elsevier") consists of your license details and the terms and conditions provided by Elsevier and Copyright Clearance Center.

License Number

5906131150449

License date

Nov 11, 2024

Licensed Content Publisher

Elsevier

Licensed Content Publication

Cell

Licensed Content Title

Targeting Strategies for Tissue-Specific Drug Delivery

Licensed Content Author

Zongmin Zhao,Anvay Ukidve,Jayoung Kim,Samir Mitragotri

Licensed Content Date

Apr 2, 2020

Licensed Content Volume

181

Licensed Content Issue

1

Licensed Content Pages

17

Start Page

151

End Page

167

Type of Use

reuse in a thesis/dissertation

Figure G.2. Copyright permission for Figure 2.1 (page 2).

Portion

figures/tables/illustrations

Number of figures/tables/illustrations

1

Format

both print and electronic

Are you the author of this Elsevier article?

No

Will you be translating?

No

Title of new work

MICROBUBBLE DYNAMICS FOR DELIVERY OF NANOMEDICINE TO TUMORS

Institution name

Bogazici University

Expected presentation date

Nov 2024

Portions

Fig. 2

The Requesting Person / Organization to Appear on the License

Bogazici

Figure G.3. Copyright permission for Figure 2.2 (page 2).

ELSEVIER LICENSE
TERMS AND CONDITIONS

Dec 12, 2024

This Agreement between Bogazici University ("You") and Elsevier ("Elsevier") consists of your license details and the terms and conditions provided by Elsevier and Copyright Clearance Center.

License Number	5906140751817
License date	Nov 11, 2024
Licensed Content Publisher	Elsevier
Licensed Content Publication	Journal of Pharmaceutical Sciences
Licensed Content Title	Microbubbles as ultrasound triggered drug carriers
Licensed Content Author	Steliyan Tinkov,Raffi Bekeredjian,Gerhard Winter,Conrad Coester
Licensed Content Date	Jun 1, 2009
Licensed Content Volume	98
Licensed Content Issue	6
Licensed Content Pages	27
Start Page	1935
End Page	1961
Type of Use	reuse in a thesis/dissertation
Portion	figures/tables/illustrations
Number of figures/tables/illustrations	1
Format	both print and electronic
Are you the author of this Elsevier article?	No
Will you be translating?	No
Title of new work	MICROBUBBLE DYNAMICS FOR DELIVERY OF

Figure G.4. Copyright permission for Figure 2.6.

	NANOMEDICINE TO TUMORS
Institution name	Bogazici University
Expected presentation date	Nov 2024
Portions	Figure 1
The Requesting Person / Organization to Appear on the License	Bogazici University
Requestor Location	Mrs. Seymen Ilke Kaykanat Bogazici University, KB406,Bebek, 34342, Istanbul, Istanbul 34342 Turkey
Publisher Tax ID	GB 494 6272 12
Total	0.00 USD

Figure G.5. Copyright permission for Figure 2.6 (page 2).

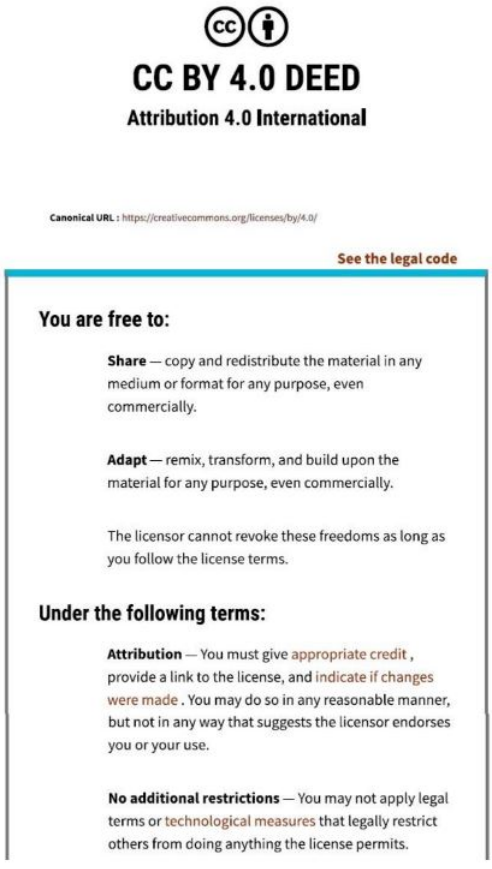

CC BY 4.0 DEED

Attribution 4.0 International

Canonical URL : https://creativecommons.org/licenses/by/4.0/

See the legal code

You are free to:

Share — copy and redistribute the material in any medium or format for any purpose, even commercially.

Adapt — remix, transform, and build upon the material for any purpose, even commercially.

The licensor cannot revoke these freedoms as long as you follow the license terms.

Under the following terms:

Attribution — You must give appropriate credit , provide a link to the license, and indicate if changes were made . You may do so in any reasonable manner, but not in any way that suggests the licensor endorses you or your use.

No additional restrictions — You may not apply legal terms or technological measures that legally restrict others from doing anything the license permits.

Figure G.6. Copyright permission for Figures 2.3, 2.4, 2.5, 2.7, 2.8, 4.18, 4.19, 4.20, 4.75, 4.76, 4.77.

AIP PUBLISHING LICENSE
TERMS AND CONDITIONS

Dec 12, 2024

This Agreement between Bogazici University ("You") and AIP Publishing ("AIP Publishing") consists of your license details and the terms and conditions provided by AIP Publishing and Copyright Clearance Center.

License Number	5926440608332
License date	Dec 12, 2024
Licensed Content Publisher	Acoustical Society of America
Licensed Content Publication	The Journal of the Acoustical Society of America
Licensed Content Title	Stability analysis of ultrasound thick-shell contras agents
Licensed Content Author	Lu, Xiaozhen; Chahine, Georges L.
Licensed Content Date	Jan 13, 2012
Licensed Content Volume	131
Licensed Content Issue	1
Type of Use	Thesis/Dissertation
Requestor type	Student
Format	Print and electronic
Portion	Figure/Table
Number of figures/tables	2
Will you be translating?	No
Title of new work	MICROBUBBLE DYNAMICS FOR DELIVERY OF NANOMEDICINE TO TUMORS
Institution name	Bogazici University
Expected presentation date	Dec 2024
Portions	Fig.2 and Fig.4

Figure G.7. Copyright permission for Figures 3.12 and 4.2.

The Requesting Person / Organization to Appear on the License	Bogazici University
Requestor Location	Mrs. Seymen Ilke Kaykanat Bogazici University, KB406,Bebek, 34342, Istanbul, Istanbul 34342 Turkey
Billing Type	Invoice
Billing Address	Mrs. Seymen Ilke Kaykanat Bogazici University, KB406,Bebek, 34342, Istanbul, Turkey 34342
Total	0.00 USD

Figure G.8. Copyright permission for Figure 3.12 and 4.2 (page 2).

AIP PUBLISHING LICENSE
TERMS AND CONDITIONS

Dec 12, 2024

This Agreement between Bogazici University ("You") and AIP Publishing ("AIP Publishing") consists of your license details and the terms and conditions provided by AIP Publishing and Copyright Clearance Center.

License Number	5926441469435
License date	Dec 12, 2024
Licensed Content Publisher	AIP Publishing
Licensed Content Publication	Physics of Fluids
Licensed Content Title	Surface stability of a bubble in a liquid fully confined by an elastic solid
Licensed Content Author	Liu, Yunqiao; Wang, Qianxi
Licensed Content Date	Dec 28, 2018
Licensed Content Volume	30
Licensed Content Issue	12
Type of Use	Thesis/Dissertation

Figure G.9. Copyright permission for Figure 4.1.

AIP PUBLISHING LICENSE
TERMS AND CONDITIONS

Nov 11, 2024

This Agreement between Bogazici University ("You") and AIP Publishing ("AIP Publishing") consists of your license details and the terms and conditions provided by AIP Publishing and Copyright Clearance Center.

License Number	5905950734043
License date	Nov 11, 2024
Licensed Content Publisher	AIP Publishing
Licensed Content Publication	Biomicrofluidics
Licensed Content Title	The role of acoustofluidics and microbubble dynamics for therapeutic applications and drug delivery
Licensed Content Author	Kaykanat, S. I.; Uguz, A. K.
Licensed Content Date	Apr 10, 2023
Licensed Content Volume	17
Licensed Content Issue	2
Type of Use	Thesis/Dissertation
Requestor type	Author (original article)
Format	Print and electronic
Portion	Figure/Table

Figure G.10. Copyright permission for Tables 2.1, 2.2, 2.3, 2.4, 2.5, 2.6, 2.7, 2.8.

Number of figures/tables	6
Will you be translating?	No
Title of new work	MICROBUBBLE DYNAMICS FOR DELIVERY OF NANOMEDICINE TO TUMORS
Institution name	Bogazici University
Expected presentation date	Nov 2024
Portions	Table 1, Table 2, Table 3, Table 4, Table 5, Table 6
The Requesting Person / Organization to Appear on the License	Bogazici University
Requestor Location	Mrs. Seymen Ilke Kaykanat Bogazici University, KB406,Bebek, 34342, Istanbul, Istanbul 34342 Turkey
Billing Type	Invoice
Billing Address	Mrs. Seymen Ilke Kaykanat Bogazici University, KB406,Bebek, 34342, Istanbul, Turkey 34342
Total	0.00 USD

Figure G.11. Copyright permission for Tables (page 2).

OHN WILEY AND SONS LICENSE
TERMS AND CONDITIONS

Dec 12, 2024

This Agreement between Bogazici University ("You") and John Wiley and Sons ("John Wiley and Sons") consists of your license details and the terms and conditions provided by John Wiley and Sons and Copyright Clearance Center.

License Number	5926520184983
License date	Dec 12, 2024
Licensed Content Publisher	John Wiley and Sons
Licensed Content Publication	Medical Physics
Licensed Content Title	Vaporization dynamics of volatile perfluorocarbon droplets: A theoretical model and in vitro validation
Licensed Content Author	Paul A. Dayton, Ayache Bouakaz, Paul S. Sheeran, et a
Licensed Content Date	Nov 30, 2016
Licensed Content Volume	41
Licensed Content Issue	10
Licensed Content Pages	10
Type of use	Dissertation/Thesis
Requestor type	University/Academic
Format	Print and electronic
Portion	Figure/table
Number of figures/tables	2
Will you be translating?	No
Title of new work	MICROBUBBLE DYNAMICS FOR DELIVERY OF NANOMEDICINE TO TUMORS
Institution name	Bogazici University
Expected presentation date	Dec 2024

Figure G.12. Copyright permission for Figure 4.3 and Table 4.4.

Portions	Figure 2, Table 1
The Requesting Person / Organization to Appear on the License	Bogazici University
Requestor Location	Mrs. Seymen Ilke Kaykanat Bogazici University, KB406,Bebek, 34342, Istanbul, Istanbul 34342 Turkey
Publisher Tax ID	EU826007151
Total	0.00 USD

Figure G.13. Copyright permission for Figure 4.3 and Table 4.4 (page 2).